Conceptual Design of a Lead-Bismuth Cooled Fast Reactor with In-Vessel Direct-Contact Steam Generation

by

Jacopo Buongiorno

B.A.Sc., Polytechnic of Milan, Milan (1996)

Submitted to the Department of Nuclear Engineering
in partial fulfillment of the requirements for the degrees of

DOCTOR OF PHILOSOPHY

at the

MASSACHUSETTS INSTITUTE OF TECHNOLOGY

February 2001

Signature of the Author:_______________________________
Department of Nuclear Engineering
September 26, 2000

Certified by:_______________________________
Prof. Neil E. Todreas
Thesis Supervisor

____
Prof. Mujid S. Kazimi
Thesis Supervisor

____
Prof. Kenneth R. Czerwinski
Thesis Supervisor

Accepted by:_______________________________
Prof. Sow-Hsin Chen
Chairman, Department Committee on Graduate Students

Conceptual Design of a Lead-Bismuth Cooled Fast Reactor with In-Vessel Direct-Contact Steam Generation

by

Jacopo Buongiorno

Submitted to the Department of Nuclear Engineering
in partial fulfillment of the requirements for the degrees of

DOCTOR OF PHILOSOPHY

MASSACHUSETTS INSTITUTE OF TECHNOLOGY, February 2001

Abstract

The feasibility of a lead-bismuth (Pb-Bi) cooled fast reactor that eliminates the need for steam generators and coolant pumps was explored. The working steam is generated by direct contact vaporization of water and liquid metal in the chimney above the core and then is sent to the turbine. The presence of a lighter fluid in the chimney drives the natural circulation of the Pb-Bi within the reactor pool. Three key technical issues were addressed: 1) the maximum thermal power removable by direct contact heat transfer without violating the fuel, clad and vessel temperature limits, 2) the consequences of Pb-Bi aerosol transport on the design and operation of the turbine and 3) the release of radioactive polonium (a product of coolant activation) to the steam.

Modeling of the multi-phase phenomena occurring in the chimney confirmed the effectiveness of the direct contact heat transfer mode within a well-defined design envelope for the reactor power, chimney height and steam superheat. A 1260MWth power is found possible for 10m chimney height and 25°C superheat. The temperature of the low-nickel steel clad is maintained below 600°C, which results in limited corrosion if tight control of the coolant oxygen concentration is adopted.

Generation, transport and deposition of Pb-Bi aerosols were also modeled. It was found that the design of a chevron steam separator reduces the heavy liquid metal in the steam lines by about three orders of magnitude. Nevertheless, the residual Pb-Bi is predicted to cause embrittlement of the turbine blades. Four solutions to this problem were assessed: blade coating, employment of alternative materials, electrostatic precipitation and oxidation of the Pb-Bi droplets.

An experimental campaign was conducted to investigate the polonium release from a hot Pb-Bi bath to a gas stream. The thermodynamics of the polonium hydride formation reaction (free-energy vs. temperature), as well as the vapor pressure of the lead-polonide were measured and then utilized to model the polonium transport in the reactor. It was found that the polonium concentration in the steam and on the surface of the power cycle components is significantly above the acceptable limits, which makes the very concept of a direct contact reactor open to question.

Thesis Supervisors: Neil E. Todreas, Mujid S. Kazimi, Kenneth R. Czerwinski

ACKNOWLEDGEMENTS

I would like to express my deepest gratitude and affection to the Fabulous Four (Neil Todreas, Mujid Kazimi, Michael Driscoll and Kenneth Czerwinski), the quartet of supervisors that guided my studies through the perilous waters of fast reactor technology. Their enthusiasm and competence have made participating in this project pleasant and intellectually rewarding.

I would like to thank the following MIT people for their key help on specific issues of my work: Jonathan Plaue for the development of the polonium electrodeposition methodology, Pavel Hejzlar for providing a core design to play with, Dohyoung Kim for the decay heat and fuel thermal conductivity calculations, Fred McWilliams of the Reactor RPO for trouble-shooting with the experimental apparatus, Deying Sun of the Campus RPO for the liquid scintillator measurements, Peter Stahle for his occasional but always accurate advice on the experimental apparatus. My office friends, Emanuele, Roberto, Rick, Tina and Yi for helping me out with computer related problems and creating a pleasant environment to work in.

A big 'Thank You' to the NED administrative staff (Paula, Amy, Mike… and earlier Sonia, Mary…) for being cooperative, supportive and making things easier when they could be terribly complicated.

Special thanks to my colleagues and friends of the Idaho National Lab reactor design group (Phil, Cliff, Kevan, Eric, Steve) for the financial support of this project and the opportunity to exchange many interesting ideas. Also, thanks to Ning Li of the Los Alamos National Lab, Ron Ballinger and Jeongyoun Lim for reviewing the chapter on materials corrosion.

Heartfelt thanks to all my teachers and professors from the past 23 years of studies to which this doctoral degree represents some sort of grand finale.

Needless to say, the biggest 'Thank You' of them all goes to my family: my sweet wife Hannele for her love, patience and comfort, my beloved mom Norma for teaching me the value of knowledge and education and my dog Max for providing much needed entertainment at the end of many hard days.

TABLE OF CONTENTS

LIST OF FIGURES

Chapter 1 Page

Chapter 2

Chapter 3

Chapter 4

Chapter 5

Chapter 6

Chapter 7

Chapter 8

Appendix A

Appendix C

Appendix D

Appendix F

Appendix G

Appendix I

LIST OF TABLES

Appendix G

Chapter 1

- INTRODUCTION TO HEAVY LIQUID METAL COOLANTS -

1.1 Lead-Bismuth Cooled Nuclear Systems

1.1.1 The Early Programs

While considerable design work has been done in the United States, Europe, and Japan on fast reactors, including actinide burners, it has mostly been done for sodium cooled reactors. A liquid metal fuel (U-Bi alloy) reactor cooled by Pb-Bi eutectic was considered in the United States and in the United Kingdom in the 1950s [Williams 1958, Frost 1958]. However, it was abandoned in favor of sodium cooling for two reasons: (1) lead bismuth coolant at the temperatures of interest can be very corrosive to structural materials; and (2) the doubling time of sodium cooled fast reactors can be significantly shorter than that of lead-bismuth cooled reactors as a result of the higher power density removable in sodium cooled cores due to the larger thermal conductivity of sodium. Whereas a short doubling time was considered an important performance characteristic in the 1950s, it is of little significance today, as we do not foresee a depletion of low cost uranium resources in the near future, and we have a significant inventory of actinides which can be burned in a fast reactor.

1.1.2 The Russian Experience

The Russians adopted Pb-Bi for use in their most advanced nuclear submarines, the so-called "Alpha" class submarines [Zrodnikov 1999]. The Russians have built and operated seven Pb-Bi reactors in submarines and two on-shore prototypes. More recently they have studied the design of a variety of lead and lead-bismuth reactors for electric power generation, some of which can operate with one core loading for many years and do not require any fuel reprocessing [Lopatkin 1999].

1.1.3 Current Research

Lead-bismuth cooled fast reactors with very long-lived cores have been investigated in Japan [Zaki 1995], in the US at the University of California at Berkeley [Greenspan 2000], at the

Argonne National Laboratory [Spencer 2000a], at the Idaho National Laboratory [Weaver 2000] and currently at MIT.

A lead-bismuth cooled, accelerator-driven, sub-critical actinide burner has been proposed by the Los Alamos National Laboratory for burning the actinides and long-life fission products from spent light water reactor fuel [LANL 1999b]. This design is based on a particle accelerator that supplies high energy protons colliding on a target to produce spallation neutrons that induce fission in the actinide loaded fuel of a subcritical core. The Los Alamos system has been labeled Accelerator-driven Transmutation of Waste (ATW). A similar system has also been proposed in Europe by the CERN laboratory [Rubbia 1994]. MIT and INEEL have more recently proposed a core design that achieves the same actinide burning capability of the ATW, but operates in a critical mode [Hejzlar 2000], hence eliminating the need for the accelerator. It is envisioned that this critical reactor could operate in concert with ATWs in a program to burn the plutonium and minor actinides inventory from the current generation of light water reactors. In this scheme the actinides would be fed to the core of the critical systems where they are burned (at lower cost) until the core reactivity does not allow to. The spent fuel of the critical systems would then be fed to the ATWs for deep burning of the residual actinides. It should also be noted that there exists a R&D synergy between the ATW and a critical system: they share similar coolant and fuel technologies with the result that either system can greatly benefit from improvements achieved for the other. A more detailed discussion is presented in **Appendix A**, that compares the accelerator-driven subcritical system and the critical reactor with regard to the actinide burning mission.

1.2 Liquid Metal Coolants for Nuclear Systems

1.2.1 General Characteristics

The choice of lead or lead alloys as coolants of a fast reactor offers enhanced safety and reliability [Spencer 2000b]. The advantages of heavy liquid metals over sodium (and more generally over light water) are related to the following material characteristics: higher atomic number; lower vapor pressure at operating temperatures; higher boiling temperature; and chemical inertness with air and water. The basic properties of Pb, Pb-Bi and sodium are compared in **Table 1.I**[1]. These properties lead to the following advantages for heavy metal coolant:

- harder neutron spectrum and, therefore, improved neutron economy, when burning actinides or converting fertile nuclides into fissile nuclides;
- better reflection properties, yielding high conversion ratios even without blankets;
- practical impossibility of creating a major void in the core by coolant overheating due to the high boiling temperature (1670°C for Pb-Bi versus 883°C for sodium);
- high solubility of the actinides in the coolant, which prevents re-criticality events upon core melting;
- possibility of eliminating the intermediate coolant loop, and reducing capital costs;
- simpler containment structure due to the impossibility of fires and explosions;
- better shielding against gamma-rays and energetic neutrons.

Table 1.I. Basic characteristics of liquid metal coolants.

Coolant	Mass #	Absorption Cross Section (mb)[2]	Melting Point (°C)	Boiling Point (°C)	Chemical Reactivity (with air and water)
Pb-Bi	~208	3.82	125	1670	Inert
Pb	207	2.75	327	1737	Inert
Na	23	2.35	98	883	Highly reactive

However, the use of Pb-Bi vs. sodium for cooling a fast reactor also presents several drawbacks in addition to the material compatibility problems already mentioned. These include:

- high material cost (see **Section 1.2.2**);
- higher melting temperature (327 and 125°C for Pb and Pb-Bi, respectively versus 98°C for sodium);

---

[1] The thermophysical properties of the Pb-Bi eutectic can be found in **Appendix B**. A useful collection of the main thermophysical properties of pure lead and sodium is reported in reference [Lyon 1952].

[2] All cross sections are averaged over the fission spectrum [BNL 2000]. Note that the absorption cross section is typically a decreasing function of neutron energy. Consequently, comparing different liquid metal coolants at the same neutron energy is not entirely correct, because heavy liquid metal coolants do not moderate neutrons and they produce a harder spectrum, which may result in smaller parasitic absorptions.

- for Pb-Bi only, production of the relatively long-lived α-emitter ^{210}Po by (n,γ) reaction on ^{209}Bi as opposed to the shorter-lived β-emitter ^{24}Na for sodium;
- high toxicity of lead;
- large static pressure on the bottom of the reactor vessel due to the high coolant density;
- increased seismic isolation requirements due to the high coolant density;
- larger pumping requirements, for a given core geometry.

1.2.2 Lead-Bismuth vs. Lead

Lead and lead-bismuth share very similar neutronic properties, as can be seen in **Table 1.I.** The chief advantage of using the Pb-Bi eutectic over pure lead is the considerably lower melting point, which greatly simplifies the design and operation of the whole plant because the likelihood of coolant freezing is reduced. The variation of the melting point of lead-bismuth alloys as a function of the relative fraction of lead and bismuth is best illustrated by means of the liquidus curve of **Figure 1.1.** It can be seen that at approximately 45%Pb-55%Bi, a eutectic mixture is formed whose melting point is about 125°C, well below the melting point of pure lead and pure bismuth.

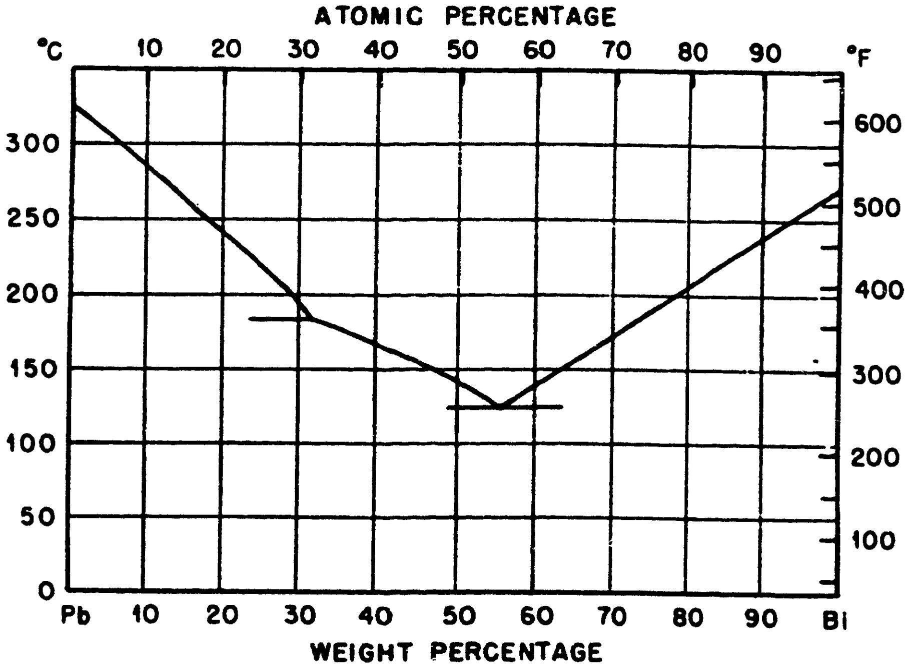

Figure 1.1. Liquidus curve for the lead-bismuth alloy (from [Lyon 1952]).

For a given operational temperature, the solubility of the main stainless steel components (particularly that of nickel) is lower in lead than in lead-bismuth as reported in **Table 1.II**, which makes pure lead potentially a less corrosive coolant [Weeks 1971]. However, note that, due to its higher melting point, a lead reactor might have to operate at higher temperatures, thus somewhat offsetting the solubility effect.

Table 1.II. Solubility of structural materials in Pb, Bi and Pb-Bi eutectic (from [Weeks 1971]).

Solute	T (°C)	Pb (ppm)	Pb-Bi (ppm)	Bi (ppm)
Cu	500	6.7	33	125
	700	3600	7200	14,800
Fe	500	0.8	2.3	15
	600	2.6	10	50
Cr	600	730	-	150
Ni	600	5370	-	66,000
Co	600	10.2	-	450
Ti	600	-	300	3,700
Zr	600	-	329	3,215

Production of radiologically hazardous activation products (e.g. ^{210}Po) is greatly reduced in pure lead. This mitigates the consequences of coolant spills or leakage and also improves the accessibility of the primary system components, hence easing maintenance. The reduction of coolant activation is of the greatest importance when a direct contact heat transfer reactor concept is considered, as is the case in the present study. In this type of reactor, the primary coolant system is not sealed. Steam is generated by vaporization of liquid water in the bulk of the hot liquid metal. As a result, there is no barrier to prevent the release of radioactive nuclides from the primary to the secondary coolant. However, it should be emphasized that realization of a direct contact reactor with pure lead presents rather serious challenges due once again to its much higher melting point. To prevent freezing, liquid water would have to be injected at temperatures above 327°C, which requires very high pressurization. On the other hand, if dry or superheated steam were to be used, it would have to be generated outside the reactor pool, which would considerably complicate the power cycle design.

Finally, because bismuth is a relatively costly and scarce material, the capital cost of a Pb-Bi alloy increases with the fraction of bismuth. It is important to estimate the magnitude of this increase and evaluate its impact on the cost of electricity. To do so, we make use of the following assumptions:

- Market cost of lead [USDI 1998]: ~ \$1/kg
- Market cost of bismuth [USDI 1998]: ~ \$7/kg
- Cost of Lead-Bismuth eutectics (55.2w% Bi, 44.8w% Pb): $C_{Pb\text{-}Bi}$ ~ \$4.3/kg
- Load factor (f): 0.85
- Coolant lifetime (N): 60yrs
- Marginal tax rate (τ): 30%
- After-tax averaged cost of capital (x): 8%
- Net salvage value of the coolant at the end of lifetime: \$0
- Linear depreciation schedule
- $m_{Pb\text{-}Bi}$ is the Pb-Bi mass per unit electric power (kg/kWe)

The capital cost of coolant, c_e, levelized over the plant lifetime can be then calculated as:

$$c_e = \frac{m_{Pb-Bi} C_{Pb-Bi}}{8.760 f} \Phi \qquad \textbf{Eq.1.1}$$

where c_e is in mills/kWh and Φ is the levelized annual capital carrying charge factor, calculated as follows:

$$\Phi = \frac{\left[(A/P,x,N) - \frac{\tau}{N} \right]}{1-\tau} \approx 10.8\% \qquad \textbf{Eq.1.2}$$

where $(A/P,x,N)$ is the so-called uniform-series capital recovery factor [Park 1990] defined as:

$$(A/P,x,N) = \frac{x(1+x)^N}{(1+x)^N - 1} \approx 8.1\% \qquad \textbf{Eq.1.3}$$

Figure 1.2 shows the value of c_e for pure lead and Pb-Bi eutectic as a function of $m_{Pb\text{-}Bi}$. For comparison, the capital cost of heavy water in a CANDU reactor and that of sodium in the Advanced Liquid Metal Reactor (ALMR) are also reported. These figures are based on a unit cost of heavy water and metallic sodium of $250/kg [Hejzlar 1994] and $0.4/kg [USDI 1998], respectively, that ignores the cost of their storage under proper conditions to avoid fires and/or contaminants. The coolant mass per unit power of the ALMR is taken from [GE 1991] and is equal to 1.5kg/kWe. The coolant mass per unit power of the reference PBWR configuration of **Figure 4.9** is about 8.6kg/kWe.

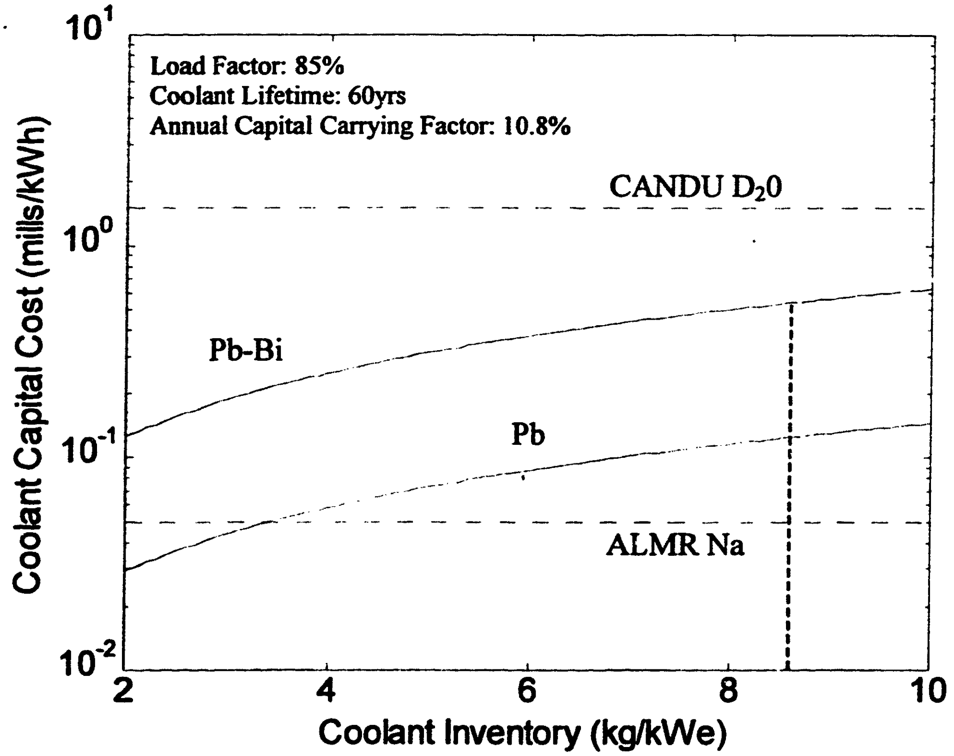

Figure 1.2. The capital cost of heavy liquid metal coolants.

It can be seen that the cost gap between lead and lead-bismuth can range up to 0.5mills/kWh. The cost of lead is comparable with that of the ALMR sodium whereas the cost of Pb-Bi is significantly above that of sodium for all values of the coolant inventory. On the other hand, both lead and lead-bismuth are economically preferable to the CANDU heavy water, whose production requires isotope separation. Although the cost difference between Pb and Pb-Bi is not negligible, it is felt that the overall simplification of the plant design and operation due to the considerably lower Pb-Bi melting point may more than compensate for the economic penalty associated with the higher coolant cost. Similarly, the compensation of Pb-Bi vs. Na by plant simplification may offset their cost difference.

1.2.3 Forced Circulation Performance

Liquid metal cooled fast reactors have mostly been designed to operate in forced circulation mode under normal steady-state conditions. Both mechanical and electromagnetic pumps were utilized to sustain the coolant flow through the core. Electromagnetic pumps display rather low efficiencies (between 40 and 50%), but they are generally thought to be very reliable because they do not have any rotating elements. On the other hand, mechanical pumps (e.g. centrifugal pumps) feature considerably higher efficiency (between 85 and 95%), but they have rotating parts. With the goal of emphasizing plant safety and reliability, the most recent Western sodium cooled fast reactor design, the GE S-Prism, adopts electromagnetic pumps as the preferred choice [Boardman 2000a].

Whether mechanical or electromagnetic pumps are utilized, it is always desirable to minimize the pumping power requirements, which has a beneficial effect on the capital as well as operational cost of the plant (i.e. reduction of the pump size and electric consumption, respectively). In this section a comparison will be made between Pb-Bi and Na in terms of pumping requirements and heat removal capability under forced circulation conditions. The selected figure of merit is the ratio of the fuel pin heat release rate, $\dot{q}$, to the pumping power required to remove that heat, W_p. It is assumed that the fuel pins of diameter D and active length L are arranged on a square lattice of pitch P and cell flow area A. The linear heat generation rate is q' and the coolant temperature rise across the core is ΔT. The friction coefficient is f.

The equations are:

Definition of pin power: $\dot{q} = q'L$ **Eq.1.4**

Energy conservation: $q'L = \rho V A c \Delta T$ **Eq.1.5**

Definition of pumping power: $W_p = VA\Delta P_{frict}$ **Eq.1.6**

Friction pressure drops: $\Delta P_{frict} = f\dfrac{L}{D_e}\dfrac{\rho V^2}{2}$ **Eq.1.7**

Friction coefficient: $f = \dfrac{0.184}{\left(\dfrac{\rho V D_e}{\mu}\right)^{0.2}}$ **Eq.1.8**

Definition of the hydraulic diameter D_e: $D_e = \dfrac{4A}{\pi D}$ **Eq.1.9**

Cell flow area: $A = P^2 - \frac{\pi}{4} D^2$ **Eq.1.10**

where V is the coolant velocity, ρ the coolant density, μ the viscosity and c its specific heat. Taking the ratio of **Eq.1.4** to **Eq.1.6**, eliminating V by means of **Eq.1.5, 1.7** and **1.8** and using **Eq.1.9** and **Eq.1.10** it can be readily demonstrated that:

$$\frac{\dot{q}}{W_p} = 14.5 \frac{\rho^2 c^{2.8}}{\mu^{0.2}} \frac{\Delta T^{2.8}}{q'^{1.8}} \frac{D^{4.8}\left[(P/D)^2 - \pi/4\right]^3}{L^{2.8}} \qquad \textbf{Eq.1.11}$$

To compare Pb-Bi and sodium, we shall now assume that the core geometry (i.e. L, D, P/D) is fixed. For simplicity, let us also assume that the same clad materials are used for both coolants. Further, the core outlet temperature and the temperature rise across the core are also fixed because in a liquid metal system the dissolution of the clad materials is driven by the maximum temperature and the coolant temperature rise. Finally, to simplify the comparison we shall also assume that the linear heat generation (and hence the pin power) is fixed. This enables clearly seeing what fluid requires more pumping power to remove a given heat load from a fuel pin. Under these circumstances, **Eq.1.11** shows that the $\frac{\dot{q}}{W_p}$ ratio is proportional to $\frac{\rho^2 c^{2.8}}{\mu^{0.2}}$ only. The value of $\frac{\rho^2 c^{2.8}}{\mu^{0.2}}$ does not significantly change with temperature and for Pb-Bi is typically about 4 times smaller than for sodium (see **Table 1.III**), resulting in larger pumping requirements for heavy liquid metal systems.

Table 1.III. Thermophysical properties groups for forced and natural circulation (at 400°C).

Liquid Metal	Forced Circulation, $\frac{\rho^2 c^{2.8}}{\mu^{0.2}}$ (normalized)	Natural Circulation, $\frac{\rho^{1.1} c \beta^{0.5}}{\mu^{0.1}}$ (normalized)
Pb-Bi	1.00	1.00
Na	4.19	1.05

However, neutronic considerations allow higher values of P/D in Pb-Bi than in sodium. Hence, if the fuel pin geometry (L and D) is kept fixed, while the pitch-to-diameter ratio P/D is allowed to change, the difference between Pb-Bi and sodium becomes less apparent. The $\frac{\dot{q}}{W_p}$ ratio is plotted (and normalized) in **Figure 1.3** as a function of P/D. It can be seen that, as already mentioned, sodium displays significantly better performance than Pb-Bi for a given P/D ratio. Nevertheless, the superior neutronic characteristics of lead-bismuth (i.e. higher atomic number) allow designing a core with a looser lattice (i.e. higher P/D). **Figure 1.3** indicates that, if for a sodium P/D ratio of 1.1 (as is the case in ALMR), a Pb-Bi P/D ratio of at least 1.21 is required to achieve a better heat removal to pumping power ratio[3]. Similarly, for a sodium P/D ratio of 1.2, the minimum required Pb-Bi P/D ratio is 1.36, and so forth.

In conclusion, due to the advantageous neutronic characteristics of Pb-Bi, the freedom to enlarge the P/D for Pb-Bi vs. Na yields effectively no difference between sodium and heavy liquid metals in terms of pumping power requirements.

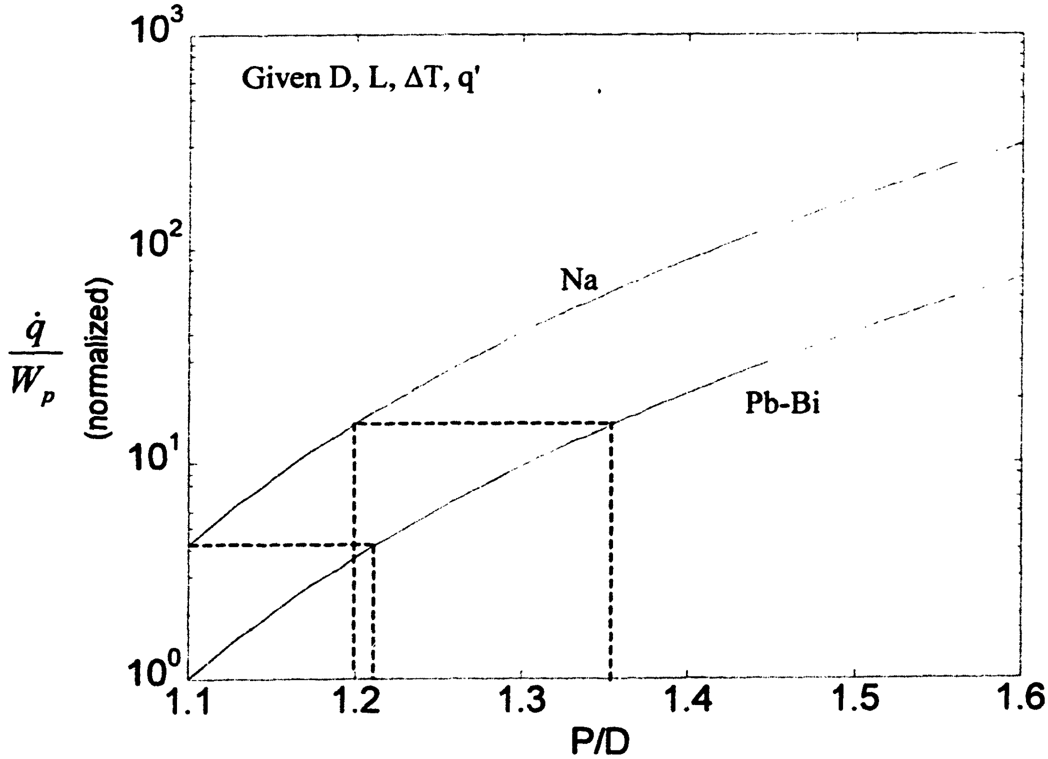

Figure 1.3. Forced circulation performance of Pb-Bi and sodium.

---

[3] Note that the reference core of this study has a P/D ratio equal to 1.2.

1.2.4 Natural Circulation Potential

In most sodium cooled fast reactors, natural circulation is relied upon only to remove the decay heat from the core in case of a loss of the external power forcing the pumps out of service. However, to simplify the primary system and make operation and maintenance less expensive, it would be desirable to remove the thermal power produced in the core exclusively by means of coolant natural circulation even under normal operating conditions. To achieve full power natural circulation, it is necessary to design the primary system to allow a substantial relative elevation (i.e. the so-called gravitational head) between the core and the heat sink. Also, friction and form pressure losses must be minimized everywhere in the primary system. Note that these requirements may be in conflict with the need to keep the size of the system within reasonable limits and with the neutronic constraints on the fuel lattice openness[4].

In this section the natural circulation potential of Pb-Bi and sodium is analyzed under the assumption that most pressure losses occur in the core. The figure of merit is the thermal power removable by natural circulation, $\dot{q}$. Again it is assumed that the fuel pins are arranged on a square lattice.

The equations are:

Loop momentum conservation: $\beta\rho\Delta TgH = f\frac{L}{D_e}\frac{\rho V^2}{2}$ **Eq.1.12**

Energy conservation: $\dot{q} = \rho VAc\Delta T$ **Eq.1.13**

where in addition to the nomenclature already introduced for the forced convection case, $\dot{m}$ is the coolant mass flow rate, g is the gravitational acceleration, β is the coolant thermal expansion coefficient and H is the gravitational head, i.e. the relative altitudes of the core and the heat sink (i.e. the steam generator or the heat exchanger if the secondary coolant is water or a gas, respectively).

Eliminating V from **Eq.1.12** and **1.13** (by means of **Eq.1.8**) and using **Eq.1.9** and **1.10**, the following expression can be readily obtained:

$$\dot{q} = 4.41\frac{\rho^{1.1}c\beta^{0.5}}{\mu^{0.1}}\left(g\Delta T\frac{H}{L}\right)^{0.56} D^{2.67}\left[(P/D)^2 - \pi/4\right]^{1.67} \quad \textbf{Eq.1.14}$$

---

[4] A lattice with very large pitch-to-diameter ratio may not be neutronically acceptable because it increases the capture in the coolant and worsens the void reactivity feedback.

Again we will assume that D, L and ΔT are fixed (see **Section 1.2.3**). Also H will be kept constant, while the P/D ratio will be varied. **Figure 1.4** illustrates the variation of $\dot{q}$ (normalized). For a given P/D ratio, there is a slight advantage for sodium as suggested by the natural circulation property group reported in **Table 1.III**. However, taking into account that a heavy liquid metal coolant allows designing a looser lattice than sodium, it can be seen that Pb-Bi could yield significantly better natural circulation performance.

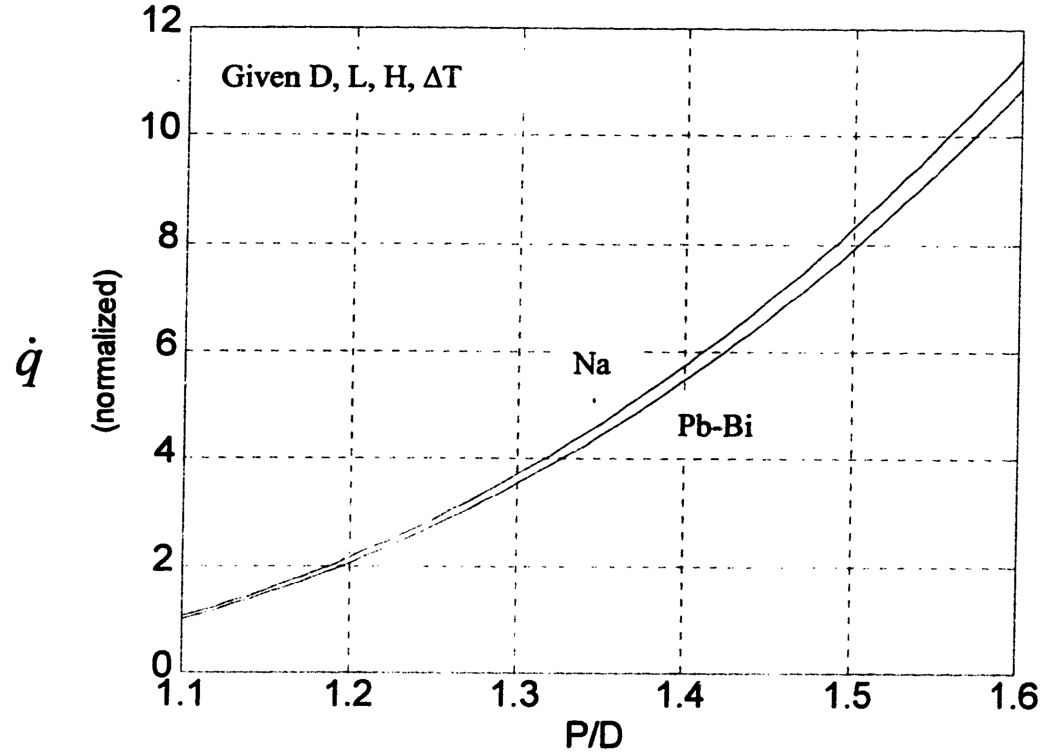

Figure 1.4. Natural circulation potential of Pb-Bi and sodium.

1.3 Motivation for a Direct Contact Heat Transfer Reactor

The analysis of the neutronic characteristics of a metallic fueled Pb-Bi cooled reactor shows that a tight lattice (P/D~1.2) is required to improve the neutronic safety and economics of the core. At low P/D ratios it is easier to design a core exhibiting a negative void reactivity coefficient [Hejzlar 2000]. Further, in a system whose main purpose is actinide burning, the actinide transmutation rate is enhanced as the P/D ratio decreases. A tight lattice is also beneficial in a breeding or high conversion reactor because it decreases the parasitic captures in the coolant and hardens the spectrum hence improving the neutron yield (i.e. the so-called η factor) of the fissile nuclides. Unfortunately, these improvements are achieved at the expense of the coolability of the core, particularly when the reactor operates in natural circulation mode. The thermal power removable by natural circulation is a strong increasing function of the P/D ratio, as can be seen from **Eq.1.14**. In previous studies conducted at MIT [Buongiorno 1999a and 1999b], a detailed analysis of the natural circulation performance of a pool-type Pb-Bi cooled reactor was undertaken. It was demonstrated that significant core power densities (up to 200kW/liter) can be removed in natural circulation even at reasonable gravitational heads (H~10m) if the reactor core (where most pressure losses occur) has a lattice of relatively large pitch-to-diameter ratio (P/D>1.3). However, at smaller pitch-to-diameter ratios, full power natural circulation requires (i) a large gravitational head (H>20m) and/or (ii) a large diameter (>5m) core to increase the flow area and thus decrease the hydraulic resistance to the flow. In both cases the overall size of the reactor and the bismuth inventory increase, which negatively affects the reactor economic acceptability. On the other hand, if a lighter fluid (e.g. helium or steam) is mixed with the Pb-Bi in the region above the core and then separated at the top of the reactor pool, a large driving density difference can be attained that enables full power natural circulation even in very tight fuel lattices (P/D≤1.2). This is essentially a gas-assisted pump and has been proposed for the reactor pool of the European ATW [Cinotti 1997].

In this thesis work an innovative Pb-Bi cooled critical reactor is explored that achieves full power natural circulation by injecting liquid water into Pb-Bi. Direct contact heat transfer between the two fluids occurs, which causes water vaporization and hence the creation of voids that drive the Pb-Bi natural circulation. The steam so generated operates a direct Rankine cycle. Because it eliminates the coolant pumps and the steam generators, this reactor offers significant potential for economic improvement and plant simplification.

1.4 Thesis Structure

A description of the core, vessel and the general characteristics of the system are given in **Chapter 2**. Direct contact heat transfer phenomena and their stability, as well as heavy liquid metal/steam two-phase flow, are discussed in **Chapter 3**. The objective is to establish the relationship between the fundamental thermal-hydraulic variables (e.g. Pb-Bi and water temperature and mass flux) and the chimney length required to obtain complete water vaporization or a desired degree of steam superheat.

The thermal-hydraulic analysis of the primary system, which enables selection of the reactor thermal power and yields the temperature distribution in the core and in the reactor pool, is presented in **Chapter 4**, where the Decay Heat Removal System (DHRS) is also discussed. The time-dependent response of the PBWR primary system to anticipated transients as well as a dynamic stability analysis are also presented in **Chapter 4**.

In **Chapter 5** the rate of heavy liquid metal aerosol carry-over from the surface of the reactor pool is evaluated. A steam dryer design is selected and its performance is estimated. The transport of the heavy metal aerosols through the steam lines is also discussed as are the consequences of liquid metal carry-over on the operation and design of the turbine.

Special attention is given to the issue of coolant activation due to the α-emitter ^{210}Po. The problem is first framed theoretically (**Chapter 6**) and then the results of an experimental campaign conducted by the author at MIT are presented (**Chapter 7**).

A brief discussion of the materials corrosion issue and a strategy for oxygen control in the PBWR are presented in **Chapter 8**. Finally, a summary of conclusions and recommendations for future work are provided in **Chapter 9**.

Chapter 2

- THE PB-BI DIRECT CONTACT HEAT TRANSFER REACTOR (PBWR) -

2.1 General Description of the Plant and Main Features

A schematic of the explored concept is illustrated in **Figure 2.1**. The primary coolant is lead-bismuth eutectic, which flows through the core and removes the heat generated by fission in the fuel. Slightly subcooled water is injected into the hot primary coolant above the core. The direct contact heat transfer between the fluids causes water to rapidly vaporize leading to the formation of steam bubbles in the reactor chimney. The large density difference between the chimney and the downcomer provides the pressure head that drives the natural circulation of Pb-Bi in the vessel[1]. The reactor chimney is partitioned into square channels (one per fuel assembly) to prevent radial drifting of the steam bubbles and maintain a uniform steam distribution. At the pool free surface, steam and Pb-Bi are separated by gravity and most residual liquid metal aerosols are collected in the steam dryer. Then the steam is sent to the turbine and operates a Rankine cycle analogous to a BWR that can achieve thermal efficiencies above 32%. However, contrary to BWRs, this design offers the possibility to superheat the steam and achieve even larger thermal efficiencies.

The primary system is pressurized at a reference pressure of 7.0MPa to take full advantage of BWR experience. In terms of height, diameter and thickness, the required vessel is within the design envelope of advanced BWR concepts [Rao 1999]. If it is designed to operate at relatively low temperatures, the vessel can be constructed with conventional austenitic stainless steels, which are known to be compatible with Pb-Bi at temperatures up to 450°C [Weeks 1971]. On the other hand, special ferritic/martensitic stainless steels ought to be used, if the vessel is to operate at higher temperatures.

The main features of this Pb-Bi/Water direct contact heat transfer reactor (designated PBWR from this point forward) are:

1) elimination of the primary coolant pumps,

---

[1] Note that gas assisted pumping of Pb-Bi in a ATW system was also proposed in reference [Cinotti 1997], although that concept retains the use of steam generators.

2) elimination of the heat exchangers due to direct water vaporization in the bulk of the primary coolant,
3) achievement of primary coolant full power natural circulation in a relatively short reactor pool, due to the large natural draft generated in the chimney by the steam bubbles,
4) achievement of high Pb-Bi velocity in the core (over 3m/s), which enables maintaining the fuel and clad temperature with beneficial effects on the fuel reliability and performance.

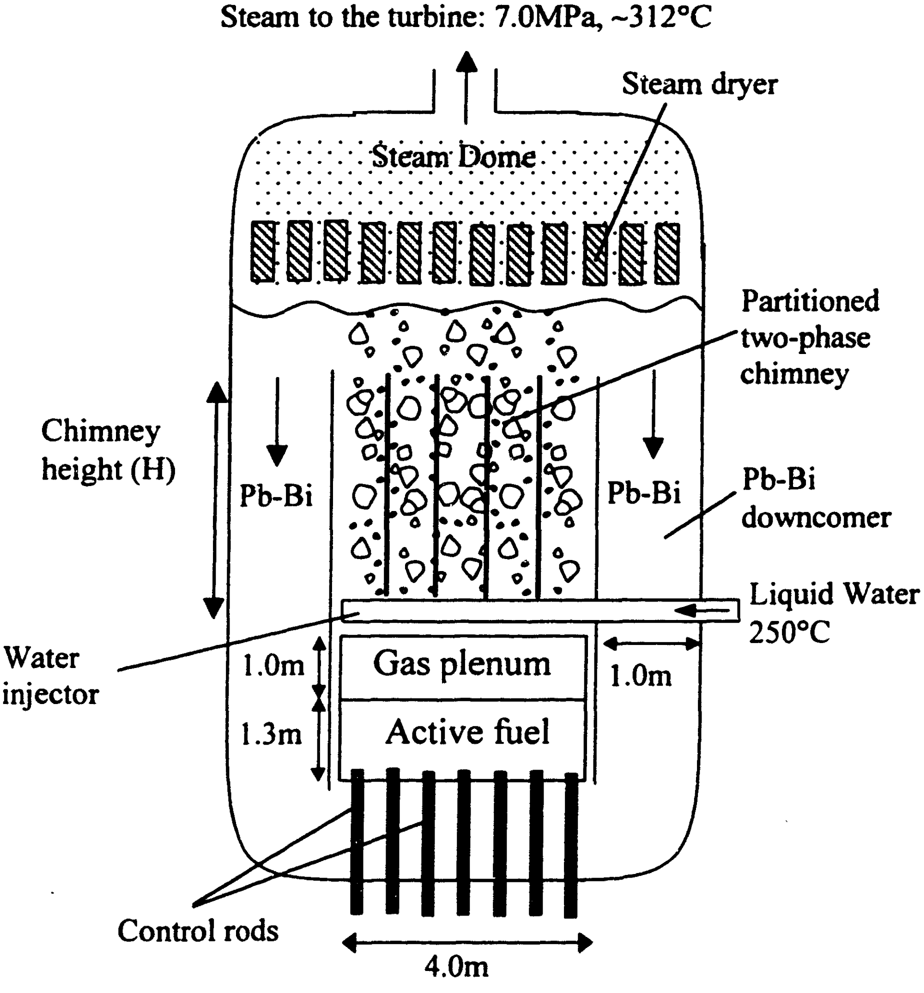

Figure 2.1. Schematic of the PBWR.

The presence of a steam/Pb-Bi two-phase mixture in the reactor chimney does not degrade the core neutronic economy and safety. Monte Carlo simulations show that the neutron reactivity is not appreciably affected by the variation of density in the two-phase chimney (see **Figure 2.2**).

This is because neutron reflection above the core is mostly due to the Pb-Bi flowing in the gas plenum region, which is relatively long[2] hence acting as neutron insulation between the core and the chimney.

This result has two major consequences:

1) This reactor concept does not require an increase of the fissile load in the fuel, since it does not increase neutron leakage.
2) The coupling of the chimney thermal-hydraulics and the core neutronics is very weak, which reduces the concern regarding coupled two-phase flow and neutronic instabilities. With respect to a traditional BWR, this significantly simplifies the design and operation of the reactor.

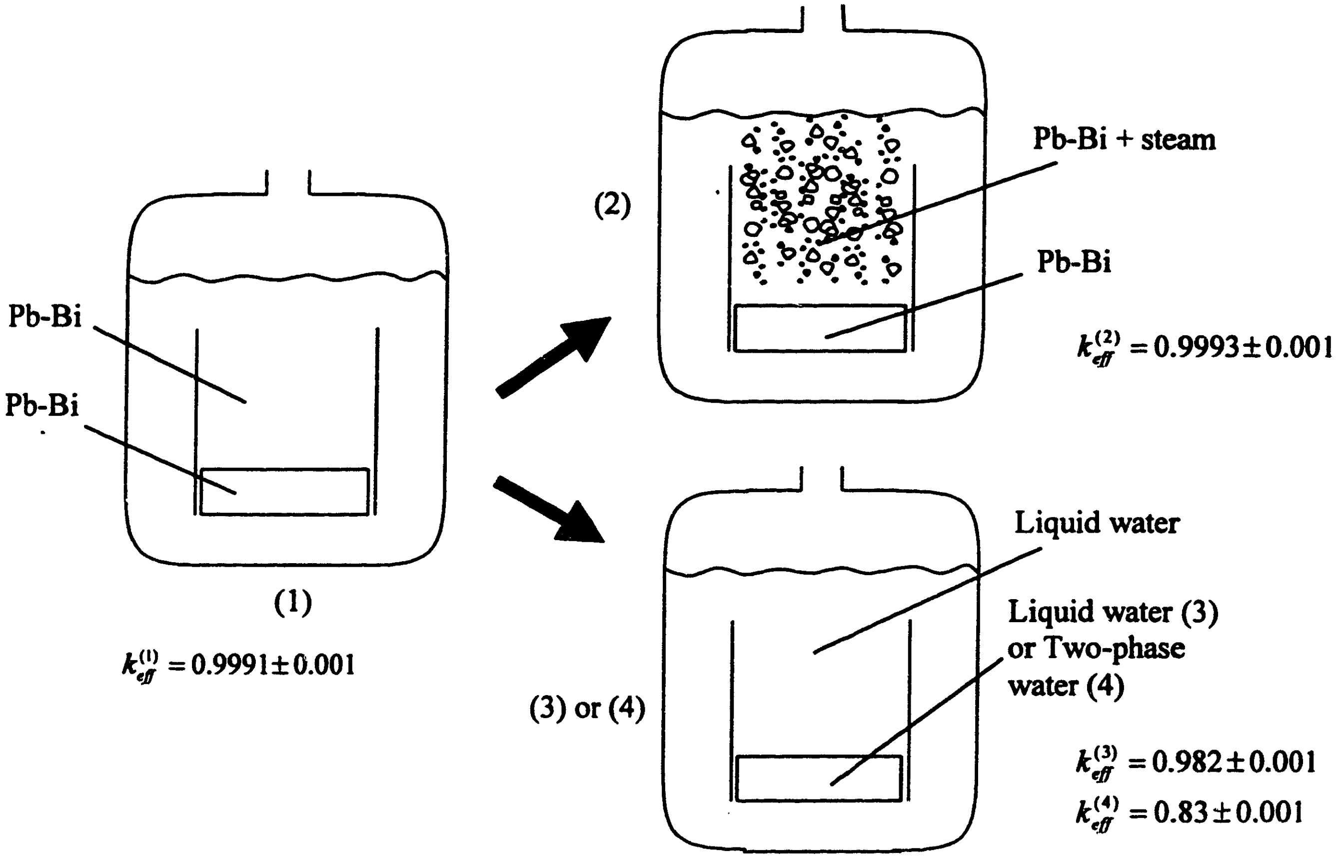

Figure 2.2. Effect of the chimney thermal-hydraulic conditions on the neutron reactivity.

---

[2] For a detailed description of the core and its neutronic characteristics see **Section 2.2.**

Monte Carlo simulations also indicate that accidental flooding of the core with water (as may be the case if the Pb-Bi primary coolant is drained from the core as a result of a vessel rupture) causes reactivity to decrease (see **Figure 2.2**) because, upon spectrum softening, (i) the parasitic captures in the fuel sharply increase and (ii) the fission cross section of non-fissile isotopes (e.g. ^{237}Np in an actinide burning core) decreases. These effects compensate for the fission cross section increase of the fissile isotopes (e.g. ^{235}U and ^{239}Pu) due to spectrum softening. However, note that a fully thermalized spectrum is not achieved in this core even upon water flooding, because the tight lattice prevents effective moderation of the neutron.

Because the Pb-Bi coolant needs to be maintained above its freezing point (125°C) and because is activated with the relatively long-lived alpha-emitter ^{210}Po, it is not feasible to remove the reactor vessel head and refuel the core while the primary coolant is in place. However, it is possible to depressurize the system, drain the Pb-Bi coolant out of the reactor vessel and replace it with liquid water to provide fuel cooling and radiation shielding during the refueling operation, which would then closely resemble that of a BWR where the fuel assemblies are shuffled and/or removed underwater. This would also allow visual inspection of the core and vessel internals during refueling. When collected in a drain tank, the Pb-Bi coolant could be maintained liquid by the decay heat of the polonium purification system (see **Section 6.5.2**) or by dedicated heaters, and pumped back into the reactor vessel after refueling operation. The chemical compatibility of Pb-Bi and water makes coolant switching a rather straightforward operation. It is important to emphasize again that flooding the core with liquid water does not raise a reactivity concern.

2.2 The Core

In this section we illustrate the essential geometric and neutronic characteristics of the Pb-Bi cooled core for actinide burning that is adopted in the present study. However, note that the concept of a reactor based on Pb-Bi/water direct contact heat transfer is not restricted to an actinide burning core and can be applied to cores with other missions such as fuel breeding or high conversion long cycle operation. For a more comprehensive and detailed description of the reference core, the reader is encouraged to consult reference [Hejzlar 2000], from which most information presented here is extracted.

2.2.1 Actinide Burning in Pb-Bi Cooled Reactors: the Neutronic Challenges

To burn actinides from LWR spent fuel in a dedicated fast spectrum nuclear system, it is desirable (1) to maximize actinide fission, hence minimize the conversion ratio in order to prevent production of higher transuranics and (2) to make a large surplus of neutrons available for the incineration. The first requirement can be fulfilled by non-fertile fuels, i.e. fuels whose matrix does not consist of fertile isotopes, such as ^{238}U or ^{232}Th, which would allow buildup of higher actinides through neutron capture. The second desirable characteristic can be achieved in fuels with low absorption rate. For this purpose a metal, fertile-free fuel has been selected, which consists of a metallic alloy of zirconium, plutonium and Minor Actinides (MA).

Metal fuels with a zirconium matrix provide a good neutron economy due to the low absorption rate in zirconium and due to the hard spectrum achievable in the absence of any strongly moderating isotopes. However, the employment of this type of fuel raises four key neutronic issues:

1) Large positive coolant void reactivity coefficient. The sign and magnitude of the coolant void coefficient is typically the result of the relative importance of three effects occurring upon coolant voiding: the leakage effect, the capture effect and the spectrum effect. When coolant voids:
   a) the neutron leakage increases,
   b) the parasitic capture in the coolant decreases,
   c) the spectrum hardens resulting in a larger fission-to-capture ratio.

   Effects b) and c) normally prevail over effect a) and the net outcome is a reactivity increase unless leakage is greatly enhanced.
2) Small Doppler effect. The amount of fertile isotopes in the metallic fuel is very small (mostly ^{240}Pu). Moreover, the hard spectrum of the metal-fuel lattice leads to a decrease of absorption rate in the resonance region. Both of these factors result in a very significant drop in the Doppler feedback.
3) Large rate of reactivity loss with burnup. The absence of fertile isotopes results in a faster net depletion of the fissile material and hence faster decrease of reactivity with burnup. As a consequence, if an acceptably long irradiation cycle is to be achieved, the reactivity excess at BOL must be large, which makes these systems more exposed to accidents involving malfunctions of control rod mechanisms.

4) Small delayed neutron fraction. Plutonium and the minor actinides display very small delayed neutron fraction (~0.002) which makes the control of this reactor somewhat more challenging than a LWR.

2.2.2 The Core Geometry

Of the above neutronic issues, the reactivity feedback upon coolant voiding is the most challenging. Most strategies to reduce the coolant void coefficient in fast reactors are based on increasing the leakage effect. If only the central region of the core is voided, this approach generally does not work, because leakage from the core center is prevented by the coolant that remains on the core periphery. Therefore, the design of a streaming Fuel Assembly (FA) that allows leakage of neutrons in both radial and axial directions directly from the center of the core was developed in [Hejzlar 2000] and adopted here. The arrangement of the streaming FA with its Control Rods (CRD) is shown in **Figure 2.3** and its characteristics are reported in **Table 2.I**.

The assembly contains 21×21 positions with 240 fuel rods, 152 square streaming tubes arranged in two rows at the FA periphery and 7×7 positions in the FA center. The streaming tubes are filled with gas and sealed. In addition to their neutron streaming function, they also provide structural support. In case of failure of a streaming tube, the tube will be flooded with coolant leading to a very small reactivity increase. To achieve a significant reactivity change in such a scenario, a large number of these tubes would have to be flooded. Widespread void flooding is thus extremely unlikely. The thickness of the walls of the square tubes was taken the same as that of cladding, i.e. 0.63mm. The central region of each FA contains a 5×5 void space to enhance neutron streaming. Two grids (in the bottom and top regions of the assembly) and a honeycomb spacer (at the assembly midplane) ensure proper separation of the fuel pins.

Table 2.I. Design parameters of the PBWR core.

Design parameter	Value
Fuel pellet OD	8.64mm
Fuel composition (Pu+MA)/Zr (wt%)	23/77* inner batch, 29/71 outer batch
Gap thickness (lead bond)	0.2mm
Cladding thickness	0.63mm
Pin outer diameter (clad outer)	10.3mm
Pitch	12.55mm
P/D	1.2
Heated core length	1.3m
Gas plenum height	1.0m**
Number of fuel pin spacers	3
Number of fuel assemblies (FA)	157
Number of positions in FA	21×21
Number of fuel rods per FA	240 (17×17 array)
Number of CRD fingers per FA	24
Number of void positions in FA center	5×5
Number of void positions in FA periphery	152
CRD material	B_4C and BW (90% ^{10}B)
Equivalent core diameter	3.73m
Core barrel thickness	2cm

* In the initial core, the outer core region contains 29wt% TRU-enriched fuel; the inner core region is loaded with 23wt% TRU-enriched fuel.

** The plenum accommodates the gaseous fission products. The length of the plenum relative to the fuel pin was selected on the basis of the Integral Fast Reactor (IFR) metallic fuel experience and set equal to 80% of the active fuel length. Detailed calculations of fission gas release were not performed for this metallic fuel.

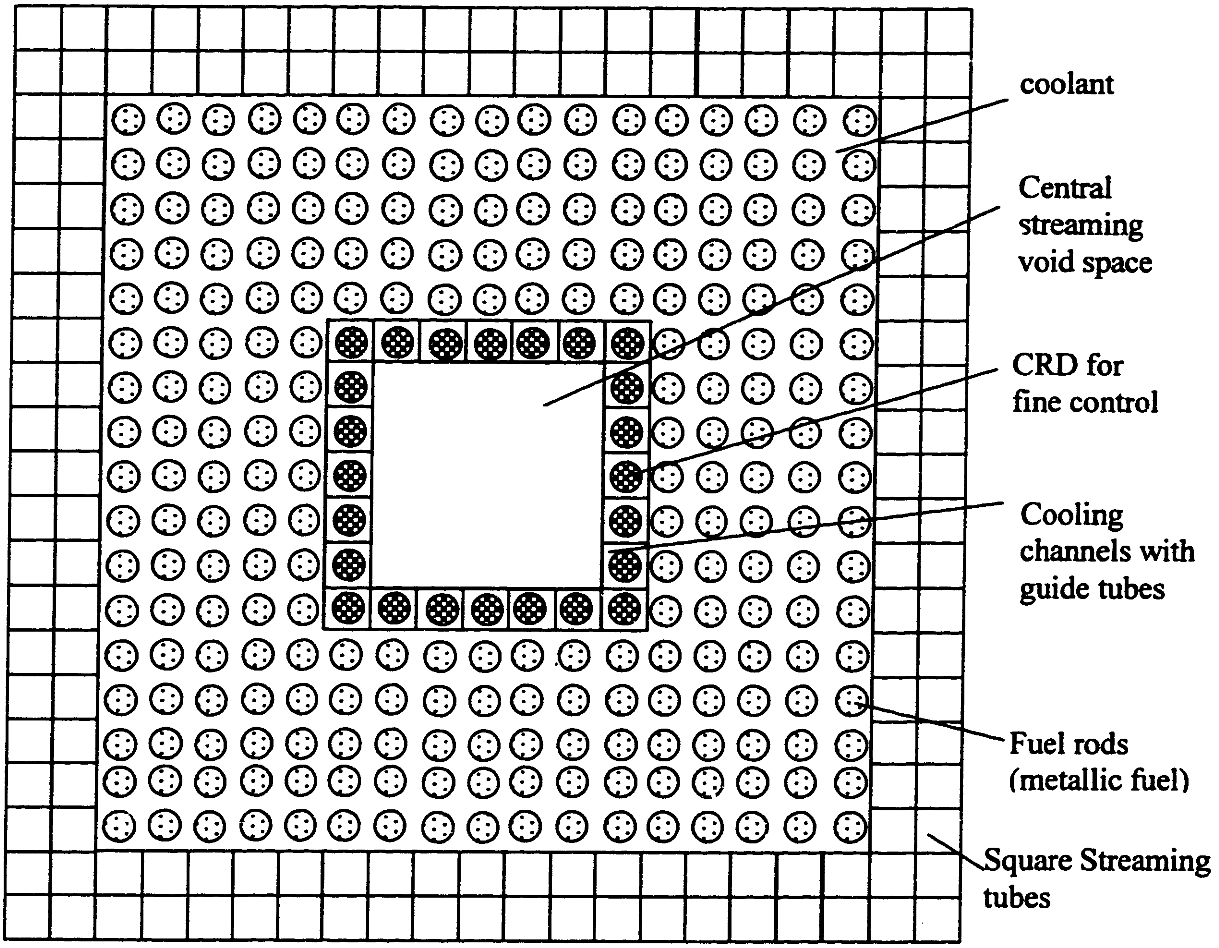

Figure 2.3. The streaming fuel assembly (from [Hejzlar 2000]).

In each FA there are four types of subchannels (see **Figure 2.4**), whose geometric characteristics are reported in **Table 2.II**.

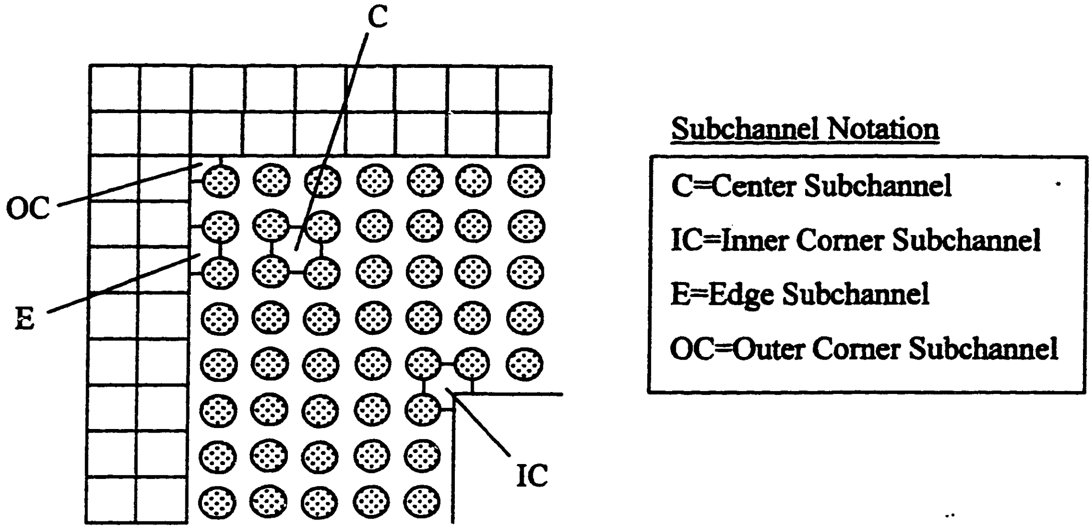

Figure 2.4. The subchannels of the streaming FA.

Table 2.II. Subchannel geometric characteristics.

Subchannel	Subchannels per assembly	Flow Area (cm^2)	Wetted Perimeter (mm)	Equivalent Hydraulic Diameter (mm)
C	192	0.694	32.4	8.6
IC	4	0.520	36.6	5.7
E	100	0.347	28.5	4.9
OC	4	0.173	20.4	3.4

There are 157 FAs with two different Pu+MA loadings to optimize the fuel cycle. The core equivalent diameter is about 3.7m, as illustrated in **Figure 2.5**. To minimize the axial power peaking, two sets of CRDs are provided inserting from the top and from the bottom of the core (see **Section 2.5**).

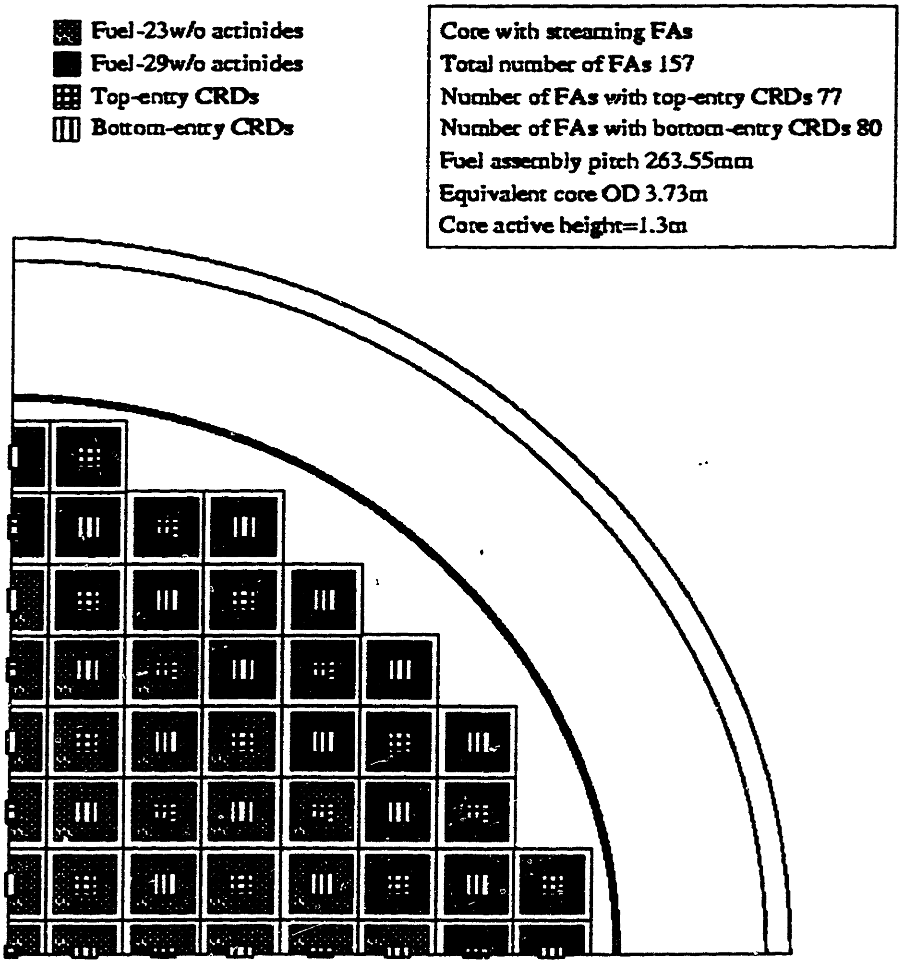

Core with streaming FAs
Total number of FAs 157
Number of FAs with top-entry CRDs 77
Number of FAs with bottom-entry CRDs 80
Fuel assembly pitch 263.55mm
Equivalent core OD 3.73m
Core active height=1.3m

Core with streaming fuel assemblies and double-entry CRDs
scale = 1/20 real scale

Figure 2.5. The PBWR core (from [Hejzlar 2000]).

2.2.3 The Fuel

Metallic alloys of zirconium, uranium and plutonium have been the subject of extended studies at Argonne National Laboratory (ANL) and demonstrated to perform extremely well in irradiation tests [Pitner 1993] and in overpower transients [Tsai 1994]. Good experience exists up to a burnup of 100MWD/kg. To maximize breeding, the continuum phase of the ANL fuels was always a heavy metal (e.g. uranium). On the other hand, because the mission of the metallic fuel of the PBWR is to burn the actinides, it is not desirable to have uranium or other fertile materials in the fuel, and thus zirconium is the continuum phase while the actinides (Pu+MA) are the dispersed component. Note that a larger fraction of Zr is beneficial since it provides more diluent material for the retention of fission products, allowing a significant increase in discharge burnup. The specific properties of this type of fuel involve a relatively tall gas plenum above the fuel pin (to accommodate the large release of fission gases due to the high burnup) and a large gap between the fuel pellet and cladding to allow for fuel swelling at high burnup. The ANL experience leads to a preferred smear density of 75 to 80%. The gap is filled with bonding material (i.e liquid lead) to enhance the thermal conductivity of the gap and thus to maintain acceptable fuel temperatures.

In the PBWR core there are two-fuel batches with two different Pu+MA contents, 23 and 29wt%, respectively. The relative isotopic composition of the higher actinides (as per the spent fuel of a typical LWR) is reported in **Table 2.III.**

Table 2.III. Higher actinides from LWR spent fuel.

Isotope	Weight percent
Pu composition	**100%=80% total**
Pu238	2%
Pu239	58%
Pu240	26%
Pu241	10%
Pu242	4%
MA composition	**100%=20% total**
Np237	43%
Am241	45%
Am242	0%
Am243	9%
Cm244	3%

2.2.3.1 Neutronic Performance

The main neutronic characteristics of the PBWR actinide burning reference core at BOL are summarized in **Table 2.IV**. It can be seen that the streaming assembly concept enables achieving a negative neutron reactivity feedback upon voiding of the whole core (core-average coolant density = $0 g/cm^3$) as well as upon local voiding of the central or peripheral assemblies.

The presence of the resonance absorber ^{240}Pu provides a (small) negative Doppler reactivity coefficient. The reactivity response to fuel temperature increase is enhanced by the negative fuel thermal expansion coefficient. Although the excess reactivity at BOL is very large and the delayed neutron fraction is relatively small, the worth of any single control rod is not sufficient to cause prompt criticality upon complete ejection.

Table 2.IV. Reactivity performance of the PBWR core at BOL[3].

Description	
Reference case (core-average coolant density =$10.25 g/cm^3$) [a]	$k_{eff}=1.0081\pm0.0006$
Delayed neutron fraction	0.0025
Prompt Neutron Lifetime	8×10^{-6}s
Doppler coefficient	-0.040±0.02¢/K
Fuel thermal expansion	-0.043±0.02¢/K
Core-average coolant density =$8 g/cm^3$	$k_{eff}=1.0020\pm0.0007$
Core-average coolant density =$6 g/cm^3$	$k_{eff}=0.9943\pm0.0007$
Core-average coolant density =$0 g/cm^3$	$k_{eff}=0.9246\pm0.0007$
The most reactive fuel assembly (FA) is partially voided [b]	$k_{eff}=1.0068\pm0.0006$
Peripheral streaming tubes of the core central FA flooded [c]	$k_{eff}=1.0071\pm0.0007$
Central void region of the core central FA flooded	$k_{eff}=1.0067\pm0.0007$
All compensation CRDs withdrawn	$k_{eff}=1.2276\pm0.0007$
Average CRD worth	0.5$
Worth of the most reactive compensating CRD	0.7$

[a] For all cases, bottom and top CRD are inserted 60cm in the core, unless noted otherwise

[b] Partially voided central 50% of the most reactive (central) fuel assembly

[c] Flooded with coolant to simulate massive failures of sealed streaming tubes

---

[3] These figures do not change significantly throughout the irradiation cycle and the same conclusions on the core neutronic performance can be drawn at EOL (see reference [Hejzlar 2000]).

To reduce reactivity excess at BOL while attaining the objective of a sufficiently long refueling interval (1.5years), a 2-batch refueling scheme is used, and the initial core has two regions with different Pu+MA loading, as shown in **Figure 2.5**. The strategy for core management is as follows:

- the initial core is loaded with 23wt% Pu+MA in the central region and 29wt% Pu+MA in the peripheral region,
- after operation of about 600 days (1^{st} nominal 18 month cycle for a 1800MWth core power), the reactor is shut down, fuel from the outer region is moved to the central region and the outer region is loaded with fresh fuel having 29wt% TRU,
- operation of the reactor for another 600 days (2^{nd} cycle) and repeating the above refueling procedure.

The variation of the core reactivity as a function of time is illustrated in **Figure 2.6** at a thermal power of 1800MWth. Note that the core neutronic life (i.e. the time to reach k_{eff}=1) is inversely proportional to the reactor thermal power, as illustrated in **Figure 2.7**. It can be seen that, because the reference power of the PBWR is 1260MWth (see **Chapter 4**), refueling must be performed approximately every 2.3yrs.

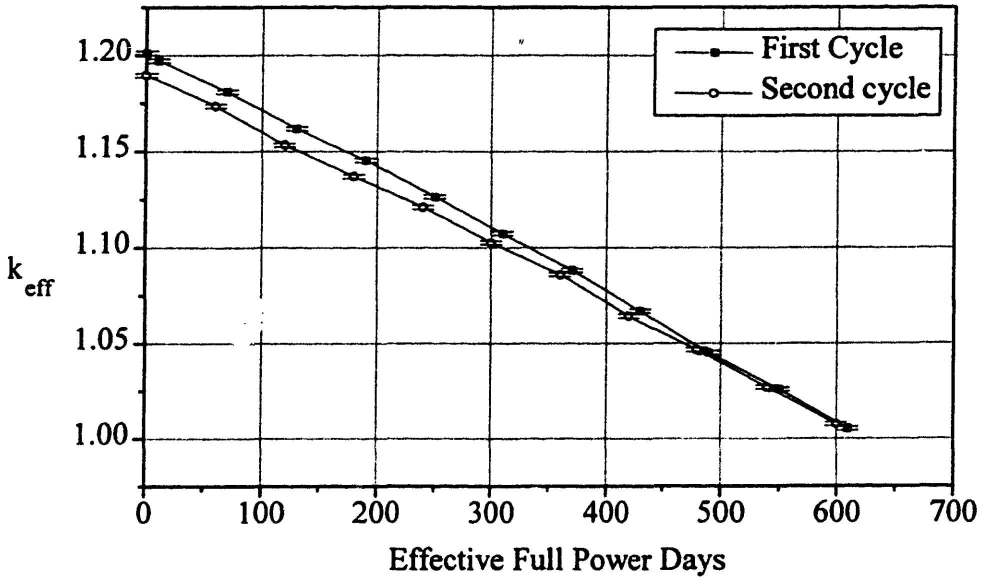

Figure 2.6. Reactivity swing of the PBWR core (at 1800MWth) (from [Hejzlar 2000]).

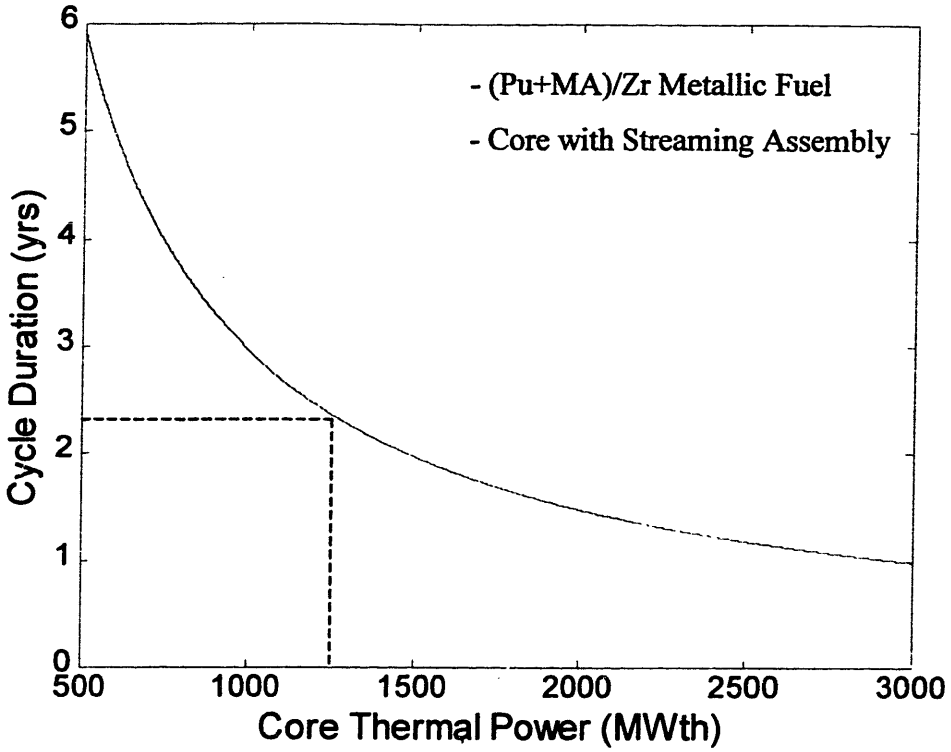

Figure 2.7. The neutronic life of the PBWR core.

The actinide burning rate of the two-batch reference core at 1800MWth is approximately 660kg per full power year. The change of the inventory of the individual nuclides is illustrated in **Figure 2.8**. As expected, the fuel experiences a large depletion of ^{239}Pu, which is the main fissile isotope, while the ^{238}Pu content actually increases due to the neutron captures in ^{237}Np. The results of **Figure 2.8** can be readily scaled to the PBWR reference power 1260MWth to yield an actinde burning rate of 462kg per full power year.

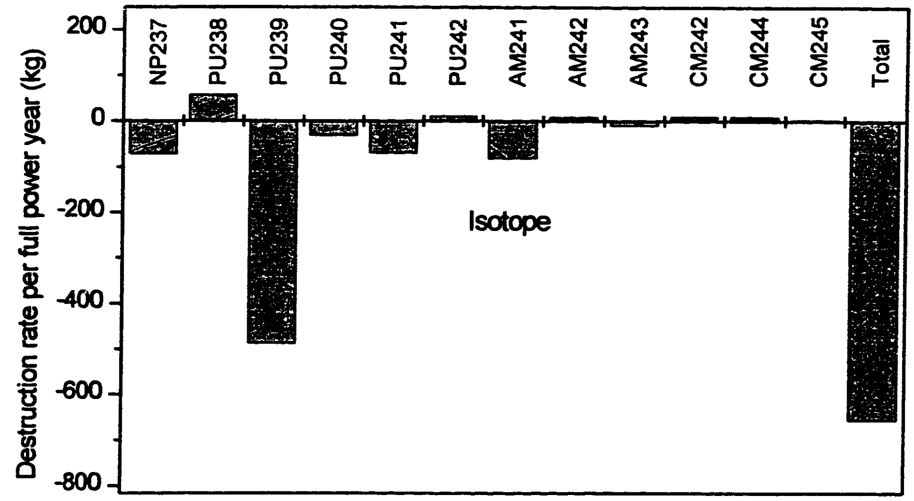

Figure 2.8. Actinide burning rate of the PBWR core (at 1800MWth) (from [Hejzlar 2000]).

2.2.3.2 Melting Point

Due to the lack of availability of experimental data for this fuel, a simplifying assumption is made that to a first approximation the thermo-physical and thermodynamic properties of the minor actinides can be set equal to those of plutonium. This assumption should be rather accurate because of their similar chemical properties and because the MA constitute only a small fraction of the fuel materials. Therefore an estimate of the melting point and crystalline phase transitions of the fuel can be gained from the phase diagram of the Pu-Zr binary alloy (see **Figure 2.9**). It can be seen that the alloy melting point (along with its crystalline stability) is an increasing function of the zirconium content, ranging between 1600 and 1700°C for a Zr weight fraction between 70 and 80%.

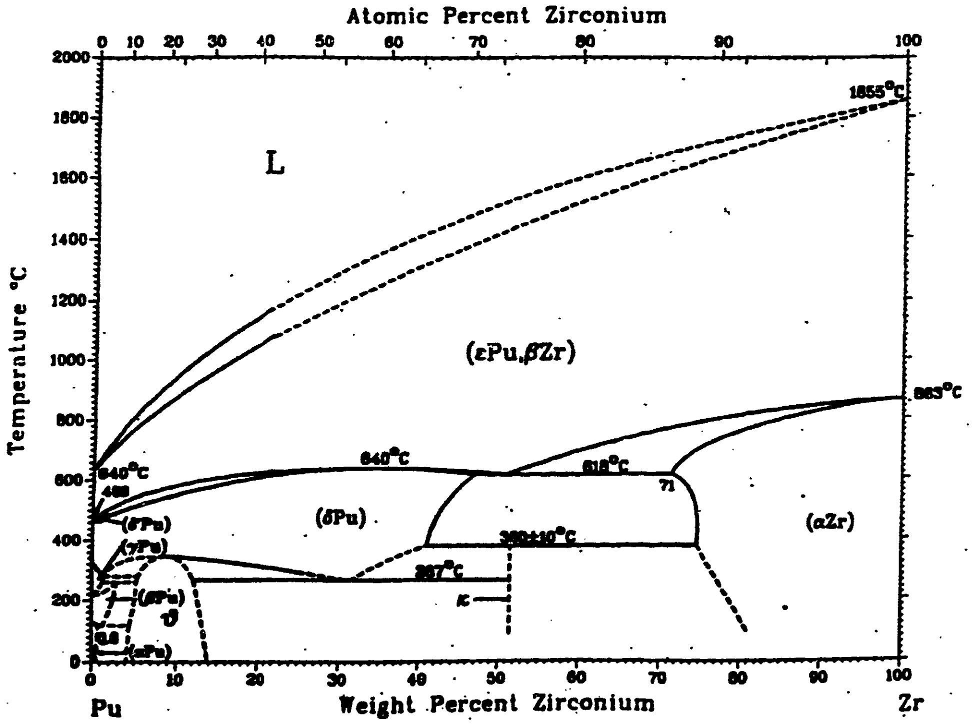

Figure 2.9. The phase diagram of Pu-Zr (from [Hofman 1985]).

2.2.3.3 Thermal Conductivity

To evaluate the thermal performance of the fuel, it is essential to know its thermal conductivity as a function of temperature and burnup. The variation of the ANL metallic fuel thermal conductivity with burnup displays a minimum at 26% porosity [Bauer 1993]. The mechanism leading to a minimum is briefly described as follows: the thermal conductivity initially decreases with burnup as the released fission gases increase the fuel porosity. When the number and size of gas filled pores become very large (i.e. above 26%), most pores agglomerate into larger interconnected cavities, which are rapidly filled by the gap bond, leading to a sharp increase of the effective fuel thermal conductivity.

An estimate of an alloy property can be in principle obtained by taking an appropriate average over its components. Here the thermal conductivity of pure βZr and εPu (see **Figure 2.9**) are averaged by means of their respective weight fraction to yield the thermal conductivity of the unirradiated fuel at any temperature above 973K (i.e. 700°C):

$$k = 0.74k_{Zr} + 0.26k_{Pu} = a + b_1T + b_2T^2 + b_3T^3 \qquad \textbf{Eq.2.1}$$

where T is in K, k is in W/cm·K and the values of the numerical coefficients are:

a=0.19856, b_1=-1.04439×10^{-4}, b_2=1.96148×10^{-7} and b_3=-5.00737×10^{-11}.

A benchmark of this method against the experimental values of thermal conductivity of other Pu metallic binary alloys indicates a systematic tendency of this approach to overpredict the thermal conductivity with an error of at most 30% [Buongiorno 1999c].

The pore effect on thermal conductivity (i.e. the burnup effect) can be estimated by means of the following equation [Bauer 1993]:

$$\frac{k_e}{k} = (1-P)^{(3\varepsilon/2)} \qquad \textbf{Eq.2.2}$$

where k_e is the thermal conductivity of the irradiated fuel and k is the thermal conductivity of the unirradiated fuel, P is the fuel porosity and ε is the pore shape factor (ε=1.0 if spherical pores are assumed). In **Figure 2.10** the predicted thermal conductivity of the fuel is plotted as a function of temperature for P=0.26. This information on the fuel thermal conductivity is taken from [Buongiorno 1999c], which should be consulted for a more comprehensive discussion.

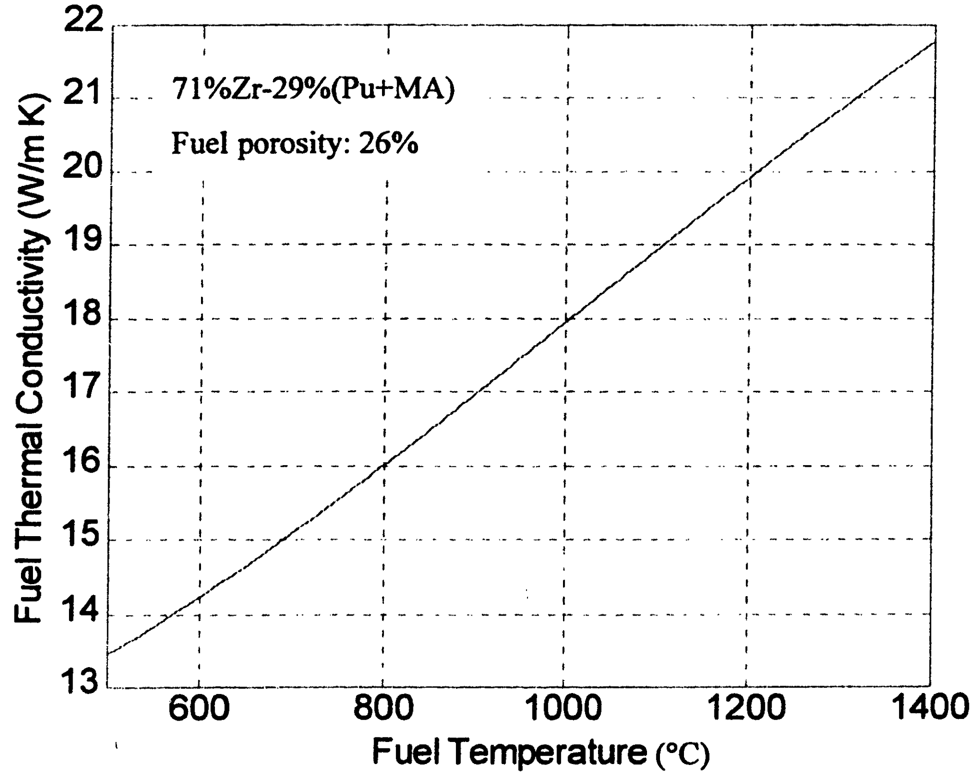

Figure 2.10. Predicted thermal conductivity of the metallic Zr-(Pu+MA) fuel.

2.2.4 The Clad

Selection of a suitable cladding material for a Pb-Bi cooled reactor is a serious technical challenge. Traditional austenitic stainless steels cannot be used due to the large solubility of nickel in bismuth (see **Table 1.II**), which would cause rapid selective leaching of that alloying element from the steel matrix and consequent loss of strength and integrity of the clad. Also, given the hard neutron spectrum and the large burnup levels of typical Pb-Bi cooled systems, the clad radiation damage requirements are exceptionally high. The possibility of employing low nickel stainless steels and/or less traditional materials (i.e. W, Nb, Ta) is currently being explored in the US [Weeks 1998, Li 1999, Loewen 2000], in Israel [Tsirlin 1999] and in Japan [Takahashi 2000].

In the past, a martensitic/ferritic steel of low nickel content (<1wt%) has been extensively tested by the Russians within their Pb-Bi cooled reactor program and it was concluded that it is suitable for cladding purposes at temperatures up to 600-650°C [Adamov 1997, Gromov 1994]. In the Russian literature this steel is designated as EP-823 and its composition is reported in **Table 2.V.** Because EP-823 is to date the only proven material for Pb-Bi applications, we select it as the reference clad material of the PBWR. The corrosion resistance of this steel relies on the formation of a protective iron/chromium oxide film that prevents rapid dissolution of the substrate. The stability of this film strongly depends on the oxygen concentration in the coolant: too little oxygen would result in a reducing environment that could dissolve the oxide. On the other hand, if the oxygen concentration is too large, the precipitation of oxide slag in the primary circuit could foul the heat transfer surfaces and/or clog the core channels. As a result, it is mandatory to control the oxygen level within a relatively narrow range of values (see **Chapter 8**).

Table 2.V. Martensitic/ferritic steel composition (%wt)

	Cr	Ni	Mo	Si	V	Nb	W	C	Mn
EP-823	12	0.8	0.9	1.3	0.4	0.4	0.8	0.2	0.6
HT-9	12	0.5	1.0	0.2	0.3	0.3	0.5	0.2	0.6

Because the thermo-physical, mechanical and irradiation properties of EP-823 are not readily available in the literature, they are set equal to those of the Western martensitic/ferritic steel HT-

9, of very similar composition (see **Table 2.V**). HT-9 was extensively and successfully tested for fusion and sodium fast reactor applications and it exhibits excellent irradiation properties.
The basic properties of this steel are [Lewis 1977]:

- Phase: martensitic BCC
- Young's Modulus: $E \approx 320$GPa at 20°C and 180GPa at 530°C.
- Poisson's Modulus: $\nu \approx 0.3$
- Thermal Conductivity: $k \approx 25$W/m·K at 90°C and 29W/m·K at 530°C
- Linear Thermal Expansion Coefficient: $\alpha \approx 10\times10^{-6}K^{-1}$ at 130°C and $12\times10^{-6}K^{-1}$ at 730°C
- Melting Point: ~1500°C

It is assumed [GE 1991] that no irradiation swelling occurs in HT-9 at fast neutron fluences below 3.3×10^{23}n/cm^2 (i.e. ~300dpa for neutrons of energy above 1MeV). Above this threshold HT-9 swells at a rate of 1% ($\Delta V/V$) per 10^{22}n/cm^2.

The Ductile-to-Brittle-Transition Temperature (DBTT) of unirradiated HT-9 ranges between −10°C and 0°C [Gelles 1987]. **Figure 2.11** illustrates the DBTT shift as a function of the neutron dose (dpa) and irradiation temperature.
The irradiation creep strain rate of HT-9 can be calculated by means of the following correlation [Amodeo 1985]:

$$\varepsilon_I = A_C \sigma_e \delta \qquad \textbf{Eq.2.3}$$

where:

$A_C = 2.9\times10^{-6}$ dpa^{-1}MPa^{-1}

σ_e = Von Mises equivalent stress (MPa)

δ = neutron dose (dpa)

The fast neutron flux (E_n>1MeV) on the PBWR fuel clad was calculated in reference [Hejzlar 2000] and found to be 3.03×10^{11}n/cm^{2}s per MWth. For a 1260MWth core with two fuel batches that refuels every 2.3yrs (see **Section 2.2.3.1**), the total fluence on the clad Φ is $3.03\times10^{11}\times1260\times(2.3\times365\times24\times3600)\times2=5.7\times10^{22}$n/cm^2, which is equivalent to a dose effect of about 50dpa. Therefore, no significant irradiation swelling is expected. It can be seen from **Figure 2.11** that the calculated neutron dose on the clad is beyond the experimental database of reference [Gelles 1987]. The clad operates at about 600°C. The curves for 500 and 550°C indicate that irradiation embrittlement does not strongly increase with the dose at high temperature (probably due to the self-annealing effect). Therefore, from **Figure 2.11** the DBTT shift is expected to be around 50°C for the PBWR clad. Considering that the DBTT of un-irradiated HT-9 ranges between –10 and 0°C [Gelles 1987], the consequences of a 50°C shift are negligible.

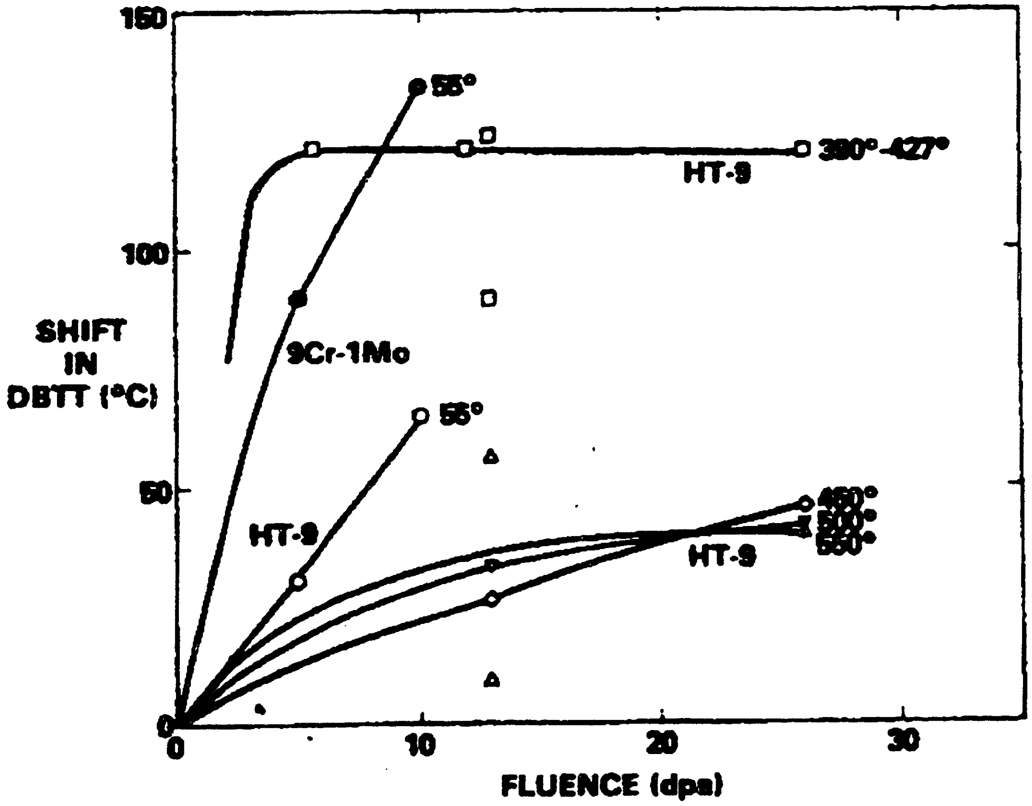

Figure 2.11. The effect of neutron irradiation on HT-9 ductility (from [Gelles 1987]).

The gap between the cladding and fuel requires bonding material to enhance thermal conductivity. The proven bonding material from the ANL Integral Fast Reactor program is sodium. However, to avoid the use of another material in the core, pure lead was selected as the bond between the fuel pellets and the stainless steel cladding. A research program will be required to confirm its compatibility with Zr-based fuel and stainless steel cladding. Sodium bonding as in EBR-II and IFR is an alternative in case lead does not provide satisfactory performance. In any event, the amount of bonding agent is not large enough to significantly affect the core neutronic characteristics presented in the fuel section.

2.2.5 The Control Rods

The control rods (CRD) are made of B_4C with 90% ^{10}B enrichment and are utilized for both reactivity compensation and control. High neutron heating requires cooling of control rods with coolant. This can be effectively achieved by placing the CRD for reactivity compensation and control outside of the fuel assembly's neutron streaming regions, as indicated in **Figure 2.3**. The guide tubes direct the control rod movement and protect it from jamming in case of fuel rod bowing against the CRD channels. The 157 control rods have ample margin to shut down the reactor. In addition, the central void boxes can contain normally out-of-core backup safety rods used only for emergency shutdown: for example if operational control rods are denied entry by coolant freezing, oxide slag accumulation, or buoyancy forces. These scram rods do not require cooling during normal operation. During shutdown, radiative cooling will be sufficient.

To minimize the axial power peaking, the control rod system employs both top- and bottom-entry rod insertion, as indicated on **Figure 2.12**. Half of the CRD are inserted from the top into the core and the other half are pulled into the core from the bottom. Control rod drives (and their respective sliding seals) for both these sets of control rods need to be mounted at the bottom of the vessel (as in a BWR) due to the presence of the steam dryer and chimney structures above the core.

Bottom and top CRD are arranged in a staggered "checkerboard" layout. The bottom-entry CRD reside in the extended space between the core lower plate and core bottom. The bottom-entry CRD are made of boron carbide, which has about four times lower specific density than Pb-Bi coolant, hence they are drawn into the core by buoyancy force. To attain passive insertion of top-entry CRD by gravity, tungsten boride (WB), which has higher density than lead-bismuth, can be used. Another alternative for the top-entry CRDs is to use tungsten slugs above and below the CRD active height to achieve gravity-driven insertion. Both alternatives were analyzed and found to perform satisfactorily.

2.2.6 Power Peaking

Knowledge of the radial, axial and local power peaking factors is key when the temperature distribution and the safety margins are to be calculated within the reactor core. The use of Pb-Bi as a coolant enables achieving a remarkably flat power distribution throughout the core due to the hard spectrum and low capture cross section, which yield a rather large neutron mean free path. This can be seen in **Figure 2.13,** where the normalized neutron flux distribution is shown at BOL. **Figure 2.14** illustrates the normalized power distribution at BOL, which differs from the neutron flux distribution because of the different fissile loading in the two fuel batches. The radial power peaking factor P_{rad} is 1.24.

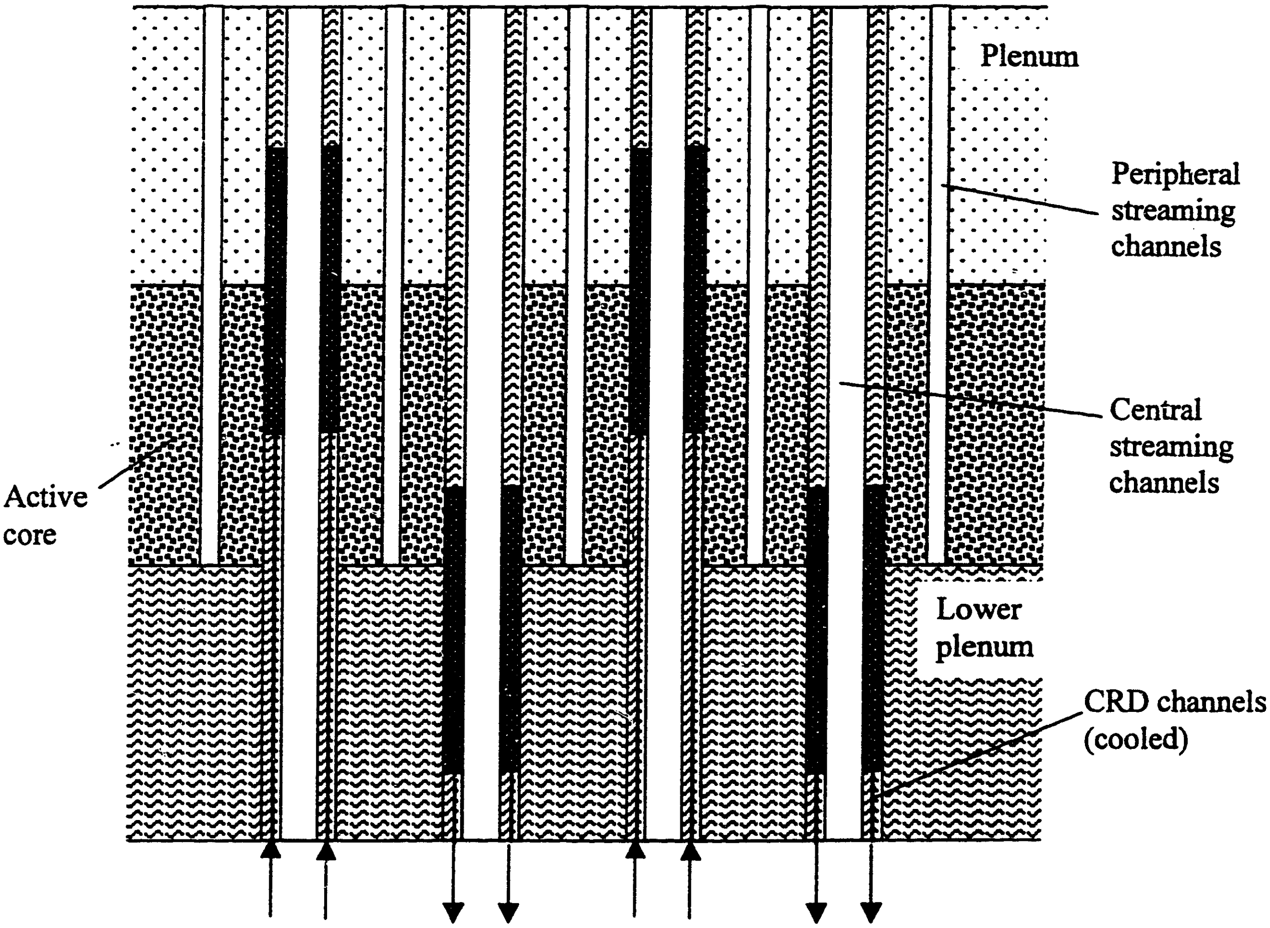

Figure 2.12. Schematic of the arrangement of double-entry control rods (from [Hejzlar 2000]).

The power distribution within the hottest fuel assembly is illustrated in **Figure 2.15.** As expected, the local peaking factor P_{loc}, is very small, i.e. P_{loc}=1.039. This value does not significantly change with burnup.

Finally, the normalized axial power at BOL and EOL is shown in **Figure 2.16.** Note that the double-entry CRD system provides an effective means to maintain the axial peaking relatively small throughout the whole irradiation cycle. The axial peaking factor P_{ax} ranges between 1.1 and 1.2.

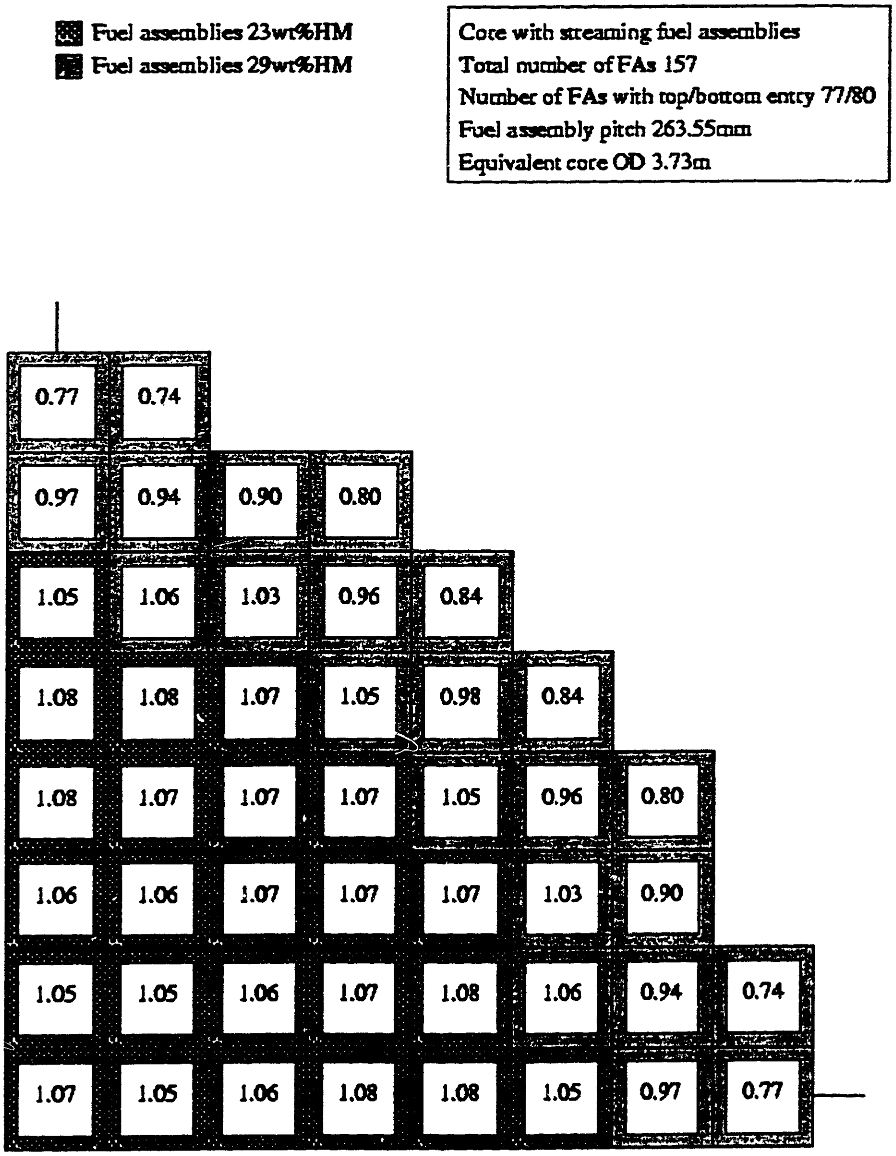

Neutron flux distribution - Core with double-entry CRDs
scale = 1/12 real scale

Figure 2.13. Radial neutron flux distribution in the core at BOL (from [Hejzlar 2000]).

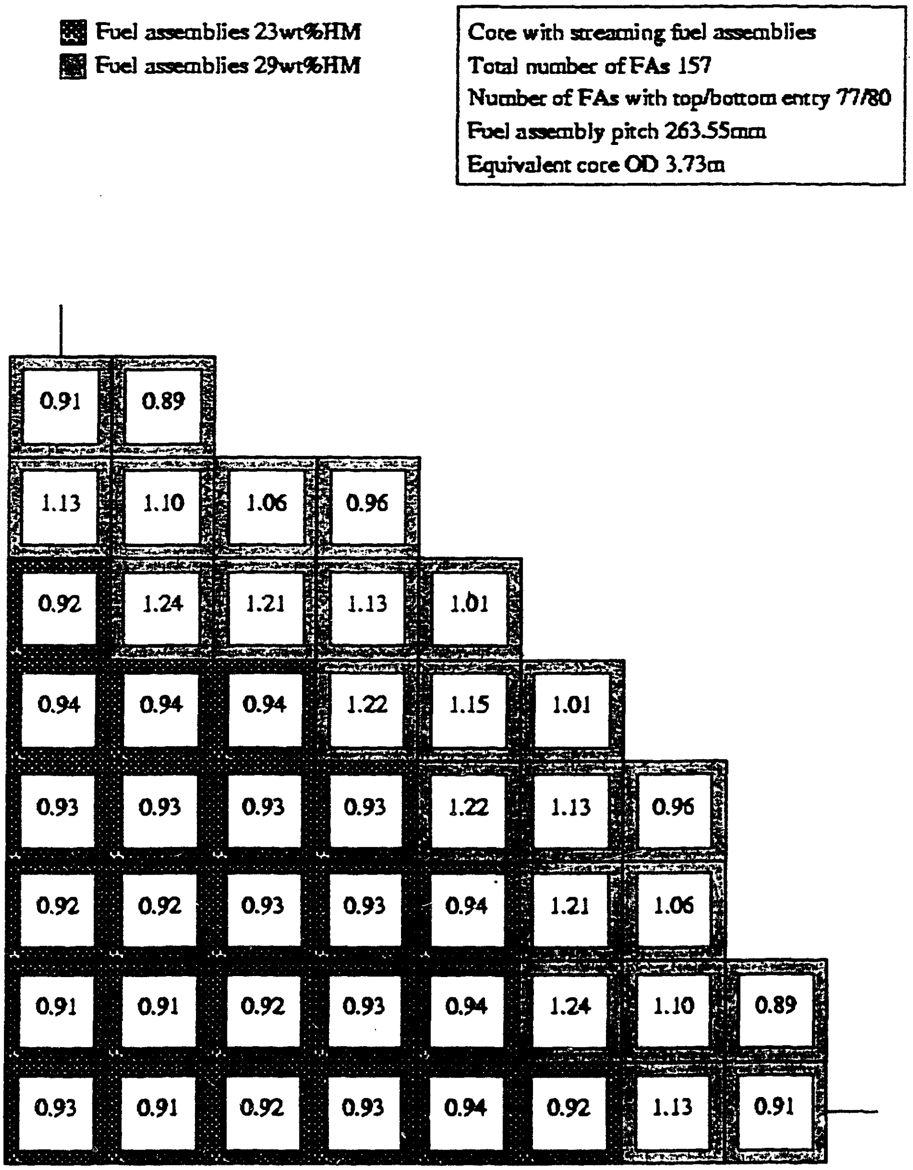

▨ Fuel assemblies 23wt%HM
▨ Fuel assemblies 29wt%HM

Core with streaming fuel assemblies
Total number of FAs 157
Number of FAs with top/bottom entry 77/80
Fuel assembly pitch 263.55mm
Equivalent core OD 3.73m

0.91	0.89						
1.13	1.10	1.06	0.96				
0.92	1.24	1.21	1.13	1.01			
0.94	0.94	0.94	1.22	1.15	1.01		
0.93	0.93	0.93	0.93	1.22	1.13	0.96	
0.92	0.92	0.93	0.93	0.94	1.21	1.06	
0.91	0.91	0.92	0.93	0.94	1.24	1.10	0.89
0.93	0.91	0.92	0.93	0.94	0.92	1.13	0.91

Assembly power distribution - Core with double-entry CRDs
scale = 1/12 real scale

Figure 2.14. Radial power distribution in the core at BOL (from [Hejzlar 2000]).

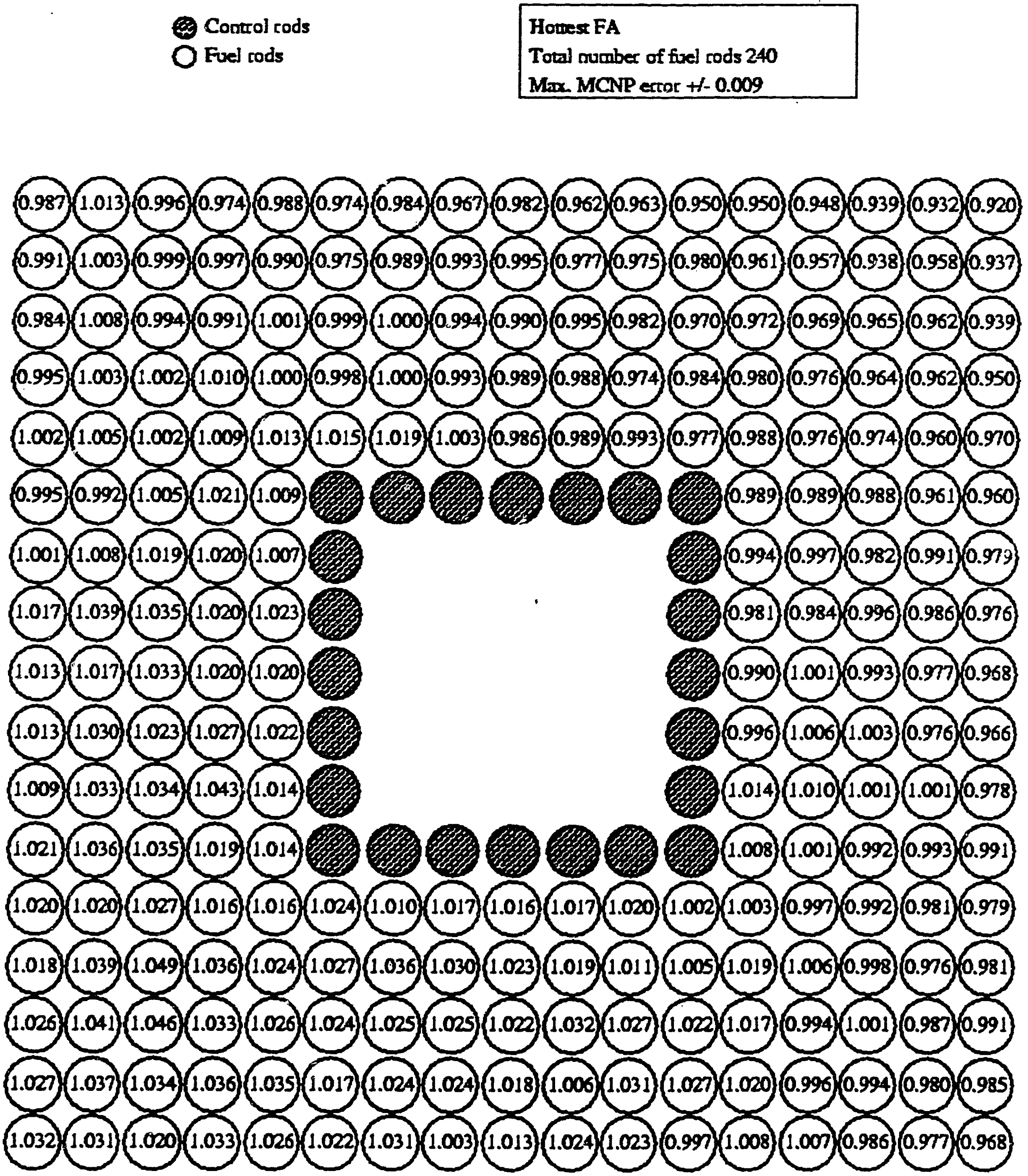

0.987	1.013	0.996	0.974	0.988	0.974	0.984	0.967	0.982	0.962	0.963	0.950	0.950	0.948	0.939	0.932	0.920
0.991	1.003	0.999	0.997	0.990	0.975	0.989	0.993	0.995	0.977	0.975	0.980	0.961	0.957	0.938	0.958	0.937
0.984	1.008	0.994	0.991	1.001	0.999	1.000	0.994	0.990	0.995	0.982	0.970	0.972	0.969	0.965	0.962	0.939
0.995	1.003	1.002	1.010	1.000	0.998	1.000	0.993	0.989	0.988	0.974	0.984	0.980	0.976	0.964	0.962	0.950
1.002	1.005	1.002	1.009	1.013	1.015	1.019	1.003	0.986	0.989	0.993	0.977	0.988	0.976	0.974	0.960	0.970
0.995	0.992	1.005	1.021	1.009	▨	▨	▨	▨	▨	▨	▨	0.989	0.989	0.988	0.961	0.960
1.001	1.008	1.019	1.020	1.007	▨						▨	0.994	0.997	0.982	0.991	0.979
1.017	1.039	1.035	1.020	1.023	▨						▨	0.981	0.984	0.996	0.986	0.976
1.013	1.017	1.033	1.020	1.020	▨						▨	0.990	1.001	0.993	0.977	0.968
1.013	1.030	1.023	1.027	1.022	▨						▨	0.996	1.006	1.003	0.976	0.966
1.009	1.033	1.034	1.043	1.014	▨						▨	1.014	1.010	1.001	1.001	0.978
1.021	1.036	1.035	1.019	1.014	▨	▨	▨	▨	▨	▨	▨	1.008	1.001	0.992	0.993	0.991
1.020	1.020	1.027	1.016	1.016	1.024	1.010	1.017	1.016	1.017	1.020	1.002	1.003	0.997	0.992	0.981	0.979
1.018	1.039	1.049	1.036	1.024	1.027	1.036	1.030	1.023	1.019	1.011	1.005	1.019	1.006	0.998	0.976	0.981
1.026	1.041	1.046	1.033	1.026	1.024	1.025	1.025	1.022	1.032	1.027	1.022	1.017	0.994	1.001	0.987	0.991
1.027	1.037	1.034	1.036	1.035	1.017	1.024	1.024	1.018	1.006	1.031	1.027	1.020	0.996	0.994	0.980	0.985
1.032	1.031	1.020	1.033	1.026	1.022	1.031	1.003	1.013	1.024	1.023	0.997	1.008	1.007	0.986	0.977	0.968

Figure 2.15. Power distribution within the hottest assembly (from [Hejzlar 2000]).

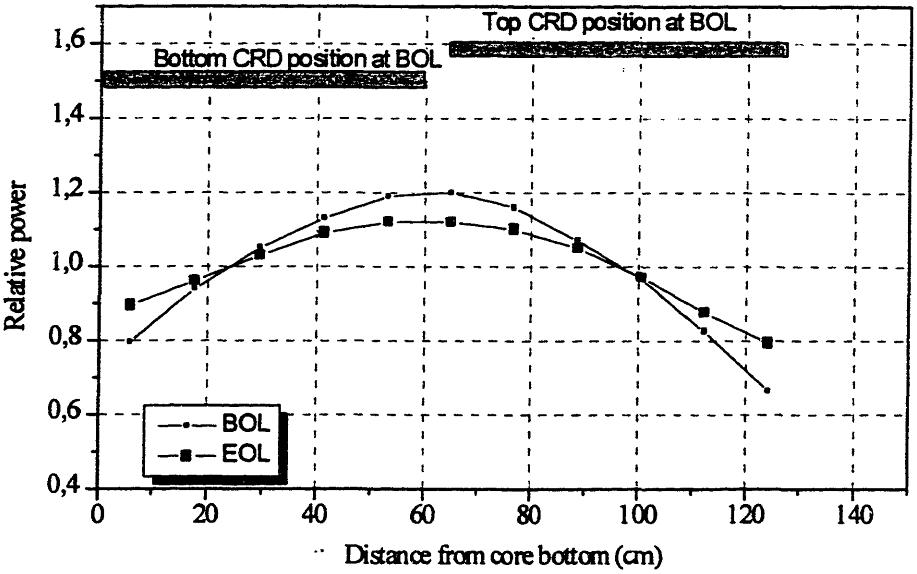

Figure 2.16. Axial power distribution in the core (from [Hejzlar 2000]).

2.3 The Reactor Vessel

The reactor vessel is one of the main barriers to the release of radioactivity into the environment. Moreover, under accidental conditions (e.g. loss of the normal heat sink) the core decay heat is discharged to the environment through the vessel wall. It is assumed that the vessel structural material is the Russian ferritic/martensitic steel EP-823, especially developed for Pb-Bi systems (see **Section 2.2.4**). The scope of this section is to a) identify the loads acting on the reactor vessel and c) conduct a structural analysis to establish the vessel temperature limit as a function of the vessel thickness. A temperature limit is set by the structural analysis because the strength of the vessel material is a decreasing function of temperature. Therefore, for given loads and vessel thickness, there exists a maximum temperature that the vessel can withstand without exceeding the safety limit set by the ASME code (see below). The vessel temperature limit will be then used in **Chapter 4** as a constraint (along with the fuel and clad temperature limits) to assess the maximum power removable from the PBWR core under normal and loss-of-heat-sink conditions.

2.3.1 Allowable Stress Intensity and Thermal Creep

We note again that due to the lack of information on EP-823 in the West, it is assumed that the properties of EP-823 are equal to those of the Western steel HT-9. The relevant properties of the HT-9 steel are reported in **Section 2.2.4**. However, because the structural analysis of the reactor vessel is undertaken following the recommendations of the ASME code case N-47, the maximum allowable stress intensity[4] of the structural material is also required, which is defined as the lowest of S_m and S_t, where:

S_m is the lowest of

- 1/3 Ultimate Stress at room temperature
- 1/3 Ultimate Stress at operating temperature
- 2/3 Yield stress at room temperature
- 2/3 Yield stress at operating temperature

S_t is the lowest of

- 2/3 minimum stress to cause creep rupture in time t
- 80% minimum stress to cause tertiary creep in time t
- Minimum stress to produce 1% creep strain in time t

Figure 2.17 shows the HT-9 allowable design stress intensity vs. temperature curve for several operating times at that temperature [Amodeo 1985]. The time dependence of the stress intensity limit is due to thermal creep. It should be noticed that the effects of thermal creep are negligible below 450°C.

2.3.2 Thin Shell Theory

A schematic of the PBWR reactor vessel is shown in **Figure 2.18**. The vessel beltline thickness is varied between 15 and 30cm (with a reference value of 25cm). The thickness of the lower and upper heads is selected to be 2/3 of the beltline thickness to minimize the discontinuity

---

[4] At any location in the vessel, the stress intensity is defined as the largest of the following stress differences: (hoop-radial), (hoop-axial), (axial-radial).

stresses. The lower and upper heads are modeled as hemispherical shells of diameter equal to the cylinder diameter.

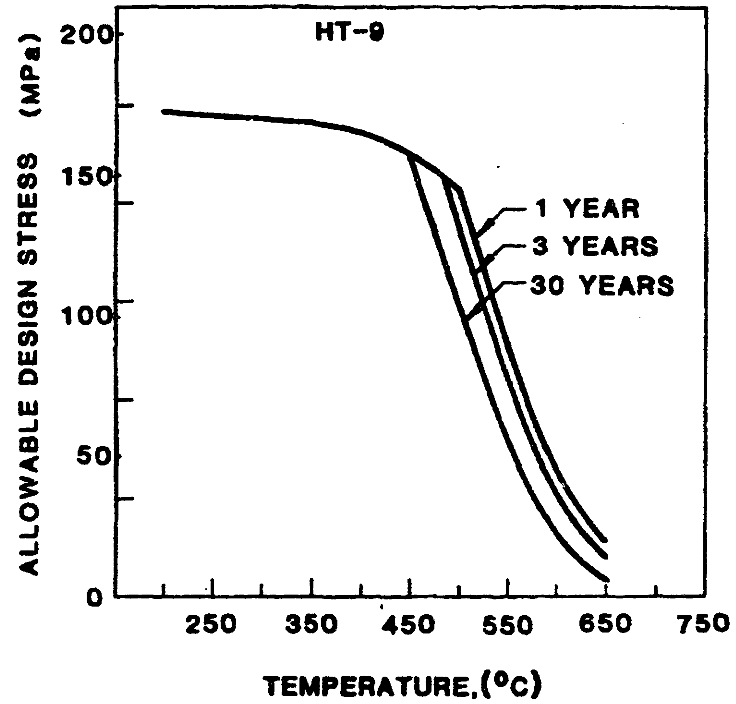

Figure 2.17. HT-9 allowable stress intensity (from [Amodeo 1985]).

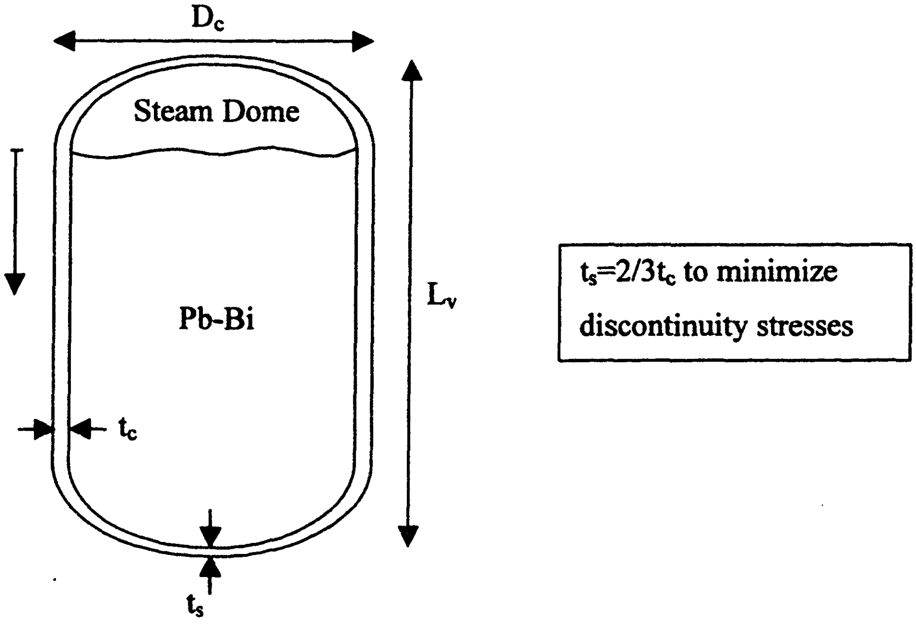

t_s=2/3t_c to minimize discontinuity stresses

Figure 2.18. The reactor vessel geometry.

2.3.2.1 Loads (Mechanical, Thermal and Irradiation)

The vessel wall is subjected to the following loads:

a) Operating pressure. The nominal pressure in the steam dome is 7.0 MPa. Due to the high density of Pb-Bi, the pressure increases linearly with depth (approximately 0.1MPa/m) thus reaching its maximum at the bottom of the lower head. The external pressure is 0.1MPa (i.e. atmospheric pressure).

b) Pb-Bi and vessel weight. This load (together with the operating pressure) determines the axial stress at any axial depth z (see **Figure 2.19**).

c) Radial temperature gradient across the vessel thickness (especially when the decay heat is removed through the vessel). It should be noted that in this structure the radial temperature gradient induces hoop and axial thermal stresses whose average over the vessel thickness is zero. These stresses have to be taken into account in a fatigue analysis only. Since the frequency of use of the Decay Heat Removal System (DHRS) is expected to be low, fatigue considerations are relatively unimportant and the thermal load will be neglected.

d) Fast neutron flux. Depending on the downcomer thickness (from 50 to 100cm), the fast neutron flux (E_n>1MeV) at the vessel surface can range up to 1.2×10^{12}n/cm^{2}s for a 1260MWth core power [Hejzlar 2000], leading to a total fluence over 30 years of vessel lifetime up to 1.1×10^{21}n/cm^2. The corresponding dose effect is about 1.1dpa.

2.3.2.2 Variables and Assumptions

The independent variables are the vessel temperature, thickness, diameter and height, designated as T, t_c, D_c an L_v, respectively. The following assumptions are made:

a) The upper and lower heads are assumed to be hemispherical.

b) The thin shell theory ($D/t_c>20$) is applied to find the:
   - primary membrane stresses,
   - discontinuity membrane and bending stresses at the junction of the beltline with the lower and upper head,
   - elastic, thermal and irradiation creep strains and displacements.

c) The ASME code case N-47 is applied to determine the stress intensity acceptability.

d) As pressure varies axially along the vessel, some primary bending stresses are expected in the cylinder. To avoid computational complications, these stresses are not considered in this analysis. This will not significantly affect the results because we will show that the limit is dominantly set by the primary membrane stresses.

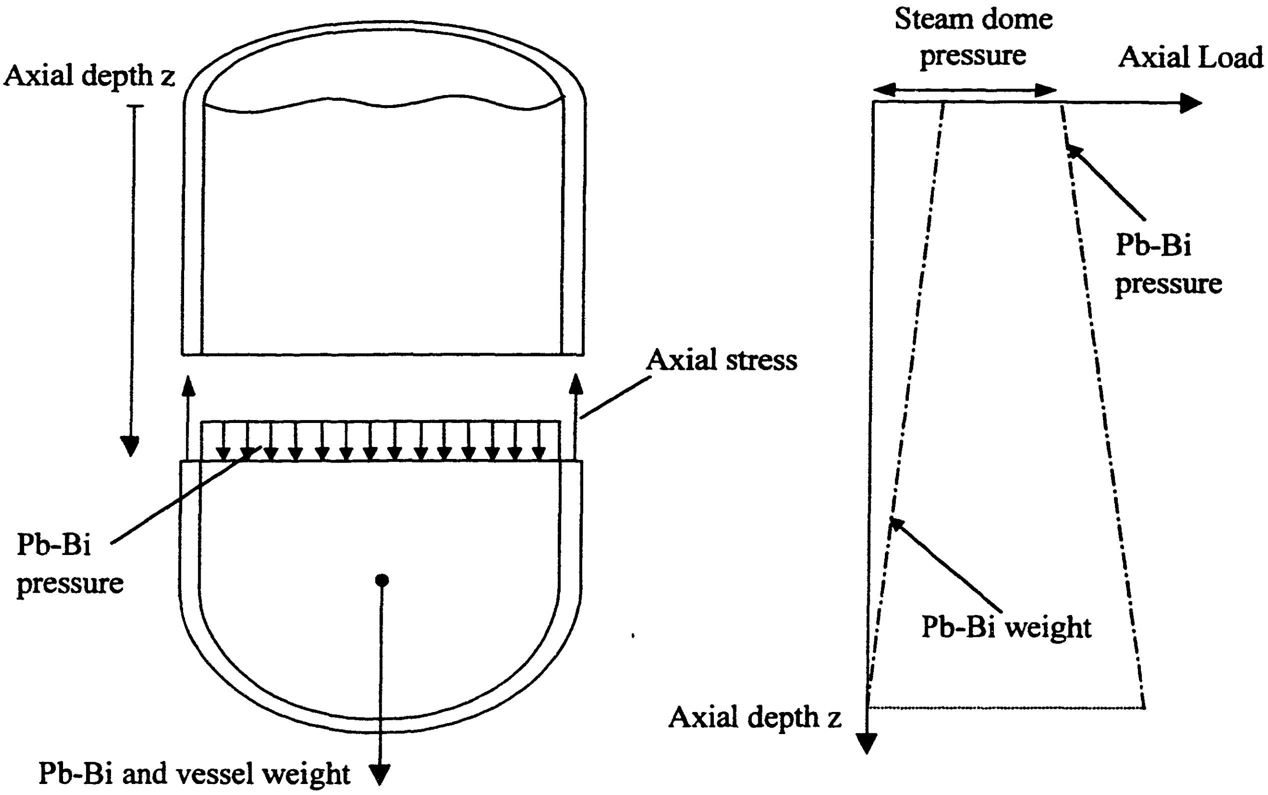

Figure 2.19. Force diagram for the determination of the axial primary membrane stress.

2.3.2.3 Safety Margin

Following the ASME code case N-47 the safety margin is defined at any location in the vessel as:

$$\text{Primary Membrane Stress Safety Margin (PMSSM)} = \frac{S_{design}}{S_{pm}}$$

where S_{design} is taken from **Figure 2.17** at the vessel membrane temperature (i.e. temperature averaged across the vessel thickness) and S_{pm} is the primary membrane stress intensity.

Analogously:

$$\text{Primary + Secondary Stress Safety Margin (PSSSM)} = \frac{3S'_{design}}{S_{ps}}$$

where S'_{design} is taken from **Figure 2.17** at the vessel local temperature and S_{ps} is the primary + secondary stress intensity.

2.3.2.4 Results

As an example of the output of the structural analysis, **Figure 2.20** illustrates the axial variation of the PMSSM and PSSSM at the outer and inner surface of a 25cm thick vessel of diameter 6m and height 20.5m (see **Section 4.6**) operating at 440°C. Points z=0 and z=10m represent the junction of the cylinder with the upper and lower heads, respectively. Therefore, points of negative z represent the upper head (see **Figure 2.18**) and points of z>10m represent the lower head.

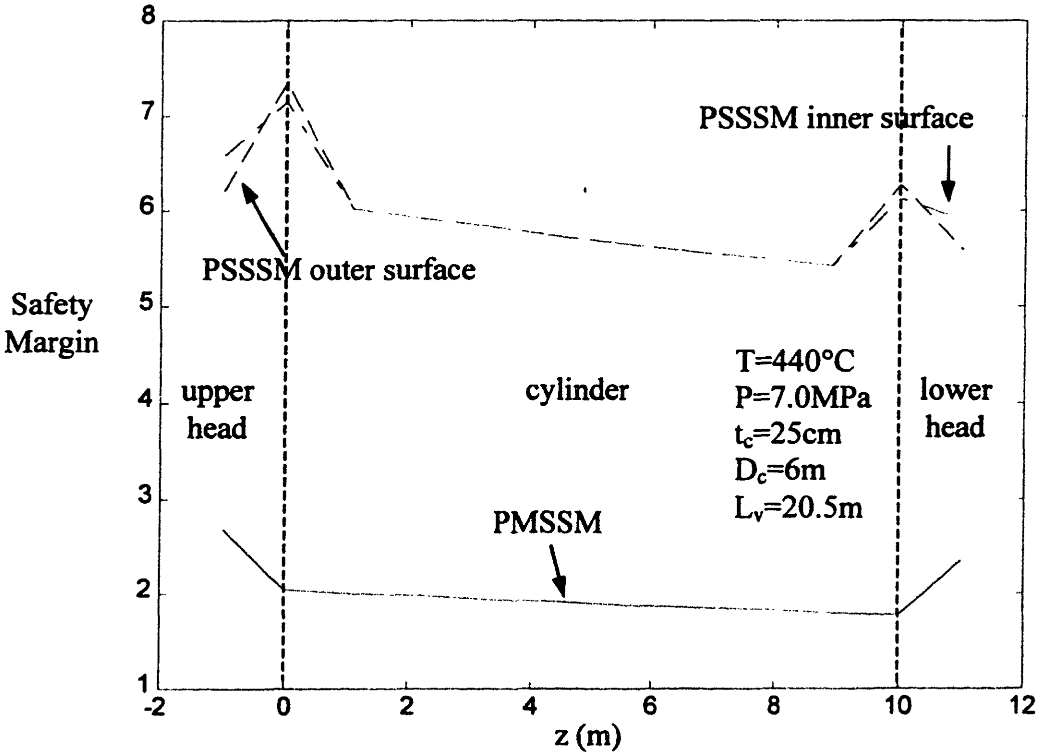

Figure 2.20. Primary and secondary stresses in the vessel.

As expected, the primary membrane stresses in the upper and lower heads are smaller than those in the cylinder due to their spherical geometry. Also, the PMSSM is smaller than the PSSSM at any location in the vessel, indicating that the structural limit is really set by the membrane stresses. The PMSSM decreases with z in the cylinder as does PSSSM far from the junctions, because all primary membrane stresses increase with z due to the increasing pressure. The most critical location in the vessel (the location of lowest safety margin) is the cylinder/lower head junction. As for the secondary stresses, the PSSSM displays a minimum slightly before the cylinder/lower head junction due to the discontinuity stresses. Also, note that no significant differences are observed between the secondary stresses on the inner and outer surface of the vessel.

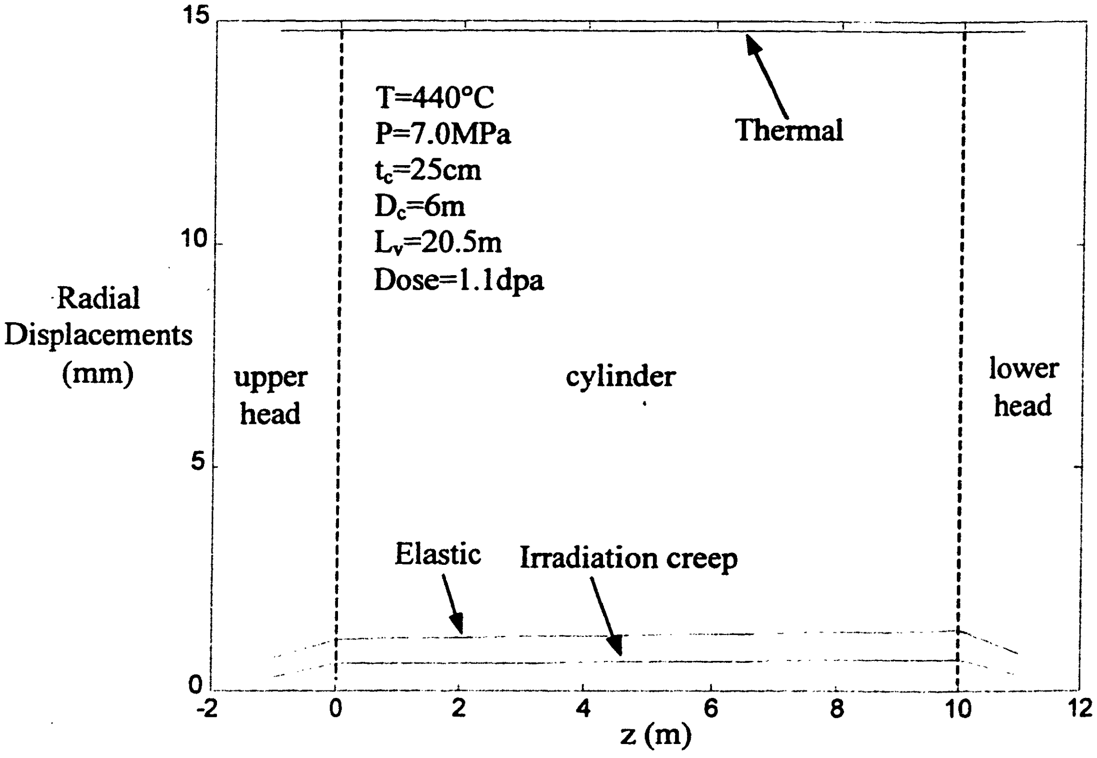

Figure 2.21. The vessel radial displacements.

Figure 2.21 illustrates the elastic, thermal and irradiation creep displacements as a function of the axial location for the same vessel of **Figure 2.20**. Note that the thermal displacements are calculated with respect to a 30°C reference temperature. As expected, thermal displacements are considerably larger than elastic displacements. Irradiation creep displacements are small, confirming the excellent irradiation characteristics of martensitic/ferritic steels like HT-9 and EP-823.

Figure 2.22 the relation between the maximum allowable vessel temperature, T_{mav}, and the vessel thickness for several different values of the vessel diameter and for a reference vessel height of 20.5m. It can be seen that for a given thickness, as the diameter increases, the stresses increase[5] and thus the maximum allowable temperature decreases. In **Figure 2.23** the effect of the vessel height on T_{mav} is shown for a reference vessel diameter of 6m. Because the pressure (and thus the stresses) at the bottom of the vessel increase with the vessel height, the temperature limit decreases with the vessel height. However, note that the magnitude of this effect is not large: for example, doubling the vessel height reduces the vessel temperature limit by only about 20°C. The T_{mav} from **Figure 2.22** and **2.23** will be used as a constraint in the thermal-hydraulic analysis of **Chapter 4**.

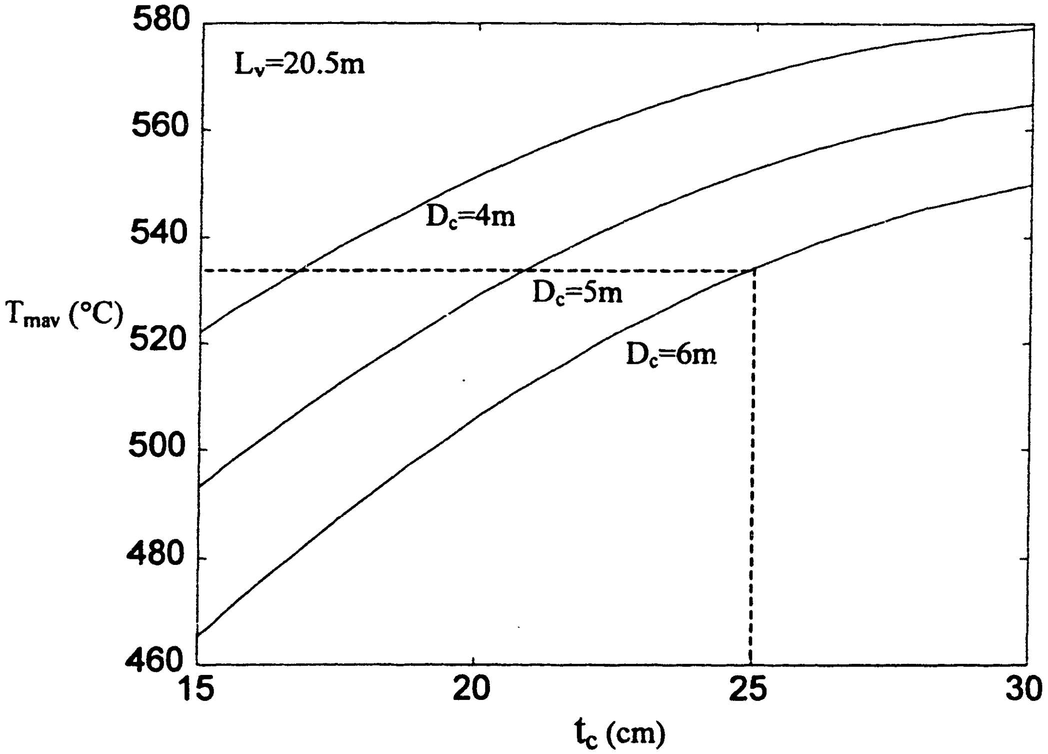

Figure 2.22. The diameter effect on the vessel temperature limit.

Other important results of the structural analysis are listed below:

- Irradiation creep strain is negligible for a fast neutron irradiation of 1.2×10^{21}n/cm^2 (see **Figure 2.21**) corresponding to 30 effective full power years at 1260MWth in the PBWR reference core.

---

[5] Both the hoop and axial stresses are proportional to the D_c/t_c ratio.

- Given that the maximum neutron irradiation of the reactor vessel is below 2.0×10^{21} n/cm^2, it can be confidently stated that irradiation swelling of the reactor vessel is not a concern.
- Irradiation embrittlement is expected to shift the vessel Ductile-To-Brittle-Temperature by at most 10°C (see **Figure 2.11**).
- Discontinuity stresses are relatively small under the analyzed conditions.

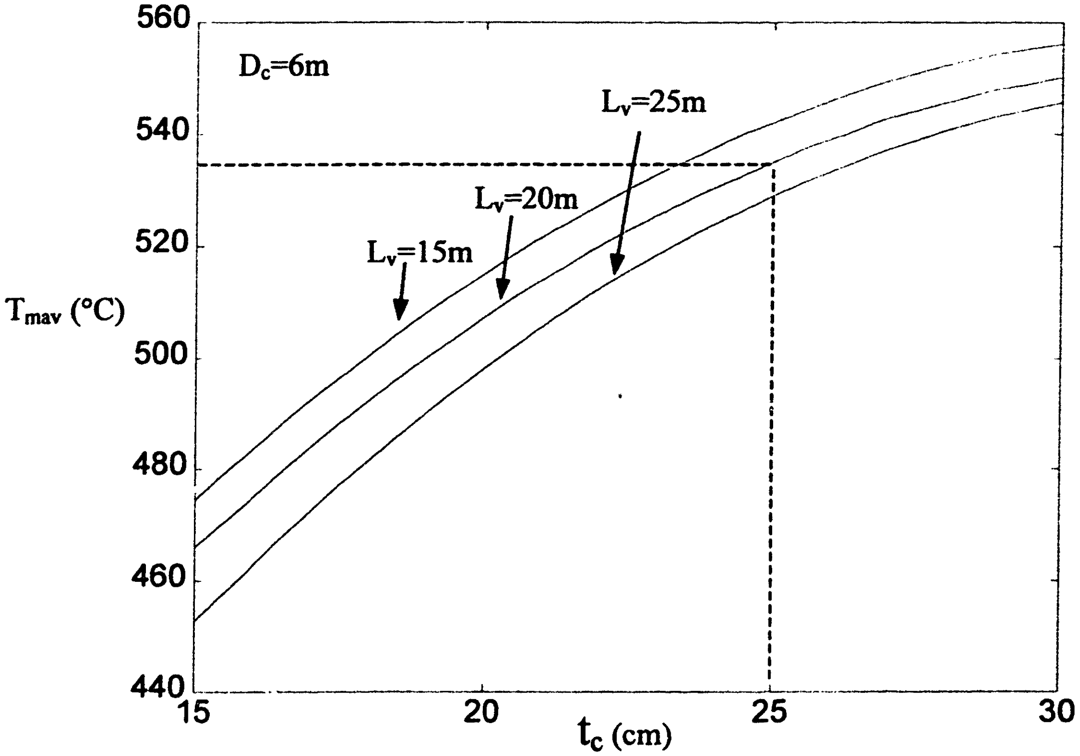

Figure 2.23. The height effect on the vessel temperature limit.

2.4 Decay Heat Removal System

Accurate knowledge of the decay power in the first few hours after shutdown is essential to design the DHRS and to predict the consequences of most accidents. In **Figure 2.24** the normalized decay heat rate of the PBWR actinide burning fuel (indicated as “trans”, i.e.

transmutation) is compared to that of a typical PWR for several values of the burnup[6]. As expected the difference appears to be within the inherent uncertainties of the utilized model.

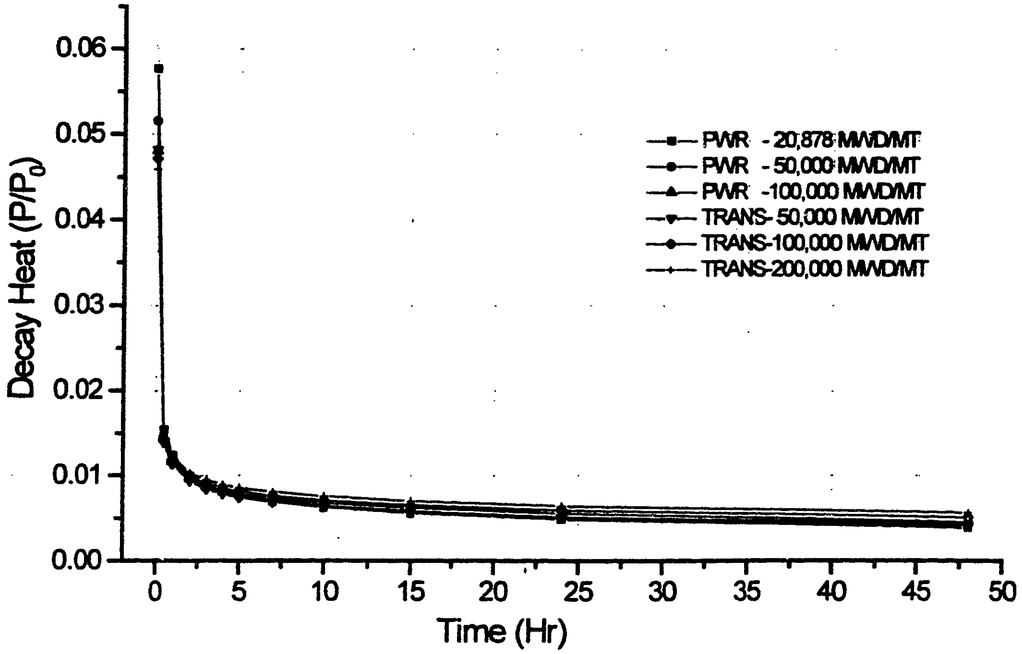

Figure 2.24. Normalized decay power after shut-down (from [Buongiorno 1999c]).

After the reactor has been shut-down, the heat produced by the radioactive decay of the residual fission fragments must be properly removed to ensure the integrity of the nuclear fuel. In the PBWR this heat will be normally removed from the reactor pool by the water injected directly in the Pb-Bi coolant above the core, but means must be provided to ensure continuous cooling of the nuclear fuel should that heat removal path fail (e.g. upon loss of the feedwater pumps). This is usually accomplished with the help of a dedicated Decay Heat Removal System (DHRS).

To enhance the social acceptability of the PBWR concept, it is desirable to design this DHRS with a high degree of passive safety. The most widely accepted DHRS for fast reactors is the so-called Reactor Vessel Auxiliary Cooling System (RVACS), developed by the American vendor General Electric for their sodium cooled reactor PRISM [GE 1991, Boardman 2000a]. A

---

[6] All decay powers were calculated by means of the ORIGEN 2.1 code.

schematic of the GE RVACS is illustrated in **Figure 2.25**. In this system, the decay heat is ultimately removed by natural circulation of air on the outer surface of the reactor containment.

The heat produced in the core is conveyed by naturally circulating Pb-Bi to the surface of the reactor vessel. The gap between the vessel and the containment is filled with an inert gas (e.g. nitrogen). The heat is transferred through the gap mainly by radiation. Air enters the reactor building through two inlets and flows through the downcomer to the containment bottom. From here it flows upward in the riser where it is heated and it is finally discharged to the atmosphere through the stacks that supply the gravitation head needed to passively drive the air through the circuit.

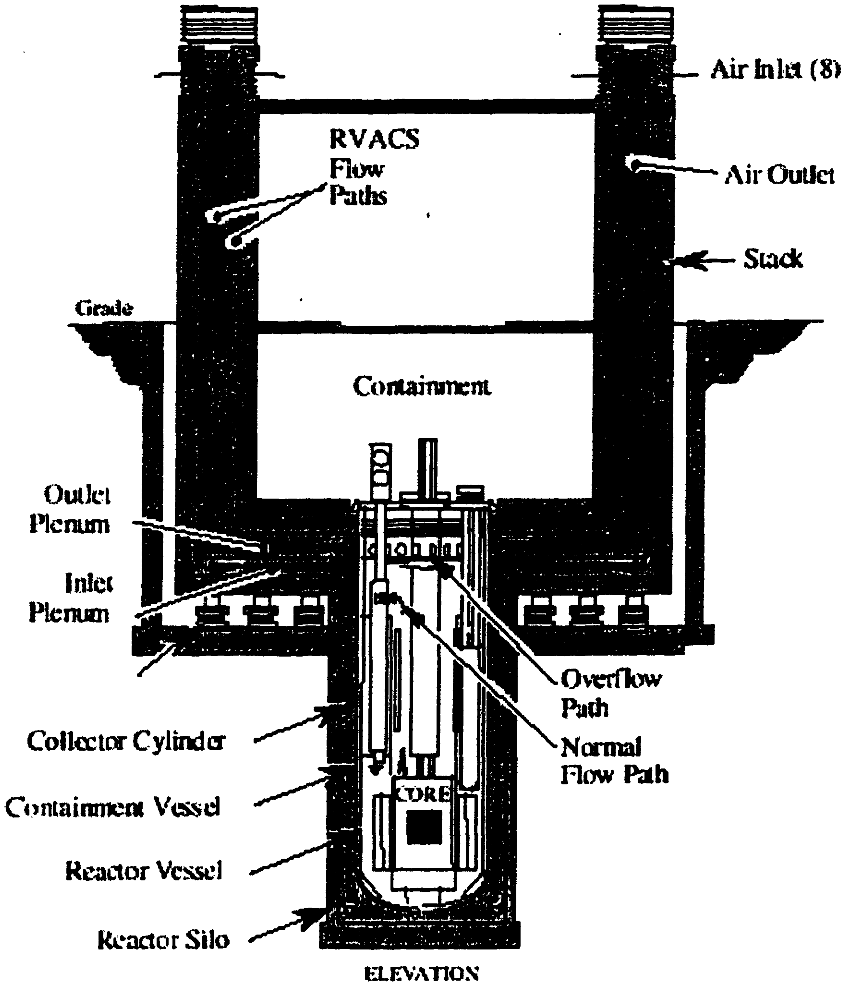

Figure 2.25. Schematic of a typical RVACS (from [Boardman 2000a]).

Because of the poor heat transfer characteristics of air and because of the large thermal resistance in the vessel/containment gap, the rated power of a RVACS is relatively small. Since the decay power is proportional to the nominal power, a small DHRS capacity results in a small acceptable nominal reactor power. Therefore, if larger reactor powers are desirable to improve the reactor economics, it is necessary to enhance the DHRS capacity. Means to do so along with a complete analysis of the PBWR DHRS will be presented in **Chapter 4**.

2.5 Main Technical Challenges

The explored reactor concept presents several technical challenges. Below the most significant ones are identified. A thorough assessment of their magnitude and possible remedies is the objective of this thesis work and is presented in the following chapters.

1) It is necessary to produce the maximum thermal power removable by direct contact heat transfer without violating the fuel, clad and vessel temperature limits. This is a difficult task that requires accurate thermal-hydraulic modeling of the multi-phase phenomena occurring in the reactor chimney as well as identification of the appropriate limits.
2) The separation of Pb-Bi and steam in the steam dryer is not complete. It is expected that a certain amount of Pb-Bi aerosol remains entrained in the steam stream and is carried over to the power cycle components with major consequences on their design and operation (e.g. liquid metal embrittlement of the stressed parts of the turbine, clogging of the condenser drain pipes).
3) The direct contact of Pb-Bi and steam significantly aggravates the issue of polonium contamination. The primary and secondary coolants (Pb-Bi and water, respectively) are not physically segregated and a substantial amount of radioactive polonium might be released into the secondary system and eventually to the environment.
4) The injection of water in the Pb-Bi primary coolant may increase the production of lead and bismuth oxides hence calling for the injection of a reducing agent (e.g. hydrogen) to prevent fouling of the heat transfer surfaces and/or clogging of the core and vessel flow channels.

2.6 Summary

In this chapter a general description of the Pb-Bi/Water Direct Contact Heat Transfer Reactor (PBWR) was provided and its main features were discussed. The geometric and neutronic characteristics of the PBWR reference core were also presented. This core was designed to burn plutonium and minor actinides from spent LWR fuel. The fuel is made of a metallic alloy of zirconium (continuum phase) and actinides (dispersed phase), which yields a very hard spectrum and a good neutron economy. The core design is based on neutron streaming assemblies that enable achieving a negative coolant void reactivity coefficient over a wide range of operating and accidental conditions.

The essential properties of the fuel and clad (e.g. thermal conductivity, melting point) as well as the radial, axial and local power peaking factors that are relevant to the thermal analysis of the next chapters were also reported.

A structural analysis of the reactor vessel, which is assumed to be made of ferritic/martensitic stainless steel, was undertaken and enabled assessing the vessel temperature limit as a function of its height, thickness and diameter. Further, an introduction to the Decay Heat Removal System (DHRS) was provided.

Moreover, three main technical challenges associated with the development of the PBWR were identified. These are: 1) the transport of Pb-Bi aerosol to the turbine, 2) the release of polonium from the Pb-Bi coolant to the steam and 3) the oxidation of the Pb-Bi coolant upon contact with water.

Chapter 3

- DIRECT CONTACT HEAT TRANSFER IN THE PBWR -

3.1 Introduction

The PBWR concept studied in this thesis work is based on direct contact vaporization of water in the reactor chimney to remove the core thermal power and generate steam for the power cycle (see **Figure 2.1**). This heat transfer mode can be remarkably effective because the primary coolant (i.e. the hot lead-bismuth) and the secondary coolant (i.e. the water) are not separated by a solid barrier (e.g. a tube wall in a conventional steam generator), but are in intimate contact and share a larger interfacial area. The actual rate of heat transfer between the two fluids determines the chimney height required to fully vaporize the water as well as the density difference between the chimney and the downcomer, which in turn strongly affects the natural circulation flow in the whole reactor pool and ultimately the temperature distribution in the core. Therefore, it should be clear that the prediction and understanding of the direct heat transfer phenomena occurring in the reactor chimney upon injection of liquid water in the bulk of the hot lead-bismuth coolant is crucial to evaluate the feasibility and performance of the PBWR system.

Direct contact heat transfer has been proposed and/or investigated in the past with regard to a variety of applications, ranging from geological heat extraction [Blair 1976, Jacobs 1977] to fuel-coolant-interaction in the analysis of disruptive accidents in nuclear reactors [Smith 1982], from magnetic hydrodynamic systems for dc electricity generation [Branover 1989, Kaushik 1995] to steam generators for sodium cooled reactors [Kinoshita 2000, Grachev 1999]. However, most early experimental work focused on organic or refrigerant fluids [Blair 1976, Smith 1982] and/or a single droplet situation [Sideman 1964, Shimizu 1988] which enables neglecting interference of the dispersed phase particles and thus yields a clean observation of the fundamental mechanisms involved. Nevertheless, if significant power is to be removed from the PBWR core maintaining a reasonably short chimney, large flow rates of the dispersed phase (i.e. water) are required and interference between contiguous dispersed phase particles (i.e. droplets, bubbles) becomes important. A transition from bubbly to intermittent flow is likely to occur at high water flow rates, which may cause a marked reduction of the interfacial area and consequently of the heat transfer rate.

Some preliminary insight into direct contact heat transfer can be indeed gained by considering the evolution of a single liquid water droplet (i.e. the dispersed fluid) in a hot stagnant liquid metal (i.e. the continuum fluid). A schematic of the regions and phenomena involved is illustrated in **Figure 3.1**, where for sake of generality it is assumed that the temperature of the droplet is initially below the saturation point at the system operating pressure. Let us focus on the stable phase transition sequence first.

In the subcooled region the water droplet remains mostly liquid and its temperature increases as the heat is supplied at the interface with the liquid metal. Depending on the bulk temperatures and the thermo-physical properties of both fluids, the temperature at the interface may quickly rise to the point where heterogeneous nucleation takes place and a stable vapor film is generated that blankets the subcooled liquid within the droplet (see **Section 3.4.1**). If this occurs the system exhibits three phases in the subcooled region: the liquid metal, the water vapor and the liquid water.

When the saturation temperature is achieved, a massive vaporization of the liquid water begins, the droplet/bubble rapidly expands and its shape may become rather irregular. Note that by definition three phases are present in the saturated region: the liquid metal, the water vapor and the liquid water.

The liquid water nucleus within the vapor bubble eventually dries out and only two phases are left: the liquid metal and the vapor bubbles, whose shape can greatly vary (e.g. spherical, ellipsoidal, cap-shaped, bullet-shaped) depending on the fluids, the droplet initial mass, the system geometry and operating conditions.

Under certain operating conditions, the vaporization of water can be very rapid and violent thus leading to fragmentation of the droplet and to the formation of a pressure shock wave that can damage the channel and/or the surrounding [Furuya 1996]. This phenomenon is known as steam explosion and must be prevented if a stable and controllable phase transition is to be obtained. However, steam explosion is thought to be a minor issue in our case primarily due to the high operating pressure of the PBWR. This issue will be briefly discussed in **Section 3.4.1.1**.

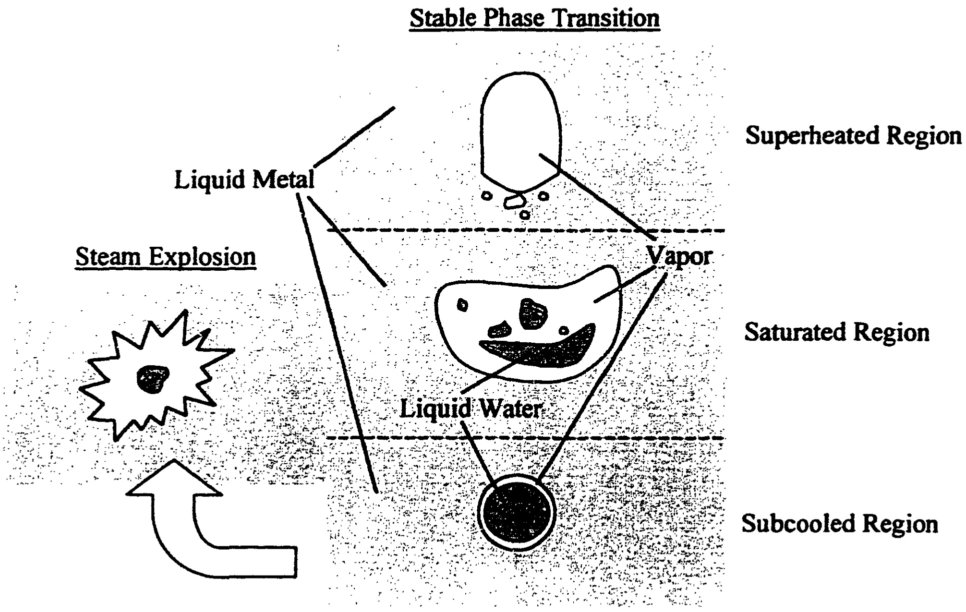

Figure 3.1. Direct contact vaporization of a single droplet.

3.2 The Volumetric Heat Transfer Coefficient

Let us now switch to a more realistic and practically useful situation where several particles (i.e. droplets or bubbles) of the dispersed fluid are present in the bulk of the continuum fluid. A schematic of this situation can be seen in **Figure 3.2**. Again we will refer to Pb-Bi and water as the continuum and dispersed fluid, respectively. Because the interfacial area is generally not known a priori, it is convenient to describe the direct contact heat transfer between the two phases as a volumetric phenomenon. This leads to the introduction of the so-called volumetric heat transfer coefficient (vhtc), which represents the rate of heat exchanged by the two fluids per unit volume of the flow and per unit temperature difference. Its SI units are W/m^3·K.

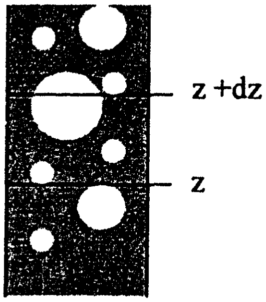

Figure 3.2. A multi-particle direct contact channel.

Knowledge of the vhtc is key to calculating the thermal performance of a direct contact heat exchanger (e.g. the chimney of the PBWR). To illustrate this point, let us write the steady-state energy conservation equations for the system of **Figure 3.2** where it is assumed that the dispersed (colder) fluid is the water and is experiencing a change of phase:

$$-\dot{m}_p c_p dT_p = h_v A(T_p - T_w)dz \qquad \textbf{Eq.3.1}$$

$$\dot{m}_w h_{fg} dx_w = h_v A(T_p - T_w)dz \qquad \textbf{Eq.3.2}$$

where $\dot{m}$ is the mass flow rate, T the temperature[1], x_w the steam quality[2], h_v the volumetric heat transfer coefficient and A the channel flow area. The subscripts p and w refer to the continuum and dispersed fluid, respectively. c_p and h_{fg} are the Pb-Bi specific heat and the water vaporization enthalpy, respectively. Note that in **Eq.3.1** and **Eq.3.2** h_v is actually a vhtc averaged over the flow area A.

If the value of h_v is known, the integration of **Eq.3.1** and **Eq.3.2** enables establishing the relationship between the inlet conditions of the fluids, their mass flow rates, the channel flow area and the length required to achieve target outlet conditions. For example, if **Figure 3.2** describes a Pb-Bi/water channel of the PBWR chimney and the mass flow rates and the inlet conditions are known, **Eq.3.1** and **Eq.3.2** can be used to predict the chimney length required to achieve complete water vaporization.

Therefore, it can be stated that the goal of the direct contact heat transfer analysis process is to find the value of the vhtc for the fluids and thermal-hydraulic conditions of interest. Ideally, it would be desirable to make use of correlations of proven accuracy for such conditions in a way similar to what is done for the surface heat transfer coefficient in the analysis of traditional thermal systems where the fluids are separated by a conductive wall, e.g. one uses the Dittus-Boelter correlation for single-phase internal forced convection or the Chen correlation for saturated boiling. Unfortunately, the database for direct contact heat transfer is not wide particularly for liquid metal/water systems at high pressure and temperature, i.e. the PBWR situation.

An alternative approach builds on the following definition of the vhtc:

---

[1] Note that in the case of saturated water, T_w is the saturation temperature of water, known if the system pressure is given.

[2] Defined as the flow rate of vapor over the total water flow rate (liquid + vapor).

$$h_v = ha_i \qquad \textbf{Eq.3.3}$$

where h is the local surface heat transfer coefficient (W/m^2K) and a_i is the interfacial area concentration (m^2/m^3), i.e. the interface area between the fluids per unit volume of the flow. The problem of finding the vhtc is then broken into the separated problems of finding the local surface heat transfer coefficient and the interfacial area concentration where a_i describes the internal geometric structure of the flow and the available area to transfer energy from one phase to another. Its value depends mainly on the droplet/bubble size, shape and number and therefore depends ultimately on the flow regime. The value of h also depends on the internal geometry of the flow, as well as on the relative velocity of the phases and on the thermodynamic conditions of the fluids (e.g. saturated vs. superheated water).

In this chapter we will try to estimate the value of h and a_i on the basis of mechanistic models of the hydraulic and thermal phenomena occurring in the PBWR chimney. The predictions so generated will be benchmarked with experimental data where possible.

3.3 Multi-Phase Flow

As already mentioned, the interfacial area concentration (and thus the vhtc) depends on the flow pattern. In this section the flow map of the Pb-Bi/water mixture at typical PBWR conditions (312°C and 7.0MPa) is derived from simple flow regime transition criteria (**Sections 3.3.1** and **3.3.2**). Then expressions are provided to estimate the void fraction and the interfacial area concentration for each relevant flow regime (**Sections 3.3.3** and **3.3.4**).

A fundamental assumption is made here that there is no velocity slip between the steam and the liquid water, i.e. the two water phases rise with the same velocity[3]. This is well justified by visual observations of the direct contact vaporization process of water in hot liquid metal at 0.1MPa, which show that water rises as two-phase bubbles where a liquid nucleus is always surrounded by a vapor film [Nishi 1998]. This assumption greatly simplifies the analysis because it allows treating the water effectively as one phase only characterized by a single velocity and a single density, ρ_w, given by the following expression:

$$\frac{1}{\rho_w} = \frac{x_w}{\rho_g} + \frac{1 - x_w}{\rho_f} \qquad \textbf{Eq.3.4}$$

---

[3] On the other hand, velocity slip between the two-phase water bubbles and the liquid metal is considered.

where ρ_g and ρ_f are the vapor and liquid water density, respectively and x_w is the steam quality, defined in **Section 3.2**. This assumption also enables making use of the traditional two-phase flow correlations for bubble rise velocity and void fraction treating the water and the liquid metal as the two phases, avoiding the complications of a third independently moving phase. Due to the large density of Pb-Bi compared to water (either liquid or vapor), we will call 'void fraction' the volume fraction of water in the chimney for all values of x_w.

It is emphasized here that the chimney is partitioned into 157 square channels each corresponding to a fuel assembly. Therefore the chimney hydraulic diameter[4] is approximately 26cm. Partitioning prevents bubble radial drifting hence yielding uniform mixture quality and heat transfer throughout the reactor chimney.

3.3.1 Flow Regime Transitions

At the bottom of the reactor chimney, the subcooled liquid water is injected in the lead-bismuth in the form of fine droplets. For all water flow rates of practical interest, the mean distance between these droplets is sufficiently large so that the droplet interaction (e.g. droplet coalescence) can be neglected. Although a thin vapor film will rapidly develop around the droplet as a result of homogeneous nucleation induced by the high Pb-Bi temperature, the size of the droplets does not change significantly because the droplet bulk remains liquid. Under these circumstances, the mixture displays an ideal bubbly flow pattern, with small spherical bubbles steadily rising at a more or less fixed distance between the bubbles.

When the temperature of the liquid nucleus reaches saturation, a vigorous vaporization is initiated. The droplet/bubble size begins to increase as does the flow void fraction. The flow regime remains bubbly until the mean distance between contiguous bubbles is so small that the rate of coalescence becomes significant and bubbly flow gradually disappears. At this stage there is considerable bubble entrainment and larger bubbles are formed that move at a higher velocity than in bubbly flow. The flow becomes agitated and unsteady. Smaller bubbles are also formed by break-up of the larger bubbles due to collision with turbulent eddies and/or by shear off at the bubble periphery. These two competing effects (bubble coalescence and break-up) result in an intermittent flow, where roughly two groups of bubbles are present: (i) large bubbles whose

---

[4] Note that in a square channel the hydraulic diameter (4*flow area/wetted perimeter) is equal to the square side.

shape markedly deviates from spherical and (ii) small spherical/ellipsoidal bubbles [Fu 2000] flowing in the wake of the large bubbles. If the large bubbles occupy the whole channel flow area and have a bullet elongated shape, the intermittent flow is called "slug flow". If the channel diameter is large, the bullet-shaped bubbles are not stable and slug flow does not occur. Instead the bubbles have a cap hemispherical shape of diameter significantly smaller than the channel diameter and the intermittent flow is called "cap flow". The transition to intermittent flow results in a larger average velocity of the bubbles and generally in a marked reduction of the interfacial area between water and Pb-Bi due to the presence of the large bubbles whose surface to volume ratio is small.

If the volumetric flow rate of the dispersed phase further increases, the large bubbles begin to agglomerate and create a central water streaming and channeling region where elongated irregular filaments of dispersed fluid are present (this is the so-called "churn flow") until the transition to an actual annular flow takes place, where most liquid metal is displaced to the channel wall and a continuum steam/liquid water core flows in the middle of the channel.

Several criteria have been proposed in the past to assess the relative boundary of the aforementioned flow regimes. The use of these criteria enables generating a flow map that can be used to roughly identify the geometry of the flow and thus to model the interfacial area and the local surface heat transfer coefficient.

3.3.1.1 Bubbly Flow Boundary

Radovich and Moissis [1962] examined the behavior of an idealized model of bubbly flow and came to the conclusion that, for void fractions below 0.1, the bubble collision frequency is relatively low. Above this value the frequency rises steeply until, at void fraction equal to 0.3, the rate of collision and coalescence is so large that a rapid transition to intermittent flow is expected.

Assuming rectangular packing of spherical bubbles Taitel [1980] postulated that significant coalescence in bubbly flow occurs when the distance between the surface of two contiguous bubbles falls below half bubble radius. This results in a void fraction of about 0.25 at the bubbly to intermittent flow transition. On the other hand, Mishima and Ishii [1984] assumed tetrahedral bubble packing and postulated that coalescence occurs when the gap between the surface of two bubbles is less than a bubble diameter and, consequently, they identified the bubbly to intermittent transition at a void fraction of about 0.3.

Visual observations reported by Kataoka and Ishii [1987] indicated that, at reduced superficial velocities above 0.5, large slug and cap bubbles appear. The reduced superficial velocity of interest is dimensionless and defined as:

$$j_w^+ = \frac{j_w}{\left[\frac{\sigma g(\rho_p - \rho_w)}{\rho_p^2}\right]^{0.25}} \qquad \textbf{Eq.3.5}$$

where g, σ and ρ_p are the gravity acceleration, the continuum phase surface tension and density, respectively. j_w is the superficial velocity of the dispersed phase (in our case water).

The intermediate flow pattern between bubbly and intermittent flow is sometimes called "churn-turbulent" [Wallis 1969, Zuber 1965]. Wallis proposed that this intermediate flow regime (characterized by significant entrainment of the bubbles in each other's wake) begins when the bubble diameter reaches a critical value, D_{cr}, given by the following expression:

$$D_{cr} = 4\sqrt{\frac{\sigma}{g\rho_p}} \qquad \textbf{Eq.3.6}$$

In reference [Kim 2000] the transition to "churn-turbulent" is assumed to occur at a void fraction around 0.05. However, depending on the injection mode, ideal bubbly flow with little or no coalescence can be maintained for void fractions up to 0.3, as illustrated in [Wallis 1969].

It can be seen that there is significant discrepancy between the different criteria. This is due to the fact that the identification of a flow regime is somewhat subjective, which results in large uncertainties when it comes to establishing criteria for the transition between one flow regime and another. The degradation of ideal bubbly flow is likely to begin at fairly low void fractions (perhaps as low as 0.05) and there seems to be general agreement that at void fractions above 0.3 the transition to intermittent flow is complete. Therefore, in modeling the interfacial area concentration, we will interpolate between the ideal bubbly flow geometry and the intermittent flow geometry conservatively assuming that the transition starts at 0.05 and is completed by 0.3 (see **Section 3.5**). However, for the purpose of generating the flow regime map we will adopt the intermediate 0.25 void fraction transition criterion proposed by Taitel, which is recommended in recent well-known text-books [Todreas 1990, Collier 1996].

Taitel noticed that this criterion holds only at low flow rates of the continuum fluid. At higher flow rates, bubble break-up is dominant and a stable bubbly flow can exist up to a void fraction of approximately 0.52. This latter flow regime is sometimes called "finely dispersed bubbly flow". Taitel proposed that finely dispersed bubbly (as opposed to bubbly) flow exists when the stable maximum diameter $D_{disp,max}$ of the dispersed bubbles is less than a critical diameter $D_{disp,cr}$. Expressions for $D_{disp,max}$ and $D_{disp,cr}$ are [Collier 1996]:

$$D_{disp,max} = \left(0.725 + 4.25\beta^{0.5}\right)\left(\frac{\sigma}{\rho_p}\right)^{0.6} K^{-0.4} \qquad \textbf{Eq.3.7}$$

$$D_{disp,cr} = 2\left[\frac{0.4\sigma}{g(\rho_p - \rho_w)}\right]^{0.5} \qquad \textbf{Eq.3.8}$$

where β is the water volumetric flow fraction (see **Eq.3.23**) and K is the rate of energy dissipation per unit mass:

$$K = \frac{2f_{TP}}{D} j^3 \qquad \textbf{Eq.3.9}$$

D is the channel equivalent diameter, j is the total superficial velocity (see **Eq.3.24**) and f_{TP} is the friction factor of the Pb-Bi/water mixture. For simplicity f_{TP} is given here by the HEM model [Todreas 1990].

3.3.1.2 Intermittent Flow Boundary

The existence of bullet shaped bubbles in large diameter channels was questioned by Kataoka and Ishii in their study on void fraction for a pool situation [Kataoka 1987]. The drift-flux correlation they proposed implies that the maximum stable bubble diameter is:

$$D_{max} = 30\sqrt{\frac{\sigma}{g(\rho_p - \rho_w)}} \qquad \textbf{Eq.3.10}$$

Therefore, if the channel equivalent diameter is smaller than D_{max}, slug flow can develop, otherwise cap flow will be present with cap bubbles of diameter approximately equal to D_{max}. At PBWR conditions[5] D_{max} is about 6cm, whereas the chimney channel equivalent diameter is 26cm. Thus, slug flow with bullet shaped bubbles can be ruled out. Rather cap flow will exist.

---

[5] Note that in **Eq.3.10** the water density can be neglected with respect to the Pb-Bi density. Therefore, D_{max} does not depend on the steam quality x_w.

A transition from intermittent to annular flow occurs when the dispersed phase superficial velocity increases further. Again several criteria to describe this transition were proposed in the past [Wallis 1969, Taitel 1980]. Because it is anticipated that the PBWR chimney will not operate near the annular flow, an accurate identification of this transition is not needed. Therefore, we will make use of the simple criterion proposed by Wallis [1969] and recommended in reference [Collier 1996] for first order estimates. Then the transition to annular flow occurs when:

$$j_w > 0.9\sqrt{\frac{gD(\rho_p - \rho_w)}{\rho_w}} \qquad \textbf{Eq.3.11}$$

3.3.2 The Flow Map

Figure 3.3 shows how the above criteria can be used to generate a flow map for the conditions of interest. The two variables selected to describe the flow are the Pb-Bi superficial velocity j_p and the water superficial velocity j_w. Note that the flow regime boundaries depend on the water density and therefore on the steam quality x_w (e.g. see **Eq.3.8** and **11**). Therefore, in principle a set of curves for different values of the water density should be drawn for each transition in **Figure 3.3**. However, to simplify the map, only the boundaries for x_w=1 (i.e. dry steam) were drawn.

The bubbly and finely dispersed bubbly to intermittent flow criteria, which are based on the void fraction (α_{trans} equal 0.25 and 0.52, respectively), were converted into a superficial velocity criterion by assuming uniform void and velocity distribution across the channel and a water drift velocity u_{wj} equal to $1.53\left[\frac{\sigma g(\rho_p - \rho_w)}{\rho_p^2}\right]^{0.25}$ as recommended by Zuber [1965] for bubbly flow. Then the drift flux theory yields the following relationship between j_p and j_w at the flow transition:

$$j_p = \frac{1-\alpha_{trans}}{\alpha_{trans}} j_w - u_{wj} \qquad \textbf{Eq.3.12}$$

Figure 3.3 also shows line A describing the flow regime evolution within the chimney channel as the water progressively vaporizes and its superficial velocity (which is inversely proportion to density) increases. Line A is drawn for the reference conditions $\dot{m}_p$=517kg/s and

$\dot{m}_w$=4.4kg/s. It will be shown in **Chapter 4** that these values are the mass flow rates at the nominal conditions selected for the PBWR chimney channels. It can be seen that upon vaporization a transition from bubbly to intermittent flow occurs, more specifically a transition to cap flow, as explained in **Section 3.3.1.2**. **Figure 3.3** shows that the PBWR reference conditions are well within the bubbly/intermittent region and far from the annular and finely dispersed bubbly flow regions.

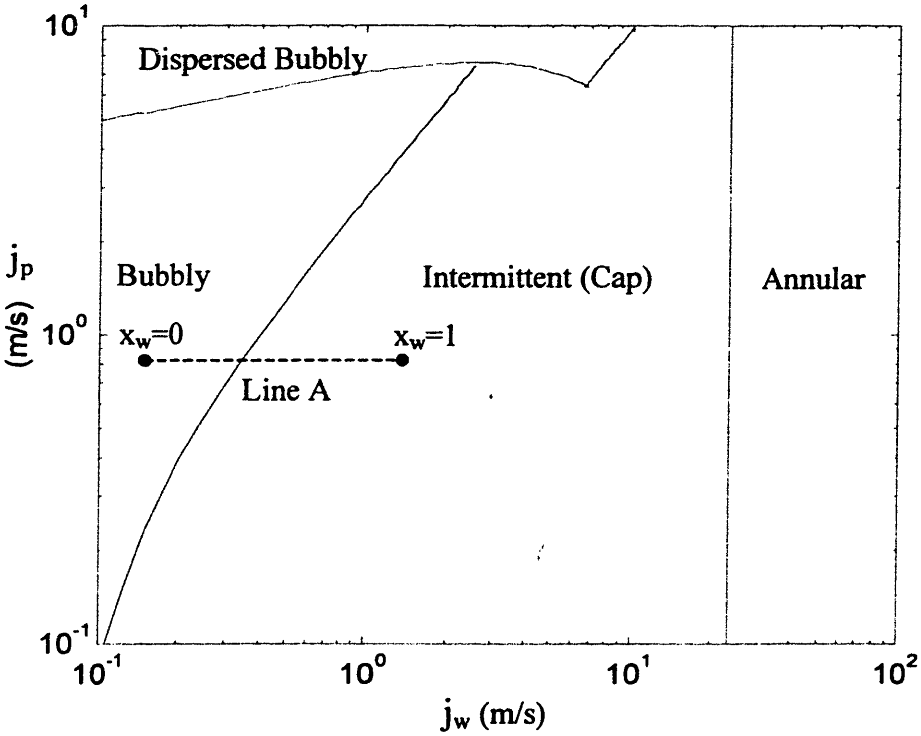

Figure 3.3. The PBWR chimney flow map (P=7.0MPa, 312°C, D=0.26m).

To increase the thermal efficiency of the system and to reduce the erosion damage of the turbine, it is desirable to achieve a certain degree of steam superheat in the chimney. At the end of this chapter it will be shown that, even at modest values of the steam superheat, the length of the saturation region is significantly smaller than the length of the superheat region due to the inferior heat transfer characteristics of the latter. This means that the majority of the chimney channel is occupied by the superheated region, whose flow regime is intermittent (see rightmost end of line A in **Figure 3.3**). As a result, the knowledge of the void fraction for intermittent flow is key to predicting (i) the natural circulation flow in the primary circuit, (ii) the interfacial area concentration and thus the heat transfer rate in the majority of the chimney. Therefore, the next section of this chapter deals with the selection of an adequate void fraction correlation to be used for high temperature high pressure Pb-Bi/steam intermittent flow in large channels.

3.3.3 Void Fraction Prediction in the PBWR Chimney

Most models and correlations for the prediction of the void fraction in two-phase flow were developed only for steam/water and air/water systems. The considerably different thermo-physical properties (e.g. density and surface tension) of liquid metal/steam mixtures makes the application of these water based correlations to the PBWR chimney open to question.

3.3.3.1 The El-Boher/Lesin Correlation

To the author's knowledge, there is only one void fraction correlation whose database contains a significant amount of heavy liquid metal/steam experimental points for vertical upflow. This is the El-Boher/Lesin Correlation (EBLC), which is given by the following equation:

$$\alpha = \frac{1}{\left[1 + 0.27 Q_R^{-0.69} Fr^{-0.177} \left(\frac{\mu_p}{\mu_w}\right)^{0.378} \left(\frac{\mathrm{Re}}{We}\right)^{0.067}\right]}$$ **Eq.3.13**

The non-dimensional numbers are calculated as:

$Q_R = x\rho_p / [(1-x)\,\rho_w] = j_w / j_p$ **Eq.3.14**

$Fr = j_p^2/(gD)$ **Eq.3.15**

$Re = \rho_p j_p D/\mu_p$ **Eq.3.16**

$We = j_p^2 \rho_p D/\sigma$ **Eq.3.17**

where μ_p is the Pb-Bi dynamic viscosity and x is the flow quality defined as:

$$x = \frac{\dot{m}_w}{\dot{m}_w + \dot{m}_p}$$ **Eq.3.18**

The EBLC was developed on the basis of the data collected at the Pb-Bi/steam facility ETGAR-3 of the Ben Gurion University in Israel [El-Boher 1988]. The main ETGAR-3 thermal-hydraulic parameters are reported in **Table 3.I**[6]: within this range, **Eq.3.13** predicts the void fraction with a reported accuracy of approximately ±10%. It was shown in reference [Buongiorno 2000] that most ETGAR-3 experimental data lie in the intermittent region with a significant 'tail' in the bubbly flow region. However, the temperature and pressure at which the ETGAR-3 experiments were conducted are very different from those of the PBWR chimney.

Table 3.I. ETGAR-3 thermal-hydraulic conditions.

Fluids: Pb-Bi and steam
$T = 160°C$
$P = 0.35$ MPa
$D = 0.2$ m; $L = 7$ m
$j_p = 0.6 - 2.0$ m/s; $j_w = 0.1 - 8.0$ m/s
$G = 6{,}000 - 20{,}000$ kg/s m^2; $x = 3\times10^{-5} - 8\times10^{-4}$

Moreover, in vertical two-phase flow the phase relative velocity is a strong function of the density of the two phases. **Table 3.II** reports the value of the density ratio for several different systems relevant to this study. It should be noted that, based on the density ratio, the PBWR reactor two-phase flow is substantially different from ETGAR-3 or a traditional BWR and is more hydrodynamically similar to a low pressure water/air system. It is therefore expected that, when applied to the PBWR conditions, the EBLC (valid for the high ρ_p/ρ_w ETGAR-3 conditions) will systematically over-predict the relative velocity and thus under-predict the void fraction. On the other hand, the correlations of proven accuracy for BWR thermal-hydraulic conditions are expected to under-predict the relative velocity and over-predict the void fraction.

Table 3.II. Hydrodynamic relevant parameters of two-phase systems.

	ETGAR-3	**Air/Water**	**PBWR**[7]	**BWR**
P (MPa)	0.35	0.35	7.0	7.0
ρ_p/ρ_w	~ 6,000	~ 250	~ 250	~ 20
D (m)	0.2	N/A	~ 0.2	~ 0.02

---

[6] L designates the channel length and G the mixture mass flux, i.e. $G=\frac{\dot{m}_w+\dot{m}_p}{A}$.

[7] The density ratio reported here is calculated assuming $x_w=1$.

Also, it should be noted that **Eq.3.13** is a purely empirical correlation. It is not based on a hydrodynamic model (e.g. drift-flux or HEM) and its coefficients do not change with the flow regime. For all the above reasons, the extrapolation of the EBLC beyond the conditions of **Table 3.I** is not prudent and needs to be justified.

3.3.3.2 Other Void Fraction Correlations

In the quest for a predictive tool suitable to the PBWR conditions, several other void fraction correlations for intermittent flow are considered in this study. Mostly they are based on the drift-flux model. In this type of correlation the void fraction is expressed as:

$$\alpha = \frac{\beta}{C_0 + u_{wj}/j} \qquad \textbf{Eq.3.19}$$

Each of the correlations selected provides an expression for the coefficients C_0 and u_{wj}, which can be found in the reported references.

The correlations considered are:

- Zuber-Findlay slug flow [1965]. This model assumes that the diameter of the bullet-shaped bubbles in slug flow is equal to the channel diameter. However, as already mentioned, the existence of big bullet-shaped bubbles in large diameter channels is questionable as shown by the visual observations in [Kataoka 1987] and [Kawanishi 1990].
- Zuber-Findlay churn flow [1965]. This model assumes that at high vapor superficial velocity large bubbles are unstable because they are broken by turbulent eddies. The maximum diameter of the resulting smaller bubbles is determined by the surface tension.
- EPRI [Chexal 1992]. This correlation was benchmarked against a wide range of steam/water and water/air data [Chexal 1991 and 1992]. The authors claim it can be applied to all flow regimes, at any pressure, mass flux and channel diameter. However, at very low void fraction (i.e.<0.1, typical of bubbly flow) it yields a global slip ratio smaller than one. This might result from a prevalence of water subcooled boiling data in the low void fraction region of the correlation database.
- Ishii-Kataoka-Rouhani (IKR). It was initially developed by Ishii-Kataoka [Kataoka 1987] for pool systems only. When adapted by Rouhani to flow systems [Rouhani 1992] the expression for the Ishii-Kataoka vapor drift velocity u_{wj} was retained, but a new expression for the distribution parameter C_0 was adopted (given by the modified Rouhani correlation [Rouhani

1969]). In this model particular attention is given to the effect of the channel diameter on the size, shape and velocity of the rising bubbles. Experiments with large diameter channels [Kataoka 1987, Kawanishi 1990] indicate that there is a maximum stable size of the bubbles, independent of the channel diameter (see also discussion in **Section 3.3.1.2** of the present chapter). Moreover, due to the turbulence of the two-phase flow, these bubbles display significant deviation from the ideal bullet shape of a slug bubble. Also they appear to rise at higher velocity than predicted by the theory for bullet-shaped bubbles [Zuber 1965].

- Kawanishi [1990]. This correlation is meant for steam/water systems only and its dependence on the pressure is dimensional. For application to our Pb-Bi/steam two-phase flow, we inserted in the correlation the value of the pressure that makes the steam/water density ratio equal to PBWR density ratio.
- Corradini-Casas [1992]. This correlation was developed for low pressure heavy liquid metal/steam pool conditions, typical of core-melt accident analysis in nuclear reactors (e.g. corium/concrete interactions). In these systems the density ratio is large (i.e. $\rho_f/\rho_g \approx$ 6,000) and significantly differs from that of the PBWR (see **Table 3.II**). Because it is based on relatively shallow pool experimental data, an effect of the pool height was observed on the radial distribution of voids. As the bubbles move upward, they tend to drift to the pool center thus increasing the distribution coefficient C_0. However, in adiabatic steady-state long channels (L/D>10) the flow is expected to be fully-developed and little dependence on the channel length (or on the mode of vapor injection) should be observed. Therefore, to make the correlation suitable to two-phase flow in long channels the value of the distribution parameter was arbitrarily assumed independent of the pool height and equal to the maximum value in Corradini's experiment.
- Dix [1971]. This correlation was mainly developed for LWR applications. It assumes there is no local slip between the two phases but it allows for a radial distribution of void and velocity. Effectively, it is a drift-flux correlation where u_{wj} is set equal to zero. The Dix model does not display a dependence on the channel diameter and the mass flux.
- Homogeneous Equilibrium Model (HEM). Because the global slip ratio is set equal to one, the HEM prediction represents the physically acceptable upper limit to the value of the void fraction since a value of the slip ratio smaller than unity is physically unacceptable (see **Section 3.3.3.3**). Effectively, it can be obtained from a drift-flux correlation where u_{wj} and C_0

are set equal to zero and one, respectively. HEM does not display a dependence on the channel diameter and the mass flux.

A summary of the essential characteristics of all the correlations considered in this study is reported in **Table 3.III**.

Table 3.III. The correlations for intermittent flow regime.

Correlation	Type	Database			
		Fluid	Flow Regime	Pressure (MPa)	Diameter (m)
Zuber-Findlay (slug)	Drift-flux	Steam/water air/water	Intermittent (slug)	0.1-18.0	0.05-0.6
Zuber-Findlay (churn)	Drift-flux	Steam/water air/water	Intermittent (churn)	0.1-18.0	0.05-0.6
EPRI	Drift-flux	Steam/water Air/water	All flow regimes	0.1-18.0	0.005-0.5
IKR	Drift-flux	Steam/water air/water	Bubbly, Intermittent	0.1-18.0	0.01-0.6
Kawanishi et al.	Drift-flux	Steam/water	Bubbly, Intermittent	0.5-1.5	0.02-0.1
Corradini-Casas	Drift-flux	Nitrogen/heavy metal	Bubbly, Intermittent (churn)	0.1	0.15
EBLC	Empirical	Steam/heavy metal	Bubbly, Intermittent	0.35	0.2
Dix	No local slip	Steam/water	All flow regimes	1.0-7.0	N/A
HEM	No global slip	N/A	N/A	N/A	N/A

3.3.3.3 Testing the Acceptability of a Void Fraction Correlation

The application of any of the above void fraction correlations to the PBWR chimney conditions represents an extrapolation beyond their database. We shall now present a rather general methodology, which enables evaluating the acceptability of a void fraction correlation when it is desirable to use it beyond the range of its experimental database.

The correlation is to be tested against six postulated criteria. The goal is to establish the "domain of physically acceptable applicability", i.e. the region of the flow map where the correlation can be meaningfully utilized. It should be emphasized that this domain does not define a region where the correlation is accurate, but only one where the correlation does not produce results in contradiction with the known characteristics of two-phase vertical upflow.

To establish the "domain of physically acceptable applicability", the correlation is tested against six criteria that fit the conditions under investigation:

1) $S \geq 1$. Because the density of the vapor phase is smaller than the density of the liquid phase, the global slip ratio must be greater than unity in adiabatic fully-developed steady-state vertical upflow. Clearly, this criterion does not necessarily hold for heated channels where subcooled boiling occurs (e.g. in the subcooled region of the steam/water channels of a BWR): in this case the bubbles are created at the heated wall and remain relatively close to it (where the velocity is low). As a result the global slip can be smaller than unity.

2) $\lim\limits_{G \to \infty} S = 1$ (in dispersed bubbly flow). At high mass flux, only small diameter bubbles exist (because bigger bubbles are broken and dispersed by turbulent eddies), the effect of gravity is small and the local slip ratio must approach unity. Moreover, at high mass flux the radial velocity profile is flat. Therefore, the global slip ratio must also approach unity.

3) $\left(\dfrac{\partial \alpha}{\partial x}\right)_G > 0$. For a given mass flux, an increase of the flow quality must cause an increase of the void fraction.

4) $\left(\dfrac{\partial \alpha}{\partial G}\right)_x > 0$. For a given flow quality, an increase of the mass flux flattens the radial velocity profile in the channel, reduces the global slip ratio hence causing an increase of the void fraction. Again it should be noted that this criterion does not necessarily hold for diabatic flows (e.g. subcooled boiling) where the bubbles may be concentrated in the region of low velocity near the wall.

5) $\dfrac{x}{\alpha}\left(\dfrac{\partial \alpha}{\partial x}\right)_G > \dfrac{G}{\alpha}\left(\dfrac{\partial \alpha}{\partial G}\right)_x$. This criterion postulates that the void fraction must primarily depend on the quality and only to a smaller extent on the mass flux. In other words, it is postulated that the effect described in 3) must be dominant over the effect described in 4).

6) $\dfrac{\partial(\beta/\alpha)}{\partial(1/j)} = u_{wj} > 0$. The drift flux velocity of the vapor phase u_{wj} (i.e. the terminal velocity of a vapor bubble in the stagnant liquid) must be positive.

It should be noted that the above criteria are postulated for adiabatic fully-developed steady-state two-phase upflow only (i.e. the dispersed phase is not concentrated at the channel wall), which is applicable to the PBWR chimney situation.

A second class of more general formal criteria to test the acceptability of a void fraction correlation was proposed by Chexal et al. [Chexal 1991]. However, these criteria are not relevant to the present study because they address:

- the $x \to 1$ and $P \to 0$ limits, which are clearly beyond the range of interest of PBWR applications,
- the $P \to P_{crit}$ limit, which is not meaningful for a two component mixture, since generally there is no pressure at which the two phases will share the exact same thermophysical properties.

To illustrate the methodology, let us now apply the testing criteria to the EBLC. **Eq.3.13** can be rewritten as:

$$\alpha = \frac{1}{1 + K \dfrac{(1-x)^{0.269}}{x^{0.69} G^{0.421}}} \qquad \textbf{Eq.3.20}$$

where $K = 0.27 \dfrac{\rho_w^{0.69} \mu_p^{0.311} (gD)^{0.177} \sigma^{0.067}}{\rho_p^{0.269} \mu_w^{0.378}}$

Recalling that by definition the slip ratio, S, is:

$$S = \frac{x}{1-x} \frac{1-\alpha}{\alpha} \frac{\rho_p}{\rho_w}, \qquad \textbf{Eq.3.21}$$

Eq.3.20 yields:

$$S = K \frac{x^{0.31}}{(1-x)^{0.731} G^{0.421}} \frac{\rho_p}{\rho_w} \qquad \textbf{Eq.3.22}$$

It is also useful to recall the following definitions to test the EBLC against criterion 6):

$$\beta = \frac{1}{1 + \dfrac{1-x}{x} \dfrac{\rho_w}{\rho_p}} \qquad \textbf{Eq.3.23}$$

$$j = \left(\frac{x}{\rho_w} + \frac{1-x}{\rho_p} \right) G \qquad \textbf{Eq.3.24}$$

$$j_p = \frac{1-x}{\rho_p} G \qquad \textbf{Eq.3.25}$$

$$j_w = \frac{x}{\rho_w} G \qquad \textbf{Eq.3.26}$$

By means of **Eq.3.20, Eq.3.23** and **Eq.3.24** the following relations are derived for the β/α ratio:

$$\frac{\beta}{\alpha} = f(x,j) = \frac{1}{1+\frac{1-x}{x}\frac{\rho_w}{\rho_p}}\left[1 + K\frac{(1-x)^{0.269}}{x^{0.69} j^{0.421}}\left(\frac{x}{\rho_w}+\frac{1-x}{\rho_p}\right)^{0.421}\right] \qquad \textbf{Eq.3.27}$$

$$\frac{\beta}{\alpha} = f(G,j) = \frac{\rho_p - \frac{G}{j}}{\rho_p - \rho_w}\left[1 + \frac{K}{G^{0.421}}\left(\frac{\rho_p}{\rho_w}-1\right)^{0.421}\frac{\left(\frac{\rho_p}{\rho_w}+\frac{j\rho_p}{G}\right)^{0.421}}{\left(\frac{j\rho_p}{G}-1\right)^{0.69}}\right] \qquad \textbf{Eq.3.28}$$

Note that, because the testing criteria are expressed in terms of the variable G and x, their geometric representation is more straightforward in the G-x plane, as opposed to the j_p-j_w plane. We emphasize that the two planes are entirely equivalent because, for given temperature and pressure, there is a one-to-one relation between the two sets of variables, as indicated by **Eq.3.25** and **26.**

Therefore:

- Setting S=1 in **Eq.3.22** a line can be plotted in the G-x plane above which S<1 and the EBLC cannot be used (see **Figure 3.4**)[8].
- For G approaching infinity, S approaches zero. Therefore, the EBLC cannot be used in dispersed bubbly flow because it does not display the correct asymptotic behavior given by criterion 2).
- Performing the proper derivatives of **Eq.3.20** it can be proven that the correlation fulfills criteria 3), 4) and 5) for any G and x.

---

[8] Again it must be emphasized that the density of the dispersed phase ρ_w is calculated assuming x_w=1.

- **Eq.3.27** yields $\left[\frac{\partial(\beta/\alpha)}{\partial(1/j)}\right]_x > 0$ for any G and x. On the other hand, taking the derivative of **Eq.3.28** with respect to 1/j and setting it equal to zero, a line can be plotted in the G-x plane below which $u_{wj}<0$ and the EBLC cannot be used (see **Figure 3.4**).

In addition to the region of applicability defined by the above criteria, it is also assumed that the EBLC cannot be utilized in annular flow because it is not based on experimental data in this flow regime. Then, the shaded area in **Figure 3.4** represents the "domain of physically acceptable applicability" of the EBLC for the PBWR conditions of 312°C, 7.0MPa and D=0.26m. It can be seen that the application of the testing criteria restricts the use of the EBLC to a relatively small region of the G-x plane where intermittent flow is the dominant flow regime. Therefore, at this pressure and temperature, the EBLC cannot be used to predict the void fraction of Pb-Bi/steam mixtures in bubbly, dispersed bubbly or annular flow.

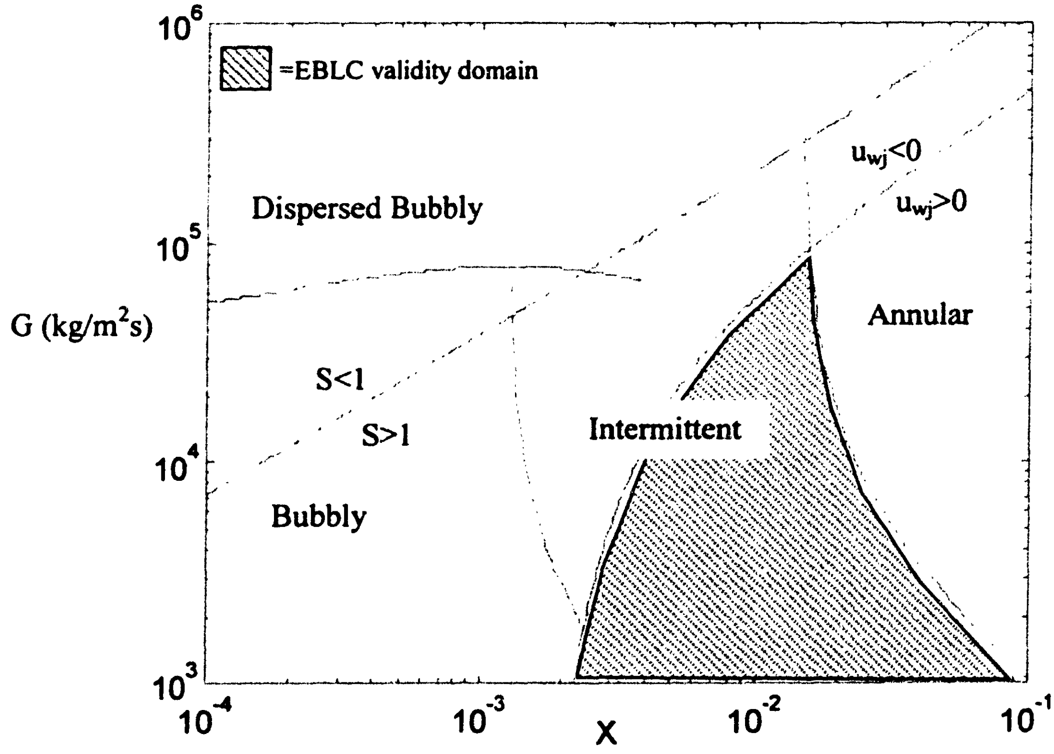

Figure 3.4. The domain of physically acceptable applicability of the EBLC correlation.

We can now test the other correlations against the proposed criteria. All drift-flux correlations satisfy criterion 6) by definition. Due to the way they are constructed they also satisfy criteria 3), 4), 5) and 6), as can be readily demonstrated by performing the proper derivatives of **Eq.3.19** (see **Appendix E**). Substituting **Eq.3.19** in **Eq.3.21** it can be proven that the global slip ratio S is larger or equal than unity if the following relation holds:

$$(C_0 - 1) + \frac{u_{wj}}{j} \geq 0 \qquad \textbf{Eq.3.29}$$

All the drift-flux correlations considered yield $C_0>1$ for intermittent upflow because in this flow regime the voids are not concentrated at the wall. Hence, since criterion 6) is also satisfied as stated above, **Eq.3.29** implies that the drift-flux correlations also satisfy criterion 1). As for criterion 2), it is not considered here because we mainly focus on intermittent flow. We shall just observe that **Eq.3.29** suggests that, when $G\rightarrow\infty$ (i.e. $j\rightarrow\infty$), the slip ratio equals one only if $C_0=1$. Therefore, to correctly predict the void fraction in dispersed bubbly flow, a drift-flux correlation must yield $C_0=1$ in the limit of high mass flux.

As for the final two correlations, the Dix correlation satisfies criterion 3), but, at low void fraction, not criterion 1). It does not satisfy criterion 2) either. The HEM model satisfies criteria 1), 2) and 3). Criteria 4), 5) and 6) do not apply to HEM and Dix because the void fraction is not a function of the mass flux in these models.

In **Figure 3.5** the void fraction is plotted against the mass flow quality at reference mass flux (i.e. G=7600kg/m^{2}s) and nominal conditions (i.e. T=312°C, P=7.0MPa and D=0.26m). In **Figure 3.6** the void fraction is plotted against the mass flux for reference quality (i.e. x=0.0084) and again at nominal PBWR conditions. As expected, the modified Corradini-Casas and EBLC correlations (based on heavy liquid metal/gas data at low pressure) mostly predict a smaller void fraction than the water-based correlations.

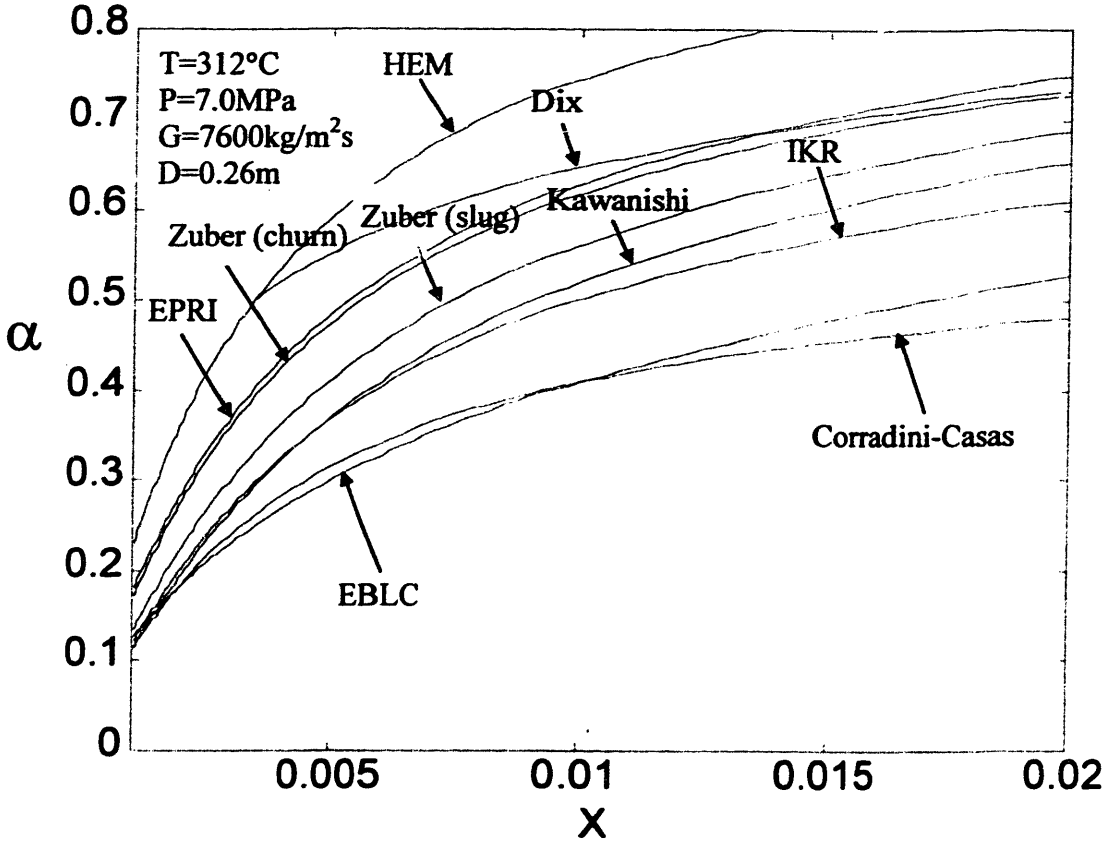

Figure 3.5. The quality effect on the void fraction.

Surprisingly, large differences (up to 40%) are observed between the IKR, the Zuber-Findlay, the EPRI and the Kawanishi correlations at 7600 kg/m^{2}s. Even larger discrepancies (up to 130%) between the same correlations are observed at low mass flux (see **Figure 3.6**), with the EPRI correlation predicting the largest void fraction, hence the smallest slip ratio. However, under these low mass flux conditions (i.e. G=1000 kg/m^{2}s) the system is hydrodynamically similar to a pool situation (i.e. vapor bubbling through a stagnant liquid) and the low value of the relative vapor drift velocity u_{wj} predicted by the EPRI, the Zuber (slug) and Zuber (churn) correlations is in conflict with the large diameter channel experiments in references [Kataoka 1987, Kawanishi 1990]. On the other hand, at high mass flux (i.e. G=10000 kg/m^{2}s) the differences among the water-based drift-flux correlations are small (i.e. within 20%), as illustrated in **Figure 3.6**, indicating that they all predict similar values of the distribution parameters C_0 [9].

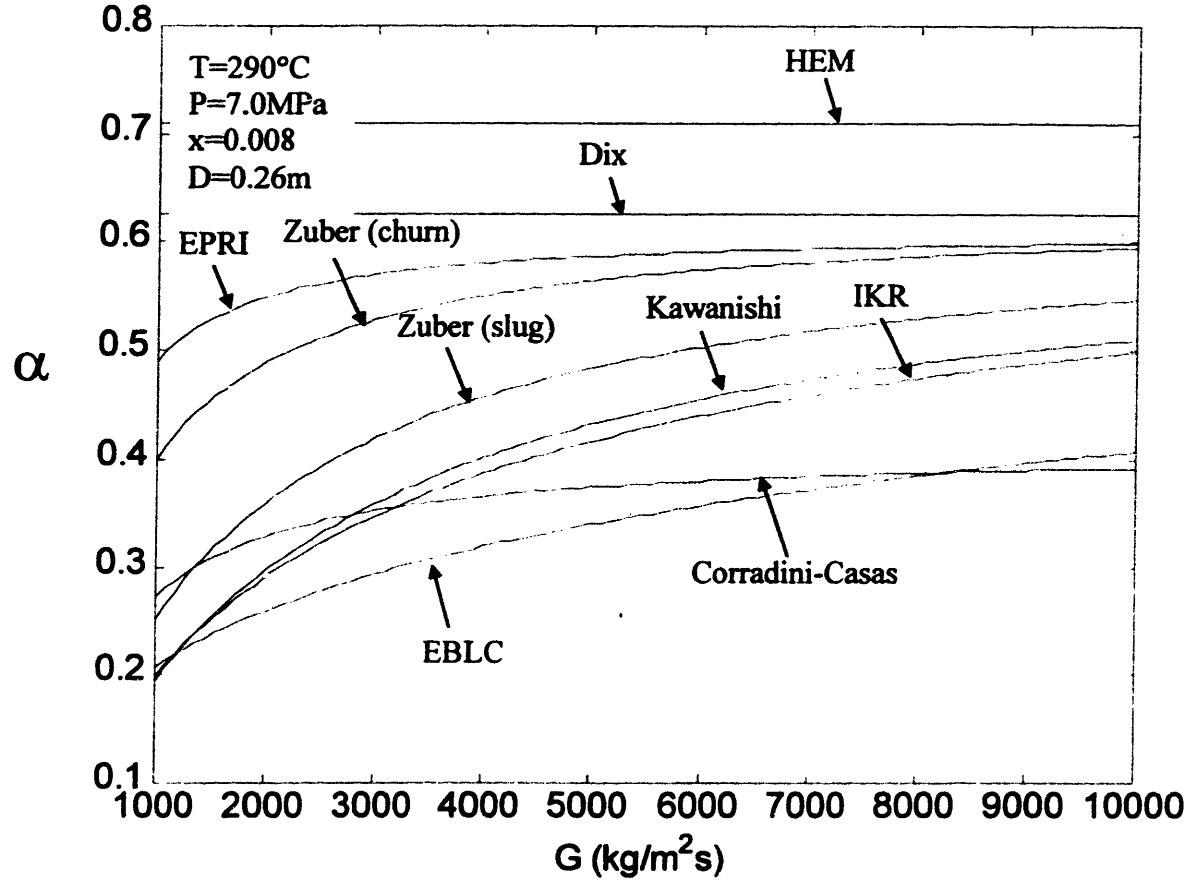

Figure 3.6. Mass flux effect on the void fraction.

The following recommendations are made:

- Given the significant discrepancies observed between the correlations considered in this study, an experimental assessment of the void fraction under typical PBWR conditions is strongly recommended (see **Appendix C**).
- For interim calculations, the EBLC should be used when a conservatively low prediction of the void fraction at PBWR conditions is required, but never outside its domain of applicability because it becomes physically unacceptable (see **Figure 3.4**).

---

[9] From **Eq.3.19** it can be seen that, at high G (i.e. high j), the void fraction depends mainly on C_0 and not on u_{wj}.

- The IKR correlation should be used when a more realistic assessment is required. The IKR correlation was chosen over the Zuber-Findlay and the EPRI correlations due to its emphasis on the channel diameter effect (i.e. the impossibility of establishing slug flow in a large diameter channel), its relative simplicity (as opposed to the complexity of the EPRI correlation) and its good agreement with experiments at low mass flux. Moreover, the IKR correlation was chosen over the Kawanishi correlation because the pressure dependence of the former is non-dimensional.

3.3.3.4 The Ishii-Kataoka-Rouhani Correlation

Because the IKR correlation has been selected as our preferred void fraction correlation, we will now report the equations that define it. The dispersed phase drift velocity u_{wj} to be used in **Eq.3.19** for large diameter channels (defined by **Eq.3.10**) is:

$$u_{wj} = 0.03\left[\frac{\sigma g(\rho_p - \rho_w)}{\rho_p^2}\right]^{0.25}\left(\frac{\rho_p}{\rho_w}\right)^{0.157} N_{\mu p}^{-0.562} \qquad \textbf{Eq.3.30}$$

where $N_{\mu p}$ is defined as:

$$N_{\mu p} = \frac{\mu_p}{\sqrt{\rho_p \sigma \sqrt{\dfrac{\sigma}{g(\rho_p - \rho_w)}}}} \qquad \textbf{Eq.3.31}$$

The distribution parameter C_0 is given by the following expressions:

$$C_0 = C_\infty - (C_\infty - 1)\left(\frac{\rho_w}{\rho_p}\right)^{1/2} \qquad \textbf{Eq.3.32}$$

$$C_\infty = 1 + 0.2\left[\frac{\rho_p \sqrt{gD}}{G + 0.001}\right]^{1/2} \qquad \textbf{Eq.3.33}$$

where G is in kg/m^{2}s.

3.3.4 Interfacial Area Concentration

We will now turn our attention to the prediction of the interfacial area concentration. Several methods have been proposed to assess the interfacial area concentration a_i in two-phase flow. This parameter is of key importance in any hydraulic model that relies on a separate set of conservation equations for each phase. In these models, estimates of the transfer terms between the phases must be provided to close the problem. Because mass, momentum and energy transfer takes place at the phase interface, all these terms strongly depend on the value of a_i. The most general method to evaluate a_i treats this parameter as a developing property of the flow. A transport equation for a_i is written, which enables predicting the internal geometric structure of the two-phase flow as a function of space and time [Kocamustafaogullari 1995]. Solution of this equation requires the provision of constitutive relations, i.e. source and sink terms for a_i due to bubble coalescence and break-up. The source and sink terms of the transport equation have to date been well characterized only for bubbly flow, where they would be less needed in our application given the relatively simple flow geometry. The development of the source and sink terms for intermittent flow, which is more relevant to our application, is still the object of current investigations [Fu 1999 and 2000] and few data are available. Therefore, in this study we do not follow the transport equation approach, but derive the expressions for the interfacial area concentration based on the assumed flow regime geometry. These expressions will be used in **Eq.3.3** to calculate the vhtc. In this section we also assume that the local thermal conditions of the two fluids (e.g. temperatures, steam quality x_w) are known.

3.3.4.1 Bubbly Flow

The following assumptions are made for bubbly flow:

a) The initial diameter of the injected liquid water droplets is known.

b) The droplets are injected uniformly across the channel.

c) The droplets and the bubbles (resulting from droplet vaporization) are spherical[10].

d) Bubble coalescence and break-up can be ignored.

e) The dispersed phase drift velocity u_{wj} is:

$$u_{wj} = (1-\alpha)^{1.5} V_\infty \qquad \textbf{Eq.3.34}$$

where V_∞ is the asymptotic velocity of a dispersed phase bubble in a stagnant pool of the continuum phase, given by Zuber for bubbly flow [Zuber 1965] as:

$$V_\infty = 1.53\left[\frac{\sigma g(\rho_p - \rho_w)}{\rho_p^2}\right]^{0.25} \qquad \textbf{Eq.3.35}$$

---

[10] This is a conservative assumption because for a given volume a spherical bubble has a minimum interfacial area.

In **Eq.3.34** the term depending on the void fraction accounts for the observed reduction of a bubble rise velocity in the presence of other bubbles.

Because bubble interaction is not important in this flow regime, assumption b) implies that the two-phase bubbles are also distributed uniformly across the channel. Hence $C_0=1$ and the void fraction in bubbly flow can be readily calculated from **Eq.3.19** and **3.34** as:

$$\alpha = \frac{\beta}{1 + u_{wj}/j} \qquad \textbf{Eq.3.36}$$

where β and j are found from **Eq.3.23** and **3.24.**

Due to assumption d), the bubble diameter D_b at any value of x_w can be obtained by a simple mass balance of the dispersed phase as:

$$D_b = D_{b0}\left(\frac{\rho_{w0}}{\rho_w}\right)^{1/3} \qquad \textbf{Eq.3.37}$$

where D_{b0} and ρ_{w0} are the initial droplet diameter and density, respectively. Then the number of bubbles per unit volume, n_b, can be found as:

$$n_b = \frac{\alpha}{\frac{\pi}{6} D_b^3} \qquad \textbf{Eq.3.38}$$

The average distance L_b between the centers of two contiguous bubbles can be calculated as:

$$L_b = \frac{1}{\sqrt[3]{n_b}} \qquad \textbf{Eq.3.39}$$

Finally, the interfacial area concentration a_i in bubbly flow is:

$$a_i = \pi D_b^2 n_b = \frac{6\alpha}{D_b} \qquad \textbf{Eq.3.40}$$

Note that the initial droplet diameter, D_{b0}, is related to the size of the nozzles of the water injector and thus can be more or less independently varied by varying the design of the injector. If it is assumed that at droplet detachment the buoyancy forces equal the surface tension, the following equation holds [Hetsroni 1981]:

$$V_d(\rho_p - \rho_w)g = \pi\sigma D_N \qquad \textbf{Eq.3.41}$$

where V_d and D_N are the droplet volume and the injector nozzle diameter, respectively. Then the droplet initial diameter is:

$$D_{b0} = \sqrt[3]{\frac{6\sigma D_N}{g(\rho_p - \rho_w)}} \qquad \textbf{Eq.3.42}$$

For example, at PBWR conditions and for D_N=1mm, **Eq.3.42** yields $D_{b0}\approx$3mm.

3.3.4.2 Intermittent Flow

It was explained in **Section 3.3.1.2** that the intermittent flow of interest to our application is cap flow characterized by large cap bubbles with smaller bubbles flowing in their wake (see **Figure 3.7**). The following assumptions are made:

a) The shape of the cap bubbles is hemispherical and their diameter is given by **Eq.3.10**:

$$D_{cap} = 30\sqrt{\frac{\sigma}{g(\rho_p - \rho_w)}} \qquad \textbf{Eq.3.43}$$

b) The shape of the small bubbles is spherical and their diameter is equal to 1.5 times the Laplace length as indicated in [Fu 2000]. Then:

$$D_{small} = 1.5\sqrt{\frac{\sigma}{g(\rho_p - \rho_w)}} \qquad \textbf{Eq.3.44}$$

c) The cap and small bubbles have the same drift velocity (and thus the same absolute velocity) given by **Eq.3.30**.

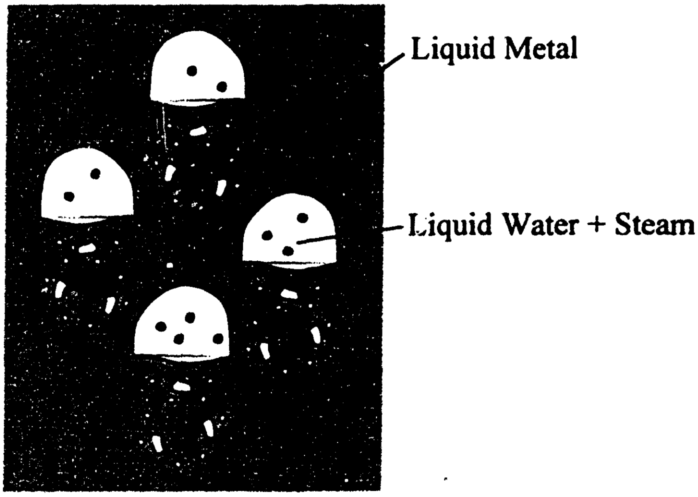

Figure 3.7. The cap flow regime.

The void fraction in the cap flow regime is calculated by means of **Eq.3.19, 3.30** and **3.32** as discussed in **Section 3.3.3**. We will indicate by f_c the fraction of α due to the cap bubbles. With this definition, $f_c\alpha$ represents the volume fraction of the cap bubbles in the flow. Consequently, $(1-f_c)\alpha$ is the volume fraction of the small bubbles. Then, the interfacial area concentration in cap flow can be calculated as:

$$a_i = f_c\alpha\frac{9}{D_{cap}} + (1-f_c)\alpha\frac{6}{D_{small}} \qquad \textbf{Eq.3.45}$$

where $9/D_{cap}$ and $6/D_{small}$ are the interfacial area per unit volume of the cap and small bubbles, respectively, derived from elementary geometry. Similar equations were proposed in reference [Ishii 1987].

Based on the data in reference [Fu 2000] it is assumed that the value of f_c is equal to 0.75 when the transition from bubbly to cap flow is completed. Therefore, we will set $f_c=0.75$ when the value of the void fraction α equals 0.3 (see discussion in **Section 3.3.1.1**). At higher values of the void fraction, entrainment of the small bubbles in the cap bubble wake occurs and the number of small bubbles decreases. This results in an increasing value of f_c which reaches unity at the transition to annular flow where the small bubbles have completely disappeared.

3.4 Local Heat Transfer Coefficient

To calculate the vhtc it is also necessary to evaluate the rate of heat transfer at the interface of the dispersed and continuum phases. To do so, we divide the PBWR chimney in three heat transfer regions according to the thermodynamic state of the dispersed phase: the subcooled, the saturation and the superheat region (see also **Figure 3.1**).

3.4.1 The Subcooled Region

To calculate the heat transfer coefficient in the subcooled region, we first evaluate whether a vapor film separates the droplet liquid bulk from the hot lead-bismuth. It is demonstrated in reference [Incropera 1990] that, when two materials at different temperatures (T_w and T_p) come in contact, the temperature at the interface, T_i , instantaneously reaches an intermediate value given by the following expression:

$$T_i = \frac{(\rho ck)_w^{1/2} T_w + (\rho ck)_p^{1/2} T_p}{(\rho ck)_w^{1/2} + (\rho ck)_p^{1/2}} \qquad \textbf{Eq.3.46}$$

where ρ, c and k are the density, specific heat and thermal conductivity of the material, respectively. The subscripts w and p refer to the first and second material (in our case water and Pb-Bi, respectively). The value of the (ρck) group of Pb-Bi is about an order of magnitude larger than that of water. As a result, T_i is expected to be much closer to T_p than to T_w.

Because the water droplet surface is rather regular, it can be assumed that no nucleation sites for heterogeneous boiling are present. Therefore, a vapor film can form only if T_i is large enough to induce homogeneous nucleation, which requires large values of liquid superheat. The temperature of homogeneous nucleation of water can be calculated from the Lienhard correlation [Collier 1996]:

$$T_{rHN} = 0.905 + 0.095 T_{rSAT}^{8} \qquad \textbf{Eq.3.47}$$

where T_{rHN} and T_{rSAT} are the reduced temperatures[11] of homogeneous nucleation and saturation, respectively. The temperature of homogeneous nucleation is plotted in **Figure 3.8** as a function of the water saturation pressure (the critical pressure and temperature of water are 22.1MPa and 374.15°C, respectively). It can be seen that, at PBWR conditions (7.0MPa), a vapor film will form if T_i exceeds approximately 330°C. It will be shown that for most PBWR situations, T_i is above this value and thus it can be assumed that a vapor film always blankets the liquid droplets in the subcooled region.

The surface heat transfer coefficient in the subcooled region, h_{sub}, can be calculated from the sum of two thermal resistances in series: (i) the heat transfer resistance from the bulk of liquid metal to the interface and (ii) the heat transfer resistance across the vapor film. Then is:

$$\frac{1}{h_{sub}} = \frac{1}{h_p} + \frac{1}{h_{film}} \qquad \textbf{Eq.3.48}$$

Note that in **Eq.3.48** the internal thermal resistance of the liquid water is neglected, which is equivalent to assuming effective mixing in the droplet in accordance with the results reported by Smith [1982].

---

[11] Reduced temperature=(temperature in K)/(critical temperature in K)

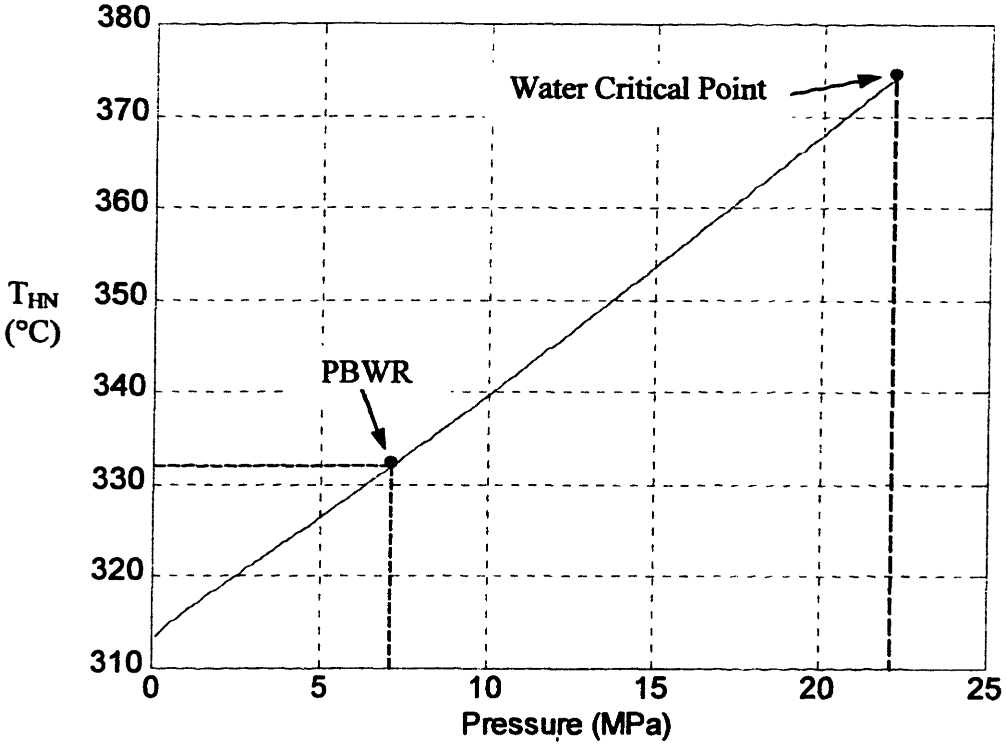

Figure 3.8. The temperature of homogeneous nucleation of water.

To calculate h_p we will make use of the following liquid metal correlation, recommended in reference[12] [Kim 2000]:

$$Nu_b = \frac{h_p D_b}{k_p} = 2 + 1.12 Pe^{0.5} \qquad \textbf{Eq.3.49}$$

where Pe is the Peclet number defined as:

$$Pe = \frac{\rho_p c_p D_b u_{wp}}{k_p} \qquad \textbf{Eq.3.50}$$

u_{wp} is the relative velocity of the droplets with respect to the lead-bismuth. u_{wp} can be readily calculated from the void fraction and the superficial velocities as:

$$u_{wp} = u_w - u_p = \frac{j_w}{\alpha} - \frac{j_p}{1-\alpha} \qquad \textbf{Eq.3.51}$$

As for h_{film} we will make use of a correlation proposed by Dhir and Lienhard [Lienhard 1981] for film boiling on a sphere:

---

[12] A similar correlation was proposed in reference [Nishi 1998], too.

$$h_{film} = 0.67\left[\frac{g(\rho_f - \rho_g)\rho_g k_g^3 h'_{fg}}{D_h \mu_g (T_i - T_{sat})}\right]^{0.25} \qquad \textbf{Eq.3.52}$$

where the subscripts g and f refer to the saturated steam and liquid water, respectively. h'_{fg} is an effective enthalpy of vaporization that accounts for the effect of steam superheat in the film and is defined as:

$$h'_{fg} = h_{fg}\left[1 + 0.34\frac{c_g(T_i - T_{sat})}{h_{fg}}\right] \qquad \textbf{Eq.3.53}$$

In **Section 3.6** it will be shown that at typical PBWR conditions $h_{film} << h_p$. This is expected due to the small thermal conductivity of steam with respect to the Pb-Bi liquid metal.

3.4.1.1. Steam Explosion

An issue associated with the evolution of the liquid droplets in the subcooled region is that of steam explosion. Under certain conditions (typically low operating pressure and high subcooling) the vapor film (blanketing the liquid droplet) is not stable and a violent expansion of the droplet can occur, which causes a shock wave that can damage the channel. There seems to be general agreement that steam explosion can occur only if:

a) the interface temperature T_i is above the temperature of homogeneous nucleation of the dispersed phase [Henry 1974, Reid 1983, Furuya 1996],
b) T_i is below the critical temperature of the dispersed phase [Henry 1975, Furuya 1996],
c) the operating pressure is below a threshold value [Henry 1978, Branover 1992, Furuya 1996, Kinoshita 2000].

Several fluid pairs have been found to satisfy these conditions, ranging from liquified natural gas/water to refrigerant/water, from refrigerant/oil to water/Pb-Bi. Condition a) expresses the fact that no vapor bubble nucleation can occur if the liquid at the interface is not sufficiently superheated. On the other hand, if homogenous nucleation occurs, a vapor film quickly forms at the interface. This film may be unstable resulting in oscillations of the interface, which eventually lead to the film collapse and to consequent violent vaporization [Matsumura 1996]. If the interface temperature is above the critical temperature of the dispersed phase, the film is relatively thick and does not collapse [Henry 1975]. Finally, if the system pressure is large, the vapor embryos generated at the interface by homogenous nucleation cannot grow rapidly. This is due to the large density of vapor at high pressure. Consequently, the generated vapor can be easily accommodated by a moderate volume increase of the vapor embryos and the phase change is not explosive. The value of the pressure above which no steam explosion occurs was found to be ~0.2MPa for R-22/water and R-22/oil [Henry 1977], 0.5MPa for water/molten NaCl [Henry 1978], 0.5MPa for water/Pb-Bi [Furuya 1996] and ~0.2MPa for butane/ethylene [Branover 1992].

At typical PBWR conditions, the interface temperature in the subcooled region is well above the homogeneous nucleation temperature as well as the critical temperature, i.e. T_i>400°C. Therefore, condition a) for steam explosion is met, but condition b) is not. Moreover, because the PBWR operating pressure (7.0MPa) is well above the threshold value for water/Pb-Bi, condition c) is not met either. Therefore, it can be concluded that the PBWR features ample safety margin to steam explosion under normal operating conditions. However, scenarios can be envisioned where an accidental depressurization of the reactor pool takes place. In this case, the possibility of steam explosion depends on the magnitude of the depressurization and on the Pb-Bi temperature during the transients. Accident analysis is beyond the scope of this study, but a more thorough investigation of this issue will have to be undertaken, should the development of the PBWR concept be considered in the future.

3.4.2 Saturated Region

It was noticed that the liquid water does not wet the Pb-Bi surface after the droplet reaches saturation, i.e. the liquid water is always segregated from the Pb-Bi by a vapor blanket. Therefore, the same equations of **Section 3.4.1** can be used to calculate the local heat transfer coefficient of the saturated region, h_{sat}, that will be given again by the sum of two thermal resistances in series: liquid metal heat convection and film boiling. However, depending on the flow regime[13], the geometry in the saturated region may change, hence requiring some modifications. Note that in the saturated region there is no temperature gradient within the liquid water and thus its internal thermal resistance can be rigorously neglected.

In bubbly flow it can be assumed that all the bubbles are spherical and have the same diameter D_b obtained for any value of x_w by means of **Eq.3.37**. Therefore the local heat transfer

---

[13] which is always bubbly in the subcooled region

coefficient may be found from **Eq.3.48** through **3.53** with no change other than replacing h_{sub} with h_{sat}. Typical values of h_{sat} in our system range from 1000 to 2000W/m^{2}K, close to the data reported by Nishi [1998] based on neutron imaging of a Pb-Bi/water channel.

On the other hand, in intermittent flow there are two groups of bubbles of different size and geometry and thus two different values of the local heat transfer coefficient, which ought to be properly averaged prior to their use in **Eq.3.3**. To identify the correct averaging method, let us consider the two groups of bubbles as they move in the channel axially from z to z+dz. The steam quality change in the small and cap bubbles (dx_{small} and dx_{cap}, respectively) is given by the conservation of energy as:

$$\dot{m}_{small} dx_{small} h_{fg} = h_{sat,small} a_{i,small} (T_p - T_{sat}) A dz \qquad \textbf{Eq.3.54}$$

$$\dot{m}_{cap} dx_{cap} h_{fg} = h_{sat,cap} a_{i,cap} (T_p - T_{sat}) A dz \qquad \textbf{Eq.3.55}$$

where $\dot{m}_{small}$ and $\dot{m}_{cap}$ are the water mass flow rate carried by the small and cap bubbles, respectively. $h_{sat,small} a_{i,small}$ and $h_{sat,cap} a_{i,cap}$ are the vhtc of the small and cap bubbles, respectively. A is the flow area. If we now consider the total water flow, the energy conservation equation becomes:

$$\dot{m}_w dx_w h_{fg} = h_{sat} a_i (T_p - T_{sat}) A dz \qquad \textbf{Eq.3.56}$$

By definition the steam flow rate is:

$$\dot{m}_w dx_w = \dot{m}_{small} dx_{small} + \dot{m}_{cap} dx_{cap} \qquad \textbf{Eq.3.57}$$

Then, combining **Eq.3.54** through **3.57**, we get:

$$h_{sat} = h_{sat,small} \frac{a_{i,small}}{a_i} + h_{sat,cap} \frac{a_{i,cap}}{a_i} \qquad \textbf{Eq.58}$$

which indicates that the local heat transfer coefficient in the saturated region can be found as the weighted sum of the local heat transfer coefficient of the small and cap bubbles, with the interfacial area concentrations as the weights. Note that $a_{i,cap}$ and $a_{i,small}$ are the two right-hand terms of **Eq.45**, respectively. $h_{sat,small}$ and $h_{sat,cap}$ are calculated from **Eq.48** through **3.53**, with D_b replaced by D_{small} and D_{cap}, respectively.

3.4.3 Superheated Region

It is assumed that, when the steam equilibrium quality reaches unity, all liquid has dried out and therefore further heat exchange superheats the steam bubbles. In reality at unity equilibrium quality, there may exist some residual liquid water along with slightly superheated steam. However, neglecting the presence of evaporating water in the superheated region is conservative because it leads to underestimating the heat transfer rate between the fluids.

The heat transfer coefficient in the superheated region is the sum of the liquid metal thermal resistance and the thermal resistance within the bubble in series. The heat transfer in the bubble occurs mostly by conduction. We will demonstrate here that the solution of the heat conduction equation in spherical geometry yields a value of the heat transfer coefficient equal to $4k_g/D_b$. Although the temperature of a single bubble actually changes with time, we will make the assumption that this change is slow enough so as to treat the heat transfer process as quasi-static. We can then solve the conduction equation neglecting the time-dependent terms. A more rigorous time-dependent treatment of heat conduction in the steam bubbles can be found in [Abdulla 2000].

Therefore, the temperature distribution within the spherical bubble is described by the following equation:

$$\frac{1}{r^2}\frac{d}{dr}\left(r^2 k_g \frac{dT}{dr}\right) = 0 \qquad \textbf{Eq.3.59}$$

Integrating and setting the boundary condition $T(r_b)=T_i$, one gets:

$$T_i - T(r) = \frac{r_b^2 q_i''}{k_g}\left(\frac{1}{r} - \frac{1}{r_b}\right) \qquad \textbf{Eq.3.60}$$

where $r_b=D_b/2$ and q_i'' is the heat flux at the bubble surface. We define the conduction heat transfer coefficient h_{cond} as:

$$h_{cond} = \frac{q_i''}{T_i - T_b} \qquad \textbf{Eq.3.61}$$

where T_b is the bubble bulk temperature defined as:

$$T_b = \frac{\int_0^{r_b} T(r) 4\pi r^2 \rho_g(T) dr}{\int_0^{r_b} 4\pi r^2 \rho_g(T) dr} \qquad \textbf{Eq.3.62}$$

$\rho_g(T)$ is the steam density at temperature T, which ultimately makes it a function of the location r. However, in our application typical values of the temperature in the bubble bulk and at the interface are around 300 and 450°C, respectively. The variation of ρ_g over this temperature range is only 20% (as readily estimated from the ideal gas equation) and to a first approximation we can assume that ρ_g is constant in **Eq.3.62**, which greatly simplifies the integration. Then the combination of **Eq.3.60** and **3.62** yields:

$$T_i - T_b = \frac{r_b q_i''}{2k_g} = \frac{D_b q''}{4k_g} \qquad \textbf{Eq.3.63}$$

And from **Eq.3.61**:

$$h_{cond} = \frac{4k_g}{D_b} \qquad \textbf{Eq.3.64}$$

Eq.3.64 is to be used in **Eq.3.48** to evaluate the local heat transfer coefficient in the superheated region, h_{sup}. The liquid metal heat transfer coefficient h_p is given again by **Eq.3.49**.

In bubbly flow, the above equations can be applied directly with D_b being the bubble diameter given by **Eq.3.37**. On the other hand, in intermittent cap flow, it is necessary to average the value of the local heat transfer over the two bubble groups. Following a procedure similar to that of **Section 3.4.2** (see **Eq.3.54** through **3.58**) and assuming that the temperature drop within the small and cap bubbles is similar, it can be demonstrated that:

$$h_{sup} = h_{sup,small} \frac{a_{i,small}}{a_i} + h_{sup,cap} \frac{a_{i,cap}}{a_i} \qquad \textbf{Eq.3.65}$$

where again $a_{i,cap}$ and $a_{i,small}$ are the two right-hand terms of **Eq.3.45**, respectively and $h_{sup,small}$ and $h_{sup,cap}$ are calculated replacing D_b with D_{small} and D_{cap}, respectively.

3.5 The Computational Algorithm

The expressions developed in **Sections 3.3** and **3.4** are now combined to predict the thermal and hydraulic evolution of the flow along the channel. It is assumed that all the inlet conditions are known. These are the water and Pb-Bi mass flow rates and temperatures and the water droplet diameter. The water outlet conditions are also given by setting the degree of steam superheat (i.e. the water outlet temperature) that is to be achieved. Note that this fixes the power exchanged in the channel and provides the Pb-Bi outlet temperature by means of a simple energy balance. The channel flow geometry (flow area, equivalent diameter) is given except for the channel length, which is one of the main outputs of the calculation.

The algorithm is based on a nodalization of the range of water temperature in the subcooled and superheated regions and the range of steam quality in the saturated region. The number of nodes per region are given and equal to N_{sub}, N_{sup} and N_{sat}, respectively.

The conservation of energy provides the axial length, z_n-z_{n-1}, of the region associated with any node n:

$$\dot{m}_w c_{wf}(T_{w,n} - T_{w,n-1}) = h_{v,n} A(T_{p,n} - T_{w,n})(z_n - z_{n-1}) \qquad \textbf{Eq.3.66}$$

$$\dot{m}_w h_{fg}(x_{w,n} - x_{w,n-1}) = h_{v,n} A(T_{p,n} - T_{w,n})(z_n - z_{n-1}) \qquad \textbf{Eq.3.67}$$

$$\dot{m}_w c_{wg}(T_{w,n} - T_{w,n-1}) = h_{v,n} A(T_{p,n} - T_{w,n})(z_n - z_{n-1}) \qquad \textbf{Eq.3.68}$$

where **Eq.3.66, 3.67** and **3.68** refer to the nodes in the subcooled, saturated and superheated region, respectively. The value of the vhtc at node n, $h_{v,n}$, is calculated from **Eq.3.3** where h and a_i for the thermal region and flow regime of interest are found from the proper expressions developed in **Sections 3.3** and **3.4**. A summary of these expressions is given in **Table 3.IV**.

Table 3.IV. The constitutive relations.

	Bubbly Flow			Intermittent		
	α	a_i	h	α	a_i	h
Subcooled Region	**Eq.3.34-3.36**	**Eq.3.40**	**Eq.3.48-3.53**	**N/A**	**N/A**	**N/A**
Saturated Region	**Eq.3.34-3.36**	**Eq.3.40**	**Eq.3.48-3.53**	**Eq.3.19, 3.30-3.33**	**Eq.3.45**	**Eq.3.58**
Superheated Region	**Eq.3.34-3.36**	**Eq.3.40**	**Eq.3.49-3.51, 3.64**	**Eq.3.19, 3.30-3.33**	**Eq.3.45**	**Eq.3.65**

Special care is given to avoiding sharp discontinuities of the flow parameters (e.g. void fraction, interfacial area concentration), which are not physical, at the transition from bubbly to intermittent flow. The equations providing the dependent variables for bubbly and intermittent flow are interpolated so that at void fraction 0.05 the flow is dominantly bubbly while at void fraction 0.3 the flow is dominantly intermittent. The interpolation is not linear, but exponential to yield continuous curves with continuous derivatives. For example, the water drift velocity u_{wj} is given by the following equation at any value of the void fraction:

$$\frac{u_{wj}-u_{wj,\mathrm{int}}}{u_{wj,bub}-u_{wj,\mathrm{int}}}=\exp\left(-3\frac{\alpha-0.05}{0.3-0.05}\right) \qquad \textbf{Eq.3.69}$$

where $u_{wj,bub}$ and $u_{wj,int}$ are given by **Eq.3.34** and **3.30**, respectively. Analogous expressions apply for the distribution parameter C_0, the interfacial area concentration a_i and the local heat transfer coefficient h. However, a step-like discontinuity of h is allowed at the transition from the saturated to the superheated region due to the sudden disappearance of evaporative heat transfer. Further, the fraction of void associated with the cap bubbles, f_c, is varied from 0 (at α=0.05) to 0.75 (at α=0.3) to 1 (at α=1), indicating the increasing importance of coalescence and formation of cap bubbles at high void fractions.

3.6 Validation of the Models and Results

In this section the model to estimate the vhtc is applied to several different conditions to ensure that all the expected trends are properly generated. In **Chapter 4**, the algorithm will be integrated with the momentum and energy equations of the whole PBWR primary circuit to predict the steady-state natural circulation performance of the reactor.

In the rest of this discussion we will consider only water and liquid Pb-Bi (designated by the subscripts w and p, respectively), flowing in a square channel of side 0.26m. The operating pressure is 7.0MPa unless specified otherwise. The water inlet temperature is 250°C (i.e. the water subcooling at the channel inlet is about 136°C). The Pb-Bi inlet temperature, the Pb-Bi mass flow rate, the mixture quality x, and the inlet droplet diameter are specified in each figure as is the Degree Of Steam Superheat (DOS) to be achieved.

Figure 3.9 illustrates the variation of the Pb-Bi and water temperatures in the PBWR chimney channel at reference conditions. The temperature at the Pb-Bi/water interface is also drawn. Note that the interface temperature at any location in the channel is very close to the Pb-Bi bulk temperature indicating that the thermal resistance in the liquid metal is negligible compared with the thermal resistance in the water droplets/bubbles. This is particularly true in the superheated region where the heat within the steam bubbles is transferred only by conduction. Also, note that the interface temperature in the subcooled region is significantly above the homogeneous nucleation and critical temperatures of water at the PBWR operating pressure (see **Figure 3.8**). Thus, the assumption of a vapor film blanketing the water droplet in the subcooled region is valid, as is that of no steam explosion. As expected, the length of the superheated region is considerably larger than that of the subcooled and saturated regions even for a modest value of the steam superheat (DOS=25°C), reflecting the abrupt change in the dominant heat transfer mode (from liquid water evaporation to steam conduction) at the boundary of the saturated and superheated regions (see **Figure 3.12**). Finally, the Pb-Bi temperature change in the saturated region is largest because most energy exchange in the channel is associated with the vaporization of the liquid water in this region.

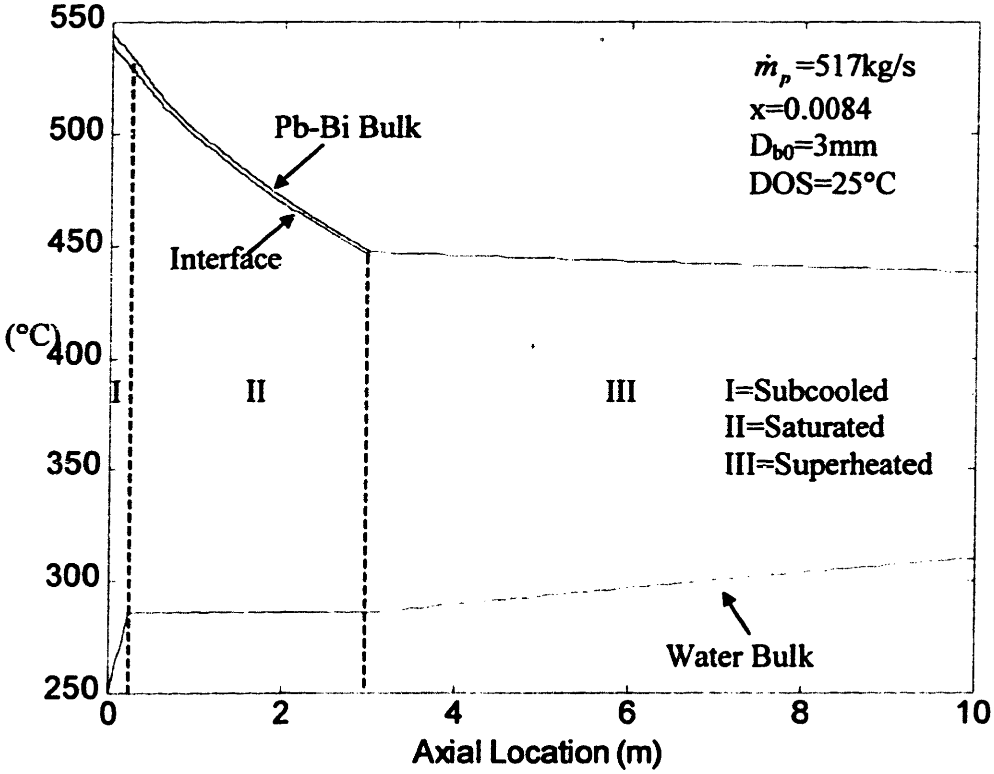

Figure 3.9. The temperature profile in the channel.

In **Figure 3.10** the void fraction variation along the channel is illustrated for the same inlet conditions of **Figure 3.9**. The void fraction rapidly increases at the inlet of the saturated region as massive water evaporation begins. However, as the bubbles swell and their mutual distance decreases, coalescence becomes important and the formed larger bubbles rise at higher velocity hence causing the water/Pb-Bi slip to increase. Therefore, the void fraction in this region, is the result of two competing effects: (i) the increasing water volumetric flow due to water vaporization and (ii) bubble coalescence. With regards to **Eq.3.19**, effect (i) results in an increase of β, which tends to increase the void fraction. Effect (ii) results in an increase of u_{wj}, which tends to decrease the void fraction. The net result is a slower increase of the void fraction until the superheated region is reached, where effect (i) becomes negligible and effects (ii) dominates, causing a slow reduction of the void fraction in this region. It should be noted that as the flow progresses in the channel, the velocity and void profiles become fully-developed, the bubbles tend to drift towards the center of the channel and the distribution coefficient C_0 increases, which further contributes to the void fraction reduction (again see **Eq.3.19**). Moreover, since the model assumes that the transition from bubbly to intermittent flow is completed by $\alpha=0.3$, it can be concluded that part of the saturated region and the entire superheated region are in intermittent flow.

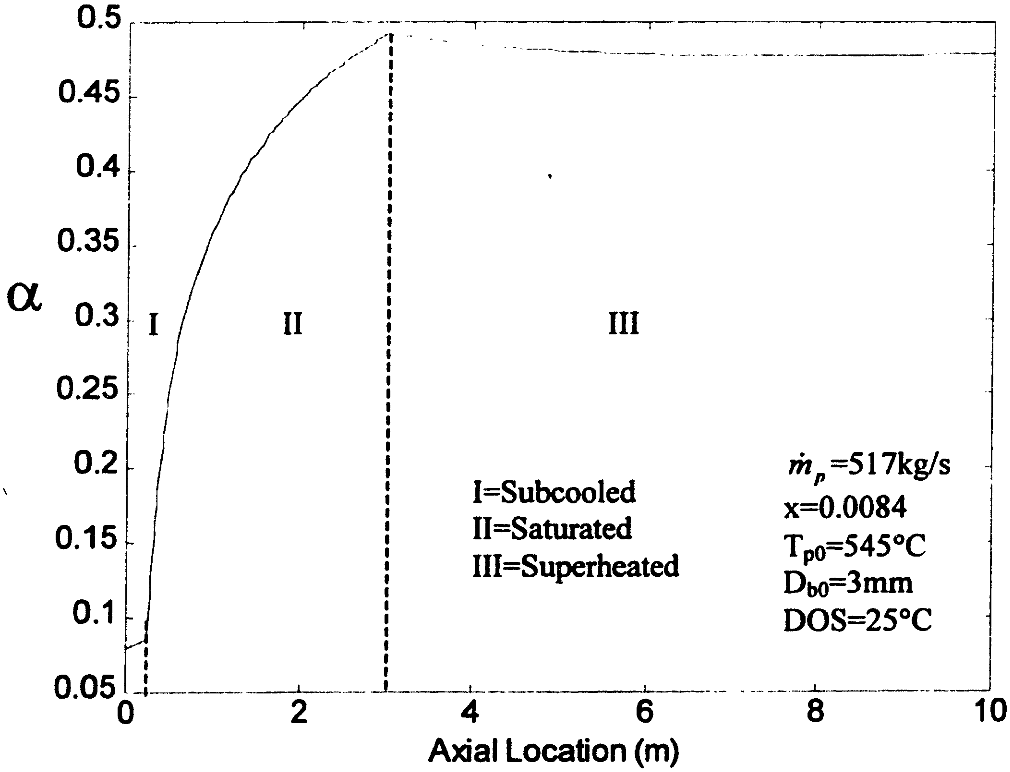

Figure 3.10. The void fraction profile in the channel.

To illustrate the effect of bubble coalescence, the variation of the interfacial area concentration, a_i, in the saturated region is plotted in **Figure 3.11** for three different droplet inlet diameters and for a convenient flow quality x=0.0084. In the first part of the saturated region coalescence is not important and the bubbles grow undisturbed (i.e. bubbly flow). This means that the value of n_b (the number of bubbles per unit flow volume), does not change appreciably with the axial location. When n_b is constant, the interfacial area concentration increases with the bubble diameter and thus with the axial location. This can be proven by eliminating the void fraction α from **Eq.3.38** and **Eq.3.40**.

As the void fraction increases, coalescence becomes important, larger bubbles form and the transition from bubbly to intermittent flow begins. As the transition proceeds, the interfacial area drops to an approximate constant value given by **Eq.3.45** corresponding to fully-developed intermittent flow.

Note that in bubbly flow (i.e. before the a_i maximum), the interfacial area depends on the mode of injection. This is expected because, for a given value of the void fraction (which does not depend on the bubble diameter, see **Eq.3.34-3.36**), the interfacial area concentration is inversely proportional to the bubble diameter (see **Eq.3.40**), which, in turn, is directly proportional to the droplet inlet diameter (see **Eq.3.37**). As a result, in bubbly flow the interfacial area concentration is a decreasing function of the droplet inlet diameter D_{b0}.

On the other hand, bubble interaction (i.e. coalescence) destroys the effect of the injection mode and when the transition to intermittent flow is complete, the value of a_i is practically independent on the droplet inlet diameter.

Note that the length of the saturation region (i.e. the length required to completely vaporize the water) is slightly larger for larger values of D_{b0}, as expected given the dependence of a_i (and thus of the vhtc) on D_{b0} in the bubbly flow region. Finally, we shall mention that the interfacial area concentration in the superheated region (not drawn in **Figure 3.11**) remains approximately constant and equal to its value at the outlet of the saturated region. Thus, with the exception of the first 0.5m (or 5% of the length) the interfacial area can be considered constant of about $180m^2/m^3$, a remarkable feature which can be used for quick estimate of the heat transfer in the chimney.

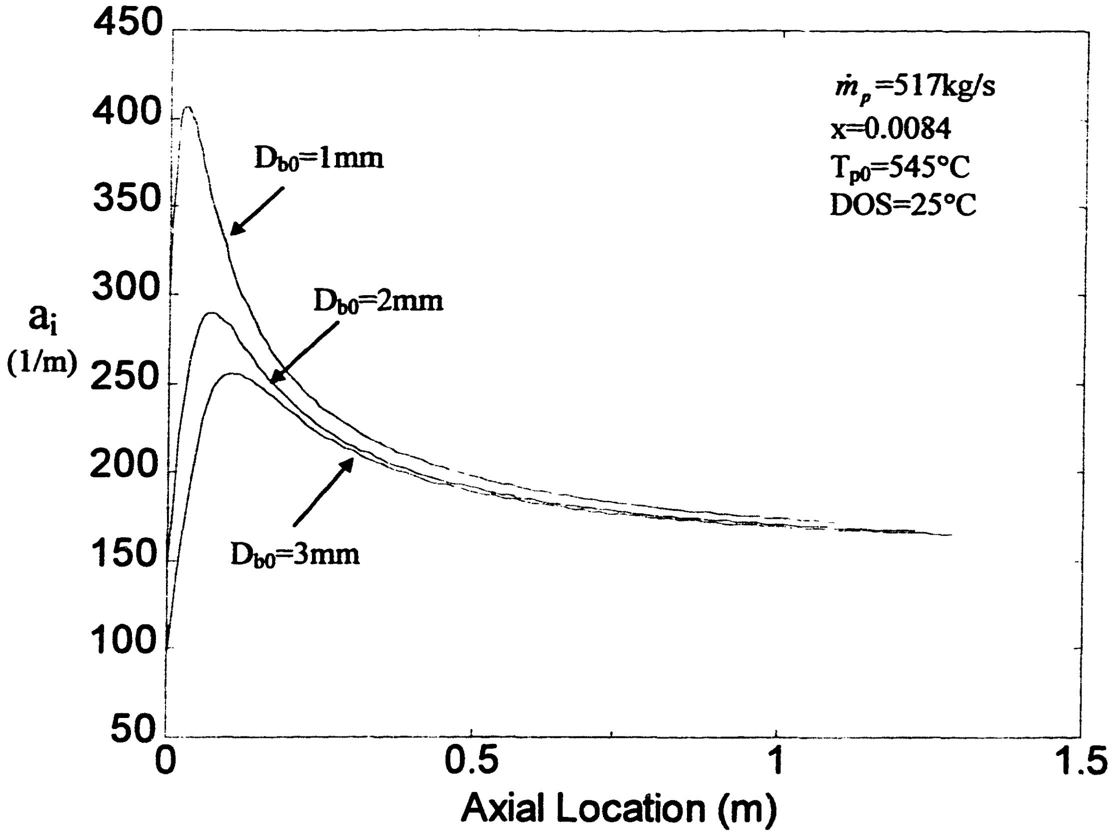

Figure 3.11. The interfacial area concentration in the saturated region.

In **Figure 3.12** the value of the vhtc is plotted as a function of the axial location in the channel. The vhtc in the saturated region follows the same behavior of the interfacial area concentration (see **Figure 3.11**). It should be noted that a similar variation of the vhtc in the saturated region was observed in reference [Sideman 1966]. Sideman [1966] and Blair [1976] also report similar absolute values of the vhtc, although for different fluid pairs (water/pentane and water/freon, respectively vs. Pb-Bi/water in our case). This is not too surprising given that the dominant thermal resistance in the saturated region is film boiling whose heat transfer coefficient is relatively insensitive to the thermo-physical properties of the fluids.

Finally, note that, as expected, a marked reduction of the vhtc occurs when the liquid water dries out in the bubbles and the superheated region begins.

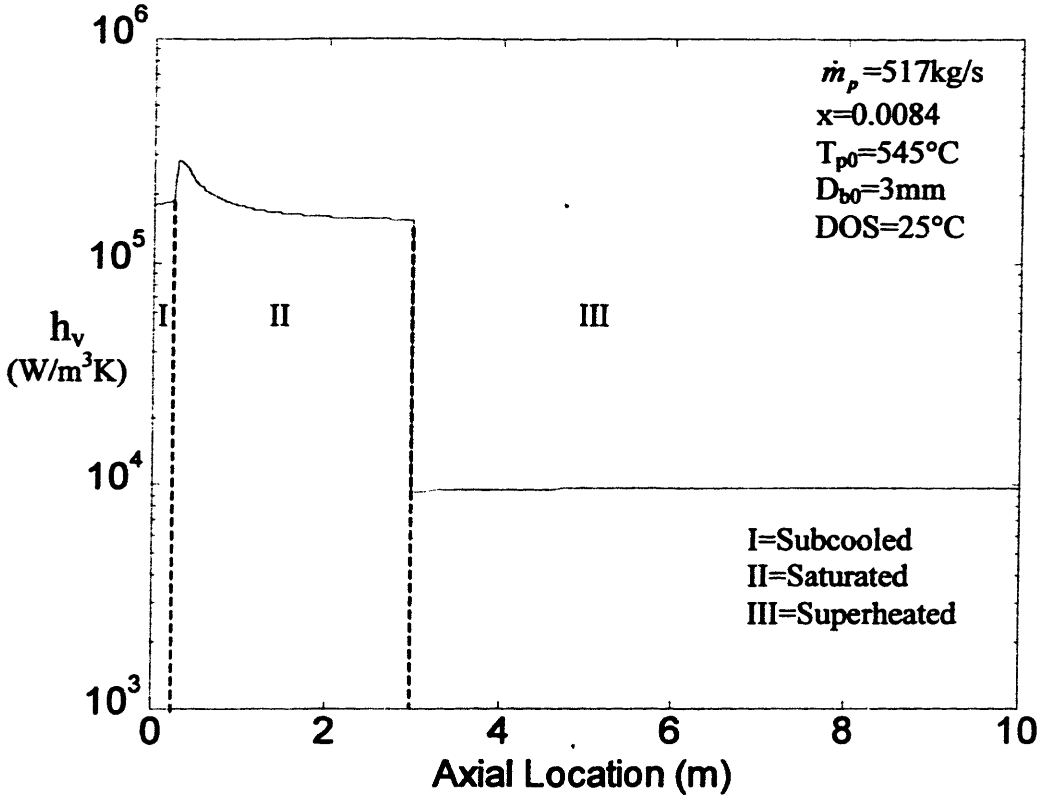

Figure 3.12. The volumetric heat transfer coefficient in the channel.

It was reported [Kinoshita 2000, Smith 1982] that the length required to completely vaporize the water, L_{sat}, is a decreasing function of the temperature difference T_{psat}-T_{sat} (where T_{psat} is the Pb-Bi temperature at the inlet of the saturation region) so that the product $L_{sat}\cdot(T_{psat}-T_{sat})$ is approximately independent of T_{psat}-T_{sat}. **Figure 3.13** shows that our model is capable to reproduce this trend very well, particularly at low mixture qualities (i.e. low water mass flow rates). However, a significant deviation is observed at larger values of x. To explain this deviation let us refer to **Eq.3.1** and **3.2**. Assuming that the vhtc is approximately constant, this equations can be readily integrated to yield an expression for the saturation region length:

$$L_{sat} = -\frac{\dot{m}_p c_p}{h_v A}\log\left(1-\frac{\dot{m}_w h_{fg}}{\dot{m}_p c_p (T_{psat}-T_{sat})}\right) \qquad \textbf{Eq.3.70}$$

For low values of the $\frac{\dot{m}_w}{\dot{m}_p}$ ratio (i.e low values of x) a Taylor expansion of the logarithm provides a simplified expression for L_{sat}:

$$L_{sat} = -\frac{\dot{m}_w h_{fg}}{h_v A(T_{psat} - T_{sat})} \qquad \textbf{Eq.3.71}$$

which indicates that, for a given vhtc, the product $L_{sat} \cdot (T_{psat} - T_{sat})$ does not depend on $T_{psat} - T_{sat}$. However, at high values of x, **Eq.3.70** should be used instead which explains the deviation of **Figure 3.13**. The logarithmic term in **Eq.3.70** is due to the Pb-Bi temperature change in the saturated region. This change is large at high values of x, but relatively small at low x. Note that the experiments of Kinoshita [2000] were conducted at low values of the mixture quality so that the Pb-Bi could be considered isothermal and **Eq.3.71** is appropriate. To obtain an isothermal continuum phase (necessary to test their direct contact model), Smith et al [1982] conducted their experiments in the form of short transients in a stagnant pool.

The product $L_{sat} \cdot (T_{psat} - T_{sat})$ slightly increases with $T_{psat} - T_{sat}$ at values of x below 0.01, indicating that the vhtc is a decreasing function of $T_{psat} - T_{sat}$. This is a result of the dominant film boiling thermal resistance in the saturated region, whose heat transfer coefficient is inversely proportioned to the 1/4th power of the temperature difference between the continuum and dispersed phase (see **Eq.3.52**). This trend was observed by Sideman [1966].

Finally, the product $L_{sat} \cdot (T_{psat} - T_{sat})$ is substantially independent of x (i.e. independent of $\dot{m}_w$) at low values of x. Therefore, **Eq.3.71** indicates that the vhtc must be proportional to $\dot{m}_w$ in this region. Note that at low x the flow regime is likely to be bubbly, for which the bubble density n_b (and thus the interfacial area concentration and the vhtc) is directly proportional to x. This trend was observed by Kinoshita [1997], Sideman [1966] and Smith [1982]. On the other hand, at higher values of x, the flow regime is intermittent and the vhtc actually decreases with x, because the interfacial area concentration is a decreasing function of the void fraction via f_c (see **Eq.3.45**).

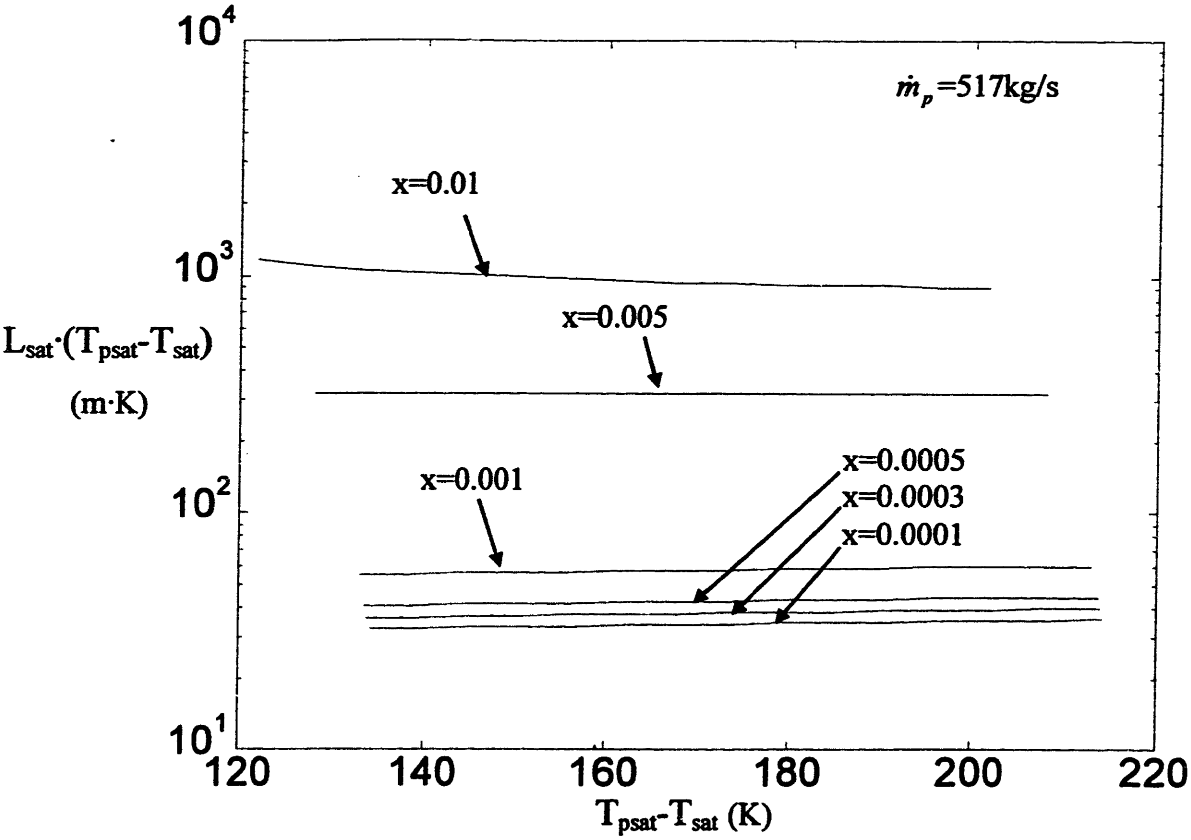

Figure 3.13. The L_{sat} / $(T_{psat}-T_{sat})$ relation

It is also interesting to evaluate the variation of the product $L_{sat}\cdot(T_{psat}-T_{sat})$ with the system pressure. Kinoshita [2000] observed that $L_{sat}\cdot(T_{psat}-T_{sat})$ increased with pressure in his experiments. However, the direction of this variation can be in general positive or negative, being the result of two opposing effects a) and b):

a) A higher pressure corresponds to a larger density of the dispersed phase. This results in a smaller dispersed phase volumetric flux (see **Eq.3.26**) and smaller void fraction, which has two opposite consequences depending on the flow regime:
   - in bubbly flow (i.e. low values of x), it lowers the interfacial area concentration and thus the vhtc,
   - in intermittent flow (i.e. higher values of x), it lowers f_c and thus increases the interfacial area concentration and the vhtc.

b) A higher pressure corresponds to a smaller heat of vaporization. Thus, for a given x, the energy required to vaporize the dispersed phase is smaller and so is the length of the saturated region (see **Eq.3.71**).

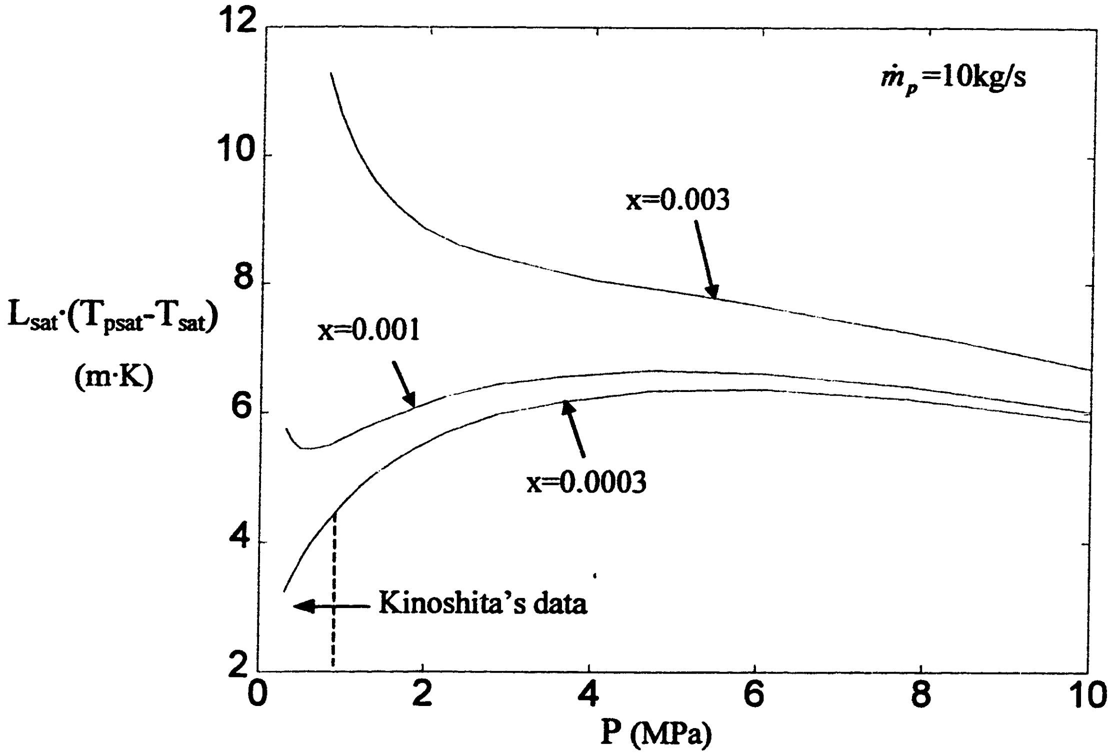

Figure 3.14. The effect of pressure on the $L_{sat}\cdot(T_{psat}-T_{sat})$ product.

In **Figure 3.14** the variation of the $L_{sat}\cdot(T_{psat}-T_{sat})$ product with the system pressure is shown for three different values of x and for a small value of $\dot{m}_p$ (typical of Kinoshita's experiments). It can be seen that the trend observed by Kinoshita at low x and low pressure is correctly reproduced. Moreover, the values of $L_{sat}\cdot(T_{psat}-T_{sat})$ in this region are in good agreement with those of Kinoshita [2000]. However, at higher pressures, effect b) becomes dominant and $L_{sat}\cdot(T_{psat}-T_{sat})$ decreases with pressure. The situation at low pressure strongly depends on the value of x (as explained in a)). At low x, the flow regime is bubbly and the pressure effect is to increase $L_{sat}\cdot(T_{psat}-T_{sat})$. At high x, the flow is intermittent and $L_{sat}\cdot(T_{psat}-T_{sat})$ decreases with pressure. At intermediate values of x, as the pressure increases, a change of flow regime occurs (from intermittent to bubbly), that results in a local minimum of $L_{sat}\cdot(T_{psat}-T_{sat})$.

Figure 3.15 illustrates the effect of the DOS on the total length of the channel, L_{tot}, for given Pb-Bi mass flow rate and mixture quality, but for different Pb-Bi inlet temperatures. As expected, L_{tot} is a strong function of the specified DOS reflecting the dominant importance of the superheated region in the channel. This suggests that it is not desirable to significantly superheat the steam, if the reactor pool height is to be maintained within reasonable limits. However, a certain degree of superheat is needed in order to ensure that all liquid is vaporized. Finally, note that the channel length required to achieve a given DOS can be considerably shortened if the Pb-Bi inlet temperature (and thus the mean Pb-Bi/water temperature difference) is increased.

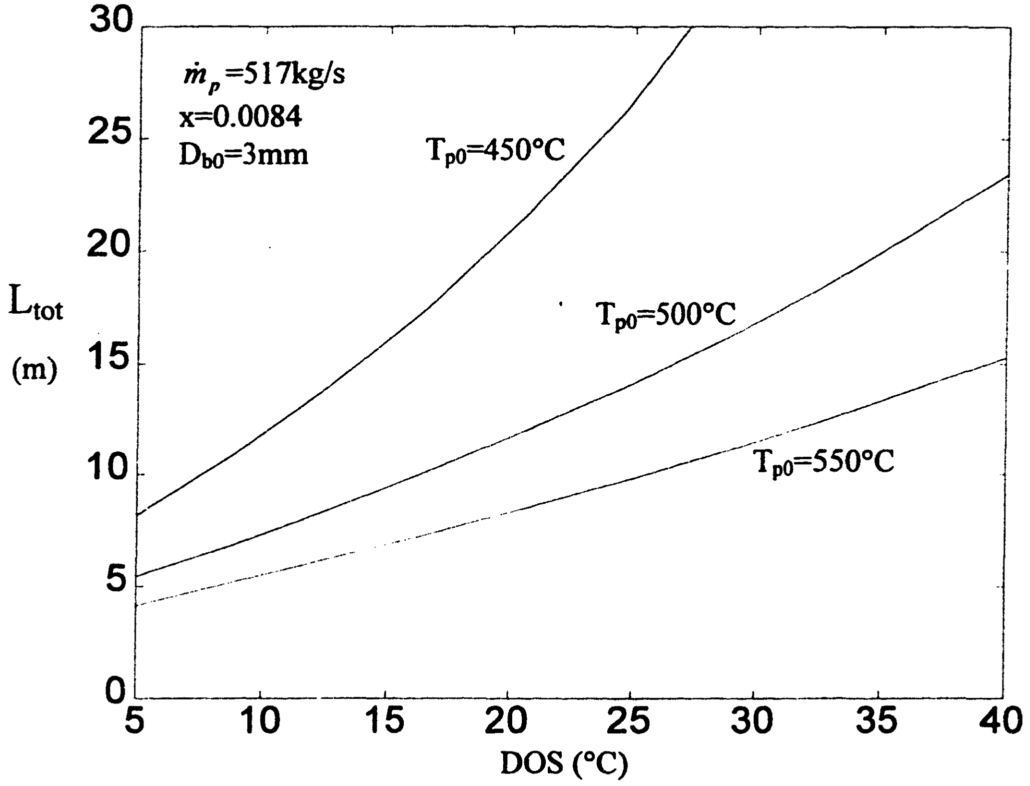

Figure 3.15. The effect of the steam superheat on the length of the channel.

3.7 Summary

Simple models were assembled to predict the evolution of the relevant thermal-hydraulic variables in the PBWR chimney. These models generate both the theoretically expected and experimentally observed trends. However, it must be emphasized that some uncertainties are present in these models as they are based on (i) correlations extrapolated beyond their database and (ii) heuristic assumptions aiming at simplifying the problem. For example, the void fraction in bubbly and intermittent flow is found from the drift-flux coefficients provided by the Zuber and IKR models, respectively, which are based on experimental data from water systems. Also, the interfacial area concentration is calculated from simple geometric considerations and not from the more general theory of interface transport due to the lack of information on the source and sink terms of the transport equation for intermittent flow.

The discussion in **Section 3.6** provides evidence that the models developed in this chapter capture the essence of the direct contact heat transfer phenomena occurring in the PBWR chimney. Therefore these models will be utilized to get a first estimate of the natural circulation performance of the PBWR primary system. Nevertheless, it is strongly recommended that a thorough experimental investigation be conducted of direct contact heat transfer phenomena at prototypical PBWR conditions, should the PBWR concept be further considered in the future. A conceptual framework for this investigation is provided in **Appendix C**.

Chapter 4

- THERMAL-HYDRAULICS OF THE PBWR PRIMARY SYSTEM -

4.1 Introduction

In **Chapter 3** we have assembled a model that predicts the evolution of the key thermal-hydraulic variables (e.g. temperature, void fraction) describing the direct contact heat transfer between Pb-Bi and water in the PBWR chimney. That model requires the knowledge of the chimney inlet conditions (e.g. Pb-Bi and water mass flow rate and inlet temperature, diameter of the injected droplets) as input. However, because the system operates in natural circulation, these inlet conditions are not known a priori and in fact depend on the characteristics of the whole primary circuit including the chimney itself. For example, a change of the void fraction in the chimney produces a change of the Pb-Bi coolant flow rate, which in turn affects the mixture quality in the chimney and ultimately the void fraction itself. Therefore, the thermal-hydraulics of the chimney is coupled to the thermal-hydraulics of the primary circuit (i.e. core and downcomer). In order to close the problem, it is necessary to integrate the models of **Chapter 3** with the momentum and energy equations of the whole primary circuit. On the basis of the clad, fuel and reactor vessel temperature constraints, it is possible to assess the maximum power removable by direct contact heat transfer as a function of the main independent variables, e.g. the chimney height and specified degree of steam superheat (**Section 4.6**). This is the main objective of this chapter.

Next the characteristics of a suitable emergency system that can remove the decay heat in loss-of-normal-heat-sink situations are investigated to evaluate the acceptability of the selected steady-state nominal power level (**Section 4.8**).

A brief qualitative discussion on the dynamic behavior of the PBWR during the most important anticipated transients is also presented (**Section 4.9.1**, **4.9.2** and **4.9.3**). Finally, the PBWR susceptibility to thermal-hydraulic instabilities is evaluated by means of a dynamic analysis in the frequency domain (**Section 4.9.5**).

4.2 Temperature Constraints

4.2.1 The Fuel

There are two fuel batches of different zirconium content (71 and 77%wt) in the PBWR core. In this range, the melting point of the Zr/(Pu+MA) alloy ranges from about 1600 to 1800°C (as shown in **Figure 2.9**). This suggests that the fuel temperature limit be a function of the location in the core. To avoid complications, we shall conservatively assume that the maximum fuel temperature (occurring at the fuel pin centerline) is to be kept below 1400°C, i.e. 200°C below the melting point of the Zr/(Pu+MA) alloy in the fuel batch of minimum zirconium content. Although this choice is rather arbitrary, we will later demonstrate that at typical PBWR conditions, the fuel temperature limit is much less constraining than the clad and the vessel limits. Therefore an accurate definition of this limit is not strictly necessary at this point.

4.2.2 The Clad

As already mentioned in **Section 2.2.4**, there exists a corrosion database in Russia on ferritic/martensitic stainless steels for Pb-Bi cooled reactor applications, which were found to be suitable for cladding purposes at temperatures up to 600-650°C. The clad is thermally bonded to the fuel by a film of liquid lead. The maximum clad temperature occurs at the clad inner surface and therefore one would expect to observe the largest rate of corrosion there. However, the liquid lead inventory between the clad and the fuel is small and quickly becomes saturated with the products of steel dissolution (e.g. iron, chromium), which prevents further clad dissolution. On the other hand, the dissolution products are carried away at the clad outer surface by the Pb-Bi coolant flow and further dissolution of the clad can proceed. Thus, it is clear that the clad temperature limit should be set on the clad outer surface. We shall conservatively assume that this limit is 600°C.

4.2.3 The Reactor Vessel

The temperature limit for a martensitic/ferritic stainless steel reactor vessel was established as a function of the vessel thickness, diameter and height in **Section 2.3** (see **Figures 2.23** and **2.24**). For example, for a reference 25cm thickness, 6m diameter and 20.5m height the temperature limit is about 535°C. Note that this limit is set on the membrane temperature (i.e. the temperature average across the vessel thickness), which coincides with the surface temperature under normal operating conditions (because there is no thermal gradient across the vessel), but differs from it in a loss-of-primary-heat-sink situation where the decay heat is discharged to the environment through the reactor vessel.

4.3 The Assumptions about the Primary System

A schematic of the reactor and a detailed description of the core geometry are reported in **Chapter 2.**

Four general assumptions are made here.

- The analysis is performed for steady-state conditions.
- Acceleration pressure losses are negligible. Preliminary calculations show that the friction pressure drop in the core and in the chimney is two and one orders of magnitude greater than the acceleration terms, respectively, hence confirming the validity of this assumption.
- The steam dome pressure is 7.0MPa.
- Friction losses in all single-phase sections of the primary system are calculated from the McAdams correlation for smooth tubes:

  $$f = \frac{0.184}{\mathrm{Re}^{0.2}} \qquad \textbf{Eq.4.1}$$

  where f is the friction factor and Re is the Reynolds number.

A list of assumptions for the specific components of the primary system follows.

4.3.1 Core

- The form losses due to contraction and expansion of the flow area at the inlet and outlet of the core are set equal to 0.5 and 1.0 kinetic heads, respectively. This choice is conservative as indicated in reference [Todreas 1990].
- The form loss coefficient due to spacers and grids is calculated as:

  $$K_{form} = C_V \left(A_s / A_v\right)^2 \qquad \textbf{Eq.4.2}$$

where A_s and A_v are the total projected frontal area of the spacer (or grid) and A_v is the unrestricted flow area of the assembly. C_v is the modified drag coefficient and its expression was derived by interpolating the data of Rehme from reference [Todreas 1990] as:

$$C_V = 6.5 + 3.0(5 - \log_{10} \mathrm{Re}) \qquad \textbf{Eq.4.3}$$

The Reynolds number and the form loss coefficient are both based on the Pb-Bi velocity in the unrestricted region far from the spacers and grids.

- The radial and axial power peaking factors in the core are conservatively assumed to be 1.25 and 1.23, respectively (see **Section 2.2.6**). The axial power profile of **Figure 2.16** is treated as a cosine curve of the following form:

$$q'(z) = q'_{\max} \cos\left[\frac{\pi}{L_e}(z - L_f/2)\right] \qquad \textbf{Eq.4.4}$$

where z is the axial location of interest starting from the core bottom, q'(z) and $q'_{\max}$ are the linear heat generation rates at location z and at the fuel midplane, respectively. L_f is the active fuel length and L_e=1.86m is a parameter selected to yield the specified 1.23 axial peaking factor.

- The heat transfer coefficient in the core is calculated from the Zhukov correlation for liquid lead flow in square rod array bundles [Zhukov 1994]:

$$Nu = 7.55(P/D) - 14/(P/D)^5 + 0.007Pe^{0.64+0.247(P/D)} \qquad \textbf{Eq.4.5}$$

where Nu is the Nusselt number based on the fuel assembly hydraulic diameter, Pe is the Peclet number and P/D is the pitch-to-diameter ratio of the square fuel lattice.

4.3.2 Chimney

- The liquid water is injected at 250°C, i.e. about 125°C above the Pb-Bi freezing point.
- The initial diameter of the water droplets is 3mm, corresponding to a water injector nozzle of 1mm diameter (see **Eq.3.42**).
- The temperature and void fraction profiles in the chimney are calculated from the equations of **Chapter 3**.
- The two-phase pressure drops are calculated from the Friedel correlation [Hetsroni 1982], which consists of the following equations:

$$f_{TP} = E + 3.24\frac{FK}{Fr_{TP}^{0.0454}We_{TP}^{0.035}} \qquad \textbf{Eq.4.6}$$

$$E = (1-x)^2 + x^2\left(\frac{\rho_p}{\rho_w}\right)\left(\frac{\mu_w}{\mu_p}\right)^{0.25} \qquad \textbf{Eq.4.7}$$

$$F = x^{0.78}(1-x)^{0.224} \qquad \textbf{Eq.4.8}$$

$$K = \left(\frac{\rho_p}{\rho_w}\right)^{0.91}\left(\frac{\mu_w}{\mu_p}\right)^{0.19}\left(1-\frac{\mu_w}{\mu_p}\right)^{0.7} \qquad \textbf{Eq.4.9}$$

$$Fr_{TP} = \frac{G^2}{gD\rho_{TP}^2} \qquad \textbf{Eq.4.10}$$

$$\rho_{TP} = \frac{x}{\rho_w} + \frac{1-x}{\rho_p} \qquad \textbf{Eq.4.11}$$

$$We_{TP} = \frac{G^2 D}{\rho_{TP}\sigma} \qquad \textbf{Eq.4.12}$$

where f_{TP} is the two-phase friction factor and x is the mixture quality defined as the ratio of the water mass flow rate to the total (water + Pb-Bi) mass flow rate. The subscripts p and w indicate the Pb-Bi and water, respectively. The water density ρ_w is calculated from **Eq.3.4.** A similar expression was adopted for the water viscosity μ_w. G is the mixture mass flux, D the chimney hydraulic diameter and σ the Pb-Bi surface tension. Because the properties of water change along the chimney due to vaporization, the coefficient f_{TP} is actually a function of the location in the chimney.

- The form losses due to the water injector are set equal to 2.0 kinetic heads of the primary coolant. This is a rather arbitrary assumption, which however should not significantly affect the analysis because the overwhelmingly dominant pressure drops occur in the core.
- Transport of mass and momentum out of the reactor pool due to Pb-Bi droplet carry-over at the top of the chimney is negligible. It will be demonstrated in **Chapter 5** that a steam separator can be designed that efficiently removes the Pb-Bi droplets from the steam stream.

4.3.3 Downcomer

- Reduction of the density head due to steam carry-under in the downcomer is neglected. It is shown in **Appendix D** that steam carry-under can be virtually eliminated by increasing the width of the downcomer and utilizing a horizontal ring (mounted at the core barrel lip) that facilitates steam bubble rise to the free surface of the pool.

- The form losses due to the Pb-Bi coolant flow 180° bend at the top and at the bottom of the downcomer are set equal to 1.0 and 1.0 kinetic heads, respectively.
- The reference value of the downcomer width is 1m. For a 4m core diameter (like the PBWR core), this corresponds to a reactor vessel diameter of 6m.

4.4 The Conservation Equations

4.4.1 Mass

It was already mentioned that Pb-Bi carry-over and steam carry-under are neglected in this analysis, therefore it can be assumed that:

a) the Pb-Bi inventory of the reactor pool is constant, and

b) all the water injected at the bottom of the chimney exits the reactor pool as steam through the steam separator.

4.4.2 Momentum

The momentum equation integrated over the whole PBWR pool is:

$$gH(\rho_{dc} - \bar{\rho}_c) = \sum_i \left(K_i + f_i \frac{L_i}{D_i} \right) \frac{\dot{M}_i^2}{2\rho_i A_i^2} \qquad \textbf{Eq.4.13}$$

where H is the chimney height, K_i, f_i, L_i, D_i, ρ_i, A_i and $\dot{M}_i$ are the form coefficient, the friction coefficient, the length, the hydraulic diameter, the density, the flow area and the mass flow rate in the i-th section of the reactor pool[1]. ρ_{dc} is the Pb-Bi density in the downcomer and $\bar{\rho}_c$ is the chimney average density defined as:

$$\bar{\rho}_c = \frac{1}{H} \int_0^H [\alpha \rho_w + (1-\alpha)\rho_p] d\ell \qquad \textbf{Eq.4.14}$$

where α is the local void fraction in the chimney and ℓ is the axial location in the chimney.

---

[1] Note that in the chimney $\dot{M}_i$ is the sum of the Pb-Bi and water mass flow rates.

4.4.3 Energy

The conservation of energy for the Pb-Bi coolant is:

$$\dot{Q} = \dot{M}_p c_p (T_{p0} - T_{pi}) \qquad \textbf{Eq.4.15}$$

where $\dot{Q}$ is the reactor power, $\dot{M}_p$ is the Pb-Bi mass flow rate, c_p is the Pb-Bi specific heat[2] and T_{p0} and T_{pi} are the Pb-Bi core outlet and inlet temperature, respectively. Note that $\dot{m}_p$ of **Chapter 3** and $\dot{M}_p$ are related as $\dot{M}_p = \dot{m}_p N_{ass}$, where N_{ass} is the number of assemblies in the core.

Because all the thermal power is transferred to the secondary coolant (i.e. the water), the conservation of energy yields:

$$\dot{Q} = \dot{M}_w [c_{wf}(T_{sat} - T_{wi}) + h_{fg} + c_{wg} DOS] \qquad \textbf{Eq.4.16}$$

where $\dot{M}_w$ is the water mass flow rate, T_{wi} and T_{sat} are the water inlet and saturation temperature, c_{wf} and c_{wg} are the specific heat of the subcooled water and of the superheated steam, respectively[3]. h_{fg} is the enthalpy of vaporization and DOS is the Degree Of Steam Superheat.

The peak linear heat generation rate in the hot assembly (to be used in **Eq.4.4**) is:

$$q'_{\max} = P_{rad} P_{ax} \left(\dot{Q} / N_{ass} / N_{pin}\right) / L_f \qquad \textbf{Eq.4.17}$$

where P_{rad} and P_{ax} are the radial and axial power peaking factors, respectively. N_{pin} is the number of fuel pins per assembly. Then, the coolant profile for the average fuel pin in the hot assembly can be found by integrating the conservation of energy equation:

$$\left(\dot{m}_p / N_{pin}\right) c_p \frac{dT_p(z)}{dz} = q'(z) \qquad \textbf{Eq.4.18}$$

The temperature on the outer surface of the clad at location z, $T_c(z)$, and the fuel centerline temperature at location z, $T_f(z)$, are related to $T_p(z)$ by the following equations, respectively:

$$T_c(z) = T_p(z) + q'(z) \frac{1}{h_p \pi d} \qquad \textbf{Eq.4.19}$$

$$T_f(z) = T_p(z) + q'(z) \left[\frac{1}{4\pi \bar{k}_f} + \frac{1}{2\pi k_g} \log\left(\frac{d_{ci}}{d_f}\right) + \frac{1}{2\pi k_c} \log\left(\frac{d}{d_{ci}}\right) + \frac{1}{h_p \pi d} \right] \qquad \textbf{Eq.4.20}$$

---

[2] The Pb-Bi specific heat does not change significantly with temperature so it will be treated as constant.

[3] Calculated at the intermediate temperatures $(T_{wi}+T_{sat})/2$ and T_{sat}+DOS/2, respectively.

where h_p is the heat transfer coefficient from the Zhukov correlation (see **Eq.4.5**), d is the fuel pin diameter, d_{ci} the inner diameter of the clad, d_f the outer diameter of the actual fuel rod, k_c and k_g the thermal conductivity of the clad and of the gap thermal bond, respectively. $\bar{k}_f$ is the average fuel thermal conductivity defined as:

$$\bar{k}_f = \frac{1}{T_f - T_{fo}} \int_{T_{fo}}^{T_f} k_f(T)dT \qquad \textbf{Eq.4.21}$$

where T_{fo} is the temperature at the fuel surface and $k_f(T)$ is given in **Figure 2.10**.

4.5 The Computational Algorithm

The key inputs to the calculations are: the reactor power, the chimney height and the DOS. Then **Eq.4.16** immediately yields the water mass flow rate (because the water inlet temperature, T_{wi}, is always fixed at 250°C). As a result, **Eq.4.13, 4.14, 4.15** and the models for α and h_v of **Chapter 3** effectively constitute a system of 5 equations in the 5 unknowns $\bar{\rho}_c$, α, T_{p0}, T_{pi} and $\dot{M}_p$, which can be solved as follows.

A guess is made for the Pb-Bi mass flow rate and for the Pb-Bi core outlet temperature T_{p0}. These two data (along with the water mass flow rate and inlet temperature, the initial droplet diameter and the DOS) are fed to the algorithm of **Chapter 3**, which calculates the void fraction profile in the chimney as well as the chimney height required to achieve the specified DOS. The relative difference between this chimney height and the actual chimney height (which is an input of the calculation) is computed and T_{p0} is increased or decreased accordingly until convergence is achieved. Then **Eq.4.15** and **Eq.4.13** give the Pb-Bi inlet temperature, T_{pi}, and the new value of the Pb-Bi mass flow rate, respectively. This procedure is repeated until convergence of the Pb-Bi mass flow rate is also achieved.

When the Pb-Bi mass flow rate and T_{pi} are known, the coolant, clad and fuel temperature profiles in the core can be calculated from **Eq.4.18, 4.19** and **4.20**, respectively.

4.6 Selection of the Reactor Power: Normal Operating Conditions

The above algorithm can be used in concert with the temperature constraints of **Section 4.2** to assess the maximum thermal power that can be removed by direct contact heat transfer under normal operating conditions. To do so, the reactor power is varied (for given DOS and chimney height) until one of the three temperature constraints of **Section 4.2** is reached. The calculations show that the first constraint to be reached is always the clad temperature limit, i.e. for T_c=600°C the fuel and the vessel operate below their respective temperature limits. **Figure 4.1** illustrates the maximum acceptable reactor power as a function of the chimney height and the DOS. Because the Pb-Bi temperatures are limited by the 600°C clad constraint, an increase of the specified DOS results in a decrease of the average driving temperature difference in the chimney and ultimately in a decrease of the reactor power. On the other hand, the maximum power is an increasing function of the chimney height due to the increased natural circulation driving head.

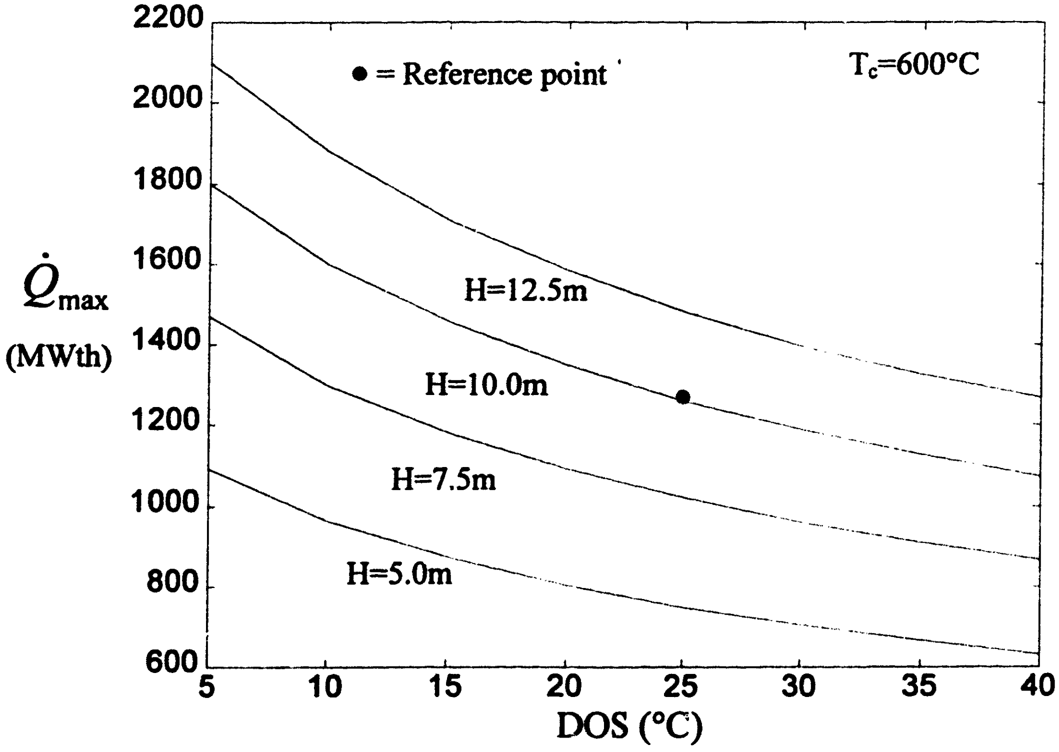

Figure 4.1. Maximum acceptable reactor power.

The results of **Figure 4.1** indicate that it is beneficial to select a long reactor pool to maximize the thermal power. A static structural analysis shows that rather long vessels (up to

25m) could be designed to operate at the required PBWR temperatures and do not violate the safety margins dictated by the ASME code (see **Figure 2.23**). However, it is expected that an upper limit on the acceptable reactor pool height will come from a seismic analysis of the reactor vessel, which is beyond the scope of this study. Here a chimney height of 10m (H=10m) is selected, that corresponds to a vessel height of about 20.5m (L_v=20.5m) (see **Figure 4.9**). The reference values of the vessel diameter and thickness are 6m and 25cm, respectively. A pressure vessel with these characteristics (i.e. 20.5m height, 5m diameter, 25cm thickness operating at 7.0MPa) is within the design envelope of current advanced light water reactors, (e.g. see the ESBWR [Rao 1999]) and thus thought to be suitable for the PBWR, too.

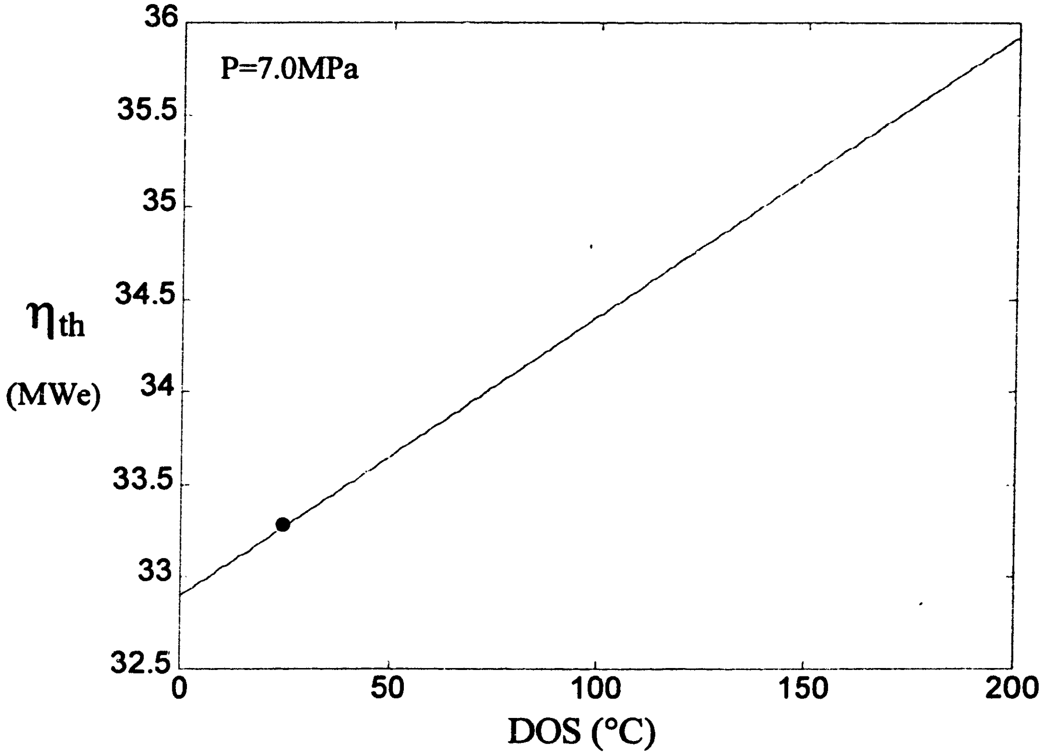

Figure 4.2. The effect of the DOS on the thermal efficiency of the Rankine cycle.

With regard to the DOS, **Figure 4.1** suggests that it should be kept rather low in order to maximize the reactor thermal power. On the other hand, a higher DOS results in a larger thermal efficiency of the power cycle. The cost of the electricity generated by the reactor is inversely proportional to the electric power, which is the product of the thermal power and the thermal efficiency. Therefore, it is the electric power output that should be maximized. The variation of the thermal efficiency, η_{th}, with the DOS for a simple Rankine cycle at 7.0MPa was found in [Keenan 1970] and is plotted in **Figure 4.2** where it is assumed that for DOS=0°C, the thermal efficiency equals that of a typical BWR, i.e. η_{th}=32.9% [Todreas 1990]. Note that the effect of the DOS on the thermal efficiency is very small. This is confirmed by the case of the Babcox & Wilcox PWRs, which are designed to generate superheated steam at 15°C DOS and they exhibit a thermal efficiency only less than 1% larger than "saturated" PWRs [Toledo Edison Company 1970]. The variation of the electric power with the DOS (for H=10m) is illustrated in **Figure 4.3**.

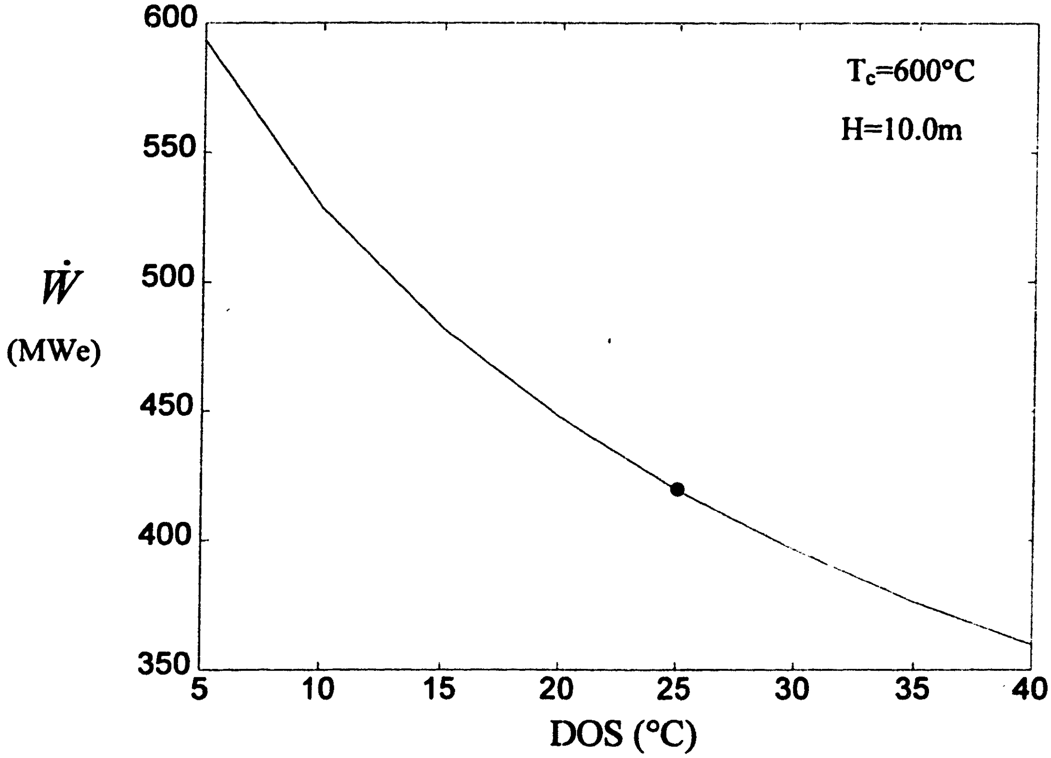

Figure 4.3. The electric power (for H=10m).

As expected, the dominant effect is the decrease of the thermal power (**Figure 4.1**) which cannot be compensated by the slight increase of the thermal efficiency. As a result, the electric power decreases with the DOS. This suggests that in the PBWR large values of the DOS are in principle not desirable. However, the core power cannot be chosen arbitrarily large: it will be shown in **Section 4.8** that for a reactor vessel of 6m diameter and 20.5m height (H=10m), the maximum allowable power compatible with the Decay Heat Removal System (DHRS) is about 1340MWth. **Figure 4.1** suggests that a DOS=25°C would then be acceptable because ensures that the decay heat can be safely removed in a loss-of-heat-sink situation. Note that maintaining a certain degree of superheat also helps to ensure that under normal operating conditions the steam fed to the turbine is dry, as demonstrated in **Appendix H**.

Figure 4.1 indicates that for DOS=25°C and H=10m, the reactor thermai power would be about 1260MWth. This is the core power reference value. Therefore the reference electric power is about 419MWe. The neutronic life of the actinide burning core at this power level can be found from **Figure 2.7** and is equal to about 2.3yrs.

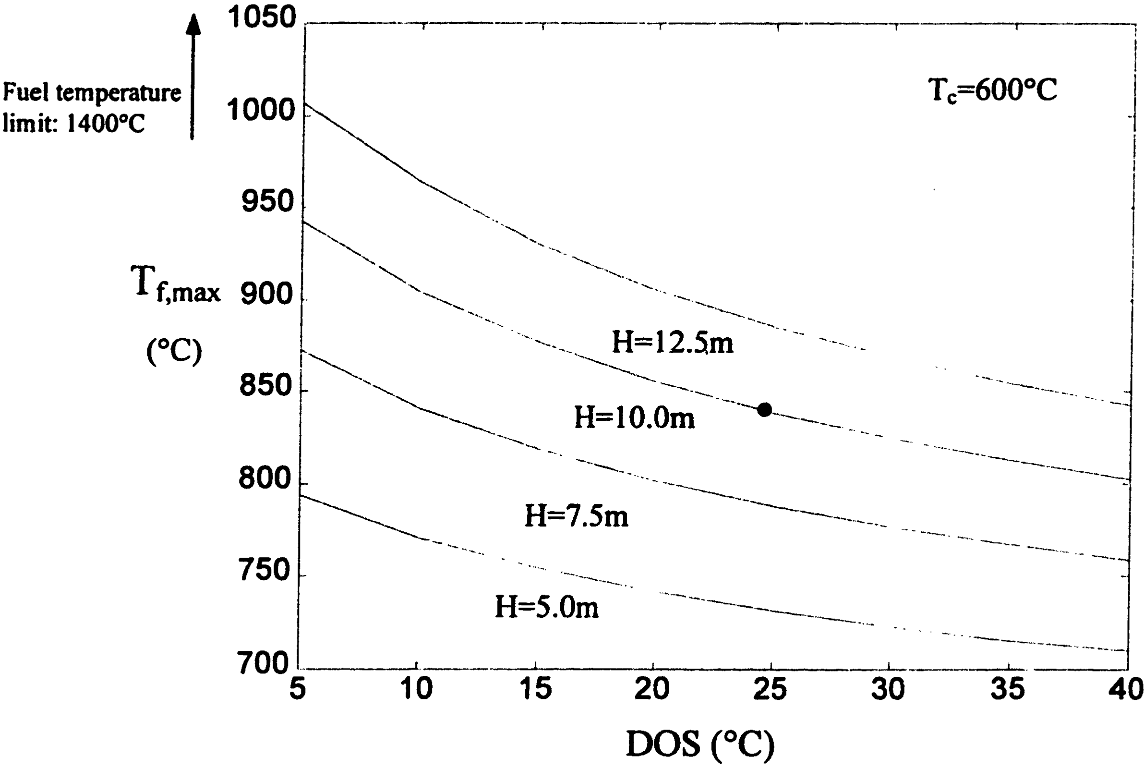

Figure 4.4. Fuel centerline temperature.

In **Figures 4.4**, **4.5**, **4.6** and **4.7** the hot assembly fuel centerline temperature, the Pb-Bi core outlet and inlet temperatures and the Pb-Bi core velocity are plotted, respectively for conditions that correspond to the curves of **Figure 4.1**. The values corresponding to the reference case (H=10m and DOS=25°C) are indicated by a dot. The fuel centerline temperature displays the same trends as the core power in **Figure 4.1**. This is expected because the fuel temperature mostly depends on the linear heat generation rate, which, for a given core, is directly proportional to the core power. Note that the fuel operates well below its temperature limit.

The Pb-Bi core outlet temperature (which is also the Pb-Bi chimney inlet temperature) increases with the DOS because, for a given chimney height, a larger Pb-Bi to water temperature difference is required to achieve a larger DOS.

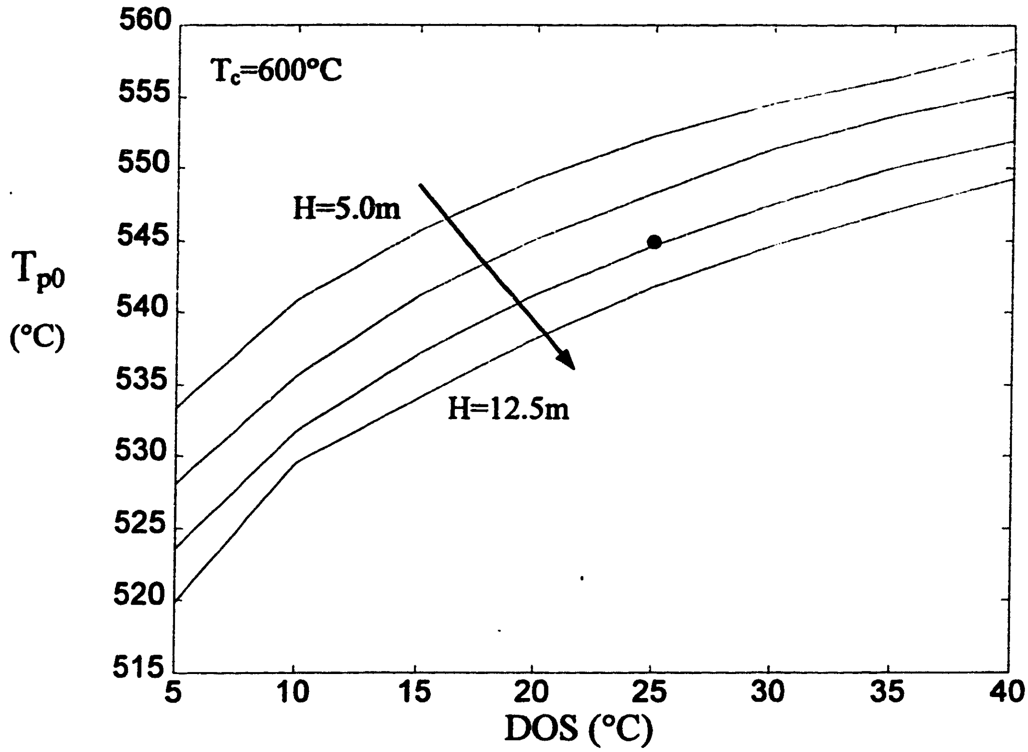

Figure 4.5. Pb-Bi core outlet temperature.

Under normal operating conditions the reactor vessel operates at the Pb-Bi core inlet temperature, T_{pi} and thus **Figure 4.6** provides the vessel temperature, too. The vessel temperature limit for the reference vessel (6m diameter, 20m height, 25cm thickness) is also drawn. It can be seen that also the vessel operates below its temperature limit.

As expected, the Pb-Bi core velocity strongly increases with the chimney height due to the enhanced natural circulation (see **Figure 4.7**), but is only weakly affected by the DOS because the void fraction (i.e. the water volume fraction) in the chimney does not significantly depend on the DOS. The Pb-Bi mass flow rate (not plotted) follows the same trends as the core velocity and ranges from 50,000 (at H=5m) to 95,000kg/s (at H=12.5m).

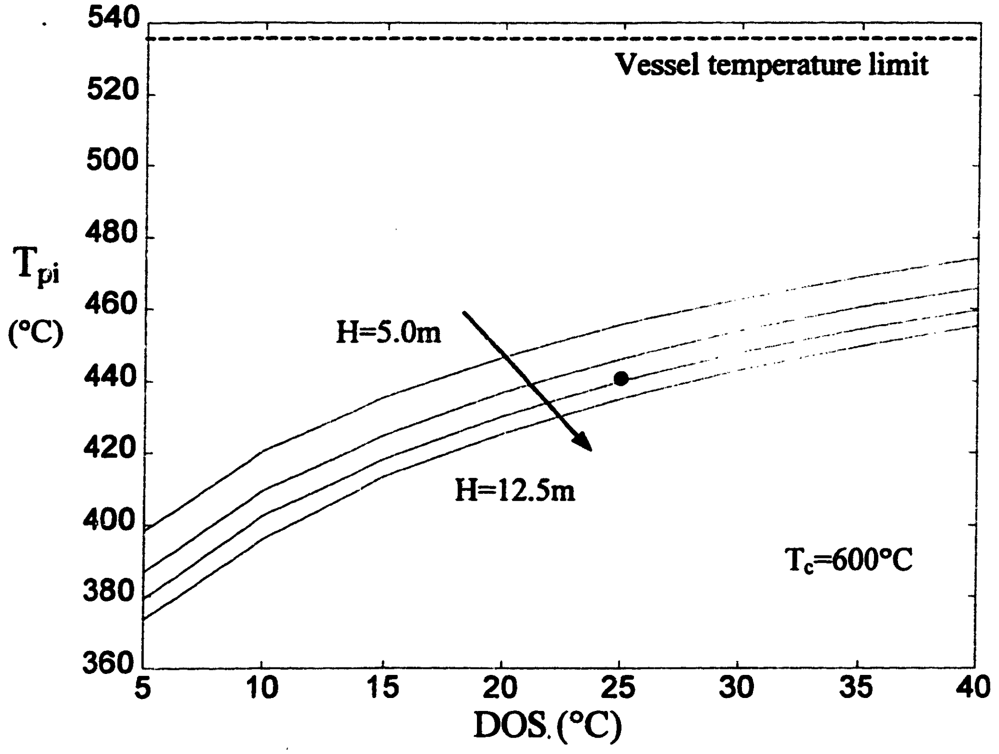

Figure 4.6. Vessel and Pb-Bi core inlet temperature.

A summary of the relevant characteristics of the primary system at our selected reference conditions is reported in **Table 4.I**. The coolant, clad and fuel axial profiles in the hot assembly are plotted in **Figure 4.8** for the reference conditions of **Table 4.I**. As expected, the clad temperature maximum occurs very close to the fuel upper end due to the relatively flat axial power profile and large Pb-Bi heat transfer coefficient.

The reference geometry of the PBWR pool is shown in **Figure 4.9**. The 3m Pb-Bi plenum in the upper region of the pool ensures that, upon loss of feedwater and consequent collapse of the voids, the Pb-Bi free surface remains significantly above the chimney lip (i.e.>1.0m), as can be readily demonstrated from the conservation of the liquid volume for a value of the void fraction equal to about 0.5 (see **Figure 3.10**). This enables Pb-Bi flow from the chimney to the downcomer under loss-of-primary-heat-sink situations, which is key to removing the decay power from the core (see **Section 4.8** below).

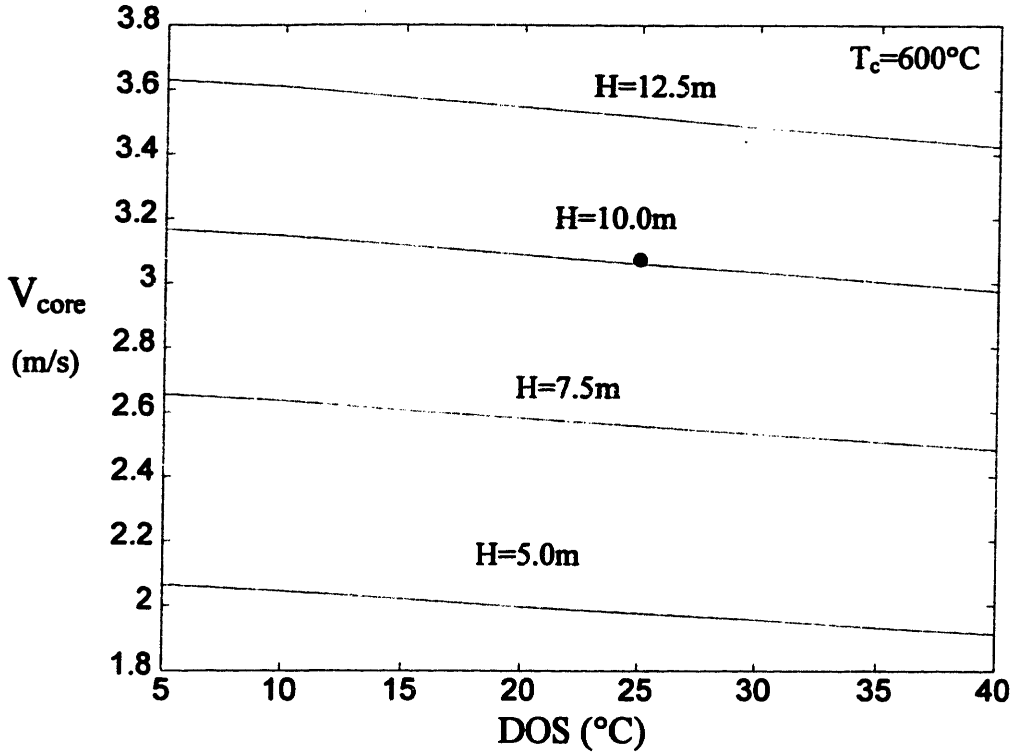

Figure 4.7. Pb-Bi velocity in the core.

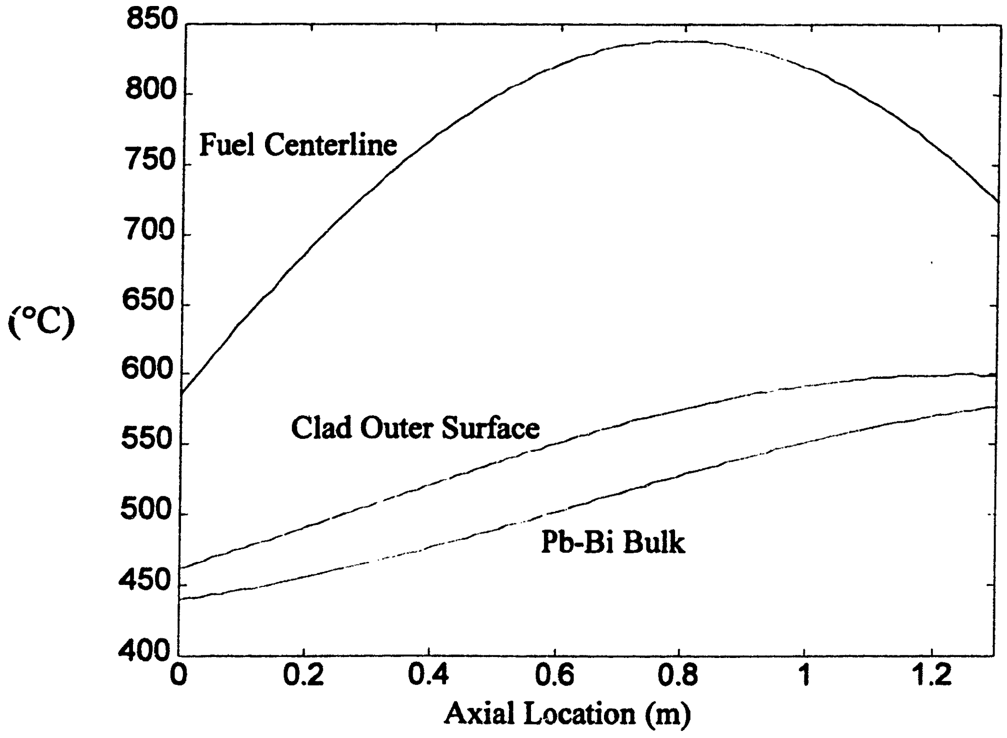

Figure 4.8. Temperature axial distribution in the hot assembly.

Table 4.I. The PBWR primary system reference conditions.

Parameter	Value
Reactor Thermal Power (MW)	1260
Reactor Electric Power (MW)	419
Thermal Efficiency (%)	33.3
Pb-Bi Core Inlet/Outlet Temperature (°C)	440/545
Pb-Bi Mass Flow Rate (kg/s)	~81,110
Pb-Bi Core Velocity (m/s)	~3.1
Average Linear Heat Generation Rate (kW/m)	25.7
Peak Linear Heat Generation Rate (kW/m)	41.1
Peak Fuel Temperature (°C)	838
Peak Clad Temperature (°C)	600
Steam Dome Operating Pressure (MPa)	7.0
DOS/Steam Outlet Temperature (°C)	25/311.7
Steam/Feedwater Mass Flow Rate (kg/s)	~686
Feedwater Temperature (°C)	250
Chimney Height (m)	10
Vessel Height/Diameter/Thickness (m)	20.5/6/0.25
Vessel Operating Temperature (°C)	440
Pb-Bi Inventory (kg)	$\sim 3.6 \times 10^6$

For the conditions of **Table 4.I**, the temperature and void fraction profiles in the chimney are plotted in **Figure 3.9** and **3.10**, respectively. The mixture quality in the chimney is 0.0084 and the flow regime is cap flow throughout almost the entire chimney.

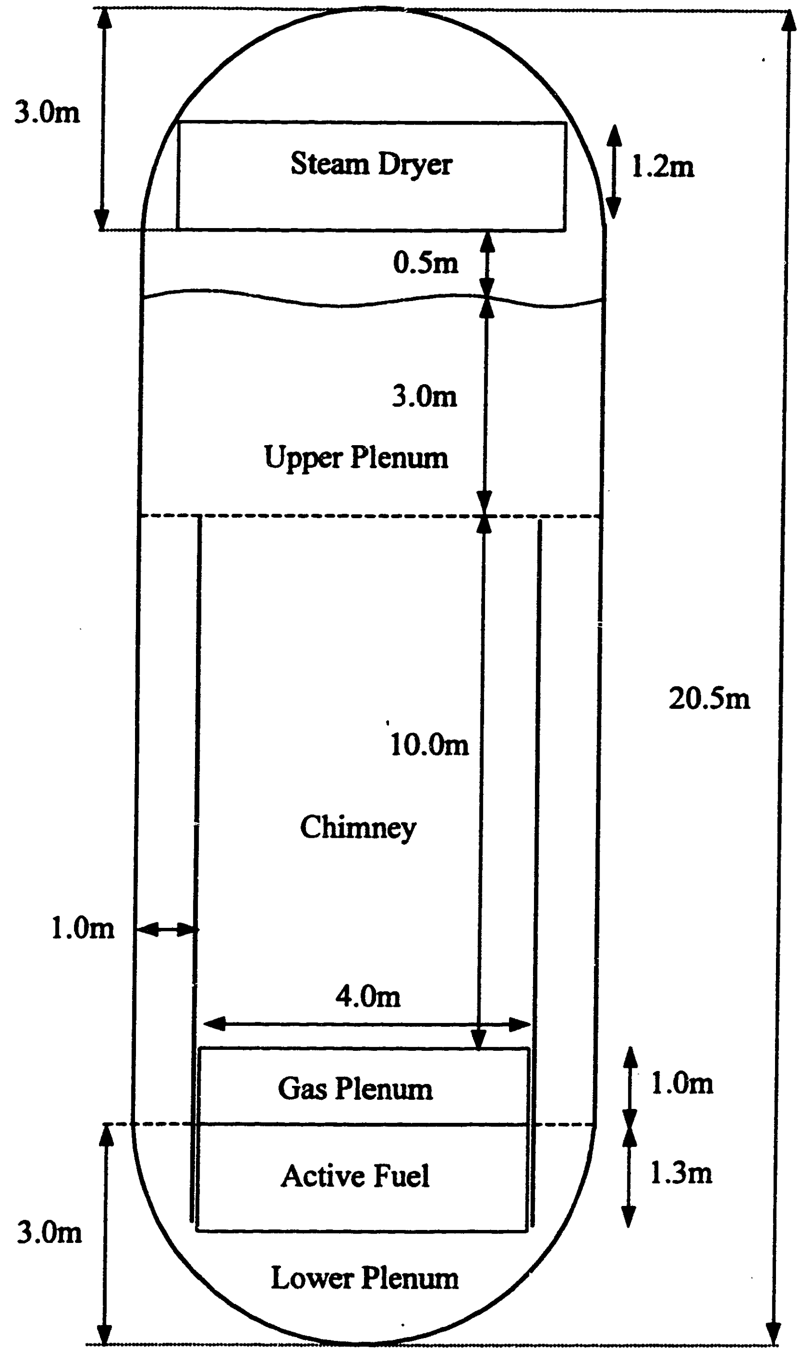

Figure 4.9. The reference geometry of the PBWR primary system.

4.7 Subchannel Considerations

Although the analysis of **Section 4.6** does take into account the radial and axial peaking power factors, the different subchannels within the hot fuel assembly were not considered. However, in principle the temperature limits will be set by the hot subchannel within the hot assembly. An accurate subchannel analysis of the PBWR core would require the use of sophisticated thermal-hydraulic codes like SAS or SuperEnergy and is beyond the scope of this study. Here we will present only some qualitative considerations. With reference to **Figure 2.4** it is expected that the coolant flow rate in subchannels IC, E and OC be smaller than in subchannel C. Assuming temperature independent fluid properties, a roughly constant friction factor and equal pressure drops in all subchannels, it can be readily demonstrated that the ratio of mass flow rate of any two subchannels j and k is:

$$\frac{\dot{m}_j}{\dot{m}_k}=\frac{A_j}{A_k}\sqrt{\frac{D_j}{D_k}} \qquad \textbf{Eq.4.22}$$

where A is the subchannel flow area and D its hydraulic diameter. Indicating with q_j the power discharged in subchannel j, the ratio of the coolant temperature rise in any two subchannels j and k is:

$$\frac{\Delta T_{cool,j}}{\Delta T_{cool,k}}=\frac{q_j}{q_k}\frac{\dot{m}_k}{\dot{m}_j} \qquad \textbf{Eq.4.23}$$

where ΔT_{cool} is the coolant temperature rise.

From **Eq.4.22** the ratio of the coolant velocity in any two subchannels j and k is:

$$\frac{V_j}{V_k}=\frac{\dot{m}_j}{\dot{m}_k}\frac{A_k}{A_j}=\sqrt{\frac{D_j}{D_k}} \qquad \textbf{Eq.4.24}$$

where V is the velocity. The ratio of the heat transfer coefficient in any two subchannels j and k can be calculated from the definition of Nusselt number and from **Eq.4.5** as[4]:

$$\frac{h_j}{h_k}=\frac{D_k}{D_j}\left(\frac{V_jD_j}{V_kD_k}\right)^{0.96}=\left(\frac{D_k}{D_j}\right)^{0.04}\left(\frac{V_j}{V_k}\right)^{0.96} \qquad \textbf{Eq.4.25}$$

---

[4] The exponent of the Pe number in **Eq.4.5** is 0.96 for P/D=1.2.

where h is the heat transfer coefficient. Because the heat flux is approximately the same for all subchannels (i.e. the local peaking factor is small, see **Figure 2.15**), the ratio of the temperature difference across the Pb-Bi boundary layer is:

$$\frac{\Delta T_{bl,j}}{\Delta T_{bl,k}} = \frac{h_k}{h_j} \qquad \textbf{Eq.4.26}$$

where ΔT_{bl} is the coolant temperature difference across the boundary layer. For the data of **Table 2.II**, the results of **Eq.4.22, 4.23, 4.24, 4.25** and **4.26** are reported in **Table 4.II**. All values are normalized to the nominal C subchannel. The far-most right column reports the expected peak clad temperature calculated on the basis of ΔT_{cool} and ΔT_{bl}.

Table 4.II. Subchannel thermal-hydraulics.

Subchannel	$\dot{m}_j$	q_j	$\Delta T_{cool,j}$	V_j	h_j	$\Delta T_{bl,j}$	$T_{clad,peak}$ (°C)
C	1.00	1.00	1.00	1.00	1.00	1.00	600
IC	0.61	0.75	1.23	0.81	0.83	1.20	636
E	0.38	0.50	1.32	0.75	0.78	1.28	650
OC	0.16	0.25	1.56	0.63	0.67	1.50	688

As expected, the peak clad temperature in the IC, E and OC subchannels exceeds that of the nominal subchannel C. Although we conservatively selected 600°C as the clad temperature limit, several investigators claim that the EP-823 clad can safely operate at up to 650°C (see discussion in **Section 2.2.4**). However, while subchannels IC and E remain within this extended limit, subchannel OC significantly exceeds it. One way to reduce the peak temperature in subchannel OC is to decrease the fissile enrichment of the four OC pins in the hot assembly. It is estimated that the enrichment reduction required to lower the OC peak temperature below 650°C is approximately 15%. So small an enrichment change in just four pins of a single assembly (which has 240 fuel pins) should not significantly affect the core neutronics.

Finally, note that radial thermal conduction was conservatively neglected in this analysis. However, it is an effective mechanism of heat transfer in a liquid metal system and is expected to flatten the temperature differences between contiguous subchannels, thus reducing the peak clad temperature in the critical subchannels IC, E and OC.

4.8 The Decay Heat Removal System

After reactor shut-down, the heat produced by the radioactive decay of the residual fission fragments must be properly removed to ensure the integrity of the nuclear fuel. The variation of the PBWR fuel decay power with time after shut-down is illustrated in **Figure 2.24**. Normally this heat is removed from the reactor pool by vaporization of liquid water in the chimney, but other means must be provided to ensure continuous cooling of the nuclear fuel should that heat removal path fail (e.g. upon loss of the feedwater pumps). In this section the characteristics of a suitable Decay Heat Removal System (DHRS) are explored.

To increase the reliability of the emergency decay heat removal, it is desirable to select a system that operates passively. A widely investigated and accepted DHRS is the so-called Reactor Vessel Air Cooled System (RVACS), designed by GE for the advanced sodium-cooled reactor project [GE 1991]. A schematic of this DHRS is shown in **Figure 4.10** (see also **Figure 2.25**). The heat produced in the core is conveyed by the naturally circulating primary coolant (in our case Pb-Bi) to the surface of the reactor vessel. The gap between the vessel and the containment is filled with an inert gas (e.g. argon). The heat is transferred through the gap mainly by radiation. Air enters the reactor building and flows through the downcomer to the containment bottom. From here it flows upward in the collector, it removes the decay heat from the containment wall and it is finally discharged to the atmosphere through a stack that supplies the gravitation head needed to passively drive the air through the circuit[5]. This design is adopted as our base DHRS configuration.

4.8.1 Assumptions and Equations

We will now quantitatively analyze the characteristics of the DHRS. The following general assumptions are made:

- Steady-state conditions. Although decay heat situations are generally time-dependent, the maximum power removable by a DHRS is more readily calculated at steady-state.
- Water is not injected into the reactor pool. Therefore, natural circulation of the Pb-Bi coolant is driven only by the Pb-Bi temperature difference between the void-free reactor chimney and downcomer.

---

[5] In **Figure 4.10** the air inlets and the exhaust stack are not shown.

- The gap between the vessel and the containment is filled with argon and the heat is transferred by radiation and free convection.
- Part of the heat flux at the containment outer surface is transferred by convection directly to the air and the other part by radiation to the collector wall. It is assumed that the outer surface of the collector wall is insulated so that all the radiated energy is ultimately discharged into the air flowing upward in the collector. Radiation heat transfer to the collector wall is very important because it effectively doubles the heat exchange surface through which the heat is transferred to the air.

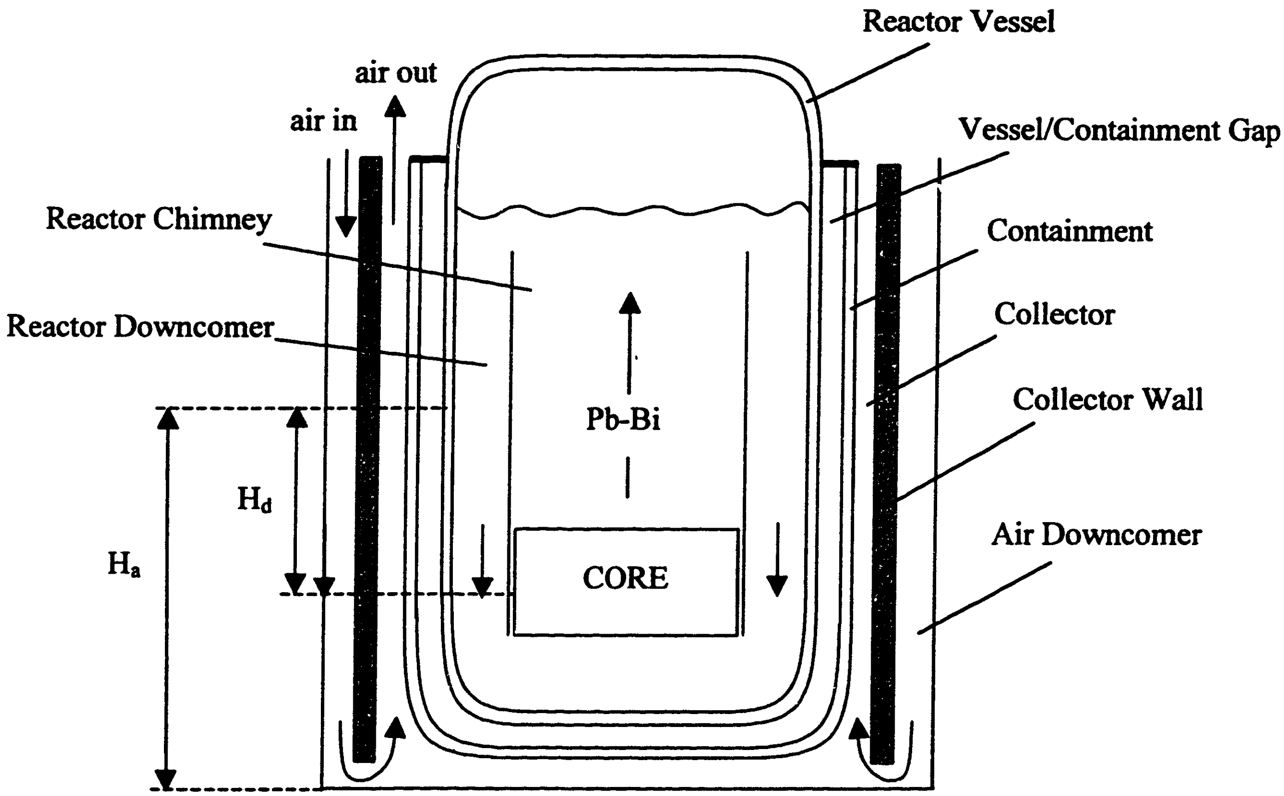

Figure 4.10. Schematic of the DHRS (configuration a)).

The thermal-hydraulics of the reactor pool is described by the following equations:

$$gH_d(\rho_{dc}-\rho_c)=\sum_i\left(K_i+f_i\frac{L_i}{D_i}\right)\frac{\dot{M}_d^2}{2\rho_i A_i^2} \qquad \text{Eq.4.27}$$

$$\dot{Q}_d=\dot{M}_d c_p(T_{p0}-T_{pi}) \qquad \text{Eq.4.28}$$

where, in addition to the symbols of **Eq.4.13** and **4.15,** ρ_{dc} and ρ_c are the Pb-Bi density in the downcomer and chimney, respectively. $\dot{Q}_d$ is the decay power. $\dot{M}_d$ is the Pb-Bi mass flow rate and H_d the gravity head[6]. Note that, because the heat is discharged through the vessel wall, the thermal center of the hot Pb-Bi is located approximately halfway between the vessel bottom and the Pb-Bi free surface (see **Figure 4.10**). The friction and form loss coefficients in the Pb-Bi pool are calculated as in **Section 4.4.**

The clad and fuel temperature profiles can be calculated again by means of **Eq.4.18, 4.19** and **4.20** where $\dot{Q}$ and $\dot{M}_p$ are replaced by $\dot{Q}_d$ and $\dot{M}_d$, respectively. However, because the decay power is only a small fraction of the nominal core thermal power, the temperature drop across the fuel and the clad is much smaller than under normal operating conditions and to a first approximation it can be assumed that the fuel, the clad and the coolant are all at the same temperature.

Newton's law of cooling provides the vessel inner surface temperature, $T_{v,i}$, as:

$$T_p - T_{v,i} = \frac{q''_{v,i}}{h_{v,i}} \qquad \textbf{Eq.4.29}$$

where T_p is the Pb-Bi temperature in the downcomer and $q''_{v,i}$ is the heat flux at the vessel inner surface. The heat transfer coefficient at the inner surface of the vessel, $h_{v,i}$ is calculated from the Seban correlation for liquid metal flow in annuli [Todreas 1990]:

$$Nu = 5.8 + 0.02 Pe^{0.8} \qquad \textbf{Eq.4.30}$$

The decay heat is transferred through the vessel wall by conduction. Then:

$$T_{v,i} - T_{v,o} = q''_{v,i} \frac{t_v}{k_v} \qquad \textbf{Eq.4.31}$$

where $T_{v,o}$ is the vessel outer surface temperature, t_v and k_v are the vessel thickness and thermal conductivity, respectively. The HT-9 vessel thermal conductivity is obtained by linearly interpolating the reference values of **Section 2.2.4.** In **Eq.4.31** the curvature of the vessel is ignored. Note that the vessel temperature limit of **Section 4.2** is on the membrane temperature $T_{v,m}$ defined as:

$$T_{v,m} = \frac{T_{v,i} + T_{v,o}}{2} \qquad \textbf{Eq.4.32}$$

---

[6] The subscript d stands for "at decay heat conditions".

The heat flux at the vessel outer surface, $q''_{v,o}$, is:

$$q''_{v,o} = h_g(T_{v,o} - T_{c,i}) + \varepsilon_g \sigma(T_{v,o}^4 - T_{c,i}^4) \qquad \textbf{Eq.4.33}$$

where $T_{c,i}$ is the containment inner temperature and σ is the Stefan-Boltzmann constant (σ=5.67×10^{-8}W/m^{2}K^4). ε_g is the vessel/containment gap equivalent emissivity calculated as:

$$\frac{1}{\varepsilon_g} = \frac{1}{\varepsilon_v} + \frac{1}{\varepsilon_c} - 1 \qquad \textbf{Eq.4.34}$$

where ε_v and ε_c are the emissivity of the vessel and containment, respectively. Following the ALMR design, the containment is made of 2¼Cr-1Mo construction steel, whose emissivity reference value is assumed to be 0.80 [GE 1991]. The vessel emissivity is assumed to be 0.75, which is representative of the average experimental data for stainless steels collected for the ALMR test program and reported by Hunsbedt [Hunsbedt 1988]. h_g is the gap heat transfer coefficient and is calculated from the MacGregor correlation for free convection in rectangular enclosures [Incropera 1990]:

$$Nu = 0.046 Ra^{1/3} \qquad \textbf{Eq.4.35}$$

where the Rayleigh number is based on the gap width t_g, which is set equal to that of the GE ALMR (t_g=12.7cm). Note that the radial displacement of the vessel due to thermal expansion (see **Figure 2.21**) can be readily accommodated in this gap.

Heat conduction through the containment wall yields:

$$T_{c,i} - T_{c,o} = q''_{c,i} \frac{t_c}{k_c} \qquad \textbf{Eq.4.36}$$

where $T_{c,o}$ is the containment outer surface temperature, t_c and k_c are the containment thickness and thermal conductivity, respectively. The containment is not a pressure barrier and its thickness is set equal to that of the ALMR (t_c=2.5cm). The 2¼Cr-1Mo steel thermal conductivity is calculated by linearly interpolating between the following two reference values: 42W/m·K at 130°C and 25W/m·K at 730°C [Incropera 1990]. In **Eq.4.36** the curvature of the containment is ignored.

The following equations hold for heat transfer at the outer surface of the containment:

$$q''_{c,o} = h_{air}(T_{c,o} - T_{air}) + \varepsilon_{coll} \sigma(T_{c,o}^4 - T_{coll}^4) \qquad \textbf{Eq.4.37}$$

$$\varepsilon_{coll} \sigma(T_{c,o}^4 - T_{coll}^4) = h_{air}(T_{coll} - T_{air}) \qquad \textbf{Eq.4.38}$$

where $T_{c,o}$ is the containment outer temperature, T_{air} is the air temperature and T_{coll} is the collector wall temperature. ε_{coll} is the collector equivalent emissivity and can be calculated from **Eq.4.34** where ε_v is replaced by ε_{cw} , i.e. the collector wall emissivity, again set equal to 0.8 because the collector wall is also made of 2¼Cr-1Mo construction steel [GE 1991]. The air heat transfer coefficient h_{air} is calculated from the Dittus-Boelter correlation.

Natural circulation of in the air circuit is described by the following two equations:

$$gH_a\left(\rho_{air,in} - \rho_{air,out}\right) = \sum_i \left(K_i + f_i \frac{L_i}{D_i}\right)\frac{\dot{M}_a^2}{2\rho_i A_i^2} \qquad \textbf{Eq.4.39}$$

$$\dot{Q}_d = \dot{M}_a c_a (T_{air,in} - T_{air,out}) \qquad \textbf{Eq.4.40}$$

where H_a is the altitude of the thermal center of the stack, $\rho_{air,atm}$ and $\rho_{air,stack}$ are the density of the cold atmospheric air and of the hottest air in the stack, respectively. $T_{air,in}$ and $T_{air,out}$ are the inlet and outlet air temperature, respectively. $\dot{M}_a$ is the air mass flow rate.

4.8.2 The Computational Algorithm

In principle, knowledge of the characteristics of the air circuit (e.g. pipe geometry, stack height, inlet and outlet form losses) is required to solve **Eq.4.39**. However, it was shown by Davis [MIT/INEEL 2000] that a satisfactorily accurate reproduction of the GE RVACS data can be achieved by i) neglecting the driving head provided by the stack, ii) considering the friction pressure losses as occurring in the air collector only (of variable width t_{ac}) and iii) modeling the pressure drops in the rest of the circuit as a concentrated form loss equal to 0.33 kinetic heads. Note that assumption i) implies that the hot air thermal center is approximately halfway between the containment bottom and the Pb-Bi free surface (see **Figure 4.10**).

The main input of the calculation is the decay power. The air atmospheric temperature $T_{air,in}$ is always fixed at 37°C as assumed in [GE 1991]. The solution of **Eq.4.39** and **4.40** yields $T_{air,out}$ and $\dot{M}_a$. The temperature T_{air} to be used in **Eq.4.37** and **4.38** is then calculated as:

$$T_{air} = \frac{T_{air,in} + T_{air,out}}{2} \qquad \textbf{Eq.4.41}$$

The temperatures T_{coll} and $T_{c,o}$ are found from **Eq.4.37** and **38**. The temperatures $T_{c,i}$, $T_{v,o}$, $T_{v,i}$ and $T_{v,m}$ are calculated from **Eq.4.37, 4.33, 4.31** and **4.32**, respectively.

The temperature T_p to be used in **Eq.4.29** is defined as:

$$T_p = \frac{T_{p0} + T_{pi}}{2} \qquad \textbf{Eq.4.42}$$

Then **Eq.4.27, 4.28** and **4.29** constitute a system of three equations in the three unknowns T_{p0}, T_{pi} and $\dot{M}_d$, which closes the problem. Note that the heat flux in **Eq.4.29, 4.31, 4.33, 4.36** and **4.37** is known from the decay power and the geometry of the system.

To evaluate the reliability of the predictions generated with this model, a benchmark against the thermal-hydraulic code ATHENA was undertaken for a vessel of 22m height, 6m diameter, and 5cm thickness at a decay power level of 4MWth. The air collector width was set equal to 17.8cm. The results of the benchmark are reported in **Table 4.III**. It can be seen that the agreement of our DHRS model with ATHENA is excellent. Similarly accurate results were obtained for different decay power levels and vessel sizes.

Table 4.III. Benchmark of the DHRS model.

Parameter	ATHENA	Present Study
$\dot{Q}_d$ (input)	4.0MW	4.0MW
$T_{air,in}$ (input)	37°C	37°C
T_{p0}	799.1°C	796.4°C
T_{pi}	785.9°C	785.7°C
$\dot{M}_d$	2,592kg/s	2,564kg/s
$T_{v,i}$	701.3°C	693.6°C
$T_{v,o}$	674.5°C	670.6°C
$T_{c,i}$	525.8°C	525.8°C
$T_{c,o}$	512.8°C	514.5°C
T_{coll}	397.1°C	412.1°C
$T_{air,out}$	198.9°C	196.8°C
$\dot{M}_a$	24.2kg/s	24.8kg/s

4.8.3 Results and Discussion

The effect of the air collector width is analyzed first. **Figure 4.11** illustrates the variation of the containment outer temperature with the air collector width for reference vessel diameter and height, D_c=6m and L_v=20.5m and for three different values of the decay power. Increasing the collector width decreases the hydraulic resistance of the air circuit and therefore larger air mass flow rates are attained along with smaller air bulk temperatures (for a given decay power). On the other hand, a decrease of the collector width implies a smaller flow area, which tends to increase the air velocity and thus the heat transfer coefficient. The result of these two effects is that for each power level there exists an optimum value of the collector width. Note that the optimum value only slightly increases with the decay power and ranges from 20 to 25cm. The intermediate value of 23cm was selected as the reference collector width, which will be used throughout the rest of this section.

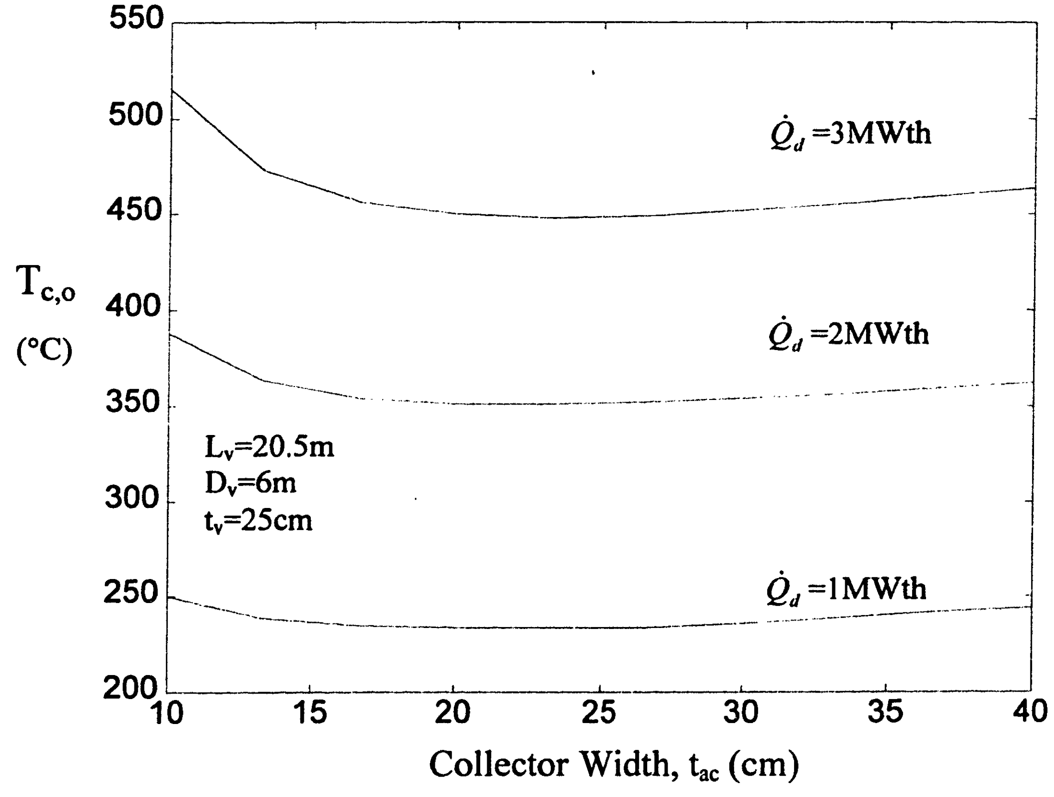

Figure 4.11. The air collector width effect.

To illustrate the relative importance of the different thermal resistances in the DHRS, all the relevant temperatures are plotted in **Figure 4.12** as a function of the decay power (for a 6m diameter, 20.5m height, 25cm thickness vessel). The temperature constraints are again from **Section 4.2** and are drawn in **Figure 4.12** as horizontal shaded lines (the fuel temperature limit is 1400°C, not shown in **Figure 4.12**). As expected, the largest temperature drops take place in the vessel/containment gap ($T_{v,o}$-$T_{c,i}$) and at the outer surface of the containment ($T_{c,o}$-$T_{air,out}$). Also, the temperature drop across the vessel is significant due to the large vessel thickness. Finally, note that the most constraining limit is again the clad temperature, although the vessel limit is relatively close to it (1.9 vs. 2.2MWth).

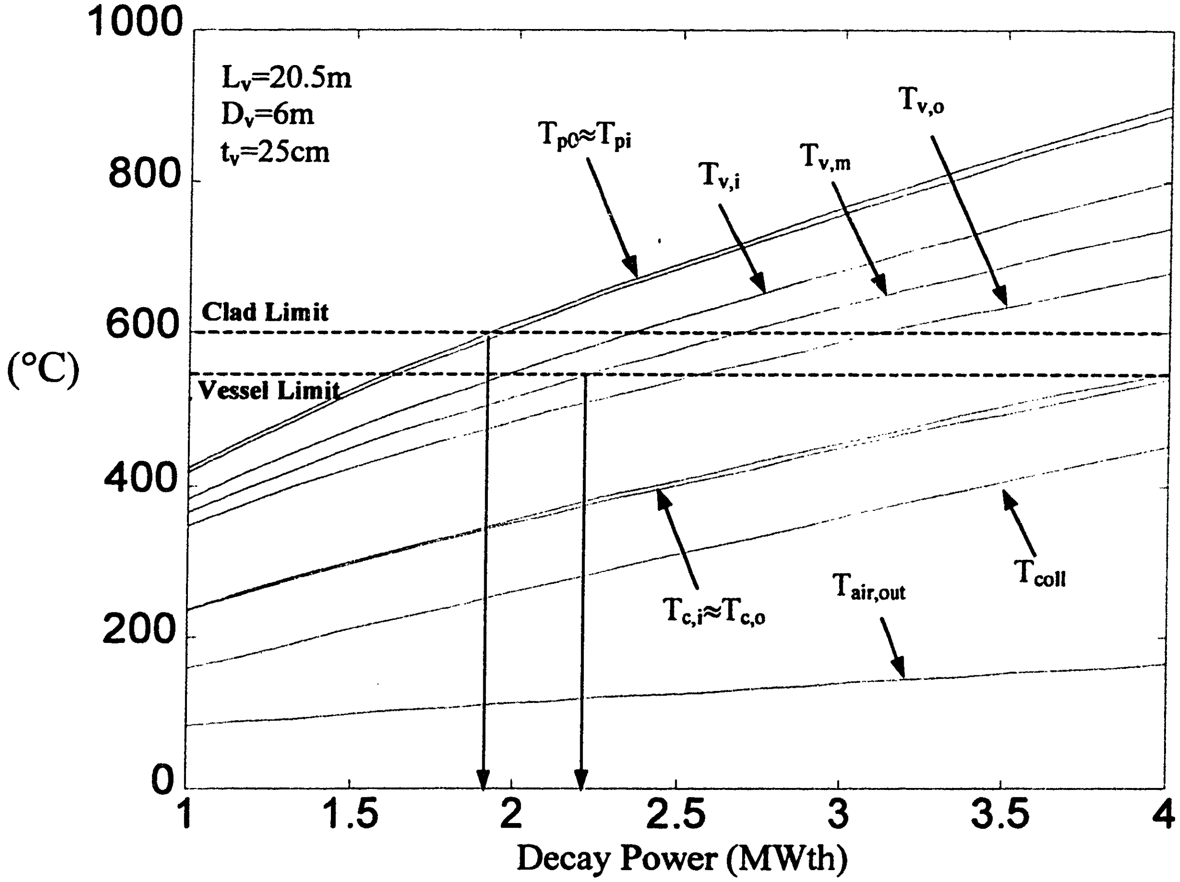

Figure 4.12. DHRS temperature variation with decay power.

The DHRS performance can be enhanced by reducing the dominant thermal resistances. If the vessel/containment gap is filled with a liquid metal acting as a thermal bond, the power removable by the DHRS increases substantially. In our case the natural choice for the thermal bond material is liquid Pb-Bi. However, the presence of a liquid metal in the gap makes online inspection and access to the reactor vessel and containment harder. We shall assume that the heat is transferred in the gap by free convection. **Eq.4.33** is still applicable once the emissivity is set equal to zero[7] and a proper correlation is utilized to compute the heat transfer coefficient h_g:

$$Nu = 0.028Ra^{0.355} \qquad \textbf{Eq.4.43}$$

Eq.4.43 is recommended in reference [Tang 1978] for free convection of liquid metal in vertical enclosures in the $4\times10^4<Ra<10^8$ range.

Figure 4.13 illustrates the variation of the relevant temperatures with decay power for a DHRS with a thermal bond in the gap. The improvement over the base design of **Figure 4.12** is apparent, since the limit is now about 2.65MWth.

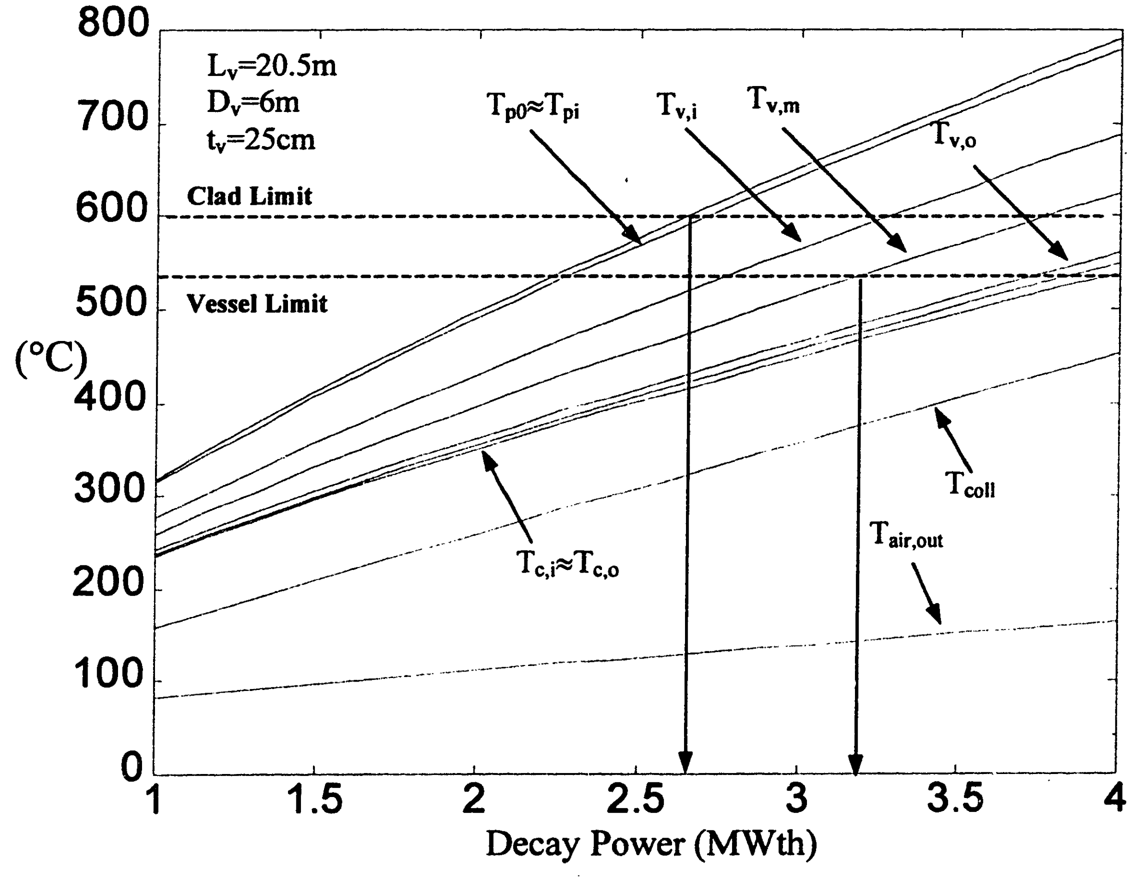

Figure 4.13. Temperatures in the DHRS with thermal bond.

---

[7] radiation heat transfer does not occur through an opaque fluid

An even more drastic modification of the DHRS base design consists of replacing air with liquid water as the ultimate heat sink on the outer surface of the containment. If the collector is flooded with water and the heat flux is sufficiently high, boiling occurs and the containment temperature can be maintained close to the water saturation temperature (100°C at atmospheric pressure). A schematic of this DHRS design is illustrated in **Figure 4.14.** Note that use of the thermal bond in the vessel/containment gap is retained. The heat transfer coefficient at the outer surface of the containment, $h_{c,o}$, is calculated from the Rohsenow correlation for pool boiling [Incropera 1990]:

$$h_{c,o} = \left[\frac{g(\rho_f - \rho_g)}{\sigma}\right]^{1/2} \left(\frac{c_{p,f}\mu_f^3 h_{fg}^2}{C_{fm}\Pr_f^n}\right)^3 (T_{c,o} - T_{sat})^2 \qquad \textbf{Eq.4.44}$$

where ρ, μ, and σ are the density, viscosity and surface tension, respectively. The subscripts f and g refer to saturated liquid water and saturated steam, respectively. T_{sat} is the water saturation temperature and Pr the Prandtl number. C_{fm} and n are two empirically determined coefficients that depend on the fluid/material pair. For boiling water on steel, it is C_{fm}=0.013 and n=1.

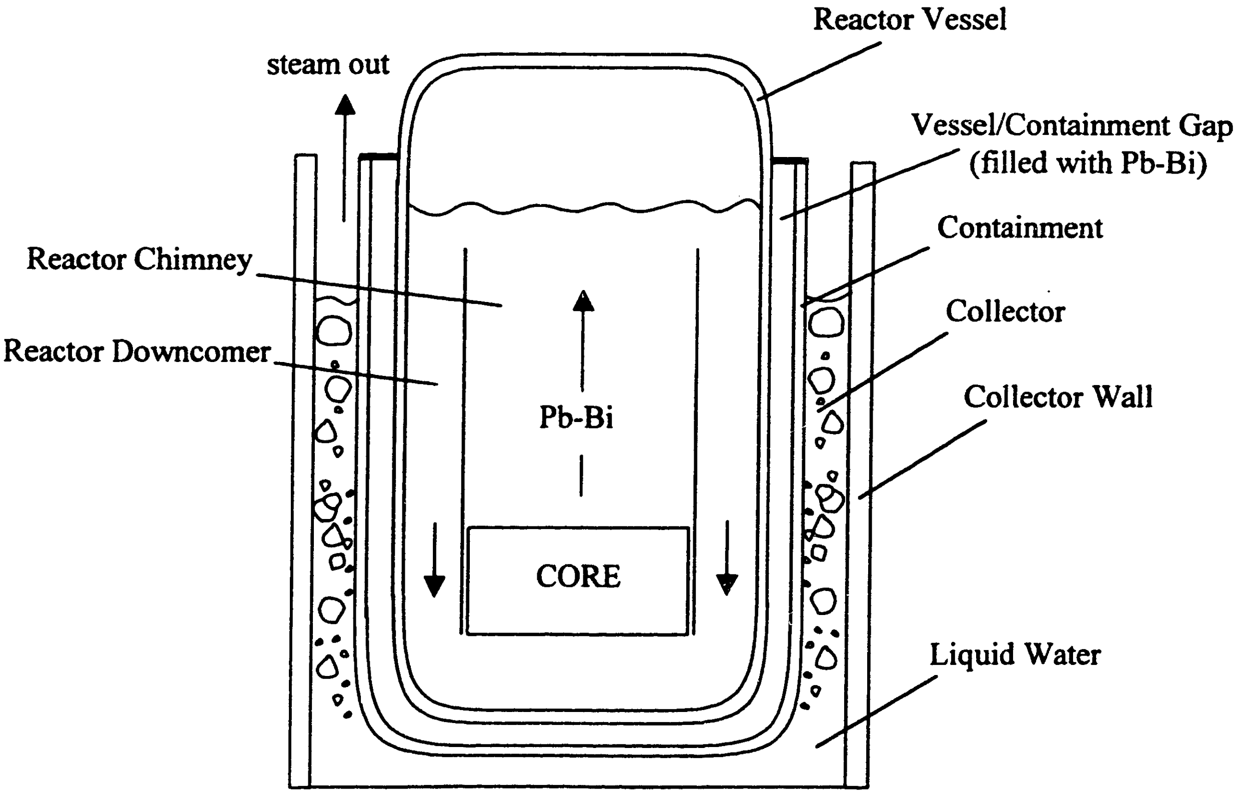

Figure 4.14. Schematic of the water cooled DHRS.

In **Figure 4.15** the relevant temperatures are plotted vs. the decay power for this DHRS design. It can be seen that the largest temperature drops now occur in the vessel and at the inner surface of the vessel. Although this DHRS provides superior heat removal capability (up to 7.6MWth), its mode of operation may raise a concern about the degree of passivity of the system. A continuous supply of water must be provided at the outer surface of the containment to prevent dry-out and consequent reduction of the heat transfer coefficient. This can be accomplished passively only if a water reservoir is located at a higher elevation than the reactor.

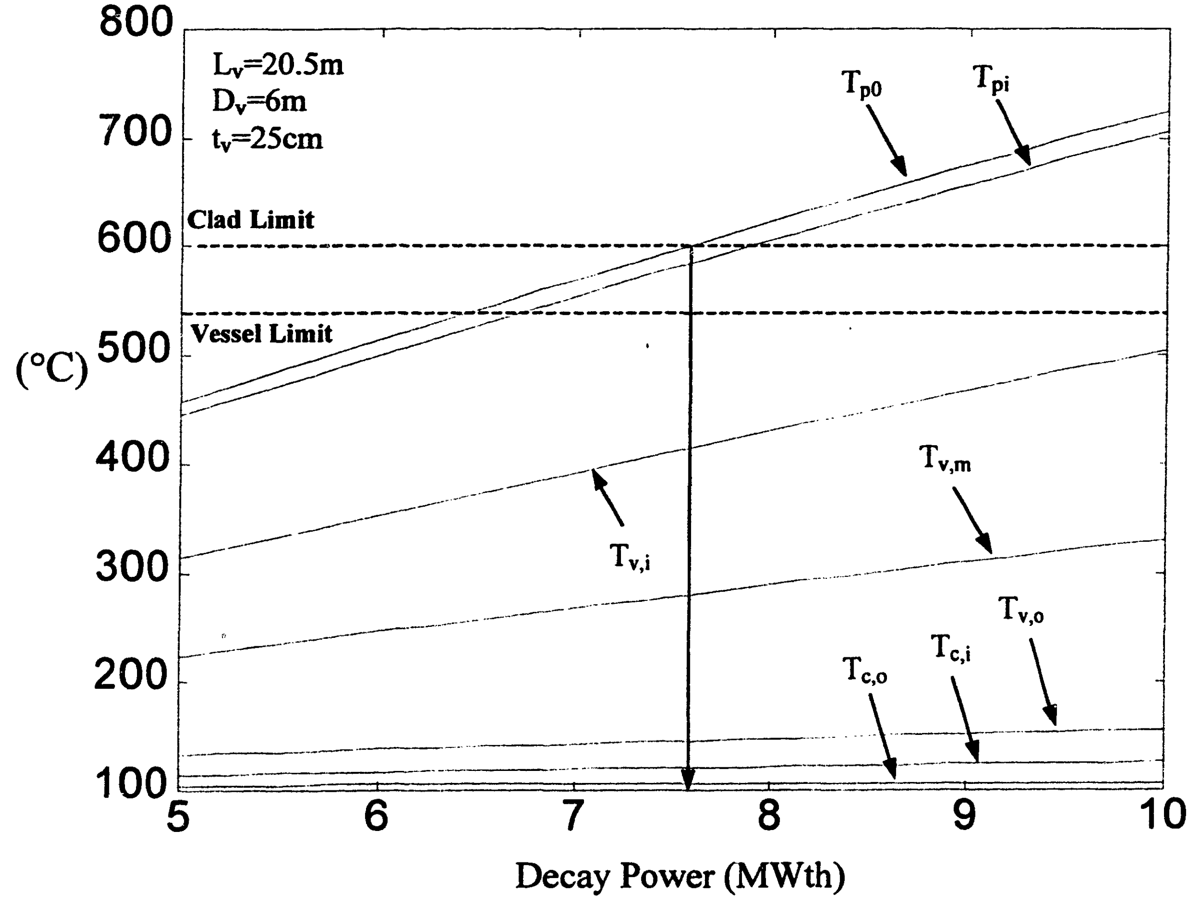

Figure 4.15. Temperatures in the DHRS cooled by water.

4.8.4 Maximum Removable Decay Power

In the previous sections we identified three different DHRS configurations: 1) a traditional RVACS with argon in the vessel/containment gap and air as the heat sink, 2) a modified RVACS with a liquid Pb-Bi thermal bond in the gap and air as the sink, and 3) a DHRS with a liquid Pb-

Bi thermal bond in the gap and boiling water on the outer surface of the containment as the heat sink. We will now systematically assess their performance. The selected figure of merit is the maximum removable decay power. The constraints are once again the temperature limits of the fuel, clad and reactor vessel reported in **Section 4.2.**

Transient analysis of these systems conducted by Davis [MIT/INEEL 2000] showed that peak temperatures in the fuel, clad and vessel are achieved approximately 25 to 30 hours after shutdown, when the decay power is between 0.55 and 0.57% of the nominal reactor thermal power (see **Figure 2.24**). It was also found that the transients are very slow and can be effectively treated as quasi-static. These considerations indicate that a suitable DHRS can be selected on the basis of a steady-state analysis, where it is proven that the system is capable of removing 0.57% of the nominal core power without violating the fuel, clad and vessel temperature limits. Conversely, the analysis can be used to determine what reactor thermal power ($\dot{Q}_{\max,d}$) is compatible with a given DHRS configuration is. We will follow this latter approach, which enables a clear comparison with the analysis of **Section 4.6.**

Figure 4.16 shows the maximum reactor thermal power compatible with DHRS configuration #1 and #2 (dashed and solid lines, respectively) as a function of the vessel diameter and height, for a vessel thickness of 25cm. Again it should be emphasized that the actual decay power removable by the DHRS is only 0.57% of the values indicated on the ordinate axis of **Figure 4.16**. Because the heat transfer surface increases with the vessel height and diameter, so does the maximum thermal power. However, these configurations do not allow the design of a high thermal power system for any reasonable values of the vessel height or diameter. For L_V=20.5m and D_V=6m (our reference reactor vessel), configuration #1 and #2 would allow a reactor power of about 340 and 465MWth, respectively, i.e. considerably below our reference 1260MWth power. Therefore, if DHRS configurations #1 or #2 are selected, the reactor could not be designed at its optimum normal operating conditions and a new (lower) value of the thermal power should be selected.

In **Figure 4.17** the maximum reactor thermal power compatible with DHRS configuration #3 is illustrated for different values of the vessel height and diameter. The power increases with the vessel height, but slightly decreases with the vessel diameter, as discussed next. In configuration #3 an important thermal resistance is the heat transfer coefficient of Pb-Bi on the inner surface of the vessel. For a given core, a smaller vessel diameter results in a narrower downcomer and thus in a larger Pb-Bi velocity and heat transfer coefficient. This more than offsets the effect of the increased heat flux associated with a smaller vessel diameter and the net result is a larger removable decay power.

For L_v=20.5m and D_v=6m, configuration #3 would allow a reactor power of about 1340MWth, i.e. above our reference 1260MWth power. Therefore, DHRS configuration 3) is compatible (although by a small margin) with the reference reactor thermal power selected in **Section 4.6**, which means that the reactor can be designed at its optimum normal operating conditions. We then select configuration #3 as our reference DHRS.

Finally, it should be noted that, when the reactor is normally operating, it is possible to let the DHRS run without dissipating too high a power (i.e. at most 0.57% of the nominal thermal power for configuration #3). In case of a sudden loss of the normal heat sink, this ensures immediate removal of the decay heat and reduces the risk of core overheating.

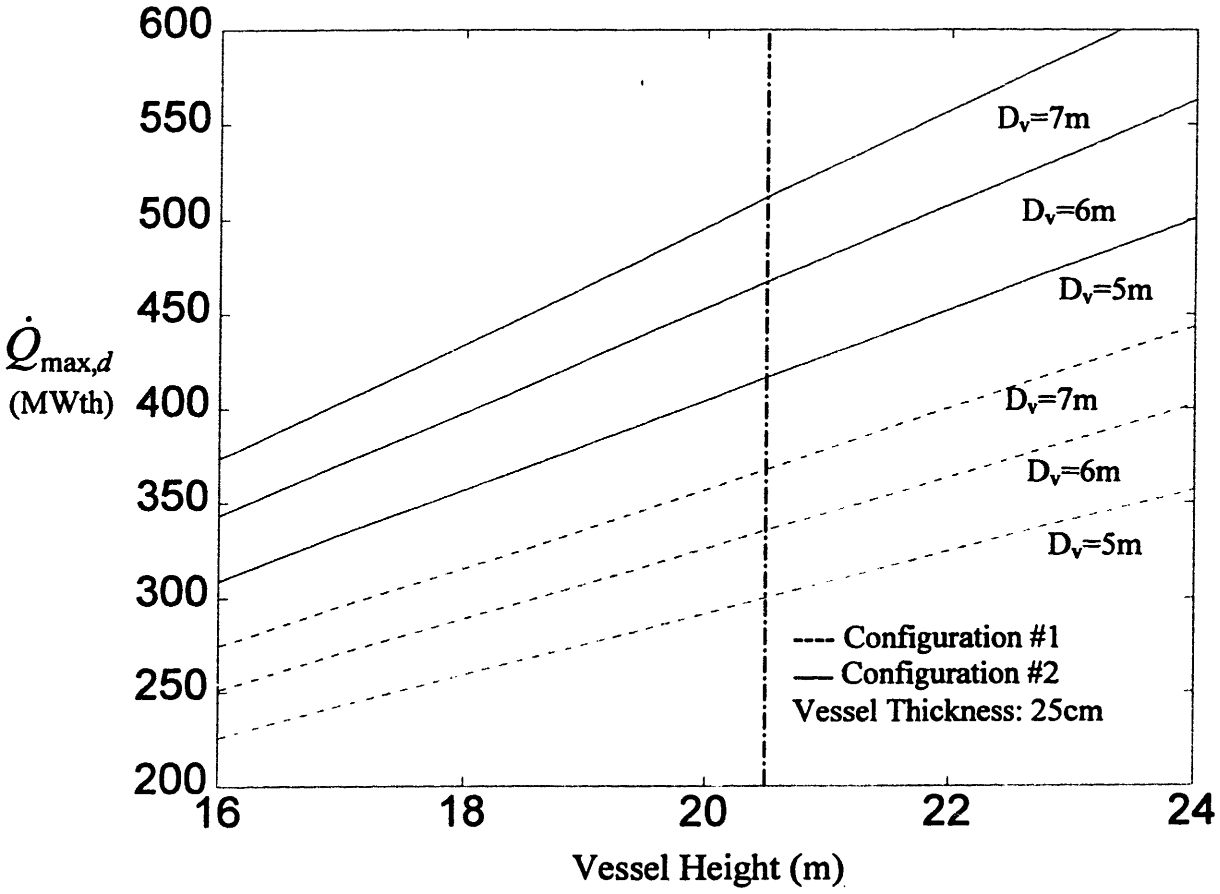

Figure 4.16. DHRS performance (configurations #1 and #2).

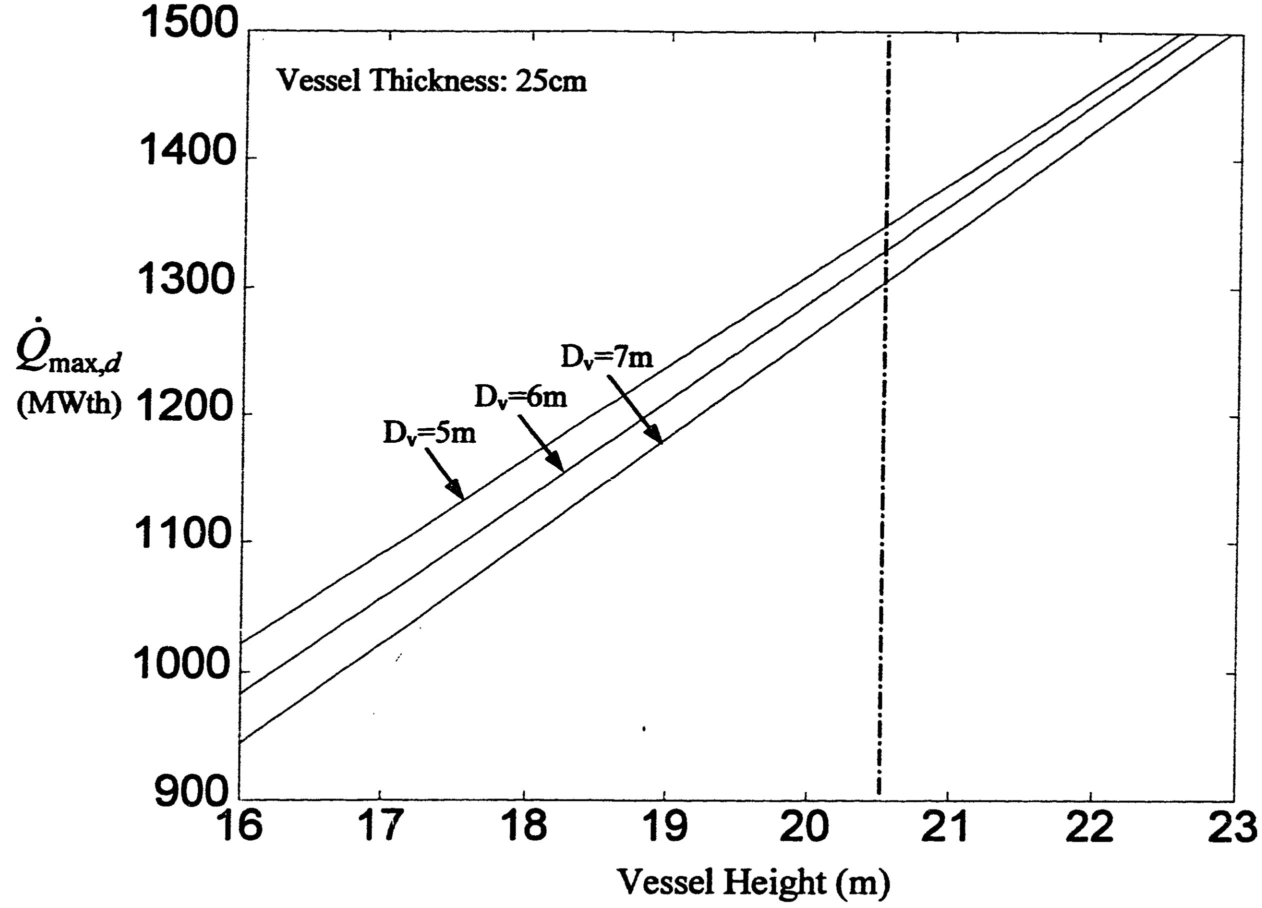

Figure 4.17. DHRS performance (configuration #3).

4.9 Dynamic Behavior of the PBWR Primary System

A rigorous analysis of the dynamic behavior of the PBWR primary system would require the use of sophisticated codes capable of modeling the time-dependent thermal-hydraulics of the direct contact heat transfer in the chimney as well as the coupling of the primary system to the power cycle. This analysis is beyond the scope of the present study. However, we will present in this section a qualitative description of the response of the PBWR to the most important anticipated transient situations: reactor start-up (**Section 4.9.1**), load change (**Section 4.9.2**) and loss of feedwater pumps with scram (**Section 4.9.3**). Also, a discussion is presented on the thermal-hydraulic instabilities that might arise in the PBWR primary circuit (**Section 4.9.4** and **4.9.5**).

4.9.1 Start-Up

It is assumed that at t=0, no water is injected into the Pb-Bi coolant and the decay heat is removed by dedicated heat exchangers in the online coolant purification system. The Pb-Bi may be maintained at a temperature around 200°C to prevent freezing. At time zero the pressure in the steam dome is low, i.e. about atmospheric. The control rods are progressively extracted from the core until the neutron counters indicate that criticality is achieved. As the neutronic power starts to rise, the feedwater pumps are activated and injection of liquid water into the reactor pool begins. It is key to inject less water than would be required to remove all of the neutronic power so that the fuel and coolant temperatures can increase. This enables the Doppler and fuel expansion effect to compensate for the increasing reactivity due to control rod extraction. In this scheme, the control rods control the coolant and fuel temperature while the water injection rate controls the neutronic power. By means of this procedure, the reactor temperatures and power can be simultaneously increased in a stable fashion until the nominal coolant temperature is achieved. We call this time t_1. At $t=t_1$ the water injection rate is allowed to fully match the neutronic power, which arrests the rise of the primary coolant temperature. The core power can be subsequently increased to its nominal value by further extraction of the control rods. Note that the fuel temperature continues to rise with the power so that the reactivity increase due to control rod extraction continues to be compensated by the Doppler and fuel expansion effects until the nominal reactor power is achieved, which occurs at time t_2.

In the first phase of the power and temperature ramp-up (until $t=t_1$), the turbine throttle and the turbine by-pass valve located at the end of the main steam lines are closed and slightly open, respectively. Therefore the steam generated upon injection of water in the Pb-Bi coolant is entirely discharged to the condenser. However, it is important to prevent excessive opening of the turbine by-pass valve so that the steam dome can be pressurized. When the pressure achieves its nominal value (which should occur sometime around t_1), the turbine by-pass valve is closed and the turbine throttle valve begins to open, which engages the turbine. At this point the generator can be connected to the grid. As the core power increases, the turbine throttle is progressively opened so that the turbine steam flow and the generator electric output increase until at $t=t_2$ the full reactor power is finally achieved.

Note that, although the system pressure is relatively low in the first phase of the reactor start-up (immediately after t=0), steam explosion phenomena are not expected because the Pb-Bi temperature is below the homogeneous nucleation limit (see **Section 3.4.1.1**).

4.9.2 Load Change

It is assumed that the reactor is connected to the grid and steadily operating at a certain power level (not necessarily the nominal full power). At t=0 the grid demands a larger load[8]. To fulfill the demand, the turbine throttle valve opens automatically and draws more steam from the steam dome. The pressure in the steam dome decreases due to the mismatch between the steam generated in the chimney and the steam flowing out of the steam dome. As a result, the pressure in the chimney also decreases and more liquid water flashes to void, which increases the natural circulation driving head. Therefore, the Pb-Bi flow rate increases which has two effects: 1) the mixture quality in the chimney decreases hence partially offsetting the effect of water flashing, and b) the fuel temperature decreases and thus the neutronic power rises due to the Doppler and fuel contraction feedbacks until the power stabilizes to the new required level.

Therefore, the PBWR exhibits the desirable characteristic of automatically following the load (like a PWR). However, it should be emphasized that allowing the reactor to follow the sequence described above (without external intervention) is not recommendable because, at the end of the transient, the fuel and coolant temperatures, as well as the steam dome pressure would be left below their nominal values. Therefore, the control system must be designed so that, when the turbine throttle opens, the control rods are automatically extracted from the core and the water injection rate is increased to match the new required power.

The transient discussed in this section and the reactor start-up of **Section 4.9.1** emphasize the need for feedwater pumps capable of injecting widely varying water flow rates. It is recommended that variable speed pumps (similar to the recirculation pumps of a BWR) be used for this purpose.

---

[8] In case of a load decrease the modifications to this discussion are obvious.

4.9.3 Loss of Feedwater Pumps with Scram

It is assumed that the reactor is connected to the grid and steadily operating at full power when at t=0 the feedwater pumps trip and the water flow to the reactor pool rapidly declines. The pressure in the steam dome markedly decreases due to the mismatch between the steam flow drawn by the turbine and the steam flow supplied by the chimney. The low pressure signal triggers a scram of the reactor, which shuts off the neutronic power. We call this time t_1. Also, at $t=t_1$ the turbine throttle closes, the generator is disconnected from the grid and the residual steam is discharged directly to the condenser. Note that the Pb-Bi flow begins to decrease immediately after the pump trip ($0<t<t_1$) due to the void reduction in the chimney. For $t>t_1$ the Pb-Bi coolant is heated in the core by the decay power and is cooled at the vessel wall by the DHRS. Because the voids in the chimney have completely disappeared, the Pb-Bi flow is sustained only by the temperature difference between the chimney and the downcomer. The average Pb-Bi temperature smoothly rises until the decay power matches the DHRS heat removal capability. We call this time t_2. The clad, fuel and vessel temperature peaks at $t=t_2$. For $t>t_2$ the temperatures coast down following the slow decrease of the DHRS.

4.9.4 Flow Excursion (Ledinegg) Instabilities

The susceptibility of the PBWR primary circuit to static instabilities of the Ledinegg type is analyzed in this section. It is assumed that the feedwater flow rate, $\dot{M}_w$, is maintained constant. The independent variable is the Pb-Bi mass flow rate $\dot{M}_p$. Consider the momentum equation of the primary circuit, **Eq.4.13**. Because the overwhelmingly dominant pressure drops in the circuit occur in the core, the right-hand term of **Eq.4.13** can be approximated as:

$$\sum_i \left(K_i + f_i \frac{L_i}{D_i}\right)\frac{\dot{M}_i^2}{2\rho_i A_i^2} \approx \left(K_{core} + f_{core}\frac{L_{core}}{D_{core}}\right)\frac{\dot{M}_p^2}{2\rho_p A_{core}^2} \qquad \textbf{Eq.4.45}$$

Since the flow in the core is single-phase and turbulent, it can be assumed that K_{core} and f_{core} are roughly independent of $\dot{M}_p$. Then **Eq.4.45** indicates that the pressure drops in the primary circuit are approximately proportional to the square of the Pb-Bi mass flow rate, as demonstrated in **Figure 4.18**, where also the pressure drops in the chimney and downcomer are considered. Let us now focus on the left-hand term of **Eq.4.13**. The density ρ_{dc} is approximately constant because the downcomer operates in single-phase flow[9]. For a given $\dot{M}_w$, an increase of $\dot{M}_p$ causes a decrease of the mixture quality (and of the void fraction) in the chimney and therefore an increase of the average density $\bar{\rho}_c$. A plot of the left-hand term of **Eq.4.13** as a function of $\dot{M}_p$ is also illustrated in **Figure 4.18** (labeled "density head"). When $\dot{M}_p$ is zero, the water rises in a stagnant pool of Pb-Bi, the average density $\bar{\rho}_c$ reaches its minimum and the density head its maximum. In **Figure 4.18** the operating condition is identified at the intersection of the two curves. This equilibrium point is stable because a decrease of $\dot{M}_p$ results in smaller pressure drops and a larger density head, which drives $\dot{M}_p$ back to its equilibrium value. Similarly, a $\dot{M}_p$ increase results in larger pressure drops and a smaller density head, thus the flow cannot be sustained and $\dot{M}_p$ is driven back to its equilibrium value again. Therefore it can be concluded that static instabilities of the Ledinegg type do not occur in the primary circuit of the PBWR.

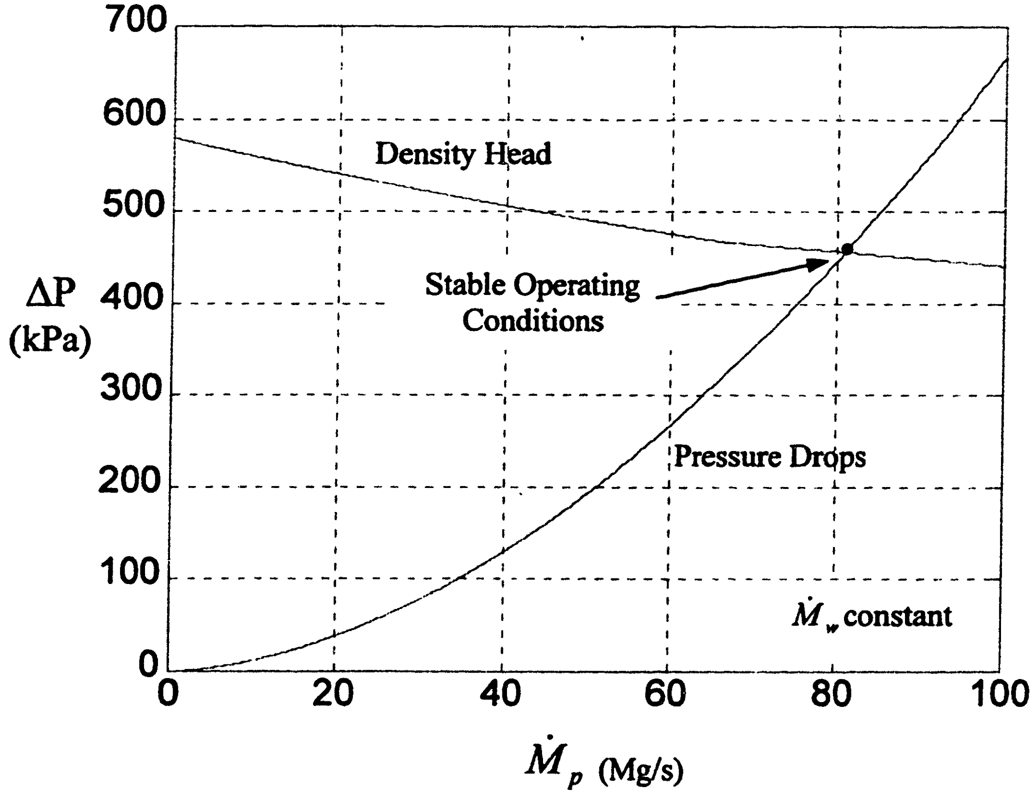

Figure 4.18. The characteristic curves of the PBWR primary circuit.

---

[9] The density change with temperature is neglected.

4.9.5 Dynamic Instabilities

4.9.5.1 Hydraulic Instabilities

Self-sustaining oscillations of the Pb-Bi mass flow rate in the primary system of the PBWR might theoretically arise due to the existence of oscillatory phase lags between the chimney and the rest of the circuit (i.e. core and downcomer). To illustrate the concept, let us assume that the feedwater flow rate is constant and the reactor is operating at steady-state. At t=0 the Pb-Bi mass flow rate in the core slightly increases[10]. Because the liquid Pb-Bi coolant is virtually incompressible, this perturbation is felt instantaneously at the chimney inlet. Since the feedwater flow is maintained constant, an increase of the Pb-Bi flow results in a smaller mixture quality (and thus a smaller void fraction). This void fraction perturbation (generated at the chimney inlet) travels up the chimney at finite velocity (i.e. the mixture velocity) and results in a decrease of the driving density head in the circuit, which in turn reduces the Pb-Bi mass flow rate in the downcomer and in the core. Note that, if the travelling velocity of the void fraction perturbation in the chimney were infinite, this feedback would have a stabilizing effect on the circuit because it would instantaneously oppose the initial Pb-Bi flow increase (as discussed in **Section 4.9.4**). However, the travelling velocity of the void fraction perturbation in the chimney is finite and a delayed reduction of the downcomer and core Pb-Bi flow is induced. The amplitude of this induced perturbation depends on the characteristics of the circuit, i.e. hydraulic resistance and void fraction dependence on the chimney Pb-Bi flow rate. If the amplitude of the induced perturbation is larger than the amplitude of the initial perturbation, the system is unstable because the oscillation grows with time. Indicating the traveling time of the Pb-Bi/water mixture in the chimney as τ (i.e. ~7s at reference PBWR conditions), the characteristic period of these instabilities would then be of the order of 2τ.

To quantitatively evaluate the susceptibility of the PBWR concept to this kind of hydraulic instability, we now undertake a dynamic analysis of the primary system in the frequency domain. The system is modeled as the coupled behavior of 4 regions, as illustrated in **Figure 4.19**. The time-dependent conservation equations for the Pb-Bi flow are:

Continuity

$$\dot{M}_1(t) = \dot{M}_4(t) \qquad \textbf{Eq.4.46}$$

---

[10] What actually causes this initial perturbation is irrelevant to the development of the transient that follows.

$$\dot{M}_2(t) = \dot{M}_1(t-\tau) \qquad \textbf{Eq.4.47}$$

$$\frac{dM_3(t)}{dt} = \dot{M}_2(t) - \dot{M}_4(t) \qquad \textbf{Eq.4.48}$$

Thus region 3 acts as a reservoir that receives flow from region 2 and provides the flow to region 4.

Momentum

$$\sum_{i=1}^{4}\frac{L_i}{A_i}\frac{d\dot{M}_i}{dt} = gL_2(\rho_4 - \rho_2) - \sum_{i=1}^{4}(K_i + f_i\frac{L_i}{D_i})\frac{\dot{M}_i^2}{2\rho_i A_i^2} \qquad \textbf{Eq.4.49}$$

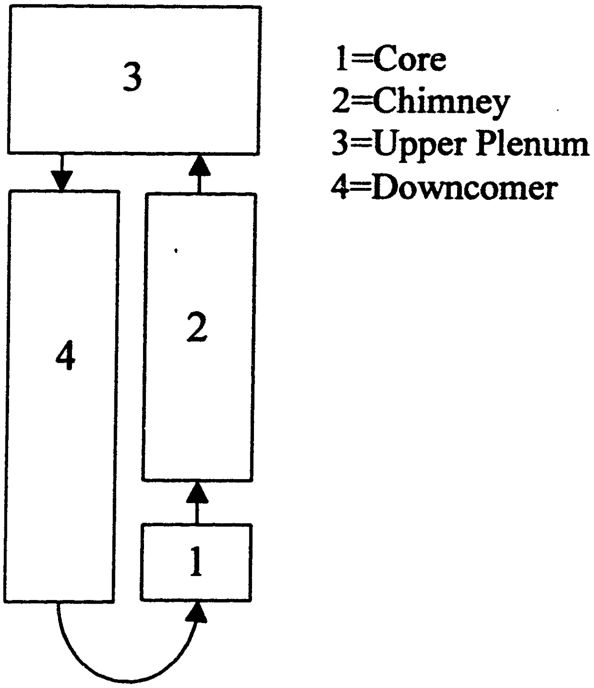

Figure 4.19. Schematic of the PBWR primary system for dynamic analysis.

Note that the acceleration term was neglected in the momentum equation. $\dot{M}_1$, $\dot{M}_2$, $\dot{M}_3$ and $\dot{M}_4$ are the core, chimney, upper plenum and downcomer Pb-Bi mass flow rates, respectively. M_3 is the upper plenum Pb-Bi mass. As already mentioned, the time delay τ is the travelling time of the mixture in the chimney[11]. L_i, A_i, D_i, K_i, ρ_i and f_i are the length, the flow area, the hydraulic diameter, the density, the form loss and friction coefficients of the i-th section, respectively. To simplify the analysis, the following assumptions are made:

a) The friction and form losses are neglected in the chimney, downcomer and upper plenum.

b) The hydraulic resistance of the core is represented by an effective form loss coefficient K_{core}.

c) The Pb-Bi velocity in the upper plenum is very small so that the $\frac{L_3}{A_3}\frac{d\dot{M}_3}{dt}$ term in **Eq.4.49** can be neglected.

d) The water density in the chimney is neglected so that the following approximation holds for the buoyancy term:

$$gL_2(\rho_4 - \rho_2) \approx gL_2\rho_p\alpha \qquad \textbf{Eq.4.50}$$

where α is the average void fraction in the chimney and ρ_p is the Pb-Bi density (assumed constant throughout the whole circuit).

e) In calculating the void fraction, the subcooled and saturated regions of the chimney are neglected. Furthermore, for simplicity, homogeneous flow is assumed and α is calculated as:

$$\alpha = \frac{1}{1 + \frac{1-x}{x}\frac{\rho_g}{\rho_p}} \approx \frac{x}{x + \frac{\rho_g}{\rho_p}} \qquad \textbf{Eq.4.51}$$

where ρ_g is the steam density and x is the mixture quality defined as:

$$x = \frac{\dot{M}_w}{\dot{M}_w + \dot{M}_2} \approx \frac{\dot{M}_w}{\dot{M}_2} \qquad \textbf{Eq.4.52}$$

Note that in **Eq.4.51** and **Eq.4.52**, the approximation is made that the feedwater mass flow rate is small compared with the Pb-Bi mass flow rate, since the quality is typically about 0.8%.

Making use of these assumptions and eliminating $\dot{M}_4$, **Eq.4.49** and **Eq.4.48** become, respectively:

---

[11] Note that there is no time delay between the downcomer and the core because they are in single-phase incompressible flow.

$$\left(\frac{L_1}{A_1}+\frac{L_4}{A_4}\right)\frac{d\dot{M}_1}{dt}+\frac{L_2}{A_2}\frac{d\dot{M}_2}{dt}=gL_2\rho_p\alpha-K_{core}\frac{\dot{M}_1^2}{2\rho_p A_1^2} \qquad \textbf{Eq.4.53}$$

$$\frac{dM_3(t)}{dt}=\dot{M}_2(t)-\dot{M}_1(t) \qquad \textbf{Eq.4.54}$$

If the feedwater flow rate $\dot{M}_w$ is a known constant, **Eq.4.47, 4.51, 4.52, 4.53** and **4.54** constitute a complete set of equations for the 5 unknowns $\dot{M}_1$, $\dot{M}_2$, M_3, α and x. To analyze the stability of the system, consider small deviations of the 5 variables from their steady-state value:

$$\xi(t)=\xi_0+\delta\xi(t) \qquad \textbf{Eq.4.55}$$

where ξ represents any of the 5 variables. Introducing these expressions in the conservation equations, canceling out the steady-state terms, eliminating the terms containing the products of two or more variations and Laplace-transforming, the following system of linear algebraic equations is obtained:

$$\delta\dot{m}_2(s)=e^{-\tau s}\delta\dot{m}_1(s) \qquad \textbf{Eq.4.56}$$

$$s\delta m_3(s)=\delta\dot{m}_2(s)-\delta\dot{m}_1(s) \qquad \textbf{Eq.4.57}$$

$$\left(\frac{L_1}{A_1}+\frac{L_4}{A_4}\right)s\delta\dot{m}_1(s)+\frac{L_2}{A_2}s\delta\dot{m}_2(s)=gL_2\rho_p\delta\alpha(s)-K_{core}\frac{\dot{M}_p}{\rho_p A_1^2}\delta\dot{m}_1(s) \qquad \textbf{Eq.4.58}$$

$$\delta\alpha(s)=\frac{\rho_g/\rho_p}{[x_0+\rho_g/\rho_p]^2}\delta x(s) \qquad \textbf{Eq.4.59}$$

$$\delta x(s)=-\frac{x_0}{\dot{M}_p}\delta\dot{m}_2(s) \qquad \textbf{Eq.4.60}$$

where the lower cases indicate the Laplace-transformed variables and s is the Laplace transform parameter. The parameters x_0 and $\dot{M}_p$ are the steady-state chimney mixture quality and Pb-Bi mass flow rate in the circuit, respectively. All the constants in **Eq.4.56** through **4.60** are taken from the steady-state analysis of the reference reactor (**Section 4.6**) and are reported in **Table 4.IV** for convenience. Note that the mixture quality, the Pb-Bi mass flow rate, the delay time τ and the core pressure loss coefficient are a function of the reactor operating conditions. Thus the values reported in **Table 4.IV** are valid only for nominal conditions (i.e. 100% power, 100% flow).

Table 4.IV. Coefficients of the dynamic equations at nominal conditions.

Parameter	**Value**
$L_1/L_2/L_4$ (m)	2.3/10/12.3
$A_1/A_2/A_4$ (m^2)	2.62/12.6/15.7
ρ_p (kg/m^3)	~10,000
ρ_g (kg/m^3)	~40
x_0	0.0084
$\dot{M}_p$(kg/s)	~81,110
τ (s)	7
K_{core}	8.8

An insightful description of the PBWR primary system feedbacks can be gained by analyzing the flow signal diagram of the above set of linear equations, which is shown in **Figure 4.20**. It can be seen that the chimney feedback on the core mass flow rate is twofold: a) via the chimney inertia ($\delta\dot{m}_2$ to $\delta\dot{m}_1$ branch) and b) via the void fraction ($\delta\alpha$ to $\delta\dot{m}_1$ branch). Also, note that the upper plenum does not generate any feedback. The function F(s) is defined as:

$$F(s) \equiv \left(\frac{L_1}{A_1}+\frac{L_4}{A_4}\right)s + K_{core}\frac{\dot{M}_p}{\rho_p A_1^2} \qquad \textbf{Eq.4.61}$$

Using the formal rules of flow signal diagrams [Cheng 1959], **Figure 4.20** can be reduced to the simple feedback loop of **Figure 4.21**, where G(s) and H(s) are defined as follows:

$$G(s) = -\frac{x_0\,\rho_g/\rho_p}{[x_0+\rho_g/\rho_p]^2\dot{M}_p}\cdot\frac{F(s)}{e^{\tau s}F(s)+\frac{L_2}{A_2}s} \qquad \textbf{Eq.4.62}$$

$$H(s) = \frac{gL_2\rho_p}{F(s)} \qquad \textbf{Eq.4.63}$$

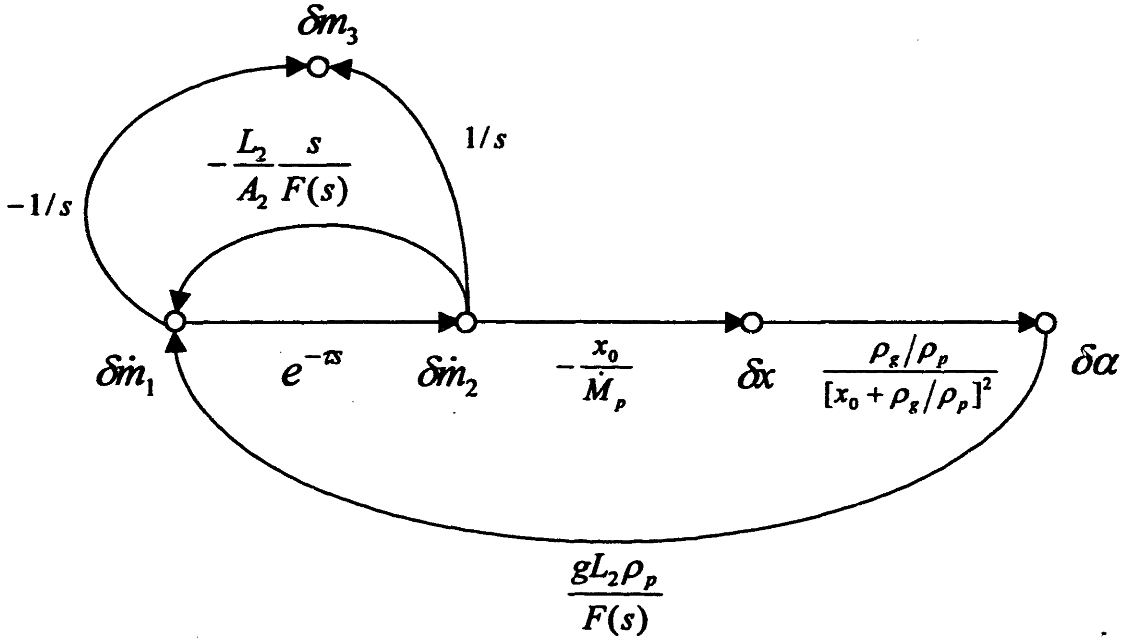

Figure 4.20. Flow signal diagram of the primary system.

To study the stability of the system, it is useful to consider the so-called open-loop transfer function G(s)H(s) and make use of the Nyquist criterion. This states that a necessary condition for a linear system to be unstable is that the complex locus of the open-loop transfer function passes through or encircles (in a clockwise fashion) the unity point on the positive real axis [Cheng 1959]. The complex locus of G(s)H(s) is illustrated in **Figure 4.22** for the values of **Table 4.IV**. Note that the locus does not encircle the (1,0) point in the complex plane and therefore the reactor is stable against hydraulic oscillations when it operates at the reference conditions of **Table 4.IV**.

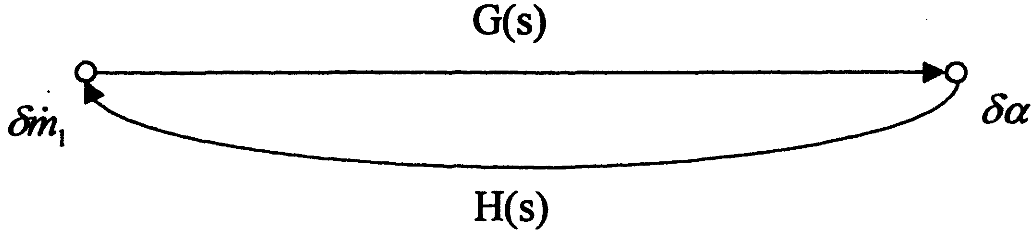

Figure 4.21. Simplified flow signal diagram of the primary system.

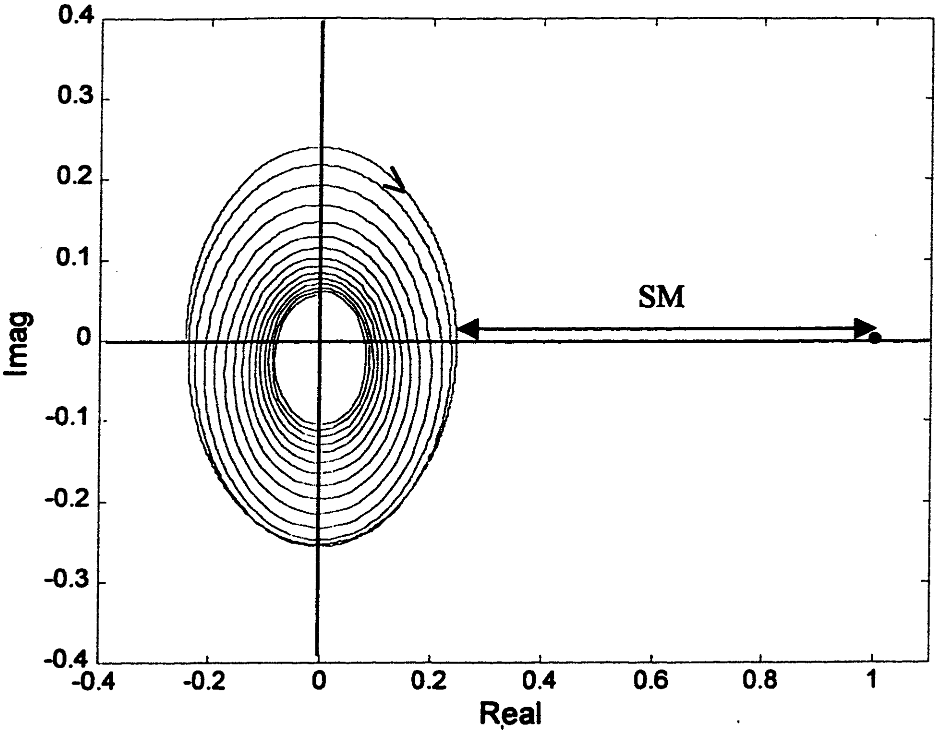

Figure 4.22. Nyquist diagram for the primary system open-loop transfer function.

If we select the distance SM between the point (1,0) and the largest locus intersect with the real axis as a measure of the stability margin, we can quantitatively identify the stabilizing and destabilizing factors in the system. With this definition, negative values of SM indicate an unstable system. **Figure 4.23** illustrates the variation of SM with the chimney travelling time τ for different values of the core pressure loss coefficient K_{core}. As expected, SM increases with K_{core}, indicating that the core hydraulic resistance has a stabilizing effect on the dynamic behavior of the primary system. On the other hand, the time delay caused by the finite velocity of the void fraction perturbation in the chimney has a destabilizing effect (i.e. SM decreases when τ increases). Note that when τ=0 the system is stable for any value of K_{core}, confirming that the time delay in the chimney is the source of instability. **Figure 4.24** illustrates the effect of $\dot{M}_p$ and x_0 on the stability of the system. Because the magnitude of the void fraction feedback is inversely proportional to $\dot{M}_p$ (see the $\delta\dot{m}_2$ to δx branch of **Figure 4.20**), a large Pb-Bi flow rate has a stabilizing effect on the system. On the other hand, the dependence of SM on x_0 is the result of two conflicting effects, which generate the minima of **Figure 4.24**: (i) the mixture quality perturbation is directly proportional to x_0 ($\delta \dot{m}_2$ to δx branch), but (ii) the void fraction perturbation decreases when x_0 increases (δx to $\delta \alpha$ branch).

Although **Figure 4.22** shows that the reactor is stable against hydraulic oscillations at nominal conditions (i.e. 100% power, 100% flow), it is important to inquire whether its stability holds under different conditions as well. Making use of the equations of **Section 4.4** of this chapter, it is possible to calculate $\dot{M}_p$, x_0, τ and K_{core} for different power levels. This enables (i) generation of a power-flow map similar to that commonly used for BWRs and (ii) assessment of the stability margin at different values of the reactor power. For our reference configuration (H=10m, Nominal Power=1260MWth), the power-flow map and the stability margin are illustrated in **Figure 4.25**. It can be seen that the PBWR stability margin decreases with the power and flow; however, it remains positive down to small values of the power level.

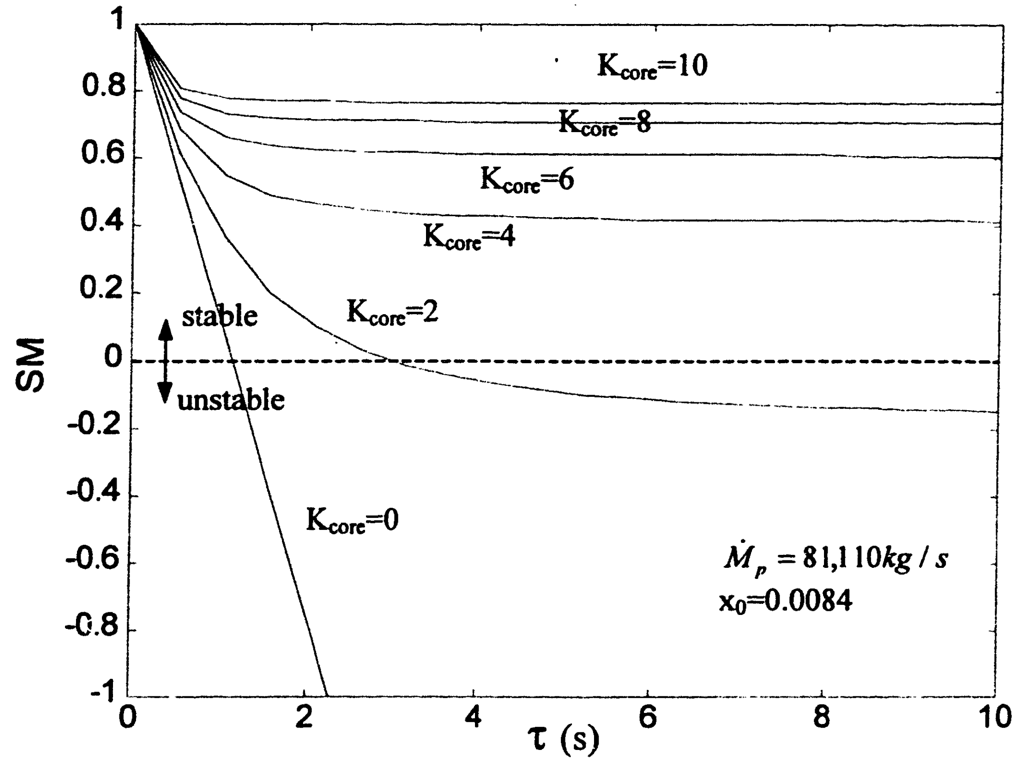

Figure 4.23. Effect of the chimney delay and core hydraulic resistance on the stability margin.

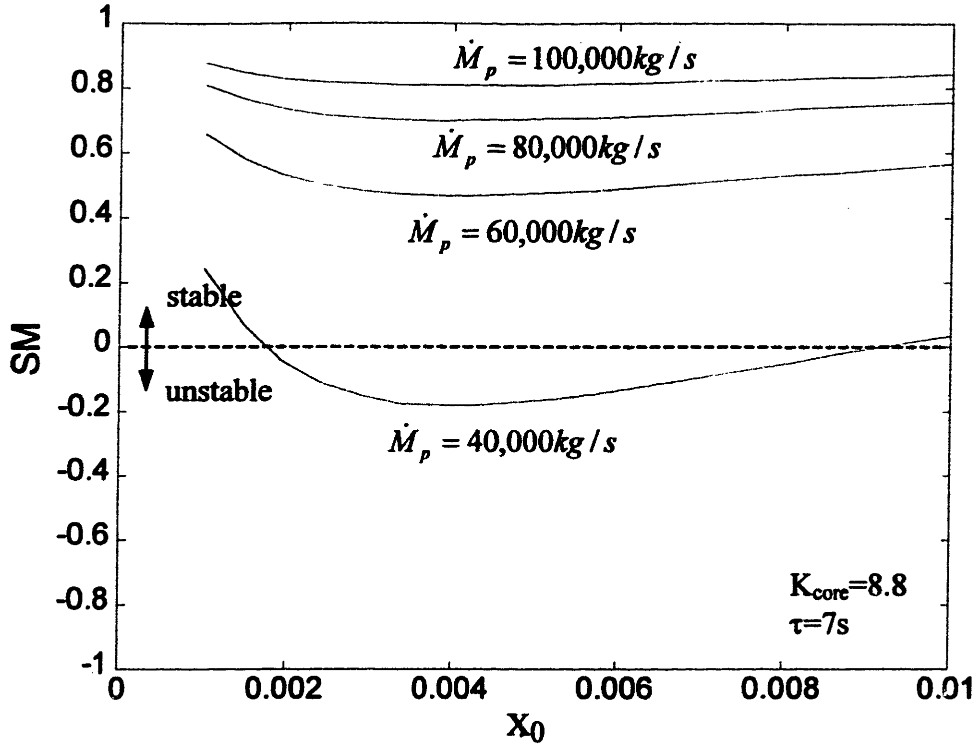

Figure 4.24. Effect of the Pb-Bi flow and chimney mixture quality on the stability margin.

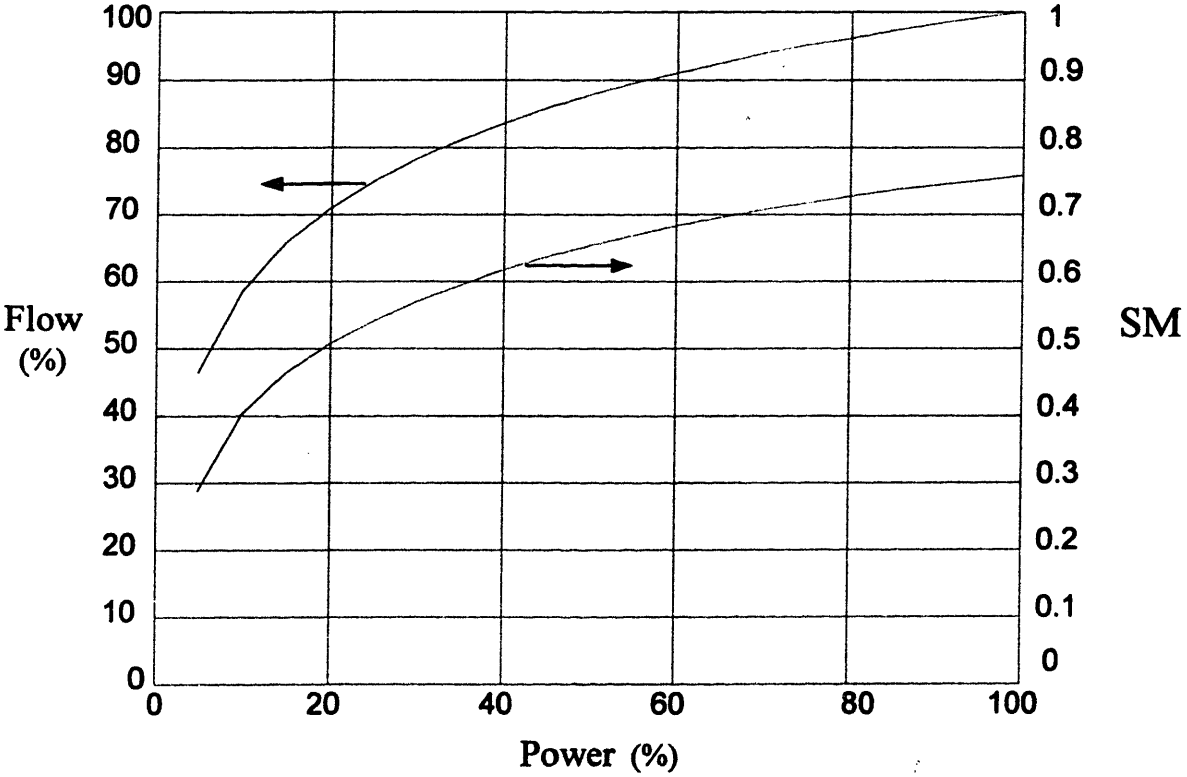

Figure 4.25. Power-flow map and stability margin of the PBWR.

4.9.5.2 Thermal and Neutronic Feedbacks

The nature of the instabilities described above is purely hydraulic. In reality, thermal and neutronic feedbacks are present too that can act to either reinforce or dampen the hydraulic oscillations. A rigorous study of these effects in the frequency domain would require coupling **Eq.4.56** through **4.60** with analogous equations for the reactor kinetics as well as for the temperature distribution in the core, chimney, downcomer and upper plenum. However, a complete dynamic analysis of the PBWR is beyond the scope of this work and here we will limit the discussion to some qualitative considerations.

Before we analyze the thermal and neutronic feedbacks, it is useful to establish whether two feedbacks (initiated by the same event, e.g. an increase of the core Pb-Bi flow mass rate) compound to yield larger or smaller oscillations. To this purpose, let us consider the two cosine waves F_1 and F_2 in **Figure 4.26** of period $m\tau$ and $n\tau$, respectively. F_{10} and F_{20} are the amplitudes of wave 1 and 2, respectively. For m=2, F_1 represents the hydraulic feedback of the previous paragraphs. F_2 is a feedback of different nature (e.g. thermal or neutronic). To evaluate whether the two feedbacks reinforce or dampen each other, we make use of the following interference integral:

$$\overline{F_1 F_2} = \frac{1}{mn\tau}\int_0^{mn\tau} F_1(t)F_2(t)dt \qquad \textbf{Eq.4.64}$$

The integration of **Eq.4.64** is straightforward and leads to the following expression for the interference indicator I_{12}:

$$I_{12} = \frac{\overline{F_1 F_2}}{F_{10}F_{20}} = \frac{1}{4\pi}\left\{\frac{1}{m+n}\sin[2\pi(m+n)] + \frac{1}{m-n}\sin[2\pi(m-n)]\right\} \qquad \textbf{Eq.4.65}$$

In **Figure 4.27** I_{12} is plotted as a function of m for n=2. A positive I_{12} indicates constructive interference (i.e. F_2 reinforces the hydraulic oscillations), while a negative I_{12} indicates destructive interference (i.e. F_2 tends to damp the hydraulic oscillations). As expected, maximum constructive interference occurs when n=2 (i.e. the two feedbacks have the same period). For n>2, any feedback with a period between 2τ and 2.5τ, 3τ and 3.5τ, etc. reinforces the hydraulic oscillations and thus has a destabilizing effect on the system. Vice versa, any feedback with a period between 2.5τ and 3τ, 3.5τ and 4τ, etc. dampens the hydraulic oscillations and thus has a stabilizing effect on the system. However, the importance of feedback interference (whether constructive or destructive) rapidly decreases with the period (for n>3).

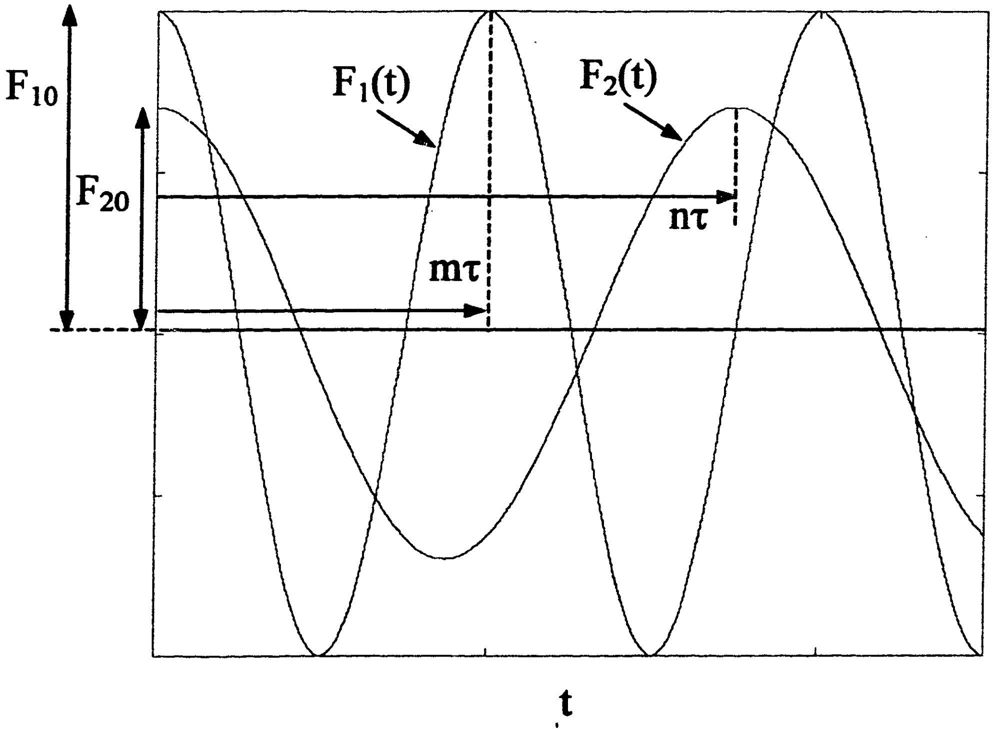

Figure 4.26. Representation of two feedback waves.

First Thermal Feedback

For given Pb-Bi core inlet temperature and core power, an increase of the Pb-Bi mass flow rate results in a decrease of the Pb-Bi temperature at the core outlet. The colder Pb-Bi travels through the fission gas plenum region and then reaches the chimney inlet. Consequently, the water is less readily vaporized, which results in a longer saturated region[12], a shorter superheated region and ultimately in a decrease of the average void fraction in the chimney. Therefore, the natural circulation driving head decreases and so does the Pb-Bi flow rate. The characteristic period of the thermal feedback can be calculated as twice the sum of following three terms: (i) the Pb-Bi travelling time in the core (~0.4s at PBWR reference conditions[13]), (ii) the Pb-Bi travelling time in the fission gas plenum region (~0.3s) and (iii) the traveling time of the void fraction perturbation in the chimney (τ=7s). Therefore, the characteristic period is 2×(0.4+0.3+7)=15.4s, equal to 2.2τ. Then **Figure 4.27** indicates that this feedback would

---

[12] The length of the saturated region is inversely proportional to the Pb-Bi inlet temperature as discussed in **Section 3.6.**

[13] The Pb-Bi core velocity is 3.1m/s, see **Table 4.I.**

significantly reinforce the hydraulic oscillations. To mitigate this effect, one can (i) select a larger DOS (and hence a longer superheated region) which would reduce the influence of the saturated region on the chimney average void fraction, and/or (ii) extend the region between the core and the chimney inlet to increase the period of the thermal feedback from 2.2τ to between 2.5 and 3τ. This will increase the vessel height, but is likely to be a more economic approach than (i).

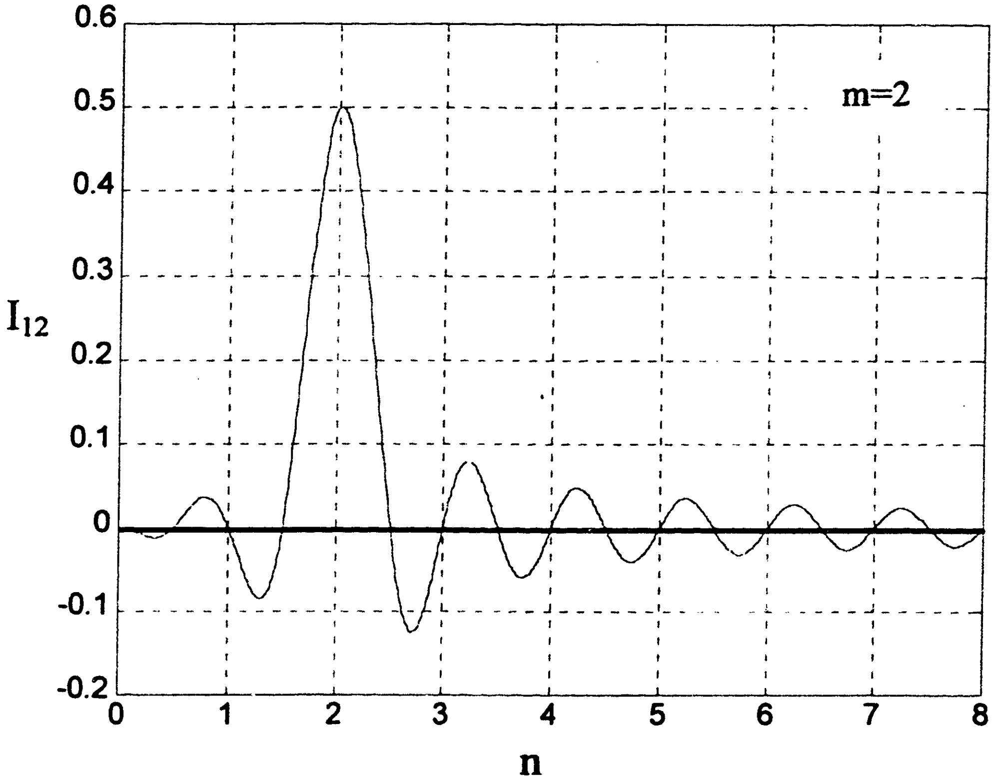

Figure 4.27. Interference of two feedbacks.

Second Thermal Feedback

Depending on the thermal inertia of the upper plenum, the temperature perturbations described above (which are generated in the core and travel along the chimney) may rapidly reach the downcomer and flow back into the core, thus creating an additional thermal feedback. The characteristic period of this second thermal feedback can be calculated as the sum of five terms: (i) the Pb-Bi travelling time in the core, (ii) the Pb-Bi travelling time in the fission gas plenum region (iii) the traveling time of the temperature perturbation in the chimney[14], (iv) the time constant of the upper plenum and (v) the travelling time of the temperature perturbation in the downcomer (i.e. about 26s at PBWR reference conditions). The time constant of the upper plenum is calculated as the ratio of the mass M_3 to the Pb-Bi mass flow rate $\dot{M}_p$ and is equal to 10s at PBWR reference conditions. Therefore, the characteristic period of this thermal feedback is approximately 0.4+0.3+7+10+26≈44s, i.e. about 6.3τ. Then **Figure 4.27** suggests that the coupling of this feedback to the hydraulic oscillations is positive (although small). If it is necessary to mitigate this feedback, one can design a larger upper plenum to increase the characteristic period from 6.3τ to between 6.5 and 7τ.

Neutronic Feedback

Let us now consider the neutronic feedbacks. For given Pb-Bi inlet temperature and core power, an increase of the Pb-Bi flow rate causes (1) a decrease of the coolant temperature in the core, and (2) an increase of the coolant heat transfer coefficient. Both effects result in a decrease of the fuel temperature and thus in an increase of the neutronic power, via the Doppler and fuel contraction reactivity coefficients (both negative for the PBWR reference core, as discussed in **Section 2.2.3.1**). The larger power generated in the fuel is then released back to the coolant, hence causing the coolant temperature to increase. The hotter Pb-Bi travels through the fission gas plenum region and reaches the chimney where it causes an increase of the void fraction, an increase of the natural circulation driving head and thus an increase of the Pb-Bi mass flow rate. The characteristic period of this feedback can be estimated as the sum of six terms: (i) the coolant travelling time in the core (=coolant temperature decrease), (ii) the fuel heat transfer time constant (=fuel temperature response to the coolant temperature decrease), (iii) the neutron prompt jump time constant (=response of neutronic power to the fuel temperature decrease), (iv) again the fuel heat transfer time constant (=heat from the fuel to the coolant), (v) the Pb-Bi traveling time in the fission gas plenum and (vi) the void fraction perturbation traveling time through the chimney. With reference to a single fuel pin, the fuel heat transfer time constant τ_f can be estimated from the following equation:

---

[14] which can be again assumed equal to τ

$$\tau_f = \frac{c_f m_f}{h_f A_f} = \frac{c_f m_f}{L_f}\left[\frac{1}{8\pi\bar{k}_f} + \frac{1}{2\pi k_g}\log\left(\frac{d_{ci}}{d_f}\right) + \frac{1}{2\pi k_c}\log\left(\frac{d}{d_{ci}}\right) + \frac{1}{h_p \pi d}\right] \quad \textbf{Eq.4.66}$$

where in addition to the nomenclature of **Eq.4.4** and **4.20**, m_f, c_f and h_f are the fuel pin mass, its specific heat and the effective heat transfer coefficient, respectively. Note that the factor 8 in place of 4 in the fuel thermal conductivity term of **Eq.4.66** is due to the fact that the fuel average temperature (as opposed to the centerline temperature in **Eq.4.20**) is considered here. At reference conditions the value of τ_f is about 0.9s.

The neutron prompt jump time constant τ_n can be evaluated as [Weaver 1963]:

$$\tau_f = \frac{\ell}{\beta} \approx 0.0032\text{s} \quad \textbf{Eq.4.67}$$

where ℓ and β are the prompt neutron lifetime and delayed neutron fraction, respectively (see **Table 2.IV**). Therefore, the characteristic period of the neutronic feedback is 0.4+0.9+0.0032+0.9+0.3+7=9.5s, equal to 1.4τ. Then **Figure 4.27** suggests that the neutronic feedback would act to dampen the hydraulic oscillations and have a stabilizing effect on the system. However, it should be emphasized that the magnitude of the neutronic feedback is expected to be small because the reactivity coefficients of the PBWR core are low.

4.9.5.3 Conclusions

A hydraulic feedback mechanism was identified due to the time delay between the natural circulation driving head (i.e. the void fraction in the chimney) and the circuit hydraulic resistance (i.e. the pressure drop in the core). This mechanism would induce Pb-Bi flow oscillations having a characteristic period of 2τ (about 14s), equal to twice the travelling time of the Pb-Bi/water mixture in the chimney. However, a quantitative dynamic analysis was undertaken to prove that these hydraulic oscillations are not self-sustaining and the reactor is stable under nominal or low power conditions.

Three additional feedbacks (two thermal and one neutronic) have been identified but were neglected in the quantitative analysis. The first is due to the effect of the Pb-Bi temperature on the chimney void fraction, the second is due to the Pb-Bi recirculation around the whole primary circuit and the third is due to the effect of the fuel temperature on the neutronic power. Based on qualitative considerations, it was found that the two thermal feedback mechanisms would compound (although to a very different extent) with the main hydraulic feedback hence decreasing the stability margin of the PBWR. The first thermal feedback mechanism is the most important because its period is similar to that of the hydraulic feedback and thus strong coupling of the two is expected. Vice versa, the period of the second thermal feedback is considerably longer than 2τ and its effect on stability should be small. Finally, the neutronic feedback appears to have a stabilizing effect on the hydraulic oscillations.

This discussion has shown that, although the PBWR appears to be quite stable against the main hydraulic feedback mechanism, the possibility of flow oscillations cannot be completely ruled out due to the anticipated coupling of the hydraulic and thermal feedback mechanisms. Therefore, it is recommended that a more comprehensive quantitative analysis that includes coupling of all feedback mechanisms (hydraulic, thermal and neutronic) be undertaken to finally ensure through appropriate design decisions the PBWR dynamic stability.

4.9.6 Feedwater Effects

In **Sections 4.9.4** and **4.9.5** it was assumed that the feedwater flow rate $\dot{M}_w$ is constant. However, in reality the feedwater flow oscillates due to vibrations of the feedwater pumps. A perturbation of the feedwater flow rate results in a perturbation of the void fraction in the chimney and thus of the Pb-Bi mass flow rate, which needs to be assessed. To this purpose, we make use of the signal flow diagram of **Figure 4.28**. Note that this diagram is identical to that of **Figure 4.20**, except for the presence of the new variable $\delta\dot{m}_w$, i.e. the Laplace transform of the feedwater mass flow rate perturbation. The transfer function of the $\delta\dot{m}_w$ to δx branch was obtained from **Eq.4.52**. It should be emphasized that, unlike that of **Section 4.9.5**, the following is not a stability analysis because the feedwater flow perturbation is treated as an external forcing term, which thus cannot affect the stability of the system.

Using the formal rules of flow signal diagrams, **Figure 4.28** can be reduced to the simpler diagram of **Figure 4.29**, where the variables $\delta\dot{m}_l$ and $\delta\dot{m}_w$ have been normalized to $\dot{M}_p$ and $\dot{M}_w$, respectively and T(s) is defined as:

$$T(s)=\frac{\dfrac{x_0\rho_g g L_2}{\dot{M}_p[x_0+\rho_g/\rho_p]^2}\left[e^{\tau s}+\dfrac{L_2}{A_2}\dfrac{s}{F(s)}\right]}{e^{\tau s}F(s)+\dfrac{L_2}{A_2}s+\dfrac{x_0\rho_g g L_2}{\dot{M}_p[x_0+\rho_g/\rho_p]^2}} \qquad \textbf{Eq.4.68}$$

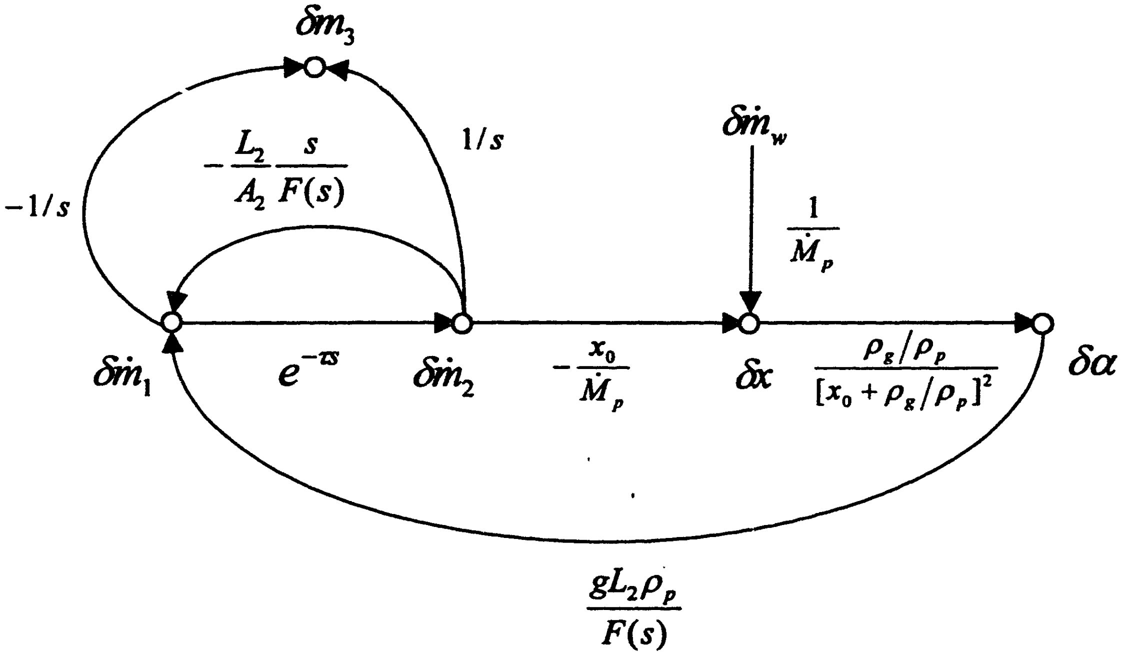

Figure 4.28. Flow signal diagram of the primary system with changing feedwater flow.

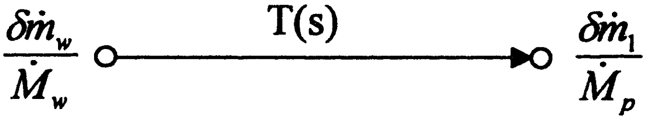

Figure 4.29. Feedwater flow to Pb-Bi flow transfer function.

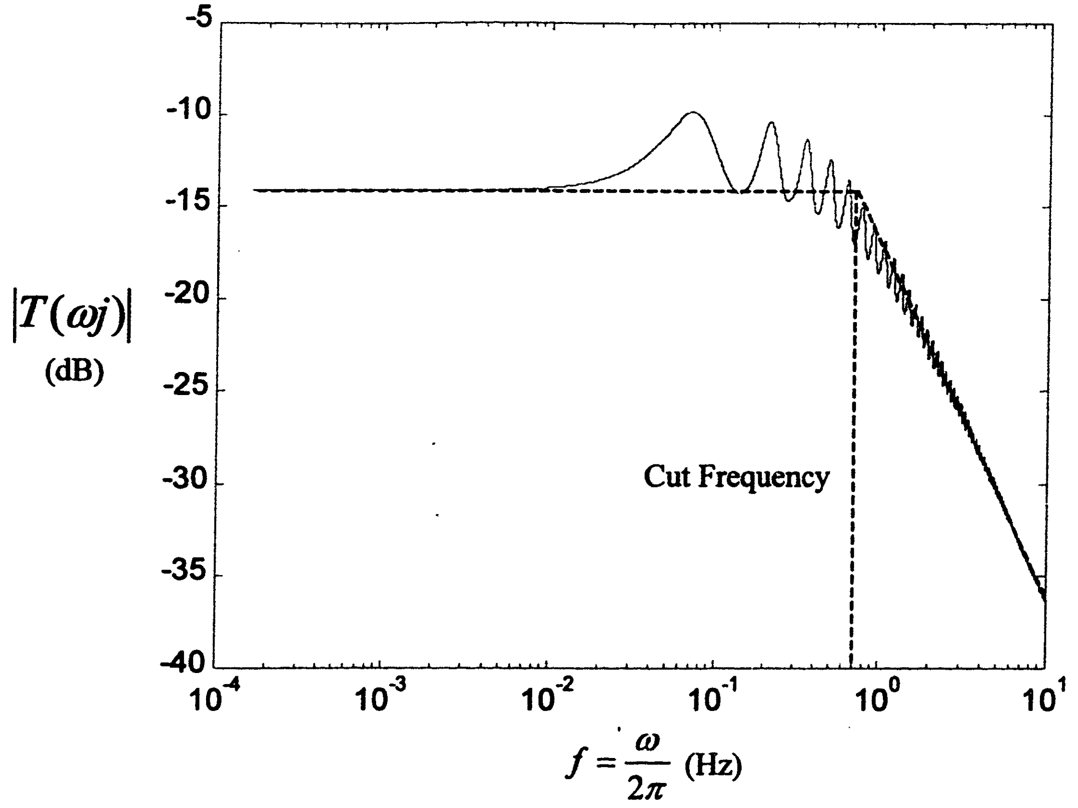

Figure 4.30. Dynamic response of the PBWR to a change of the feedwater flow.

The Pb-Bi flow response to a feedwater perturbation is best illustrated by a Bode diagram where the amplitude of the transfer function T(s) (in dB)[15] is plotted versus the frequency of the feedwater perturbation, f. The negative dB values of the amplitude indicate that the magnitude of the induced Pb-Bi flow perturbation is smaller than the magnitude of the inducing feedwater perturbation. For example, for $|T|$=-15dB, a 10% feedwater flow oscillation induces a Pb-Bi flow oscillation equal to about 1.7%. Furthermore, **Figure 4.30** indicates that the system acts as a low-pass filter with a cut frequency of about 0.7Hz. Note that the feedwater oscillations are expected to be in the high frequency region because they are produced by vibrations of the feedwater pumps, whose characteristic frequency (corresponding to the rotation of the impeller) is larger than 0.7Hz. As a result, the amplitude of the induced Pb-Bi flow oscillations is expected to be much smaller than the amplitude of the inducing feedwater oscillations.

---

[15] The amplitude in dB is defined as $20\text{Log}_{10}|T|$.

An additional effect induced by a fluctuation of the feedwater flow rate is the change of the steam DOS. For example, for a given power an increase of the feedwater flow causes a reduction of the DOS. If the magnitude of this reduction is too large, the outlet steam could reach saturation hence resulting in carry-over of liquid water droplets to the turbine. To assess the importance of this effect, let us consider small perturbations of the DOS and of the feedwater mass flow rate in **Eq.4.16**:

$$\delta DOS = -\frac{\dot{Q}}{c_{wg}\dot{M}_w}\frac{\delta\dot{M}_w}{\dot{M}_w} \qquad \textbf{Eq.4.69}$$

where retention of the capital letters for the small perturbations indicates that the variable were not Laplace-transformed. At nominal PBWR conditions is $\dot{Q}$=1260MWth, $\dot{M}_w$=686kg/s and c_{wg}=5,510J/kg°C. For these values, **Eq.4.69** suggests that a 1% oscillation of the feedwater mass flow rate[16] induces a 3.3°C oscillation of the DOS. Because the nominal value of the DOS is 25°C, it can be then concluded that the steam remains superheated. Note that, for the sake of simplicity, in deriving **Eq.4.69** it was assumed that the whole reactor power is transferred to the water secondary coolant, therefore neglecting the thermal capacity of the Pb-Bi primary coolant.

Finally, it is anticipated that the change of the DOS and steam flow rate induced by the feedwater perturbation generates no feedback (through the secondary system) on the feedwater flow itself. This is due to the fact that:

a) the thermodynamic conditions of the feedwater (temperature and pressure) are set by the condenser, whose large thermal capacity acts to dampen the steam temperature perturbation at the turbine outlet,

b) the liquid level of the condenser shrinks or swells to accommodate the perturbation of the steam flow from the turbine. As a result, the feedwater flow rate drawn by the pumps is not affected by the steam flow discharged to the condenser.

4.10 Summary

The thermal constraints of the clad, fuel and vessel were presented. On the basis of these constraints, a steady-state thermal-hydraulic analysis of the primary system was undertaken to

---

[16] Actually a very large oscillation which is not normally encountered in nuclear reactors.

evaluate the maximum acceptable reactor power. A value of 1260MWth, corresponding to a 10m chimney and 25°C steam superheat, was chosen as the reference thermal power of the PBWR. A passive Decay Heat Removal System (DHRS) in which the decay heat is ultimately removed by boiling water on the outer surface of the containment was also explored. It was demonstrated that this design is compatible with the reference 1260MWth thermal power.

The time-dependent response of the PBWR primary system to the most common anticipated transients was qualitatively analyzed and no problems were found. The susceptibility of the PBWR primary system to static and dynamic instabilities was quantitatively assessed. Static instabilities of the flow excursion type can be ruled out on the basis of the pressure drop/flow characteristic curve. It was also found that the PBWR is not prone to flow oscillations induced by the phase lag between the pressure drop in the core and the buoyancy term in the chimney. The effect of the neutronic feedbacks on the dynamic stability of the reactor was also investigated and found to be relatively unimportant.

Chapter 5

- PB-BI AEROSOL GENERATION AND TRANSPORT -

5.1 Introduction

In the PBWR chimney the lead-bismuth primary coolant is mixed with liquid water to generate steam. A Pb-Bi/steam mixture rises to the top of the chimney where the steam is separated and sent to the turbine. The objective of this chapter is to select a suitable steam separator[1] that minimizes the residual Pb-Bi carry-over to the steam lines. The transport of Pb-Bi aerosols through the steam-lines, which can result in a significant liquid Pb-Bi contamination of the turbine, is also examined. Lead-bismuth may induce embrittlement of the turbine's most stressed components like the moving blades and the rotor shaft. Particular attention is given to this phenomenon, known as Liquid Metal Embrittlement (LME) because it can lead to rapid and catastrophic failure of the turbine. Several solutions to the LME problem are then explored ranging from alternative blade materials to blade coating, from Pb-Bi removal by electrostatic precipitators to oxidation of the Pb-Bi droplets[2]. Finally, it is demonstrated that the mechanical impact of liquid or solid heavy metal particles on the surface of the turbine blades does not raise an erosion concern.

5.2 Mechanisms of Pb-Bi Aerosol Generation

Two mechanisms of heavy metal release into steam take place in the upper region of the reactor pool and operate in parallel:

i) Lead-bismuth droplet entrainment in steam.
ii) Direct evaporation of lead-bismuth.

Mechanism i) will be extensively discussed in the following section as part of the steam separator analysis. On the other hand, because of the extremely low vapor pressure of the Pb-Bi coolant, the importance of mechanism ii) is very limited. To prove this, let us estimate the mass of heavy metal transported out of the reactor pool due to Pb-Bi evaporation over 40 years of

---

[1] We will use the words "steam separator" to indicate a device that separates liquid Pb-Bi from steam.
[2] Oxides do not induce LME.

operations. Based on the data for pure lead and bismuth taken from [Weeks 1971, Lyon 1952], the variation of the lead-bismuth vapor pressure with temperature was estimated as:

$\mathrm{Log}P_{PbBi}=11.1-10660/T$ **Eq.5.1**

where P_{PbBi} and T are in Pa and K, respectively. If it is conservatively assumed that the steam flow is saturated with Pb-Bi vapor, the molar fraction of Pb-Bi in steam due to evaporation $x_{PbBi,e}$ is:

$$x_{PbBi,e}=\frac{P_{PbBi}(T)}{P} \qquad \textbf{Eq.5.2}$$

where P is the PBWR operating pressure (7.0MPa). The mass of heavy metal released by evaporation $m_{PbBi,e}$ over 40 years of operation can be calculated as:

$$m_{PbBi,e}=x_{PbBi,e}\frac{A_{PbBi}}{A_{H20}}\dot{M}_g t_{40} \qquad \textbf{Eq.5.3}$$

where A_{PbBi}=0.209kg/mol and A_{H2O}=0.018kg/mol are the Pb-Bi and steam weights, respectively. $\dot{M}_g$ is the steam mass flow rate (~686kg/s at nominal conditions) and t_{40} is 40 years expressed in seconds. In **Figure 5.1** $m_{PbBi,e}$ is plotted against the steam dome operating temperature. It can be seen that at PBWR reference conditions (T=312°C), the release of lead-bismuth over 40 years is extremely small (i.e.<0.1kg).

5.3 Steam Separator Analysis

There are two chief (and often conflicting) constraints in the selection and design of a steam separator: pressure drop and steam carry-under. Large pressure losses in the steam separator are never desirable because they decrease the thermal efficiency of the power steam cycle. Moreover, if the whole primary coolant flow is forced through the steam separator[3], the pressure drops ought to be kept to a minimum to enhance the coolant circulation throughout the primary system. If the primary system operates in a natural circulation mode, lower pressure drops can result in a significantly larger mass flow rate and hence lower temperatures in the core [Cheung 1998]. If on the other hand the forced circulation mode is adopted, lower pressure drops in the steam separator mean lower pumping power and hence better economics of the reactor.

---

[3] as is the case in the cyclone steam separator of a BWR

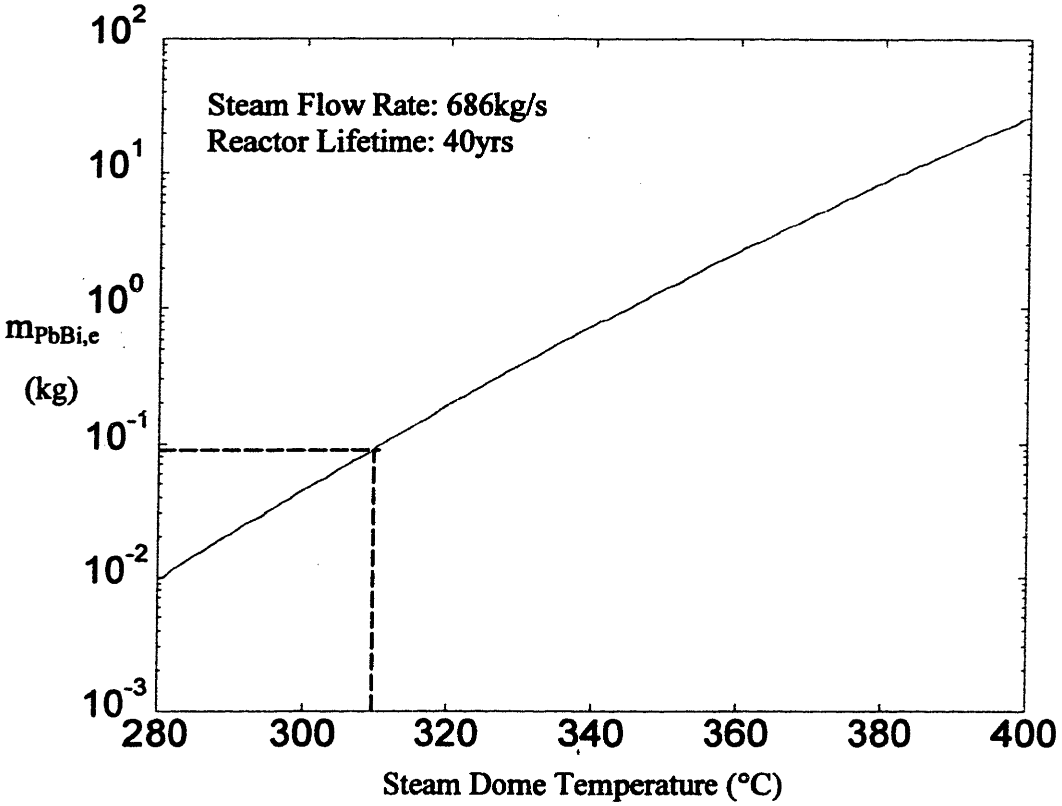

Figure 5.1. Lead-bismuth release by evaporation.

Poor selection and design of the steam separator may result in significant dragging of steam bubbles into the downcomer. This phenomenon (also known as steam carry-under) is detrimental to the primary system performance because it reduces the density driving head in natural circulation and it promotes pump cavitation in forced convection. Also the presence of low density bubbles (i.e. voids) in the core[4] would cause undesirable reactivity fluctuations that may impair reactor safety. Mitigation of carry-under may necessitate the utilization of "full flow" complex steam separators (e.g. cyclones), which usually display larger pressure drops.

5.3.1 Liquid Entrainment

The simplest way to separate the two phases at the top of the chimney is to rely on gravity for natural separation: the lighter volatile steam leaves the liquid free surface of the pool while the heavy lead-bismuth makes a U-turn and flows back into the downcomer. This configuration is

---

[4] should these bubbles in fact be able to flow from the chimney all the way through the downcomer and into the core

extremely simple, the flow path is not complex and the pressure drops are typically less than only one kinetic head [Griffith 1997]. In our case, gravity separation is clearly favored by the large density ratio of lead-bismuth to steam, which enables achievement of rather good separation efficiency (as demonstrated in **Section 5.3.1.1**). However, steam separation is not perfect and the use of a steam dryer (to further remove the liquid metal from the steam stream) is mandatory (see **Figure 5.2**). Moreover, gravity separation may be susceptible to significant steam carry-under because the liquid flows from the chimney directly into the downcomer. The carry-under characteristics of this steam separator are analyzed in **Appendix D**.

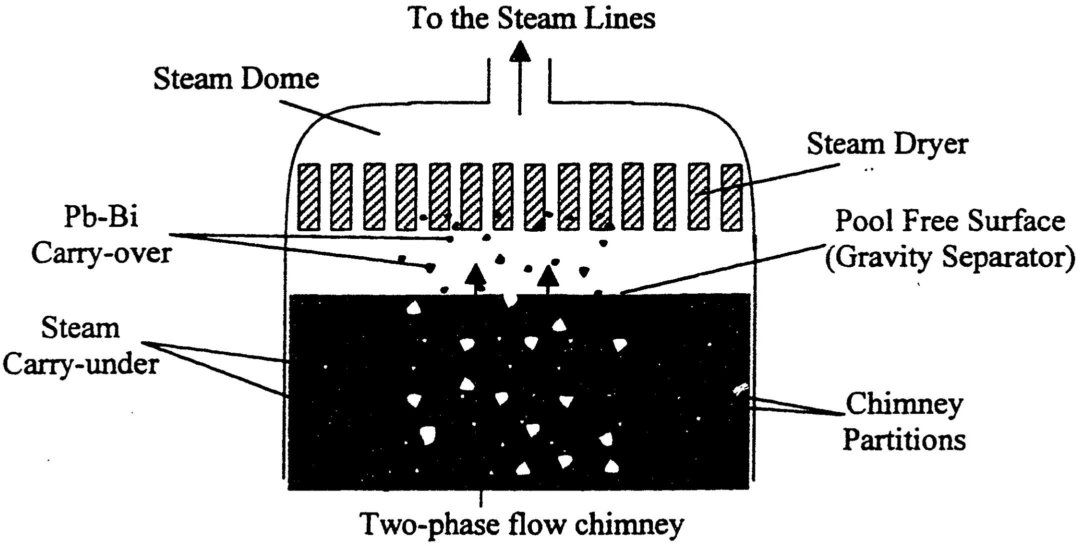

Figure 5.2. The reactor pool.

We shall now assess the gravity separator efficiency by calculating the magnitude of Pb-Bi entrainment at the liquid free surface of the reactor chimney. The relevant thermal-hydraulic characteristics of the steam separator region are summarized in **Table 5.I**. Griffith [1997] gives a suitability condition for gravity separation: the parameter F_s (defined as $j_g\sqrt{\rho_g}$) should lie between 0.25 and $15(\text{kg/m})^{1/2}/\text{s}$. In our case F_s is about $8.6(\text{kg/m})^{1/2}/\text{s}$.

In low void fraction pools (i.e. bubbly flow) the primary mechanism of entrainment is the burst of the steam bubbles, which projects the ligament and sheets of liquid away from the free surface. Also, when a bubble bursts, a concentric wave is generated that propagates toward the center of the bubble. When the wave collapses, a jet is formed that moves straight up and projects several fine droplets away from the surface [Griffith 1997].

Table 5.I. Conditions at the pool free surface.

Parameter	Description	Value
T	Steam temperature	312°C
P	Steam pressure	7.0MPa
D_c	Chimney (or core barrel) diameter	4m
A_c	Chimney flow area ($=\frac{\pi}{4}D_c^2$)	12.6m^2
D_H	Chimney hydraulic diameter[5]	0.26m
$\dot{M}_g$	Steam mass flow rate (at full power)	686kg/s
j_g	Steam superficial velocity (at full power)	~1.4m/s
V_g	Steam velocity above the free surface[6] (at full power)	~1.4m/s

However, in larger void fraction pools[7] (i.e. slug, churn or cap flow), the entrainment mechanism changes and is better explained in terms of liquid droplet shear-off by steam jets running through the free surface [Kataoka 1984]. The height reached by these droplets depends on their size and initial velocity. The steam dragging force acting on the droplets determines whether the droplet entrainment is stable or not (see **Section 5.3.1.3**). Large droplets can only reach a certain height (directly proportional to their initial velocity) and eventually fall back into the pool. On the other hand, smaller droplets are dragged away from the pool regardless of their initial velocity. Therefore, it is desirable to allow for a certain elevation above the pool free surface, so that the large droplets can precipitate back into the pool and a compact steam dryer can be employed to remove the smaller droplets only.

5.3.1.1 Entrainment Rate

The most complete study of entrainment phenomena at the free surface of a pool is that of Kataoka and Ishii [Kataoka 1984]. Their semi-empirical model (also recommended in [Griffith

---

[5] The chimney is partitioned into square channels of side 0.26m (see **Figure 2.1**), each corresponding to a fuel assembly.

[6] Note that steam absolute and superficial velocities are almost equal in the highly dispersed two-phase flow above the free surface.

[7] Under normal operating conditions, the PBWR belongs to this second case as demonstrated in **Section 3.3.2**.

1997]) is based on the liquid shear-off entrainment mechanism and was successfully benchmarked against numerous databases from steam-water and air-water systems at high and low pressure[8] (i.e. from 0.1 to 18.7MPa). The model provides a correlation for the maximum height, h, reached by the large droplets (**Eq.5.4**) and the entrainment of the small droplets, 1-x (**Eq.5.5**).

$$h^{*}=1.97\times10^{3}N_{\mu g}^{0.33}D_{H}^{*0.42}\left(\frac{\rho_{g}}{\rho_{p}-\rho_{g}}\right) \qquad \textbf{Eq.5.4}$$

$$\frac{1-x}{x}=1.99\times10^{-3}j_{g}^{*3.0}N_{\mu g}^{0.5}\left(\frac{\rho_{p}-\rho_{g}}{\rho_{g}}\right) \qquad \textbf{Eq.5.5}$$

where

$$h^{*}=\frac{h}{\sqrt{\frac{\sigma}{g(\rho_{p}-\rho_{g})}}} \qquad \textbf{Eq.5.6}$$

$N_{\mu g}$ is the gas viscosity number defined as:

$$N_{\mu g}=\frac{\mu_{g}}{\sqrt{\rho_{g}\sigma\sqrt{\frac{\sigma}{g(\rho_{p}-\rho_{g})}}}} \qquad \textbf{Eq.5.7}$$

D_{H}^{*} is the Bond number defined as:

$$D_{H}^{*}=\frac{D_{H}}{\sqrt{\frac{\sigma}{g(\rho_{p}-\rho_{g})}}} \qquad \textbf{Eq.5.8}$$

j_{g}^{*} is the dimensionless superficial gas velocity defined as:

$$j_{g}^{*}=\frac{j_{g}}{\left[\sigma g(\rho_{p}-\rho_{g})/\rho_{g}^{2}\right]^{1/4}} \qquad \textbf{Eq.5.9}$$

1-x is the liquid mass fraction in the flow above the pool[9], μ_g and ρ_g are steam viscosity and density, respectively. ρ_p and σ are the lead-bismuth density and surface tension, respectively.

---

[8] At 0.3MPa an air-water system displays the same density ratio of steam/Pb-Bi in the PBWR.

[9] the mass flow rate of lead-bismuth over the total mass flow rate (i.e. steam + lead-bismuth).

For the PBWR conditions of interest, **Eq.5.4** yields h~0.4m, which means the precipitation of large and heavy droplets will take place within a relatively short distance from the pool free surface allowing for a compact design of the reactor pool upper region. In **Figure 5.3** the liquid entrainment from the pool, 1-x, is plotted against the steam superficial velocity[10]. At j_g~1.4m/s (corresponding to full power), the liquid entrainment is ~0.13% only (or 0.9kg/s). As expected, entrainment increases with the steam velocity.

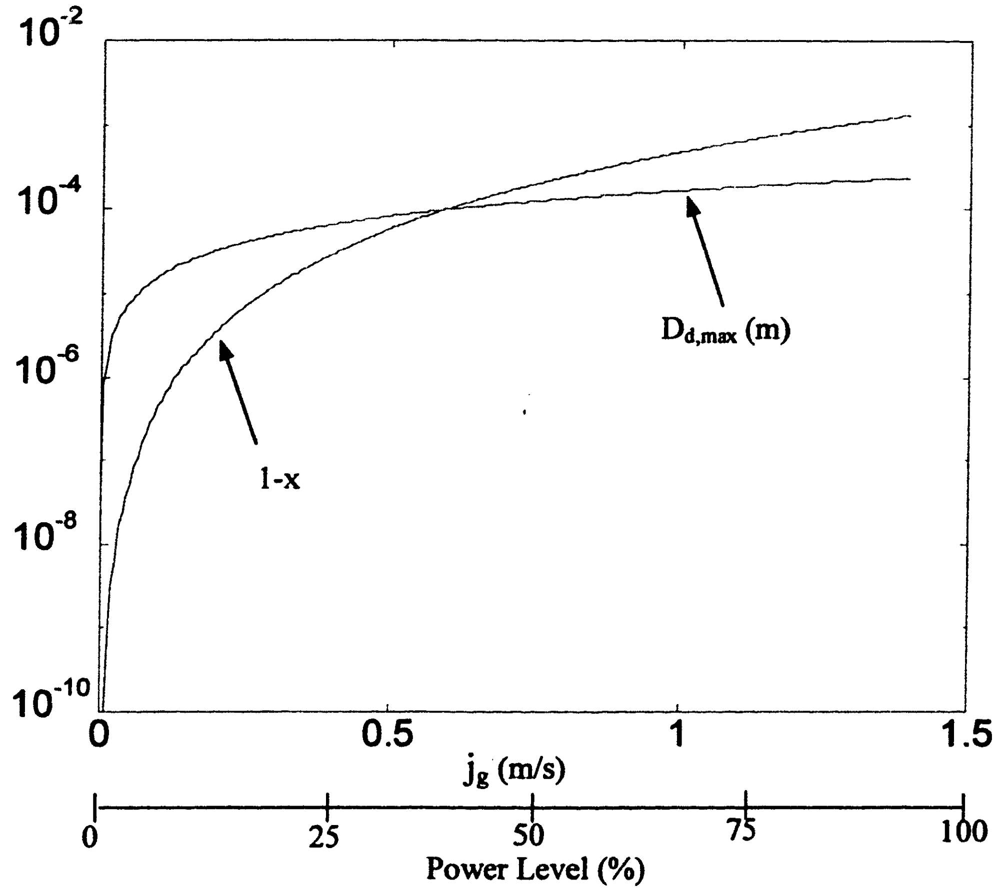

Figure 5.3. Pb-Bi Entrainment from the pool free surface

5.3.1.2 PBWR vs. BWR

To appreciate how small the liquid rate of entrainment from the lead-bismuth pool free surface is, we shall now compare it to that of liquid water from the free surface of a pool at BWR

---

[10] and hence effectively against the reactor power level, since the steam mass flow rate is directly proportional to the reactor power.

conditions. For consistency, we apply the Katoaka-Ishii model again. The reference conditions of a BWR chimney are: T~290°C, P~7.0MPa, j_g~2.8m/s [11]. Application of **Eq.5.4** and **5.5** to this system yields the following results: h~1m and 1-x~13%, respectively. Clearly, under these conditions gravity separation would not be very effective: therefore, in BWRs the whole two-phase flow coming from the core is forced through a cyclone steam separator that removes the bulk of the liquid from the steam stream. As a result the steam flow quality at the outlet of a cyclone steam separator is typically above 90%. Subsequently the steam passes through a dryer and is then sent to the turbine. However, in the PBWR case the use of a cyclone steam separator is not necessary because gravity separation is very effective and the magnitude of entrainment from the pool surface is small[12].

The absence of a cyclone steam separator will enhance natural circulation, significantly simplify the design of the reactor vessel upper region, help reduce capital cost, make refueling easier and enable shortening the reactor pool[13]. On the other hand, a gravity separator may be susceptible to carry-under: this problem is given proper attention in **Appendix D**. It should be noted that a steam dryer is required anyway to remove the small droplets from the dispersed two-phase flow above the pool free surface.

5.3.1.3 Droplet Size

The maximum diameter $D_{d,max}$ of the droplets found above h can be readily calculated by equating the drag force to the droplet weight[14]:

$$\frac{\pi}{6}D_{d,\max}^{3}\rho_{p}g = C_{D}\frac{\pi}{4}D_{d,\max}^{2}\frac{\rho_{g}V_{g}^{2}}{2} \qquad \textbf{Eq.5.10}$$

Solving for $D_{d,max}$:

$$D_{d,\max} = \frac{3}{4}\frac{C_{D}\rho_{g}V_{g}^{2}}{\rho_{p}g} \qquad \textbf{Eq.5.11}$$

---

[11] the steam superficial velocity was calculated from geometry and mass flow rate data of a 3600MWth BWR/6 as reported in [Todreas 1990].

[12] Note that the mass quality and the volumetric flow ratio in the PBWR are 1 and 2 orders of magnitude smaller than in the BWR, respectively.

[13] A typical BWR cyclone steam separator is 2m high.

[14] Here the steam/droplet relative velocity is set equal to the steam absolute velocity V_g, this being the condition that defines the maximum droplet size.

Ishii and Kataoka [Ishii 1979] recommend the use of the following expression for the drag coefficient C_D for a droplet in highly dispersed flow:

$$C_D = \frac{10.67}{\mathrm{Re}_d^{0.5}} \qquad \textbf{Eq.5.12}$$

valid for $5<\mathrm{Re}_d<1000$. Here Re_d is defined as $\mathrm{Re}_d = \frac{\rho_g V_g D_d}{\mu_g}$. Note that **Eq.5.11** is an implicit equation in $D_{d,max}$ and its solution requires iteration.

An entrained droplet may become unstable if its velocity relative to the vapor stream is large. The droplet may deform until it disintegrates into several fine droplets[15]. It is therefore necessary to verify that the diameter obtained from **Eq.5.11** is in fact stable. The stability of a droplet against disintegration is usually expressed in terms of a 'critical' Weber number. The Weber number We_d is defined as:

$$We_d = \frac{\rho_g D_d V_g^2}{\sigma} \qquad \textbf{Eq.5.13}$$

It measures the relative importance of the destabilizing aerodynamic forces (i.e. the dynamic pressure $\sim \frac{\pi}{4} D_d^2 \rho_g V_g^2$) to the stabilizing surface tension forces ($\sim \pi D_d \sigma$) [Lefebvre 1989]. The critical value of the Weber number depends in general on the liquid viscosity through the Ohnesorge number Oh:

$$Oh = \frac{\mu_p}{\sqrt{\rho_p D_d \sigma}} \qquad \textbf{Eq.5.14}$$

where μ_p is the liquid viscosity. The viscosity effect can be neglected if $Oh<0.1$ [Azzoppardi 1997]. This condition is fulfilled by any Pb-Bi droplet of practical interest ($>0.1\mu m$), signaling that in our case liquid viscosity plays no significant role in the disintegration process. Several values of the critical Weber number are found in the literature [Griffith 1997, Azzoppardi 1997, Kataoka 1983] ranging from 8 to 22 for conditions where $Oh<0.1$. In this study we conservatively select the lowest value 8. Then the diameter above which disintegration can occur is calculated from **Eq.5.13** as:

$$D \geq \frac{8\sigma}{\rho_g V_g^2} \approx 40\mathrm{mm} \qquad \textbf{Eq.5.15}$$

---

[15] A comprehensive description of several droplet disintegration mechanisms can be found in [Azzoppardi 1997].

Figure 5.3 shows the maximum diameter of the entrained droplets $D_{d,max}$ calculated from **Eq.5.11**. At j_g=1.4m/s the maximum droplet diameter is $D_{d,max}$~233μm. Droplets of this size are clearly stable against disintegration. It is shown in **Section 5.3.2.2** that these droplets can be readily removed in a chevron-type steam dryer.

5.3.1.4 Droplet Distribution

Knowledge of the size distribution of the droplets entrained at the free surface of the liquid pool must be estimated to assess the performance of the steam dryer. No droplet size distribution data for intermittent flow pool situations could be found in the literature. Reference [Griffith 1997] reports a droplet spectrum for bubbly flow pool. However, no criterion is given to scale this spectrum to different fluids and/or different thermal-hydraulic variables. Moreover, the entrainment mechanism in bubbly and intermittent flow is qualitatively different, as explained at the beginning of **Section 5.3.1**, which makes it questionable to apply bubbly flow data to an intermittent flow situation. On the other hand, there is a considerable amount of data on droplet distribution in annular two-phase channels [Azzoppardi 1997, Kataoka 1983, Kocamustafaogullari 1994]. The entrainment mechanism in annular flow is shear-off of roll-wave at the liquid film/steam core interface [Kataoka 1983], which somewhat resembles that of pool entrainment in churn flow. On this basis, we will make use of annular flow channel distribution data for our intermittent flow pool system.

Most available data fit an upper-limit lognormal distribution (first proposed by Mugele and Evans [Mugele 1951]), which is defined by the following equation:

$$\frac{dv}{d\delta}=\frac{\psi}{\sqrt{\pi}}\exp\left(-\psi^2\delta^2\right) \qquad \textbf{Eq.5.16.a}$$

$$\frac{dv}{dD_d}=\frac{D_{d,max}}{D_d(D_{d,max}-D_d)}\frac{\psi}{\sqrt{\pi}}\exp\left(-\psi^2\log^2\left(\frac{\chi D_d}{D_{d,max}-D_d}\right)\right) \qquad \textbf{Eq.5.16.b}$$

In **Eq.5.16.a** dv is the fraction of liquid volume[16] carried by droplets of parameter δ between δ and δ+dδ. In **Eq.5.16.b** dv is the fraction of liquid volume carried by droplets of diameter D_d between D_d and D_d +dD_d. The parameter δ is a convenient dimensionless variable defined as:

---

[16] and hence the fraction of liquid mass

$$\delta = \log\left(\frac{\chi D_d}{D_{d,\max} - D_d}\right)$$ **Eq.5.17**

where ψ and χ are two coefficients chosen to fit the experimental data. It was found that the values of ψ and χ do not dramatically change with the flow system variables [Kataoka 1983, Kocamustafaogullari 1994] (e.g. steam and liquid superficial velocity, channel diameter) and lie in the 0.75-0.88 and 1.93-2.13 range, respectively. We shall arbitrarily assume here the intermediate values of ψ~0.8 and χ~2.0. Note that the distribution is normalized for any choice of the parameters ψ and χ. The effect of ψ and χ is to change the distribution variance and mean, respectively. In our case $D_{d,\max}$ is given by **Eq.5.11**. The features that make this distribution appealing are its exclusive dependence on the maximum diameter and its zero value for D_d above $D_{d,\max}$. A plot of the upper-limit lognormal distribution is shown in **Figure 5.4** for $D_{d,\max}$=233μm. It can be seen that most liquid is in the form of droplets of diameter between 30 and 150μm.

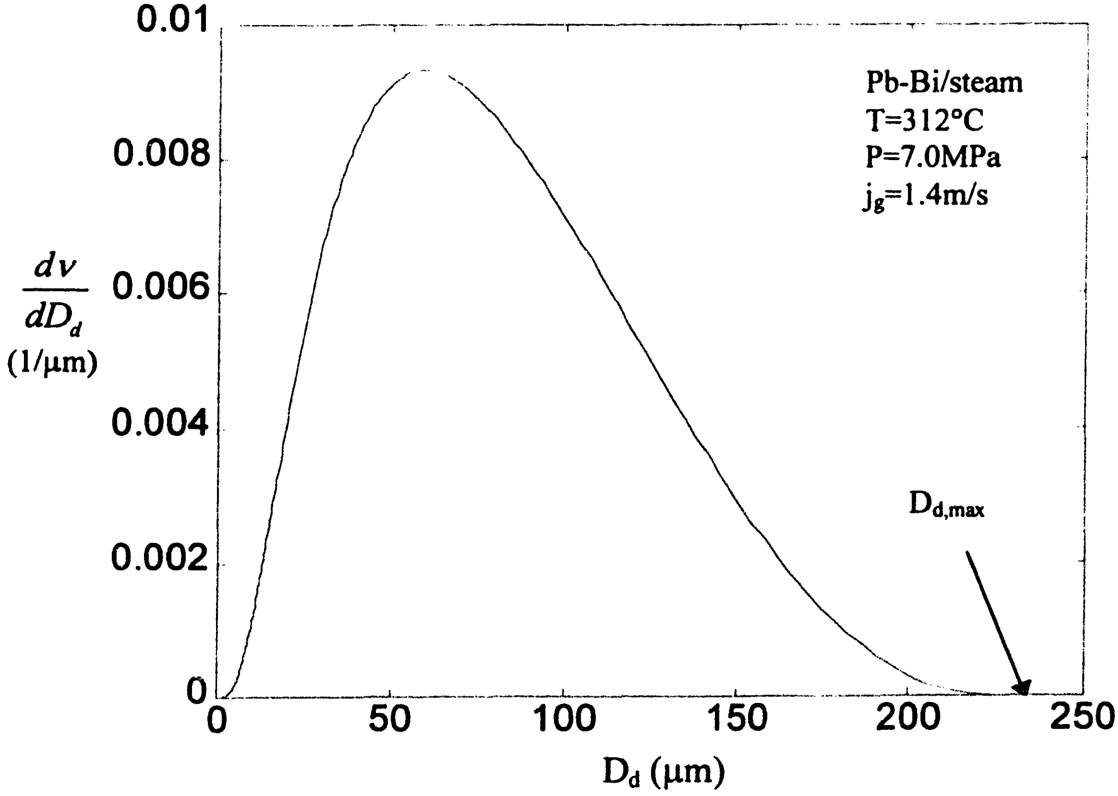

Figure 5.4. The droplet mass distribution at the steam dryer inlet.

5.3.2 The Steam Dryer

Devices to remove fine droplets from highly dispersed two-phase flow steam are known as steam dryers. In the nuclear industry they find their primary applications in the steam separator within the reactor pressure vessel of BWRs, in the steam generators of Westinghouse PWRs and in the moisture separators (between the high and low pressure sections of the turbine) of both BWRs and PWRs. The most commonly used types of steam dryers are the "wire-mesh" and the "chevron" separators. They belong to the family of the inertia separators because the heavier droplets impact the separator surface due to their inability to follow the steam flow path. The wire-mesh separator consists of a fine grid of metallic wires[17] that captures the droplets out of the steam stream. The film of liquid formed on the wire drips back into the pool by gravity. The chevron separator is made of a bank of corrugated plates (or vanes) inducing a zigzag flow path, which causes the droplets to impact the plate surface and deposit (see **Figure 5.5**). A liquid film forms on the plate surface that flows by gravity down to the drain pan at the bottom of the separator (see **Figure 5.6**). To prevent axial drag of the liquid film and facilitate wetness removal from the plate walls, the plates are equipped with drainage scoops. For a given steam velocity, wire-mesh separators generally display higher droplet removal efficiency than chevron separators because the mesh can be designed to be very tight to capture the fine droplets. However, high efficiency comes at the expense of the pressure drop, which is inversely proportional to the mesh pitch. This is true for chevron separators, too: a more involved zigzag flow path increases the droplet removal efficiency as well as the pressure drop.

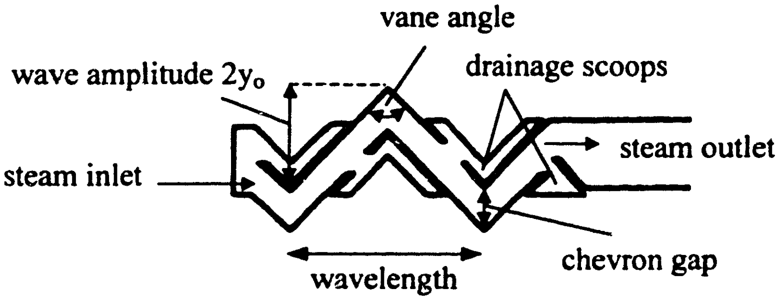

Figure 5.5. Cross-section of a chevron steam dryer vane (from [Nagase 1996]).

---

[17] which the steam flow is forced through.

In wire-mesh and chevron separators particular care must be given to the selection of the steam velocity. A low steam velocity (and hence a low droplet velocity) generally means lower efficiency. However, if the steam velocity exceeds a critical value (the so-called breakthrough velocity), re-entrainment from the liquid film may occur [Griffith 1997, Moore 1976, Keshava 1997], which results in failure of the separator function. The identified re-entrainment mechanisms are i) roll-wave shear-off of the liquid film and ii) splashing due to the impact of large droplets on the liquid film [Nakao 1999]. The breakthrough velocity is generally larger in chevron separators, which allows accommodation of higher operating steam velocity hence recovering some separating efficiency. For this reason and due to their lower pressure drop, chevrons are preferred over wire-mesh separators[18] in most modern LWRs [Cerezo 1998, Nakao 1999] and we will tentatively employ them in the PBWR steam dryer, too.

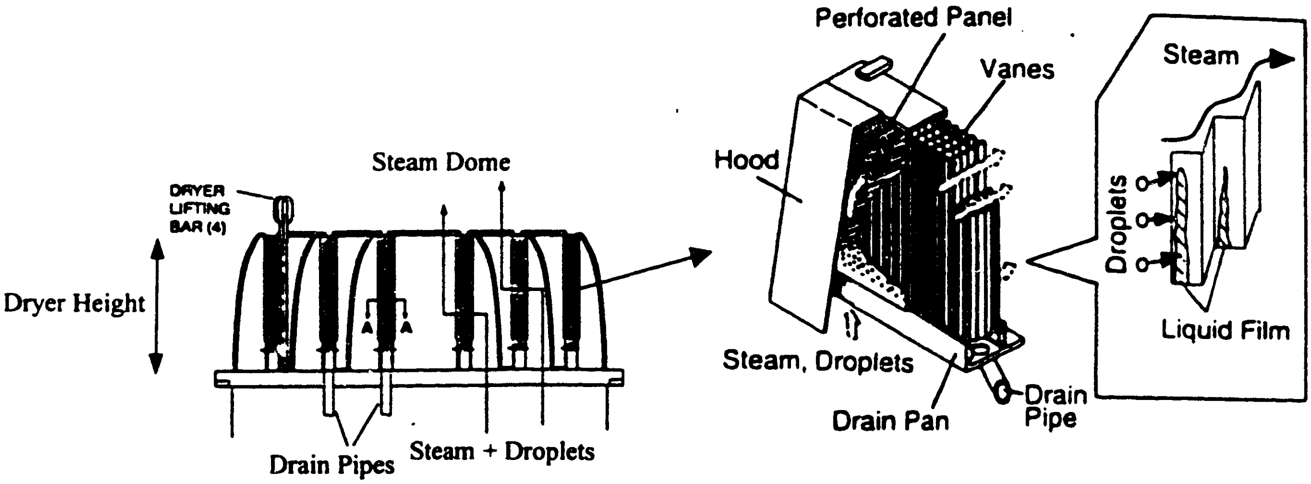

Figure 5.6. Chevron steam dryer (from [Nakao 1999] and [GE 1999]).

Numerous different chevron separator designs have been proposed in the past for LWR applications. A good review of the their technical characteristics and performance can be found in [Carson 1980] and [Griffith 1997]. Most modern chevrons are 4 wavelengths long with a 120° vane angle, but they mainly differ in the shape, size and location of the drainage scoops. Because it was recently noted that most droplets are removed within the first two wavelengths of the dryer

---

[18] Wire-mesh separators are also susceptible to droplet induced erosion due to the small diameter of the wire. For example, it is reported in [Carson 1980] that the wire-mesh demister in the moisture separator of the San Onofre

[Saito 1995], advanced chevron separators have been proposed that feature only 2 wavelengths (to reduce the pressure drop) and a smaller vane angle (to increase the efficiency). Several values of the vane angle were explored and it was established that, under prototypical BWR conditions, the optimum pressure drop vs. efficiency performance is achieved with a 90° angle-2 wavelength chevron [Nakao 1999, Nagase 1996]. As a result, it is now possible to design steam dryers with lower pressure drops and higher efficiency than in the past. The development and/or optimization of a new chevron separator for the steam dryer of the PBWR are beyond the scope of this study. Therefore we will adopt the advanced chevron design proposed in [Nakao 1999] for BWR applications and will assess its performance in our system. This 90° vane angle-2 wavelength chevron separator is shown in **Figure 5.5**. The chevron gap is 10mm, the wavelength is 50mm and the wave amplitude $2y_o$ is 25mm. The dryer height is 1.2m. The steam operating velocity, U, is 2m/s. At this velocity this chevron was found [Nagase 1996] to display approximately the same pressure drop as a BWR traditional 120° vane angle-4 wavelength chevron. The flow area A_{dryer} required to accommodate the steam flow $\dot{M}_g$ is:

$$A_{dryer} = \frac{\dot{M}_g}{\rho_g U} \approx 8.6\,\mathrm{m}^2 \qquad \textbf{Eq.5.18}$$

where ρ_g=40kg/m^3 and $\dot{M}_g$=686kg/s.

The flow area of each chevron channel (defined by two corrugated plates) is the product of the dryer height times the chevron gap: $1.2\times0.01=0.012\mathrm{m}^2$. Therefore the required number of channels is $12.5/0.012\approx715$. Because the chevrons are bundled in packs of 10 channels each, the steam dryer is made of about 71 packs (each of width $0.01\times10=0.1$m) that must be accommodated between the pool free surface and the steam dome. Following the BWR design, they will be arranged on 6 rows (of different length) as illustrated in **Figure 5.7**.

PWR failed by erosion after only three months of operation.

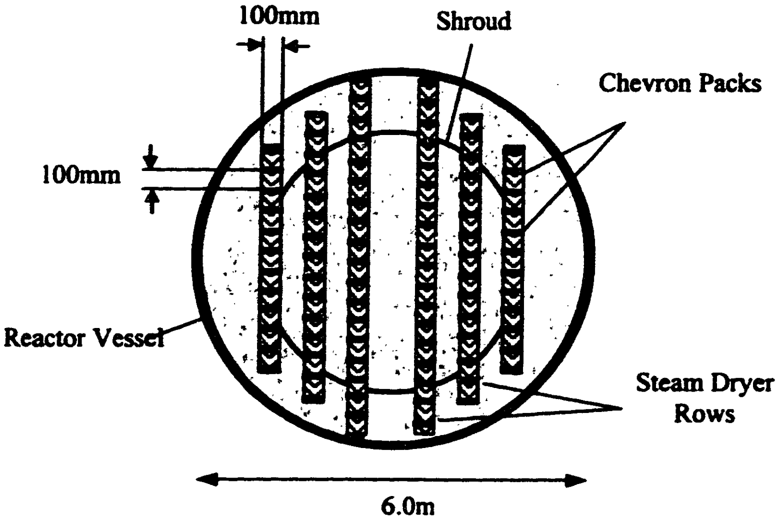

Figure 5.7. Schematic of the steam dryer arrangement.

5.3.2.1 Breakthrough Velocity

To prevent re-entrainment from the liquid film on the corrugated plate walls, it must be demonstrated that the dryer operates below a certain critical steam velocity, also known as the breakthrough velocity. At low wetness[19], the breakthrough velocity was found to be substantially independent of the liquid flow rate [Sorokin 1966]. Two correlations are available for the prediction of the re-entrainment condition in chevron steam separators: the Wilson correlation [Wilson 1965] and the Panasenko and Koslov correlation [Panasenko 1962]. They are illustrated in **Figure 5.8** where Ku is the Kutateladze number and is given by:

$$Ku = \frac{\rho_g^{1/2} U_{cr}}{\left[g\sigma\left(\rho_p - \rho_g\right)\right]^{1/4}} \qquad \textbf{Eq.5.19}$$

and U_{cr} is the breakthrough velocity. In reference [Moore 1976] the discrepancy between the two correlations is attributed to the absence of drainage scoops on the corrugated plates of Panasenko and Koslov's experiments.

Because the liquid film was not effectively drained out of the chevron separator, the breakthrough velocity was significantly smaller in these experiments. Since the chevron separator selected for the PBWR steam dryer is equipped with drainage scoops, we will rely primarily on the Wilson correlation. For PBWR conditions the ordinate $g(\rho_p-\rho_g)/\sigma \approx 0.25\text{mm}^{-2}$.

---

[19] e.g. 1-x up to 10% in water systems

The Wilson correlation yields Ku≈2 and hence $U_{cr}\approx4.5$m/s, which is considerably above the selected steam operating condition of 2m/s.

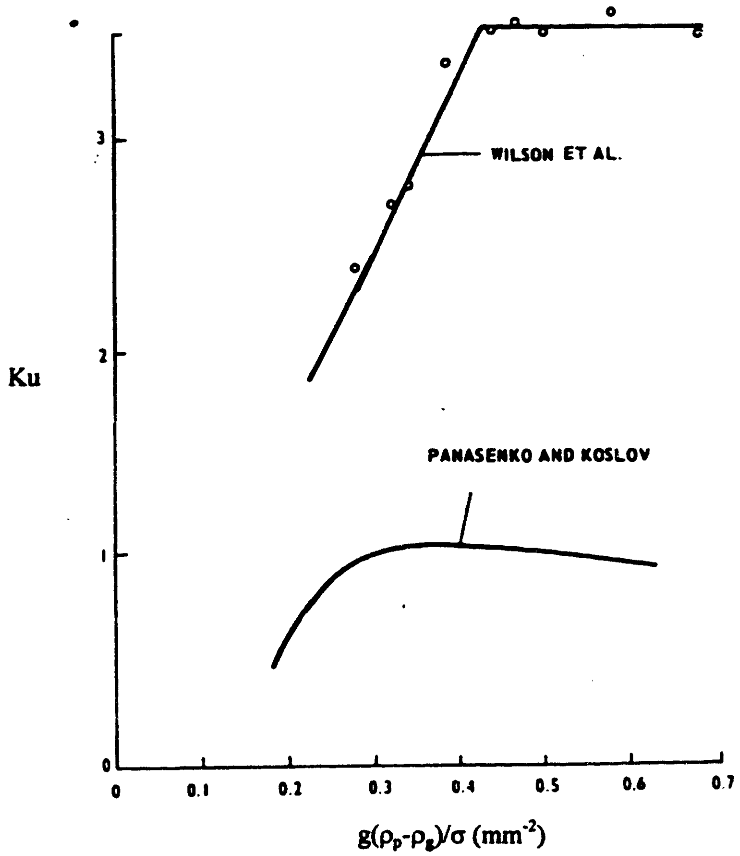

Figure 5.8. The breakthrough velocity correlations (from [Moore 1976]).

5.3.2.2 Steam Dryer Efficiency

To evaluate the droplet removal efficiency of the PBWR chevron separator, we will make use of a simple theoretical model developed by Moore and Sieverding [Moore 1976], whose assumptions can be best described with the help of **Figure 5.9**:

a) The corrugated plates display a sinusoidal profile of wavelength p and amplitude y_0', spaced from each other by a distance h.

b) The steam streamlines are also sinusoidal with the same wavelength and amplitude. The steam flows through the corrugated plates with velocity U in the x-direction.

c) The velocity of the liquid droplets in the x-direction is also U.

c) The velocity of the liquid droplets in the x-direction is also U.

d) The droplets are subjected to a drag force F_y in the y-direction which can be expressed by Stokes law as $F_y = -3\pi D_d \mu_g V_{pg,y}$ where $V_{pg,y}$ is the y-component of the steam/droplet relative velocity.

e) At the dryer inlet the droplets are uniformly distributed in the y-direction.

f) An impact on the plate surface always results in droplet deposition.

g) There is no re-entrainment from the liquid film.

h) The effect of the drainage scoops on the steam flow is neglected.

The equation of motion of the droplet is solved to generate the droplet trajectory in the gap between the plates. Due to assumption 'd' the trajectory is also a sinusoidal wave of wavelength P, but of amplitude $A=\frac{y_0'}{\sqrt{1+Stk^{-2}}}$ and phase-lag $\theta = -\arctan(Stk^{-1})$. The Stokes number Stk is defined as $Stk = \frac{\pi \rho_p D_d^2 U}{9\mu_g P}$ and measures the ratio of the droplet inertia to the viscous forces, i.e. the tendency of a droplet to deviate from the steam streamlines.

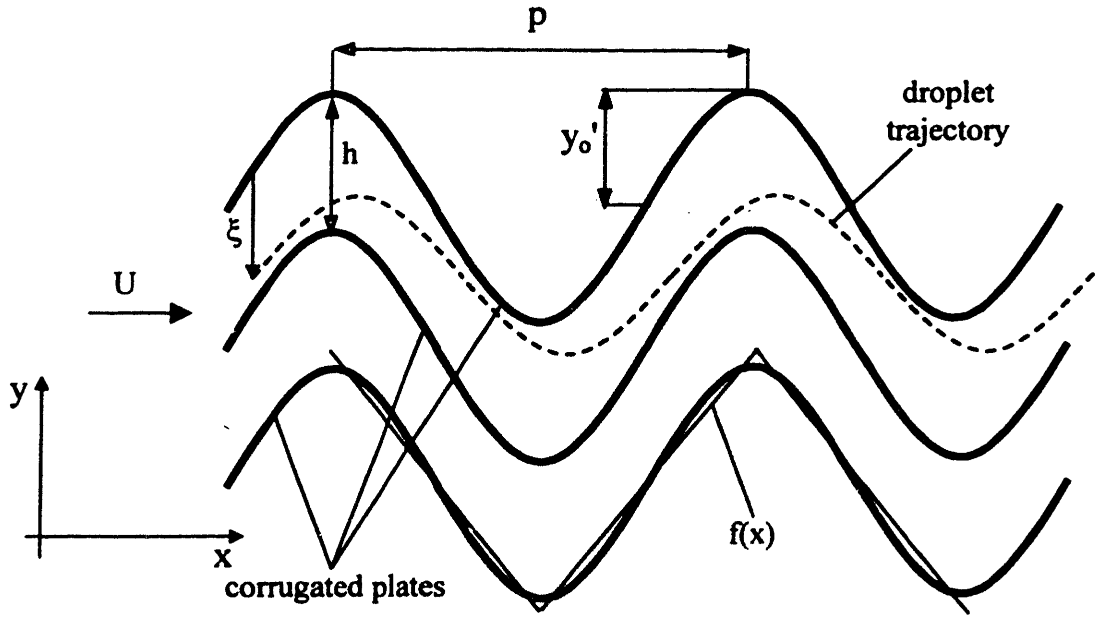

Figure 5.9. Chevron geometry for the Moore's model.

The smaller droplets faithfully follow the steam streamlines and flow through the dryer without impacting the corrugated plates. On the other hand, the larger droplets display a trajectory with significant phase-lag and are likely to deposit on the plates. For a droplet entering the dryer at a distance ξ from a corrugated plate, the condition of impact on the plate surface (expressed mathematically as the intersection of the droplet trajectory and the plate profile) is:

$$\xi < \xi_{cr} = \frac{y_0'}{\sqrt{1+Stk^{-2}}} \qquad \textbf{Eq.5.20}$$

If $h \leq 2\xi_{cr}$, all the droplets of diameter D_d deposit on the plate walls and the efficiency is equal to unit. On the other hand, if $h > 2\xi_{cr}$, the efficiency is

$$\eta = \frac{2\xi_{cr}}{h} = \frac{2y_0'/h}{\sqrt{1+Stk^{-2}}} \qquad \textbf{Eq.5.21}$$

where it is assumed that at the dryer inlet the droplets are uniformly distributed in the y-direction (assumption 'e').

However, in longer chevron separators there is some diffusion-driven redistribution of the droplets in the y-direction after the droplets close to the wall have deposited. To account for this effect, Moore and Sieverding propose the following expression for the overall dryer efficiency:

$$\eta_m = 1-(1-\eta)^{am} \qquad \textbf{Eq.5.22}$$

where m is the plate length in the x-direction (expressed in number of wavelengths p), η is given by **Eq.5.21** and 'a' is an empirical coefficient selected to fit the experimental data. A value a~0.5 is recommended as conservative in [Moore 1976] and [Keshava 1997] and will be adopted in this study. The Moore and Sieveding model was benchmarked against data from several different fluids and chevron configurations with reported satisfactory accuracy [Moore 1976].

In order to apply this model to the commercial chevron steam dryers of **Figure 5.5** it is necessary to represent their "linear zigzag" plates as a sinusoidal wave. We shall do that by approximating the periodical linear segmented curve f(x) with the first term of its Fourier series, as illustrated on the lowest plate of **Figure 5.9**. Then:

$$f(x) \approx f_1 \sin\left(\frac{2\pi x}{p}\right) \qquad \textbf{Eq.5.23}$$

where f_1 is defined as:

$$f_1 = \frac{2}{p}\int_0^p f(x)\sin\left(\frac{2\pi x}{p}\right)dx = \frac{8y_0}{\pi^2} = y_0' \qquad \textbf{Eq.5.24}$$

where y_o is the amplitude of the actual chevron[20] (see **Figure 5.5**).

Fourier series theory guarantees that this choice of the coefficient f_1 minimizes the mean square error defined as $\int_0^p \left| f(x) - f_1 \sin\left(\frac{2\pi x}{p}\right)\right|^2 dx$.

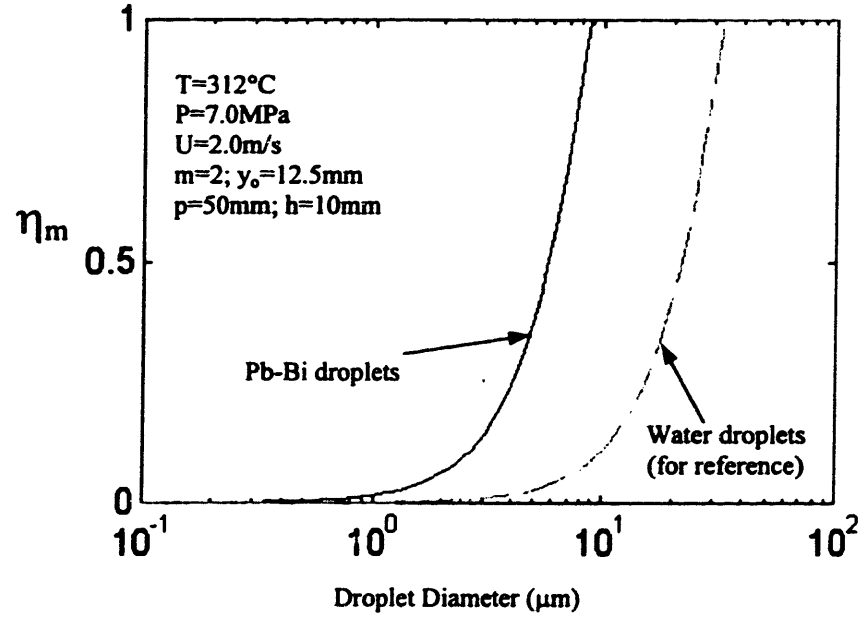

Figure 5.10. The chevron droplet removal efficiency[21].

Figure 5.10 illustrates the droplet removal efficiency of the PBWR chevron separator as a function of the droplet diameter for the selected 2m/s steam operating velocity. The chevron efficiency for liquid water droplets is also plotted for reference. As expected, for a given droplet diameter, the removal efficiency of the Pb-Bi droplets is larger than that of the water droplets due to the larger liquid density. Moreover, practically every Pb-Bi droplet above 10μm is removed from the steam stream and practically every droplet below 0.1μm is not removed. We will conservatively assume that the removal efficiency for droplets of diameter below and above

---

[20] Note that f_1 is the amplitude of the approximating sinusoidal wave and is slightly smaller than y_o.

[21] It is anticipated that there will be no liquid water droplets in the steam dryer. Therefore, the removal efficiency curve for the liquid water droplets is plotted in this figure for comparison purposes, only.

10μm is zero and unity, respectively. Then the overall efficiency of the steam dryer[22] can be readily calculated as:

$$\eta_{dryer} = \int_{10\mu m}^{233\mu m} \frac{dv}{dD_d} dD_d = \int_{10\mu m}^{233\mu m} \frac{dv}{d\delta}\frac{d\delta}{dD_d} dD_d \approx 99.68\% \qquad \textbf{Eq.5.25}$$

where the definition of dv and δ is given in **Section 5.3.1.4**. Because the Pb-Bi flow rate at the steam dryer entrance is 4kg/s, it can be concluded that the Pb-Bi carry-over at the steam dryer outlet is (1-0.9968)×0.9kg/s≈0.0029kg/s=10.4kg/hr. Also, the steam quality at the dryer outlet is $\frac{686kg/s}{686kg/s+0.0029kg/s} > 99.999\%$. The consequences of the transport of some Pb-Bi through the steam lines and to the turbine are discussed in **Section 5.4** and **5.5**, respectively.

5.4 Transport of Pb-Bi Aerosol Through the Steam Lines

The dynamics of the Pb-Bi droplets passing through the steam lines is now studied to evaluate the fraction of the Pb-Bi mass flow rate that actually reaches the turbine and the fraction that deposits on the walls of the steam lines. The relevant geometric and thermal-hydraulic characteristics of the steam lines are reported in **Table 5.II**. The geometry is taken from the BWR and deemed applicable to the PBWR.

Table 5.II. The steam lines.

Parameter	Description	Value
N_{sl}	# of steam lines	3
D	Steam line diameter	1m
A_{sl}	Steam line flow area	0.785m^2
L	Steam line length	50m
$\dot{M}_g$	Total steam mass flow rate	686kg/s
$\dot{m}_g$	Steam mass flow rate per steam line	229kg/s
V_g	Steam average velocity	7.3m/s
x	Steam quality	99.999%
$\dot{M}_p$	Total Pb-Bi mass flow rate	0.0029kg/s
$\dot{m}_p$	Pb-Bi mass flow rate per line	0.0010kg/s
T	Steam Temperature	312°C
P	Steam Pressure	7.0MPa

---

[22] defined as the ratio of the liquid removal rate to the liquid flow rate at the dryer inlet

5.4.1 Droplet Deposition

In this section we will consider two different deposition mechanisms whose relative importance depends on the droplet size.

a. Turbulent diffusion

The motion of small Pb-Bi droplets in the radial direction is dominated by turbulence. A droplet in the turbulent core is accelerated radially and its inertia (particularly if the droplet flows near the wall) may be large enough to penetrate the viscous layer and deposit on the wall. As a result the steam in the proximity of the wall is depleted of droplets. This creates a radial concentration gradient in the channel, which drives the diffusion of more droplets from the central region of the channel (i.e. the turbulent core) to the wall where a liquid film is formed.

b. Gravity deposition

Because the steam lines are horizontal, all the droplets acquire an average drift velocity (analogous to the drift velocity of the electrons of an ohmic conductor immersed in an electric field) that tends to deposit them on the bottom of the channel. At small diameters the effect of turbulence is dominant and the drift velocity is negligible. To a first approximation it can be assumed that the droplets are kept in suspension by the turbulent fluctuations and therefore do not precipitate[23]. On the other hand, droplets of large diameter do not feel the effect of turbulence and gravity can make them effectively precipitate.

Before we proceed to calculate the droplet deposition rate of these two mechanisms, it is necessary to estimate the range of droplet size to which they apply. Starting from the equation of motion of a particle under the action of a periodically oscillating external force, Fuchs [Fuchs 1964] proposed a criterion to assess when the dynamics of a droplet is dominated by turbulence. It can be assumed that complete droplet entrainment by the turbulent eddies occurs if:

$$\tau_{rel} f_t < 0.01 \qquad \textbf{Eq.5.26}$$

Vice versa if:

$$\tau_{rel} f_t > 0.1 \qquad \textbf{Eq.5.27}$$

the droplet inertia is large and turbulence does not affect the droplet motion. In the intermediate range (between 0.01 and 0.1) the two effects are comparable.

---

[23] However, they can deposit by turbulent diffusion.

In **Eq.5.26** and **5.27** τ_{rel} is the relaxation time (estimated in **Section 5.4.2** as $\tau_{rel} = \frac{D_d^2 \rho_p}{18\mu_g}$) and f_t is the frequency of the turbulent fluctuations. In our case f_t can be estimated as:

$$f_t = \frac{\langle V' \rangle}{\langle \ell_M \rangle} \qquad \textbf{Eq.5.28}$$

where $\langle V' \rangle$ and $\langle \ell_M \rangle$ are the spatially averaged turbulent eddy radial velocity and mixing length (i.e. the average radial displacement of a turbulent eddy), respectively.

By definition these quantities are:

$$\langle V' \rangle = \frac{1}{A}\int_A V' dA = \frac{1}{\frac{\pi}{4}D^2}\int_0^{D/2} 2\pi r V' dr \qquad \textbf{Eq.5.29}$$

$$\langle \ell_M \rangle = \frac{1}{A}\int_A \ell_M dA = \frac{1}{\frac{\pi}{4}D^2}\int_0^{D/2} 2\pi r \ell_M dr \qquad \textbf{Eq.5.30}$$

where A and D are the steam line flow area and diameter, respectively.

The local values of V' and ℓ_M are related by the mixing length theory of eddy diffusivity as:

$$V' = \ell_M \frac{dv_z}{dy} \qquad \textbf{Eq.5.31}$$

where v_z is the axial velocity in the channel and y=R-r is a convenient radial coordinate.

Integration of the radial component of the Navier-Stokes equation (i.e. the conservation of momentum) in a round channel yields:

$$\left[\mu_g + \rho_g \ell_M^2 \left|\frac{dv_z}{dy}\right|\right]\frac{dv_z}{dy} = \tau_w \qquad \textbf{Eq.5.32}$$

where μ_g is the steam dynamic viscosity and τ_w is the wall shear stress.

Solving **Eq.5.32** for $\ell_M \frac{dv_z}{dy}$ one gets:

$$V' = \ell_M \frac{dv_z}{dy} = \sqrt{\frac{\tau_w}{\rho_g} - \nu_g \frac{dv_z}{dy}} \qquad \textbf{Eq.5.33}$$

By means of the following transformations:

$$v^+ = \frac{v_z}{\sqrt{\tau_w/\rho_g}} \quad ; \quad y^+ = \frac{y}{\nu_g}\sqrt{\tau_w/\rho_g}$$ **Eq.5.34**

Eq.5.32 becomes:

$$V' = \sqrt{\tau_w/\rho_g}\sqrt{1-\frac{dv^+}{dy^+}}$$ **Eq.5.35**

The knowledge of the friction factor f (e.g. from Moody's diagram) enables calculating τ_w as:

$$\tau_w = f\frac{\rho_g V_g^2}{8}$$ **Eq.5.36**

where V_g is the average steam velocity in the channel (see **Table 5.II**).

The universal turbulent velocity profile [Martinelli 1947] provides an expression for $\frac{dv^+}{dy^+}$ as:

$$\begin{cases} \frac{dv^+}{dy^+} = 1 & \text{for } y^+<5 \\ \frac{dv^+}{dy^+} = \frac{5}{y^+} & \text{for } 5<y^+<30 \\ \frac{dv^+}{dy^+} = \frac{2.5}{y^+} & \text{for } y^+>30 \end{cases}$$ **Eq.5.37**

Eq.5.33, **Eq.5.35** and **Eq.5.37** can be utilized to compute the integrals in **Eq.5.29** and **5.30** and hence $\langle V' \rangle$ and $\langle \ell_M \rangle$. An analytic approximate expression for $\langle \ell_M \rangle$ is 0.14 D/2, obtained by Nikuradse for the region far from the wall.

For the conditions of **Table 5.II** it is found that $\langle V' \rangle$~0.22m/s, $\langle \ell_M \rangle$~0.07m and f_t ~ 3.1Hz. Therefore, **Eq.5.26** and **5.27** lead to the following conclusions:

a. Turbulence dominates for D_d<10μm. The droplet are kept in suspension.
b. Turbulence and the droplet inertia effects are comparable for 10μm<D_d<33μm.
c. Droplet inertia dominates (i.e. turbulence effects can be neglected) for D_d>33μm. In this range the droplets do not follow the turbulent eddy motion and the external forces (i.e. gravity) dominate.

We will then apply the turbulent diffusion theory for $D_d<10\mu m$, gravity precipitation for $D_d>33\mu m$ and both for $10\mu m<D_d<33\mu m$.

5.4.1.1 Turbulent Diffusion

The rate of droplet deposition Γ_d (kg/m^{2}s) can be calculated by means of the McCoy & Hanratty correlation [McCoy 1977] for annular two-phase flow in a round tube:

$$\Gamma_d = K_d C_d \qquad \textbf{Eq.5.38}$$

where C_d is the Pb-Bi concentration in steam (kg/m^3) and K_d is given in **Figure 5.11** as a function of τ^*, where:

$$\begin{cases} \tau^* = \dfrac{1}{18}\dfrac{\rho_p}{\rho_g}\left(\dfrac{\rho_g u^* D_d}{\mu_g}\right)^2 \\ u^* = \sqrt{\tau_w/\rho_p} \end{cases} \qquad \textbf{Eq.5.39}$$

τ_w is again the wall shear stress given by **Eq.5.36**.

For D_d below 33μm, τ^* ranges up to 10 and K_d/u^* up to approximately 0.1 (see **Figure 5.11**).

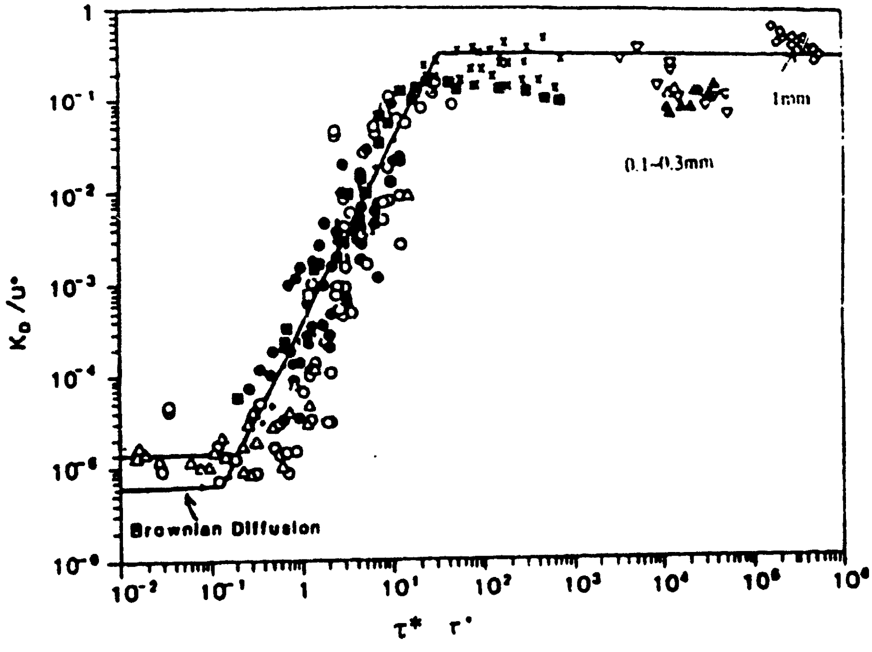

Figure 5.11. The mass transfer coefficient for turbulent diffusion (from [McCoy 1977]).

Let us now estimate the total droplet deposition (due to turbulent diffusion) in our steam lines.

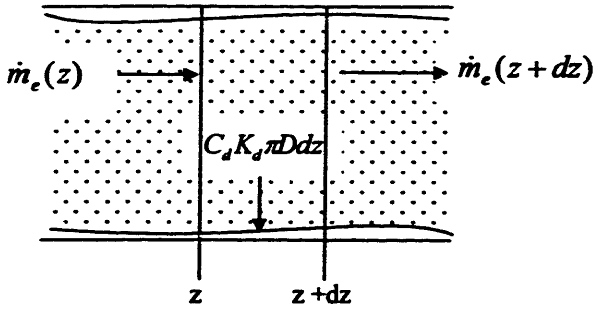

Figure 5.12. Schematic of the steam line channel.

With reference to **Figure 5.12**, a mass balance over the entrained liquid yields:

$$\dot{m}_e(z) = \dot{m}_e(z+dz) + C_d K_d \pi D dz \qquad \textbf{Eq.5.40}$$

where $\dot{m}_e$ is the entrained Pb-Bi mass flow rate.

C_d is given by:

$$C_d = \frac{\dot{m}_f \rho_g}{\dot{m}_g} \qquad \textbf{Eq.5.41}$$

Therefore **Eq.5.40** becomes:

$$\frac{d\dot{m}_e}{dz} = -\frac{K_d \pi D \rho_g}{\dot{m}_g}\dot{m}_e \qquad \textbf{Eq.5.42}$$

which can be readily integrated to yield:

$$\dot{m}_e = \dot{m}_e(0)e^{-\frac{K_d \pi D \rho_g}{\dot{m}_g}z} = \dot{m}_p e^{-\frac{K_d \pi D \rho_g}{\dot{m}_g}z} \qquad \textbf{Eq.5.43}$$

where it was assumed that, at the steam line inlet, all the Pb-Bi is entrained (i.e. $\dot{m}_e(0) = \dot{m}_p$).

The value of the coefficient $\frac{K_d \pi D \rho_g}{\dot{m}_g}$ for our system ranges up to 0.0009m^{-1} (corresponding to $K_D/u^* \sim 0.1$). Thus, **Eq.5.43** suggests that the reduction of $\dot{m}_e$ over a 50m long steam line is at most 4%. Clearly, in our system turbulent diffusion is not an effective mechanism of droplet deposition.

It must be emphasized that re-entrainment of Pb-Bi from the liquid film to the steam core was neglected in **Eq.5.40** because the Reynold's number of the film (conservatively calculated assuming that all the Pb-Bi flows in the film) is smaller than the critical value given by the Govan correlation [Govan 1988] for the onset of entrainment.

5.4.1.2 Gravity Deposition

The equation of motion of large Pb-Bi droplets (of mass m_d) in the vertical direction x can be written as (see **Figure 5.13**):

$$m_d \frac{dV_x}{dt} = -F_x + m_d(1-\frac{\rho_g}{\rho_p})g \qquad \textbf{Eq.5.44}$$

where F_x is the vertical component of the drag force. The terminal drift velocity (or precipitation velocity) in the vertical direction is then:

$$V_{drift} = \sqrt{\frac{4}{3}(\frac{\rho_p}{\rho_g}-1)\frac{gD_d}{C_D}} \qquad \textbf{Eq.5.45}$$

where:

$$C_D \equiv \frac{F_x}{\frac{\pi}{4}D_d^2 \frac{\rho_g V_{drift}^2}{2}} = 24\left(\frac{1}{\mathrm{Re}_d}+\frac{0.1}{\mathrm{Re}_d^{0.313}}\right) \qquad \textbf{Eq.5.46}$$

is the drag coefficient from [Hewitt 1982] (valid for Re_d up to 200) and

$$\mathrm{Re}_d = \frac{\rho_g V_{drift} D_d}{\mu_g} \qquad \textbf{Eq.5.47}$$

is the droplet Reynold's number.

Clearly **Eq.5.45** is an implicit equation in the only unknown V_{drift}.

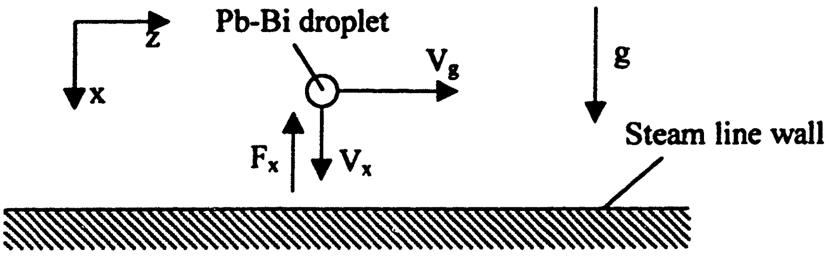

Figure 5.13. Reference system for the droplet equation of motion.

In **Figure 5.14** V_{drift} is plotted against the droplet diameter D_d. Recalling that the steam line diameter is D=1m and that the droplet traveling time in the steam line is $t_{trav}=L/V_g \approx 6.8$s, it can be readily concluded that only the droplets whose drift velocity is greater than $(D/2)/t_{trav} \sim 0.07$m/s will deposit by gravity on the bottom of the steam lines. **Figure 5.14** indicates that all the droplets of diameter greater than 20μm fulfill this requirement. Because the maximum diameter of the droplets that escape the steam dryer is about 10μm, it can be concluded that, in the PBWR steam lines, gravity precipitation is not an important deposition mechanism, either.

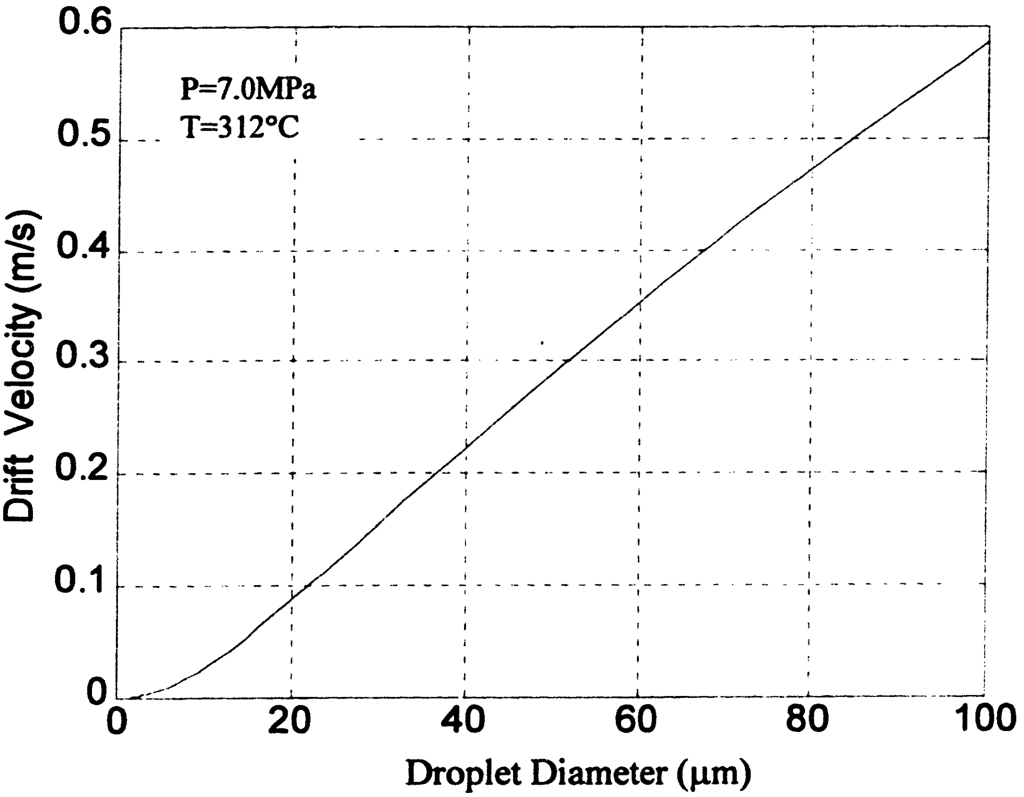

Figure 5.14. Vertical drift velocity of the droplets in the steam lines.

We have so far assumed that the medium around the droplets can be regarded as a continuum. At very small diameters (approaching the scale of the water molecule mean free path) this might not be correct and **Eq.5.46** would require the introduction of a corrective factor (i.e. the so-called Cunningham factor). To assess if this correction is necessary, we calculate the droplet Knudsen number, which is defined as the ratio of the water molecular mean free path λ to the droplet diameter. For droplet of diameter D_d>0.1μm in steam at 312°C and 7.0 MPa, the Knudsen number, Kn, is:

$$Kn = \frac{\lambda}{D_d} = \frac{A_{H2O}}{D_d \rho_g N_{av} (\frac{\pi}{2} D_w^2)} = 0.06 << 1 \qquad \textbf{Eq.5.48}$$

which confirms the validity of the continuum assumption. In **Eq.5.48** A_{H2O}, D_w and N_{av} are the water molar weight (i.e. 0.018g/mol), the diameter of the water molecules (i.e. 3.7×10^{-10}m) and Avogadro's number, respectively.

5.4.2 Droplet Coagulation

In the previous section, the interaction of contiguous droplets was neglected. This assumption is justified in the discussion that follows. The liquid dragged out of the steam dome is in the form of finely dispersed droplets. For a given Pb-Bi mass flow rate, the smaller the droplet size the larger the droplet concentration (number of droplets per unit volume). Coagulation phenomena (i.e. coalescence of droplets) become important at high concentration. A droplet may collide with another droplet and form a bigger one. As the number of droplets decreases, so does the probability of collision until the average distance between two droplets is so large that the probability of collision becomes zero. If the time scale of these collision phenomena is small compared with the traveling time of a droplet through the steam lines, coagulation dominates the size evolution of the small droplet population. In this section we will see how this sets a lower limit to the droplet diameter.

Depending on the droplet size and degree of flow turbulence, the dominant coagulation mechanism can be either Brownian (thermal) collisions or turbulent eddy induced collisions.

Brownian Coagulation

The random (thermal) motion of very small droplets in a surrounding medium can be predicted by means of statistical mechanics. The droplets are treated as (larger) molecules of the medium. Their average kinetic energy is then equal to $\frac{1}{2}kT$ as is that of the molecules, although molecules and liquid droplets considerably differ in size (i.e. 10^{-10}m vs. 10^{-8}-10^{-5}m, respectively).

As already mentioned, if the droplet concentration is large, the collision probability of two droplets may become significant.

To assess the time evolution of a droplet population under the action of Brownian coagulation, we make use of Smoluchowski's theory [Fuchs 1964], which is based on two fundamental assumptions:

- All droplets are spherical and remain spherical after coalescence with another droplet.
- Every collision is 100% effective (i.e. it produces coalescence).

Smoluchowski's theory provides a simple expression for the mean time to collision t_{coll} of two droplets in brownian motion:

$$t_{coll} = \frac{1}{N_d K_0} \qquad \textbf{Eq.5.49}$$

where N_d is the droplet concentration (Pb-Bi droplets/m^3 of steam) and K_0 is the coagulation constant:

$$K_0 \approx \frac{4}{3}\frac{kT}{\mu_g} \qquad \textbf{Eq.5.50}$$

N_d is readily obtained from conservation of mass considerations as follows. The Pb-Bi mass flux in the steam line can be calculated as:

$$\frac{\dot{m}_p}{A_{sl}} = N_d \rho_p \frac{\pi}{6} D_d^3 V_p \qquad \textbf{Eq.5.51}$$

where D_d is the droplet diameter, $\frac{\pi}{6} D_d^3$ is the volume of a single droplet and V_p is the droplet axial velocity.

The vapor mass flux in the steam line is:

$$\frac{\dot{m}_g}{A_{sl}} = \rho_g V_g \qquad \textbf{Eq.5.52}$$

Assuming that the axial velocities of the droplets and steam are equal, an expression for N_d immediately follows from **Eq.5.51** and **Eq.5.52**:

$$N_d = \frac{\dot{m}_p \rho_g}{\dot{m}_g \rho_p \frac{\pi}{6} D_d^3} \qquad \textbf{Eq.5.53}$$

We can now predict the evolution of the droplet size (due to brownian coagulation) along the steam lines. We assume that:

- all Pb-Bi enters the steam lines as droplets of diameter $D_{d,i}$
- all droplets simultaneously collide at $t=t_{coll}$

The mean axial displacement of the droplets before they collide is then:

$$L_{coll} = V_g t_{coll} \qquad \textbf{Eq.5.54}$$

As two droplets of diameter D_d collide, the conservation of mass requires that they form a bigger droplet of diameter D_d':

$$D_d' = \sqrt[3]{2} D_d \qquad \textbf{Eq.5.55}$$

From **Eq.5.53** N_d can be recalculated for the new diameter. Then **Eq.5.54** provides the average axial displacement before the droplets of diameter D_d' collide again to form even bigger droplets, and so forth.

Figure 5.15 illustrates the axial variation of the droplet size in the steam line for four different initial droplet diameters $D_{d,i}$. It can be seen that, regardless of the initial diameter, the droplet size eventually converges to a single curve. This behavior is expected because, as the diameter increases, the droplet concentration decreases and the collision probability becomes smaller and smaller. As a result, L_{coll} gets increasingly large and the droplet previous history becomes negligible.

It is important to emphasize that the assumption of brownian motion (and therefore **Eq.5.49**) holds only if $t_{coll} >> \tau_{rel}$, where $\tau_{rel} = \frac{D_d^2 \rho_F}{18\mu_g}$ is the relaxation time (i.e. a measure of the time a droplet takes to reach its terminal velocity under the action of a constant force). In our case this condition is satisfied by droplets of diameter much larger than 10^{-13}m (!). Because in this section we are dealing with droplet in the 10^{-8} to 10^{-6}m range, it can be concluded that the assumption of brownian motion is applicable.

Turbulent Coagulation

The brownian motion of the droplets takes place on a microscopic scale and is superimposed to the macroscopic motion due to turbulence in a flow system. The droplets are displaced by turbulent steam eddies that move chaotically in the radial direction. As a result they may acquire a relative velocity and collide.

Fuchs [Fuchs 1964] provides an expression for the turbulent coagulation collision time and suggests a simple criterion to estimate the magnitude of this coagulation mechanism relative to that associated with the brownian motion. Turbulent coagulation becomes significant when $\zeta>1$, where ζ is the ratio of the brownian and turbulent coagulation collision times:

$$\zeta=\frac{75}{64}\sqrt{\varepsilon\rho_g\mu_g}\,\frac{D_d^3}{kT} \qquad \textbf{Eq.5.56}$$

and ε is the rate of dissipation of turbulent energy per unit mass of steam, which can be calculated as:

$$\varepsilon=\frac{fV_g^3}{2D} \qquad \textbf{Eq.5.57}$$

f is the friction factor. Setting $\zeta>1$ in **Eq.5.56** and solving for D_d, it can be proven that in our case turbulent coagulation can be ignored for $D_d<1\mu m$.

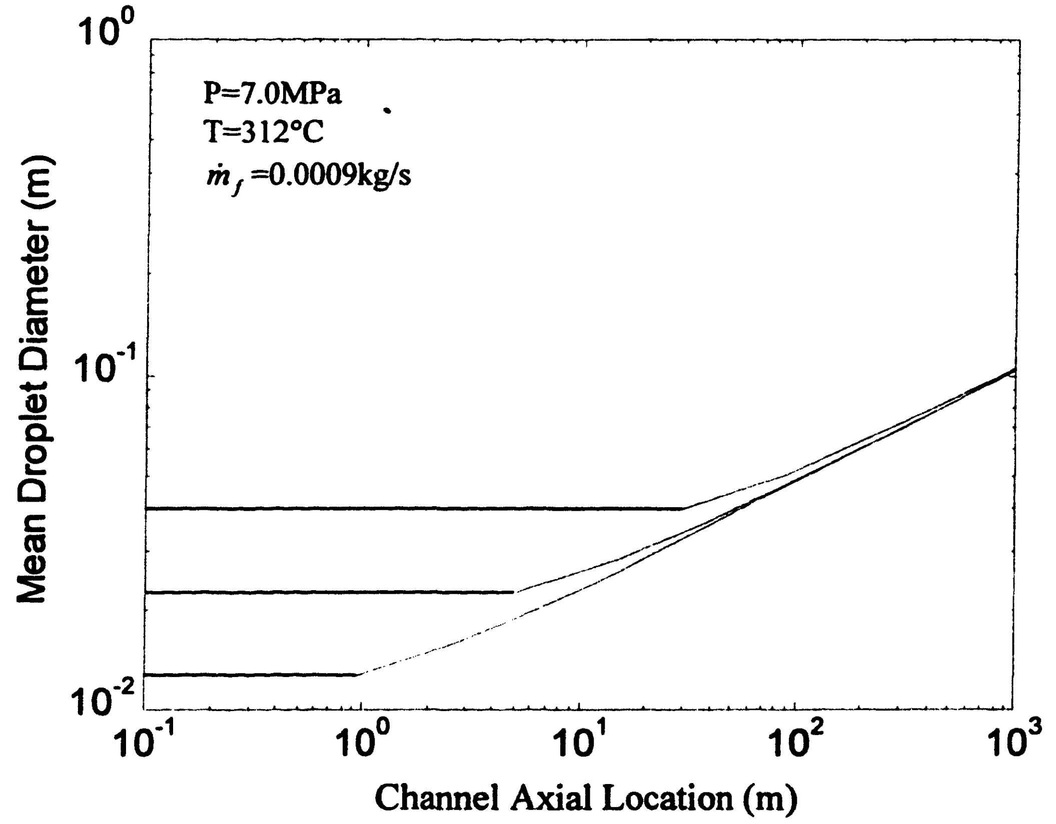

Figure 5.15. Evolution of the droplet size in the steam lines due to brownian coagulation

Because this value is substantially larger than the maximum droplet diameter reached by brownian coagulation (see **Figure 5.15**), we can conclude that the brownian to turbulent coagulation transition does not occur in the steam lines and the results obtained by means of Smoluchowski's theory hold.

The droplet removal and coagulation phenomena analyzed in **Section 5.4** and the range over which they become dominant are synoptically illustrated in **Figure 5.16**.

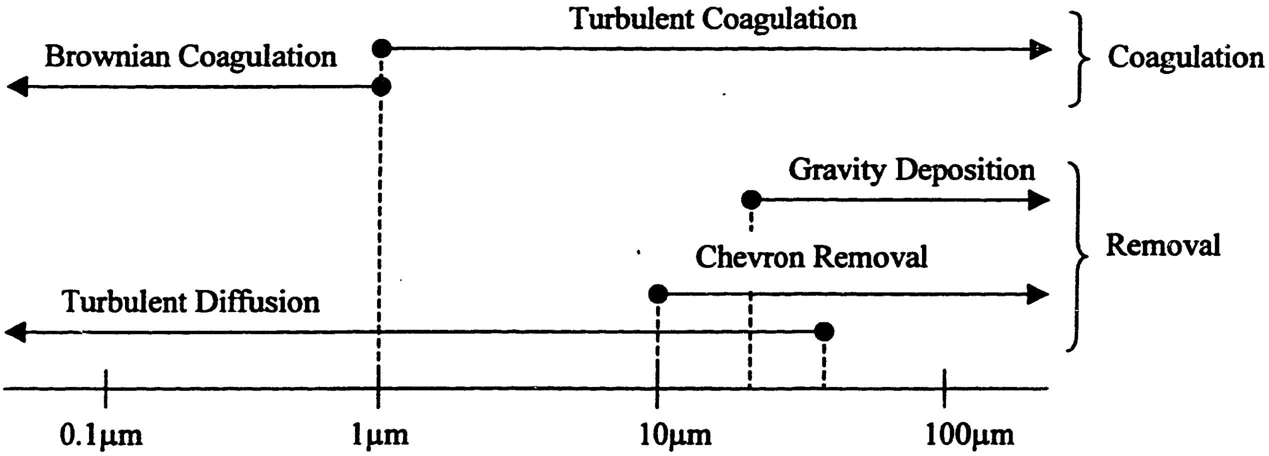

Figure 5.16. Regimes of governing droplet dynamic mechanisms.

5.5 Effect of Pb-Bi Droplet Carry-Over on Design and Performance of the Turbine

In the previous section it was estimated that a substantial amount of liquid Pb-Bi becomes entrained in the steam stream (in the form of small droplets) at the free surface of the pool. The majority of these droplets are removed in the steam dryer, but the residual droplets are transported through the steam lines and reach the turbine. In this chapter we discuss the implications of Pb-Bi droplet carry-over to the design and performance of the turbine.

The presence of heavy liquid metal droplets at the first stages of the turbine raises three basic concerns:

1) Liquid metal embrittlement of the turbine blades and other stressed components.
2) Erosion of the turbine surfaces exposed to the steam flow.
3) Accumulation of Pb-Bi and consequential contamination of the turbine surfaces by radioactive polonium.

Before we try to assess the magnitude of these technical challenges and propose possible remedies to ensure safe, reliable and economic operation of the turbine, it is prudent to concisely provide some basic turbine technology information that will be useful in the sections that follow.

5.5.1 Steam Turbine Technology

To produce the work that is converted into electricity in the generator, the steam coming from the reactor is expanded in the turbine from its maximum pressure (i.e. approximately 7.0MPa in LWRs) to sub-atmospheric pressure. A specific volume increase of several orders of magnitude (and a corresponding volumetric flow rate increase) are associated with this large pressure reduction. Because the steam velocity at the turbine outlet cannot be set arbitrarily high (due to friction losses and other design constraints), this large steam volumetric flow is accommodated by increasing the flow area and hence the length of the low pressure stage blades (where the most significant expansion takes place). The mechanical tensile stresses in a turbine blade are induced by the centrifugal force caused by the high speed rotation of the shaft on which the blades are mounted (3600rpm in the US where the electric grid operates at 60Hz). These stresses are proportional to the blade material density ρ_b and to the square of the local blade velocity V_b:

$$\sigma_{blade} \propto \rho_b V_b^2 \propto \rho_b \omega^2 r^2 \qquad \textbf{Eq.5.58}$$

where ω is the shaft angular velocity and r is the radial distance from the shaft axis. **Eq.5.58** clearly shows that increasing the blade length dramatically raises the magnitude of the tensile stresses.

The blades of a nuclear steam turbine are typically made from AISI 422[24] stainless steel [Kuehn 1993, Moore 1976]. Due to the nature of their crystalline phase (known as martensite, from which they are sometimes called martensitic) the steels of the 400 AISI series display good yield strength over a wide range of temperatures (i.e. 1GPa up to 500°C). This characteristic

---

[24] Its composition (in %wt) is 12Cr-1Mo-1W-0.8Ni-0.25V-0.23C-Fe.

makes them suitable for mechanical components in environments where high stresses and high temperatures are present simultaneously[25].

However, in large nuclear power plants (>600MWe), the volumetric steam flow is so large that the blade length (required to accommodate it) would force operating dangerously close to the failure limit of AISI 422. To overcome this problem and retain the use of AISI 422 in the Low Pressure (LP) section of the turbine (as opposed to using more expensive materials like titanium), two design modifications have been successfully implemented by the nuclear industry [Moore 1976]:

a. the angular velocity of the rotor is reduced to 1800rpm,
b. the LP section of the turbine is split into several coaxial units to reduce the flow area requirement (and hence the blade length) per unit (see **Figure 5.26**).

On the other hand, in fossil fueled plants (generally of smaller rated power than nuclear plants) economics of scale prevents the split of the LP unit and the transition to 1800rpm (i.e. the capital cost impact of these changes would be unacceptable). In this case it is indispensable to maximize the LP flow area and hence the blade length. If AISI 422 is to be used, the blade length limit (for a 3600rpm turbine) is only 800mm [Kuehn 1993, Sakamoto 1992]. However, the use of titanium (whose yield strength to density ratio is larger than AISI 422 at low temperature) allows modern turbines to utilize LP blades up to 1500mm long [Kuehn 1993]. For this reason and despite its higher cost, titanium has become the customary material for LP turbine blades for fossil fuel plants and its technology has been fully developed [Kuehn 1993]. However, the mechanical properties of titanium at high temperature are poor and this material cannot be employed in the High Pressure (HP) section of a turbine (where temperatures range from 300°C in LWRs to 550°C in supercritical conventional plants). Note that stresses in the HP section are smaller (because the blades are shorter) and the use of AISI 422 (which is less expensive and maintains its mechanical strength at high temperature) is preferred (both in 1800 and 3600rpm turbines).

Now that some useful information on steam turbine technology has been introduced, we can move on to discuss the challenges specific to the turbine of the PBWR.

---

[25] e.g. in the High Pressure (HP) section of a steam turbine

5.5.2 Liquid Metal Embrittlement

Liquid Metal Embrittlement (LME) is the brittle fracture, or loss of ductility, of a normally ductile metal (stressed in tension) upon contact with a liquid metal [Joseph 1999]. LME is manifested as a drastic reduction of the strain to rupture, although until fracture occurs, the stress-strain behavior of the solid metal remains unchanged [Lynch 1992, Westwood 1971] (the yield stress and the elastic properties are not affected by the presence of the liquid metal). Several different microscopic models have been proposed to explain the physical mechanism leading to LME. The most commonly referenced is that of Kamdar [Kamdar 1983], which postulates the presence of a micro-crack as a prerequisite. At the crack tip, liquid metal atoms replace the atoms of the solid by breaking their mutual bonds, which causes a rapid acceleration of the crack growth until the crack reaches a critical size and the solid macroscopically fails. Tensile stresses are necessary to drive the crack growth. A detailed description of LME models and phenomena is beyond the scope of this work. We will only report those characteristics that are relevant to our application. For a more comprehensive and general discussion of LME, the reader is referred to [Kamdar 1986, Joseph 1999, Lynch 1992] from which most considerations in this section are drawn.

The following is a list of the elements that should be kept in mind.

a. Although LME is not a corrosion, diffusion or intergranular penetration phenomenon, its most mandatory prerequisite is that the liquid be in intimate contact with the solid surface and be present at the tip of the propagating crack.
b. A thin oxide film (several angstroms thick) is enough to prevent the liquid metal/solid contact so that embrittlement is not observed.
c. LME does not take place in ceramic materials, but in metallic solids, only.
d. LME is a selective phenomenon in that a liquid metal may embrittle certain metals and not others.
e. LME may occur at any temperature[26]. However, in stainless steel its consequences are somewhat mitigated at high temperature (above 510 to 650°C) because the fracture induced by LME becomes ductile.
f. LME occurs in presence of tensile stresses, only.

---

[26] In fact it may occur even at temperatures below the melting point of the liquid metal. In this case the phenomenon is more appropriately called Solid Metal Induced Embrittlement.

g. LME causes a reduction of the fatigue life of the solid.

Since data on LME induced by lead-bismuth mixtures are not available in the literature, our analysis will be based on an extrapolation from the data regarding pure lead and pure bismuth only. It was reported in [Kamdar 1986] that smooth samples of stainless steels are not susceptible to lead nor bismuth LME. This is probably due to the presence of the protective chromium oxide film which prevents liquid metal/solid contact and hence embrittlement (see points a. and b.). It was also found that lead and bismuth do not embrittle titanium. On the other hand, commercial stainless steels[27] (where micro-cracks and discontinuities of the oxide film are normally present) are susceptible to severe lead LME [Kamdar 1986, Lynch 1992]. Pure bismuth does not seem to cause embrittlement in ferrous alloys. Following reference [Kamdar 1986] we will assume that a mixture of embrittling and non-embrittling species (in our case lead and bismuth, respectively) in fact causes embrittlement[28], where it is postulated that the non-embrittling species effectively acts as an inert carrier and does not affect the active agent.

The lead-bismuth droplets coming from the reactor enter the turbine and mostly impact the fixed or moving surfaces of the HP section. The droplets that manage to escape the HP section are collected in the Moisture Separator/Reheater (MSR) before they reach the LP turbine. Therefore, in our reactor the LME analysis must focus primarily on the HP turbine. Liquid metal contamination of the LP turbine is effectively prevented by the presence of the MSR and the HP turbine itself. It should be noted that LME induced failure of turbine components is not a completely new and unknown phenomenon: for example, reference [Cameron 1994] reports the case of a gas turbine stainless steel shaft cracking due to LME induced by the accidental melting of its copper bearing.

The PBWR HP turbine inlet operating temperature is 312°C. As already mentioned, the use of commercially pure titanium (which would eliminate the LME problem) is impractical at this relatively high temperature and stainless steel most likely will be used. Unfortunately, this temperature is below the brittle-to-ductile fracture transition of stainless steel (see point e.) and LME is expected. The critical components are those subjected to significant tensile stresses (see point f.) like the turbine casing (which serves as a pressure barrier between the turbine and the external environment) and the blades. Also it should be noted that, due to vibrations, the stresses

---

[27] Of the martensitic type, too.

[28] This assumption is conservative and plausible in view of the physical mechanism of LME described above.

in the blades are cyclical. LME reduces the fatigue strength of stainless steel and makes the blades more susceptible to fatigue failure.

It should be clear by now that LME can be a very serious problem in this reactor design and ways to cope with it must be identified.

5.5.2.1 Alternative Blade Materials

The most obvious way to eliminate LME would be to select an alternative structural material that is not prone to embrittlement upon contact with lead or bismuth. A list of materials immune to either lead or bismuth LME is reported in **Table 5.III**.

Table 5.III. Materials immune to lead or bismuth LME (from [Kamdar 1986]).

Material	Immune to Bi LME	Immune to Pb LME
Sn	Yes	Yes
Bi	Yes	Yes
Cd	Yes	Yes
Zn	Yes	No
Mg	Yes	Yes
Ag	Yes	Yes
Ni	Yes	No
Fe	Yes	No
Pd	Yes	Yes
Ti	Yes	Yes

Those materials in this list that are immune to both lead and bismuth embrittlement cannot practically be used in a turbine because they are either too expensive (e.g. silver, palladium) or mechanically inadequate at the temperatures of interest (e.g. titanium, tin, magnesium, cadmium, bismuth) or both. However, titanium-aluminum alloys are successfully employed in a variety of applications in gas turbines and compressors at temperatures up to 540°C [Von Boeckh 1984, Bania 1988] due to their high strength-to-density ratio. Typical Ti-Al alloys are Ti-6242 and Ti-1100 whose composition is Ti-6Al-2Sn-4Zr-2Mo-0.1Si (%wt) and Ti-6Al-2.75Sn-4Zr-0.4Mo-

$0.45Si$-$0.07O_2$-$0.02Fe$ (%wt). Aluminum is susceptible to severe lead and bismuth LME [Kamdar 1986]. However, the continuous phase of Ti-6242 is titanium[29] and thus it is conceivable that LME would not occur in this alloy. Naturally, an experimental verification of this conclusion would be necessary, should this material be considered for the PBWR turbine blades. Also, aluminum solubility in Bi is relatively high [Weeks 1971] and it must be ensured that leaching (i.e. selective attack of aluminum by bismuth) does not take place[30].

5.5.2.2 Coating

Another viable option to reduce the concerns about LME is coating the surfaces of the HP turbine critical components (which could then be made of stainless steel). The presence of a barrier to liquid metal/solid contact is known to completely prevent LME (see point b.). To ensure the integrity of this barrier, the coating material should be ceramic (see point c.). Blade coating of high temperature gas turbines is a mature and successful technology [Nakamura 1990, Burgel 1986] aiming at the reduction of blade corrosion in the presence of chemically aggressive combustion gases typical of these turbines. However, it mostly makes use of metallic coating materials (e.g. CoCrAlY, NiCrAlY, Al-Pt) that could not be used in our case because of their potential susceptibility to LME.

On the other hand, coating of HP steam turbines is a less established technology, which does not make use of metallic coating materials. However, this technology has already been adopted in the US by several utilities to mitigate the effects of Solid Particle Erosion (SPE) [Diaz-Tous 1994]. SPE is caused by ferric oxide scale formed on the walls of the steam lines. Due to the differential thermal expansion of the oxide and the metallic substrate, the oxide scale cracks and the exfoliated particles become entrained in the steam and are dragged to the turbine where they cause erosion.

This phenomenon is particularly pronounced in conventional fossil power plants where steam operating temperatures are high (up to 550°C) and the formation and cracking of the oxide scale proceeds faster. This is a severe problem that results in loss of turbine efficiency and increase of turbine maintenance. To reduce the erosion induced by the impact of the solid particles on the moving and stationary components of the HP turbine, many utilities have chosen to coat the most

---

[29] Due to the relatively small weight fraction of Al, Sn, Zr, Mo, Si and Fe.

[30] On the other hand, Ti solubility in Pb-Bi is not high [Weeks 1969] and solution of the Ti matrix is not expected.

exposed HP turbine surfaces with a high hardness cermet coating layer at a reported [Diaz-Tous 1994] cost ranging between 0.09 and 0.45$/kWe[31]. Several ceramic materials were explored for this purpose such as chromium carbide[32] (Cr_2C_3), titanium nitride (TiN) and tungsten carbide (WC). To add compactness and strength to the coating, the ceramic base is normally blended with alloying metallic particles (up to 20%wt of the final coating mixture) to form a material that is not perfectly ceramic, but ceramic-metallic (a so-called cermet). Nickel, chromium, indium, iron, aluminum and cobalt are the typical metals of choice for this purpose [Walsh 1994]. Because some of these metals are susceptible to LME (see **Table 5.III**), if this coating strategy is adopted for the PBWR, it will be necessary to test the LME susceptibility of the cermets. Also, the solubility of nickel in lead and bismuth is high [Weeks 1998, Alden 1957] and it must be ensured that this element is not prone to selective Pb-Bi attack when embedded in a cermet. However, it should be noted that, nickel (along with iron and chromium) is among the basic constituents of austenitic stainless steels, which are known to be corrosion-compatible with Pb-Bi at temperatures up to 450°C [33] [Tsirlin 1999, Orlov 1998] due to the formation of an oxide film acting as a kinetic barrier to nickel solution.

Several techniques have been developed to lay the cermet coating material on the metallic substrate to protect. Two of these seem to have gained particular attention [Walsh 1994]: detonation gun deposition and plasma deposition. In both cases the coating blend is initially in the form of a powder. In the detonation gun technique this powder is laid on the substrate by the detonation of a gas which heats the powder particles above their melting point and accelerates them to about 1000m/s. The molten powder impacts the substrate and forms a compact, uniform layer with high adhesive and cohesive strength.

In the plasma deposition technique, the process is the same except that the powder is heated and accelerated by a plasma of partially ionized inert gases (e.g. argon, nitrogen, helium). The maximum impact velocity that can be obtained with the plasma based technique is 500m/s which results in a slightly less compact and adhesive coating.

Typical characteristics of a detonation gun deposited coating are reported in **Table 5.IV**.

---

[31] For a 419MWe reactor, the cost would then range between $38,000 and $189,000.

[32] Chromium carbide based coatings were reported to have increase the SPE resistance of 422 stainless steel up to 20 times at 550°C [Walsh 1994].

[33] The operating temperature of the HP blades in the PBWR is below 320°C.

Table 5.IV. A detonation gun cermet coating.

Designation	UCAR^{TM} LC-1H
Composition (%wt)	$80Cr_2C_3$-16Ni-4Cr
Density	6,300kg/m^3
Thickness	~150μm
Tensile bond strength	>70MPa
Hardness (Vickers / Rockwell A)	1000 / 88 (from [Brady 1991])

Detonation gun chromium carbide/nichrome coatings are not new to the nuclear industry. They were extensively investigated and tested as erosion resistant coatings for core components of sodium-cooled fast reactors [Johnson 1984]. They were found to be superior to plasma and diffusion coatings in terms of irradiation damage, thermal cracking and corrosion when irradiated for 7 years (i.e. fast neutron fluence up to 6×10^{22}n/cm^2) in 625°C sodium at the Fast Flux Test Facility reactor. As a result, they are now successfully in use on the 316 stainless steel FFTF core components.

5.5.2.3 Pb-Bi Droplet Oxidation

Ceramic materials like oxides or carbides do not induce LME. In this section we illustrate a method to change the chemical state of the liquid Pb-Bi from metallic to oxide before it reaches the turbine, which eliminates the possibility of LME.

We have seen in **Section 5.3.2.2** that the expected liquid Pb-Bi mass flow rate entrained in the steam flow at the outlet of the steam dryer is about 0.0029kg/s. The liquid Pb-Bi is in the form of fine droplets of diameter smaller than 10μm (see **Figure 5.10**). If a substantial amount of pure oxygen is introduced in the steam flow, it is possible to entirely oxidize this metallic Pb-Bi hence eliminating its embrittlement potential. The oxygen can be injected in the steam flow at the beginning of the steam lines, which enables a thorough and complete oxidation before the Pb-Bi reaches the turbine.

The chemical reactions of interest are:

$Pb+1/2O_2\rightarrow PbO$ **Eq.5.59**

$2/3Bi+1/2O_2\rightarrow 1/3Bi_2O_3$ **Eq.5.60**

The free energy variation of these two reactions is, respectively [Li 1999]:

$\Delta G_{PbO}=-220.67+0.101T$ **Eq.5.61**

$\Delta G_{Bi2O3}=-194+0.094T$ **Eq.5.62**

where ΔG_{PbO} and ΔG_{Bi2O3} are in kJ/mol of oxygen and T is in K.

The respective equilibrium constants k_{PbO} and k_{Bi3O4} are:

$$k_{PbO}=e^{-\frac{\Delta G_{PbO}}{RT}}=\frac{a_{PbO}}{a_{Pb}\sqrt{P_{O2}}}$$ **Eq.5.63**

$$k_{Bi2O3}=e^{-\frac{\Delta G_{Bi2O3}}{RT}}=\frac{a_{Bi2O3}^{1/3}}{a_{Bi}^{2/3}\sqrt{P_{O2}}}$$ **Eq.5.64**

where a_{PbO}, a_{Pb}, a_{Bi3O4} and a_{Bi} are the equilibrium chemical activity of lead oxide, lead, bismuth oxide and bismuth, respectively. P_{O2} is the equilibrium partial pressure of oxygen (in atm). **Eq.5.59** and **Eq.5.60** indicate that at least ½ and ¾ moles of oxygen are needed to entirely oxidize a mole of lead and bismuth, respectively. The minimum required rate of injection of oxygen, $\dot{m}_{O2,\mathrm{min}}$ is then readily found as:

$$\dot{m}_{O2,\mathrm{min}}=\left(1/2\frac{0.45\dot{M}_p}{A_{Pb}}+3/4\frac{0.55\dot{M}_p}{A_{Bi}}\right)A_{O2}\approx 3\times 10^{-4}\mathrm{kg/s}$$ **Eq.5.65**

where $\dot{M}_p$=0.003kg/s is the mass flow rate of Pb-Bi, A_{Pb}=0.207kg/mol and A_{Bi}=0.209kg/mol are the atomic weight of lead and bismuth, respectively. A_{O2}=0.032kg/mol is the molecular weight of oxygen. In **Eq.5.65** it was also taken into account that the weight fraction of lead and bismuth in the Pb-Bi eutectic is 45 and 55%, respectively.

In practice it is necessary to inject the oxygen at a significantly larger rate than indicated by **Eq.5.65** in order to produce an effective oxygen flow to the surface of the liquid droplets which allows rapid oxidation of the Pb-Bi. It is anticipated that the phenomenon limiting the speed of the oxidation reaction is oxygen diffusion from the steam bulk to the droplet surface (see **Figure 5.17**). Because the velocity of the droplets relative to the steam is zero, convection mass transfer can be neglected and only diffusion should be considered. Assuming that the droplets are spherical, the diffusion equation in the region around a droplet of diameter D_d can be written as:

$$D_{AB}\frac{1}{r^2}\frac{d}{dr}\left(r^2\frac{d}{dr}c(r)\right)=0$$ **Eq.5.66**

where D_{AB} is the binary diffusion coefficient of oxygen in steam, r is the radial coordinate and c(r) is the concentration of oxygen (mol/m^3) in the steam at location r. A value of D_{AB} for the gas binary mixture of interest was found in reference [Hines 1985] ($D_{AB}\approx 3.52\times10^{-4}$m^2/s). However, this value is reported for a mixture at 0.1MPa and 353K and must be scaled to the high pressure, high temperature conditions of the PBWR (i.e. P=7.0MPa, T=312°C=585K). To do so, it is recommended in reference [Incropera 1990] to make use of the gas kinetic theory, which suggests a pressure and temperature dependence of the binary diffusion coefficient of the following type:

$$D_{AB}\propto\frac{T^{3/2}}{P}$$ **Eq.5.67**

where T is in K. By means of **Eq.5.67**, the appropriate value of D_{AB} was found to be 1.0×10^{-6}m^2/s.

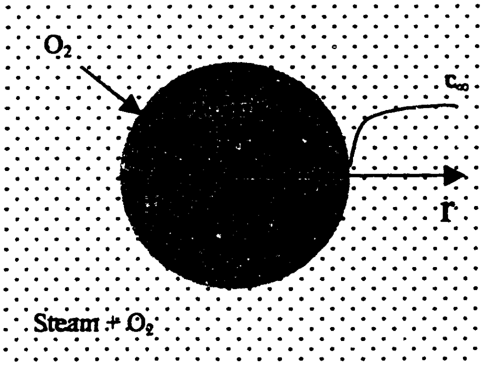

Figure 5.17. Oxygen diffusion to the surface of a Pb-Bi droplets.

The boundary conditions of **Eq.5.66** are:

$$\begin{cases} c=c_\infty \text{ for } r\to\infty & \textbf{Eq.5.68} \\ c=c_0 \text{ for } r\to D_d/2 & \textbf{Eq.5.69} \end{cases}$$

where c_∞ and c_0 are the oxygen concentration in the steam bulk and at the droplet surface, respectively. **Eq.5.66** can be readily integrated to yield:

$$c(r)=c_\infty-(c_\infty-c_0)\frac{(D_d/2)}{r}$$ **Eq.5.70**

Making use of Fick's law the oxygen flow rate to the droplet surface, $\dot{N}_{O2}$, can be calculated as:

$$\dot{N}_{O2} = \pi D_d^2 D_{AB} \frac{\partial c}{\partial r}\bigg|_{r=\frac{D_d}{2}} = 2\pi D_d D_{AB}(c_\infty - c_0) \qquad \textbf{Eq.5.71}$$

c_∞ can be related to the rate of oxygen injection, $\dot{M}_{O2}$, as:

$$c_\infty = \frac{(\dot{M}_{O2} / A_{O2})}{(\dot{M}_g / \rho_g)} \qquad \textbf{Eq.5.72}$$

where $\dot{M}_g$=686kg/s and ρ_g are the mass flow rate and density of steam, respectively.

Note that the oxygen partial pressure and the local value of the oxygen concentration are related by the simple equation:

$$c_0 = \frac{\rho_g}{A_{steam}}\left(\frac{P_{O2}}{P}\right) \qquad \textbf{Eq.5.73}$$

where A_{steam}=0.018kg/mol is the molecular weight of steam.

Therefore, assuming chemical equilibrium at the droplet surface, P_{O2} (and thus c_0) can be found from **Eq.5.63** and **Eq.5.64** where the activity of the lead and bismuth oxides can be conservatively set equal to unity, i.e. the concentration of lead and bismuth oxides equals their solubility[34]. We will also make the critical assumption that the activity of lead and bismuth, a_{Pb} and a_{Bi}, at the surface of the droplet is equal to unity. This is equivalent to assume perfect mixing within the droplet so that a continuos supply of elementary lead and bismuth is available for oxidation at the surface. Should a compact solid lead and/or bismuth oxide film form at the droplet surface, this crucial assumption would not hold and oxygen diffusion through the oxide film would become the dominant process determining the reaction speed. However, note that, if in fact a solid oxide film forms at the droplet surface, the droplets would not be able to induce LME because the liquid metal is shielded.

At 312°C and with the assumptions discussed above, **Eq.5.32** and **5.64** yield P_{O2} equal 10^{-24} and 6×10^{-20}atm, respectively, signaling that the dominant equilibrium is that of the bismuth oxide, which was expected on the basis of its larger free energy variation. Therefore, we will assume $P_{O2}=10^{-20}$atm$=10^{-15}$Pa and, from **Eq.5.73**, $c_0=3.2\times10^{-19}$mol/m^3.

---

[34] This is actually the case as soon as the first crystal of solid oxide forms in the droplet.

Now that the expressions for c_∞ and c_0 have been derived, it is possible to assess the time, τ_{ox}, required to completely oxidize a droplet of diameter D_d and mass $M_d = \rho_p \frac{\pi}{6} D_d^3$. The moles of oxygen necessary to oxidize the Pb-Bi droplet, N_{O2}, can be calculated as:

$$N_{O2} = \left(1/2\frac{0.45M_d}{A_{Pb}} + 3/4\frac{0.55M_d}{A_{Bi}}\right)A_{O2} \qquad \textbf{Eq.5.74}$$

And combining **Eq.5.74** with **5.71**:

$$\tau_{ox} = \frac{N_{O2}}{\dot{N}_{O2}} \qquad \textbf{Eq.5.75}$$

The variation of τ_{ox} with the droplet diameter and rate of oxygen injection ($\dot{M}_{O2}$) is illustrated in **Figure 5.18** for the reference case of $\dot{M}_g$=686kg/s. The droplet traveling time in the steam lines is about 6.8s and is indicated by the horizontal shaded line[35]. It can be seen that the finer droplets are readily oxidized within the steam lines even at low rates of oxygen injections. However, at an oxygen injection rate of 0.1kg/s, even the coarser droplets (D_d~10μm) rapidly oxidize in less than 2s.

This rate of oxygen injection corresponds to a weight fraction and a partial pressure of oxygen in the steam bulk of 150ppm and 6×10^2Pa, respectively. In our case, the oxygen can be easily injected immediately after the steam dryer and be effectively removed in the Off-Gas System connected to the main condenser downstream of the turbine (see **Section 6.5.2**). However, note that the proposed 150ppm oxygen level is very high if compared with current BWR steam lines and turbines whose operating oxygen concentration ranges up to about 20ppm [ABB 1988, Ruiz 1992].

---

[35] For a description of the steam lines geometry, see **Section 5.4.**

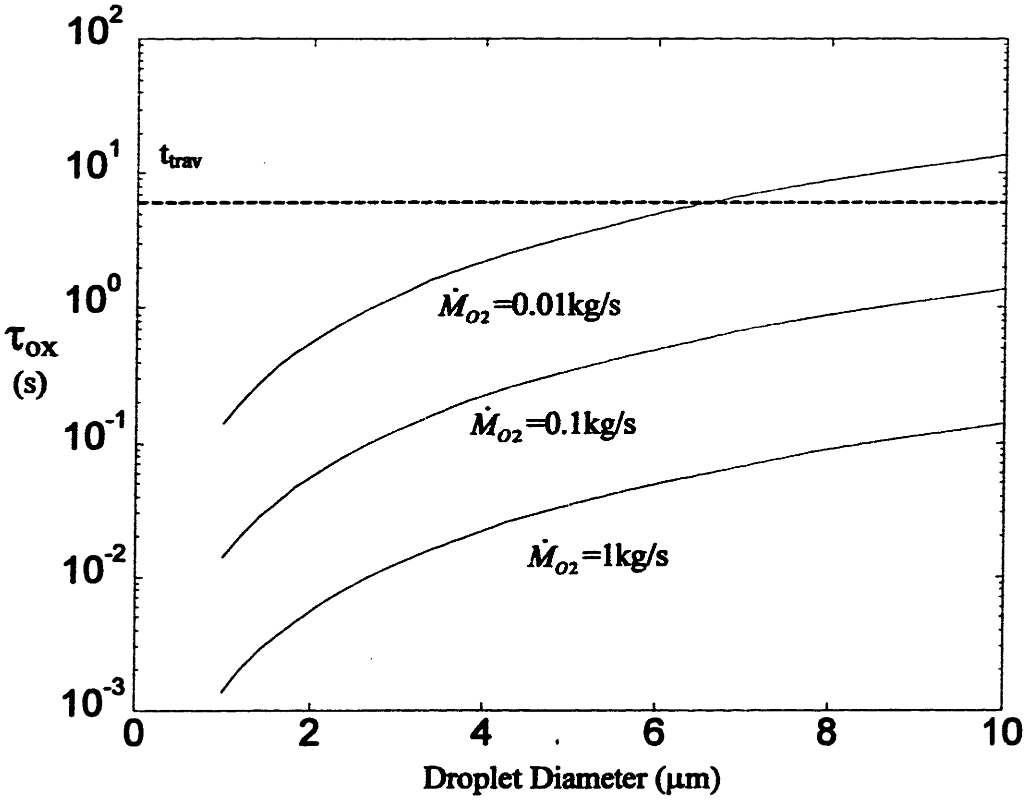

Figure 5.18. Oxidation time of the Pb-Bi droplets in the steam lines.

To assess the consequences of this high oxygen level on the corrosion rate of the turbine materials, we will now estimate the increase of the electrochemical potential (ecp) associated with a two orders of magnitude increase of the oxygen concentration. The Nernst equation for the oxygen reduction reaction provides the following relation between the ecp, E, and the oxygen partial pressure:

$$E \propto 2.31\frac{RT}{nF}\log_{10} P_{O2} \qquad \textbf{Eq.5.76}$$

where R is the gas constant (8.31J/mol·K) and F the Faraday's constant (96,500C/mol). T is the operating temperature in the turbine (in K), conservatively assumed equal to the inlet temperature 312°C=585K. In the case of oxygen reduction in aqueous environment, the value n=4 is appropriate. **Eq.5.76** indicates that, if the oxygen content increases from 20 to 150ppm, the ecp increases by about 0.025V. The internals of a steam turbine (e.g. blades, casing, shaft) are usually made of stainless steel, which operates above the primary passivation potential E_{pp}, as illustrated in the polarization diagram of **Figure 5.19**, where i is the corrosion current density. At these conditions the steel surface is protected by a passive film that maintains an approximately constant (low) rate of corrosion. If the ecp surges above a critical value E_{tp} (known as trans-passive ecp), the rate of corrosion increases substantially.

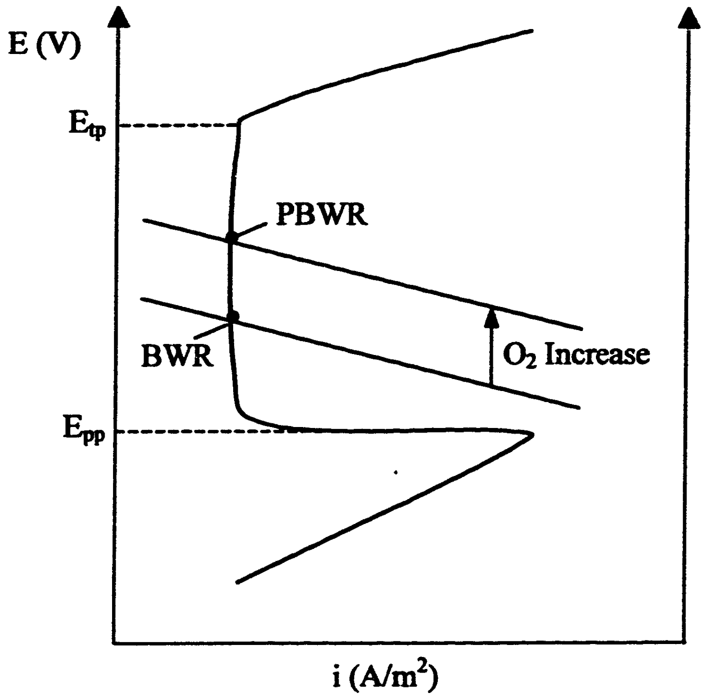

Figure 5.19. Polarization diagram for a passive metal.

The width of the region between E_{pp} to E_{tp} for stainless steels is typically about 1.0V [Kaesche 1985, Jones 1992], which is considerably larger than 0.025V. Therefore, it can be assumed that the ecp increase due to the proposed high oxygen level (two orders of magnitude above the BWRs) is not likely to place the operating ecp outside the region of passivity and then does not increase the corrosion rate of the turbine materials.

It is useful to estimate the mean distance between the droplets, L_d, to verify that the boundary condition expressed by **Eq.5.68** actually holds. The effects of droplet interference can be neglected, if $L_d >> D_d$. L_d can be evaluated as:

$$L_d \approx \frac{1}{\sqrt[3]{N_d}} \qquad \textbf{Eq.5.77}$$

where N_d is the concentration of Pb-Bi droplets in the steam flow (droplets/m^3):

$$N_d = \frac{\left(\dot{M}_p / M_d\right)}{\left(\dot{M}_g / \rho_g\right)} \qquad \textbf{Eq.5.78}$$

For $\dot{m}_p$=0.0029kg/s, $\dot{m}_{steam}$=686kg/s and D_d ranging from 1 to 10μm, the mean distance L_d ranges between 0.3 and 3mm, which demonstrates the applicability of **Eq.5.68.**

Although oxidation of the liquid Pb-Bi droplets will prevent LME of the turbine stressed parts, the issue of heavy metal carry-over remains rather challenging. The oxidized solid particles raise an erosion concern regarding the blades of the HP turbine first stages. This problem resembles that caused by Solid Particle Erosion (SPE), a phenomenon due to exfoliation of oxide scale from the walls of the steam lines and is present in most nuclear and conventional steam turbines. SPE is typically handled by means of turbine blade and casing coating technology, which could then be used to cope with the lead and bismuth oxide problem, as well. Note that the very same SPE coating technology was proposed in **Section 5.5.2.2** to prevent contact between the liquid metal and the blade stainless steel substrate, hence eliminating LME. Here the purpose of coating is different: it does not work as a barrier to liquid metal wetting of the blade stainless steel surface, but as a mechanical shielding of the substrate in order to reduce wearing induced by the solid oxide particles. In this case, the requirements on the continuity of the coating layer become less strict, to the advantage of the turbine reliability.

Downstream of the turbine, the lead and bismuth oxides can deposit on the condenser tubes, hence reducing its heat transfer efficiency. Or the oxides can form a slag in suspension that might clog the condenser outlets and (if transported throughout the whole secondary system) the pumps, the feedwater heaters and eventually even the water injector in the reactor pool, which can impair the coolability of the core. Evidently great care must be taken to effectively filter the oxides out of the system as early in the secondary loop as possible. This can certainly be done in the Moisture Separator Reheater (MSR) between the HP and LP turbines. It is anticipated that the oxide particles will either stick to the liquid water droplets (generated by homogeneous condensation in the steam bulk upon expansion in the turbine) or will impact the turbine surfaces and be washed away by the liquid water rivulets present on those surfaces. Either way, it is expected that at the inlet of the MSR the oxide particles will be entrained in the liquid water. The purpose of the MSR is to remove liquid water from the steam stream and send it to the Feedwater Reheaters (FRs). The water mass flow rate at the outlet of a typical LWR HP turbine is a relatively small fraction of the total steam flow (approximately 13% [Moore 1976])[36]. It is thought that a full flow hard porous packed solids filter installed on the water line between the MSR and the FRs would enable high efficiency removal of micronic and submicronic particles at the expense of modest pressure drops. These filters are successfully employed in naval reactors to remove particulates at a rate similar to our application (i.e. some grams per second) [Kovach 2000].

5.5.2.4 Electrostatic Precipitation

An alternative way to cope with the problem of liquid lead-bismuth or lead and bismuth oxide carry-over is to make use of electrostatic precipitators in the steam lines. The basic principle of operation of these devices is that the gas borne particles are passed through a corona or charging electric field where they receive an electric charge. The charged particles are then deflected by the electric field to move across the gas stream and deposit on the wall of the device. The collected particles are consequently removed by mechanical shock impulse and fall under gravity into hoppers beneath the field. Electrostatic precipitators are currently utilized in fossil-fueled power plants and waste incineration plants to remove dust and heavy metal particulate (e.g. Hg, Cd, Te, Pb, V) from the combustion gases before they reach the stack. They are known to be suitable for large volumetric flow rates up to 50m^3/s and above[37] [Parker 1999]. They achieve particle removal efficiencies ranging from 99 to 99.9% for particles of diameter between 0.01 and 10μm. Typical collector-to-collector spacing and operating voltage are 30cm and 60kV, respectively. Typical length of the precipitator is of the order of a few meters. Electrostatic precipitators can be used for applications at relatively high temperature (up to 540°C [Sittig 1977]). However, they typically operate at atmospheric pressure, whereas in the PBWR they would operate at high pressure (i.e. 7.0MPa).

The effect of the gas pressure on the design and operation of the electrostatic precipitator can be described by considering the migration velocity of the charged Pb-Bi particles in the space between the two electrodes, V_m. This velocity is given in [McDonald 1982] as:

---

[36] At nominal PBWR conditions the filter capacity should be 0.13×686=90kg/s.

[37] It should be noted that the reference PBWR volumetric steam flow rate in the steam lines is about 17m^3/s.

$$V_m = \frac{qE_e}{3\pi D_d \mu_g} \qquad \textbf{Eq.5.79}$$

where q is the charge acquired by the Pb-Bi particles when they pass through the corona and E_e is the electric field. **Eq.5.79** was obtained equating the electric force to the viscous force (given by Stokes's law). High migration velocities result in high removal efficiencies of the precipitator. **Eq.5.79** suggests that an effective way to increase the migration velocity is to raise the intensity of the electric field. However, there exists an upper limit to the acceptable operating value of the electric field. If the electric field is too intense, electrical breakdown of the gas between the electrodes occurs and a continuous discharge is established. The corresponding voltage is called the sparking voltage. It was reported in [Oglesby 1978] that the sparking voltage increases linearly with the gas density and thus with pressure. Therefore, in a high pressure system (like the PBWR) it should be possible to raise the operating voltage and thus increase the efficiency of the precipitator. On the other hand, gas viscosity normally increases with pressure, which somewhat offsets the beneficial effect of the higher electric field on the migration velocity. Moreover, high pressure operation complicates the design of the collected particle removal system, which becomes a pressure boundary for the whole secondary system.

Note that an electrostatic precipitator would effectively work whether the heavy metal droplets are oxidized or not and could in principle be utilized alone (i.e. without the upstream oxygen injection) to remove most liquid droplets. However, the small amount of Pb-Bi droplets that escape precipitation, could still raise a LME concern. On the other hand, the combined use of the electrostatic precipitator and the oxygen injection can effectively solve the LME issue because the very fine droplets (<1μm) are quickly oxidized and the larger droplets (>1μm) are removed by the electrostatic precipitator[38] (whether they are oxidized or not).

Again it should be emphasized that the electrostatic precipitator required in our PBWR application would operate beyond the pressure operating conditions typical of current precipitators in the fossil-fuel industry, which could seriously complicate the design of this system and reduce its reliability. Because the Pb-Bi removal system is indispensable to avoid LME failure of the turbine, the reactor could not operate when the precipitator is down. This will

---

[38] Note that this allows reducing the rate of oxygen injection.

have negative consequences on the plant load factor and, ultimately, on its economic performance.

In conclusion, the concerns associated with LME of the stressed components of the HP turbine will make it impossible to equip the PBWR with a traditional LWR turbine. Four strategies have been analyzed: alternative turbine blade materials, blade coating, Pb-Bi aerosol oxidation and electrostatic precipitation. The use of coating seems a plausible way to provide a strong and effective barrier to lead-bismuth/steel contact and hence limit these concerns. Moreover, steam turbine coating technology is relatively established and its cost is not prohibitive. However, if this approach to the LME problem is embraced, three important technical issues must be addressed:

i) verify the LME immunity of the cermet coating material,
ii) verify that nickel in the cermet is not susceptible to selective solution in lead-bismuth,
iii) ensure the continuity of the coating layer under operating conditions to prevent liquid metal wetting of the substrate.

The latter challenge is tightly connected to the magnitude of the erosion caused by Pb-Bi water droplets on the blades of the HP turbine. In the next section we will demonstrate that Pb-Bi erosion of the HP turbine is negligible when the blades are coated with a high hardness material.

With regard to the LP turbine, we have already mentioned that massive Pb-Bi contamination is not anticipated due to effective shielding by the HP turbine and the MSR. Nevertheless, it is reasonable and prudent to assume that some liquid metal will actually reach the LP turbine. To prevent LME here, two different approaches can be implemented: a) blade coating in a fashion similar to the HP turbine or b) making use of titanium (which is not embrittled by lead or bismuth) for the LP turbine blades and fixed structures. The choice of one approach over the other will be probably driven by the economic trade-off[39].

---

[39] Titanium blades can cost up to four times as much as 422 stainless steel blades [Kuehn 1993].

5.5.3 Pb-Bi Droplet Erosion

5.5.3.1 The Mechanism

Liquid droplet erosion is a well-known problem shared by all steam turbines. The most typical source of liquid is water condensation when the steam expands and becomes subcooled[40]. This phenomenon takes place mostly in the LP section of the turbine. However, in LWR turbines some liquid is fed to the HP section too because the steam coming from the reactor (or the steam generator in a PWR) is saturated and never perfectly dry. In our case the HP turbine is fed slightly superheated dry steam (i.e. no liquid water droplets), which nevertheless may carry a significant amount of liquid Pb-Bi (see **Section 5.3.2.2**).

General agreement exists on what the process responsible for liquid droplet erosion is. The liquid droplets carried by steam are small and mostly follow the steam flow without impacting the turbine surfaces [Tsubouchi 1990]. However, when the steam flow path is abruptly diverted in the fixed or moving blades, some droplets do deposit by inertial impact or by turbulent diffusion [Pouchot 1971] (a mechanism similar to that described in **Section 5.4.1.1**) and form liquid rivulets. The rivulets on the moving blades are pushed by the centrifugal force to the moving blade radial tip from where they are thrown to the turbine casing[41] [Moore 1976]. On the other hand, the rivulets on the fixed blades (not subjected to the centrifugal force) are dragged axially to the fixed blade lip by the steam flow shear. At the lip they are torn off and get re-entrained in the steam flow. In the region downstream of a fixed blade (called the fixed blade wake), the steam velocity is relatively low and only mild atomization of the rivulets takes place [Tsubouchi 1990]. As a result, the droplets leaving the fixed blade are substantially larger than those initially entrained in the steam (typically 30-300μm vs. 1-10μm). Because the absolute velocity of these large and heavy droplets is smaller than that of steam, their velocity relative to the turbine moving blades is large and they violently strike the leading edge of the moving blades, as illustrated in **Figure 5.20**.

---

[40] As the steam falls below saturation pressure, it may spontaneously condense in the bulk of the flow (homogeneous condensation) or form the embryo of a droplet around a so-called nucleation site (heterogeneous condensation). In both cases the size of the generated droplets is typically small (less than 1μm).

[41] This droplet spraying at the radial tip of the moving blades can actually cause erosion of the turbine casing as reported in [Pouchot 1971].

Impingement of droplets on the moving blades causes i) mechanical removal of the blade material (i.e. erosion) due to the large impact pressure and ii) kinetic energy loss due to slowing down of the blades (the so-called braking effect). Also, acceleration of the droplets in the fixed blade wake represents a net energy loss. If not properly taken care of, these two latter effects may result in a significant loss of turbine efficiency.

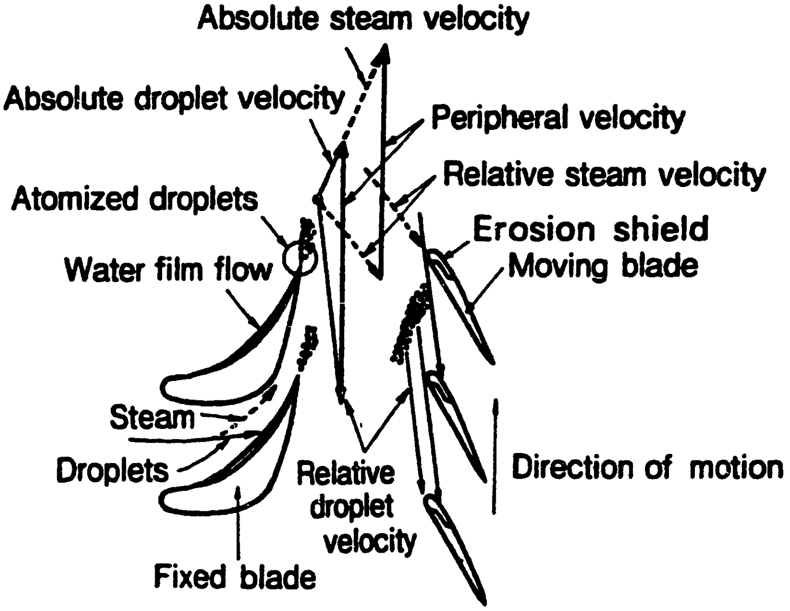

Figure 5.20. Droplet dynamics in a steam turbine (from [Tsubouchi 1990]).

5.5.3.2 Erosion Technology

Numerous remedies have been proposed to mitigate the negative effects of the presence of liquid droplets in steam turbines. The most successful and widely applied are:

Erosion shields. The region of the casing wall eroded by the droplets sprayed off the tip of the moving blades is often armored with hard chromium steel [Moore 1976]. Also, the leading edge of the moving blades (where the impingement of most droplets takes place) is equipped with a bar-nose (see **Figure 5.20** and **5.21**) made of a hard material (typically cobalt-based alloy Stellite^{TM} or titanium-based alloys) to minimize erosion. In recent years, the possibility of making use of cobalt-free shielding materials has been explored [Beaudry 1992] for nuclear applications where the transport of cobalt to the core can result in the production of undesirable radioactive ^{60}Co.

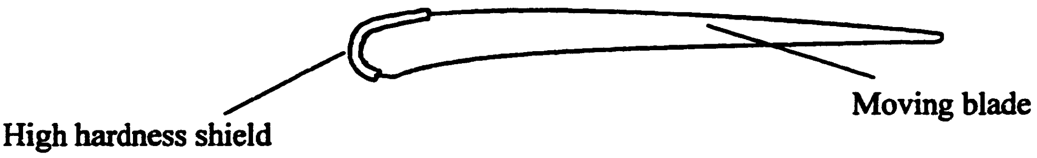

Figure 5.21. Erosion shield on a moving blade (from [Beaudry 1992]).

Peripheral Drainage Slots. The liquid radially centrifuged by the moving blades is collected and drained off the turbine by extraction rings cut in the casing wall [Moore 1976, Sakamoto 1992, Yoshida 1990]. These rings (also known as drainage slots or drainage catchers) are usually located immediately downstream the moving blade stages (see **Figure 5.22**).

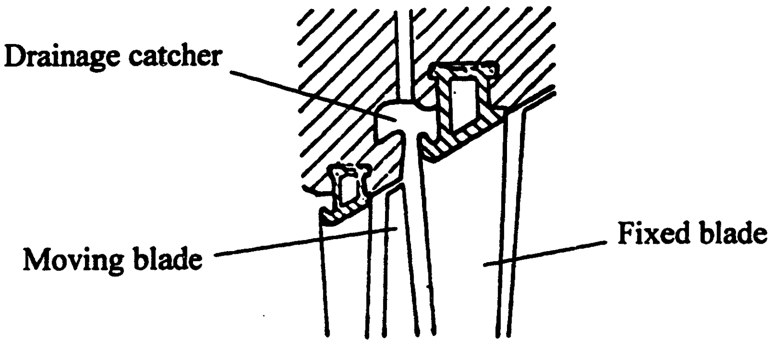

Figure 5.22. Drainage slots on the turbine casing (from [Moore 1976]).

Hollow Fixed Blades. A pressure difference is artificially maintained between the outer and inner surfaces of the (hollow) fixed blades equipped with suction slots (see **Figure 5.23**). When the liquid rivulets flowing on the surface of the fixed blades get close to the suction slots, they are pushed through and drained out of the turbine, hence reducing the formation of coarse droplets at the fixed blade lip [Moore 1976, Sakamoto 1992, Yoshida 1990].

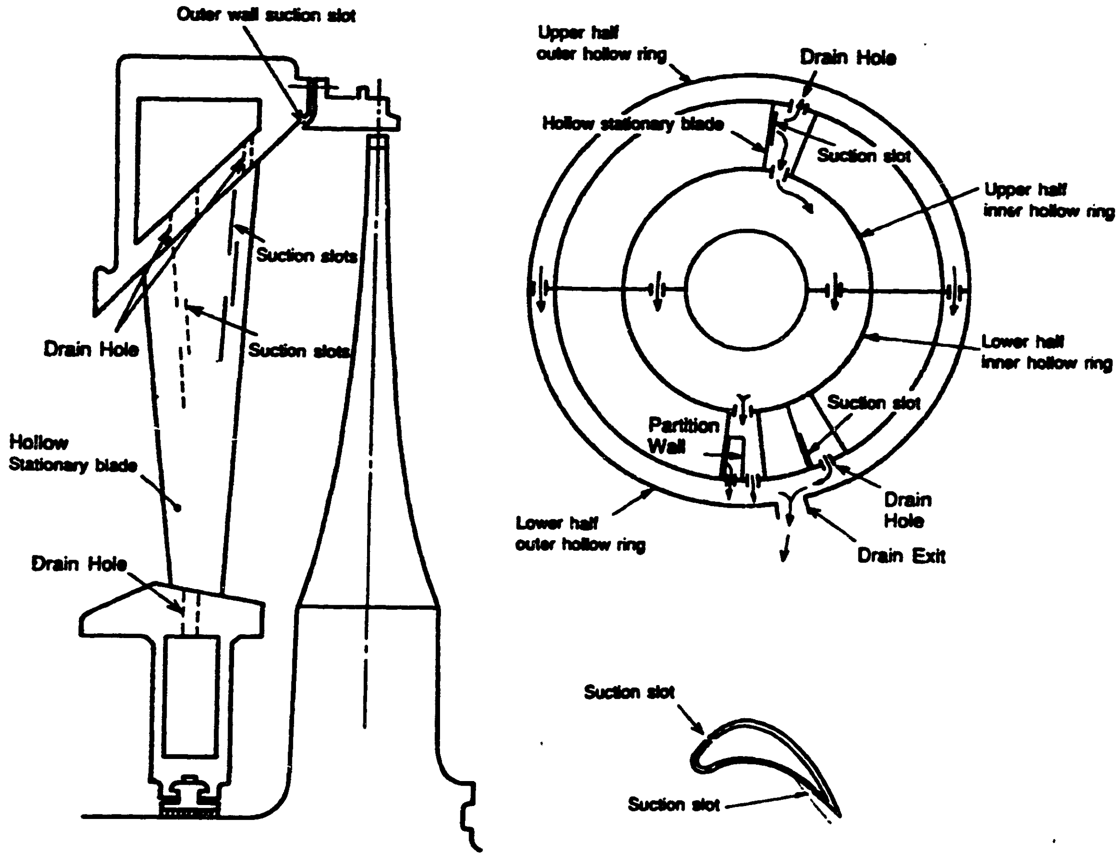

Figure 5.23. Liquid removal by hollow blades with suction slots (from [Sakamoto 1992]).

Fixed-to-Moving Blade Spacing. If the axial distance between the stationary and the moving blade stages is increased, the coarse droplets generated at the lip of the fixed blades are carried out of the wake zone and accelerated in the high speed fully-developed steam stream. Secondary atomization occurs and they are split into smaller droplets [Tsubouchi 1990]. Higher droplet velocity and lower size[42] result in less severe erosion (see **Figure 5.24**).

The application of these techniques has made liquid droplet erosion a manageable problem in steam turbines.

---

[42] We will see in **Section 5.5.3.3** that erosion increases with the size of the impacting droplets.

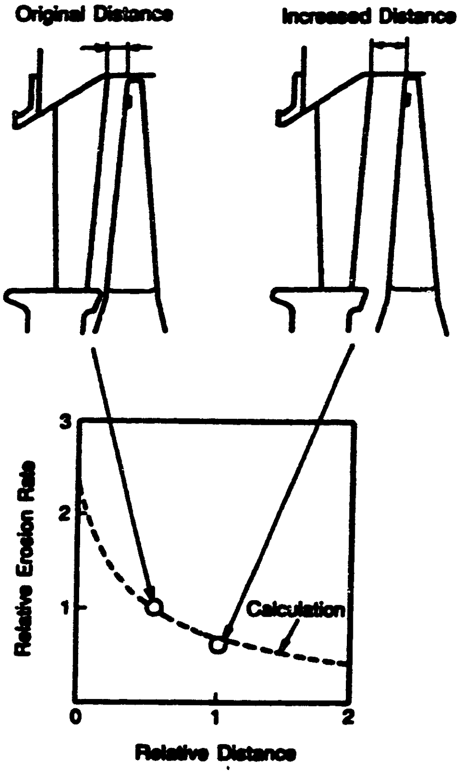

Figure 5.24. The effect of axial spacing on erosion (from [Sakamoto 1992]).

5.5.3.3 Erosion Evaluation

It will be now assessed if the presence of Pb-Bi droplets in the PBWR HP turbine introduces a new serious concern or can be handled within the framework of traditional erosion technology. For this purpose the Pb-Bi droplet erosion rate of the PBWR HP turbine blades will be compared to that induced by water droplets in a 3600rpm LP turbine. It should be noted that this approach is conservative because in a traditional steam turbine the LP moving blades is where most erosion takes place due to the large local speed and wetness. We will make use of two different predictive tools: the Pouchot model [Pouchot 1971] and the Hitachi correlation [Tsubouchi 1990].

The variation of liquid droplet erosion rate with time is known to display three different stages. In the first stage (the so-called incubation period) little or no weight loss occurs, but only plastic deformation of the surface and initiation of fatigue cracks. In the second stage the erosion rate rapidly increases, reaches a maximum and levels off at an intermediate value. In the third stage the erosion rate remains at approximately that value and no significant variation with time is observed. In **Figure 5.25** characteristic erosion rate curves are reported for 422 stainless steel bombarded by high velocity droplets typical of 3600rpm LP steam turbines. There is no agreement on what section of the erosion rate curve should be used to best represent the erosion resistance of a material. Different investigators have tried to produce models or correlations that address different sections of this curve. For example, the Pouchot model provides an expression for the peak erosion rate whereas the Hitachi correlation deals with an arbitrarily defined mean value (a time average over the three erosion stages).

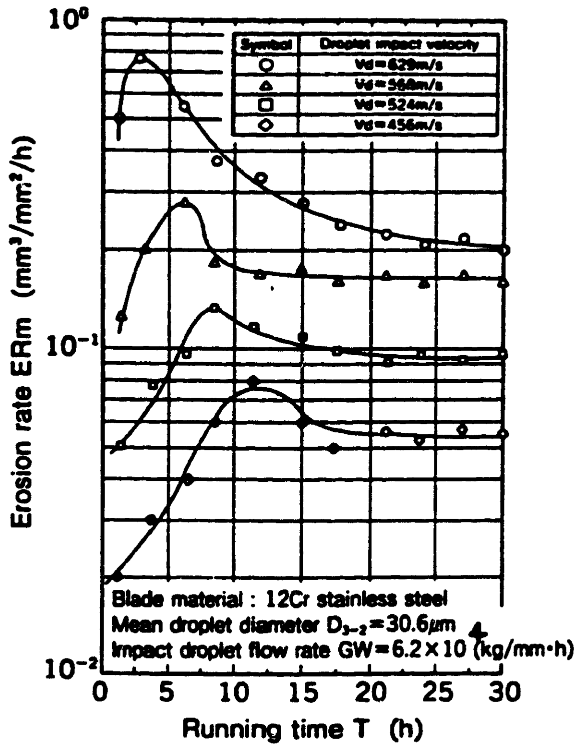

Figure 5.25. Time variation of the erosion rate (from [Tsubouchi 1990]).

Pouchot Model

The Pouchot model assumes that the liquid droplets impinge normally on the surface of the eroded material[43] with velocity equal to that of the moving blades[44]. On the basis of the experimental evidence in [Pearson 1964], Pouchot also assumes that there exists a threshold

---

[43] It was reported in [Quets 1994, Walsh 1994, Pearson 1964] that erosion increases with the impact angle (measured from the eroded surface). Therefore Pouchot's assumption is conservative.

[44] This is equivalent to assuming zero droplet absolute velocity.

velocity below which no erosion occurs. The value of this threshold depends on the droplet size[45], the droplet thermophysical properties and the material hardness. According to this model it is:

$$\delta_m \propto \frac{V^4}{c^2 S}\left(1-\frac{V_{th}}{V}\right)\frac{M_\ell}{A} \qquad \textbf{Eq.5.80}$$

where:

δ_m is the erosion rate expressed as loss of thickness per unit time,
V is the moving blade absolute velocity,
c is the speed of sound in the liquid,
S is the eroded material hardness,
V_{th} is the threshold velocity,
M_ℓ is the impinging droplet mass flow rate (kg/s),
A is the impingement area (effectively the moving blade surface area).

A semi-empirical correlation for the threshold velocity is:

$$V_{th} \propto \frac{S}{c\rho_f}\left(\frac{t}{D_d}\right)^{0.57} \qquad \textbf{Eq.5.81}$$

where ρ_f, t and D_d are the droplet density, the thickness of the liquid film forming on the moving blades (upon impingement of droplets) and the droplet diameter, respectively.

The expression for the threshold velocity adds more complexity to **Eq.5.80**. For simplicity we will conservatively neglect the threshold term in **Eq.5.80**. With this assumption, the ratio of the erosion rate of the first stage of the PBWR HP turbine to that of the last stage of a traditional 3600rpm LP turbine becomes:

$$\frac{\delta_{m,1}}{\delta_{m,2}} \propto \left(\frac{V_1}{V_2}\right)^4\left(\frac{S_2}{S_1}\right)\left(\frac{c_2}{c_1}\right)^2\frac{M_{\ell,1}}{M_{\ell,2}}\frac{A_2}{A_1} \qquad \textbf{Eq.5.82}$$

where the subscripts 1 and 2 refer to the PBWR HP turbine and the traditional LP turbine, respectively.

The values of the parameters to be used in **Eq.5.82** are reported in **Table 5.V**. The velocity V is computed as the product of the shaft angular velocity (1800/60×2π s^{-1} or 3600/60×2π s^{-1} for the HP and LP turbine, respectively) times the distance from the shaft axis (i.e. blade length +

---

[45] As the inverse of the square root.

turbine disc). The turbine disc radius (i.e. the distance between the blade root and the shaft axis) is taken approximately equal to 0.9m, for both the HP and LP turbine.

Table 5.V. Turbine parameters.

Parameter	**Description**	**Units**	**Value**	
			PBWR HP Turbine (1)	*Traditional LP Turbine (2)*
P	Pressure Range	kPa	1000-7000	7-1000
V	Blade Velocity	m/s	170	680
ω	Angular Velocity	rpm	1800	3600
S	Blade Hardness	Vickers Scale	1000	430
ρ_g	Steam Density	kg/m^3	40	0.05
σ	Liquid Surface Tension	N/m	0.4	0.07
c	Liquid Speed of Sound	m/s	1000 (estimated)	1500
M_ℓ	Liquid Mass Flow Rate	kg/s	<1	35
L_b	Blade Length	Mm	50	900
A	Impact Surface Area	m^2	0.14	7.63

The HP blades are assumed to be coated with the chromium carbide-based cermet UCAR™ LC-1H whose characteristics can be found in **Table 5.IV**. The LP blade erosion shielding material is Stellite™ (see **Section 5.5.3.2**). The speed of sound in lead is arbitrarily assumed equal to 1000m/s because no data on lead compressibility could be found[46]. The speed of sound in water is 1500m/s [CRC 2000]. The Pb-Bi droplet flow rate is conservatively assumed equal to 0.0029kg/s (see **Section 5.3.2.2**). The water droplet flow rate in the LP turbine is calculated assuming 10% steam wetness and 350kg/s steam mass flow rate. The impact surface area is the stage frontal area (i.e. the circular crown delimited by the blade tip and the blade root).

With these values of the relevant parameters, **Eq.5.82** suggests that (Pb-Bi droplet induced) erosion of the PBWR HP blades is about five orders of magnitude smaller than (water droplet induced) erosion of traditional 3600rpm LP blades.

---

[46] However, this value seems conservatively low if compared to the 1450m/s speed of sound in mercury [CRC 2000].

Hitachi Correlation

A thorough experimental investigation of droplet atomization, acceleration and impact in the wake of steam turbine fixed blades was conducted by the Japanese turbine vendor Hitachi with the goal of quantitatively characterizing the dependence of erosion on the relevant variables [Tsubouchi 1990]. Unfortunately, the Hitachi correlation considers water systems only, which makes its application to heavy liquid metal droplet erosion somewhat arbitrary. The qualitative trend with impact velocity, material hardness and impinging droplet mass flow rate is substantially similar to that of Pouchot model. However, the Hitachi investigation has revealed a strong dependence of erosion on the droplet diameter, which is missing in the Pouchot model. The Hitachi correlation can be expressed as:

$$\delta_m \propto \frac{D_d^3 V^5}{S^2} \frac{M_\ell}{A} \qquad \textbf{Eq.5.83}$$

where D_d is the average diameter of the impinging droplets[47]. This diameter is not known a priori and must be calculated. We assume that it can be estimated from the droplet Weber number We_d as:

$$D_d \propto \frac{\sigma We_d}{\rho_g V_{pg}^2} \qquad \textbf{Eq.5.84}$$

where σ is the fluid surface tension, ρ_g is the steam density and V_{pg} is the steam/fluid relative velocity when the Pb-Bi droplet becomes entrained at the lip of the fixed blades. To a first approximation the Weber number can be assumed independent of fluid (and therefore neglected in this analysis). With this assumption, the combination of **Eq.5.83** and **5.84** yields:

$$\delta_m \propto \frac{\sigma^3}{\rho_g^3 S^2 V} \left(\frac{V}{V_{pg}} \right)^6 \frac{M_\ell}{A} \qquad \textbf{Eq.5.85}$$

The ratio of the erosion rate of the first stage of the PBWR HP turbine to that of the last stage of a traditional 3600rpm LP turbine is then:

$$\frac{\delta_{m,1}}{\delta_{m,2}} \propto \left[\frac{(\sigma_1 / \rho_{g,1})}{(\sigma_2 / \rho_{g,2})} \right]^3 \left(\frac{S_2}{S_1} \right)^2 \left(\frac{V_2}{V_1} \right) \left[\frac{(V_1 / V_{pg,1})}{(V_2 / V_{pg,2})} \right]^6 \frac{M_{\ell,1}}{M_{\ell,2}} \frac{A_2}{A_1} \qquad \textbf{Eq.5.86}$$

---

[47] The other symbols are defined in the Pouchot model section

We assume that V_{pg} is the steam velocity at the fixed blade outlet[48]. The ratio V/V_{pg} (moving blade velocity / steam velocity) is dictated by design constraints related to the efficiency of the turbine stage and varies from impulse to reaction stages (being twice larger in a reaction stage than in an impulse stage [El-Wakil 1984]). HP turbine stages are typically of the impulse type while LP stages are typically of the reaction type; therefore in our case:

$$\left[\frac{(V_1/V_{pg,1})}{(V_2/V_{pg,2})}\right]^6 \approx 2^6 = 64 \qquad \textbf{Eq.5.87}$$

With the values of σ, ρ_g, S, V, M_ℓ found in **Table 5.V**, **Eq.5.86** suggests that (Pb-Bi droplet induced) erosion of the PBWR HP blades is about seven orders of magnitude smaller than (water droplet induced) erosion of traditional 3600rpm LP blades.

From the applications of the Pouchot model and the Hitachi correlation it can be concluded that the presence of Pb-Bi droplets in the PBWR HP turbine does not seem to raise a serious concern in terms of erosion.

5.5.4 Pb-Bi Removal from the Turbine

Accumulation of lead-bismuth in the turbine is to be prevented for several reasons:

a) it increases the chances of liquid metal embrittlement of the turbine components,
b) it represents a significant source of contamination due to its high concentration of radioactive polonium (see **Chapter 6**),
c) it can clog the water extraction lines,
d) it can favor re-entrainment of large Pb-Bi droplets into steam and consequently increase the magnitude of erosion and radionuclide carry-over to the condenser.

It is clear that ways to efficiently remove the heavy liquid metal should be identified if reliable operation of the turbine is to be achieved.

Because the steam produced by LWRs is generally saturated (or slightly superheated in B&W PWRs), significant water condensation occurs already in the HP section of the turbine. To prevent massive erosion of the blades and internals, HP turbines are equipped with several devices (described in **Section 5.5.3.2** of this chapter) that remove the liquid water from the steam flow. However, these devices are not sufficient to remove all the liquid and thus the whole steam

---

[48] And hence the steam velocity at the moving blade inlet, too.

flow is extracted and forced through an external MSR where it is dried and superheated[49] before entering the LP turbine (see **Figure 5.26**). Typical HP turbine extraction temperatures can range between 176 and 192°C [Moore 1976, Yarden 1997] (corresponding to a pressure between 1.0 and 1.2MPa) depending on the reactor model and power. Because the melting point of Pb-Bi is 125°C, it can be safely assumed that throughout the whole HP turbine the Pb-Bi remains liquid, which greatly simplifies its removal[50].

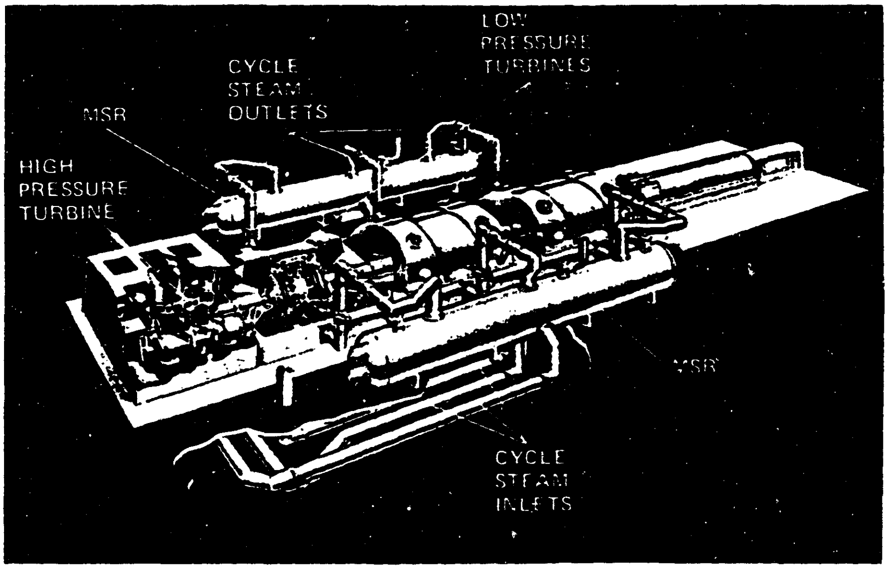

Figure 5.26. An LWR turbine with MSR (from [Moore 1976]).

It is anticipated that most Pb-Bi entering the HP turbine in the form of fine droplets will impact the turbine blade and internal surfaces and will then be removed (along with liquid water) through the drainage slots located on the turbine casing and on the hollow fixed blades (see **Figure 5.22** and **5.23**, respectively). The drained Pb-Bi will have to be filtered out of the water and returned to the reactor. However, some Pb-Bi is likely to reach the HP outlet and be conveyed to the MSR. MSRs are large pressure vessels where two distinct components are accommodated in series: the moisture separator and the steam reheater. The moisture separator is typically equipped with steam separators of the chevron or wire-mesh type[51] [Hayes 1991,

---

[49] at the expenses of high temperature steam extracted from the reactor steam line

[50] For example, the possibility of clogging of the water drainage channels is considerably reduced.

[51] Both are so-called inertia steam separators because they rely on the relatively large inertia of the liquid droplets as the separating mechanism (see **Section 5.3.2**).

Cerezo 1998] featuring a reported efficiency of up to 96% for water liquid droplets down to 13μm [Keshava 1997]. During operation of the first MSRs it was observed that the major portion of the moisture leaving the HP turbine is not entrained in the steam flow but instead flows along the walls of the connection line between the HP turbine and the MSRs[52]. This has prompted a redesign of the MSRs, which now employ a preseparator stage removing the liquid film on the wall hence raising the overall MSR separating efficiency to a remarkable 99.7% [Von Boeckh 1984]. Due to the larger density of Pb-Bi with respect to water, it is reasonable to assume that these MSRs are suitable to efficiently remove the Pb-Bi droplets and drain them from the system, as well. Again special care should be given to the drained Pb-Bi/water mixture, so that the Pb-Bi is filtered out and returned to the reactor.

In conclusion, liquid extraction, drainage and separation systems in the HP turbine and MSRs are expected to drastically minimize the magnitude of Pb-Bi carry-over to the LP turbine and condenser.

5.6 Summary

The issue of Pb-Bi carry-over in the direct contact heat transfer reactor was investigated. The rate of entrainment at the free surface of the reactor pool was calculated and found to be significantly smaller than in a water system due to the larger density difference between the phases in the PBWR. An efficient steam dryer was selected that reduces the amount of Pb-Bi entrainment by three orders of magnitude. The transport of Pb-Bi aerosols through the steam lines was also evaluated and it was found that the Pb-Bi droplets travel relatively undisturbed to the turbine. Liquid Pb-Bi can cause Liquid Metal Embrittlement (LME) of the stressed components of the turbine, particularly of the stainless steel moving blades. It is possible to prevent LME by selecting alternative blade materials that are not susceptible to LME. Titanium alloys appear to be the most promising candidates. Also, blade coating with cermet coats may be a viable option, although the LME immunity of the coating materials itself needs to be verified. In both cases, accumulation of liquid Pb-Bi in the turbine can be prevented by means of traditional wetness drainage technology already in use for steam turbines.

---

[52] probably due to liquid centrifuging at the last stage of the turbine.

In addition, Pb-Bi droplet oxidation and/or electrostatic precipitation were explored as a means to eliminate LME. Oxidation would require the injection of a significant amount of oxygen in the steam lines, which could potentially raise a corrosion problem. Electrostatic precipitation would require the development of a system that operates at pressures beyond those of currently used precipitators.

It is thought that a feasible technical answer to the LME issue can be found within the pool of solutions explored in this chapter. However, it should be emphasized that the cost of coping with this issue might seriously penalize the economic acceptability of the PBWR concept and possibly offset the benefits associated with the simplification of the primary system (i.e. elimination of the steam generators and the primary coolant pumps). To evaluate the impact of the Pb-Bi aerosol issue, it is recommended that a thorough quantitative economic analysis be performed that will ultimately measure the attractiveness of the PBWR over alternative heavy liquid metal reactor concepts.

Chapter 6

- COOLANT ACTIVATION IN THE PBWR -

6.1 Introduction

The use of molten lead-bismuth eutectic as a heavy liquid metal coolant of fast spectrum nuclear systems has been deemed preferable over pure lead [Spencer 2000a, LANL 1999a, Gromov 1997, Zaki 1995] due to its lower melting point (125°C vs. 327°C), which greatly simplifies coolant handling as well as plant design and operation. However, Pb-Bi does display several disadvantages with respect to lead including coolant availability and cost (bismuth is a relatively rare and costly material[1]), materials corrosion (at a given temperature the solubility of steel materials is larger in bismuth than in lead[2] [Weeks 1971]) and radiological hazard associated with coolant activation. ^{210}Po (an extremely toxic alpha-emitter of approximately 140 days half-life) is formed from ^{209}Bi by neutron capture. In a single-phase Pb-Bi reactor the primary system is sealed and separated from the secondary system. As a result, polonium is well retained in the Pb-Bi eutectic during normal operating conditions and can raise a problem only if a coolant leakage through the steam generator or the reactor vessel occurred. Also, some polonium migrates to the cover gas in the reactor plenum and can diffuse outside the primary system if the reactor pool is not perfectly tight. However, recent studies within the frame of the LANL ATW project [Li 1998] have shown that exposure of plant personnel to polonium can be maintained within tolerable limits even in case of massive release of cover gas or coolant into the reactor room. Nevertheless, due to its half-life, ^{210}Po may limit access to the surfaces on which it deposits, thus increasing maintenance costs and/or collective doses. Considerable experience in dealing with polonium related issues has been gained in the past 30 years in Russia where several submarines were equipped with Pb-Bi cooled nuclear reactors [Zrodnikov 1999]. A polonium technology was developed that includes special polonium filters for air cleaning, polonium adsorbing adhesive films for decontamination of large surfaces, special respirators and pressurized suits for maintenance of contaminated areas [Pankratov 1992].

---

[1] See Section 1.2.2.

[2] However, it should be noted that, due to Pb higher melting point, a Pb cooled reactor might have to operate at higher temperature which may offset the solubility difference.

However, the case of a Pb-Bi/water direct contact reactor presents a significantly more severe challenge. Under normal operating conditions, the primary system is not isolated and the radioactive polonium may be readily transported by steam to the components of the secondary system (e.g. the steam lines, the turbine, the condenser). Because leaks of some contaminated steam out of the turbine or other power cycle components are inevitable, a certain amount of polonium is likely to escape into the environment. It must be demonstrated that the polonium concentration in the leaking steam, and all other vented flows, is within the limits prescribed by the radiation protection regulations. As a result, the development of the PBWR concept calls for a substantial investigation of the mechanisms of formation of radioactive polonium and its chemical compounds, a quantitative characterization of their release and transport throughout the plant and identification of possible ways to mitigate the radiological concern associated with these phenomena. This is a major focus of this thesis work that will be illustrated in the following sections. In **Sections 6.2, 6.3** and **6.4** a literature review is presented on the nuclear characteristics of polonium, on the chemistry of its most relevant compounds and on the proposed methods of polonium extraction from the Pb-Bi coolant, respectively. Then in **Section 6.5** theoretical modeling of polonium production and transport in the PBWR concept is undertaken with the goal of evaluating the magnitude of the coolant activation issue in this concept.

6.2 Polonium Nuclear Characteristics

Polonium has no stable isotopes. However, ^{210}Po, ^{214}Po and ^{218}Po do naturally occur in the decay chain of ^{238}U [GE 1996]. The isotope of interest in our case, ^{210}Po, has a relatively long half-life and emits alpha particles of 5.3MeV with 100% yield[3]. It is produced in the Pb-Bi coolant by neutron activation of ^{209}Bi [4] according to the following reaction chain:

$$^{209}Bi + n \rightarrow {}^{210}Bi \underset{t_{1/2}=5days}{\overset{\beta^-}{\rightarrow}} {}^{210}Po \underset{t_{1/2}=138days}{\overset{\alpha}{\rightarrow}} {}^{206}Pb \qquad \textbf{Eq.6.1}$$

---

[3] And is therefore known as a pure α-emitter.

[4] The isotopic abundance of ^{209}Bi is 100% (i.e. ^{209}Bi is the only natural isotope of bismuth). For the ^{209}Bi neutron capture cross section in the PBWR spectrum, see **Section 6.5.**

To characterize its radiotoxicity, we shall make use of the concept of Derived Air Concentration (DAC). The DAC is a specific radioactivity (typically expressed in Bq/m^3, $\mu Ci/cm^3$) and can be defined as follows: a worker inhaling air (whose concentration of a certain radionuclide is equal to its DAC) for 2000hrs (at a rate of $1.2m^3/hr$), will receive a dose from that radionuclide equal to the maximum allowable annual dose (i.e. 50mSv in the US). Because ^{210}Po is an emitter of energetic alpha particles, its DAC is very stringent ($10Bq/m^3$ or $3\times10^{-10}\mu Ci/cm^3$ as reported in [EPA 1988]), which may raise a potential radiological problem. Note that ^{210}Bi is a beta emitter (electron maximum energy equal to 1.16MeV) of shorter life and consequently of lower radiotoxicity than ^{210}Po as reflected by its DAC, which is two orders of magnitude larger ($1000Bq/m^3$ vs. $10Bq/m^3$). Moreover, due to its shorter half-life the concentration of ^{210}Bi in the Pb-Bi coolant is substantially smaller than that of ^{210}Po (about $5/138\approx4\%$). Also the volatility of bismuth is lower than that of polonium and its chemical compounds. As a result, the release of ^{210}Bi from the coolant is expected several orders of magnitude smaller than that of polonium. Therefore in the rest of the chapter we will mostly neglect the presence of ^{210}Bi, which enables simplifying the coolant activation analysis.

It should be noted that in a subcritical system driven by a proton accelerator (e.g. ATW), several different polonium radioactive isotopes are also produced by (p,xn) and (α,xn) reaction on ^{209}Bi and ^{208}Pb, respectively [Yefimov 1998]. Due to these additional production channels, the specific polonium activity in the target coolant of these systems can increase by an order of magnitude compared to ^{210}Po alone [Yefimov 1998, Gromov 1994].

6.3 Polonium Chemical Characteristics

When created by neutron activation in the lead-bismuth coolant, polonium rapidly forms a stable compound with lead, known as lead polonide (PbPo) [Li 1998, Yefimov 1998]. As a result, only up to 0.2% of the polonium present in Pb-Bi is in the unbound elementary form (Po) [Li 1998]. Upon contact of PbPo with water a very volatile hydride (H_2Po) is formed [Yefimov 1998, Gromov 1996, Schipakhin 1992]. Additional parallel mechanisms of Po release into steam are direct evaporation of PbPo and simple Po [Feuerstein 1992, Hoffman 1985, Gromov 1996]. An experimental campaign was undertaken at MIT to gain a better insight of the polonium release mechanisms, with particular emphasis to the role of the hydride on which the literature is rather scarce. A detailed description of these experiments is given **Chapter 7**. In **Section 6.5** the magnitude of polonium release associated with direct evaporation and polonium hydride formation in the PBWR will be quantitatively assessed relying on the data collected at MIT as well as on data available in the literature.

We will now analyze the characteristics of several different chemical polonium compounds of interest.

Pure Polonium - Po

Polonium is a metal of atomic number 84 and density ranging between 9,200 and 9,400kg/m^3 depending on temperature and hence crystalline structure [Bagnall 1966]. Its melting and boiling points at 1atm are 250 and 962°C, respectively [Greenwood 1984]. The vapor pressure of metallic polonium is given by [Bagnall 1966, Abakumov 1974]:

$$\mathrm{Log}P_{Po}=9.457-5440/T \qquad \textbf{Eq.6.2}$$

where P_{Po} and T are in Pa and K, respectively. Also, the rate of evaporation was calculated by means of Langmuire's law (on the basis of the vapor pressure data) and is plotted as a function of temperature in **Figure 6.1**.

Lead Polonide - PbPo

This is the main form in which polonium is found in the lead-bismuth eutectic as recognized in [Feuerstein 1992, Gromov 1996]. Simulations with tellurium (chemically similar to polonium) in lead-bismuth seem to indicate that the bismuth polonide Bi_2Po_3 is much less stable than PbPo and can be neglected in practice [Yefimov 1998]. As a solid, PbPo displays ionic crystalline structure similar to NaCl (i.e. face centered cubic) of density 9,600kg/m^3 and unit cell 6.6Å [Witteman 1960]. However, it will be demonstrated that the PbPo concentration in the Pb-Bi eutectic is very low and it can be assumed that PbPo is present in a solution state only. PbPo is a chemically stable compounds of polonium and melts at 600°C. Its boiling point is 1520°C and its vapor pressure can be computed from the following equation [Abakumov 1974]:

$$\mathrm{Log}P_{PbPo}=9.061-7270/T \qquad \textbf{Eq.6.3}$$

where P_{PbPo} and T are in Pa and K, respectively. The correlation of **Eq.6.3** was originally proposed for the 640-850°C temperature range. However, the experiments conducted within the framework of this thesis validated the correlation also in the 400-550°C range.

The rate of evaporation of PbPo is also plotted as a function of temperature in **Figure 6.1**. It can be seen that in lead-bismuth eutectic the experimental points bracket the PbPo evaporation rate curve, further confirming that polonium is in the bound form PbPo and not in the elementary form Po.

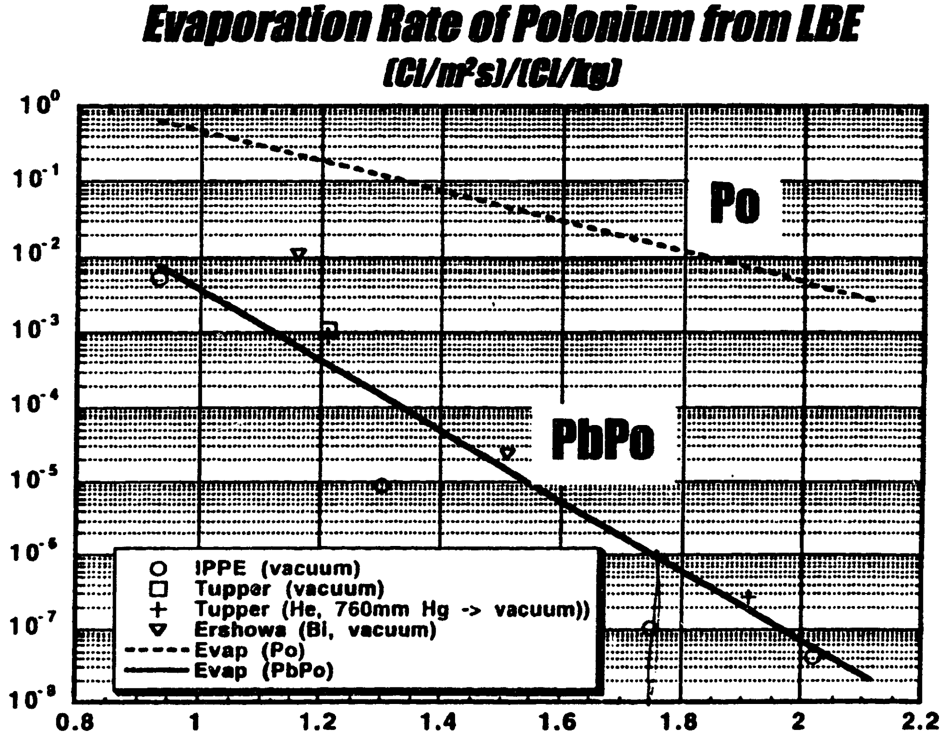

Figure 6.1. The evaporation rate of Po and PbPo from the Pb-Bi eutectic (from [Orlov 1998]).

Note that the data of **Figure 6.1** refer to Po and PbPo evaporation to a vacuum. It is reported in [Gromov 1996] that under atmospheric pressure the actual evaporation rate of Po and PbPo from a lead-bismuth eutectic decreases by approximately three orders of magnitude.

<u>Rare Earth Polonides</u> – PrPo, TmPo

In reference [Greenwood 1984] it is reported that some rare earths form extremely stable polonides of very high melting point (above 1000°C). For example, PrPo (praseodymium polonide) and TmPo (thulium polonide) display a melting point of 1253°C and 2200°C, respectively. These data suggest that it might be possible to decrease the rate of release of polonium by dissolving thulium or praseodymium in the lead-bismuth eutectic hence promoting the formation of a lower volatility species. It should be observed that the thulium capture cross section at high energy (2MeV) is rather high (~100mb) [BNL 2000] and its use in the reactor coolant requires careful neutronic investigations, as not to deteriorate neutron economy or worsen void reactivity response. On the other hand, the capture cross section of praseodymium (at 2MeV) is about 8mb, comparable to that of ^{209}Bi (~3mb) and therefore is neutronically more acceptable.

Polonium Hydride – H_2Po

In a Pb-Bi system the polonium hydride is produced by the reaction of PbPo with water:

$$PbPo_{(sol)}+H_2O_{(g)} \leftrightarrow H_2Po_{(g)}+PbO_{(sol)} \qquad \textbf{Eq.6.4}$$

where the subscripts (sol) and (g) stand for 'in solution' and 'gaseous', respectively. H_2Po is believed to be responsible for the occurrence of significant polonium release upon leakage of activated lead-bismuth in a moist atmosphere, even at low temperature [Li 1998, Gromov 1996][5]. Therefore, in a single-phase Pb-Bi cooled reactor the interest in such chemical compound is limited to accidental situations only. On the other hand, it is anticipated that in the PBWR[6] this hydride will play a key role in removing and transporting polonium from the reactor coolant to the secondary system under normal operating conditions, too.

Polonium hydride is a volatile and chemically unstable gas [Bagnall 1966, Greenwood 1984], which readily decomposes into hydrogen and polonium [Li 1998]. H_2Po is hard to produce in sizeable amounts and in the past its properties were mostly derived by extrapolation of data on selenium and tellurium hydrides, which display similar chemical behavior (see **Appendix F**). Its melting and boiling point at 1atm are thought to be –36 and 37°C, respectively [Bagnall 1966]. We extrapolated the vapor pressure equations of selenium and tellurium hydride reported in

---

[5] the rate of release of H_2Po at 20°C under 80% moisture air is reported to be $1.5\times10^{-9}(Ci/m^2s)/(Ci/m^2)$ from Russian experiments and actual submarine reactor experience [Li 1998].

[6] where water is injected in hot lead-bismuth.

[Bagnall 1966] to produce the following tentative equation for the vapor pressure of pure polonium hydride in the absence of chemical reactions:

$LogP_{H2Po}$=7.915-980/T **Eq.6.5**

where P_{H2Po} and T are in Pa and K, respectively.

However, **Eq.6.5** is of limited interest because in the PBWR the chemical reaction of **Eq.6.4** actually takes place. The free-energy variation of **Eq.6.4** was measured during the polonium experiments conducted for this thesis work and found to be (see **Section 7.4**):

$\Delta G_1(T)$=17.34+0.121T **Eq.6.6**

where ΔG_1 is in kJ/mol and T in K.

Reference [Sumathi 1990] reports calculated values of the ionization potential of the hydrides of the VI group elements (i.e. H_2O, H_2S, H_2Se, H_2Te, H_2Po). The ionization potential of polonium hydride is 8.0eV as opposed to 13.0eV for water, which in principle leaves room for a polonium removal technique based on selective ionization of the polonium hydride. However, the development of such method is beyond the scope of this study and will not be pursued any further.

A summary of the chemical characteristics of polonium and its compounds is reported in **Table 6.I** below.

Table 6.I. Polonium and its compounds.

Property	Po	PbPo	PrPo/TmPo	H_2Po
Density (g/cm^3)	9.2-9.4	9.6	N/A[7]	Mostly gaseous
Melting Point (°C) at 1atm	250	600	1253/2200	-36
Boiling Point (°C) at 1atm	962	1520	N/A	37
Vapor Pressure (Pa)	**Eq.6.2**	**Eq.6.3**	N/A	**Eq.6.5**
Evaporation Rate	**Fig.6.1**	**Fig.6.1**	N/A	N/A
Formation reaction ΔG (kJ/mol)	0	N/A	N/A	**Eq.6.6**

---

[7] N/A= 'Not-Applicable' or 'Not-Available'.

6.4 Polonium Extraction from Pb-Bi

Continuous on-line polonium extraction from the PBWR Pb-Bi coolant is essential to inhibit the formation of the volatile H_2Po, to decrease PbPo evaporation and hence to ultimately minimize the polonium transport out of the reactor pool. Even small rates of polonium extraction can result in considerable reduction of polonium concentration in Pb-Bi, as will be shown in **Section 6.5**. However, it should be emphasized that, despite the construction of several submarine Pb-Bi reactors in the former Soviet Union, there is no industrially established and proven polonium extraction technology to date. The development of such technology is not among the objectives of this study, but it is clear that thorough R&D effort on this subject is necessary should the development of commercial Pb-Bi nuclear systems (especially of the direct contact heat transfer type) be more decisively pursued in the future.

Two different techniques were proposed in the past for the extraction of polonium from heavy liquid metals: high temperature distillation and alkaline extraction.

High Temperature Distillation

The vapor pressure of PbPo is several orders of magnitude larger than that of Pb-Bi across a wide range of temperatures, which allows selective distillation of polonium from a Pb-Bi stream [Yefimov 1998]. Processing a 50 to 600kg/hr flow rate of polonium contaminated Pb-Bi[8] at 700°C was found to require a mass transfer surface area of 150m^2, which can be achieved by bubbling an inert gas through the liquid lead-bismuth [Yefimov 1998]. The removal efficiency of this process is rather high reaching up to 99%. Polonium distillation was found suitable for small scale military applications in Russia [Orlov 1998]. However, in the case of a large commercial reactor, this technique might be impractical and/or costly because of the large transfer area requirements and the need to operate the system at high temperature.

Alkaline Extraction

The alkaline extraction method is based on the following reaction [Orlov 1998]:

$$PbPo + 4NaOH \leftrightarrow Na_2Po + Na_2PbO_2 + 2H_2O \qquad \textbf{Eq.6.7}$$

---

[8] In view of an on-line utilization of the distillation process, this is a modest flow rate if compared with the nominal 81,110kg/s Pb-Bi mass flow rate of the PBWR.

which occurs when a mass of polonium contaminated Pb-Bi is put in contact with a NaOH-KOH melt. The addition of KOH to NaOH results in the formation of a low melting point eutectic, which enables operating the purification system at a relatively low temperature (250 to 500°C). Moreover, neither KOH nor the molten Pb-Bi (which acts as a polonium carrier) participates in the chemical reaction. The minimum required contact time of Pb-Bi with the sodium melt is thought to be 2 minutes, which in principle makes alkaline extraction suitable for on-line utilization. After 2 minutes contact the removal efficiency of this system is known to be approximately 90% [Yefimov 1998]. This value was found to change with the concentration of oxygen and oxides in the Pb-Bi coolant, being larger at low concentrations and vice versa. Whether it is possible to employ this method on a large scale still remains to be determined, but in this study we will select alkaline extraction as our interim polonium removal technique.

6.5 Theoretical Characterization of the Polonium Problem

6.5.1 The Governing Equations

In this section simple calculations based on available data on polonium chemistry will be used to provide a first estimate of the magnitude of the polonium challenge in the direct contact PBWR. We will do so by establishing a polonium balance over the control volume represented by the total Pb-Bi inventory in the reactor pool. A fundamental assumption is made that the steam leaving the reactor pool is saturated with the polonium species, therefore ignoring the kinetics of the reactions involved in polonium release.

The balance equation is:

$$\frac{dN_{Po}}{dt} = \Gamma_{prod} - \Gamma_{decay} - \Gamma_{extr} - \Gamma_{rel} \qquad \textbf{Eq.6.8}$$

where N_{Po} is the total number of ^{210}Po nuclei in the Pb-Bi coolant and Γ_{prod}, Γ_{decay}, Γ_{extr} and Γ_{rel} are the (n,γ) production, the decay, the extraction and release terms defined below.

Production

^{210}Po is created in the reactor core by neutron activation of ^{209}Bi. We neglect the intermediate radionuclide ^{210}Bi whose half-life is 5days (see **Eq.6.1**). The rate of ^{210}Po production in the coolant can be readily calculated as:

$$\Gamma_{prod} = \sigma\Phi N_{Bi,c} \qquad \textbf{Eq.6.9}$$

The Monte Carlo code MCNP was utilized to assess the neutron spectrum in the 1,800MWth PBWR core [Hejzlar 2000]. The one-group averaged neutron flux Φ and capture cross section σ of ^{209}Bi were found to be 2.24×10^{15}n/cm^{2}s and 4.8mb, respectively. $N_{Bi,c}$ is the number of ^{209}Bi nuclei in the core and it was calculated as:

$$N_{Bi,c} = \frac{0.55\rho_{PbBi}N_{av}}{A_{Bi}}V_c \qquad \textbf{Eq.6.10}$$

Here ρ_{PbBi} is the Pb-Bi density (~10,000kg/m^3), N_{av} is the Avogadro's number, A_{Bi}=0.209kg/mol is the bismuth atomic weight. The factor 0.55 accounts for the fact that 55%wt of Pb-Bi eutectic is bismuth.

V_c is the volume of coolant in the core calculated assuming the core is a cylinder of diameter 4m and height 1.3m entirely filled with Pb-Bi. Actually, the coolant volume fraction in the PBWR core is only 27%, due to the neutron streaming channels and the presence of the fuel (see **Figure 2.3**). So this assumption is conservative. However, the MCNP simulations indicate that the neutron flux does not rapidly decrease with distance from the core. Therefore significant production of polonium outside the core is anticipated. This effect might somewhat offset the conservative assumption of completely Pb-Bi filled core.

Decay

^{210}Po α-decays with a half-life of approximately 140 days (i.e. λ_{dec}~5.8×10^{-8}s^{-1}). The radioactive decay term can be expressed as:

$$\Gamma_{decay} = \lambda_{dec}N_{Po} \qquad \textbf{Eq.6.11}$$

Extraction

It is assumed that a fraction "f" of the total Pb-Bi mass flow rate circulating in the reactor pool is sent to the Polonium Extraction System (PES) to remove the polonium by means of the alkaline process described in **Section 6.4**, whose efficiency is ε=90%. The extraction term can then be calculated as:

$$\Gamma_{extr} = \varepsilon f \dot{m}_f \frac{N_{Po}}{M_{PbBi}} \qquad \textbf{Eq.6.12}$$

where $\dot{m}_f$ is the reactor Pb-Bi mass flow rate (81,110kg/s at nominal conditions) and $M_{PbBi} \approx 3.6 \times 10^6$kg is the total Pb-Bi inventory in the reactor pool (**Table 4.I**). The term $\frac{N_{Po}}{M_{PbBi}}$ is the concentration (nuclei/kg) of ^{210}Po in the pool.

Release

When created in the Pb-Bi coolant, polonium rapidly forms a chemically stable compound with lead (i.e. PbPo). In accordance with [Li 1998] it is assumed that 99.8% of polonium is in fact in this form and 0.2% remains in the unbound elementary Po form. Release of polonium from Pb-Bi can then occur by means of three different mechanisms: evaporation of PbPo, evaporation of Po and formation of the volatile hydride H_2Po. The rate of evaporation of PbPo and Po is provided in **Figure 6.1**. However, the use of these data requires knowledge of the Pb-Bi/steam interface transfer area, which is not easily obtainable as it depends on the two-phase flow regime and thermal-hydraulic conditions in the chimney. Therefore, we will conservatively calculate the rate of release of polonium assuming that the steam passing through the chimney becomes saturated with H_2Po, PbPo and Po. This enables the use of the equilibrium data of **Section 6.3** (see **Eq.6.6, 6.3** and **6.2**, respectively). Consequently, the release term Γ_{rel} (polonium nuclei per unit time) can be expressed as:

$$\Gamma_{rel} = x'_{Po,tot} \dot{m}_g \frac{N_{av}}{A_{H2O}} = \dot{m}_g \frac{N_{av}}{A_{H2O}} \left(x_{PbPo} \frac{P_{PbPo}(T)}{P} + x_{Po} \frac{P_{Po}(T)}{P} + \frac{P'_{H2Po}}{P} \right) \qquad \textbf{Eq.6.13}$$

where $\dot{m}_g$=686kg/s is the steam mass flow rate, $x'_{Po,tot}$ is the total molar fraction (PbPo + Po + H_2Po) of polonium in the steam and A_{H2O}=0.018kg/mol is the steam molecular weight. P is the system pressure (7MPa) and T is the system temperature. $P_{PbPo}(T)$ and $P_{Po}(T)$ are given by **Eq.6.3** and **6.2**, respectively. P'_{H2Po} is the partial pressure of H_2Po in steam and x is the molar fraction in liquid lead-bismuth. In **Eq.6.13** we made use of Rault's law for ideal solutions to relate the molar fractions of PbPo and Po in the liquid and in the steam[9]. The molar fractions of PbPo and Po in the liquid, x_{PbPo} and x_{Po}, can be readily calculated as:

$$x_{PbPo} = 0.998 \frac{(N_{Po} / N_{av})}{(M_{PbBi} / A_{PbBi})} \qquad \textbf{Eq.6.14}$$

$$x_{Po} = 0.002 \frac{(N_{Po} / N_{av})}{(M_{PbBi} / A_{PbBi})} \qquad \textbf{Eq.6.15}$$

where A_{PbBi}=0.209kg/mol is the average atomic weight of Pb-Bi. Throughout this section the coolant is assumed to be a very dilute solution of polonium so that the molar fractions of the polonium species are small and the simple expressions in **Eq.6.13, 6.14** and **6.15** can be adopted. This is justified because the typical values of x_{PbPo} and x_{Po} are about 10^{-8} and 10^{-10}, respectively.

Note that it is not possible to use Rault's law to calculate P'_{H2Po} because the polonium hydride does not exist as such in the Pb-Bi melt, but is generated by the reaction of **Eq.6.4.** However, it is demonstrated in **Section 7.4** that the partial pressure of H_2Po is related to the partial pressure of hydrogen P'_{H2} in the steam and the PbPo concentration C_{PbPo} in the Pb-Bi coolant (mol/$kg_{Pb\text{-}Bi}$) by the following expression:

$$P'_{H2Po} = C_{PbPo} P'_{H2} e^{\frac{\Delta G_2 - \Delta G_1}{RT}} \qquad \textbf{Eq.6.16}$$

where ΔG_1 and ΔG_2 (the free-energy variation of the water-lead reaction **Eq.7.15**) are given by **Eq.6.6** and **7.17**, respectively and R is the gas constant (8.31J/mol·K). It should be emphasized that in order to make use of **Eq.6.16** all pressures must be expressed in atm and C_{PbPo} in mol/kg_{PbBi}, due to the definition of the standard state of the species involved. Note that the partial pressure of hydrogen in the PBWR steam is known and fixed at 5×10^{-3}atm on the basis of materials corrosion considerations (see **Section 8.3**). C_{PbPo} can be readily calculated as:

$$C_{PbPo} = 0.998 \frac{(N_{Po} / N_{av})}{M_{PbBi}} \qquad \textbf{Eq.6.17}$$

6.5.2 Results and Discussion

Now that the expressions of all the Γ terms have been derived, we get back to **Eq.6.8**, which can be re-written as:

---

[9] According to Rault's law, the partial pressure of a species A above a A+B mixture is equal to the vapor pressure of pure A times its molar fraction in the mixture.

$$\frac{dN_{Po}}{dt}=\sigma\Phi N_{Bi,c}-\lambda_{dec}N_{Po}-\varepsilon f\dot{m}_f\frac{N_{Po}}{M_{PbBi}}-\dot{m}_g\frac{N_{Po}A_{PbBi}}{M_{PbBi}A_{H2O}}\left(0.998\frac{P_{PbPo}}{P}+0.002\frac{P_{Po}}{P}+0.998\frac{P'_{H2}}{P}\frac{e^{\frac{\Delta G_2-\Delta G_1}{RT}}}{A_{PbBi}}\right)$$

$$=\sigma\Phi N_{Bi,c}-\left[\lambda_{dec}+\frac{\varepsilon f\dot{m}_f}{M_{PbBi}}+\frac{\dot{m}_g A_{PbBi}}{M_{PbBi}A_{H2O}}\left(0.998\frac{P_{PbPo}}{P}+0.002\frac{P_{Po}}{P}+0.998\frac{P'_{H2}}{P}\frac{e^{\frac{\Delta G_2-\Delta G_1}{RT}}}{A_{PbBi}}\right)\right]N_{Po}$$

$$=\sigma\Phi N_{Bi,c}-\left[\lambda_{dec}+\lambda_{extr}+\lambda_{rel}\right]N_{Po} \qquad \textbf{Eq.6.18}$$

where the following definitions are adopted:

$$\lambda_{extr}\equiv\frac{\varepsilon f\dot{m}_f}{M_{PbBi}} \qquad \textbf{Eq.6.19}$$

$$\lambda_{rel}\equiv\frac{\dot{m}_g A_{PbBi}}{M_{PbBi}A_{H2O}}\left(0.998\frac{P_{PbPo}}{P}+0.002\frac{P_{Po}}{P}+0.998\frac{P'_{H2}}{P}\frac{e^{\frac{\Delta G_2-\Delta G_1}{RT}}}{A_{PbBi}}\right) \qquad \textbf{Eq.6.20}$$

For given operating conditions λ_{extr} and λ_{rel} are not a function of time and **Eq.6.18** can be readily integrated to yield:

$$N_{Po}=\frac{\sigma\Phi N_{Bi,c}}{\lambda_{dec}+\lambda_{extr}+\lambda_{rel}}\left(1-e^{-(\lambda_{dec}+\lambda_{extr}+\lambda_{rel})t}\right) \qquad \textbf{Eq.6.21}$$

where it was assumed that $N_{Po}(0)=0$.

The value of λ_{dec} is 5.8×10^{-8} s^{-1}. For f between 0.001 and 0.1 (0.1% and 10% of the total Pb-Bi mass flow rate) the values of λ_{extr} range from 2×10^{-5} and 2×10^{-3}s^{-1}. For T between 440 and 550°C the values of λ_{rel} range from 4×10^{-10} to 10^{-9}s^{-1}. This temperature range is explored as representative of the Pb-Bi/steam interface temperature in the reactor chimney (see **Table 4.I** and **Figure 3.9**). Since it is hard to predict the evolution of the polonium species concentration and to establish whether they will reach chemical equilibrium at the high or the low temperature, it is necessary to scan the whole temperature range, if a realistic envelop is to be generated.

It is apparent from the relative values of the λ rates (λ_{extr}>>λ_{dec},λ_{rel}) that the dominant mechanism determining the polonium asymptotic inventory in the reactor pool, $N_{Po,\infty}$, is the on-line extraction. Consequently, the exponential term in **Eq.6.21** vanishes at times greater than approximately $4/\lambda_{extr}$, which ranges from 0.6hr to 56hr (corresponding to f=0.1 and 0.001, respectively). Nevertheless, it should be noted that polonium is produced by the radioactive decay of ^{210}Bi [10], whose half-life is 5 days, which is significantly larger than 37hr. Therefore it is expected that the ^{210}Bi decay time constant dominates the transient. However, even 5 days is a negligible time if compared with the typical operating time of a nuclear reactor (~18 months) and for all practical purposes the polonium transient can be neglected. Consequently, in this analysis we will deal only with the asymptotic values of the polonium quantities of interest, which are proportional to $N_{Po,\infty}$. Also, note that ignoring the ^{210}Bi decay does not affect these asymptotic values.

Then the polonium specific activity in the Pb-Bi coolant (Ci/kg) is:

$$C_{Po,cool} = \frac{\lambda_{dec} N_{Po,\infty}}{M_{PbBi}} \qquad \textbf{Eq.6.22}$$

The polonium specific activity in the steam leaving the reactor pool (Bq/m^3) can be readily calculated as:

$$C_{Po,st} = \frac{\lambda_{rel} \lambda_{dec} N_{Po,\infty}}{\dot{m}_g / \rho_g} \qquad \textbf{Eq.6.23}$$

Note that **Eq.6.23** holds under the assumption that the water entering the reactor pool is polonium-free. The validity of this assumption really depends on the transport of polonium in the secondary system, as discussed next.

Part of the radioactive polonium transported by steam remains in the secondary system because it either stays in the water or deposits on the internal surfaces of the turbine, condenser and pipes. Part is vented out of the secondary circuit through the OffGas system (OG) connected to the condenser by the Steam Jet Air Ejectors (SJAEs), whose main purpose is to separate the non-condensable gases from the condensed water. In current BWRs the OG is equipped with filters and charcoal adsorbing beds that collect the radionuclides entrained in the non-condensable gases [GE 1999]. The effluents are then monitored and finally discharged into the atmosphere through the plant stack. In the PBWR these filters and adsorbing beds will have to be re-designed and/or optimized to ensure that the polonium radioactivity of the vented effluents is within acceptable limits. However, most polonium in the condenser is likely to be in a non-volatile phase because the condenser operates at low temperature. As a result, it is anticipated

---

[10] neglected in our model

that only a small amount of polonium will actually be transported to the OG by the non-condensable gases.

Some steam may also leak out of the turbine, mainly through the shaft clearance and turbine valves. This steam expands to atmospheric pressure and therefore its polonium volumetric concentration (Bq/m^3) is smaller than calculated by **Eq.6.23**. The polonium concentration of steam at atmospheric pressure, $C^*_{Po,st}$, can be readily found from that at 7.0MPa as:

$$C^*_{Po,st} = C_{Po,st}\frac{\rho^*_g}{\rho_g} \qquad \textbf{Eq.6.24}$$

where ρ^*_g is the steam density at atmospheric pressure (0.6kg/m^3).

In **Figure 6.2** $C_{Po,cool}$ and $C^*_{Po,st}$ are plotted as a function of the temperature T and the mass flow rate fraction f sent to the extraction polonium system.

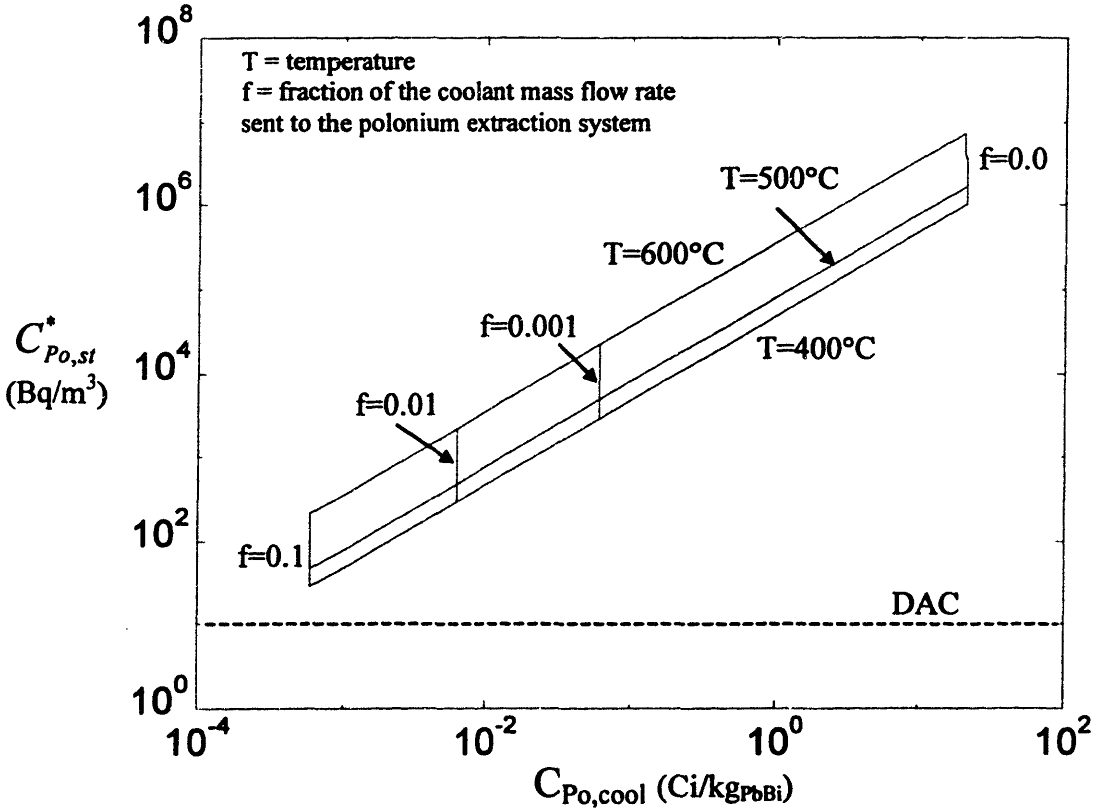

Figure 6.2. Polonium concentration in steam vs. polonium concentration in the Pb-Bi coolant.

As anticipated, the effect of the Polonium Extraction System (PES) rate on the polonium concentration in Pb-Bi is remarkable: increasing f from 0.0 (no PES) to 0.001 decreases the polonium content of Pb-Bi by almost three orders of magnitude (for a given temperature). As already noted, λ_{extr} is much larger than λ_{dec} and λ_{rel} even at modest values of f. This makes $N_{Po,\infty}$ and hence $C_{Po,cool}$ practically independent of λ_{rel} and consequently independent of temperature for a given f, as illustrated in **Figure 6.2**.

It can be seen that for all temperatures and extraction rates, the magnitude of polonium contamination of the leaking steam is above the allowed limits (expressed as the ^{210}Po DAC, see **Section 6.2**). This might not constitute a severe concern because modern BWR turbines are equipped with a dedicated Gland Steam Sealing System (GSSS) that virtually eliminates steam leakage [Sawyer 1999, Todd 2000]. This system consists of an evaporator that delivers clean steam to the turbine shaft and major valves. The steam is forced to flow through a labyrinth packing gland outward to the turbine building atmosphere hence providing a seal to the radioactive steam.

We shall now estimate the polonium contamination of the surfaces of the main secondary system components: the steam lines, the turbine and the condenser. Unprotected maintenance of these surfaces can be carried out for an α-activity up to 0.9μCi/m^2. Above this threshold, access to the surface requires decontamination and/or the use of radiation protection equipment like sealed suits and respirators. The rate of polonium release (in Ci/s) from the reactor pool can be calculated from **Eq.6.13**[11] as $\lambda_{dec}\Gamma_{rel}$. For T between 440 and 550°C and f=0.001, this rate ranges from 0.1 to 0.3mCi/s. We will assume that all this polonium deposits on a single component of internal surface S. This will provide an upper bound to the value of the surface activity for that component. Taking into account the radioactive decay, the equilibrium α-activity of that component, α_s, can be readily calculated as:

$$\alpha_s = \frac{\Gamma_{rel}}{S} \qquad \textbf{Eq.6.24}$$

The PBWR has 3 steam lines of 1m diameter and 50m length (see **Section 5.4**), which result in a total steam line surface area S of about 470m^2. For this value of S **Eq.6.24** yields a surface

---

[11] Note that **Eq.6.12** and **Eq.6.13** actually expresses a rate in polonium nuclei per second and must be multiplied by λ_{dec} if the activity rate is wanted.

activity ranging from 3 to 10 Ci/m^2, i.e. several orders of magnitude above the free-access threshold.

Assuming a tandem-compound 2 flow HP turbine with 10 stages per flow, 5cm blade length (L_b) and 0.9m turbine disc radius (i.e. R_d = the distance between the blade root and the shaft axis), the surface area S_{HP} of the HP turbine blades can be calculated as:

$$S_{HP} = \pi\left[(R_d + L_b)^2 - R_d^2\right] \cdot 10 \cdot 2 \cdot 2 \approx 2\pi R_d L_b \cdot 10 \cdot 2 \cdot 2 \approx 11.3\text{m}^2 \quad \textbf{Eq.6.25}$$

where the approximation $L_b \ll R_d$ was utilized and the factor 2 in the end accounts for the rear face of the blades. Assuming a tandem-compound 4 flow LP turbine with 6 stages per flow, 50cm average blade length and 0.9m turbine disc radius, the surface area S_{LP} of the LP turbine blades can be calculated as:

$$S_{LP} = \pi\left[(R_d + L_b)^2 - R_d^2\right] \cdot 6 \cdot 4 \cdot 2 \approx 217.1\text{m}^2 \quad \textbf{Eq.6.26}$$

Therefore, the total turbine blade surface area S is $S_{HP}+S_{LP} \approx 228.5\text{m}^2$. Consequently **Eq.6.24** yields a surface activity ranging from 7 to 21Ci/m^2, also considerably above the limit for unrestricted maintenance.

As for the condenser, it is assumed to be of the shell-and-tube type, with 2 separate shells and 2 tube passes per shell. Each shell collects half steam flow exhausted at the outlet of the turbine. The total power exchanged in the condenser is 832MWth (416MWth/shell) corresponding to a reactor power of 1260MWth and a cycle thermal efficiency of 33%. The cooling water inlet temperature is 27°C and the condensing water temperature is 40°C. For such condenser, the recommended heat transfer surface area is 52,000m^2 [El-Wakil 1984]. For this value of S, **Eq.6.24** yields an α-activity ranging from 0.03 to 0.09Ci/m^2, again much larger than the free-access limit.

These simple calculations suggest that, if a significant deposition of polonium does in fact take place on the components of the PBWR secondary system, their maintenance cost may considerably rise since extensive surface decontamination and/or the use of special radiation protection equipment will be required.

We will now calculate the polonium concentration in the secondary system assuming all polonium remains in the water (i.e. no steam leakage, no deposition). Then the feedwater polonium concentration is:

$$C_{Po,fw} = \frac{(\lambda_{dec}\Gamma_{rel})}{\lambda_{dec}M_w} = \frac{\Gamma_{rel}}{M_w} \qquad \textbf{Eq.6.27}$$

where M_w is the total water inventory of the secondary system, which amounts to about 200,000 gallons, i.e. ~760m^3 [Sawyer 1999]. $C_{Po,fw}$ ranges from 2.1 to 6.3mCi/kg. The Annual Limit of Intake by ingestion for ^{210}Po is 3μCi [EPA 1988], suggesting that accidental ingestion of even small amounts of secondary water must be absolutely avoided. Also, dilution of this water must be insured before it reaches public areas.

We have mentioned that extraction accounts for most polonium removal from the reactor pool. The rate of polonium radioactivity extraction can be calculated as $\lambda_{dec}\Gamma_{extr}$. For f=0.001, the result is 4.4Ci/s. Accumulation of polonium in the Polonium Extraction System (PES) is balanced by radioactive decay. Therefore the equilibrium Po activity in the PES is about 76MCi. The heat generation associated with this activity is 2.4MW. This is a considerable thermal output that will require active cooling of the PES under normal operating conditions. However, profitable use of this energy source could be made by (i) keeping the Pb-Bi coolant above the solidification point when the reactor is shutdown, (ii) coupling the PES to a small evaporator to supply steam to the GSSS or to drive safety related systems (e.g. the High Pressure Coolant Injection Turbine) during LOCAs or loss of off-site power events.

For f=0.001 and $\dot{m}_f$=81,000kg/s, the Pb-Bi mass flowing through the PES is 81kg/s. Because the alkaline process requires a 2min Pb-Bi/NaOH contact, the total Pb-Bi inventory in the PES is 81kg/s×120s≈9700kg, which is less than a cubic meter of Pb-Bi and suggests that a rather compact PES can be designed.

6.5.3 Critical Review of the Models and Conclusions

This theoretical evaluation has shown that the problem of polonium release and transport in the PBWR is very serious, potentially a show-stopping issue. The radiation level in the steam, in the feedwater and on the surface of the main secondary system components exceeds the EPA limits for inhalation, ingestion and unrestricted maintenance, respectively, under any polonium extraction rate in the reactor pool and over the whole range of temperatures considered. However, the uncertainties affecting this analysis are very significant. They are as follows:

a) We have conservatively assumed that the steam leaving the reactor pool is saturated with the polonium species, therefore ignoring the kinetics of the reactions involved in polonium release.

b) We have ignored the effect of dissolving additives in the Pb-Bi coolant that could inhibit polonium release by several orders of magnitude (i.e. thulium and/or praseodymium).

c) We have not considered the effect of a polonium extraction system in the secondary circuit. This could be a full-load system located upstream of the turbine or a smaller system part of the Chemistry and Volume Control System. In either case, the amount of polonium circulating in the secondary system could be easily decreased by orders of magnitude.

To reduce these uncertainties and acquire a more realistic evaluation of the polonium issue it is recommended to experimentally investigate the kinetics of the polonium hydride formation and of the PbPo evaporation. Further, serious consideration should be given to dissolution of rare-earths in the Pb-Bi coolant that could decrease the volatility of polonium. Finally, the interaction of the polonium chemical compounds of interest with the structural materials of the primary and secondary system should also be considered.

6.6 Summary

In this chapter, the basic chemical and nuclear characteristics of polonium (the most important product of neutron activation of the Pb-Bi coolant) were presented. The mechanisms and rate of release of polonium from the Pb-Bi coolant to the working steam as well as its transport through the secondary system were also investigated. It was found that online polonium extraction from the Pb-Bi coolant greatly reduces polonium release to the steam. However, the specific polonium activity of steam remains high, i.e. above the allowed DAC level. Also, if deposition of all polonium released is assumed to occur on the components of the secondary system (i.e. steam lines, turbine, condenser), the surface activity would exceed the unrestricted maintenance limit.

Chapter 7

- THE POLONIUM EXPERIMENTS -

7.1 Experiment Objectives

In **Chapter 6** we have theoretically characterized the issue associated with polonium generation and release in the primary system of the PBWR. That analysis required the use of data on the chemistry of some polonium species (i.e. polonium hydride and lead polonide). Given the importance of the polonium issue in determining the viability of the PBWR concept, it was decided to undertake an experimental effort to generate data on these species and in particular on:

1) The equilibrium concentration of polonium hydride in steam in the 200 to 600°C temperature range as a function of hydrogen partial pressure[1] and polonium concentration in the Pb-Bi melt.
2) The vapor pressure of lead-polonide at low temperature (<500°C).

These experiments and their results are described in this chapter.

7.2 Description of the Experimental Apparatus

7.2.1 The Cell

A high temperature reaction cell was deployed at MIT to accommodate a liquid Pb-Bi bath and radioactive polonium. The radioactive polonium was produced by irradiation of 99.99% bismuth samples in the MIT research reactor (see **Appendix G**). The cell consists of a single autoclave which hosts the molten Pb-Bi and polonium. The desired gas mixture is injected in the autoclave and then bubbled through two polonium traps in series. The alpha-activity of the trapping solution is then measured by means of two alternative methods: a) in a low background alpha-spectrometer after electroplating the polonium on a nickel disk and b) in a liquid

---

[1] For the role of the hydrogen potential in the chemistry of the polonium hydride see **Section 7.4**.

scintillator. A description of these techniques is reported in **Appendix I**. A schematic of the cell is illustrated in **Figure 7.1** and a photo of the actual apparatus is illustrated in **Figure 7.2**.

The whole apparatus is mounted on a table located in a ventilation hood in the back-lab of the MIT nuclear reactor. The hood prevents heavy contamination of the laboratory environment in case of polonium leakage from the autoclaves. It also provides a monitored path for disposal of the exhausted gases from the polonium traps (see **Appendix F**).

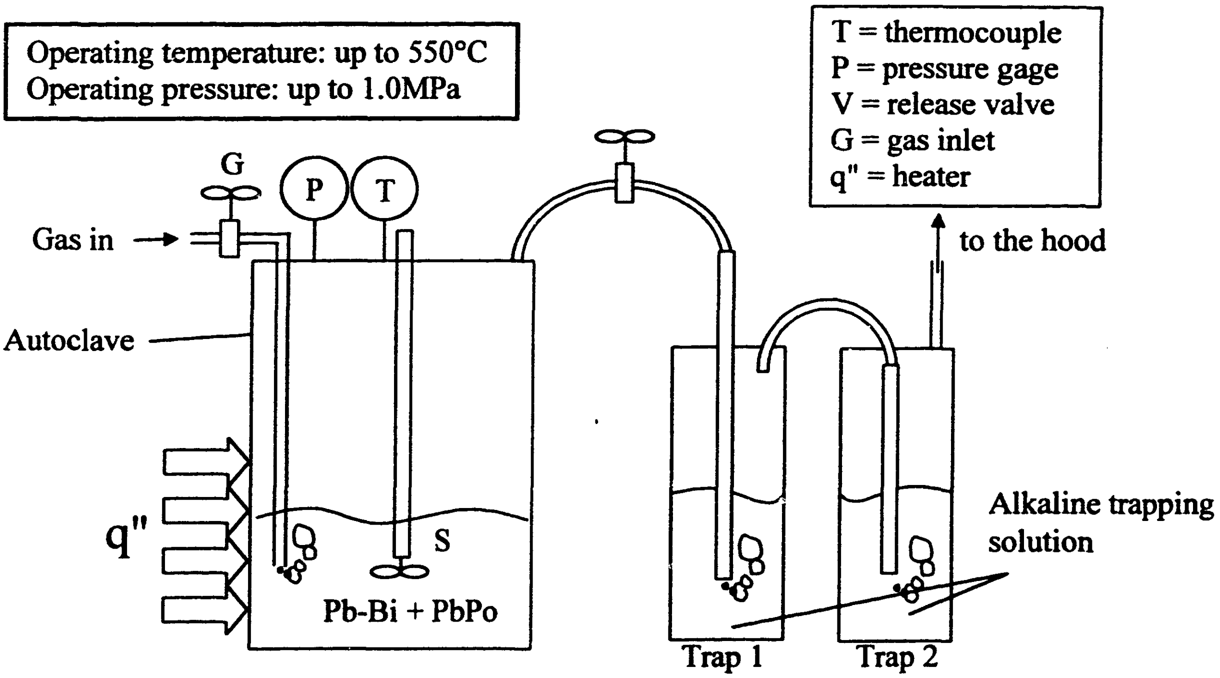

Figure 7.1. Schematic of the polonium experimental apparatus.

7.2.1.1 The Autoclave

The autoclave was supplied by Parr Instrument Company of Moline IL. It is a Parr model 4576-FG-GP-SS-115-VS 12-2000-4842 of 2.5"ID (63.5mm), 3.25"IL (82.55mm) and 250ml nominal capacity vessel rated for use at up to 4000psi (27.58MPa) at 550°C [2]. The autoclave head, the cylinder, the internal wetted parts and the external fittings are made of T316 stainless steel. The autoclave is equipped with a magnetic stirrer (also made of T316SS) of 16 in-lb torque with gas entrainment impeller (see **Figure 7.3**) and removable baffles. The stirrer is driven by a 1/8hp motor with speed control (0-1500rpm) and ensures mixing of the Pb-Bi melt as well as

---

[2] prior to shipping, the autoclave was tested by Parr at high pressure and temperature and received the ASME certification for pressure vessels.

recirculation of the cover gases through the Pb-Bi melt. The stirrer is connected to the electric motor by an arm and a magnetic drive (see **Figure 7.2** and **7.4**), which needs to be water cooled when the autoclave is operated above 100°C. The autoclave head (see **Figure 7.3** and **7.4**) accommodates: (i) the gas inlet with valve and dip tube, (ii) the pressure gage, (iii) the inconel safety rupture disc, (iv) two vertical connections (one 1/4"NPTF fitting and one 1/16"NPTF fitting) for additional instrumentation (as needed), (v) gas release port to the traps, (vi) thermowell with Type-J thermocouple and (vii) the stirrer. Head/cylinder sealing is provided by a gasket made of flexible graphite. The heat is supplied by a 1500W, 115V electric heater. The heater and the stirrer are controlled by a PID temperature/speed controller (model 4842) with extended length cables (5ft) (see **Figure 7.5**). The heater is equipped with a lateral cavity accommodating a High Temperature Limit bayonet thermocouple (HTL) that measures the temperature on the outer surface of the autoclave (i.e. the autoclave maximum temperature). The HTL is used as a safety system: if its reading exceeds a threshold set point the heaters are held off until the temperature falls back below the threshold value. This prevents the development of excessive thermal stresses in the autoclave shell as well as a local reduction of the vessel strength due to high temperature.

This polonium experiment deals with chemically and radiologically toxic substances like molten lead and polonium, respectively. To prevent uncontrolled release of these species that would cause poisoning and/or contamination of the people involved with the experiment, it is necessary to thoroughly test for leaks the autoclaves with their valves and connections. For this purpose, prior to the insertion of the heavy metals, the autoclave was first pressurized with argon gas at about 2.0MPa and 450°C. After ten hours the pressure did not appreciably change indicating a good sealing of the autoclave. Also, simulations of the experimental procedures were undertaken with (non-radioactive) molten lead prior to the actual experiments.

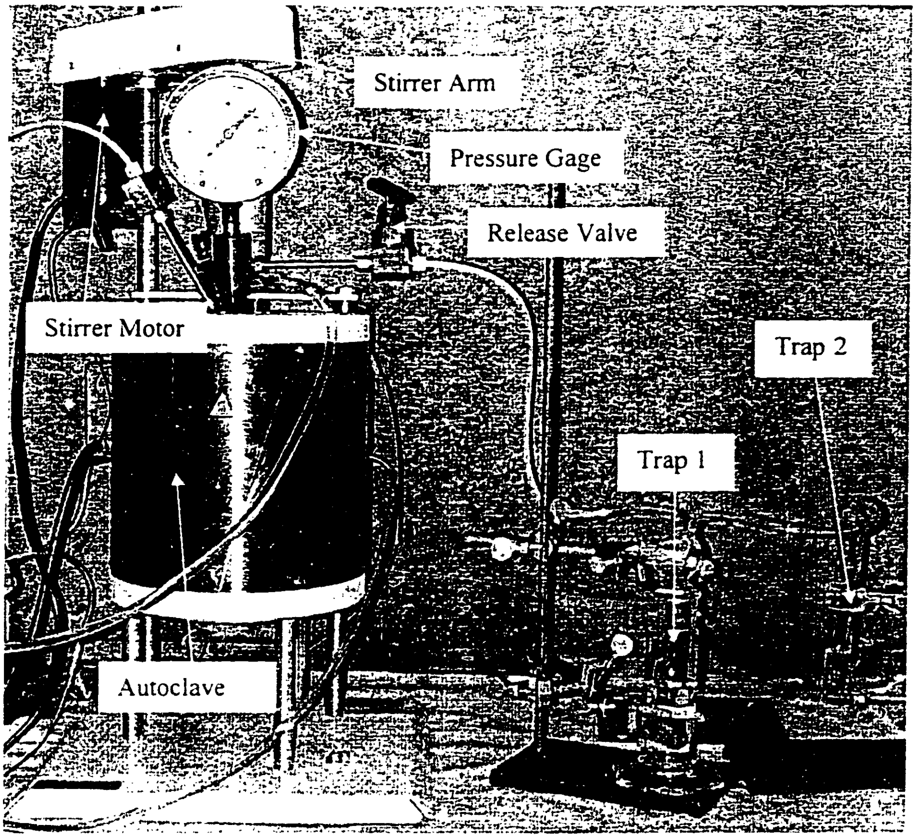

Figure 7.2. Overview of the experimental apparatus.

7.2.1.2 The Traps

The gases released from the autoclave are bubbled through two polonium traps in series. Trapping is provided by an alkaline aqueous solution of 0.1N NaOH. It is demonstrated in **Appendix F** that this kind of solution exhibits a trapping efficiency of the volatile polonium hydride of at least 99.8%. To maximize the interfacial area between the gases and the trapping solution, gas washing bottles with fritted spargers are employed (**Figure 7.6**) of capacity ranging from 125 to 250ml. The hydraulic connections between the autoclave and the traps are made of 1/4"OD nylon tubing.

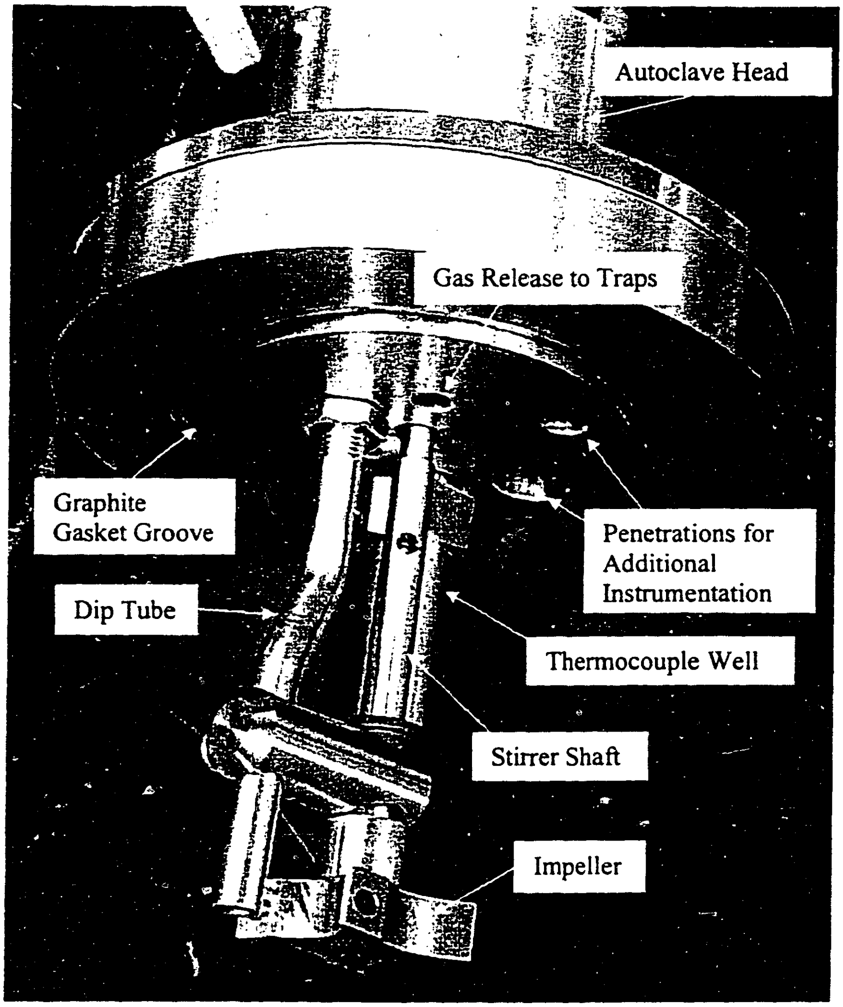

Figure 7.3. Penetrations of the autoclave head.

7.2.1.3 The Gases

For the PbPo experiments, a tank of 99.97% argon gas was used with a standard 1.4MPa N_2 regulator. For hydrogen control in the polonium hydride experiments, a tank of argon containing 1000ppm H_2 was used with a 0.4MPa hydrogen regulator. The concentration of oxygen was rated to be <2ppm. Both gas tanks were supplied by BOC Gases. The steam for the polonium hydride experiments was generated in a separate autoclave from de-ionized water through which the H_2/Ar mixture was bubbled for 10 minutes to scavenge the oxygen.

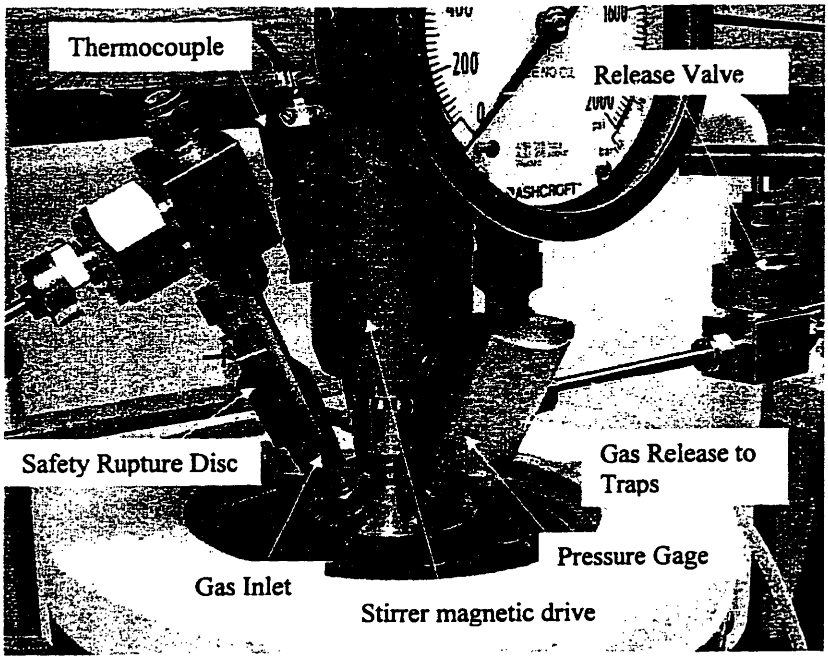

Figure 7.4. The autoclave head.

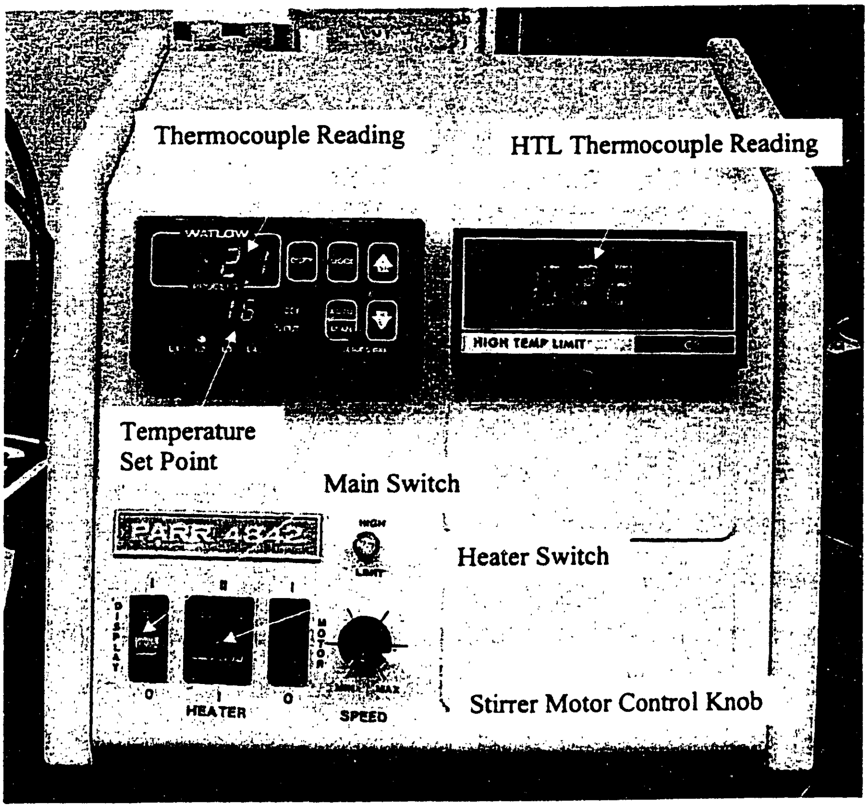

Figure 7.5. The temperature controller.

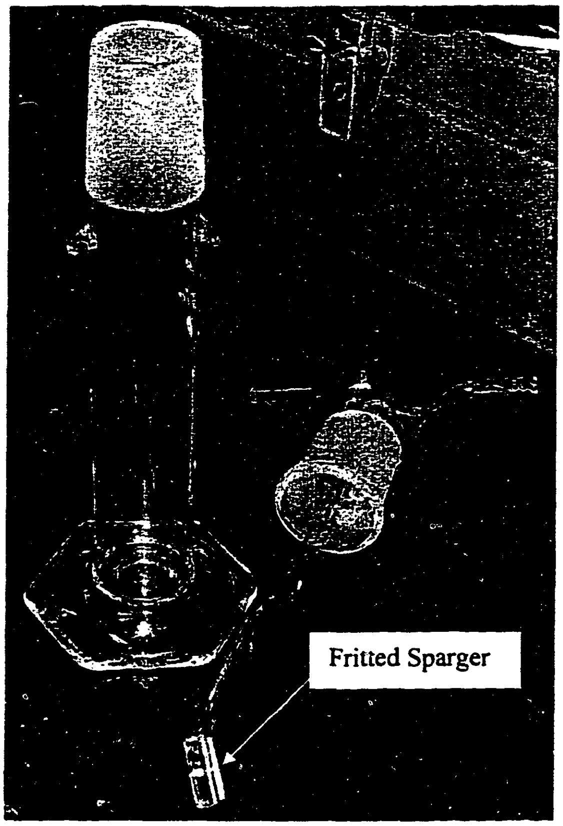

Figure 7.6. The gas washing bottle for the trapping solution.

7.2.2 The Pb-Bi Bath

The mass of the Pb-Bi eutectic melt in the autoclave is 500g of which 275g is 99.99% bismuth (supplier Sidech SA, Belgium) and 225g is 99.9% lead (supplier Alfa Aeser, USA). The polonium was produced by irradiation of bismuth samples in the high neutron flux channel of the MIT nuclear reactor. The irradiation and related measurements are described in detail in **Appendix G**. The polonium specific activity of the Pb-Bi melt is illustrated in **Figure G.3**, which is reported also here for convenience.

Although the nominal volume of the autoclave is 250ml, the actual volume was measured by Parr [Parr 2000] to be 282ml. The presence of the stirrer shaft, the impeller, the thermowell and the dip tube reduce the free volume of the autoclave to 271ml [Parr 2000]. Considering that approximately 50ml are occupied by the Pb-Bi melt, the net volume available to the gases is about 221ml.

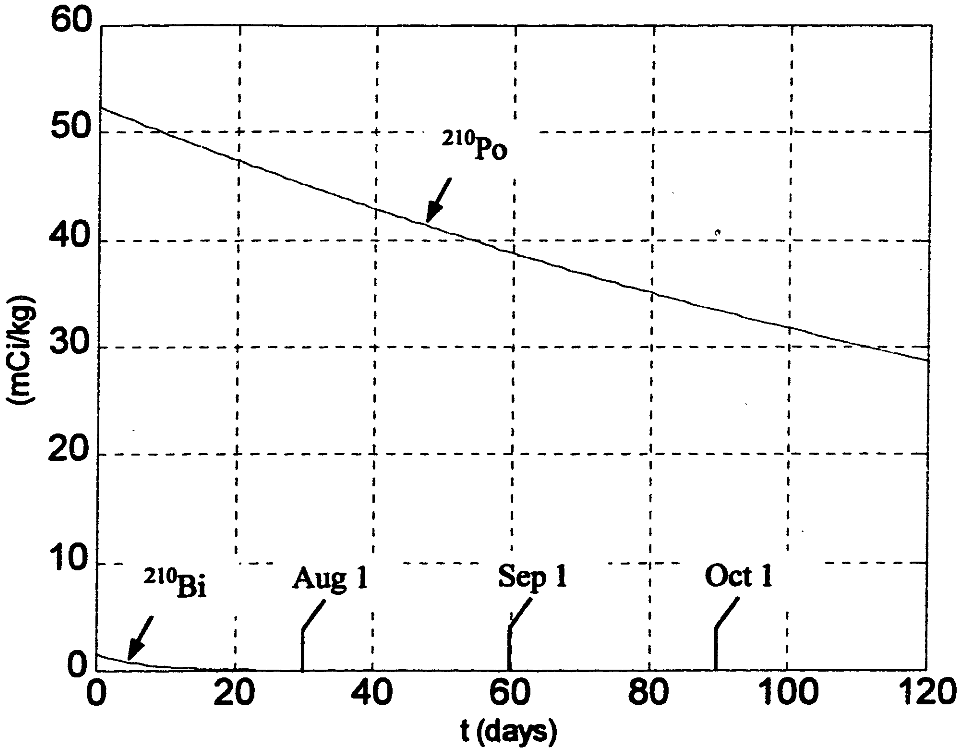

Figure G.3. Specific radioactivity of the Pb-Bi melt.

7.3 Measurements of the Lead-Polonide Vapor Pressure

The first set of experiments aims at the determination of the vapor pressure of the stable compound lead-polonide (PbPo) at relatively low temperatures (<550°C). Note that a PbPo vapor pressure correlation already exists in the literature, i.e. the Abakumov correlation [Abakumov 1974], **Eq.6.3**. This correlation was developed on the basis of data at high temperature (>640°C). In this study the Abakumov correlation is extrapolated to the temperature range of interest to the PBWR application and used to assess the plausibility of our experimental approach.

A typical run for the measurement of the PbPo vapor pressure at a given temperature consists of the following operations:

1. The autoclave is heated up to the specified temperature.
2. The autoclave is pressurized at about 1.0MPa with argon gas.
3. The stirrer is activated.
4. While the stirrer is on, the release valve is opened to discharge the gas into the traps.

5. The alpha-activity of the traps is counted.

The alpha-activity in the traps can be related to the PbPo vapor pressure by modeling the gas release during the depressurization that follows the opening of the release valve (step 4 above). The pressure variation dP corresponding to an amount of gas dN flowing out of the autoclave, is given by the following relation:

$$dP = \frac{RT}{V} dN \qquad \textbf{Eq.7.1}$$

where the gas mixture above the Pb-Bi bath (Ar + PbPo) is considered ideal[3]. R is the gas constant (8.31J/mol·K), V is the volume occupied by the gases in the autoclave and T is the specified temperature. Indicating by x'_{PbPo} the molar fraction of PbPo in the gas mixture, the number of PbPo moles flowing out of the autoclave, dN_{PbPo}, is:

$$dN_{PbPo} = x'_{PbPo} dN = x'_{PbPo} \frac{V}{RT} dP \qquad \textbf{Eq.7.2}$$

where x'_{PbPo} can be calculated as:

$$x'_{PbPo} = \frac{P'_{PbPo}}{P} \qquad \textbf{Eq.7.3}$$

The PbPo partial pressure above the Pb-Bi bath, P'_{PbPo}, can be evaluated from Rault's law as:

$$P'_{PbPo} = x_{PbPo} P_{PbPo}(T) \qquad \textbf{Eq.7.4}$$

where x_{PbPo} is the PbPo molar fraction in the Pb-Bi bath and P_{PbPo} is the PbPo vapor pressure, which depends only on the temperature T. Combining **Eq.7.2** through 7.4, one gets:

$$dN_{PbPo} = x_{PbPo} P_{PbPo}(T) \frac{V}{RT} \frac{dP}{P} \qquad \textbf{Eq.7.5}$$

Integrating **Eq.7.5** and solving for $P_{PbPo}(T)$ yields:

$$P_{PbPo}(T) = \frac{RT}{V} \frac{N_{PbPo}}{x_{PbPo}} \frac{1}{\log\left(\frac{P_i}{P_f}\right)} \qquad \textbf{Eq.7.6}$$

where P_i and P_f are the autoclave pressure before and after the gas release, respectively.

The total alpha-activity in the traps, Λ_{PbPo}, is given by:

---

[3] Note that because no water or hydrogen is present in this set of experimental runs, PbPo is the only expected form of polonium in the gas.

$$\Lambda_{PbPo} = \lambda_{dec} N_{av} N_{PbPo}$$ **Eq.7.7**

where λ_{dec} is the decay constant of ^{210}Po and N_{av} is the Avogadro's number.

Assuming that all polonium in the Pb-Bi bath exists as PbPo, the specific alpha-activity of the Pb-Bi bath C_{Po} (Bq/kg) can be calculated as:

$$C_{Po} = \lambda_{dec} N_{av} \frac{x_{PbPo}}{A_{PbBi}}$$ **Eq.7.8**

where A_{PbBi} is the average atomic weight of Pb-Bi (i.e. 0.208kg/mol). Solving **Eq.7.7** and **7.8** for N_{PbPo} and x_{PbPo}, respectively and substituting in **Eq.7.6**, one finally gets:

$$P_{PbPo}(T) = \frac{RT}{V} \frac{\Lambda_{PbPo}}{A_{PbBi} C_{Po}} \frac{1}{\log\left(\frac{P_i}{P_f}\right)}$$ **Eq.7.9**

Eq.7.9 enables calculation of $P_{PbPo}(T)$ from the knowledge of Λ_{PbPo}, which is measured by alpha-counting of the trap solution. Note that in **Eq.7.9** T is specified, V is known (221ml), C_{Po} is known from **Figure G.3** and P_i and P_f are read from the pressure gage.

A key assumption in deriving **Eq.7.9** is the applicability of Rault's law to estimate the partial pressure of PbPo in the gas mixture. This assumption holds only if the PbPo in the gas mixture is in equilibrium with the PbPo in the Pb-Bi bath at all times during the gas release. To ensure the validity of this assumption, the gas release to the traps is performed very slowly, i.e. at a rate of about 1.0MPa per hour. Moreover, the stirrer is activated prior to and during the gas release. The stirrer vigorously mixes the Pb-Bi melt and also recirculates the gases through the Pb-Bi melt, hence promoting equilibrium.

Also, **Eq.7.9** assumes that all polonium released from the autoclave is captured in the traps. To assess the validity of this assumption, the inner surface of the trap bottles and the inner surface of the tubing connecting the autoclave to the traps were extensively wiped with 1.5" paper discs. Counting of these paper discs with the alpha-spectrometer showed that polonium deposition does not occur other than in the trapping solution.

The PbPo experiments consist of 15 runs. The parameters and results from each run are reported in **Table 7.1**, where the runs are listed in chronological order. $\Lambda_{PbPo,1}$ and $\Lambda_{PbPo,2}$ are the alpha-activity of trap 1 and 2, respectively, i.e. $\Lambda_{PbPo}=\Lambda_{PbPo,1}+\Lambda_{PbPo,2}$. Both alpha-counting techniques (alpha-spectrometer and liquid scintillation) were utilized to measure the activity of the traps. However, only the values obtained with the alpha-spectrometer are reported in **Table 7.1** because in this set of experimental runs the activities of the 1ml samples extracted from the traps were mostly below the lower limit of detection of the RPO liquid scintillator (see **Appendix I**).

In **Table 7.1** the values of the PbPo vapor pressure predicted by the Abakumov correlation (**Eq.6.3**) are also reported for comparison. The discrepancy (rightmost column) is defined as the relative difference between the prediction of the Abakumov correlation and that of the present study.

Table 7.1. The experimental runs for the measurement of the PbPo vapor pressure.

Run #	T (°C)	C_{Po} (mCi/kg)	P_i (MPa)	P_f (MPa)	$\Lambda_{PbPo,1}$* (Bq)	$\Lambda_{PbPo,2}$* (Bq)	P_{PbPo} ** (Pa)	P_{PbPo} $^+$ (Pa)	Discr. (±%)
1	495	51	1.0	0.2	13.40	0.44	0.63	0.390	61
2	400	48	0.95	0.2	0.56	0.08	0.03	0.018	55
3	445	48	0.95	0.2	2.68	0.27	0.14	0.086	61
4	500	48	1.0	0.2	16.70	0.34	0.83	0.452	84
5	540	48	1.05	0.2	52.85	1.70	2.72	1.312	107
6	440	47	1.0	0.2	2.27	0.23	0.11	0.073	57
7	465	47	1.0	0.2	6.79	0.71	0.36	0.162	121
8	515	47	1.0	0.2	23.86	1.41	1.28	0.682	88
9	550	47	1.0	0.2	21.90	2.07	1.27	1.684	-24
10	392	46	1.0	0.2	0.11	0.0	0.004	0.013	-64
11	495	46	0.95	0.2	4.07	0.02	0.21	0.392	-46
12	497	46	1.0	0.2	5.20	0.26	0.28	0.415	-33
13	400	45	1.0	0.2	0.14	0.0	0.006	0.018	-63
14	497	45	0.9	0.2	3.20	0.20	0.19	0.415	-54
15	495	45	1.0	0.2	1.68	0.19	0.10	0.392	-75

* Obtained by electroplating and counting of 0.1ml of trapping solution in the alpha-spectrometer.

** Calculated from **Eq.7.9**.

$^+$ Calculated from **Eq.6.3**.

Although, as expected, the alpha-activity in Trap 1 is consistently larger than in Trap 2, the alpha-activity of Trap 2 is not entirely negligible, which indicates that the trapping efficiency in this set of experiments is not as high as predicted in **Appendix F**. This can probably be explained by the fact that, while the traps are chemically designed for optimal retention of the polonium hydride, in this set of experiments the chemical species of interest is PbPo, which is much more stable and thus more difficult to trap.

The data of **Table 7.1** are also illustrated in **Figure 7.7** along with the predictions generated by the Abakumov correlation. The statistical deviation (calculated as the inverse of the square root of the counts) ranges up to ±25%. It can be seen that our data are significantly scattered about the correlation curve but the temperature dependence is well reproduced. These results indicate the reliability of the experimental approach adopted in this study and confirm the validity of the Abakumov correlation at temperatures lower than those it was developed for.

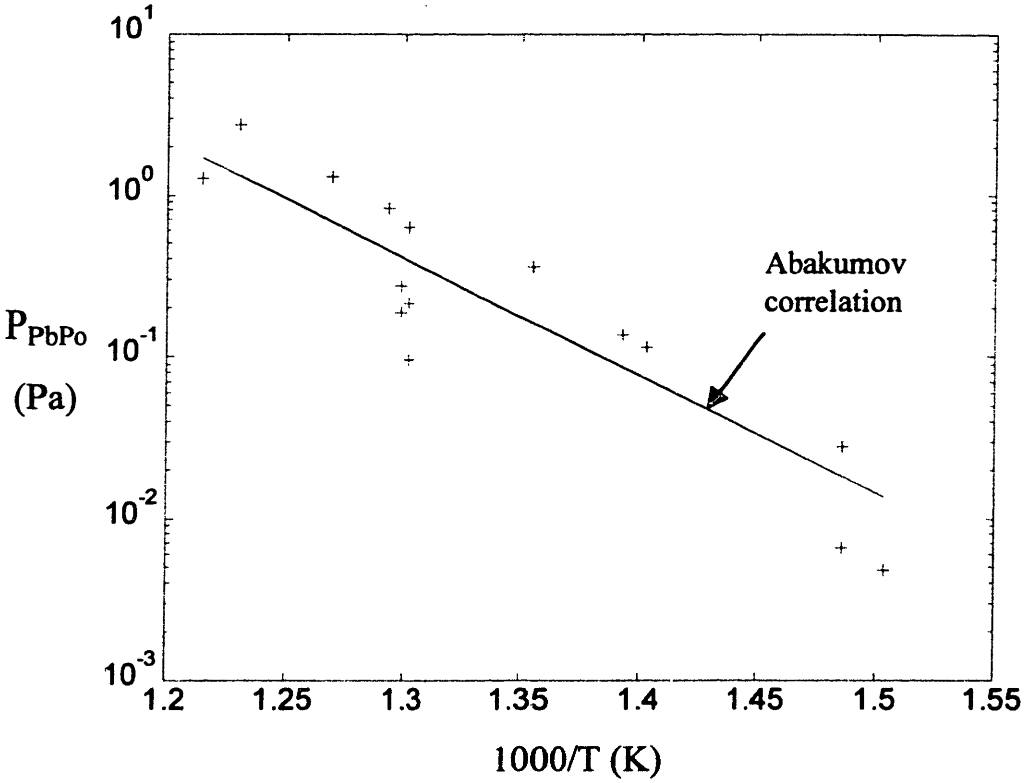

Figure 7.7. The PbPo vapor pressure.

7.4 Investigation of the Polonium Hydride Chemistry

The second set of experiments aims to investigate the chemistry of the polonium hydride formation reaction:

$PbPo_{(sol)}+H_2O_{(g)} \leftrightarrow H_2Po_{(g)}+PbO_{(sol)}$ **Eq.7.10**

where the subscripts (sol) and (g) stand for 'in solution' and 'gaseous', respectively. In particular, it is desired to evaluate the free-energy variation of this reaction as a function of temperature. A typical experimental run consists in the following operations:

1. The autoclave is heated up to the specified temperature.

2. The autoclave is pressurized at about 1.0MPa with known partial pressures of argon, hydrogen and steam.
3. The stirrer is activated.
4. While the stirrer is on, the release valve is opened to discharge the gas into the traps.
5. The alpha-activity of the traps is counted.

The alpha-activity in the traps can be related to the free-energy variation of **Eq.7.10** by modeling the gas release during the depressurization that follows the opening of the release valve (step 4 above) in a way somewhat similar to that of **Section 7.3**. The pressure variation dP corresponding to an amount of gas dN flowing out of the autoclave, is given again by **Eq.7.1.** Indicating by x'_{H2Po} the molar fraction of H_2Po in the gas mixture, the number of H_2Po moles flowing out of the autoclave, dN_{H2Po}, is:

$$dN_{H2Po} = x'_{H2Po} dN = x'_{H2Po} \frac{V}{RT} dP \qquad \textbf{Eq.7.11}$$

where x'_{H2Po} can be calculated as:

$$x'_{H2Po} = \frac{P'_{H2Po}}{P} \qquad \textbf{Eq.7.12}$$

In **Eq.7.12**, P'_{H2Po} is the H_2Po partial pressure above the Pb-Bi bath. Substituting **Eq.7.12** in **7.11**, one gets:

$$dN_{H2Po} = \frac{P'_{H2Po}}{P} \frac{V}{RT} dP \qquad \textbf{Eq.7.13}$$

An expression for the polonium hydride partial pressure in the gas mixture above the Pb-Bi melt can be derived by considering the equilibrium constant of **Eq.7.10**, k_1:

$$k_1 = e^{-\frac{\Delta G_1(T)}{RT}} = \frac{P'_{H2Po} a_{PbO}}{C_{PbPo} P'_{H2O}} \qquad \textbf{Eq.7.14}$$

where $\Delta G_1(T)$ is the unknown free-energy variation of the reaction, P'_{H2O} is the steam partial, a_{PbO} is the chemical activity of PbO in the Pb-Bi melt and C_{PbPo} is the concentration of PbPo in the Pb-Bi melt (mol_{PbPo}/kg_{PbBi}). Note that with this definition of the reaction equilibrium constant, the reference state for the lead-polonide PbPo is one for which C_{PbPo}=1mol/kg.

Let us know consider the following chemical equilibrium:

$$Pb + H_2O_{(g)} \leftrightarrow H_{2(g)} + PbO_{(sol)} \qquad \textbf{Eq.7.15}$$

The corresponding equilibrium constant, k_2, is:

$$k_2 = e^{-\frac{\Delta G_2(T)}{RT}} = \frac{a_{PbO}P'_{H2}}{a_{Pb}P'_{H2O}} = \frac{a_{PbO}P'_{H2}}{P'_{H2O}}$$ **Eq.7.16**

where the activity of lead was set equal to one. P'_{H2} is the partial pressure of hydrogen in the gas mixture above the Pb-Bi. $\Delta G_2(T)$ is the free-energy variation of **Eq.7.15** that can be readily derived from the thermodynamic properties of lead, lead-oxide, water and hydrogen (see, for example, [Li 1999]):

$\Delta G_2(T)=24.9+0.047T$ **Eq.7.17**

where $\Delta G_2(T)$ is in kJ/mol and T is in K.

Eliminating a_{PbO} from **Eq.7.14** and **7.16** and solving for P'_{H2Po}, one gets:

$$P'_{H2Po} = C_{PbPo}P'_{H2}e^{\frac{\Delta G_2-\Delta G_1}{RT}}$$ **Eq.7.18**

Substituting **Eq.7.18** in **7.13**:

$$dN_{H2Po} = C_{PbPo}\frac{P'_{H2}}{P}e^{\frac{\Delta G_2-\Delta G_1}{RT}}\frac{V}{RT}dP$$ **Eq.7.19**

The ratio $\frac{P'_{H2}}{P}$ is the molar fraction of hydrogen in the mixture gas, x_{H2}, which is known and remains constant during the depressurization because hydrogen flows out of the autoclave along with the other gases. Therefore **Eq.7.19** can be readily integrated to yield:

$$N_{H2Po} = C_{PbPo}x_{H2}e^{\frac{\Delta G_2-\Delta G_1}{RT}}\frac{V}{RT}(P_i - P_f)$$ **Eq.7.20**

where the same nomenclature of **Eq.7.6** is adopted. Solving **Eq.7.20** for ΔG_1 yields:

$$\Delta G_1 = \Delta G_2 - RT\log\left[\frac{RT}{V}\frac{N_{H2Po}}{C_{PbPo}x_{H2}(P_i - P_f)}\right]$$ **Eq.7.21**

The alpha-activity in the traps due to the polonium hydride, Λ_{H2Po}, is by definition:

$$\Lambda_{H2Po} = \lambda_{dec}N_{av}N_{H2Po}$$ **Eq.7.22**

Assuming that all polonium in the Pb-Bi bath exists as PbPo, the specific alpha-activity of the Pb-Bi bath, C_{Po}, can be calculated as:

$$C_{Po} = \lambda_{dec}N_{av}C_{PbPo}$$ **Eq.7.23**

Solving **Eq.7.22** and **7.23** for N_{H2Po} and C_{PbPo}, respectively and substituting in **Eq.7.21**, one finally gets:

$$\Delta G_1 = \Delta G_2 - RT\log\left[\frac{RT}{V}\frac{\Lambda_{H2Po}}{C_{Po}x_{H2}(P_i - P_f)}\right] \qquad \textbf{Eq.7.24}$$

Note that in this equation T is specified, ΔG_2 and V are known, C_{Po} is known from **Figure G.3**, x_{H2} is evaluated from the knowledge of the initial argon, steam and hydrogen partial pressures and P_i and P_f are read from the pressure gage. Therefore **Eq.7.24** enables calculation of $\Delta G_1(T)$ from the knowledge of Λ_{H2Po}. Note that in this set of experiments the total alpha-activity of the trap (which is the only quantity actually measured) is given by the sum of two contributions due to the polonium hydride and the lead-polonide, respectively. Therefore, Λ_{H2Po} can be calculated by subtracting the PbPo contribution (obtained by solving **Eq.7.9** for Λ_{PbPo} and using the Abakumov correlation for $P_{PbPo}(T)$) from the measured total alpha-activity of the trap solution.

A key assumption of the derivation above is the applicability of **Eq.7.18** to estimate the partial pressure of H_2Po in the gas mixture. This assumption holds only if the chemical equilibria of the reactions of **Eq.7.10** and **7.15** exist in the autoclave. To ensure the validity of this assumption, the gas release to the traps is performed very slowly, i.e. at a rate of about 1.0MPa per hour. Moreover, the stirrer is activated prior to and during the gas release. The stirrer vigorously mixes the Pb-Bi melt and also recirculates the gases through the Pb-Bi melt, hence promoting equilibrium.

The H_2Po experiments consist of 19 runs. The parameters and results from each run are reported in **Table 7.2**, where the runs are listed in chronological order. $\Lambda_{Po,1}$ and $\Lambda_{Po,2}$ are the total alpha-activity of Trap 1 and 2, respectively. The alpha-activity of Trap 1 was measured with the liquid scintillator and that of Trap 2 with the alpha-spectrometer. Λ_{H2Po} is the net polonium hydride contribution to the activity and ΔG_1 is calculated from **Eq.7.24**.

Note that the alpha-activities are generally larger than those in **Table 7.1**, suggesting the presence of a new channel of polonium release in addition to PbPo evaporation. To verify that this additional mechanism of polonium release is in fact the formation of the volatile H_2Po and not the steam-assisted transport of polonium contaminated lead aerosols, samples from Trap 1 were searched for lead with a ICP plasma spectrometer[4]. No traces of lead could be found, i.e. the concentration of lead was below the background of the plasma spectrometer (i.e. <5μM).

---

[4] For a brief description of the ICP plasma spectrometer, see **Section F.4**.

Also, the alpha-activity of Trap 1 is consistently much larger than that of Trap 2, which confirms the excellent H_2Po trapping characteristics of the 0.1M NaOH solution.

Table 7.2. The experimental runs for the measurement of the H_2Po formation reaction free-energy variation.

Run #	T (°C)	C_{Po} (mCi/kg)	x_{H2} (10^{-4})	P_i (MPa)	P_f (MPa)	$\Lambda_{Po,1}$ (Bq)	$\Lambda_{Po,2}$ (Bq)	Λ_{H2Po}* (Bq)	ΔG_1 (kJ/mol)
1	260	43	5.0	0.8	0.1	32.0	0.60	32.6	79.8
2	346	43	4.7	0.85	0.1	48.5	0.48	48.9	85.9
3	385	43	5.3	0.75	0.1	6.0	0.45	6.2	100.6
4	444	43	3.6	1.1	0.1	27.5	0.19	25.2	98.7
5	300	42	4.0	1.0	0.1	21.5	0.16	21.6	85.6
6	290	42	4.0	1.0	0.1	7.5	0.38	7.8	89.3
7	305	42	4.0	0.6	0.1	10.0	0.32	10.3	89.3
8	387	42	6.7	1.0	0.1	22.7	0.16	22.5	93.8
9	405	42	4.0	1.0	0.1	24.5	0.25	24.1	95.1
10	400	42	4.0	1.0	0.1	17.0	0.86	17.3	96.5
11	395	42	4.0	1.0	0.1	11.0	0.22	10.8	98.7
12	487	41	4.0	1.0	0.1	15.5	0.19	7.8	109.9
13	490	41	4.0	1.0	0.1	10.5	0.35	2.2	118.2
14	497	41	4.0	1.0	0.1	22.5	0.16	12.2	108.1
15	550	41	4.0	1.0	0.1	42.8	0.32	3.6	121.8
16	203	40	3.3	1.2	0.1	35.5	0.45	35.9	73.9
17	195	40	4.4	0.9	0.1	8.0	0.25	8.2	78.7
18	200	40	2.5	0.8	0.1	19.3	0.22	19.5	73.1
19	200	40	3.6	1.1	0.1	10.5	0.35	10.8	78.3

*$\Lambda_{H2Po} \equiv \Lambda_{Po,1}+\Lambda_{Po,2}-\Lambda_{PbPo}$

The free-energy data of **Table 7.2** are plotted in **Figure 7.8** along with ΔG_2 from **Eq.7.17.** The statistical deviation of the experimental points ranges up to ±3%. The data are fitted (in a least mean-square sense) by the following curve:

$\Delta G_1(T)=\Delta H_1-T\Delta S_1=17.34+0.121T$ **Eq.7.25**

where T is in K and the coefficients $\Delta H_1=17.34$kJ/mol and $\Delta S_1=0.121$J/mol·K represent the enthalpy and entropy variation of **Eq.7.10**, respectively. From **Figure 7.8** it can be seen that within the temperature range 450-850K (180-580°C), **Eq.7.25** reproduces the experimental data with an accuracy of ±10%.

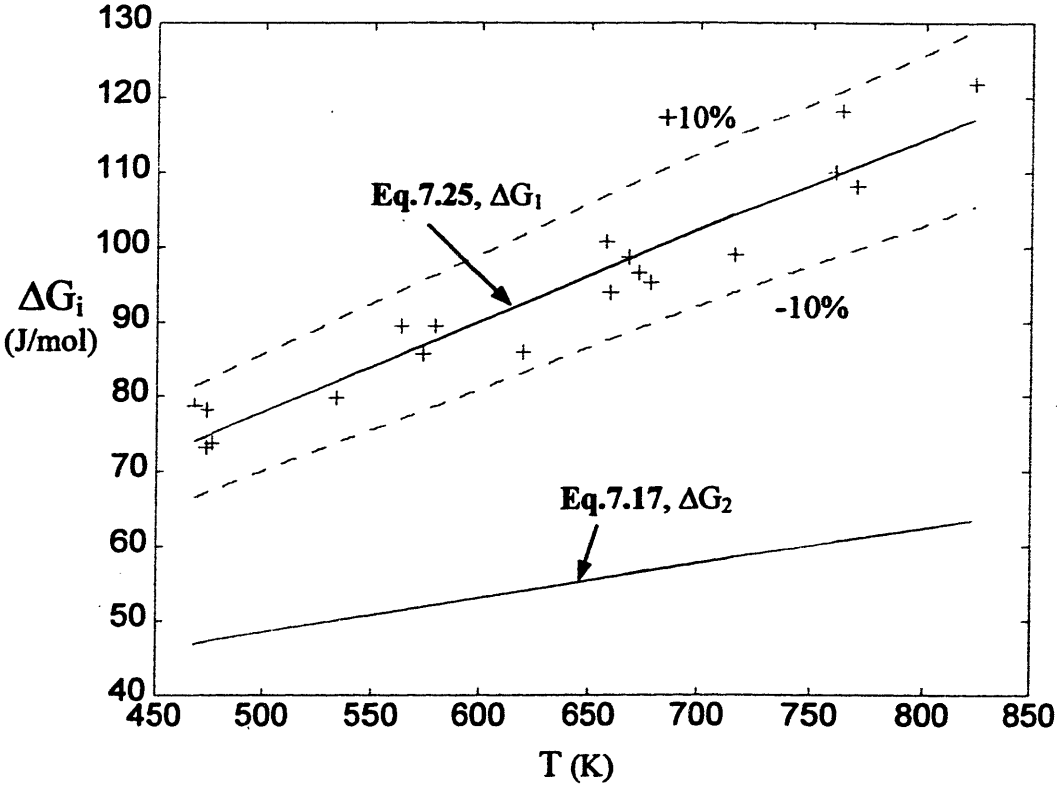

Figure 7.8. Free-energy variation of the polonium hydride formation reaction.

Because $\Delta H_1 > 0$, the polonium hydride formation reaction appears to be endothermic. Moreover, because ΔG_1 increases with temperature, the reaction favorably proceeds at low temperatures. Note also that $\Delta G_1 > \Delta G_2$, which indicates that **Eq.7.10** is thermodynamically less favored than **Eq.7.15**, an indirect confirmation of the polonium hydride chemical instability. In combination with **Eq.7.14**, **Eq.7.25** enables calculation of the polonium hydride equilibrium partial pressure in systems for which the temperature, hydrogen partial pressure and polonium concentration in the Pb-Bi melt are known (e.g. see **Chapter 6**). Again it should be emphasized that in **Eq.7.14** the units of C_{PbPo} are mol_{PbPo}/kg_{PbBi}.

7.5 Summary

An experimental campaign was undertaken at MIT to measure the characteristics of the polonium chemical compounds key to assessing alpha-activity release from an activated Pb-Bi bath upon contact with a gas stream. As a result, the vapor pressure of lead polonide was measured over the 400-550°C temperature range and found to be in good agreement with an existing correlation derived from data at higher temperatures. Also, it was experimentally confirmed that the presence of steam in the gas stream above the Pb-Bi melt substantially increases the amount of polonium released, which suggests the formation of the volatile compound H_2Po. The free-energy variation of the H_2Po formation reaction was estimated from the release data and a fitting curve that correlates the data within ±10% in the 180-580°C range was generated.

Chapter 8

- MATERIALS CORROSION IN THE PBWR -

8.1 Introduction

The selection of structural materials suitable for cladding and containment purposes is key to the development of all lead and lead-bismuth cooled nuclear systems and thus also of the PBWR concept presented in this study. Traditional austenitic stainless steels can be used at moderate temperatures only (up to 450°C). However, they are not suitable for the higher temperatures typical of fast reactor applications due to the large solubility of nickel in bismuth (see **Table 1.II**), which would cause rapid selective leaching of that alloying element from the steel matrix and consequent loss of strength and integrity of the structures. The possibility of employing low nickel martensitic/ferritic stainless steels was extensively studied in Russia [Adamov 1997, Gromov 1994] and currently in the US [Weeks 1998, Li 1999, Loewen 2000], Japan [Takahashi 2000] and Israel [Tsirlin 1999], as well. The Russian research program culminated with the development of a steel designated EP-823, which is claimed to be suitable for Pb-Bi applications at up to 600-650°C. The corrosion resistance of the low nickel steels relies on the formation of a protective iron oxide film that prevents rapid dissolution of the metallic substrate. The stability of this film depends on the oxygen concentration in the coolant: too little oxygen would result in a reducing environment that could dissolve the oxide. On the other hand, if the oxygen concentration is too large, the precipitation of oxide slag in the primary circuit could foul the heat transfer surfaces and/or clog the core channels. As a result, it is necessary to control the oxygen concentration in the Pb-Bi coolant within a relatively narrow range.

Because the EP-823 steel was selected as the PBWR interim reference structural material (**Section 2.2.4** and **2.3**), the objective of this chapter is to demonstrate the feasibility of tight oxygen control in a direct contact system where the Pb-Bi coolant is mixed with water.

8.2 Corrosion Mechanisms in Pb-Bi Cooled Systems

Before discussing the oxygen control strategy, it is important to gain some insight of the corrosion mechanisms of structural materials immersed in liquid Pb-Bi. To do so, let us first consider the primary system of a generic Pb-Bi cooled reactor and assume that (i) the Pb-Bi coolant and the structures are all at the same temperature, (ii) the surface of the structures is clean (i.e. no oxide film is present) and (iii) there is no oxygen in the Pb-Bi. If it is also assumed that the initial concentration of iron in the Pb-Bi coolant is zero, dissolution of the structures will proceed until the iron concentration in Pb-Bi equals the solubility limit at the given temperature. Then, the Pb-Bi is saturated with iron and no further corrosion can occur. The iron dissolution reaction is:

$Fe_{(s)} \rightarrow Fe_{(sol)}$ **Eq.8.1**

where the subscripts (s) and (sol) stand for 'solid' and 'in solution', respectively. The iron solubility in Pb-Bi, $c_{Fe,s}$, is given in [Li 1999] as:

$\mathrm{Log}(c_{Fe,s})=6.01-4380/T$ **Eq.8.2**

where Log is the 10 base logarithm, $c_{Fe,s}$ is in wt ppm and T in K. The iron solubility is also illustrated in **Figure 8.1**.

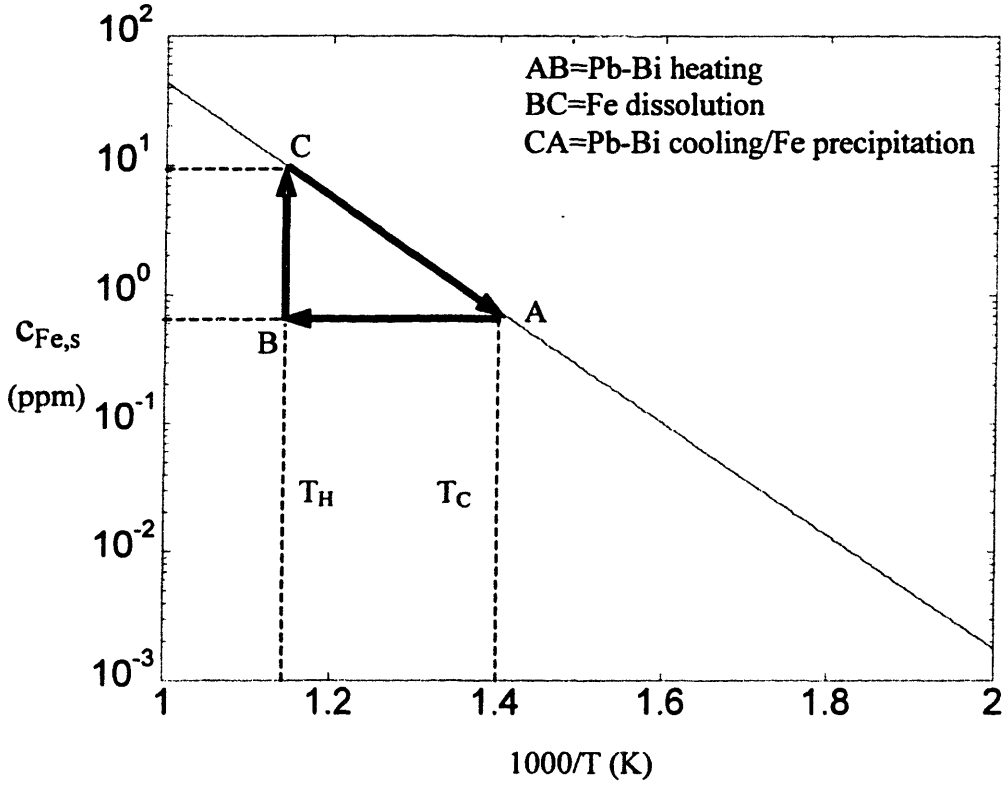

Figure 8.1. Iron solubility in Pb-Bi.

Let us now consider the same system, but allow for two temperature regions. We will call the corresponding cold and hot temperatures T_C and T_H, respectively. The assumptions of clean surfaces, no oxygen and no initial iron in the Pb-Bi are retained. In this case, structure dissolution proceeds throughout the entire system until the solubility limit corresponding to T_C is reached. Then further dissolution takes place only in the hot region (because the solubility limit at T_H is higher). However, when the hot iron-rich Pb-Bi is cooled down to T_C, the iron in excess of the solubility limit at T_C precipitates on the surfaces of the cold region structures. This mechanism effectively transfers mass from the hot to the cold region and may result in severe corrosion of the hot region structures. This process is also illustrated by the ABC loop of **Figure 8.1** for two reference temperatures 440 and 600°C [1], where it was assumed that iron dissolution in the hot region is rapid enough to reach the solubility limit at T_H. It can be seen that the corrosion driving force is the iron solubility difference between the hot and the cold regions, which can be evaluated from **Eq.8.2** or **Figure 8.1** as (10-0.7)ppm=9.3ppm (i.e. length of the BC arrow).

Let us now consider a third situation where oxygen is present in the Pb-Bi. Again it is assumed that there are two temperature regions, no pre-existing oxide on the surfaces and zero initial iron concentration in the Pb-Bi. In this case, iron dissolution by **Eq.8.1** proceeds in parallel with the following iron oxidation reaction at the structure surface:

$3Fe_{(s)}+4PbO_{(sol)} \rightarrow Fe_3O_{4(s)}+4Pb$ **Eq.8.3**

Note that oxygen in solution does not exist as O_2 or O, but mostly in the form of lead oxide. Depending on the local conditions (i.e. oxygen concentration in the Pb-Bi bulk, Pb-Bi velocity, temperature), a Fe_3O_4 film may form that completely segregates the iron substrate from the liquid Pb-Bi. If this happens and no iron is present in the Pb-Bi, the film cannot be stable and rapidly dissolves according to the following reaction:

$4Pb+Fe_3O_{4(s)} \rightarrow 3Fe_{(sol)}+4PbO_{(sol)}$ **Eq.8.4**

If on the other hand, the iron concentration in Pb-Bi was sufficiently large, the oxide film would be stable. As a result, dissolution of the iron substrate by **Eq.8.1** is greatly reduced due to the low diffusion rate of iron through the film (the diffusion coefficient of iron in Fe_3O_4 at 600°C is about $10^{-17}m^2/s$ [Samsonov 1982]). A schematic of the processes described by **Eq.8.3** and **8.4** is illustrated in **Figure 8.2**.

---

[1] These are the Pb-Bi core inlet temperature and clad peak temperature in the PBWR, respectively.

Therefore, it is very important to establish the conditions of stability of the oxide film. In particular, one should assess (a) the minimum amount of oxygen in solution to promote film formation and (b) the minimum amount of iron in solution to prevent film dissolution.

The equilibrium constant k_{film} of **Eq.8.3** (equal to the inverse of the equilibrium constant of **Eq.8.4**) is:

$$k_{film} = e^{-\frac{\Delta G_{film}(T)}{RT}} = \frac{a_{Fe3O4} a_{Pb}^{4}}{a_{Fe}^{3} a_{PbO}^{4}} \qquad \textbf{Eq.8.5}$$

where R is the gas constant (8.31J/molK), T is the system temperature (in K), a_{Fe3O4}, a_{Pb}, a_{Fe} and a_{PbO} are the chemical activities of Fe_3O_4, lead, iron and lead-oxide in solution, respectively and $\Delta G_{film}(T)$ is the free-energy variation of the reaction of **Eq.8.3**, given as:

$$\Delta G_{film}(T) = -225.6 - 0.143T \qquad \textbf{Eq.8.6}$$

where ΔG_{film} is in kJ/mol_{Fe3O4}.

Eq.8.6 was derived combining the free-energy variation of the following two reactions [Li 1999]:

$$3Fe_{(s)} + 2O_{2(g)} \leftrightarrow Fe_3O_{4(s)} \qquad \textbf{Eq.8.7}$$

$$Pb + \frac{1}{2}O_{(g)} \leftrightarrow PbO_{(sol)} \qquad \textbf{Eq.8.8}$$

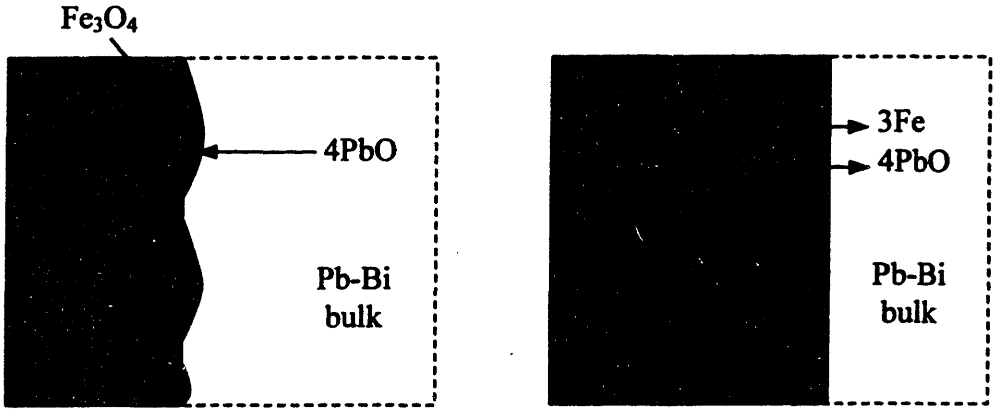

Film Formation (**Eq.8.3**)

Film Dissolution (**Eq.8.4**)

Figure 8.2. Oxide film dynamics.

In **Eq.8.5** the activity of iron in solution is defined as:

$$a_{Fe} \equiv \frac{c_{Fe}}{c_{Fe,s}} \qquad \textbf{Eq.8.9}$$

The activity of lead-oxide in solution is given by Henry's law as:

$$a_{PbO} = \frac{c_O}{c_{O,s}} \qquad \textbf{Eq.8.10}$$

where c_{Fe} and c_O are the iron and oxygen concentration, respectively. The iron and oxygen solubility in Pb-Bi, $c_{Fe,s}$ and $c_{O,s}$, are given by **Eq.8.2** and by the following equation [Li 1999], respectively:

$$\mathrm{Log}(c_{O,s}) = 5.2 - 3400/T \qquad \textbf{Eq.8.11}$$

where $c_{O,s}$ is in ppm.

In **Eq.8.5** the lead activity (a_{Pb}) can be always set equal to unity and so can the iron oxide activity (a_{Fe3O4}) provided that there exists at least a single crystal of iron oxide on the surface. While the film is forming on the surface, a_{Fe} can also be set equal to unity because the solid iron substrate is exposed to the Pb-Bi melt (thus at the surface is $c_{Fe}=c_{Fe,s}$). Then, the minimum oxygen concentration required to sustain the formation of the oxide film can be readily found from **Eq.8.5** as:

$$c_{O,\min} = c_{O,s} e^{\frac{\Delta G_1(T)}{4RT}} \qquad \textbf{Eq.8.12}$$

On the other hand, once the Fe_3O_4 film is formed, the iron substrate is segregated from the Pb-Bi coolant. Therefore, the chemical activity of iron cannot generally be set equal to unity, but depends on the value of the iron concentration in the Pb-Bi as per **Eq.8.9**. In fact, if it is assumed that the oxygen concentration is given, the equilibrium iron concentration $c_{Fe,\min}$ can be calculated from **Eq.8.5** as:

$$c_{Fe,\min} = c_{Fe,s} \frac{e^{\frac{\Delta G_{film}(T)}{3RT}}}{\left(c_O/c_{O,s}\right)^{4/3}} \qquad \textbf{Eq.8.13}$$

Note that, being the equilibrium iron concentration, $c_{Fe,\min}$ is indeed the minimum iron concentration required to stabilize the oxide film, i.e. if c_{Fe} near the film is lower than $c_{Fe,\min}$, dissolution of the film by **Eq.8.4** will proceed until $c_{Fe}=c_{Fe,\min}$.

Eq.8.12 and **8.13** can be compactly represented in a c_O vs. T diagram (with $c_{Fe,\min}$ as a parameter), as illustrated in **Figure 8.3**. At any given temperature there exists an upper acceptable limit to the amount of oxygen in solution, which corresponds to the precipitation of lead oxide by means of **Eq.8.8**. Formation of lead oxide slag in the coolant may foul the heat transfer surfaces or clog the core channels and thus should be prevented. This limit is, by definition, the oxygen solubility in Pb-Bi, $c_{O,s}$, of **Eq.8.10**, also plotted in **Figure 8.3**.

Figure 8.3 can be used to understand the corrosion mechanism in Pb-Bi systems with oxide films. Let us assume that the oxygen concentration is maintained at a given value. In an isothermal system, dissolution of the oxide film would stop when the iron concentration in the Pb-Bi reaches the value of $c_{Fe,min}$ corresponding to the given temperature and oxygen concentration. On the other hand, in a non-isothermal system the oxide film dissolves in the hot region because $c_{Fe}<c_{Fe,min}(T_H)$ and (ii) grows in the cold region because $c_{Fe}>c_{Fe,min}(T_C)$. This process is described by the ABA cycle of **Figure 8.3**. To prevent complete dissolution of the oxide film in the hot region, it must be ensured that the supply of oxygen (in the form of PbO) to the iron substrate is large enough, so that the oxide film can be continuously replenished. Note that under these circumstances, corrosion of the hot region structures occurs via reduction of the oxide film and not via direct iron dissolution (**Eq.8.1**), which is greatly mitigated by the presence of the oxide film. Therefore, the driving force for corrosion is the $c_{Fe,min}$ difference between the hot and the cold region. For example, for an oxygen concentration of about 0.4ppm and T_C and T_H equal to 440 and 600°C, respectively, this corrosion driving force can be estimated from **Eq.8.13** (or from **Figure 8.3**) to be approximately $(10^{-4}-10^{-7})\text{ppm}\approx10^{-4}\text{ppm}$. This value is about 5 orders of magnitude smaller than the corrosion driving force in a system with no protective oxide film (e.g. loop ABC in **Figure 8.1**), indicating that the presence of a stable oxide film enables a very significant reduction of the Pb-Bi induced corrosion.

Figure 8.3 also suggests that the corrosion driving force would further decrease if the oxygen concentration was maintained at an even larger value (cycle A'B'A'). However, care should be taken in preventing line A'B' from intersecting the $c_{O,s}$ curve hence causing PbO precipitation in the cold region (point A'). Therefore, in order to minimize corrosion without generating lead oxide slag, the oxygen concentration in the system should be kept slightly below the value of $c_{O,s}$ corresponding to the cold temperature T_C. For example, for T_C=440°C it can be calculated that c_O should be maintained below 2.7ppm. Assuming again T_H=600°C, the corresponding $c_{Fe,min}$ difference between the cold and the hot region would be then about 10^{-5}ppm, i.e. 6 orders of magnitude smaller than a system without protective oxide film.

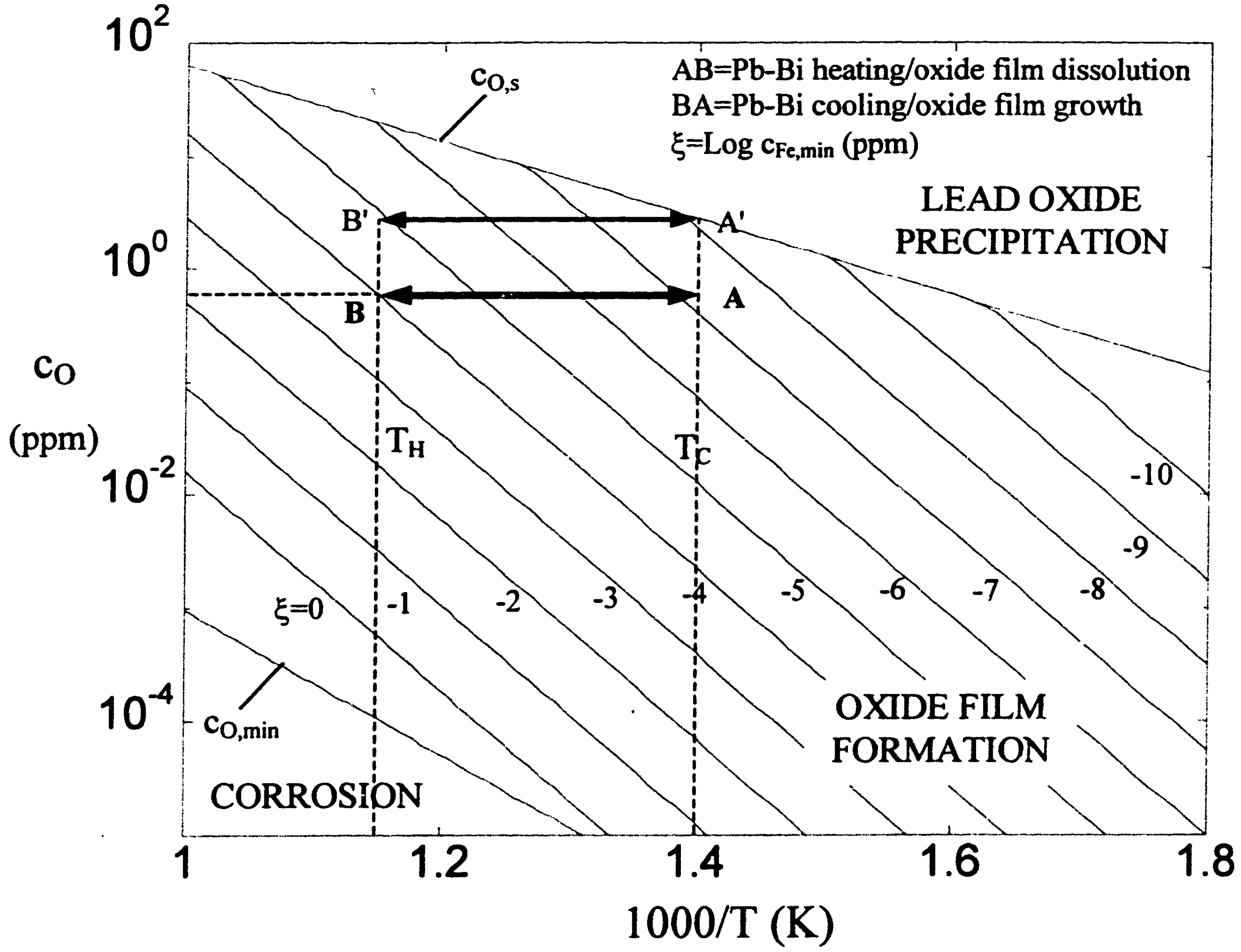

Figure 8.3. Corrosion map for a Pb-Bi system with oxygen.

The corrosion rate corresponding to this situation can be estimated as follows. If it is assumed that the iron concentration in Pb-Bi reaches $c_{Fe,min}$ in the hot region, the rate of iron release from the structures $\dot{m}_{Fe}$ can be calculated as:

$$\dot{m}_{Fe} = c_{Fe,\min}(T_H)\dot{M}_p \qquad \textbf{Eq.8.14}$$

where $\dot{M}_p$ is the Pb-Bi mass flow rate in the pool. Further, we conservatively assume that all this iron is released from the fuel clad. Then the clad thickness reduction δ_c due to corrosion can be readily evaluated as:

$$\delta_c = \frac{\dot{m}_{Fe}}{S_{clad}\rho_{Fe}} \qquad \textbf{Eq.8.15}$$

where S_{clad} and ρ_{Fe} are the clad total surface (2840m^2 for the PBWR core) and the iron density (about 7870kg/m^3), respectively. For reference PBWR values T_H=600°C and $\dot{M}_p$=81,110kg/s, **Eq.8.15** yields δ_c=1.1μm/yr=0.045mpy. Because the service time of the clad is equal to two refueling cycles (4.5yrs for the reference actinide burning fuel), the total loss of clad thickness due to corrosion is expected to be about 5μm, equal to 0.8% of the nominal clad thickness and thus thought to be acceptable.

It should be emphasized that this estimate is conservative because it assumes that dissolution of the oxide film proceeds until the iron concentration in the Pb-Bi bulk reaches $c_{Fe,min}$. However, in reality an iron concentration boundary layer forms that enables reaching $c_{Fe,min}$ in the Pb-Bi near the wall significantly before than in the bulk, hence rapidly arresting further iron oxide dissolution.

8.3 Oxygen Control

In the previous section we have demonstrated that if the oxygen concentration in the Pb-Bi is properly controlled, it is possible to reduce the corrosion of reactor materials by several orders of magnitude. In the PBWR system the most straightforward way to control the oxygen concentration in the Pb-Bi melt is to control the oxygen partial pressure in the steam dome. The following chemical equilibrium exists in the steam dome:

$H_{2(g)}+\frac{1}{2}O_{2(g)} \leftrightarrow H_2O_{(g)}$ **Eq.8.16**

where the subscript (g) stands for 'gaseous'.

The equilibrium constant of the above reaction is:

$$k_{H2O} = e^{-\frac{\Delta G_{H2O}(T)}{RT}} = \frac{P_{H2O}}{P_{H2}P_{O2}^{1/2}} \quad \textbf{Eq.8.17}$$

where P_{H2O}, P_{H2} and P_{O2} are the steam, hydrogen and oxygen partial pressures in the steam dome, respectively. The free-energy variation of this reaction is [Li 1999]:

$\Delta G_{H2O}(T)$=-245.57+0.054T **Eq.8.18**

where ΔG_{H2O} is in kJ/mol$_{H2O}$ and T in K.

It should be emphasized that the temperature of interest in **Eq.8.17** and **8.18** is not the steam bulk temperature (312°C at PBWR reference conditions), but the temperature at the steam/Pb-Bi interface, which was shown to be approximately equal to the Pb-Bi temperature (see T_i in **Section 3.6**). Therefore, in the following discussion it will be assumed that the oxygen in the Pb-Bi is in equilibrium with the oxygen partial pressure in the steam at this interfacial temperature (~440°C at PBWR reference). The assumption of equilibrium between the oxygen in the steam dome and the oxygen in the whole Pb-Bi pool holds only if:

a) The partial pressure of oxygen in the steam dome is not above the value that would cause lead-oxide precipitation. In this case the oxygen concentration in the Pb-Bi would remain equal to its solubility limit (**Eq.8.10**).
b) There is vigorous turbulent mixing of the Pb-Bi so that the concentration of oxygen is uniform throughout the pool. Note that the Pb-Bi/water two-phase flow provides excellent Pb-Bi mixing in the chimney and upper plenum. Furthermore, fully turbulent Pb-Bi flow exists in the core and in the downcomer where the Reynolds number is 1.3×10^5 and 3.0×10^6, respectively.

It is convenient to establish the relationship between the oxygen partial pressure in the steam dome and the oxygen concentration in Pb-Bi so that **Eq.8.17** can be used in concert with **Figure 8.3** to identify an oxygen control strategy. The reaction of oxygen dissolution in lead is:

$\frac{1}{2}O_{2(g)} \leftrightarrow O_{(sol)}$ **Eq.8.19**

The corresponding equilibrium constant, k_O is:

$$k_O = e^{-\frac{\Delta G_O(T)}{RT}} = \frac{a_O}{P_{O2}^{1/2}}$$ **Eq.8.20**

where ΔG_O is in kJ/mol$_O$ and given in [Alcock 1964] as:

$\Delta G_O(T) = -219.16 + 0.101T$ **Eq.8.21**

Combining **Eq.8.10** and **Eq.8.20**, the relation between the oxygen concentration in the Pb-Bi and the oxygen partial pressure in the dome is:

$$c_O = c_{O,s} P_{O2}^{1/2} e^{-\frac{\Delta G_O(T)}{RT}}$$ **Eq.8.22**

Therefore **Eq.8.17** yields:

$$c_O = c_{O,s} \frac{P_{H2O}}{P_{H2}} e^{\frac{\Delta G_{H2O}(T) - \Delta G_O(T)}{RT}}$$ **Eq.8.23**

In **Figure 8.4** the oxygen concentration from **Eq.8.23** is plotted as a function of temperature for several values of the hydrogen partial pressure and for the reference steam pressure P_{H2O}=7.0MPa. The limiting curve $c_{O,s}$ is also drawn. In the previous section we have demonstrated that at PBWR reference conditions it is desirable to control the oxygen concentration in Pb-Bi at about 2.7ppm. **Figure 8.4** (or **Eq.8.23**) indicates that this can be readily accomplished by maintaining the hydrogen partial pressure in the steam dome at about 5×10^{-3} atm. In this scheme, the hydrogen partial pressure controls the oxygen partial pressure in the steam dome, which in turn sets the oxygen concentration in the upper plenum Pb-Bi. Finally, turbulent mixing ensures that the oxygen concentration throughout the whole reactor pool (i.e. downcomer and core) is equal to that of the upper plenum. Therefore, special attention should be given to designing the Pb-Bi coolant flow path throughout the reactor pool to prevent stagnation regions with poor oxygen circulation, which would promote dissolution of the oxide film and consequent corrosion of the structural materials.

The rate of hydrogen injection needed to control the oxygen concentration in the Pb-Bi melt is estimated as follows. Indicating by x_{H2} the molar fraction of hydrogen in the steam dome and treating steam, oxygen and hydrogen as a mixture of ideal gases, the following relation holds:

$$x_{H2} = \frac{P_{H2}}{P_{H2O} + P_{H2} + P_{O2}} \approx \frac{P_{H2}}{P_{H2O}} \qquad \textbf{Eq.8.24}$$

Therefore the hydrogen mass flow rate $\dot{m}_{H2}$ to be injected in the feedwater in order to maintain the desired hydrogen partial pressure in the steam dome is:

$$\dot{m}_{H2} = x_{H2}\frac{A_{H2}}{A_{H2O}}\dot{M}_w \approx \frac{P_{H2}}{P_{H2O}}\frac{A_{H2}}{A_{H2O}}\dot{M}_w \qquad \textbf{Eq.8.25}$$

where A_{H2} and A_{H2O} are the hydrogen and water molecular weights and $\dot{M}_w$ is the feedwater mass flow rate. At reference PBWR conditions, it is $\dot{m}_{H2}\approx$0.0054kg/s=20kg/hr. The corresponding hydrogen concentration in the feedwater is about 8ppm.

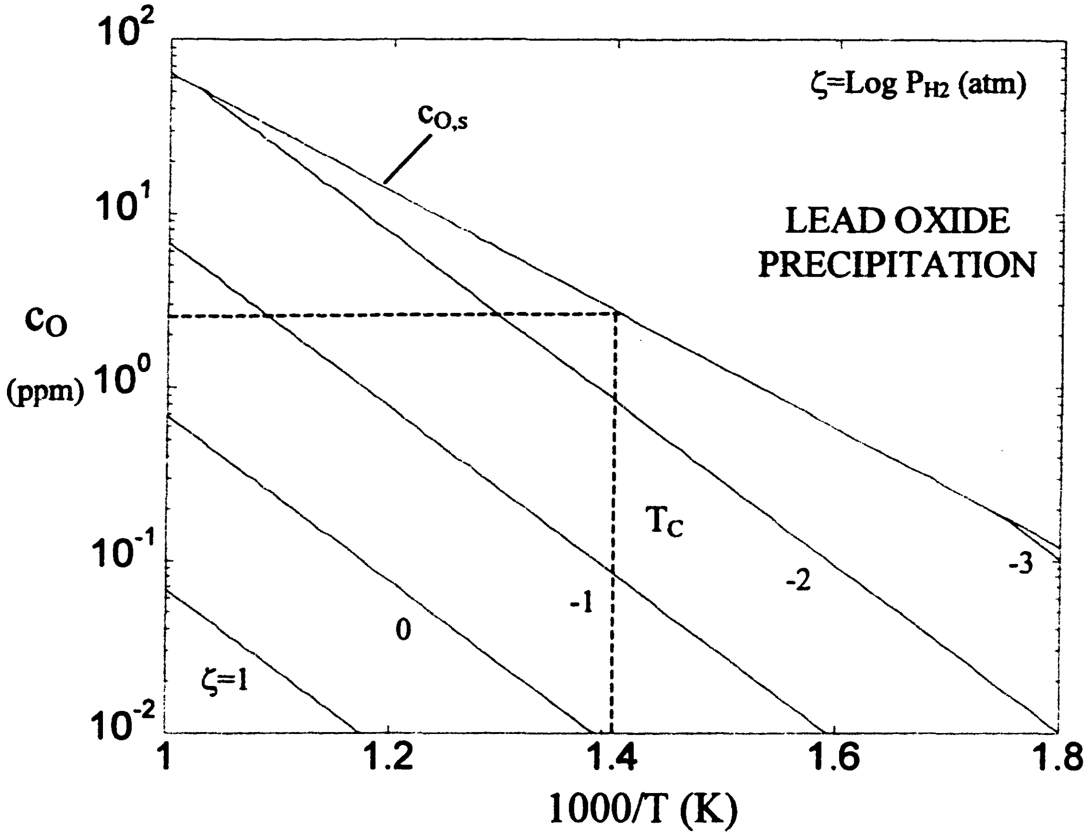

Figure 8.4. Oxygen control by hydrogen.

8.4 Summary

The mechanisms of degradation of structural materials for heavy liquid metal applications were identified. It was found that the formation of an iron oxide film on the exposed surfaces greatly reduces the rate of corrosion of the substrate. To maintain a stable oxide film, it is necessary to control the oxygen concentration in the coolant within a well-defined range. The lower limit of this range is dictated by the thermodynamic conditions required to oxidize the iron, while the upper limit is related to the precipitation of lead-oxide and consequent formation of a solid slag that could foul the surfaces and/or clog the flow channels of the core. It was demonstrated that the oxygen can be adequately control by dissolving minutes quantities of hydrogen in the feedwater. It was also estimated that at reference PBWR conditions, the relative reduction of the fuel clad thickness over its 4.5 years lifetime is less than 1%.

Chapter 9

- SUMMARY, CONCLUSIONS AND RECOMMENDATIONS FOR FUTURE WORK [1]-

The choice of lead or lead alloys as the coolant of a fast reactor offers enhanced safety and reliability. The advantages of heavy liquid metals over sodium (and more generally over light water) are related to the following material characteristics: higher atomic number; lower vapor pressure at operating temperatures; higher boiling temperature; and chemical inertness with air and water. These properties lead to several advantages for a heavy metal coolant including harder spectrum for actinide transmutation, practical impossibility of creating a void in the core, elimination of the intermediate coolant loop and better shielding against gammas and neutron radiation (**Section 1.2**).

In an effort to make this class of coolants even more attractive for application in the nuclear systems of the next generation, an innovative fast reactor concept that eliminates the need for steam generators and main coolant pumps and thus offers potential for substantial capital and operating cost reduction was explored in this thesis work. A schematic of the explored concept[2] is illustrated in **Figure 2.1**. The primary coolant is lead-bismuth eutectic, which flows through the core and removes the heat generated by fission in the fuel. Slightly subcooled water is injected into the hot primary coolant above the core. The direct contact heat transfer between the fluids causes water to rapidly vaporize leading to the formation of steam bubbles in the reactor chimney. The large density difference between the chimney and the downcomer provides the pressure head that drives the natural circulation of Pb-Bi in the vessel. The reactor chimney is partitioned into square channels (one per fuel assembly) to prevent radial drifting of the steam bubbles and maintain a uniform steam distribution. At the pool free surface, steam and Pb-Bi are separated by gravity and most residual liquid metal aerosols are collected in the steam dryer. Then the steam is sent to the turbine and operates a Rankine cycle analogous to a BWR that can achieve thermal efficiencies above 32%. However, contrary to BWRs, this design offers the possibility to superheat the steam and achieve even larger thermal efficiencies.

---

[1] The underlined paragraphs of this chapter highlight the areas where the most significant original contributions of this thesis work were made.

[2] To which we will refer as the Pb-Bi/Water direct contact heat transfer reactor (PBWR).

The core design developed at MIT for burning of actinides from LWR spent fuel was adopted as the PBWR reference core (**Section 2.2**). The fuel is made of a metallic alloy of zirconium, plutonium and minor actinides and cladded by a martensitic/ferritic stainless steel specifically designed by the Russians for high temperature Pb-Bi applications and designated EP-823 (**Section 2.2.4**). The core design is based on neutron streaming fuel assemblies and displays excellent neutronic properties, e.g. negative Doppler and void coefficients, small axial and radial power peaking (**Section 2.2.3.1**). It was demonstrated that the presence of a lighter phase in the reactor chimney does not perturb the neutronic performance of this core. Moreover, it was found that, if the core is accidentally flooded with liquid or two-phase water, the neutron reactivity decreases making the PBWR concept very resilient to loss of primary coolant situations (**Section 2.1**).

The explored reactor concept also presents several technical challenges. The most significant ones are identified below.

1) It is necessary to evaluate the maximum thermal power removable by direct contact heat transfer without violating the fuel, clad and vessel temperature limits. This is a difficult task that requires accurate thermal-hydraulic modeling of the multi-phase phenomena occurring in the reactor chimney.
2) The separation of Pb-Bi and steam in the steam dryer is not complete. It is expected that a certain amount of Pb-Bi aerosol remains entrained in the steam stream and is carried over to the power cycle components with major consequences on their design and operation (e.g. liquid metal embrittlement of the stressed parts of the turbine, clogging of the condenser drain pipes).
3) The direct contact of Pb-Bi and steam significantly aggravates the issue of polonium contamination. The primary and secondary coolants (Pb-Bi and water, respectively) are not physically segregated and a substantial amount of radioactive polonium might be released into the secondary system and eventually to the environment.
4) The injection of water in the Pb-Bi primary coolant may increase the production of lead and bismuth oxides hence calling for the injection of a reducing agent (e.g. hydrogen) to prevent fouling of the heat transfer surfaces and/or clogging of the core and vessel flow channels. Water injection might also have consequences on corrosion of the reactor structural materials.

STEADY-STATE THERMAL-HYDRAULICS OF THE PRIMARY SYSTEM

The chimney channels above the core, where direct contact vaporization of water occurs, were modeled as three axial regions defined by the thermodynamic state of water: the subcooled, saturated and superheated region. The flow regime map of the Pb-Bi/water multi-phase channel was generated applying the flow transition criteria available in the literature (**Section 3.3.1**). It was found that the flow regimes of interest are bubbly flow (mostly in the subcooled region) and cap flow (in the saturated and superheated regions). On the basis of the flow geometry, expressions for the local heat transfer coefficient (**Section 3.4**) and the interfacial area concentration (**Section 3.3.4**) were derived with the goal of estimating the volumetric heat transfer coefficient. Then an energy balance on the channel enabled relating the inlet conditions of the two fluids to the exchanged power or, for a given power, to the necessary channel length (**Section 3.2** and **3.5**). Also, it was found that at typical PBWR temperature and pressure conditions, a violent phase transition from liquid water to steam (the so-called steam explosion) does not occur because the vapor film that rapidly forms around the water droplets upon injection in the Pb-Bi coolant is stable (**Section 3.4.1.1**).

The void fraction in the chimney, needed to evaluate the density head for natural circulation in the reactor pool, was calculated by means of the Ishii-Kataoka-Rouhani drift-flux correlation for steam/water and air/water systems (**Section 3.3.3.4**). Extrapolation of this two-phase flow correlation to the PBWR three-phase flow application was made possible by the assumption of no slip between the steam and liquid water phases. Moreover, the superiority of this correlation over several other correlations considered was proven by means of a newly developed and rather general methodology based on a set of formal criteria drawn from the expected characteristics of steady-state two-phase upflow (**Section 3.3.3.3**).

All the models assembled to describe the PBWR chimney thermal-hydraulics were then benchmarked against the direct contact heat transfer data available in the literature. It was demonstrated that they generate both the theoretically expected and experimentally observed trends and values (**Section 3.6**). These trends are: smooth decrease of the volumetric heat transfer coefficient upon bubbly-to-cap flow transition, sharp drop of the volumetric heat transfer coefficient in the superheated region due to the change of heat transfer mode from evaporation to conduction, independence of the product of the saturation region length and Pb-Bi/water temperature difference from the mixture quality and the increase of this product with pressure. It was concluded that the model captures the essence of the direct contact heat transfer phenomena.

This model was then integrated into the steady-state momentum and energy equations for the entire reactor pool (i.e. core + chimney + downcomer) to calculate the natural circulation performance of the PBWR (**Section 4.4**). A fixed feedwater temperature and a fixed steam dome pressure were selected as the boundary conditions of this analysis. On the other hand, the steam dome temperature (i.e. the degree of steam superheat), the reactor power and the chimney height were allowed to vary. The friction pressure drop in the chimney region was calculated with the Friedel correlation for two-phase upflow. However, the dominant pressure drop occurs in the core. A complete list of the assumptions of this calculation can be found in **Section 4.3**. For given steam superheat and chimney height, the reactor power was changed until either the clad, the fuel or the vessel temperature limits[3] were reached. It was found that the clad limit in the hot assembly is always the most restrictive constraint. This calculation enabled generation of a design envelope for the reactor power as a function of the steam superheat and chimney height (**Figure 4.1**). As expected, the maximum power is an increasing function of the chimney height due to the increased natural circulation driving head. An intermediate chimney height value of 10m was selected as reference: this translates into a 20.5m vessel height, which is within the range of advanced BWR pressure vessels. On the other hand, because the Pb-Bi temperatures are limited by the clad constraint, an increase of the specified steam superheat results in a decrease of the average temperature difference that sustains the heat transfer in the chimney and ultimately in a decrease of the reactor thermal power. Moreover, because it was demonstrated that adoption of a large steam superheat does not yield a substantial increase of the thermal efficiency (**Section 4.1**), an intermediate steam superheat of 25°C was chosen as reference. This value guarantees complete vaporization of the residual liquid water droplets entrained by the steam and transported to the steam lines (**Appendix H**). The corresponding thermal and electric power are 1260 and 419MW, respectively. The temperature distributions of the coolant, clad and fuel were also calculated. A summary of the reference steady-state thermal-hydraulic conditions of the PBWR can be found in **Table 4.I**.

---

[3] The vessel temperature limit was established by means of a structural analysis based on ASME code case N-47 (**Section 2.3**).

A semi-qualitative subchannel analysis of the hot assembly (**Section 4.7**) showed that the peak clad temperature in the inner corner and edge subchannels only slightly exceeds that of the nominal central subchannel whereas the outer corner subchannel significantly exceeds it[4]. It was proposed to decrease the fissile enrichment of the four outer corner fuel pins in the hot assembly by approximately 15% with the understanding that so small an enrichment change in just four pins of a single assembly (which has 240 fuel pins) should not significantly affect the core neutronics.

DYNAMIC BEHAVIOR OF THE PRIMARY SYSTEM

A qualitative description of the response of the PBWR to the most important anticipated transient situations was undertaken. In particular the following events were considered: reactor start-up (**Section 4.9.1**), load change (**Section 4.9.2**) and loss of feedwater pumps with scram (**Section 4.9.3**). It was shown that the PBWR can be safely started and brought to full power by the combined adjustment of the control rods and feedwater flow rate. Moreover, the reactor appears to exhibit the desirable characteristic of automatically following the load (like a PWR).

The susceptibility of the PBWR primary circuit to static instabilities of the Ledinegg type was also analyzed (**Section 4.9.4**). Because the overwhelmingly dominant pressure drops in the primary circuit occur in the single-phase flow core, the characteristic curve of the PBWR is roughly proportional to the square of the coolant mass flow rate and no flow excursions are expected.

A quantitative dynamic analysis in the frequency domain was undertaken with the goal of evaluating the margin of the PBWR to loop perturbations (**Section 4.9.5**). The primary system was sectionalized in four regions (i.e. core, chimney, upper plenum and downcomer). The mass and momentum equations for these regions were written, perturbed and Laplace-transformed to obtain a linear system of algebraic equations, whose stability was then analyzed by means of flow signal and Nyquist diagrams.

A hydraulic feedback mechanism was identified due to the time delay between the natural circulation driving head (i.e. the void fraction in the chimney) and the circuit hydraulic resistance

---

[4] For a definition of the subchannel geometry see **Section 2.2.2**.

(i.e. the pressure drop in the core). This mechanism would induce Pb-Bi flow oscillations having a characteristic period of about 14s, equal to twice the travelling time of the Pb-Bi/water mixture in the chimney. However, the quantitative analysis showed that these hydraulic oscillations are not self-sustaining and the reactor is stable under nominal or low power conditions.

Three additional feedbacks (two thermal and one neutronic) have been identified but were neglected in the quantitative analysis (**Section 4.9.5.2**). The first is due to the effect of the Pb-Bi temperature on the chimney void fraction, the second is due to the Pb-Bi recirculation around the whole primary circuit and the third is due to the effect of the fuel temperature on the neutronic power. Based on qualitative considerations, it was found that the two thermal feedback mechanisms would compound (although to a very different extent) with the main hydraulic feedback hence decreasing the stability margin of the PBWR. The first thermal feedback mechanism is the most important because its period is similar to that of the hydraulic feedback and thus strong coupling of the two is expected. Vice versa, the period of the second thermal feedback is considerably longer than 14s and its effect on stability should be small. Finally, the neutronic feedback appears to have a stabilizing effect on the hydraulic oscillations.

Finally, the effect of a feedwater perturbation (for example due to vibration of the feedwater pumps) on the Pb-Bi flow in the primary system and on the steam conditions in the steam dome was explored and found to be negligible.

THE DECAY HEAT REMOVAL SYSTEM

After reactor shut-down, the heat produced by the radioactive decay of the residual fission fragments must be properly removed to ensure the integrity of the nuclear fuel. Normally this heat is removed from the reactor pool by vaporization of liquid water in the chimney, but other means must be provided to ensure continuous cooling of the nuclear fuel should that heat removal path fail (e.g. upon loss of the feedwater pumps). This task is performed by a dedicated system called the Decay Heat Removal System (DHRS). To increase the reliability of the emergency decay heat removal, it was decided to select a system that operates passively. The widely investigated and accepted Reactor Vessel Air Cooled System (RVACS), designed by GE for the advanced sodium-cooled reactor project was chosen as the base configuration (configuration #1). A schematic of this DHRS is shown in **Figure 4.10** (see also **Figure 2.25**). The heat produced in the core is conveyed by the naturally circulating primary coolant (in our case Pb-Bi) to the surface of the reactor vessel. The gap between the vessel and the containment is filled with an inert gas (e.g. argon). The heat is transferred through the gap mainly by radiation. Air enters the reactor building and flows through the downcomer to the containment bottom. From here it flows upward in the collector, removes the decay heat from the containment wall and is finally discharged to the atmosphere through a stack that supplies the gravitation head needed to passively drive the air through the circuit.

Two additional enhanced DHRS configurations were explored: one in which the vessel/containment gap is filled with a liquid metal acting as a thermal bond[5] (configuration #2) and one in which the air is replaced with liquid water as the ultimate heat sink on the outer surface of the containment (configuration #3, **Figure 4.14**). The use of a thermal bond in the vessel/containment gap was retained in this latter configuration.

A single-axial-node scheme was adopted to calculate the temperature distribution throughout the system (i.e. core, vessel, containment, collector) for the three DHRS configurations (**Section 4.8.1**). The goal was to evaluate the maximum decay power removable without violating the clad, fuel and vessel temperature limits. The friction pressure losses occurring in the air intake and outtake circuit were modeled as a concentrated form loss equal to 0.33 kinetic heads. It was demonstrated in [Davis 2000] that this approach accurately reproduces the GE RVACS data. Radiation heat transfer was considered in the collector of configuration #1 and #2 as well as in the vessel/containment gap of configuration #1. Natural convection heat transfer was considered in the vessel/containment gap of configuration #1 (gap filled with argon) as well as configurations #2 and #3 (gap filled with liquid metal bond). The validity of this simple approach was successfully benchmarked against the results generated with the more sophisticated thermal-hydraulic code ATHENA (**Section 4.8.2**).

As expected, it was found that the maximum removable decay power increases from configuration #1 to #2 and #3. Also, while configuration #1 and #2 are not compatible with the selected 1260MWth reference power, it was demonstrated that configuration #3 ensures effective removal of the decay heat at this power level and maintains the fuel, clad and vessel temperatures within acceptable limits (**Section 4.8.4**). Therefore, configuration #3 was selected as the PBWR reference DHRS.

---

[5] In our case the natural choice for the thermal bond material is liquid Pb-Bi.

PB-BI AEROSOL GENERATION AND TRANSPORT

Two mechanisms of heavy metal release into steam that take place in the upper region of the reactor pool and operate in parallel were considered: (i) lead-bismuth droplet entrainment by steam, (ii) direct evaporation of lead-bismuth. It was showed that the importance of mechanism ii) is very limited due to the extremely low vapor pressure of the Pb-Bi coolant (**Section 5.2**). The rate of Pb-Bi droplet entrainment by steam at the free surface of the pool was evaluated by means of the Kataoka-Ishii model and found to be about 1kg/s at PBWR reference conditions (**Section 5.3.1.1**). The maximum diameter of the entrained droplets was calculated by a force balance and found to be about 230μm (**Section 5.3.1.3**). In accordance with other investigations in the literature, the droplet size distribution was assumed to be an upper-limit lognormal (**Section 5.3.1.4**). Because the rate of entrainment and the droplet size are relatively small, it was decided to avoid the employment of complicated cyclone steam separators, but to rely on natural gravity separation instead. To appreciate the performance of gravity separation in the PBWR, the liquid rate of entrainment from the lead-bismuth pool free surface was compared to that of liquid water from the free surface of a pool at BWR conditions (**Section 5.3.1.2**). It was also proven that gravity separation in the PBWR is not prone to steam dragging into the downcomer (the so-called carry-under) if the downcomer width is sufficiently large, i.e. at least 1m (**Appendix D**).

However, it is desirable to remove the small Pb-Bi droplets from the steam before they reach the steam lines. For this purpose, a steam dryer of the chevron type was selected (**Section 5.3.2**) and its droplet removal efficiency was evaluated by means of the Moore-Sieverding model. Due to their large density, the Pb-Bi droplets are very efficiently removed and as a result the amount of Pb-Bi at the inlet of the steam lines is over three orders of magnitude smaller than at the steam dryer inlet (**Section 5.3.2.2**).

The dynamics of the Pb-Bi droplets passing through the steam lines was studied to evaluate the fraction of the Pb-Bi mass flow rate that actually reaches the turbine and the fraction that deposits on the walls of the steam lines. Two different deposition mechanisms were considered whose relative importance depends on the droplet size: turbulent diffusion and gravity deposition (**Section 5.4.1**). It was found that neither effect results in a significant deposition of Pb-Bi in the steam lines. Changes of the droplet distribution due to coagulation phenomena in the steam lines were also considered to evaluate the size of the Pb-Bi droplet reaching the turbine. Two mechanisms of coagulation were analyzed: brownian coagulation and turbulent coagulation (**Section 5.4.2**). Again it was showed that neither has a significant effect on the droplet size distribution. A synoptic description of the droplet dynamics in the steam lines is illustrated in **Figure 5.16**.

The presence of heavy liquid metal droplets at the first stages of the turbine raises three basic concerns: (i) erosion of the turbine surfaces exposed to the steam flow, (ii) accumulation of Pb-Bi and consequential contamination of the turbine surfaces by radioactive polonium, (iii) Liquid Metal Embrittlement (LME) of the turbine blades and other stressed components.

The rate of erosion of the first stages of the PBWR HP turbine was estimated by means of two predictive tools (i.e. the Pouchot model and the Hitachi correlation). It was then compared to the erosion rate of the last stage of a typical LP steam turbine and found to be negligible (**Section 5.5.3**).

It is thought that Pb-Bi accumulation in the turbine can be effectively prevented by making use of the erosion control technology for traditional steam turbines (e.g. hollow fixed blades, drainage slots on the turbine casing, axial spacing between the fixed and the moving blades). The Pb-Bi that deposits in the turbine would then be drained along with the condensed water. Note that this is a viable strategy because Pb-Bi is liquid at HP turbine temperatures (**Section 5.5.4**).

Several solutions to the LME problem were explored. The investigation of alternative blade materials not susceptible to LME led to the identification of titanium-aluminum alloys as a candidate for the PBWR HP turbine blades. However, selective leaching of aluminum (whose solubility in Pb-Bi is relatively high) should be evaluated prior to adoption of these alloys (**Section 5.5.2.1**). Coating of the blades could prove successful as it prevents Pb-Bi wetting of the stainless steel substrate. A suitable detonation gun coating, that is utilized in traditional steam turbines to control solid particle erosion, was selected. However, this coating contains nickel (whose solubility in Pb-Bi is very high) and again selective leaching might occur (**Section 5.5.2.2**).

Ceramic materials like oxides or carbides do not induce LME. Therefore, if the chemical state of the liquid Pb-Bi is changed from metallic to oxide before it reaches the turbine, the possibility of LME is eliminated. This can be realized by introducing a substantial amount of pure oxygen in the steam flow. The oxygen can be injected in the steam flow at the beginning of the steam lines, which enables a thorough and complete oxidation before the Pb-Bi reaches the turbine. The diffusion driven oxygen supply to the surface of the droplets was modeled and it was found that complete oxidation of the Pb-Bi aerosol prior to impact with the turbine blades can be achieved if at least 0.1kg/s of oxygen are injected in the steam lines (**Section 5.5.2.3**). It was also demonstrated that the consequences of this additional oxygen on the corrosion of the steam lines and turbine materials are not significant.

Finally, electrostatic precipitation of the Pb-Bi droplets in the steam lines was explored as a means to reduce the LME concern. Although this would be an effective way to remove the Pb-Bi droplets from the steam flow, it was found that the required operating conditions (particularly the pressure) are beyond the range of typical electrostatic precipitators, which would call for the development of a special system for the PBWR (**Section 5.5.2.4**).

COOLANT ACTIVATION

The alpha-emitter ^{210}Po is produced by neutron activation of the stable isotope ^{209}Bi. In a single-phase Pb-Bi reactor the primary system would be sealed and separated from the secondary system. As a result, polonium would be well retained in the Pb-Bi eutectic during normal operating conditions and could raise a problem only if a coolant leakage through the steam generator or the reactor vessel occurred. However, the case of a Pb-Bi/water direct contact reactor presents a significantly more severe challenge. Under normal operating conditions, the primary system is not isolated and the radioactive polonium may be readily transported by steam to the components of the secondary system (e.g. the steam lines, the turbine, the condenser). Because leaks of some contaminated steam out of the turbine or other power cycle components are inevitable, a certain amount of polonium is likely to escape into the environment. It should be demonstrated that the polonium concentration in the leaking steam, and all other vented flows, is within the limits prescribed by the radiation protection regulations. As a result, the development of the PBWR concept called for a substantial investigation of the mechanisms of formation of radioactive polonium and its chemical compounds, a quantitative characterization of their release and transport throughout the plant and identification of possible ways to mitigate the radiological concern associated with these phenomena.

Two chemical compounds of polonium were identified (polonium hydride and lead polonide) that contribute significantly to the release of alpha-activity from the Pb-Bi coolant (**Section 6.3**). Due to the lack of data in the literature and given the importance of the polonium issue in determining the viability of the PBWR concept, it was decided to undertake an experimental campaign to generate data on these species and in particular on (i) the free-energy variation of the polonium hydride formation reaction as a function of temperature, hydrogen partial pressure[6] and polonium concentration in the Pb-Bi melt and (ii) the vapor pressure of lead-polonide as a function of temperature. This is a significant contribution to the chemistry of polonium from which all heavy liquid metal cooled nuclear systems could benefit. A high temperature reaction cell was deployed at MIT to accommodate a liquid Pb-Bi bath and radioactive polonium (**Chapter 7.2.1**). The radioactive polonium was produced by irradiation of pure bismuth samples in the MIT research reactor (**Appendix G**). The cell consists of a single autoclave which hosts the molten Pb-Bi and polonium. The desired gas mixture is injected in the autoclave and then bubbled through two polonium traps in series (**Figure 7.1** and **Appendix F**). The alpha-activity of the trapping solution is then measured by means of two alternative methods: a) in a low background alpha-spectrometer after electroplating the polonium on a nickel disk and b) in a liquid scintillator (**Appendix I**).

The vapor pressure of lead polonide was measured over the 400-550°C temperature range and found to be in good agreement with an existing correlation derived from data at higher temperatures (**Section 7.3**). Also, it was experimentally confirmed that the presence of steam in the gas stream above the Pb-Bi melt substantially increases the amount of polonium released, which suggests the formation of the volatile compound polonium hydride. The free-energy variation of the polonium hydride formation reaction was estimated from the release data and a fitting curve that correlates the data within ±10% in the 180-580°C range was generated (**Section 7.4**).

The experimental data were then utilized in the theoretical modeling of polonium production and transport in the PBWR concept. A polonium balance over the control volume represented by the total Pb-Bi inventory in the reactor pool was established (**Section 6.5.1**). A fundamental conservative assumption was made that the steam leaving the reactor pool is saturated with the polonium species, therefore ignoring the kinetics of the reactions involved in polonium release.

Four terms were considered: production in the core, radioactive decay, extraction in an online dedicated system and release to the steam. Of three extraction methods proposed in the Russian

---

[6] For the role of the hydrogen potential in the chemistry of the polonium hydride see **Section 7.4**.

literature, one based on alkaline striping of the polonium was adopted as reference (**Section 6.4**). It was found that online polonium extraction from the Pb-Bi coolant greatly reduces the source term for polonium release to the steam (**Section 6.5.2**, in particular **Figure 6.2**). The mechanisms of release include the direct evaporation of pure polonium and lead-polonide as well as the formation of the polonium hydride. Despite the release reduction due to extraction, the specific polonium activity of steam was found to remain high, i.e. above the allowed DAC level. Also, if deposition of all polonium released was assumed to occur on the components of the secondary system (i.e. steam lines, turbine, condenser), the surface activity would exceed the unrestricted maintenance limit.

MATERIALS CORROSION

Traditional austenitic stainless steels are not suitable for high temperatures typical of fast reactor applications due to the large solubility of nickel in bismuth (**Table 1.II**), which would cause rapid selective leaching of that alloying element from the steel matrix and consequent loss of strength and integrity of the structures. The possibility of employing low nickel martensitic/ferritic stainless steels was extensively studied in Russia and currently in the US, Japan and Israel, as well. The Russian research program culminated with the development of a steel designated EP-823, which is claimed to be suitable for Pb-Bi applications at up to 600-650°C. The mechanisms of degradation of this structural material were identified (**Section 8.2**). It was found that the formation of an iron oxide film on the exposed surfaces greatly reduces the rate of corrosion of the substrate. To maintain a stable oxide film, it is necessary to control the oxygen concentration in the coolant within a well-defined range. The lower limit of this range is dictated by the thermodynamic conditions required to oxidize the iron, while the upper limit is related to the precipitation of lead-oxide and consequent formation of a solid slag that could foul the surfaces and/or clog the flow channels of the core. It was demonstrated that the oxygen can be adequately controlled by dissolving minutes quantities of hydrogen in the feedwater (**Section 8.3**). It was also estimated that at reference PBWR conditions, the relative reduction of the fuel clad thickness over its 4.5 years lifetime is less than 1%.

CONCLUSIONS

The explored innovative reactor concept exhibits potential for substantial capital and operating cost reduction due to primary system simplification associated with the elimination of the steam generators and the main coolant pumps. It was confirmed that direct contact between the Pb-Bi coolant and water is an effective heat transfer mode enabling design of a medium size system (<1300MWth) that generates slightly superheated steam, which ultimately results in a 419MW net electric output. This reactor concept is found not to be susceptible to thermal-hydraulic instabilities of dynamic or static nature. It was also demonstrated that the decay heat generated by this reactor can be passively removed by a suitable DHRS based on boiling water on the outer surface of the containment. Finally, it was shown that careful control of the oxygen concentration in the Pb-Bi coolant reduces the corrosion of the fuel clad to negligible levels.

Nevertheless, two major issues were identified: 1) liquid metal embrittlement of the turbine stressed parts and 2) polonium transport out of the reactor pool. A set of potential technical solutions to the embrittlement problem was identified. However, it should be emphasized that adoption of any of these solutions might significantly offset the cost benefits of the present reactor concept. Because the assessment of this economic trade-off was not undertaken in this study, it is hard to draw any conclusions on the viability of the PBWR concept from a liquid metal embrittlement standpoint.

On the other hand, the polonium issue seems to represent a very serious technical obstacle to the development of a Pb-Bi/water direct contact reactor. Despite the use of an online polonium extraction system, the alpha-activity in the working steam, on the surfaces of the power cycle components and in the feedwater is well above acceptable limits. Operation of the reactor at these levels of radioactive contamination might result in excessive exposure of the plant personnel and/or prohibitive maintenance costs.

FUTURE WORK

Several key calculations in this study (e.g. assessment of the volumetric heat transfer coefficient in the chimney, estimate of the Pb-Bi aerosol at the free surface of the reactor pool) were performed with the help of models and/or correlations that were originally developed for more traditional nuclear reactor coolants like water, gas or liquid sodium. Although an effort was made to justify the extrapolation of these models to the PBWR application, it should be emphasized that a thorough experimental validation of the results presented in this study will be needed, should the concept of a direct contact heat transfer reactor be further pursued in the future. A framework for future experimental investigation in the area of direct contact thermal-hydraulics is presented in **Appendix C**. In particular, it is proposed to explore the possibility of using imaging techniques like ultrasound, neutron and X-Ray radiography to gain insight of the vaporization mechanisms upon injection of liquid water in a hot heavy liquid metal bath at high pressure. Also, the direct contact heat transfer model could be refined by means of a more rigorous treatment of the interfacial area concentration that built on the solution of the Ishii and Kocamustafaogullari's transport equation. However, the closure relations of this equation for the flow regime of interest (i.e. cap flow in large diameter channels) are not available in the literature at this time.

Due to the key importance of the polonium issue in proving the feasibility of the PBWR concept, it is recommended that the possibility of utilizing rare-earth additives in the Pb-Bi coolant be explored to drastically reduce the polonium source of release to the working steam. Moreover, the basic chemical characteristics of the polonium extraction technique based on molten sodium hydroxide should be further investigated to demonstrate its suitability for an online coolant purification system. Also, other polonium extraction methodologies (e.g. hydrogen washing of the Pb-Bi bath to produce the volatile hydride, rare-earth filters) should be given proper attention. Note that both direct and indirect cycle Pb-Bi reactors share the polonium management issue and both would consequently benefit from these investigations.

Although it was shown that a coolant chemistry strategy based on tight oxygen control can significantly reduce corrosion of the core and reactor structural materials (i.e. martensitic/ferritic steel of low nickel content), the development of innovative materials based on low solubility elements (e.g. tantalum, niobium, tungsten) should also be considered. These might allow achievement of substantially higher temperatures in the primary system (i.e. 700-800°C) and thus of higher plant thermal efficiencies and/or higher margins to fuel failure.

Finally, an accurate economic analysis should be undertaken that establish the trade-off between simplification of the primary system (i.e. elimination of the steam generators and main coolant pumps) and the need for dedicated systems to cope with the Pb-Bi aerosol and polonium issues (e.g. turbine blade coating, electrostatic precipitator, polonium extraction system). This analysis will ultimately determine the attractiveness of the direct contact reactor concept.

Appendix A

- ACTINIDE BURNING: ACCELERATOR-DRIVEN SYSTEM VS. CRITICAL REACTOR -

Undesirable yet inevitable by-products of the nuclear fission reaction are the fission fragments. These fragments are typically radioactive relatively lighter nuclei whose lifetime may range from a few milliseconds to a few hundreds years. These radionuclides account for most of the radioactivity present in the fuel of an operating nuclear reactor hence constituting the most serious hazard to the public in case of a severe accident. However, in the very long-term the radioactivity and toxicity level of the nuclear spent fuel is not determined by the fission fragments but by the very long-lived actinides. The lifetime of the actinides is significantly longer than that of fission fragments and can range up to hundreds of thousands of years. It is mainly because of this time scale that the designers of nuclear waste permanent repositories are required to demonstrate the integrity and reliability of the barriers to radioactivity release for thousands of years. The inherent uncertainties associated with such unusual design requirements triggered in past years a debate about the legacy of the nuclear age to the future generations.

Operation of US utility nuclear reactors has produced so far about 70,000 metric tons of spent fuel containing approximately 600 tons of minor actinides. It is clear that finding ways to reduce the hazard associated with these actinides is crucial to improving the acceptability of the nuclear power technology.

The strategy to burn plutonium and other minor actinides from LWR spent fuel and/or decommissioned nuclear weapons in an accelerator driven subcritical system (ATW) has gained considerable support in Europe and in the US in the last decade [LANL 1999b, Gromov 1997]. Processing the actinides by means of these systems has a substantial effect on the long-term hazard of the spent fuel of current Light Water Reactors, as illustrated in **Figure A.1**: here the specific ingestion toxicity is plotted versus the decay time for the Direct Disposal option as well as for Actinide Burning assisted disposal (indicated in **Figure A.1** as ATW-assisted Repository). After 1,000 years the toxicity of the actinide-depleted fuel is approximately three orders of magnitude smaller than in the direct disposal option.

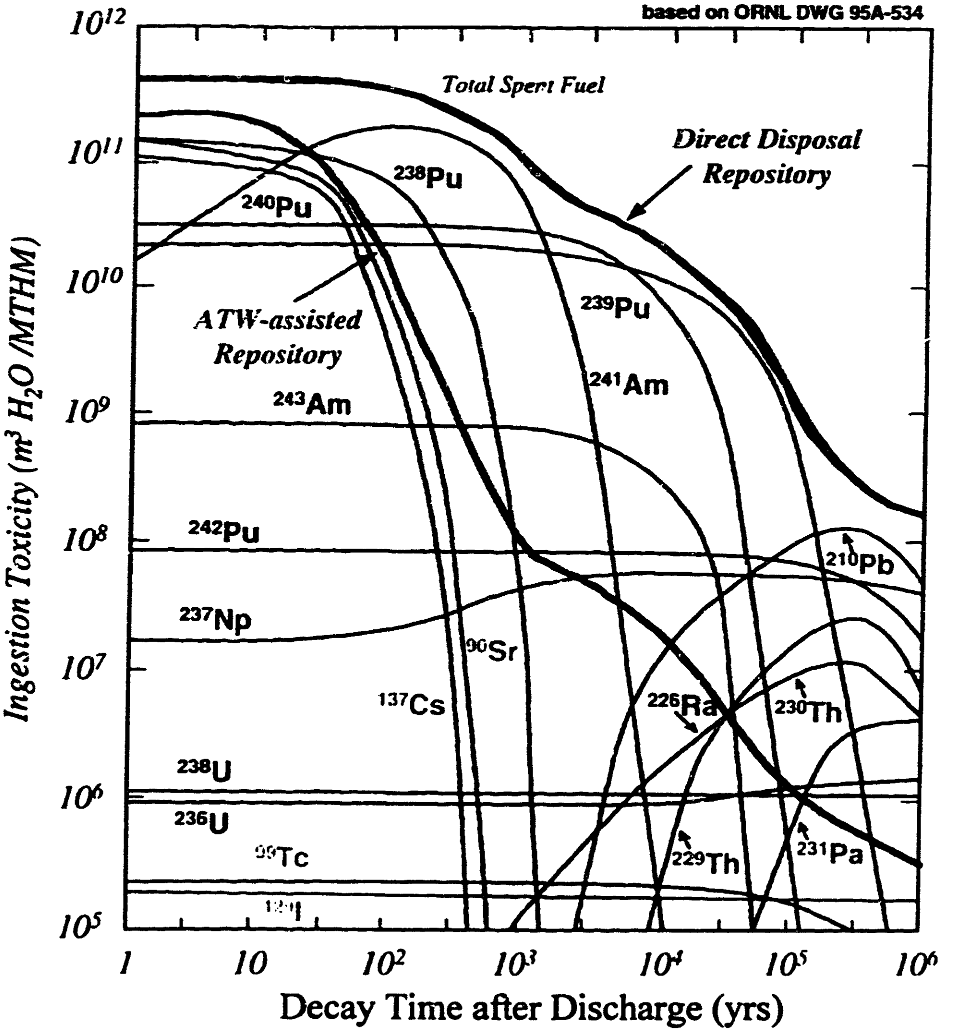

Figure A.1. The effect of actinide burning on the toxicity of LWR spent fuel.

The subcritical system offers potential in terms of reactivity safety margin, but it does not remove the key issue of preventing fuel melting when the system is shut-down and subject to decay heat release in the fuel. Further, the high cost of the accelerator, the lack of demonstrated high accelerator availability and some materials concerns specifically associated with the spallation target must be considered when comparing this design to alternative means to achieve the transmutation mission.

To effectively transmute plutonium and minor actinides from LWR spent fuel, it is desirable to minimize the waste of neutrons in order to attain a large surplus available for transmutation. Metallic fuels based on a zirconium matrix provide excellent neutron economy due to the low parasitic absorption cross-section of zirconium and due to the hard spectrum achievable because the fuel does not contain any moderating isotope. To maximize the actinide transmutation capability of the system, breeding of new fissile material must be minimized hence making the presence of the fertile isotopes U238 or Th232 undesirable. The choice of fuel composition is then restrained to the to-be-transmuted plutonium and minor actinides (20-30% wt.) and to the zirconium matrix (70-80% wt.) constituting the structural component of the fuel rods. This fuel raises four major neutronic challenges (see **Section 2.2.1**):

- Void Reactivity Coefficient. Spectrum hardening and decreased parasitic captures in the coolant might cause a large reactivity increase upon coolant voiding.
- Doppler Feedback. The scarcity of resonance absorption nuclides and the hard spectrum make the Doppler feedback very small.
- Reactivity Change with Burnup. The lack of plutonium breeding causes rapid depletion of the fissile nuclides in the fuel hence preventing operation of the system for long times.
- Delayed Neutron Fraction. Plutonium and minor actinides display very small delayed neutron fraction (<0.002) which makes the control of this reactor somewhat more challenging than a LWR.

These challenges are particularly significant for a critical system that must rely on reactivity feedback to control the fission chain reaction. However, the reactivity feedback concerns are considerably reduced in a subcritical system, where the margin to prompt criticality is large. For example, at k_{eff}=0.97 a rapid insertion of 1$ reactivity determines a power excursion of only 5%. Because of its substantial insensitivity to reactivity feedback, ATW offers greater fuel flexibility, e.g. the possibility of burning weapon plutonium, which would not provide adequate Doppler response in a critical reactor. However, rapid reactivity decrease with burnup takes place in a subcritical system, too and must be compensated for by a corresponding increase of the accelerator beam power to maintain a constant total power output. Therefore, the accelerator is mostly operated below its design power, which results in further economic penalization of the ATW system. Also, the presence of an intense neutron source at the center of the subcritical blanket is expected to generate large power peaking in the ATW system, whereas a Pb-Bi cooled critical core generally features remarkably low radial and axial power peaking (**Section 2.2.6**).

The actinide burning rate per unit thermal power is slightly larger in a critical reactor (**Section 2.2.3.1**), because all energy comes from fission of plutonium and minor actinides whereas in ATW a (small) part of the energy is supplied directly by the accelerator. This also means that, for a given thermal power, the reactor displays a larger electric output.

A subcritical system also requires the design of a spallation target. This represents a significant engineering challenge due to the radiation damage of the structural materials involved and the extremely high thermal load to be removed, which calls for a dedicated cooling loop. Moreover, the spallation by-products alter the chemistry of the target cooling loop and might result in more severe corrosion of the structural materials.

Assuming the employment of the same Pb-Bi eutectic coolant, the critical reactor and the subcritical system share the problem of radioactive ^{210}Po production by neutron capture on bismuth. However, several additional isotopes of polonium can be produced by proton bombardment of the Pb-Bi coolant in a subcritical system, hence resulting in a polonium specific activity up to an order of magnitude larger than in the reactor [Yefimov 1998, Gromov 1994].

Finally, the main disadvantage of the accelerator-driven system over a critical reactor is the capital cost of the accelerator itself and its related systems (e.g. target cooling loop), which can be only partially offset by the elimination of most reactivity control systems.

Appendix B

- THERMOPHYSICAL PROPERTIES OF LEAD-BISMUTH -

The data from reference [Kutateladze 1958] were fitted by means of the least-mean-squares method to yield the following expressions (T in °C) for the main thermophysical properties of the lead-bismuth eutectic (45%Pb-55%Bi), valid in the range 125 to 700°C.

Density (kg/m^3):

ρ=10728-1.2159T **Eq.B.1**

Isobaric expansion coefficient (1/°C):

$\beta=5.0027\times10^{-5}+6.2868\times10^{-7}T-2.1103\times10^{-9}T^2+3.0586\times10^{-12}T^3-1.5928\times10^{-15}T^4$ **Eq.B.2**

Thermal diffusivity (10^{6}m^2/s):

$\alpha=6.0107+0.0078713T$ **Eq.B.3**

Kinematic viscosity (10^{7}m^2/s)

$\nu=61.423/T^{0.61106}$ **Eq.B.4**

Thermal Conductivity (W/m°C):

$k=9.6254+0.010169T$ **Eq.B.5**

Specific Heat (J/kg°C):

$c_p=146.37$ **Eq.B.6**

Prandtl Number:

$Pr=3.7362/T^{0.90183}$ **Eq.B.7**

On the basis of the data in [Lyon 1952], Shieh [1999] generated the following fitting curve for the surface tension (N/m):

$\sigma=0.411-5.5\times10^{-5}T$ **Eq.B.8**

Appendix C

- FRAMEWORK FOR FUTURE INVESTIGATION OF DIRECT CONTACT HEAT TRANSFER PHENOMENA -

The models of **Chapter 3** have been utilized to get a first estimate of the natural circulation performance of the PBWR primary system. Nevertheless, it is strongly recommended that a thorough experimental investigation be conducted of Pb-Bi/water direct contact heat transfer phenomena at prototypical PBWR conditions, should the PBWR concept be further considered in the future.

The objective should be to experimentally assess the thermal-hydraulic characteristics of heavy liquid metal/water direct contact heat transfer with the goal of generating a predictive tool (i.e. correlation and/or model) to be used in the design of the Pb-Bi/water reactor (i.e. PBWR) chimney.

C.1 The Experimental Approach

Two experimental approaches are identified.

C.1.1 Integral Measurement Approach

The average volumetric heat transfer coefficient is calculated from knowledge of the inlet temperatures and mass flow rates, from measurement of the outlet temperatures and by means of an energy balance over the test section. For example, with regard to the vhtc in the saturated region, **Eq.3.70** can be used for this purpose.

The advantages of this experimental approach are:

(i) It is simple and relatively inexpensive because it does not require the use of sophisticated machines and/or techniques.

(ii) It is flexible because there is virtually no constraint on the size and geometry of the channel and/or the selection of the fluids.

(iii) A predictive correlation can be readily generated for the conditions of interest.

The disadvantages are:

(i) It provides little physical insight of the heat transfer and hydrodynamic mechanisms.

(ii) The results obtained with this approach can hardly be extrapolated beyond the experimental database conditions.

C.1.2 Local Measurement Approach

The interfacial area concentration is measured by means of an imaging technique. The local heat transfer coefficient is modeled and the product of the two provides the vhtc.

The advantages of this approach are:

(i) An insightful view of the direct contact vaporization process can be gained. Note that the local phenomena in the subcooled region could probably be modelled without the help of an imaging technique due to their relatively simple geometry. However, the vaporization of water (which occurs in the saturated region) displays a rather irregular interfacial geometry and might require a direct local measurement.

(ii) Because it is based on a description of the local heat transfer phenomena, this approach enables producing meaningful predictions beyond the experimental database.

The shortcomings of the local approach are:

(i) In order to estimate the average volumetric heat transfer coefficient (which is the engineeringly useful parameter), this approach must be coupled to a mechanistic model that assesses the local surface heat transfer coefficient. The relation between the average volumetric and local surface heat transfer coefficient (i.e. $\bar{h}_v$ and h_s, respectively) is:

$$\bar{h}_v = \frac{1}{V}\int_V a_i h_s dV \qquad \textbf{Eq.C.1}$$

where V is the test section volume.

(ii) Because it involves modeling, the predictions generated by means of this approach must be validated by the integral approach, anyway.

(iii)The use of imaging techniques may considerably increase the cost of the investigation.

(iv)The selection of an imaging technique may constrain the acceptable fluids and the geometry of the test section.

C.2 Selection of the Fluids

The reference thermal-hydraulic conditions of the PBWR chimney are reported in **Table C.I.**

Table C.I. Reference characteristics of the PBWR chimney.

Parameter	Value
Fluids	Pb-Bi, water
Pb-Bi temperature range	440-550°C
Water temperature range	250-320°C
Pressure	7.0MPa
Water Quality, x	0.8%
Channel equivalent diameter	26cm

The cost of designing and operating an experimental apparatus at these conditions may be rather high. Therefore it might be desirable to conduct the investigation at considerably lower pressure and temperature. Also it may be convenient to make use of different fluids. The selection of a suitable simulating fluid requires some discussion.

<u>Pb-Bi Simulants</u>: Pb-Bi, Pb-Bi-Sn, Wood's metal, mercury, highly subcooled liquid water.

<u>Water Simulants</u>: water, low boiling point fluids (e.g. liquid xenon, refrigerants, organics).

If fluids other than Pb-Bi/water are selected as simulants of Pb-Bi/water, the experimental results must be correlated and interpreted in terms of dimensionless numbers to allow a meaningful conversion to different fluids and/or thermal-hydraulic conditions. Some restrictions apply to the fluid selection in relation to the experimental approach.

If the integral measurement approach is selected, the use of water as a simulant of Pb-Bi is probably not a viable option, because the mechanisms of heat transfer in a liquid metal are qualitatively (and of course quantitatively) different from those in a large Prandtl number fluid.

This point requires some more explanation. We will refer for simplicity to the superheated region[1]. It is anticipated that the main resistance to heat transfer between lead-bismuth and steam is represented by conduction within the steam bubble. Likely, the thermal resistance in the liquid metal is negligible due to its large thermal conductivity. If water (i.e. a fluid of small thermal conductivity) is used as a simulant of Pb-Bi, it is conceivable that its thermal resistance cannot be neglected, which may substantially alter the mechanisms of heat transfer. It is therefore proposed that the selection of the simulating fluids be based on the (non-dimensional) ratio of the dispersed (vapor) to continuum phase thermal resistance. Again, we shall designate the continuum and the dispersed phases by means of the subscripts p and w, respectively (see **Figure C.1**) with the understanding that they could now refer to any couple of experimental fluids.

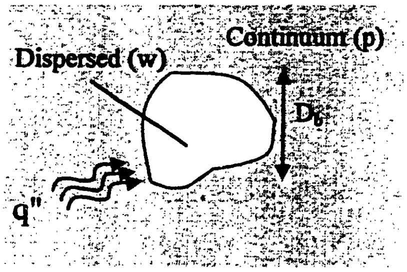

Figure C.1. Phases and geometry of the superheated region.

The thermal resistance in the continuum phase is:

$R_p=(T_p-T_i)/q''=1/h_p$ **Eq.C.2**

where T_i and q" are the temperature and the heat flux at the interface and h_p is the heat transfer coefficient.

The resistance to heat transfer within the vapor bubble can be estimated as:

$R_w=(T_i-T_w)/q''=D_b/k_w$ **Eq.C.3**

where D_b is the characteristic length of the bubble and k_w is the vapor thermal conductivity.

The ratio of R_w to R_p is called the Biot number (Bi) [Incropera 1990]. Its expression in our case is:

$Bi=h_pD_b/k_w$ **Eq.C.4**

To calculate the Biot number, an estimate of D_b and h_w must be provided. The diameter of the bubbles depends on the flow regime and, in bubbly flow, on the mode of injection of the

---

[1] It was demonstrated in **Section 3.6** that this is the longest region of the PBWR chimney.

dispersed phase (see discussion in **Section 3.6**). For the sake of simplicity, we assume that D_b can be calculated as [Kataoka 1987, Kawanishi 1990]:

$$D_b \propto \sqrt{\frac{\sigma}{g(\rho_p - \rho_w)}} \qquad \textbf{Eq.C.5}$$

As for h_p, we shall assume that it can be given by a forced convection correlation for liquid metals. Thus:

$$h_p \propto \frac{k_p}{D_b} Pe^{0.8} \qquad \textbf{Eq.C.6}$$

where $Pe = \frac{\rho_p u_{wp} D_b c_p}{k_p}$ is the Peclet number of the continuum phase and u_{wp} is the bubble velocity relative to the continuum phase approximated as [Zuber 1965]:

$$u_{wp} \propto \left[\frac{\sigma g(\rho_p - \rho_w)}{\rho_p^2}\right]^{1/4} \qquad \textbf{Eq.C.7}$$

Combining **Eq.C.4** through **C.7**, an expression for the Biot number can be obtained as:

$$Bi \propto \frac{k_p^{0.2} \rho_p^{0.2} c_p^{0.8} \sigma_p^{0.6}}{k_w g^{0.2}\left(1 - \frac{\rho_w}{\rho_p}\right)^{0.2}} \approx \frac{k_p^{0.2} \rho_p^{0.2} c_p^{0.8} \sigma_p^{0.6}}{k_w g^{0.2}} \qquad \textbf{Eq.C.8}$$

where the $\rho_p >> \rho_w$ approximation was made.

It is recommended that **Eq.C.8** be used in selecting the simulating fluids so that the Biot number (i.e. the ratio of the dispersed to continuum phase thermal resistance) be kept approximately the same as the Pb-Bi/water combination, i.e. Bi=3200. **Eq.C.8** suggests that in principle this can be accomplished (for any pair of simulating fluids) by controlling the magnitude of the body forces g (e.g. by means of a centrifuge).

The Biot number can provide a useful tool to select simulating fluids even if the local measurement approach is selected (where the objective is to measure the interfacial area). However, if it can be assumed that the geometric characteristics of the phase interface are primarily determined by hydrodynamic phenomena (as opposed to heat transfer phenomena), the use of any fluid pair (e.g. water/liquid xenon, Wood's metal/water) would be suitable. However, it should be emphasized that, if the bubble geometry is highly irregular, the use of some imaging technique (e.g. NMR) might be problematic (see below).

C.3 Imaging Considerations

Seven experimental techniques are considered: Ultrasound (US), Low Frequency Sound (LFS), Electric Conductivity Measures (ECM), Hot Wire Probe/Electric Conductivity Probe (HWP/ECP), Neutron Radiography (NR), X-Ray Radiography (XRR), Nuclear Magnetic Resonance (NMR).

C.3.1 Technique Description

US. Mechanical waves of varying (high) frequency are generated at the channel periphery and scattered by the vapor bubbles. The size of the bubbles is determined by measuring the distribution of the scattered waves. The US waves are scattered at the surface of the vapor bubbles and therefore do not enable measuring the size of the water droplets inside (in the saturated region).

LFS. The velocity of low frequency mechanical waves is measured as they travel transversally through the channel. Because this velocity is a function of the average density (i.e. of the void fraction) and elastic properties of the fluid, this technique enables measuring the relative volumetric fraction of the three phases.

ECM. A current is imposed transversally through the channel and the electric potential is measured at several locations on the channel periphery. By means of this information the average conductivity (and consequently the vapor fraction) can be calculated. It should be noted that because the electric conductivity of the liquid continuum phase (e.g. lead-bismuth) is much larger than that of vapor bubbles, the electric current will flow in the liquid only, therefore providing no information about the water droplets inside the bubbles.

HWP/ECP. HWP is a phase indicator based on measuring the temperature fluctuations in an electrically heated probe (at a specific location in the channel) due to the different heat transfer coefficient of the liquid and vapor phases. ECP measures the potential drop across two close probes and hence the electric conductivity of the interposed medium, which enables determination of which phase is in contact with the probes at a given time. Information on the velocity and size of the bubbles and/or droplets can be collected by placing two or more probes at a fixed distance and measuring the signal time correlation. The size of these probes is approximately 1mm which would probably make them unsuitable to detect the liquid water droplets inside the vapor bubbles. Four-sensor ECP is currently the preferred technique for measuring the interface area concentration in water based systems [Kim 1998].

NR. The channel is bombarded with a neutron beam. Neutrons are scattered with significantly different efficiency by liquid water, liquid lead and vapor. By measuring the neutron intensity beyond the channel it is possible to visualize the three phases [Nishi 1998].

XRR. The channel is bombarded with a X-ray beam. X-rays are attenuated with significantly different efficiency by heavy elements (i.e. liquid lead-bismuth) and light elements (i.e. vapor and liquid water). By measuring the X-ray intensity beyond the channel it is possible to visualize the three phases. However, if the attenuation coefficient of the heavy element is overwhelmingly dominant, it may be hard to separate liquid water and vapor. This technique has been selected by a group of researchers at the University of Wisconsin for measurement of a_i in their Pb-Bi/water rig.

NMR. A volumetric magnetization is generated in the materials by means of a static magnetic field. The intensity of this magnetization depends on the permeability of the material and it is measured from the electromotive force produced when the magnetization vector rotates under the action of external radio-frequency electromagnetic waves.

This technique can deliver satisfactory images of smooth surfaces (i.e. spheres, cylinders), but it is thought to be much less effective with highly irregular geometries.

C.3.2 Comparative Elements

LFC and ECM are capable of measuring the relative volumetric fraction of the phases, US is more suitable to measure the size of the bubbles. NR, XRR and NMR may enable measuring both quantities at the same time.

These techniques also differ in terms of the hydrodynamic nature of the information they deliver: XRR, NR, NMR and US enable following the time evolution of a single droplet through the vaporization process (Lagrangian approach), HWP/ECP provides information at a given location in the channel as a function of time (Eulerian approach). LFS and ECM can supply information averaged over the entire cross-section (at a given axial location in the channel) as a function of time (integral Eulerian approach).

These techniques are subjected to different fluid, geometry and size constraints. NMR is not suitable for heavy metal experimention in channels larger than a few millimeters. If a planar (i.e. one-dimensional) XRR or NR is selected to measure the bubble/droplet size, the width of the channel in the beam direction must be small to ensure that only one bubble is scanned so that the measurement does not represent a chordal average over several bubbles. On the other hand, ECM, US, HWP/ECP and LFC have virtually no constraints on geometry and size.

XRR, NR, NMR, HWP/ECP, LFC can in principle supply information on the three phases whereas US and ECM cannot.

By definition, NR and XRR require a radiation source (e.g. accelerator, reactor, X-ray tube) which may make them rather costly. On the other hand ECM, LFC and US are known to be relatively inexpensive and simple experimental techniques.

Table C.II summarizes the main characteristics of the selected techniques.

Table C.II. The imaging technique for experimental characterization of direct contact heat transfer.

Technique	Geometry Constraints	Fluid Separating Property	Phase Detection	Type of Data
US	None	Surface Discontinuity	Liquid Metal and Vapor	Lagrangian/ Bubble Size
LFS	None	Density, Compressibility	Three Phases	Integral Eulerian/ Volumetric Fraction
ECM	None	Electric Conductivity	Liquid Metal and Vapor	Integral Eulerian / Volumetric Fraction
HWP/ECP	None	Thermal and Electric Conductivity	Three Phases	Eulerian
NR	Narrow Test Section	Macroscopic Cross Section	Three Phases	Lagrangian
XRR	Narrow Test Section	Atomic Number, Density	Three Phases	Lagrangian
NMR	Smooth Surfaces	Magnetic Permeability	Three Phases	Lagrangian

Appendix D

- STEAM CARRY-UNDER IN THE CHIMNEY UPPER PLENUM -

Most steam flowing out of the reactor chimney reaches the free surface of the pool where it separates from the liquid due to its lower density. However, if the liquid velocity in the downcomer is large enough, the steam bubbles may follow the liquid backward into the downcomer. This phenomenon is known as steam carry-under and significantly degrades the performance of a system based on natural circulation. The presence of steam bubbles in the downcomer reduces the density difference between the downcomer and the chimney, hence decreasing the driving force for coolant circulation in the primary system. The occurrence and magnitude of steam carry-under mainly depends on i) the downcomer liquid velocity, ii) the system pressure and temperature[1], iii) the geometry of the chimney-to-downcomer plenum.

To quantitatively study the importance of steam carry-under phenomena in our particular situation, we shall make use of a simple model proposed by Petrick [Petrick 1963], whose assumptions can be explained with the help of **Figure D.1**. The liquid and steam bubble velocities in the reactor chimney and downcomer are $V_{p,c}$, $V_{g,c}$, $V_{p,d}$ and $V_{g,d}$, respectively. The liquid/bubble relative velocity (assumed equal in the chimney and in the downcomer) is V_{pg} [2]. The chimney radius and the downcomer width are R_c and w_d, respectively. The assumptions of the model are:

a) The liquid streamlines in the chimney-to-downcomer plenum are half-circles[3] running between ξ and ξ', for which the following relation holds: $\frac{\xi}{R_c} = \frac{\xi'}{w_d}$.

b) The steam distribution in the chimney is flat (i.e. the steam bubbles in the chimney are uniformly distributed over R_c).

c) The tangential component of the liquid velocity $V_{p,\theta}$ is described by the following equation:

---

[1] which affect the Pb-Bi/steam relative velocity hence determining whether the bubbles can be dragged into the downcomer

[2] Here is V_{pg}=0.59m/s, as calculated by means of the Ishii-Kataoka-Rouhani drift flux correlation (see **Section 3.3.3.4**).

[3] this assumption is accurate when $h>(w_d+R_c)/2$.

$$V_{p,\vartheta}=\frac{1}{2}\left[(V_{p,c}+V_{p,d})+(V_{p,c}-V_{p,d})\cos\vartheta\right]$$ **Eq.D.1**

Note that this equation fulfills the boundary conditions $V_{p,\theta}=V_{p,c}$ at $\theta=0$ and $V_{p,\theta}=V_{p,d}$ at $\theta=\pi$.

d) The y-component of the liquid/bubble relative velocity is V_{pg} at any point on the bubble trajectory. Therefore is:

$V_{g,y}=V_{p,y}+V_{pg}$ **Eq.D.2**

e) The x-components of the liquid and bubble velocities are equal:

$V_{g,x}=V_{p,x}$ **Eq.D.3**

f) All the bubbles whose trajectory would end at $\eta>w_d$ are not carried-under (i.e. they are not dragged into the downcomer).

Eq.D.1, **D.2** and **D.3** and the rectangular-to-polar coordinate transformation enable calculation of the bubble trajectory as a function of w_d, R_c, $V_{p,c}$, $V_{p,d}$ and V_{pg}. The results are:

i. For $V_{p,c}<V_{pg}$ the bubble trajectory diverges and carry-under does not occur. This is an intuitive result, which is expected on the basis of simple kinematic considerations: the velocity in the downcomer is not large enough to sustain the downward bubble motion.

ii. For $V_{p,c}>V_{pg}$ the bubbles with $\xi<\xi_{cr}$ display a trajectory that ends within the downcomer width. ξ_{cr} is given by the following equation:

$$\xi_{cr}=\frac{2w_d}{(1+\frac{w_d}{R_c})\left(\frac{V_{p,c}-V_{pg}}{V_{p,d}-V_{pg}}\right)^{\frac{2V_{pg}}{V_{p,c}-V_{p,d}+2V_{pg}}}-(1-\frac{w_d}{R_c})}$$ **Eq.D.4**

Therefore, due to assumption b), the steam flow rate in the downcomer $\dot{M}_{g,d}$ (i.e. the rate of steam carry-under) is:

$$\dot{M}_{g,d}=\frac{\xi_{cr}}{R_c}\dot{M}_g$$ **Eq.D.5**

and the steam quality in the downcomer is:

$$x_d=\frac{\dot{M}_{g,d}}{\dot{M}_{g,d}+\dot{M}_p}=\frac{1}{1+\frac{R_c}{\xi_{cr}}\frac{\dot{M}_p}{\dot{M}_g}}$$ **Eq.D.6**

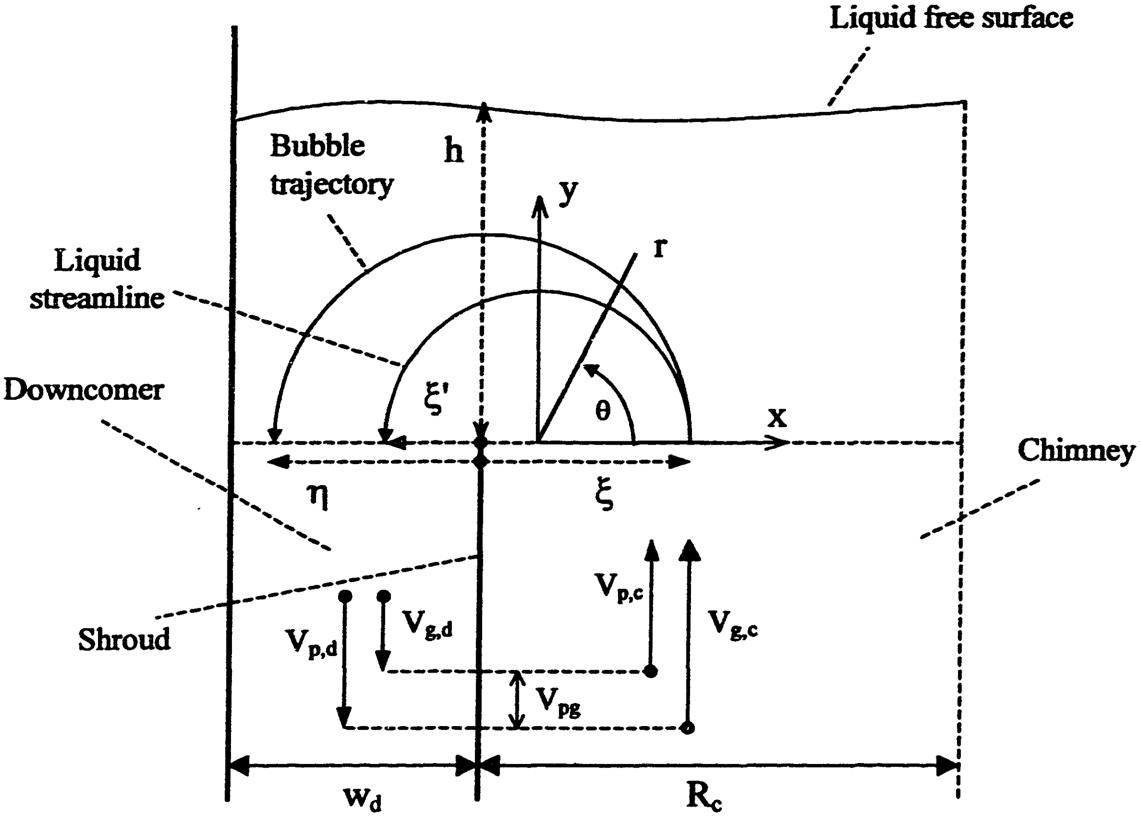

Figure D.1 Geometry and nomenclature for the steam carry-under analysis.

It is important to note that $V_{p,d}$ (the Pb-Bi velocity in the downcomer) is not only a function of the downcomer flow area $A_{dc}=\pi(2R_c w_d+w_d^2)$ and the Pb-Bi mass flow rate $\dot{M}_p$ (which are known a priori), but of the downcomer void fraction α_d as well:

$$V_{p,d}=\frac{\dot{M}_p}{\rho_p A_{dc}(1-\alpha_d)} \qquad \text{Eq.D.7}$$

But α_d depends on x_d by definition as:

$$\alpha_d=\frac{1}{1+\frac{1-x_d}{x_d}\frac{\rho_g}{\rho_p}\frac{V_{g,d}}{V_{p,d}}}=\frac{1}{1+\frac{1-x_d}{x_d}\frac{\rho_g}{\rho_p}\frac{V_{p,d}-V_{pg}}{V_{p,d}}} \qquad \text{Eq.D.8}$$

Therefore, **Eq.D.4, D.6, D.7** and **D.8** represent a system of four equations in the unknown x_d, α_d, $V_{p,d}$ and ξ_{cr} with w_d, R_c, $V_{p,c}$, V_{pg} and $\dot{M}_p$ as known parameters. Given the non-linearity of the equations, the solution of this system requires the use of iterations. These equations can be used to evaluate the magnitude of steam carry-under as a function of the downcomer width as illustrated in **Figure D.2**, where x_d is plotted against w_d for a given chimney radius, chimney steam flow rate and Pb-Bi flow rate. Note that, in an all-liquid downcomer ($\alpha_d=0$), $w_{d,cr}=0.86$m is the critical value of w_d at which $V_{p,d}$ is equal to V_{pg}.

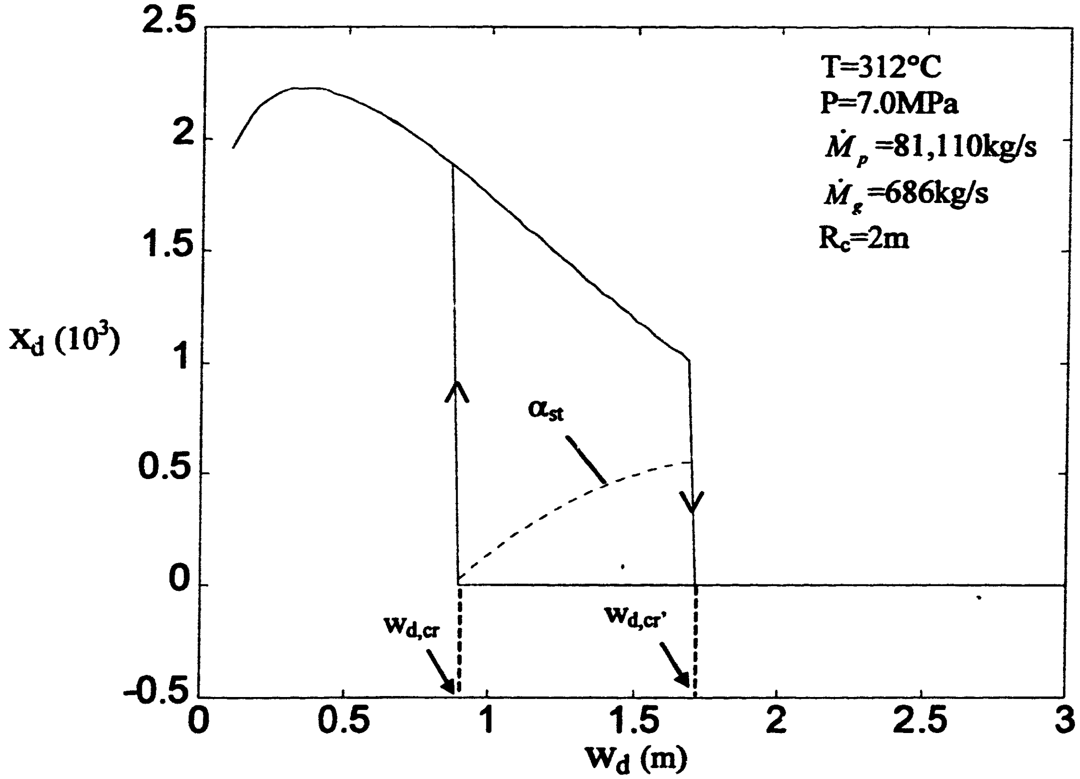

Figure D.2. The effect of the downcomer width on steam carry-under.

Figure D.2 displays several noteworthy characteristics that ought to be explained.

- $w_d<w_{d,cr}$

  The maximum value of x_d is the result of two conflicting effects: i) at very low w_d most bubbles (in their trajectory) hit the vessel wall before reaching the downcomer (see assumption f)) and are not carried-under, ii) as w_d increases the liquid velocity in the chimney-to-downcomer plenum decreases and fewer bubbles are dragged down to the downcomer.

- $w_{d,cr}<w_d<w_{d,cr}'$

  x_d is a multi-valued function in this geometry region. For any w_d there are two different possible values of x_d, one corresponding to no carry-under ($x_d=0$) and one corresponding to some carry-under ($x_d>0$). They are both valid and physically acceptable solutions of **Eq.D.4, D.6, D.7** and **D.8**. The $x_d>0$ solution arises from the positive feedback effect described by **Eq.D.7**: the greater the rate of carry-under, the greater the downcomer void fraction, the greater the downcomer liquid velocity, the greater the rate of carry-under. The relative stability of the two solutions in a practical situation depends on the initial presence of steam in the downcomer. If the amount of steam in the downcomer is initially "small", the situation evolves towards the $x_d=0$ solution because the liquid velocity in the downcomer is low ($V_{p,d}<V_{pg}$) and cannot sustain carry-under. On the other hand, if the downcomer is initially perturbed by the presence of a "large" amount of steam, the liquid velocity may be large enough to sustain carry-under and the $x_d>0$ solution will hold. It is of paramount importance to determine the magnitude of the initial perturbation that leads to the $x_d>0$ solution. In other words, it is important to establish the domain of stability of the two solutions. The iterative solution of **Eq.D.4, D.6, D.7** and **D.8** readily lends itself to this purpose: it can be shown that, depending on the first guess of the downcomer void fraction α_d, the unknown x_d converges to either the zero or the positive finite value. The value of the void fraction first guess at which this transition occurs is also plotted in **Figure D.2** (this curve is designated α_{st}). It can be then concluded that, for w_d between $w_{d,cr}$ and $w_{d,cr'}$, an initially steam-free downcomer remains so until a steam perturbation of magnitude α_{st} occurs.

- $w_d>w_{d,cr'}$

  In this region the downcomer is so wide (hence the downcomer liquid velocity so small) that the only possible solution of the equations is $x_d=0$ and no carry-under can take place.

Clearly, the only way to guarantee that no carry-under occurs in our reactor would be to select a downcomer of width greater than $w_{d,cr'}\approx1.7$m. However, this is likely to not be economically viable: a wide downcomer greatly increases the total Pb-Bi inventory[4] and the overall size of the reactor pool. Therefore, it might be necessary to design the downcomer within the multi-valued region ($w_{d,cr}<w_d<w_{d,cr'}$). This leaves room to the theoretical possibility of carry-under. Nevertheless, at w_d equal (for example) to 1.0m the inception of carry-under does not take place until a 0.18 void fraction perturbation is induced: the occurrence of such a large perturbation is

---

[4] Bismuth is relatively costly (see **Section 1.2.2**)

unlikely and for any practical purposes steam carry-under could be ruled out. Thus, 1.0m is selected as the reference value of the PBWR downcomer width.

The presence (under certain conditions) of two different (but both valid) solutions of the equations describing steam carry-under suggests the possibility of a hysteresis cycle. This can be clearly observed by plotting x_d (the magnitude of carry-under) vs. $\dot{M}_p$ (the Pb-Bi mass flow rate) for a given system geometry and steam quality in the chimney[5], as illustrated in **Figure D.3**.

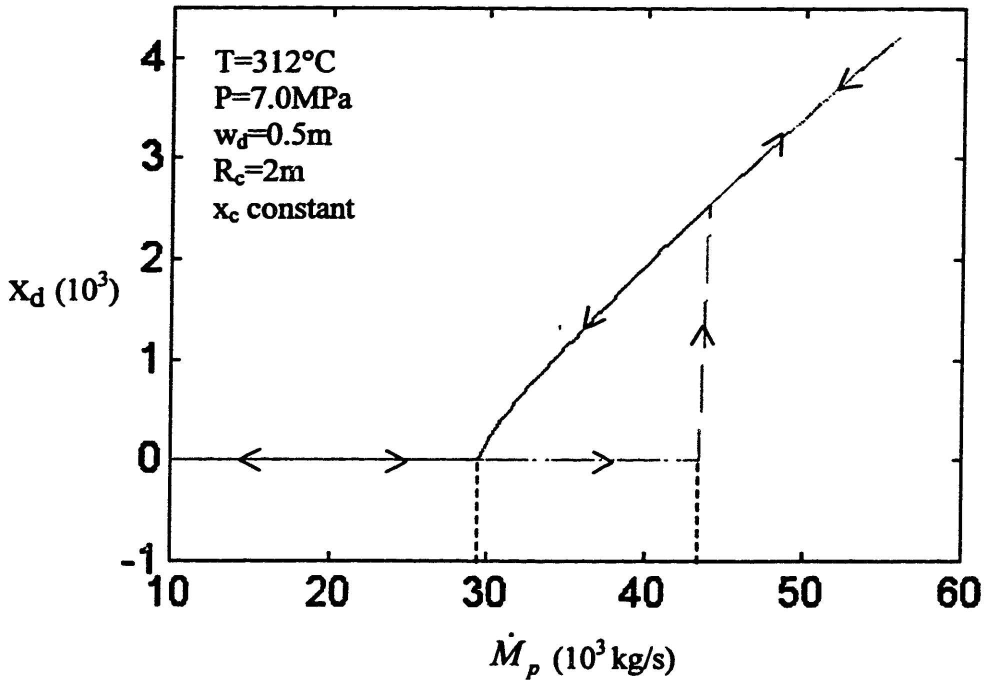

Figure D.3. Steam carry-under hysteresis cycle.

Starting at low values of $\dot{M}_p$ the liquid velocity in the downcomer is small and no carry-under takes place. At approximately 43,000kg/s [6], carry-under inception occurs, x_d jumps up to a finite positive value and then smoothly increases with $\dot{M}_p$. When $\dot{M}_p$ is decreased, x_d follows the smooth curve past 43,000kg/s and all the way down to 29,000kg/s where again x_d=0. Although steam carry-under in a plenum pertains to a relatively simple and basic system (i.e. a gravity

---

[5] This means that the steam mass flow rate in the chimney is increased proportionally to the Pb-Bi mass flow rate.
[6] corresponding to $V_{p,d}=V_{pg}$

steam separator), the literature on this topic is relatively scarce and to the author's knowledge, this hysteresis cycle has not been theoretically identified or experimentally observed yet.

One of the fundamentals assumptions made in this study is that the steam/Pb-Bi relative velocity V_{pg} is the same in the chimney and in the downcomer. This is not the case in reality where the chimney and the downcomer can be in two distinct flow regimes (e.g. churn flow in the chimney, bubbly flow in the downcomer) due to the different flow direction and steam quality. Also, the assumption that there exists a single V_{pg} within one region (e.g. the chimney) is not necessarily correct. V_{pg} varies with the bubble diameter and, because in any two-phase flow there is a distribution of bubbles, it is reasonable to conclude that there is a distribution of V_{pg} as well. Therefore, our analysis only approximates the actual situation: this approximation is rather accurate if the relative velocity distribution can be effectively described by a single average value. Note that the presence of a distribution of relative velocities V_{pg} tends to smoothen the sharp carry-under inception discontinuities in **Figure D.2** and **D.3**, because different bubbles are carried-under in the downcomer at different liquid velocities. Also, if very small bubbles are present in the flow[7], the possibility of completely eliminating carry-under becomes questionable, as experimentally verified in [Petrick 1963].

Marshall [Marshall 1964] observed a sharp increase of carry-under rate in water-air gravity separators at low pressure upon formation of a stationary air slug in the downcomer. This stable slug occurs at a threshold downcomer liquid velocity and is the result of bubble coalescence after the liquid boundary layer separates from the shroud. Reference [Marshall 1964] gives a correlation to estimate the threshold liquid superficial velocity in the downcomer as:

$$j_{pc,th} = 0.35\sqrt{2g(R_c + w_d)} \qquad \textbf{Eq.D.9}$$

For R_c=2m and w_d=1m, the above equation yields $j_{pc,th}\approx 2.7$m/s, which is well above the PBWR downcomer operating liquid superficial velocity at $\dot{M}_p$=81,110kg/s. Although Marshall's correlation is based on water-air data in relatively small vessels only (and therefore cannot be very reliably applied to our case), it gives an indication that this type of instability (i.e. the slug bubble in the downcomer) is not likely to take place in the PBWR.

Finally we shall observe that it is possible to improve the design of the chimney upper plenum to minimize steam carry-under. The Petrick model indicates that most carry-under

---

[7] the relative velocity V_{pg} is generally a decreasing function of the bubble size

emanates from the peripheral region of the chimney where the liquid streamlines curving 180° into the downcomer are short and tight: as a result, the bubbles of this region are efficiently dragged to the downcomer. However, if the sharp U-turn is prevented by installing the straightening ring shown in **Figure D.4**, the passage time of the peripheral bubbles in the plenum increases and so does their probability of flowing up to the liquid free surface where the steam leaves the pool.

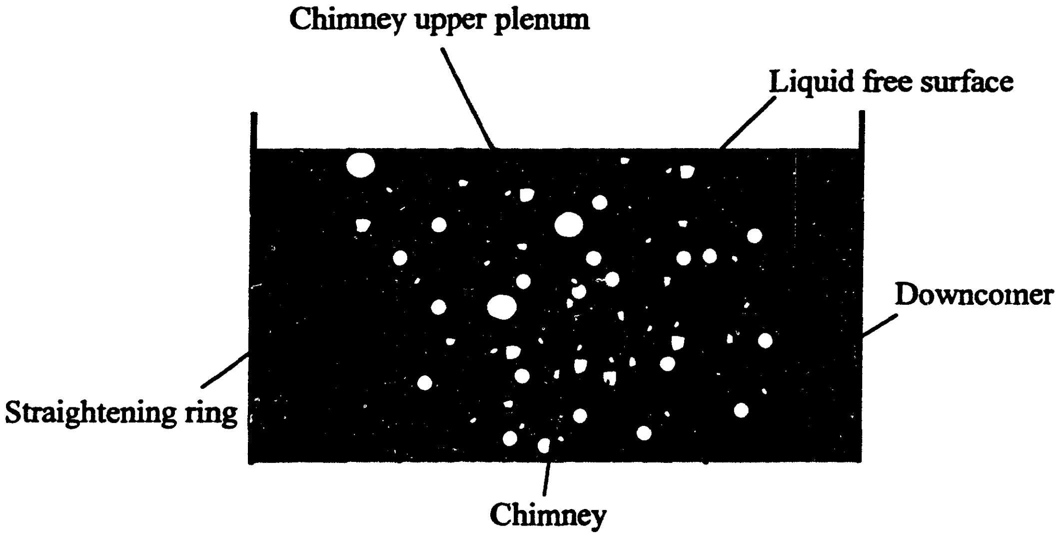

Figure D.4. The effect of the liquid flow path on the bubble trajectory.

Appendix E

- DERIVATIVES OF THE DRIFT-FLUX VOID FRACTION CORRELATIONS -

In this appendix, it is demonstrated that a void fraction correlation based on the drift-flux model satisfies criteria 3), 4) and 5) in **Section 3.3.3.3.**

The general form of the drift-flux correlations is:

$$\alpha = \frac{\beta}{C_0 + u_{wj}/j} \qquad \textbf{Eq.3.19}$$

Using **Eq.3.23** and **3.24, Eq.3.19** becomes:

$$\alpha = \frac{x/\rho_w}{\left[\frac{x}{\rho_w} + \frac{1-x}{\rho_p}\right] C_0 + \frac{u_{wj}}{G}} \qquad \textbf{Eq.E.1}$$

In principle the drift-flux coefficients C_0 and u_{wj} should depend only on the flow regime and not on x and G. This is rigorously correct for the Zuber slug and churn correlations as well as for the Kawanishi and Corradini-Casas correlations. On the other hand, the coefficients of the EPRI and IKR correlations depend (although weakly) on G and x. To simplify the analysis, this dependence is neglected here. Then for all drift-flux correlations the following relations hold:

$$\left(\frac{\partial \alpha}{\partial x}\right)_G = \frac{\frac{1}{\rho_w}\left(\frac{C_0}{\rho_p} + \frac{u_{wj}}{G}\right)}{\left\{\left[\frac{x}{\rho_w} + \frac{1-x}{\rho_p}\right] C_0 + \frac{u_{wj}}{G}\right\}^2} \qquad \textbf{Eq.E.2}$$

$$\left(\frac{\partial \alpha}{\partial G}\right)_x = \frac{\frac{x u_{wj}}{\rho_w G^2}}{\left\{\left[\frac{x}{\rho_w} + \frac{1-x}{\rho_p}\right] C_0 + \frac{u_{wj}}{G}\right\}^2} \qquad \textbf{Eq.E.3}$$

Because C_0, u_{wj}, x and G are positive by definition, **Eq.E.2** and **E.3** imply that $\left(\frac{\partial \alpha}{\partial x}\right)_G > 0$ and $\left(\frac{\partial \alpha}{\partial G}\right)_x > 0$ for any value of x and G, respectively and thus the drift-flux correlations satisfy criterion 3) and 4).

Multiplying **Eq.E.2** times x and **Eq.E.3** times G, respectively, and canceling out the denominators, it can be readily demonstrated that criterion 5) is also satisfied for any values of x and G.

Appendix F

- THE POLONIUM TRAP -

To measure the activity of gaseous polonium compounds, it is necessary to vent the residual gases off the autoclave and bubble them through a solution that traps the polonium. The alpha-activity of the contaminated trapping solution can be then counted in a liquid scintillator. Therefore, the function of the trap is twofold:

a. To convert the volatile polonium hydride into a form that is suitable for measurements in a liquid scintillator or an alpha-spectrometer.
b. To minimize the release of toxic polonium into the environment.

F.1 Selenium as a Polonium Homologue

Given the potential hazard posed by the radiotoxicity of ^{210}Po, it is indispensable to ensure that the trapping efficiency of the solution is large (i.e. as close to 100% as possible). For this purpose, prior to the radioactivity portion of the experimental campaign, the performance of the trapping solution was tested by means of H_2Se whose chemical behavior closely resembles that of H_2Po. In fact the values of the trapping efficiency so obtained are a conservative estimate of the actual trapping efficiency for polonium, as H_2Se is chemically more stable than H_2Po.

In this section the use of selenium as a chemical homologue of polonium is discussed and justified. Polonium is a metal that belongs to Group VI of the table of elements along with oxygen, sulfur, selenium and tellurium. In general, elements of the same group share similar chemical characteristics and it is therefore natural to look for a chemical homologue of polonium within this group. Oxygen and sulfur are discarded because they do not display metallic behavior[1].

---

[1] Metallic sulfur can actually be stable but in a very limited region of the potential-pH diagram.

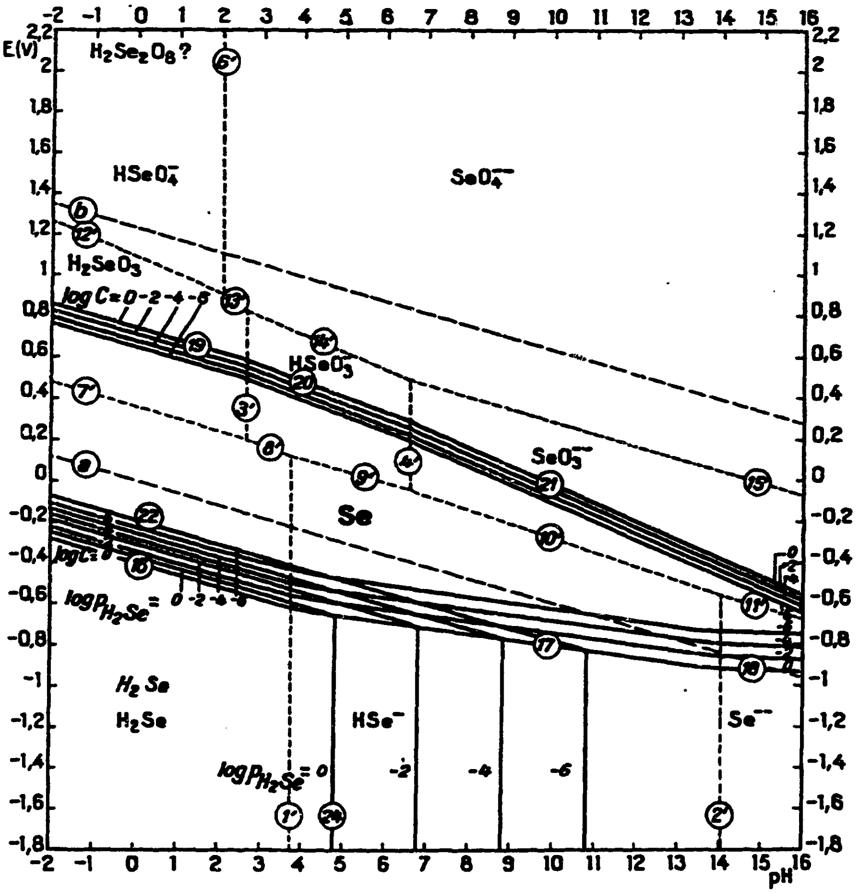

Figure F.1. Pourbaix diagram of Selenium (from [Pourbaix 1966]).

The potential-pH diagram (i.e. Pourbaix diagram) of selenium, tellurium and polonium is shown in **Figure F.1**, **F.2** and **F.3**, respectively. It can be seen that the hydride stability domain is limited to the low pH region and lies below the hydrogen oxidation line (a). Clearly, the stability of the hydride decreases from selenium to polonium as indicated by the increasingly negative reversible potential of the reaction:

$M+2H^++2e^-\leftrightarrow H_2M$ (the metal is designated as M) **Eq.F.1**

A good stability of the hydride is desirable as it renders its production and handling easier.

On the basis of this criterion, selenium is selected as a viable chemical homologue of polonium and will be used to test the efficiency of the polonium trap. Also, given the larger stability of H_2Se with respect to H_2Po, the values of the trapping efficiency so obtained will be a conservative estimate of the actual efficiency for polonium.

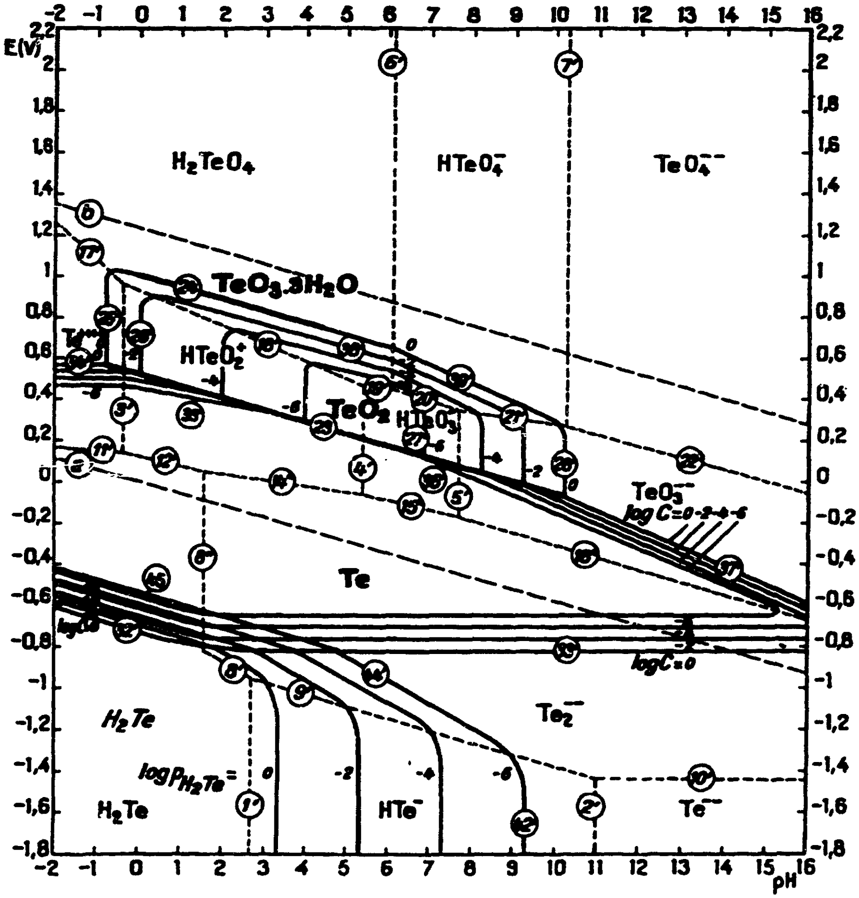

Figure F.2. Pourbaix diagram of Tellurium (from [Pourbaix 1966]).

It is interesting to observe that **Figure F.3** seems to indicate that, at low potentials, polonium hydride is stable at any pH as opposed to selenium and tellurium hydrides, which decompose into selenide and telluride ions, respectively. However, it is reasonable to assume that, given the scarcity of data on polonium hydride, its decomposition into polonide ions at high pH was ignored in [Pourbaix 1966] and the chemical behavior of polonium actually resembles that of selenium and tellurium in alkaline solutions, too.

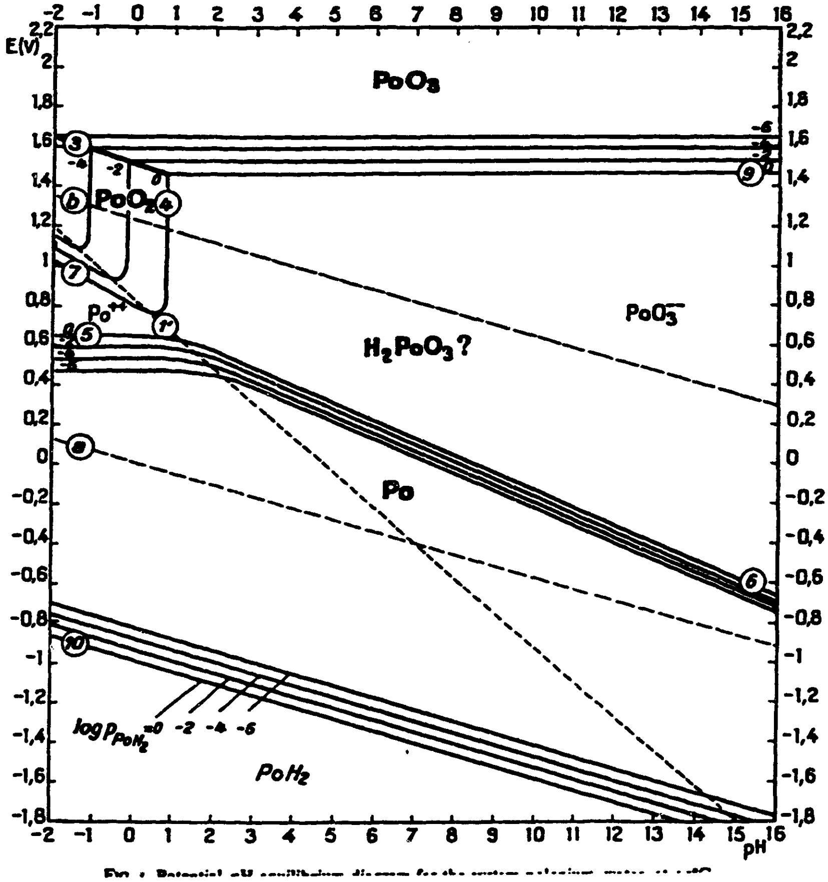

Figure F.3. Pourbaix diagram of Polonium (from [Pourbaix 1966]).

F.2 Chemical Design of the Trap

Because H_2Se is gaseous at room temperature[2], it is indispensable to chemically decompose it into a solution specie for analysis.

In aqueous solution the following ionic equilibria exist:

$H_2Se \leftrightarrow H^+ + HSe^-$	$k_{H2Se}=1.8\times10^{-4}$	**Eq.F.2**
$HSe^- \leftrightarrow H^+ + Se^{2-}$	$k_{HSe}=9.8\times10^{-15}$	**Eq.F.3**

These equilibria suggest that the concentration of H^+ can be adjusted to select the desired relative concentration of H_2Se, HSe^- and Se^{2-}. A plot of the relative concentration of these species vs. the solution pH is shown in **Figure F.4**.

---

[2] H_2Se boiling point at 1atm is –41°C.

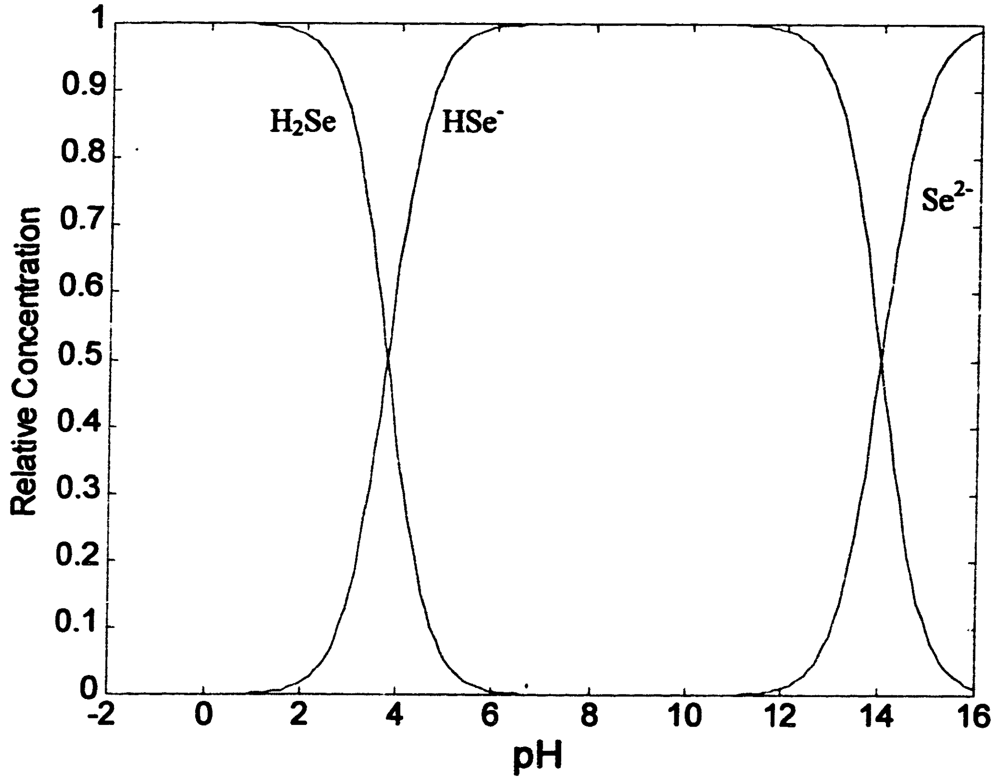

Figure F.4. Speciation of selenium species in aqueous solution.

Clearly, a very alkaline solution can ensure effective H_2Se decomposition to Se^{2-}, hence providing adequate trapping efficiency. A 0.1M solution of potassium hydroxide KOH is selected to achieve a suitable alkalinity (i.e. pH≈13). However, **Figure F.1** shows that the stability region of Se^{2-} lies below the oxygen reduction line (b), hence suggesting that, if the trapping solution is aerated, Se^{2-} is oxidized to $Se0_3^{2-}$, which is soluble and non-volatile thus representing a suitable form to measure and dispose of selenium.

Therefore, the process of selenium hydride trapping takes place through two distinct reactive events upon contact with the trapping solution:

$H_2Se \leftrightarrow 2H^+ + Se^{2-}$ **Eq.F.4**

$Se^{2-}+6OH^- \rightarrow Se0_3^{2-}+3H_2O+6e^-$ **Eq.F.5**

F.3 Production of H_2Se

Selenium hydride is a colorless gas with a foul smell, highly toxic and irritating to eyes and skin. It finds industrial application in the semiconductor industry. It is commercially available from several suppliers in the US (as pressurized pure liquid or as gaseous mixture with hydrogen), but in relatively large quantities only (>500g). However, for the purpose of our experiment, it was decided to produce it at MIT because:

a. Its cost is rather high (i.e. a 500g cylinder runs at $500) and delivery times may be long (i.e. up to 6 weeks).
b. Safe handling and disposing of substantial quantities of selenium hydride may be difficult.
c. Testing the efficiency of the trap does not require more than few milligrams of selenium hydride.

A rather straightforward way to produce selenium hydride is the hydrolysis of aluminum selenide Al_2Se_3 in acid solutions at room temperature [Greenwood 1984] as:

$Al_2Se_3+6H^+ \rightarrow 3H_2Se+2Al^{3+}$ **Eq.F.6**

Aluminum selenide is an inexpensive and toxic dark brown crystalline solid. One gram of 99.8% aluminum selenide was purchased from the chemical supplier Alfa Aeser.

F.4 Measuring Selenium

Selenium was detected and quantitatively measured by means of a ICP Atomic Emission Spectrometer. In this machine the solution that contains selenium is nebulized and passed through a plasma torch (which excites the atomic energy levels) and the characteristic emitted radiation is measured by a multi-channel spectrometer. The output is in the form of counts per seconds (i.e. photons per seconds) at a given wavelength.

Prior to utilization in our experiment, it was necessary to assess the lower and upper limit of selenium detection of the ICP and the background noise at characteristic selenium wavelengths. A set of selenium solution samples of concentration ranging from 1μM to 10mM was used to generate the selenium calibration curve.

This curve is shown in **Figure F.5** where the net ICP output (net cps=total cps-background cps) is plotted (in log-log scale) against the solution concentration. The background noise is 1235±21cps. The best fitting curve (in a least-square sense) is:

$C_{Se}=7.61\times10^{-9}\,(cps_0)^{1.02}$ **Eq.F.7**

where C_{Se} is the selenium concentration (in M) and cps_0 is the net cps.

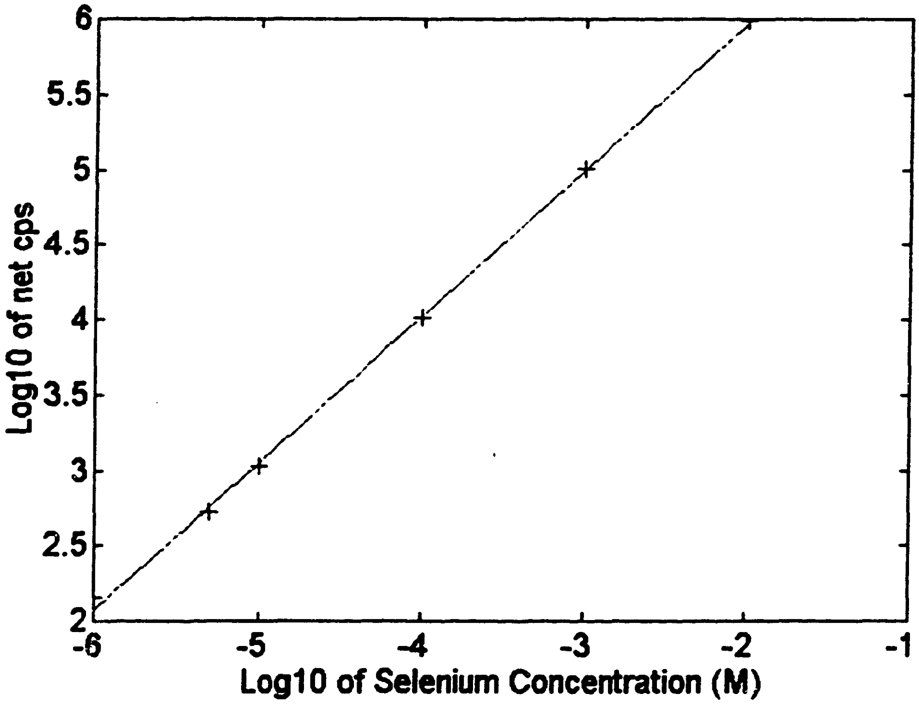

Figure F.5. Calibration curve of the ICP spectrometer.

It can be seen that the response is almost linear over the entire concentration range. The lower limit of detection is fixed at 1µM because, at this low concentration, the ICP output becomes comparable (within two standard deviations) with the background noise.

Because the calibration curve does not display any tendency to level off at 10mM, it is safe to assume that the upper limit of detection is at least 10mM.

F.5 The Experimental Apparatus

A schematic of the experimental apparatus utilized to test the trap efficiency is illustrated in **Figure F.6.**

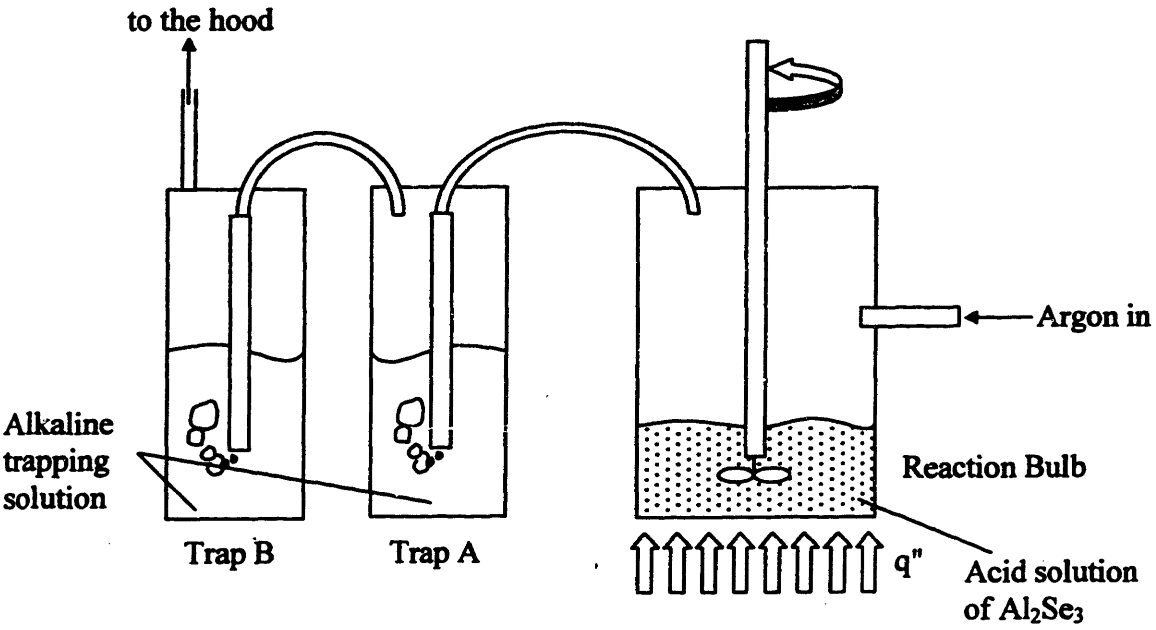

Figure F.6. Trap testing apparatus.

The reaction bulb is connected to two traps in series to maximize the trapping efficiency.

The following operations were performed.

Some aluminum selenide (i.e. 161.6mg) was placed in the reaction bulb. A controlled amount (i.e. 27.5ml) of 0.097M nitric acid (HNO_3) solution was added to the Al_2Se_3 crystals via an automatic burette. Heat was supplied and vigorous stirring was provided to improve the kinetics of the hydrolysis reaction. A constant argon flow ensured effective convection of the selenium hydride to traps A and B. After few minutes, the initially colorless trap solution began to turn darker whereas trap B remained unchanged, signaling effective selenium trapping in A. Despite the addition of heat and vigorous stirring, solid undissolved crystals of Al_2Se_3 were still visible in the reaction bulb after 1hr. Because measurements by ICP require species in solution, any assessment of the trapping efficiency involving a mass balance over the reaction bulb was considered impractical. However, the two trap configuration readily enables measuring the trapping efficiency by comparing the selenium concentration in trap A and B[3]. This point requires some explanation. If the efficiency η of a single trap is defined as the ratio of the captured to supplied selenium, then the selenium flow in the experimental apparatus can be schematically represented as in **Figure F.7**.

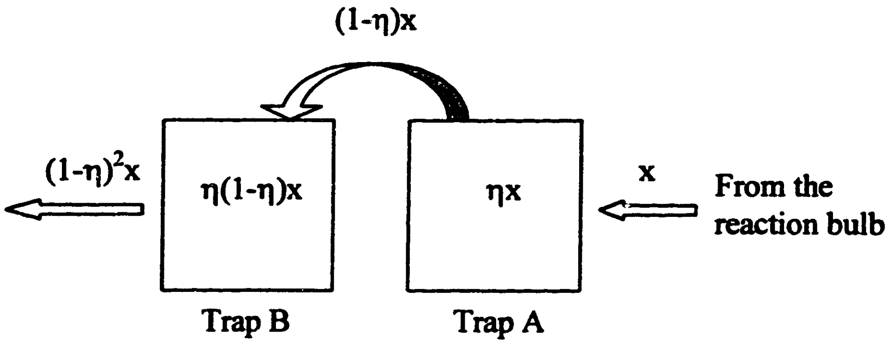

Figure F.7. Selenium flow in the traps[4].

In **Figure F.7** x is the (unknown) amount of selenium hydride leaving the reaction bulb. Therefore, the efficiency of a single trapping stage can be evaluated by taking the ratio of the (measured) selenium concentration in trap B and trap A. This ratio is equal to $1-\eta$, does not depend on x and does not require any measure on the reaction bulb.

The ICP output for trap A and B is 63782±875cps and 1253±16cps, respectively. The selenium concentration in trap A is then 594±8μM as can be readily calculated from **Eq.F.7** (the calibration curve). Because the cps output of trap B is within the background noise, it can be conservatively assumed that the selenium concentration in trap B be at most 1±0.01μM.

Then the ratio of selenium concentration in the traps yields:

$1-\eta=1/594 \Rightarrow \eta=0.998\pm0.003$ **Eq.F.8**

In view of the fact that polonium hydride is expected to be chemically more unstable than selenium hydride (as discussed in **Section F.1**) and thus more readily captured, it can be stated that the efficiency of the polonium hydride trapping solution will be in excess of 99.8%, which is considered satisfactory.

A ICP measurement of the aluminum concentration of trap A and B solutions was undertaken with the goal of confirming that selenium hydride (as opposed to Al_2Se_3) was transported from

---

[3] Note that selenium is present in the traps as the soluble species SeO3- and therefore can be measured in the ICP.

[4] It is assumed that the two traps be identical.

the reaction bulb to the traps. Because the aluminum cps are within the background, this measurement demonstrates that the reaction of formation of selenium hydride actually took place in the bulb.

Appendix G

- POLONIUM PROCUREMENT BY IRRADIATION OF BISMUTH SAMPLES IN THE MITR -

Although polonium is a naturally occurring element[1], all its isotopes are radioactive and have no major industrial applications. Procurement of significant polonium from a commercial supplier is somewhat problematic and expensive also due to the toxicity and intense radioactivity of the material. For example, it is possible to buy 5mCi of ^{210}Po as polonium chloride in aqueous solution from Isotope Products Labs at a rated cost of $2,250. On the other hand, 5μCi/ml ^{209}Po solution of 5M nitric acid from the Oak Ridge National Laboratory runs at $3,618 per μCi. However, ^{210}Po can be readily obtained by irradiating bismuth samples in a nuclear reactor hence making use of the reaction of **Eq.6.1**. Annual funds for research related irradiation are available at the MIT Reactor (MITR), that would make the procurement of our polonium very inexpensive. Moreover, it will be demonstrated below that polonium activities up to several hundreds of mCi can be quickly achieved in the irradiation channels of the MITR. Consequently, it was decided not to buy the polonium from an external supplier, but to produce it on-campus instead.

The MITR has several irradiation channels featuring different neutron spectra and fluxes. The neutron capture cross section of ^{209}Bi, σ, varies with energy, being larger at low energy (30mb averaged over a Maxwellian thermal spectrum vs. 4.7mb averaged over the fission spectrum [BNL 2000]). Therefore, it is decided to conduct the irradiation in the MITR high flux thermal spectrum channel, which enables a higher rate of polonium production hence minimizing the irradiation time. The thermal neutron flux, Φ, in this channel is nominally rated at 5×10^{13}n/cm^{2}s. This channel also has a fast flux component of 4×10^{12}n/cm^{2}s. The maximum allowed irradiation time is t_{irr}=12hrs.

---

[1] ^{210}Po, ^{214}Po and ^{218}Po are part of the decay chain of ^{238}U

G.1 Irradiation Design

We will now estimate the ^{210}Po and ^{210}Bi activity resulting from neutron bombardment of the bismuth samples. The activation analysis is based on the solution of the following system of ordinary differential equations:

$$\begin{cases} \dfrac{dB}{dt} = \sigma N_{Bi}\Phi - \lambda_B B & \textbf{Eq.G.1} \\ \dfrac{dP}{dt} = \lambda_B B - \lambda_P P & \textbf{Eq.G.2} \end{cases}$$

where B and P are the density of ^{210}Bi and ^{210}Po nuclei, respectively. N_{Bi} is the density of ^{209}Bi nuclei in the sample. λ_B ($\sim 1.6\times 10^{-6}s^{-1}$) and λ_P ($\sim 5.8\times 10^{-8}s^{-1}$) are the decay constants of ^{210}Bi and ^{210}Po, respectively. The initial conditions are B(0)=0 and P(0)=0. Φ is set identically equal to zero for $t>t_{irr}$.

Eq.G.1 and **Eq.G.2** are solved by means of an implicit finite difference method, which is stable for any choice of the time discretization. The calculation output is illustrated in **Figure G.1** for the reference case t_{irr}=12hr and $\Phi=5\times 10^{13}$n/cm^{2}s. As expected the ^{210}Bi specific activity raises rapidly until the end of the irradiation and then decays with a half-life of 5 days. Consequently, the ^{210}Po specific activity reaches its maximum (~0.21Ci/kg) approximately 25 days after the end of the irradiation and then starts to decay with a half-life of about 140 days. Note that within 25 days after the irradiation (equal to five ^{210}Bi half-lives) the ^{210}Bi activity decreases by a factor 2^5=32. It was also calculated that, assuming the mass of each bismuth sample is 56g, the total activity per sample due to ^{210}Bi and ^{210}Po is about 0.35Ci, 0.31Ci and 0.023Ci at the end of the irradiation, 1 day after the irradiation and 25 days after the irradiation, respectively.

It is important to assess the rate of heat generation by radioactive decay of the two nuclides to ensure that the temperature of the sample does not become too high as to cause melting of the sample itself. The thermal power per unit mass of the sample is plotted versus time in **Figure G.2**. Clearly, the radioactive heat deposition rate is negligibly small for all practical purposes.

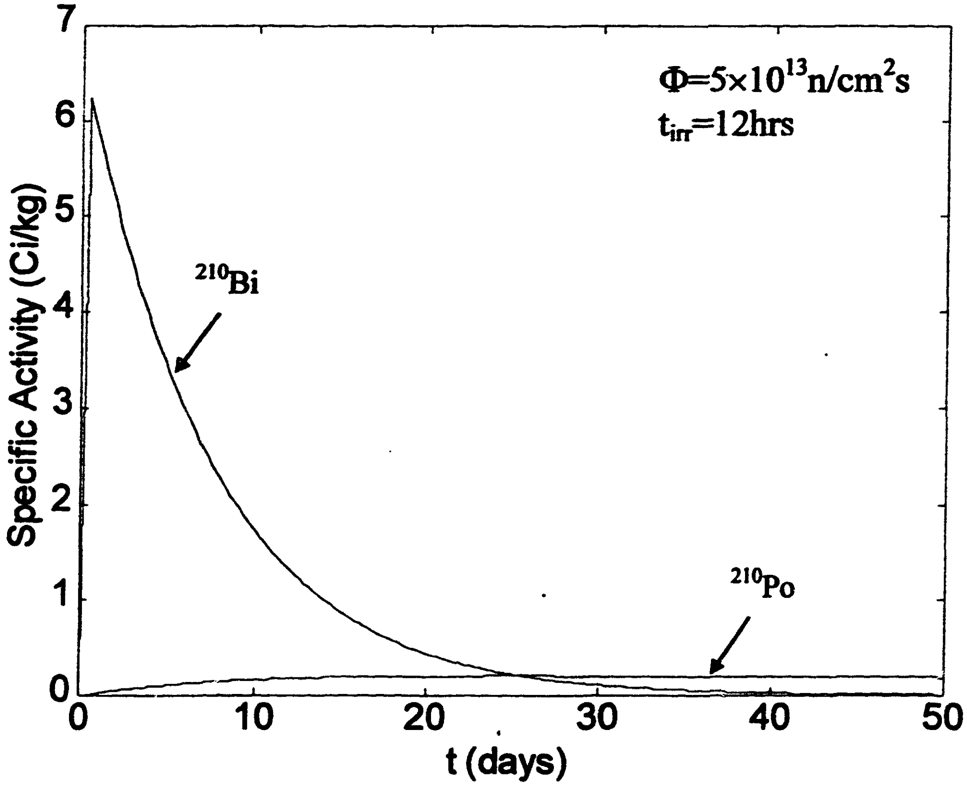

Figure G.1. Radioactivity of the bismuth samples.

Also, it should be demonstrated that sample heating due to the gamma field in the irradiation channel is not excessive. The gamma exposure $\dot{R}$ in the selected MITR channel is known to be about 10^7R/hr. One roentgen is defined as the exposure resulting in an ionization of 1esu (1esu=3.33×10^{-10}C) per cm^3 of air at 0°C and 1atm. Therefore the exposure $\dot{R}$ is a specific ionization and can be computed as:

$$\dot{R}=e\frac{\varepsilon_\gamma \mu_{air}\Phi_\gamma}{I_{air}}=e\frac{\varepsilon_\gamma \rho_{air}(\mu/\rho)_{air}\Phi_\gamma}{I_{air}} \qquad \textbf{Eq.G.3}$$

where e is the electronic charge, ε_γ is the average energy of the gamma photon, μ_{air} is the attenuation coefficient in air (1/cm), Φ_γ is the gamma flux (gammas/cm^{2}s), I_{air} is the average ionization potential of air (34eV) and ρ_{air} is the air density at reference conditions (0.129g/cm^3). On the other hand, the rate of gamma heat deposition per unit mass of the bismuth sample, $\dot{W}_{Bi}$ is:

$$\dot{W}_{Bi}=\varepsilon_\gamma(\mu/\rho)_{Bi}\Phi_\gamma \qquad \textbf{Eq.G.4}$$

Assuming that the reduced attenuation coefficient (μ/ρ) is independent of the medium[2], **Eq.G.3** and **Eq.G.4** yield the following conversion relation:

$$\dot{W}_{Bi} = \frac{I_{air}}{e\rho_{air}}\dot{R} \qquad \textbf{Eq.G.5}$$

Therefore, for $\dot{R}=10^7$R/hr, it is $\dot{W}_{Bi}\approx 2.4\times10^{-4}$W/g, which is larger than the radioactive decay heating, but still negligibly small.

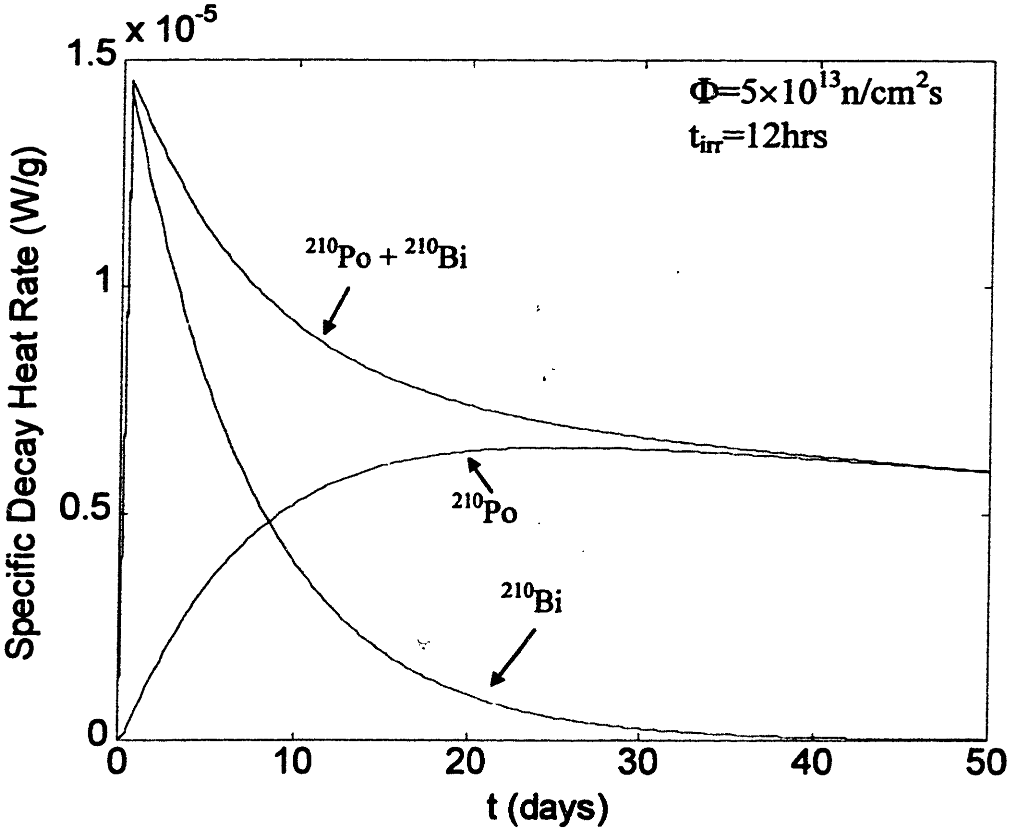

Figure G.2. Decay heat in the bismuth samples.

We have seen above that the maximum ^{210}Po specific activity achieved in the bismuth samples is 0.21Ci/kg, which translates into a 0.55×0.21=0.116Ci/kg specific activity when the irradiated bismuth is molten and mixed with lead to form the Pb-Bi eutectic. From **Figure 6.2** it can be seen that such specific activity in the Pb-Bi melt corresponds to an estimated polonium

---

[2] This is a rather accurate approximation for gammas of energy around 1MeV, for which Compton scattering is the dominant mechanism of interaction.

activity of about 5×10^3Bq/m^3 in steam of atmospheric pressure at 400°C. Because the volume of the autoclave is about 250ml=2.5×10^{-4}m^3, the total polonium activity in the autoclave is expected to be at least 1.2Bq, which is thought to be detectable by either the Liquid Scintillator of the RPO or the Alpha-Spectrometer (see Appendix I). Therefore, it is concluded that a bismuth sample specific activity of 0.21Ci/kg, as obtained in a 12hr irradiation at 5×10^{13}n/cm^{2}s, is acceptable.

G.2 Bismuth Impurities and Preliminary Irradiation

The irradiation samples are made of "technical grade" 99.99% bismuth purchased (in form of 2.8mm shots) from the Belgian supplier Sidech SA at a cost of $80/kg + shipment. Chemical analyses performed at Sidech guarantee the quality of the product and characterize the composition of the impurities as reported in **Table G.I.** Although the goal of the irradiation is to produce ^{210}Bi and hence ^{210}Po, the generation of undesirable radioactive by-products is inevitable due to the presence of these impurities. It is necessary to assess the number and amount of the relevant by-products to ensure that they do not raise a radiological concern and/or affect the outcome of the experiment.

Table G.I. Impurities in 99.99% Sidech bismuth.

Element	Weight Fraction (ppm)
Ag	2.2
Pb	3.4
Cd	0.2
Zn	0.2
Cu	1.1
Sb	3.0
Fe	0.7
Ni	5.0

To this purpose, a preliminary short irradiation of a small bismuth sample (0.5334g) was conducted in the 5×10^{13}n/cm^{2}s MITR irradiation channel[3]. After two minutes of neutron irradiation, several radionuclides were detected and their respective specific activity[4] (μCi/g$_{Bi}$) was measured by means of a High Purity Germanium Reverse Electrode Gamma Spectroscope, as reported in **Table G.II**. It is thought that all these nuclides are the products of a (n,γ) reaction on an isotope of the same element. This preliminary irradiation indicates the presence of additional impurities that were not identified by Sidech's chemical analysis (see **Table G.I**): sodium, aluminum, chlorine, vanadium, manganese, indium, tin, platinum and gold.

It is anticipated that the impurities will give birth to several other longer-lived radionuclides that were not seen after the short preliminary irradiation such as: ^{110m}Ag, ^{115m}Cd, ^{65}Zn, ^{59}Fe, ^{63}Ni, ^{60}Co. The radioisotope ^{60}Co is the result of a fast (n,p) reaction on ^{60}Ni.

Table G.II. Results of the preliminary irradiation.

Radionuclide	**Half-Life**	**Specific Activity** (μCi/g$_{Bi}$)
^{24}Na	15h	0.0108
^{28}Al	2.3m	0.9318
^{38}Cl	37m	0.023055
^{52}V	4m	0.0527
^{56}Mn	2.6h	0.0076198
^{116}In	54m	0.00242
^{125}Sn	9.5m	0.000875
^{197}Pt	1.6h	0.0617
^{198}Au	2.5d	0.002
^{66}Cu	5m	0.053349

It is necessary to calculate the activities of these longer-lived radionuclides as well as to scale up the activities of **Table G.II** to the duration of the actual polonium production irradiation (i.e. 12 hours). The specific activity, a_{irr} (Ci/kg$_{Bi}$), resulting from an irradiation time t_{irr} at a flux Φ_k

---

[3] i.e. the same channel where the long irradiation of the bismuth samples will take place.

[4] The reported values of the specific activity are actually decay-adjusted.

and the specific activity, a_{dec} (Ci/kg$_{Bi}$), after 24 hours decay time, t_{dec}, can be calculated as, respectively:

$$a_{irr,j} = \sigma_k \frac{N_k}{\rho_{Bi}} \Phi_k \left(1 - e^{-\lambda_j t_{irr}}\right) \qquad \textbf{Eq.G.6}$$

$$a_{dec,j} = a_{irr,j} e^{-\lambda_j t_{dec}} \qquad \textbf{Eq.G.7}$$

where j and k indicate the initial stable isotope and its product of neutron activation, respectively. Φ_k is the flux relevant to the reaction on the isotope k (i.e. the thermal flux 5×10^{13}n/cm^{2}s for the (n,γ) reaction and the fast flux 4×10^{12}n/cm^{2}s for the (n,p) reactions). λ_j is the decay constant of the radionuclide j. ρ_{Bi} is the bismuth density (~9,750kg/m^3). σ_k and N_k are the capture cross section and atomic density of the isotope k. N_k can be calculated as:

$$\frac{N_k}{\rho_{Bi}} = f_k \frac{N_{av}}{A_k} w_k \qquad \textbf{Eq.G.8}$$

w_k and A_k are the weight fraction and the atomic weight of the element the nuclide k is an isotope of (e.g. for ^{62}Ni w_k and A_k are 5ppm and 58.7g/mol). f_k is the abundance of the isotope k (e.g. for ^{62}Ni f_k is 4%).

To scale the activities of the radionuclides of **Table G.II**, **Eq.G.6** can be used to yield:

$$a_{irr,j} = a^{\bullet}_{irr,j} \frac{1 - e^{-\lambda_j t_{irr}}}{1 - e^{-\lambda_j t^{\bullet}_{irr}}} \qquad \textbf{Eq.G.9}$$

where $a^{\bullet}_{irr,j}$ and $t^{\bullet}_{irr}$ are the preliminary irradiation specific activity and duration, respectively.

The results obtained from **Eq.G.6, G.7** and **Eq.G.9** are shown in **Table G.III**. After 24 hours decay time, only few radionuclides display a significant activity (>1mCi/kg$_{Bi}$): ^{24}Na, ^{197}Pt, ^{198}Au. However, they have a half-life of the order of few days or hours and they are expected to decay to negligible levels within a week or two from the end of the irradiation. As for the longer-lived radionuclides that should be considered in view of disposal of the Pb-Bi eutectic, only ^{65}Zn and ^{110m}Ag display relevant activities of the order of few μCi/kg$_{Bi}$. It should be noted that the specific activity of none of the radionuclides in **Table G.III** is comparable to that of ^{210}Po activity, which peaks at 0.32Ci/kg$_{Bi}$ approximately 25 days after the end of irradiation[5] (see **Section G.1**).

---

[5] Note that the dominant activity immediately after irradiation is ^{210}Bi, which then decays to ^{210}Po.

Table G.III. Activation by-products of the bismuth samples.

Radioisotope j	**Half-life[6]**	$a_{irr,j}$ (Ci/kg$_{Bi}$)	$a_{dec,j}$ (Ci/kg$_{Bi}$)
^{24}Na	β^-, 15h	3.0×10^{-3}	9.7×10^{-4}
^{28}Al	β^-, 2.3m	2.0×10^{-3}	0
^{38}Cl	β^-, 37m	6.3×10^{-4}	0
^{52}V	β^-, 4m	1.7×10^{-4}	0
^{56}Mn	β^-, 2.6h	8.3×10^{-4}	1.4×10^{-6}
^{66}Cu	β^-, 5m	2.2×10^{-4}	0
^{116}In	β^-, 54m	9.6×10^{-5}	9.6×10^{-13}
^{125}Sn	β^-, 9.5m	6.4×10^{-6}	0
^{197}Pt	β^-, 18.3h	1.8×10^{-2}	7.2×10^{-3}
^{198}Au	β^-, 2.7d	6.7×10^{-4}	5.2×10^{-3}
^{115m}Cd	β^-, 2.2d	1.8×10^{-5}	1.3×10^{-5}
^{65}Zn	ε, 244d	1.3×10^{-6}	1.3×10^{-6}
^{110m}Ag	β^-, 250d	4.9×10^{-5}	4.8×10^{-5}
^{63}Ni	β^-, 100a	3.8×10^{-7}	3.8×10^{-7}
^{60}Co	β^-, 5.3a	6.7×10^{-10}	6.7×10^{-10}
^{59}Fe	β^-, 44d	3.1×10^{-7}	3.1×10^{-7}

The total specific activity due to all impurities at the end of the irradiation and 24 hours after the end of the irradiation is 25 and 9mCi/kg$_{Bi}$, respectively. These specific activities are negligible when compared to the species of interest, ^{210}Po and ^{210}Bi (see **Figure G.1**).

G.3 Polonium Production

The bismuth samples to be irradiated are made of 99.99% "technical grade" Sidech bismuth in the form of spherical shots of approximately 2.8mm diameter. Five bismuth samples of

---

[6] In this table the following nomenclature is adopted: s=sec, m=min, h=hour, d=day, a=year, β^-=negative beta decay, ε=electron capture.

56±0.1g each (a total 280g) were irradiated for 12 hours in the 2ph channel of the MITR at 5×10^{13}n/cm^{2}s thermal neutron flux. The irradiation schedule is reported in **Table G.IV**.

Table G.IV. The irradiation schedule (all dates are for the year 2000).

Sample #	**Starting time**	**Ending time**	Δt (hrs)
1	5/8 @ 18:55	5/9 @ 6:55	12
2	5/9 @ 15:51	5/10 @ 3:51	12
3	5/10 @ 8:47	5/10 @ 20:47	12
4	5/10 @ 21:00	5/11 @ 9:00	12
5	5/11 @ 10:00	5/11 @ 22:00	12

At the end of the irradiation, the samples were shielded and stored in the MITR for 40 days to reduce the beta activity and the activity of the irradiation by-products. A single bismuth shot was extracted from each sample in order to measure the actual specific activity of the species of interest (^{210}Po and ^{210}Bi) by means of the MIT radiation protection office liquid scintillator (Packard TRI-CARB 2700TR). To prevent self-absorption of the alpha particles in the solid bismuth, each shot was completely dissolved in 11ml of 15.56M nitric acid. Then 1.5μl of the resulting solution were diluted in 10ml of the scintillation cocktail (Packard Ultima Gold AB). The diluting factor is then $11\times10^{-3}/1.5\times10^{-6}\approx7333$. The results of the liquid scintillator measurements (performed on 6/26/2000 @ 15:45) are reported in **Table G.V**. It can be seen that the measured specific activities are systematically about half the specific activities expected on the basis of **Eq.G.1** and **G.2** (column (h)), which can probably be attributed to deviations (in energy and intensity) from the nominal neutron flux in the irradiation channel. On the other hand the calculated and measured values of the alpha-to-beta-activity-ratio, which does not depend on the neutron flux, are in good agreement (column (g)), indicating that the measurements are reliable. The average alpha-to-beta-activity-ratio error, defined as $\frac{1}{5}\sum_{i=1}^{5}\left[\frac{(\alpha/\beta)_{meas,i}}{(\alpha/\beta)_{calc,i}}-1\right]$, is +8%.

Table G.V. Measured activity of the irradiated bismuth samples (on 6/26/2000 @ 15:45).

(a)	(b)	(c)	(d)		(e)		(f)		(g)		(h)	
Sample #	Bi shot weight (g)	Time after irradiation (days)	Liquid Scintillator Reading (Bq)		Measured Specific Activity (Ci/kg$_{Bi}$)		Calculated Specific Activity (Ci/kg$_{Bi}$)		α/β Ratio		Meas./Calc. Ratio	
			α	β	α	β	α	β	Meas.	Calc.	α	β
1	0.1702	48.4	95.1	3.87	0.110	0.0045	0.190	0.0085	24.4	22.4	0.579	0.529
2	0.1608	47.5	89.3	4.08	0.110	0.0050	0.191	0.0098	21.9	19.5	0.576	0.510
3	0.1642	46.8	86.8	4.75	0.105	0.0057	0.1915	0.0108	18.3	17.7	0.548	0.528
4	0.1513	46.3	75.8	4.23	0.099	0.0055	0.192	0.0116	17.9	16.6	0.517	0.474
5	0.1837	45.8	117.6	5.92	0.127	0.0064	0.194	0.0124	19.9	15.6	0.654	0.516

G.4 Activity of the Pb-Bi Bath

The following amounts of bismuth were extracted from the irradiated samples to prepare the Pb-Bi bath required to conduct the experiments described in **Chapter 7**.

Sample 1: 23.7g; Sample 2: 55.0g; Sample 3: 55.2g; Sample 4: 56.0g; Sample 5: 52.6g. The total alpha and beta activities (on June 26 @ 15:45) can be readily calculated from **Table G.V** (column (e)) and are equal to 26.7 and 1.3mCi, respectively. The irradiated bismuth was mixed with 32.5g of fresh bismuth and 225g of pure lead to yield 500g of Pb-Bi eutectic (Pb 45wt%-Bi 55wt%). Then the specific alpha and beta activities of the Pb-Bi mixture are 53.4 and 2.6mCi/kg$_{PbBi}$, respectively. These are also the initial conditions of the decay equations (similar to **Eq.G.1** and **G.2**, but with the neutron flux Φ=0) that enable predicting the activity of the Pb-Bi melt at any time after June 26, 2000, as illustrated in **Figure G.3**. This information is very important because it characterizes the polonium source in the experiments of **Chapter 7**.

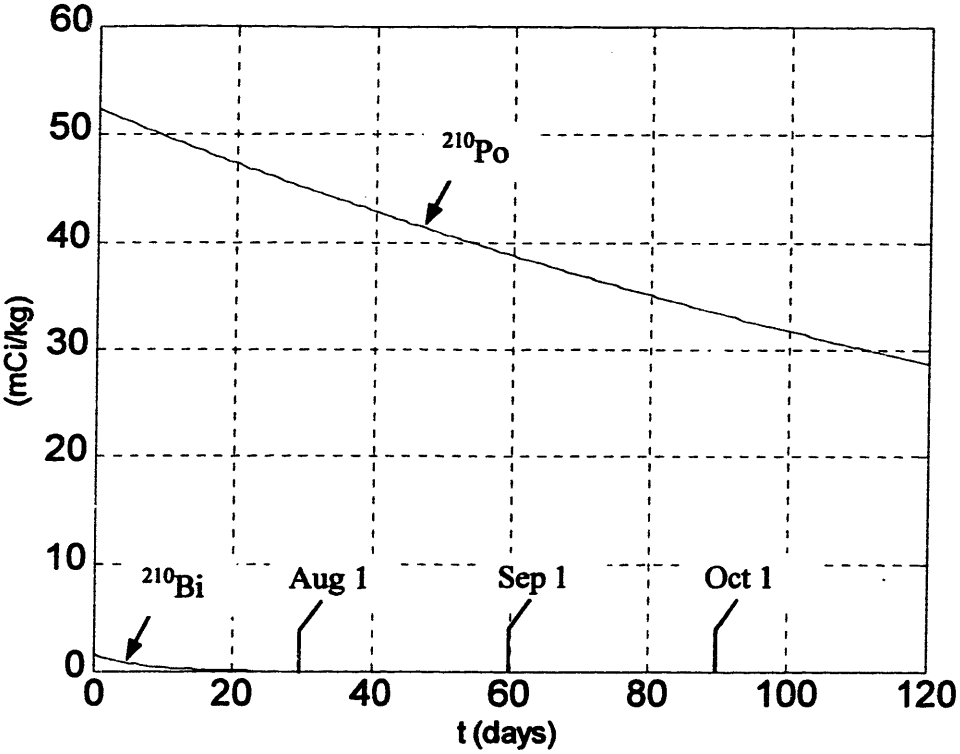

Figure G.3. Specific radioactivity of the Pb-Bi melt.

Appendix H

- EVAPORATION OF LIQUID WATER DROPLETS IN THE STEAM LINES -

In **Chapter 3** an assumption was made that when the equilibrium quality reaches unity, all the liquid water has dried out. In reality, a residual amount of liquid water (at saturation temperature) persists into the superheated region and possibly up to the chimney outlet. It is important to assess whether this liquid water evaporates in the steam lines or can impact the turbine blades. **Figure 5.10** indicates that water droplets of diameter above 100μm are removed in the steam dryer. The droplets that escape the steam dryer travel in the steam lines surrounded by superheated steam (DOS=25°C). To estimate the rate of liquid evaporation, the heat conduction equation is solved in spherical coordinates for the region around a water droplet:

$$\frac{1}{r^2}\frac{\partial}{\partial r}\left(r^2 k_g \frac{\partial}{\partial r}T(r)\right)=0 \qquad \textbf{Eq.H.1}$$

where T(r) is the temperature field, k_g is the steam thermal conductivity and r is the radial distance from the center of the droplet. The boundary conditions of **Eq.H.1** are:

$T(\infty)=T_g=T_{sat}+DOS$ **Eq.H.2**

$T(D_d/2)=T_{sat}$ **Eq.H.3**

where T_g=310°C is the superheated steam temperature, T_{sat}=286.7°C is the saturation temperature and D_d is the water droplet diameter. Integrating **Eq.H.1** twice and setting the boundary conditions of **Eq.H.2 and H.3, one finds:**

$$T_g - T_{sat} = DOS = \frac{\dot{q}}{2\pi D_d k_g} \qquad \textbf{Eq.H.4}$$

where $\dot{q}$ is the heat rate supplied to the droplet.

The conservation of mass for the droplet yields:

$$\frac{dM_d}{dt} = -\frac{\dot{q}}{h_{fg}} \qquad \textbf{Eq.H.5}$$

where h_{fg} is the vaporization enthalpy of water and the mass of the droplet, M_d, can be expressed as:

$$M_d = \frac{\pi}{6} D_d^3 \rho_f$$ **Eq.H.6**

where ρ_f is the liquid water density.

Substituting **Eq.H.6** in **H.5**, one gets:

$$\frac{\pi}{2} \rho_f D_d^2 \frac{dD_d}{dt} = -\frac{\dot{q}}{h_{fg}}$$ **Eq.H.7**

Solving **Eq.H.4** for $\dot{q}$ and substituting in **Eq.H.7**, one gets the following differential equation for the droplet diameter D_d:

$$D_d \frac{dD_d}{dt} = -\frac{4k_g DOS}{\rho_f h_{fg}}$$ **Eq.H.8**

which can be readily integrated between $t=0$ and $t=\tau_{ev}$ (i.e. the time to complete evaporation of the droplet) to yield:

$$\tau_{ev} = \frac{D_{d0}^2 \rho_f h_{fg}}{8k_g DOS}$$ **Eq.H.9**

where D_{d0} is the initial droplet diameter. At reference PBWR conditions (i.e. ρ_f=730kg/m^3, DOS=25°C, h_{fg}=1476kJ/kg, k_g=0.066W/m°C), the time to complete evaporation of the largest droplets (D_{d0}=100μm) is then about 0.8s, much shorter than the droplet travelling time through the steam lines (t_{trav}=6.8s see **Section 5.5.2.3**). Therefore, it can be concluded that the steam fed to the turbine does not carry liquid water droplets, although it does carry Pb-Bi droplets as discussed in **Chapter 5**.

Appendix I

- ALPHA COUNTING IN THE POLONIUM EXPERIMENTS -

The alpha-activity in the trapping solution of the polonium experiments was measured by means of two alternative methodologies: wet counting in a liquid scintillator and dry counting in an alpha-spectrometer after electroplating. In this appendix the two approaches are described.

I.1 Liquid Scintillation

At the end of each experimental run, two 1ml samples of the alkaline trapping solution (one sample from each trap) were collected and diluted in 10ml of scintillation cocktail (Packard Ultima Gold AB) hosted in plastic vials of 25ml capacity. The resulting solution was counted for 2 minutes with the liquid scintillator Packard TRI-CARB 2700TR located in the Radiation Protection Office of MIT. Note that the utilization of the Ultima Gold AB cocktail was recommended by Packard for optimum alpha counting performance.

In absence of a ^{210}Po standard source, the liquid scintillator was calibrated by means of a ^{241}Am source, which emits alpha-particles of energy similar to that of ^{210}Po (~5.5 vs. ~5.3MeV). For the sake of consistency, the scintillation cocktail utilized for the calibration samples was also Packard Ultima Gold AB. A 100% detecting efficiency was assumed as recommended for alpha-particles by the scintillator manufacturer.

In the energy range of interest, the radiation background was measured several times and found to be 5±2 counts per minute (cpm), i.e. 0.083±0.033Bq, which made the liquid scintillation approach unsuitable for the relatively low alpha-activities of the PbPo experimental runs. On the other hand, the samples from Trap 1 of the H_2Po runs were consistently above background and could be readily counted in the liquid scintillator.

I.2 Polonium Electroplating and Alpha-Spectrometry

This approach consists in electroplating small samples of the trapping solution on a metallic planchet and subsequently counting them in a low background alpha-spectrometer. A more detailed description follows.

At the end of each experimental run, a 100μl sample is collected from each trap. The samples are neutralized with 100μl of 0.1M $HClO_4$ and diluted in 4.5ml of ethanol[1]. The resulting solution is injected in a teflon coated vial of conical shape closed at one end by a nickel planchet (see **Figure I.1**). The vial is then mounted on the electroplating tray, the planchet is connected to the positive electrode and the negative electrode (a platinum wire) is dipped in the solution (**Figure I.2**). A 25ml DC current (at about 200V) is delivered to the system for 40 to 45 minutes to force the polonium (which is assumed to exist in solution as Po^{2-} from dissolution of PbPo or H_2Po) to deposit on the nickel planchet. The ethanol is subsequently drained, the planchet is dried with air and finally inserted in the alpha-spectrometer Canberra model Alpha-Analyst (the available energy window is 16 to 6000keV). Each sample is counted for 12 hours in the 5242 to 5342keV energy range. An example of the spectrometer output is illustrated in **Figure I.3** where the ^{210}Po peak at about 5300keV is clearly recognizable.

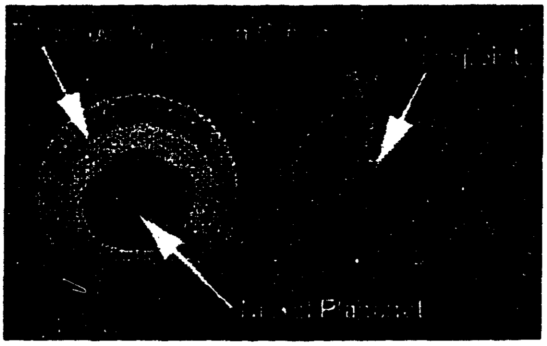

Figure I.1. The vial for polonium electroplating.

The detection efficiency of the Canberra Alpha-Analyst was measured by means of a NIST mixed standard of Pu-239, Pu-242, Am-241, and U-234 source and found to be 28%. The electroplating yield, defined as the ratio of the activity deposited on the planchet to the activity of the initial solution, was calculated applying the above described procedure to 4 samples of

---

[1] It was observed that, if not neutralized with a strong acid, the trapping solution was not soluble in ethanol.

8Bq/ml polonium reference solution and found to be 26.1±2.7%. The overall efficiency of the methodology (counts over activity in the initial 100μl of trapping solution) is then about 0.28×0.26≈0.07.

The background in the energy range of interest was measured and found to be 0 counts over 12 hours.

Because they were reused in several runs, the nickel planchets were washed with acetone prior to their use in the vials to remove deposits from the previous run.

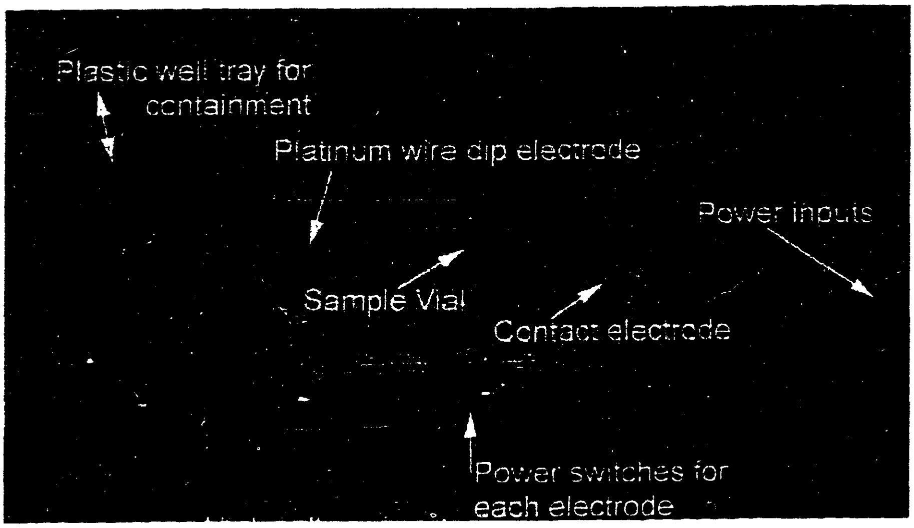

Figure I.2. Overview of the electroplating tray.

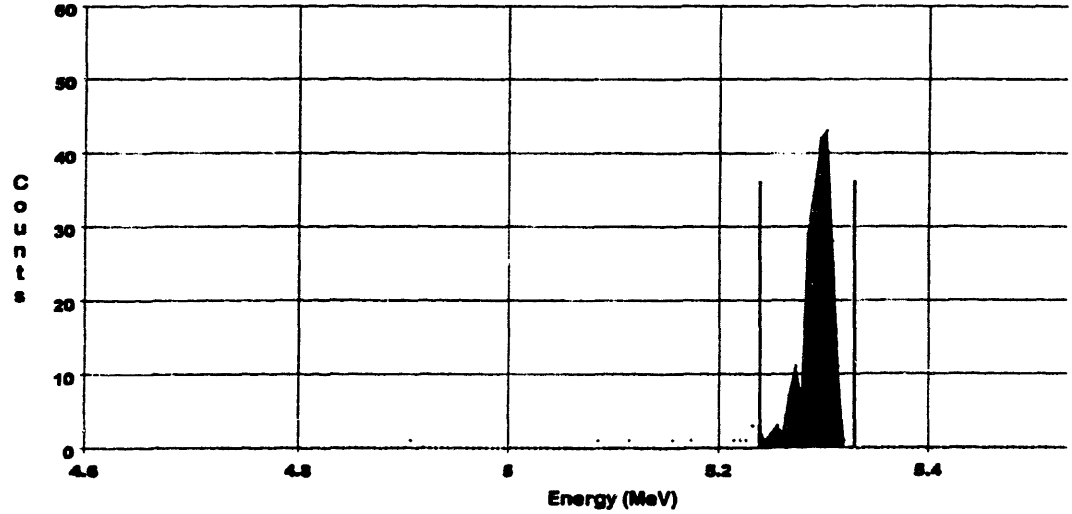

Figure I.3. A polonium peak measured by the alpha-spectrometer.

NOMENCLATURE

Symbol	Description	Units
a	Chemical activity	
	Moore model's coefficient	
a_i	Interfacial area concentration	m^2/m^3
A	Flow area	mm^2
	Atomic or molecular weight	kg/mol
	Wave amplitude	m
	Impingement area	m^2
A_C	Irradiation creep proportionality constant	$dpa^{-1}MPa^{-1}$
A_s	Spacer frontal area	mm^2
A_v	Unrestricted flow area of the assembly	mm^2
$(A/P,x,N)$	Uniform-series capital recovery factor	
B	Nuclei of ^{210}Bi	
Bi	Biot number	
c	Concentration	mol/m^3, ppm
	Speed of Sound	m/s
c, c_p	Specific heat	J/kg°C
C	Specific activity	Ci/kg
C_d	Pb-Bi concentration in steam	kg/m^3
C_D	Drag coefficient	
c_e	Capital cost of coolant	mills/kWh
C_{fm}	Rohsenow correlation coefficient	
$C_{Pb\text{-}Bi}$	Specific cost of Pb-Bi	\$/kg
cps_0	Net counts per second	1/s
C_v	Spacer form loss coefficient	
C_0	Drift-flux distribution parameter	
C_∞	Drift-flux distribution parameter in the IKR correlation	
d	Fuel pin diameter	mm
D	Fuel pin diameter	mm
	Channel equivalent diameter	m
D_{AB}	Diffusion coefficient	m^2/s
D_c	Vessel diameter	m
D_{cr}	Bubble critical diameter	m
D_e	Equivalent diameter	m
$D_{disp,cr}$	Critical bubble diameter in dispersed bubbly flow	m
$D_{disp,max}$	Maximum stable bubble diameter in dispersed bubbly flow	m
D_H	Hydraulic diameter	m
D_H^*	Bond number	

D_{max}	Maximum stable diameter of the bullet shaped-bubbles	m
D_N	Injector nozzle diameter	mm
e	Electronic charge	C
E	Young's Modulus	GPa
	Friedel correlation coefficient	
	Electrochemical potential	V
E_e	Electric field	V/m
E_n	Neutron energy	MeV
E_{pp}	Passivation potential	V
E_{tp}	Trans-passive potential	V
f	Load factor	
	Friction factor	
	Function	
	Frequency	Hz
	Isotopic fraction	
	Mass flow rate fraction to the polonium extraction system	
F	Friedel correlation coefficient	
	Transfer function	
	Cosine wave	
	Force	N
	Faraday's constant	C/mol
f_c	Volume fraction of the cap bubbles	
Fr	Froude number	
g	Gravity acceleration	m/s^2
G	Mass flux	kg/m^2s
	Transfer function	
	Gas Valve	
H	Gravitational head, chimney height	m
h	Local surface heat transfer coefficient	W/m^2K
	Heat transfer coefficient	W/m^2K
	Height	m
	Chevron spacing	mm
h^*	Normalized height	
h_{fg}	Water vaporization enthalpy	kJ/kg
h'_{fg}	Effective water vaporization enthalpy	kJ/kg
h_v	Volumetric heat transfer coefficient	W/m^3K
$\bar{h}_v$	Average volumetric heat transfer coefficient	W/m^3K
I	Interference indicator	
	Ionization potential	eV
j	Superficial velocity	m/s
j^+, j^*	Reduced superficial velocity	

k	Thermal conductivity	W/m·K
	Boltzmann constant	J/K
	Equilibrium constant	
K	Rate of energy dissipation	m^2/s^3
	Non-dimensionless coefficient of the EBLC	$kg^{0.421}/m^{0.842}s^{0.421}$
	Friedel correlation coefficient	
K_d	Coefficient of the McCoy correlation	m/s
k_e	Thermal conductivity of the irradiated fuel	W/m·K
k_{eff}	Neutron multiplication factor	
$\bar{k}_f$	Average fuel thermal conductivity	W/m·K
K_{form}	Spacer form loss coefficient	
K_0	Coagulation constant	m^3/s
Kn	Knudsen number	
Ku	Kutateladze number	
ℓ	Axial coordinate	m
	Prompt neutron lifetime	s
$\langle \ell_M \rangle$	Average eddy mixing length	m
L	Fuel active length	m
	Channel length	m
	Steam line length	m
L_b	Bubble average distance	m
L_e	Extrapolated length	m
L_f	Fuel active length	m
L_v	Vessel length	m
m	Mass	kg
	Non-dimensionless chevron length	
$\dot{m}$	Mass flow rate	kg/s
$\dot{M}$	Mass flow rate	kg/s
$m_{Pb\text{-}Bi}$	Pb-Bi mass per unit electric power	kg/kWe
n	Rohsenow correlation coefficient	
	Number of electrons	
n_b	Bubble density	$1/m^3$
N	Coolant lifetime	Yrs
	Number of nodes	
	Number of nuclei	
$\dot{N}$	Molar flow rate	mol/s
N_{av}	Avogadro's number	mol^{-1}
N_{ass}	Number of fuel assemblies	
N_d	Droplet concentration	$1/m^3$
N_{pin}	Number of fuel pin per assembly	

N_{sl}	Number of steam lines	
Nu	Nusselt number	
N_{μ}	Viscosity number	
p	Chevron wavelength	mm
P	Fuel pitch	mm
	Fuel porosity	
	Power	MW
	Pressure	MPa
	Nuclei of ^{210}Po	
	Pressure gage	
P_{ax}	Axial power peaking factor	
P_{crit}	Critical pressure	MPa
P_{loc}	Local power peaking factor	
P_{rad}	Radial power peaking factor	
Pe	Peclet number	
Pr	Prandtl number	
P/D	Pitch-to-diameter ratio	
Oh	Ohnesorge number	
q	Electric charge	C
Q'	Linear heat generation rate	kW/m
$\dot{q}$	Fuel pin power	kW
	Heat rate to the droplet	W
q''	Heat flux	kW/m^2
q_i''	Heat flux at the bubble surface	kW/m^2
$\dot{Q}$	Reactor thermal power	MWth
Q_R	Volumetric flow ratio	
r	Radius	m
	Radial coordinate	m
R	Radius	m
	Thermal resistance	m^2K/W
	Ideal gas constant	J/mol·K
$\dot{R}$	Exposure rate	R/hr
R_d	Turbine blade root to shaft axis distance	
Ra	Rayleigh number	
Re	Reynolds number	
s	Laplace transform parameter	1/s
S	Slip ratio	
	Surface	m^2
	Hardness	
S_{design}	Design stress intensity	MPa
S_m	ASME code stress intensity	MPa

S_{pm}	Primary membrane stress intensity	MPa
S_{ps}	Primary + secondary stress intensity	MPa
S_t	ASME code stress intensity	MPa
Stk	Stokes number	
t	Time	s, min, hrs, yrs
	Thickness	m
$t_{1/2}$	Half-life	s
T	Temperature	K, °C
	Transfer function	
	Thermocouple	
t_c	Vessel belt-line thickness	cm
T_{mav}	Maximum allowable vessel temperature	K, °C
T_{rHN}	Reduced homogeneous nucleation temperature	
T_{rSAT}	Reduced saturation temperature	
t_s	Vessel head thickness	cm
U^*	Shear velocity	m/s
U	Velocity	m/s
u_{wj}	Water drift-flux velocity	m/s
u_{wp}	Water/Pb-Bi relative velocity	m/s
v	Volumetric fraction	
v^+	Reduced velocity	
V	Velocity	m/s
	Valve	
$\langle V' \rangle$	Average turbulent eddy velocity	m/s
V_{core}	Core velocity	m/s
V_d	Droplet volume	m^3
V_∞	Asymptotic velocity	m/s
w	Width	m
$\dot{W}$	Electric power	MWe
	Specific heat deposition rate	W/g
W_p	Pumping power	kW
We	Weber number	
x	After-tax averaged cost of capital	
	Flow quality	
	Molar fraction	
	Spatial coordinate	m
y	Spatial coordinate	m
y^+	Reduced y-coordinate	
y_o, y_o'	Chevron wave amplitude	
z	Axial coordinate	m

Greek Letters	Description	Units
α	Linear thermal expansion coefficient	1/K
	Thermal diffusivity	m^2/s
	Void fraction	
α_{trans}	Void fraction at flow transition	
β	Volumetric thermal expansion coefficient	1/K
	Volumetric flow fraction	
	Delayed neutron fraction	
χ	Upper-limit lognormal distribution parameter	
ΔG	Free-energy variation	kJ/mol
ΔH	Enthalpy variation	kJ/mol
ΔP	Pressure drop	Pa
ΔS	Entropy variation	kJ/mol·K
ΔT	Coolant temperature rise	K, °C
$\Delta V/V$	Relative volume change	
δ	Neutron dose	dpa
	Small variation	
	Upper-limit lognormal distribution parameter	
δ_c	Clad thickness reduction	µm/yr
δ_m	Erosion rate	mm/yr
ε	Fuel pore shape factor	
	Specific energy dissipation rate	W/kg
	Efficiency	%
ε_g	Gap equivalent emissivity	
ε_I	Irradiation creep strain	
ε_γ	Gamma photon energy	MeV
Φ	Annual capital carrying factor	
	Neutron fluence	n/cm^2s
Γ_d	Droplet deposition rate	kg/m^2s
Γ_{decay}	Polonium decay rate	1/s
Γ_{extr}	Polonium extraction rate	1/s
Γ_{prod}	Polonium production rate	1/s
Γ_{rel}	Polonium release rate	1/s
η	Efficiency	%
	Spatial coordinate	m
Φ	Neutron flux	n/cm^2s
Φ_γ	Gamma flux	γ/cm^2s
λ	Mean free path	m
	Decay constant	1/s
μ	Viscosity	Pa·s
	Attenuation coefficient	1/cm
ν	Poisson's Modulus	
	Kinematic viscosity	m^2/s

θ	Phase-lag	rad
	Angle	rad
ρ	Density	kg/m^3
$\bar{\rho}_c$	Average density in the chimney	kg/m^3
ρ_{dc}	Pb-Bi density in the reactor downcomer	kg/m^3
σ	Surface tension	N/m
	Stefan-Boltzmann	W/m^{2}K^4
	Cross section	b
σ_e	Equivalent stress	MPa
τ	Marginal tax rate	
	Traveling time	s
τ^*	Reduced wall shear stress	
τ_{ev}	Evaporation time	s
τ_{ox}	Droplet oxidation time	s
τ_{rel}	Relaxation time	s
τ_w	Wall shear stress	Pa
ω	Angular frequency	rad/s
	Angular velocity	rad/s
Λ	Radioactivity	Bq
ξ	General variable	
	Spatial coordinate	m
ψ	Upper-limit lognormal distribution parameter	
ζ	Ratio of brownian to turbulent coagulation collision time	
	Logarithm of the hydrogen partial pressure	

Subscripts	Meaning
a	Air
ac	Air collector
air	Air
atm	Atmospheric
b	Bubble
	Blade
B	^{210}Bi
Bi	Bismuth
bl	Boundary layer
c	Chimney
	Clad
	Containment
	Core
	Cylinder
C	Cold
cap	Cap bubble

ci	Clad inner surface
clad	Clad
coll	Collector
	Collision
cond	Conduction
cool	Coolant
core	Core
cw	Collector wall
d	Decay heat
	Droplet
	Dowcomer
drift	Drift
e	Evaporation
	Entrained
f	Liquid water
	Final
	Fuel
Fe	Iron
Fe3O4	Iron oxide
film	Vapor film
	Oxide film
fo	Fuel outer surface
fric	Friction
fw	Feedwater
g	Steam
	Gap
H	Hot
HP	High pressure turbine
HSe	Selenium hydride ion
H2	Hydrogen
H2O	Water
H2Po	Polonium hydride
H2Se	Selenium hydride
i	Interfacial
	i^{th} term of a series
	Initial
	Inner surface
in	In
int	Intermittent
irr	Irradiation
j	j^{th} term of a series
k	k^{th} term of a series
LP	Low pressure turbine
ℓ	Liquid
m	Average

max	Maximum
min	Minimum
o	Outer surface
O	Oxygen
O2	Oxygen
out	Out
p	Primary
	Pb-Bi coolant
P	^{210}Po
Pb	Lead
PbBi	Lead-bismuth coolant
PbPo	Lead polonide
PbO	Lead oxide
Po	Polonium
s	Surface
	Saturation
	Solubility
sat	Saturated
Se	Selenium
sl	Steam line
small	Small bubble
st	Steam
	Stability
sub	Subcooled
sup	Superheated
t	Turbulence
th	Threshold
	Thermal
TP	Two-phase
tot	Total
v	Vessel
w	Water
x	x-direction
y	y-direction
z	z-direction
0	Initial
∞	Asymptotic
Acronyms	
ALI	Annual Limit of Intake
ALMR	Advanced Liquid Metal Reactor
ANL	Argonne National Laboratory
ASME	American Society of Mechanical Engineers
ATHENA	Thermal-hydraulics computer code
ATW	Accelerator Transmutation of Waste

BCC	Body Centered Cubic
B&W	Babcox & Wilcox
BNL	Brookhaven National Laboratory
BOC	Gas supplier
BOL	Beginning Of Life
BWR	Boiling Water Reactor
C	Center Subchannel
CANDU	Canadian Deuterium Uranium Reactor
CERN	Centre Europenne pour la Recherche Nuclaire
CRD	Control Rods
CVCS	Chemistry and Volume Control System
DAC	Derived Air Concentration
DBTT	Ductile-to-Brittle-Transition
DC	Direct Current
DHRS	Decay Heat Removal System
DOS	Degree of Superheat
E	Edge Subchannel
EBLC	El-Boher/Lesin Correlation
EBR-II	Experimental Breeder Reactor II
ECM	Electric Conductivity Measures
ecp	Electrochemical potential
ECP	Electric Conductivity Probe
EOL	End Of Life
EPA	Environmental Protection Agency
EPRI	Electric Power Research Institute
ER	Erosion Rate
ESBWR	European Simplified Boiling Water Reactor
FA	Fuel Assembly
FFTF	Fast Flux Test Facility
FR	Feedwater Reheater
GE	General Electric
GSSS	Gland Steam Sealing System
HEM	Homogeneous Equilibrium Model
HP	High Pressure
HPCI	High Pressure Coolant Injection
HTL	High Temperature Limit
HWP	Hot Wire Probe
IC	Inner Corner Subchannel
ICP	Plasma Spectrometer
ID	Inner Diameter
IL	Inner Length
INEEL	Idaho national Engineering and Environmental Laboratory
IFR	Integral Fast Reactor
IKR	Ishii-Kataoka-Rouhani correlation

LANL	Los Alamos National Laboratory
LFS	Low Frequency Sound
LME	Liquid Metal Embrittlement
LOCA	Loss Of Coolant Accident
LP	Low Pressure
LWR	Light Water Reactor
MA	Minor Actinides
MIT	Massachusetts Institute of Technology
MITR	MIT Reactor
MSR	Moisture Separator Reheater
NMR	Nuclear Magnetic Resonance
NR	Neutron Radiography
OC	Outer Corner Subchannel
OD	Outer Diameter
OG	OffGas System
PARR	Autoclave manufacturer
PBWR	Pb-Bi Water Reactor
PES	Polonium Extraction System
PID	Proportional Integral Derivative
PMSSM	Primary Membrane Stress Safety Margin
PSSSM	Primary + Secondary Stress Safety Margin
PWR	Pressurized Water Reactor
R&D	Research and Development
RPO	Radiation Protection Office
RVACS	Reactor Vessel Auxiliary Cooling System
SI	Systeme Internationale
SJAE	Steam Jet Air Ejector
SM	Safety Margin
SPE	Solid Particle Erosion
TRU	Transuranic
US	Ultra Sound
USDI	United States Department of Interior
vhtc	Volumetric heat transfer coefficient
XRR	X-Ray Radiography

REFERENCES

- A.Abakumov, Z.Frshova. "Vapor Tension of Polonium and Lead Polonide". Radiokhimiya. Vol.16, No.3, pp.397-401. May-June 1974.
- ABB Atom AB. "Influence of Forward-Pumped Heater Drains and Magnetic Filtration on Water Chemistry and Radiation Buildup in BWRs". EPRI NP-5864. pp.3-26, 3-27. Electric Power Research Institute. June 1988.
- S.Abdulla, X.Liu, M.Anderson, R.Bonazza, M.Corradini, D.H.Cho, A.Nguyenle. "Interfacial Transport Phenomena and Stability in Liquid-Metal/Water Systems: Year 1-Annual Progress Report". DOE-DE-FG03-99SF21928. 2000.
- E.Adamov, V.Orlov, A.Filin, V.Leonov, A.Sila-Novitski, V.Smirnov, V.Tsikunov. "The Next Generation of Fast Reactors". Nuclear Engineering and Design, vol.173, pp.143-150. 1997.
- C.B.Alcock, T.N.Belford. "Thermodynamics and Solubility of Oxygen in Liquid Metals from E.M.F. Measurements Involving Solid Electrolytes, Part I-Lead". Transactions of the Faraday Society, pp.822-835, vol.60. 1964.
- T.H.Alden, "The Solubility of Nickel and Chromium in Liquid Lead", M.S. Thesis MIT. 1957.
- R.J.Amodeo, N.M.Ghoniem. "Development of Design Equations for Ferritic Alloys in Fusion Reactors". Nuclear Engineering and Design/Fusion, vol.2, 97-110. 1985.
- B.J.Azzoppardi, G.F.Hewitt. "Maximum Drop Sizes in Gas-Liquid Flows". Multiphase Science and Technology, vol.9, pp.109-204. 1997.
- K.Bagnall. The Chemistry of Selenium, Tellurium and Polonium. Elsevier Publishing Company. 1966.
- P.J.Bania. "Advanced Alloy for Elevated Temperatures". Journal of Metals. Vol.40, no.3, pp.20-22. March 1988.
- T.H.Bauer et al. "In-Pile Measurement of the Thermal Conductivity of Irradiated Metallic Fuel". Nuclear Technology, vol.110, pp.407-421, 1993.
- R.J.Beaudry, K.S.McLeod. "The Development and Application of Welded Cobalt-Free Erosion Shields for Low Pressure Steam Turbine Blades". pp.63-68. PWR-Vol.18, Steam Turbine-Generator Development for the Power Generation Industry. ASME 1992.
- C.K.Blair, R.F.Boehm, H.R.Jacobs. "Heat Transfer Characteristics of a Direct Contact Volume Type Boiler". ASME paper 76-HT-23. 1976.
- BNL. On-line Table of Nuclides. http://necs01.dne.bnl.gov/CoN/nuchart1.html. 2000.
- C.E.Boardman, A.E.Dubberley, D.G.Carroll, M.Hui, A.W.Fanning, W.Kwant. "A Description of the S-PRISM Plant". ICONE-8168, Proceedings of ICONE-8. Baltimore, MD USA. April 2-6, 2000a.
- C.E.Boardman, A.E.Dubberley, M.Hui. "Optimizing the Size of the Super-PRISM Reactor". ICONE-8003, Proceedings of ICONE-8. Baltimore, MD USA. April 2-6, 2000b.
- G.S.Brady, H.R.Clauser. Materials Handbook. p.183. 13th Edition. McGraw-Hill, Inc. 1991.
- H.Branover. "Promising Applications of the Liquid Metal MHD Energy Conversion Technology". Proc. 24th Intersociety Energy Conversion Engineering Conf. (IECEC-89, Cat.No.89CH2781-3). Vol.2, pp.1051-1058. August 1989.
- H.Branover. "Liquid Metal MHD Research and Development in Israel". Proceedings of the 1992 Symposium on Engineering Applications of MHD. Baltimore. June-July 1992.

- H.Branover, S.Lesin, M.Tsirlin. "Heavy-Liquid-Metal Two-Phase Flow with Steam". Trans. Am. Nucl. Soc., vol.80, pp.195-196. June 1999.
- J.Buongiorno, P.Hejzlar, N.Todreas, M.Driscoll, M.Kazimi. "Actinide Transmutation by Lead-Bismuth Cooled Reactors". Report MIT-ANP-TR-065. Department of Nuclear Engineering, MIT. June 1999a.
- J.Buongiorno, M.Kazimi, N.Todreas. "Natural Circulation Potential of Pb-Bi Cooled Reactors for Power Production and Actinide Burning". Proceedings of the 1999 ANS Annual Meeting. Boston, June 1999b.
- J.Buongiorno, N.E.Todreas, M.S.Kazimi. "Thermal Design of Lead-Bismuth Cooled Reactors for Actinide Burning and Power Production". MIT Technical Report MIT-ANP-TR-066. July 1999c.
- J.Buongiorno, N.Todreas, M.Kazimi. "Void Fraction Prediction for the Pb-Bi/Water Direct Contact Nuclear Reactor". ICONE-8739. Proceedings of ICONE-8, 8th International Conference on Nuclear Engineering. Baltimore, MD USA. April 2-6, 2000.
- R.Burgel. "Coating Service Experience with Industrial Gas Turbines". Materials Science and Technology. Vol.2, no.3, pp.302-308. March 1986.
- D.V.Cameron. "Failures in Large Gas Turbines due to Liquid-Metal Embrittlement". Materials Characterization. Vol.33, no.1, pp.37-43. July 1994.
- W.R.Carson, H.K.Williams. "Method of Reducing Carry-Over and Reducing Pressure Drop through Steam Separators". EPRI NP-1607, pp.c-1,c-2. November 1980.
- L.M.Cerezo, A.L.Yarden. "MSR Upgrade Adds Megawatts at Cofrentes". Nuclear Engineering International. Vol.43, no.530, pp.38-40. September 1998.
- D.K.Cheng. Analysis of Linear Systems. pp.257-299. Addison-Wesley Publishing Company, Inc. 1959.
- Y.K.Cheung, B.Shiralkar, A.S.Rao. "Design Evolution of Natural Circulation In ESBWR". ICONE-6, San Diego, USA. May 1998.
- B.Chexal, J.Herowitz, G.Lellouche. "An Assessment of Eight Void Fraction Models". Nuclear Engineering and Design, vol.126, pp.71-88. 1991.
- B.Chexal, G.Lellouche, J.Herowitz, J.Healzer. "A Void Fraction Correlation for Generalized Applications". Progress in Nuclear Energy, vol.27, no.4, pp.255-295. 1992.
- L.Cinotti, G.Corsini. "A Proposal for Enhancing the Primary Coolant Circulation in the EA". International Workshop on Physics of Accelerator-Driven Systems for Nuclear Transmutation and Clean Energy Production. Trento, Italy. 1997.
- J.G.Collier, J.R.Thome. Convective Boiling and Condensation. pp.18-26, 137-138. 3rd Edition. Clarendon Press, 1996.
- M.Corradini, J.C.Casas. "Study of Void Fraction and Mixing of Immiscible Liquids in a Pool Configuration by an Upward Gas Flow". Nuclear Technology, vol.99. pp.104-119. July 1992.
- CRC. Handbook of Chemistry and Physics. 14-39. 80th Edition, 1999-2000.
- I.A.Diaz-Tous, A.H.Khan, T.H.McCloskey. "Solid Particle Erosion Technology Assessment". pp.247-254. PWR-Vol.26, Advances in Steam Turbine Technology for the Power Generation Industry. ASME 1994.
- G.E.Dix. "Vapor Void Fractions for Forced Convection with Subcooled Boiling at Low Flow Rates". NEDO-10491. November 1971.
- A.El-Boher, S.Lesin, Y.Unger, H.Branover. "Experimental Studies of Liquid-Metal Two-Phase Flows in Vertical Pipes". Proceedings of the 1st World Conference on Experimental

Heat Transfer, Fluid Mechanics and Thermodynamics. Dubrovnik (Yugoslavia), September 1988.

- M.M.El-Wakil. Powerplant Technology. pp.177-195, 223-230. McGraw-Hill Book Inc. 1984.
- EPA. Limiting Values of Radionuclide Intake and Air Concentration and Dose Conversion Factors for Inhalation, Submersion and Ingestion. Federal Guidance Report No.11. EPA 520/1-88-020. September 1988.
- H.Feuerstein, J.Oschinski, S.Horn. "Behavior of Po-210 in Molten Pb-17Li". Journal of Nuclear Materials 191-194, 288-291. 1992
- B.R.T.Frost, C.C.Addison, A.Chitty, G.A.Geach, P.Gross, J.A.James, G.J.Metcalfe, T.Raine, H.A.Sloman. "Liquid Metal Fuel Technology". Proceedings of the 2nd International Conference on Peaceful Uses of Atomic Energy. 7, 139. 1958.
- X.Y.Fu, S.Kim, X.Wang, M.Ishii. "Application of Four-Sensor Method for Slug and Churn-Turbulent Two-Phase Flow". Trans. Am. Nuc. Soc. vol.81, p.349. November 1999.
- X.Y.Fu, Y.Mi, M.Ishii. "Interfacial Area Measurement in a Bubbly-Slug Transition Air-Water Flow". ICONE-8327, Proceedings of ICONE-8. Baltimore, MD USA. April 2-6, 2000.
- N.A.Fuchs. The Mechanics of Aerosols. pp.80-83, 258-259, 288-290. Pergamon Press. 1964.
- M.Furuya, I.Kinoshita, Y.Nishi. "Vapor Explosions in the System of Water Droplet Impinging onto Melt Surface". Heat Transfer – Houston 1996. AIChE Symposium Series. Vol.92, n.310. pp.310-316. 1996.
- GE Nuclear Energy. "ALMR Summary Plant Design Description". 1991.
- GE. "Nuclides and Isotopes. Chart of Nuclides". Fifteenth Edition. GE Nuclear Energy, Lockheed Martin. 1996.
- GE. "The ABWR. Plant General Description". GE Nuclear Energy. April 1999.
- D.S.Gelles. "Effect of Irradiation on Ferritic Alloys and Implications for Fusion Reactor Applications". Journal of Nuclear Materials, vol.149, 192-199. 1987.
- A.H.Govan, G.F.Hewitt, D.G.Owen, T.R.Bott. "An Improved CHF Modelling Code". 2nd UK National Conference on Heat Transfer, 1, 33-48. Institute of Mechanical Engineers, London, September 1988.
- N.S.Grachev, P.L.Kirillov, P.N.Martynov. "Steam Generators with Direct Contact Between Liquid Metal and Water". Proceedings of the 9th International Topical Meeting on Nuclear Reactor Thermal Hydraulics (NURETH-9), San Francisco, October 3-8, 1999.
- E.Greenspan, H.Shimada, D.C.Wade, M.D.Carelli, L.Conway, N.W.Brown, Q.Hossain. "The Encapsulated Nuclear Reactor Heat Source Reactor Concept". ICONE-8750, Proceedings of ICONE-8. Baltimore, MD USA. April 2-6, 2000.
- N.N.Greenwood, A.Earnshaw. Chemistry of the Elements. pp.882-919. Pergamon Press. 1984.
- P.Griffith. "Steam-Water Separation". Multiphase Science and Technology. Vol.9, pp.381-437. 1997.
- B.F.Gromov, V.M.Dekusar, E.Yefimov, A.G.Kalashnikov, M.P.Leonchuk, D.Pankratov, Y.G.Pashkin, V.N.Stepanov, V.V.Chekunov, V.S.Stepanov, M.L.Kulikov, S.K.Leguenko. "Lead-Bismuth as a Perspective Coolant for Advanced Reactors and Accelerator-Based Plants". Proceedings of the International Topical Meeting on Advanced Reactors Safety. Pittsburgh, PA USA. April, 1994.
- B.F.Gromov, E.Yefimov, M.P.Leonchuk, A.A.Veremeev, V.V.Chekunov, Y.I.Orlov, D.Pankratov, V.S.Stepanov, V.T.Gorshov. "Liquid-Metal Lead-Bismuth Target for High-

Energy Protons as an Intense Source of Neutrons Controlled Systems". Atomic Energy, Vol.80, No.5, pp.378-384. 1996.

- B.F.Gromov, Y.S.Belomitcev, E.I.Yefimov, M.P.Leonchuk, P.N.Martinov, Y.I.Orlov, D.V.Pankratov, Y.G.Pashkin, G.I.Toshinsky, V.V.Chekunov, B.A.Shmatko, V.S.Stepanov. "Use of Lead-Bismuth Coolant in Nuclear Reactors and Accelerator-Driven Systems". Nuclear Engineering and Design, 173, pp.207-217. 1997.
- J.K.Hayes, S.A.Trovato, S.Misilo, J.Burger. "An Investigation and Assessment of Methods to Improve Moisture Removal and Reheating of PWR Cycle Steam". Design, Repair and Refurbishment of Steam Turbines. PWR-Vol.13. pp.115-126. ASME 1991.
- P.Hejzlar, N.E.Todreas, M.J.Driscoll. "Conceptual Design of a Large, Passive Pressure-Tube Light Water Reactor". Report MIT-ANP-TR-023. Department of Nuclear Engineering, MIT. June 1994.
- P.Hejzlar, M.J.Driscoll, M.S.Kazimi. "Neutronic Design for a Pb-Bi-Cooled Burner Fast Reactor". Trans. Am. Nucl. Soc., vol.81, pp.271-273. 1999.
- P.Hejzlar, M.J.Driscoll, M.S.Kazimi. "Conceptual Reactor Physics Design of A Lead-Bismuth-Cooled Critical Actinide Burner". Nuclear Engineering Department, MIT. Technical Report MIT-ANP-TR-069. February 2000.
- R.E.Henry, J.D.Gabor, I.O.Winsch, D.J.Quinn, E.G.Erickson, J.J.Heiberger, G.T.Goldfuss. "Large Scale Vapor Explosions". Proc. Fast Reactor Safety Meeting, Argonne IL, Conf. 740 401-P2, p.922. 1974.
- R.E.Henry, H.K.Fauske. "Energetics of Vapor Explosions". Am. Soc. Mech. Eng. Paper 75-HT-66. 1975.
- R.E.Henry, L.M.McUmber. "Vapor Explosion Potential under LWR Hypothetical Accident Conditions". Proc. Light Water React. Saf. Meet., CONF-770708, p.414-425. Sun Valley, Idaho. 1977.
- R.E.Henry. "Test Plan: Large Scale Molten Salt-Water Vapor Explosion Studies to be Conducted at Ispra, Italy". NUREG/CR-0728, ANL-79-20. Argonne National Laboratory. 1978.
- G.Hetsroni. Handbook of Multiphase Systems. pp.4-13/4-15. McGraw-Hill, 1981.
- G.Hetsroni. Handbook of Multiphase Systems. p.2-60. Hemisphere Publishing Corporation, New York. 1982.
- G.F.Hewitt, J.M.Delhaye, N.Zuber. Multiphase Science and Technology. Vol.1, p.169. 1982.
- A.L.Hines, R.N.Maddox. Mass Transfer. Fundamentals and Applications. pp.24-25. Prentice-Hall, Inc. 1985.
- N.J.Hoffman et al. "Polonium Aspects Associated with the Use of Lead-Bismuth Blankets in Fusion Applications". Fusion Technology, Vol.8, pp.1376-1384. July 1985.
- G.L Hofman, et al, "Metallic Fuels Handbook", ANL-IFR-29. Argonne National Laboratory. 1985.
- A.Hunsbedt, P.M.Magee. "Design and Performance of the PRISM Natural Convection Decay Heat Removal System," Proceedings of the International Topical Meeting on Safety of Next Generation Power Reactors, Seattle, Washington, May1-5. 1988.
- F.P.Incropera, D.P.De Witt. Fundamentals of Heat and Mass Transfer. pp.259-262, 410, 558-562, 596-600, 880, A3-A6, A-24. 3rd Edition. John Wiley & Sons, Inc. 1990.
- M.Ishii, I.Kataoka. "Drag Coefficient and Relative Velocity in Bubbly, Droplet or Particulate Flows". AIChE Journal. 25, 843. 1979.

- M.Ishii. "Interfacial Area Modeling". Multiphase Science and Technology, Vol.3. Chapter 2. 1987.
- H.R.Jacobs, S.B.Plass, A.C.Hansen. "Operational Limitations of Direct Contact Boilers for Geothermal Applications". ASME Paper 77-HT-5. 1977.
- R.N.Johnson. "Coatings for Fast Breeder Reactor Components". Thin Solid Films, 118, pp.31-47. 1984.
- D.A.Jones. Principles and Prevention of Corrosion. pp.127-128. Prentice Hall, Inc. 1992.
- B.Joseph, M.Picat, F.Barbier. "Liquid Metal Embrittlement: a State-Of-The-Art Appraisal". European Physics Journal, Applied Physics. Vol.5, no.1, pp.19-31. January 1999.
- H.Kaesche. Metallic Corrosion. p.327. National Association of Corrosion Engineers. 1985.
- M.H.Kamdar. "Treatise on Materials Science and Technology". Edited by Academic Press, 25, p.361. 1983.
- M.H.Kamdar. "Liquid Metal Embrittlement". Metals Handbook. 9th edition. Vol.11. pp.225-238. American Society for Metals, 1986.
- I.Kataoka, M.Ishii, K.Mishima. "Generation and Size Distribution of Droplets in Gas-Liquid Annular Two-Phase Flow". ANL/RAS/LWR, 81-3. 1981.
- I.Kataoka, M.Ishii, K.Mishima. "Generation and Size Distribution of Droplets in Annular Two-Phase Flow". Transactions of ASME, vol.105. June 1983.
- I.Kataoka, M.Ishii. "Mechanistic Modeling of Pool Entrainment Phenomenon". International Journal of Heat and Mass Transfer. Vol.27, no.11, pp.1999-2014. November 1984.
- I.Kataoka, M.Ishii. "Drift-Flux Model for Large Diameter Pipe and New Correlation for Pool Void Fraction". International Journal of Heat and Mass Transfer. Vol.30, No.9, pp.1927-1939. 1987.
- S.C.Kaushik, S.S.Verma, A.Chandra. "Solar-Assisted Liquid Metal MHD Power Generation: a State of the Art Study". Heat Recovery Systems & CHP. Vol.15, No.7, pp.675-689. 1995.
- K.Kawanishi, Y.Hirao, A.Tsuge. "An Experimental Study on Drift Flux Parameters for Two-Phase Flow in Vertical Round Tubes". Nuclear Engineering Design, vol.120, p.447-458. 1990.
- J.H.Keenan. Thermodynamics. p.181. MIT Press, Cambridge (MA). 1970.
- V.Keshava Iyer, A.Dasgupta, B.Venkat Rao. "Some Investigations on Flow through Chevrons of Moisture Separator and Reheater Used in Nuclear Power Plants". Proceedings of the ASME Fluids Engineering Division. FED-Vol.244. pp.381-386. ASME 1997.
- H.Kim, M.Anderson, R.Bonazza, M.Corradini, D.H.Cho. "Interfacial Transport Phenomena and Stability in Molten Metal-Water Systems". ICONE-8478, Proceedings of ICONE-8. Baltimore, MD USA. April 2-6, 2000.
- S.Kim, X.Y.Fu, X.Wang, M.Ishii. "The Local Interfacial Area Concentration Measurement in a Two-Phase Flow Using a Four-Sensor Conductivity Probe". Trans. Am. Nucl. Soc, vol.79, p.356. 1998.
- I.Kinoshita, Y.Nishi, M.Furuya. "Fundamental Heat Transfer Characteristics of Direct Contact Heat Exchanger between Melting Alloy and Water". Experimental Heat Transfer, Fluid Mechanics and Thermodynamics 1997. M.Giot, F.Myinger, G.P.Celata (editors). Edizioni ETS, pp.2071-2077. 1997.
- I.Kinoshita, Y.Nishi, M.Furuya. "On Applicability of Direct Contact Heat Transfer Steam Generators for LMFBRs". ICONE-8769, Proceedings of ICONE-8. Baltimore, MD USA. April 2-6, 2000.

- G.Kocamustafaogullari, S.R.Smits, J.Razi. “Maximum and Mean Droplet Sizes in Annular Two-Phase Flow”. Int. J. Heat Mass Transfer. Vol.37, no.6, pp.955-965. 1994.
- G.Kocamustafaogullari, M.Ishii. “Foundation of the Interfacial Area Transport Equation and its Closure Relation”. Int. J. Heat Mass Transfer. Vol.38, pp.481. 1995.
- L.Kovach. NUCON International, Inc. Personal communication to Jacopo Buongiorno. August 18, 2000.
- S.E.Kuehn. “Steam Turbine Technology Keeps Pace with Demands”. pp.18-24. Power Engineering. March 1993.
- S.S.Kutateladze, V.M.Borishanskii, I.I.Novikov, O.S.Fedinskii. Liquid-Metal Heat Transfer Media. Consultants Bureau, Inc., New York, Chapman and Hall, Ltd., London, 1959. Supplement No.2 to the journal “Atomnaia Energia”, Atomic Press, Moscow, 1958.
- LANL. “A Roadmap for Developing ATW Technology. Target-Blanket Technology”. LA-UR-99-3022. Los Alamos National Laboratory. 1999a.
- LANL. “A Roadmap for Developing Accelerator Transmutation of Waste (ATW) Technology”. DOE/RW-051. Los Alamos National Laboratory. 1999b.
- A.H.Lefebvre. Atomization and Sprays. pp.29-36. Hemisphere Publishing Company. 1989.
- J.R.Lewis. Handbook of Stainless Steels. Chapter 19. McGraw-Hill Book Company. 1977.
- N.Li, E.Yefimov, D.Pankratov. “Polonium Release from an ATW Burner System with Liquid Metal Lead-Bismuth Coolant”. LA-UR-98-1995. Los Alamos National Laboratory. April 1998.
- N.Li. “Active Control of Oxygen in Molten Lead-Bismuth Eutectic Systems to Prevent Steel Corrosion and Coolant Contamination”. LA-UR-99-4696. Los Alamos National Laboratory. 1999.
- J.H.Lienhard. A Heat Transfer Handbook. pp.410-412. Prentice Hall, In. 1981.
- E.P.Loewen, C.B.Davis, P.E.MacDonald. “A Technique for Dynamic Corrosion Testing in Liquid Lead Alloys”. ICONE-8245, Proceedings of ICONE-8. Baltimore, MD USA. April 2-6, 2000.
- A.V.Lopatkin, V.V.Orlov. “Fuel Cycle of BREST-1200 with Non-Proliferation of Plutonium and Equivalent Disposal of Radioactive Waste”. Proceedings of Global 99, International Conference on Future Nuclear Systems. Jackson Hole, WY. September 1999.
- J.C.B.Lopes, A. E.Dukler. "Droplet Entrainment in Vertical Annular Flow and its Contribution to Momentum Transfer," AIChE J. vol.32, pp. 1500-1515. 1986
- S.P.Lynch. “Metal-Induce Embrittlement”. Materials Characterization. Vol.28, no.4, pp.279-289. June 1992.
- R.N.Lyon. Liquid-Metals Handbook. Navy Press, June 1952.
- R.C.Marshall. “Carryunder in Gravity Separation of Air-Water Mixtures”. ASME 64-WA/HT-38. 1964.
- R.C.Martinelli. “Heat Transfer to Molten Metals”. Trans. ASME 69:947, 1947.
- K.Matsumura, H.Nariai. “The Occurrence of Spontaneous Vapor Explosions”. Proc. 4th ASME/JSME Joint Conference on Nuclear Engineering (ICONE-4). Vol.1, Pt.A, pp.325-332. 1996.
- D.D.McCoy, T.J.Hanratty. “Rate of Deposition of Droplets in Annular Two-Phase Flow”. International Journal of Multiphase Flow, 3, pp.319-331. 1977.
- J.McDonald, A.Dean. Electrostatic Precipitator Manual. pp.7-18. Noyes Data Corporation. 1982.

- K.Mishima, M.Ishii. "Flow Regime Transition Criteria for Upward Two-Phase Flow in Vertical Tubes". Int.J.Heat Mass Transfer. Vol.27, No.5, pp.723-737. 1984.
- MIT/INEEL. "Design of Pb-Bi Cooled Reactors for Actinide Burning and for Low Cost Electricity". MIT Nuclear Engineering Department. MIT-ANP-TR-072. June 2000.
- M.J.Moore, C.H.Sieverding. Two-Phase Steam Flow in Turbines and Separators. pp.11-19, 52-53, 282-288, 317-344. McGraw-Hill Inc. 1976.
- R.A.Mugele, H.D.Evans. "Droplet Size Distribution in Sprays". Ind. Eng. Chem., Vol.43, pp.1317. 1951.
- M.Nagase, Y.Saito, T.Nakao. "Development of Reactor Internals for Next Generation BWR". ICONE-4, vol.2, pp.511-515. ASME 1996.
- S.Nakamura, Y.Fukuy, Y.Kojima, M.Siga, S.Yamaguchi. "Development of Materials and Coating Processes for High Temperature Heavy Duty Gas Turbines". ASME Paper. 90-GT-79. 1990.
- T.Nakao, M.Nagase, G.Aoyama, M.Murasc. "Development of Simplified Wave-Type Vane in BWR Steam Dryer and Assessment of Vane Droplet Removal". Journal of Nuclear Science and Technology. Vol.36, no.5, pp.424-432. May 1999.
- Y.Nishi, I.Kinoshita, M.Furuya, N.Takenaka, M.Matsubayashi. "Visualization of Direct Contact Heat Transfer between Molten Alloy and Water by Neutron Radiography". Proceedings of the 11th International Heat Transfer Conference. Kyongju, South Korea. 1998.
- S.Oglesby, G.B.Nichols. Electrostatic Precipitation. pp.15-30. Marcel Dekker, Inc. 1978.
- Y.Orlov, E.Yefimov, J,Stbbins, M.Bjornberg, X.He, W.Gregory, N.Li. "LANL/IPPE/EDO-GP Collaboration Programs on Liquid Lead-Bismuth technology". Notes of the MIT ATW Technical Review, January 15-16, 1998.
- M.D.Panasenko, Y.V.Koslov. Teploenergetika, no.8, pp.69. 1962.
- D.Pankratov, B.F.Gromov, M.A.Solodjankin, E.I.Yefimov, V.N.Stepanov, G.I.Toshinsky, V.V.Kalchenko, V.V.Stekolnikov, V.S.Stepanov, L.N.Moskvin, O.G.Panov, Y.A.Prokhorov. "The Experience in Handling Lead-Bismuth Coolant Contaminated by Polonium-210". Transactions of the ANS. Vol.67, Supplement No.1. p.256. September 1992.
- C.S.Park, G.P.Sharp-Bette. Advanced Engineering Economics. p.48. John Wiley & Sons. 1990.
- K.R.Parker, A.Sanyal. "Effective Capture of Respirable Sized Particulates Using Electrostatic Precipitator Technology". Proceedings of the American Power Conference. Vol.61(I), pp.174-179. 1999.
- Parr. Personal communication to Jacopo Buongiorno. April 12, 2000.
- D.Pearson. "A Summary of the MEL Experiment Data on Erosion". Marchwood Engineering Laboratories, CEGB, RDD/M/MIB, Job No.30023. November 1964.
- M.Petrick. "A Study of Carry-Under Phenomena in Vapor Liquid Separation". AIChE Journal. Vol.9, no.2. pp.253-260. March, 1963.
- A.L.Pitner, R.B.Baker. "Metal Fuels Test Program in the FFTF". Journal of Nuclear Materials, vol.204, p.124, 1993.
- W.D.Pouchot, R.E.Kothman, W.K.Fentress, F.J.Heyman, T.C.Varljen, J.W.H.Chi, J.D.Milton, C.M.Glassmire, J.A.Kyslinger, K.A.Desai. "Basic Investigation of Turbine Erosion Phenomena". NASA CR-1830. November 1971.
- M.Pourbaix. Atlas of Electrochemical Equilibria in Aqueous Solutions. pp.554-576. Pergamon Press. 1966.

- J.M.Quets, P.N.Walsh, V.Srinivasan, R.C.Tucker. "High Temperature Erosion and Fatigue Resistanceo Of a Detonation Gun Chromium Carbide Coating for Steam Turbines". pp.255-260. PWR-Vol.26, Advances in Steam Turbine Technology for the Power Generation Industry. ASME 1994.
- N.A.Radovich, R.Mossis. "The Transition from Two-Phase Bubble Flow to Slug Flow". Report No.7-7673-22, Dept. of Mech. Eng., MIT. 1962.
- A.S.Rao, Y.K.Cheung, M.Huggenberger, G.Yadigaroglu. "Performance Improvements in BWR's Using Passive Features". ICONE-7393. Proceedings of ICONE-7, 7th International Conference on Nuclear Engineering. Tokio, Japan. April 19-23, 1999.
- R.Reid. "Rapid Phase Transitions from Liquid to Vapor". Advances in Chemical Engineering, vol.12, pp.105-208. Academic Press, 1983.
- S.Rouhani. "Modified Correlations for Void and Pressure Drop". AB Atomenergi, Sweden, Internal Report AE-RTC 841, March 1969.
- S.Rouhani. "TRAC-BF1 Models and Correlations". NUREG/CR-4391, EGG-2680, INEEL. August 1992.
- C.Rubbia. "A High Gain Energy Amplifier Operated with Fast Neutrons". 1994 International Conference on Accelerator-Driven Transmutation Technologies and Applications. Las Vegas, NV. American Institute of Physics Conference Proceedings 346. AIP Press. 1994.
- Ruiz, Lin, Robinson, Henshaw, Pathania. "Model Calculations of Water Radiolysis and Electrochemical Potentials in BWR Primary Coolant". Proc. Water Chemistry of Nuclear Reactor Systems, Vol.2, p.141, BNES. London 1992.
- Y.Saito et al. "Two-Phase Flow Analyses in BWR Separators and Dryers". Proc. 3rd ASME/JSME Nucl. Eng. Joint Conference (ICONE-3), vol.1, pp.155-160. 1995.
- T.Sakamoto, S.Nagao, T.Tanuma. "Investigation of Wet Steam Flow for Steam Turbine Repowering". pp.33-40. PWR-Vol.18, Steam Turbine-Generator Development for the Power Generation Industry. ASME 1992.
- G.V.Samsonov. The Oxide Handbook. pp.129-141. IFI/Plenum, New York. 1982.
- C.Sawyer. GE Nuclear Energy. Personal communication to Jacopo Buongiorno. July 7, 1999.
- S.R.Seagle. "Titanium/Titanium Alloys". Advanced Materials & Processes. Vol.137, no.1, pp.29, 90. January 1990.
- O.L.Schipakhin, N.B.Borisov, S.L.Churkin. "The Polonium-210 Problem in Thermonuclear Reactor". Transactions of the ANS. Vol.67, Supplement No.1. p.405. September 1992.
- A.Shieh. "Addition of Lead-Bismuth Eutectic as a Working Fluid in the ATHENA Code". Idaho National Engineering and Environmental Laboratory. Software Design and Implementation Document. August 1999.
- Y.Shimizu, Y.H.Mori. "Evaporation of Single Liquid Drops in an Immiscible Liquid At Elevated Pressures: Experimental Study with N-Pentane and R113 Drops in Water". Int.J.Heat Mass Transfer. Vol.31, No.9, pp.1843-1851. 1988.
- B.Shiralkar, Y.K.Cheung, A.S.Rao. "Design Evolution of Natural Circulation in ESBWR". ICONE-6, San Diego, USA. May 1998.
- S.Sideman, Y.Taitel. "Direct Contact Heat Transfer with Change of Phase: Evaporation of Drops in an Immiscible Liquid Medium". Int. J. Heat Mass Transfer, vol.7, pp.1273-1289. 1964.
- S.Sideman, Y.Gat. "Direct Contact Heat Transfer with Change of Phase: Spray-Column Studies of a Three-Phase Heat Exchanger". AIChE J., vol.12, pp.296-303. 1966.

- M.Sittig. Particulates and Fine Dust. Processes and Equipment. pp.496-501. Noyes Data Corporation. 1977.
- R.C.Smith, W.M.Rohsenow, M.S.Kazimi. "Volumetric Heat-Transfer Coefficients for Direct-Contact Evaporation". Journal of Heat Transfer. Vol.104, pp.264-270. May 1982.
- Y.L.Sorokin, I.N.Popchenkov, V.S.Burkat. Chem. Petro. Eng., no.12, p.781. 1966.
- B.W.Spencer, R.N.Hill, D.C.Wade, D.J.Hill, J.J.Sienicki, H.S.Khalil, J.E.Cahalan, M.T.Farmer, V.A.Maroni, L.Leibowitz. "An Advanced Modular HLMC Reactor Concept Featuring Economy, Safety and Proliferation Resistance". ICONE-8145, Proceedings of ICONE-8. Baltimore, MD USA. April 2-6, 2000a.
- B.W.Spencer. "The Rush to Heavy Liquid Metal Reactor Coolants – Gimmick or Reasoned". ICONE-8729, Proceedings of ICONE-8. Baltimore, MD USA. April 2-6, 2000b.
- K.Sumathi, K.Balasubramanian. "Electronic States and Potential Energy Surfaces of H_2Te, H_2Po and their Positive Ions". J.Chem.Phys. 92(11), pp.6604-6619. 1 June 1990.
- Y.Taitel, D.Bornea, A.E.Dukler. "Modelling Flow Pattern Transitions for Steady Upward Gas-Liquid Flow in Vertical Tubes". AIChE Journal. Vol.26, No.3, pp.345-354. 1980.
- M.Takahashi, N.Sawada, H.Sekimoto, M.Kotaka, T.Yano, S.Uchida, T.Tkahashi, K.Hata, T.Suzuki. "Design and Construction of Pb-Bi Corrosion Test Loop and Test Plan". ICONE-8507, Proceedings of ICONE-8. Baltimore, MD USA. April 2-6, 2000.
- Y.S.Tang, R.D.Coffield, R.A.Markley. Thermal Analysis of Liquid-Metal Fast Breeder Reactors. p.201. American Nuclear Society. 1978.
- F.Todd. Hope Creek Nuclear Power Station, PSEG. Personal communication to Jacopo Buongiorno. March 18, 2000.
- N.E.Todreas, M.S.Kazimi. Nuclear Systems I. Thermal Hydraulic Fundamentals. pp.4-5, 31, 358, 379, 386-390, 450-452, 467-474, 476-478, 488-490. Hemisphere Publishing Corporation. 1990.
- The Toledo Edison Company. "Davis-Besse Nuclear Power Station. PSAR". Vol.1. 1970.
- H.Tsai. "Performance of Metal Fuel Elements in an Operational Overpower Transient". Trans. Am. Nucl. Soc., vol.70, p.289, June 1994.
- M.Tsirlin, Sh.Lesin, H.Branover. "Some Aspects of Structural Materials Compatibility with Liquid Lead-Containing Coolants". Trans. Am. Nucl. Soc., vol.80, pp.196-197. June 1999.
- K.Tsubouchi, N.Yasugahira, S.Yoshida, R.Kaneko, T.Sato. "An Evaluation of Water Droplet Erosion for Advanced Large Steam Turbine". pp.245-251. PWR-Vol.10, Advances in Steam Turbine Technology for Power Generation. ASME 1990.
- USDI. http://minerals.usgs.gov/minerals/. U.S. Department of the Interior. U.S. Geological Survey. Fourth Quarter Report 1998.
- P.Von Boeckh, J.Hutton, J.Patrick. "Moisture Separator and Cycle Efficiency Improvements by Installing Moisture Preseparators". ASME Paper 84-JPGC-Pwr-30. 1984.
- G.B.Wallis. One-Dimensional Two-phase Flow. pp.253-255, 260-262, 345-346. Mc-Graw-Hill Book Company. 1969.
- P.N.Walsh, J.M.Quets, R.C.Tucker. "The Effects of Erodent Particle Size and Composition on the Erosion of Chromium Carbide Based Coatings". pp.261-265. PWR-Vol.26, Advances in Steam Turbine Technology for the Power Generation Industry. ASME 1994.
- L.E.Weaver. System Analysis of Nuclear Reactor Dynamics. pp.34-59. Rowman and Littlefield, Inc. 1963.

- K.D.Weaver, J.S.Herring, P.E.MacDonald. "Performance Modeling of Metallic and Nitride Fuels in Advanced Lead-Bismuth Cooled Fast Reactors". ICONE-8014, Proceedings of ICONE-8. Baltimore, MD USA. April 2-6, 2000.
- J.R.Weeks and A. J. Romano, "Liquidus Curves and Corrosion of Fe, Ti, Zr and Cu in Liquid Bi-Pb Alloys", Corrosion, 25, pp. 131-136. 1969.
- J.R.Weeks. "Lead, Bismuth, Tin and their Alloys as Nuclear Coolants". Nuclear Engineering and Design, 15, pp.363-372. 1971.
- J.R.Weeks. "Compatibility of Structural Materials with Liquid Lead-Bismuth and Mercury". Materials for Spallation Neutron Sources, pp.77-81. Edited by M.S.Wechsler, L.K.Mansur. C.L.Snead, W.F.Sommer. The Minerals, Metals & Materials Society. 1998.
- A.R.C.Westwood, C.M.Preece, M.H.Kamdar. "Adsorption-Induced Brittle Fracture in Liquid Environments". Edited by H.Leibowitz, Academic Press, 3, pp.589. 1971.
- C.Williams, R.T.Schomer. "Liquid Metal Fuel Reactor and LMFBR-I". Proceedings of the 2nd International Conference on Peaceful Uses of Atomic Energy. 10, 487. 1958.
- J.F.Wilson, R.J.Grenda, R.H.Klumb, W.E.Littleton, W.C.Meyer, H.W.Yent. ACNP 65003, 1965.
- W.Witteman, A.Giorgi, D.Vier. "The Preparation and Identification of Some Intermetallic Compounds of Polonium". J.Phys.Chem. Vol.64, No.4, pp.434-440. 1960.
- A.L.Yarden, T.W.Clement, H.W.Kang. "Kori Gains 30 MWe from MSR Reconstruction". Nuclear Engineering International. Vol.42, no.515, pp.35-39. June 1997.
- E.Yefimov, D.Pankratov, S.Ignatiev. "Removal and Containment of High-Level Radioactive Polonium from Liquid Lead-Bismuth Coolant". Materials Research Society Symposium Proceedings. Vol.506, p.679-686. 1998.
- K.Yoshida, C.Masuzawa, M.Kishimoto. "Development of Measuring Techniques and Countermeasure on Wet Steam for Steam Turbine". pp.237-244. PWR-Vol.10, Advances in Steam Turbine Technology for Power Generation. ASME 1990.
- S.Zaki, H.Sekimoto. "Safety Aspect of Long-Life Small Safe Power Reactors". Progress in Nuclear Energy, vol.22, no.11, pp.711-722, 1995.
- A.V.Zhukov, A.P.Sorokin, V.P.Smirnov, M.V.Papandin. "Heat Transfer in Lead-Cooled Fast Reactor (LCFR)". Proceedings of the 1994 International Topical Meeting on Advanced Reactors Safety, Pittsburgh, USA. 1994.
- A.V.Zrodnikov, V.I.Chitaykin, B.F.Gromov, G.I.Toshinsky, U.G.Dragunov, V.S.Stepanov. "Applications of Reactors Cooled by Lead-Bismuth Alloy in Nuclear Power Energy". Proceedings of Global '99: International Conference on Future Nuclear Systems. Jackson Hole, WY USA. August-September 1999.
- N.Zuber, J.A.Findlay. "Average Volumetric Concentration in Two-Phase Flow Systems". Journal of Heat Transfer. Vol.87. pp.453-468. 1965.